Transactions of the ASME®

Journal of Fluids Engineering

Published Quarterly by The American Society of Mechanical Engineers

VOLUME 122 • NUMBER 4 • DECEMBER 2000

Transactions of the ASME, Journal of Fluids Engineering (ISSN 0098-2202) is published quarterly (Mar., June, Sept., Dec.) by The American Society of Mechanical Engineers, Three Park Avenue, New York, NY 10016. Periodicals postage paid at New York, NY and additional mailing offices.
POSTMASTER: Send address changes to Transactions of the ASME, Journal of Fluids Engineering, c/o THE AMERICAN SOCIETY OF MECHANICAL ENGINEERS, 22 Law Drive, Box 2300, Fairfield, NJ 07007-2300.
CHANGES OF ADDRESS must be received at Society headquarters seven weeks before they are to be effective. Please send old label and new address.

INDEXED by Applied Mechanics Reviews and Engineering Information, Inc. Canadian Goods & Services Tax Registration #126148048.

649 Editorial

TECHNICAL PAPERS

650 Geometric Parameters Influencing Flow in an Axisymmetric IC Engine Inlet Port Assembly: Part I—Valve Flow Characteristics
Andreas Maier, Terry H. Sheldrake, and Dennis Wilcock

658 Geometric Parameters Influencing Flow in an Axisymmetric IC Engine Inlet Port Assembly: Part II—Parametric Variation of Valve Geometry
Andreas Maier, Terry H. Sheldrake, and Dennis Wilcock

666 Measurements and Predictions of a Highly Turbulent Flowfield in a Turbine Vane Passage
R. W. Radomsky and K. A. Thole

677 Investigation of the Flopping Regime of Two-, Three-, and Four-Plate Arrays
D. W. Guillaume and J. C. LaRue

683 Improving Startup Behavior of Fluid Couplings Through Modification of Runner Geometry: Part I—Fluid Flow Analysis and Proposed Improvement
H. Huitenga and N. K. Mitra

689 Improving Startup Behavior of Fluid Couplings Through Modification of Runner Geometry: Part II—Modification of Runner Geometry and Its Effects on the Operation Characteristics
H. Huitenga and N. K. Mitra

694 Large Eddy Simulation of a Smooth Circular Cylinder Oscillating Normal to a Uniform Flow
Mustafa Tutar and Arne E. Holdø

703 Numerical Prediction of Flow Fields Around Circular Cylinders: Forced Motion and Dynamic Response Cases
S. Lu and Ö. F. Turan

715 Image Singularity System to Represent Two Circular Cylinders of Different Diameter
D. K. Lee

720 DSMC Analysis of Rarefied Gas Flow Over a Rectangular Cylinder at All Knudsen Numbers
Chin-Hsiang Cheng and Feng-Liang Liao

730 Discharge Coefficients of Critical Venturi Nozzles for CO_2 and SF_6
Shin-ichi Nakao and Masaki Takamoto

735 Numerical Simulation on the Flow Structure Around the Injection Nozzles for Pneumatic Dimensional Control Systems
S. C. M. Yu, H. J. Poh, and C. P. Tso

743 Turbulent Transient Gas Injections
P. Ouellette and P. G. Hill

754 Numerical Study of the Three-Dimensional Structure of a Bubble Plume
Y. Murai and Y. Matsumoto

761 Two-Phase Flow Pressure Drop in Right Angle Bends
Edward Graf and Sudhakar Neti

769 Pressure Gradient and Choking Velocity for Adiabatic Pipe Flow of a Homogeneous Steam-Water-Solids Mixture
F. Fluerenbrock

(Contents continued on inside back cover)

(**Contents continued**)

Journal of Fluids Engineering **Volume 122, Number 4** **DECEMBER 2000**

774 Thin-Film Flow at Moderate Reynolds Number
Kenneth J. Ruschak and Steven J. Weinstein

779 Rise Height for Negatively Buoyant Fountains and Depth of Penetration for Negatively Buoyant Jets Impinging an Interface
P. D. Friedman and J. Katz

783 A Computational Study of Bubble-Structure Interaction
Philemon C. Chan, Kit K. Kan, and James H. Stuhmiller

791 Three-Dimensional Unsteady Simulation of Cavitating Flows in Injector Passages
R. A. Bunnell and S. D. Heister

798 A Linear Stability Analysis of Cavitation in a Finite Blade Count Impeller
Hironori Horiguchi, Satoshi Watanabe, and Yoshinobu Tsujimoto

806 Optical Observation of the Supercavitation Induced by High-Speed Water Entry
Hong-Hui Shi, Motoyuki Itoh, and Takuya Takami

811 PIV Technique for the Simultaneous Measurement of Dilute Two-Phase Flows
K. T. Kiger and C. Pan

819 A Conductance Based Solids Concentration Sensor for Large Diameter Slurry Pipelines
James F. Klausner, Feng Fu, and Renwei Mei

825 Optimization of a Deepening Load Acting on a Flexible Cable Towed Under Water
M. Gutman

830 Turbulent Mixing, Viscosity, Diffusion, and Gravity in the Formation of Cosmological Structures: The Fluid Mechanics of Dark Matter
C. H. Gibson

836 Author Index

841 Fluids Engineering Calendar

ANNOUNCEMENTS

844 First Call for Symposium Papers—2002 FED Conference

850 Final Call for Forum Papers—2001 Congress

854 Announcement—ASME Freeman Scholar Program

855 Statement of Numerical Accuracy

855 Statement of Experimental Uncertainty

855 Access to the Electronic JFE

855 Submission of Papers

Journal of Fluids Engineering

Editorial

This volume contains 26 papers covering a wide range of flow problems, analysis and simulation methods and measurement techniques. Significant fraction of these papers deal with flows in complex geometries. Maier et al., in two papers, focus on the parameters influencing the flow at the inlet to an internal combustion engine. They measure the discharge coefficient and examine the occurrence of separation, reattachment, and heat transfer in the boundary layer on the valve seat using liquid crystal. The flow seems to be highly sensitive to small geometric changes. Consequently, in the second paper they systematically examine the effects of fillet radius, cone and seat angles. The latter two have significant effects on the valve performance. Radomsky and Thole report on 3-D velocity measurements and computations of the flow in a turbine vane passage. They show that substantial changes to the turbulent kinetic energy occur along the passage, and that these changes depend on the initial turbulence levels. Their RANS simulations are performed using different stress models with significant variations in results. Guillaume and LaRue measure the pressure and velocity spectra in the wakes of multiple plates aligned normal to the flow. The wakes vary between stable modes, flopping and quasi-stable behavior, depending on the ratio of plate spacing to plate thickness. A pair of papers by Huitenga and Mitra focus on improvements to the startup behavior of fluid coupling through modifications to runner geometry. Numerical simulations are used as guidance for determining the required modifications.

Several papers deal with the flow around a single or multiple cylinders. Tutar and Holdø use Large Eddy Simulations (LES) with a near-wall model to study transitional flows around oscillating cylinders, and compare the results to experimental data. Lu and Turan examine the flow forced, deformable oscillating cylinder, combining structural equations and Navier Stokes equations. Their results show reasonable agreement with experimental data. For cases with coupled torsional and transverse oscillation their results indicate that lock-in depends on the relative phase between them. Lee introduces a singularity system to represent two circular cylinders that can be truncated for numerical simulations. A criterion for the number of singularities is obtained and emphasis is put on how to deal with discrete vortex model for the boundary layer. Finally, Cheng and Liao study the flow of rarefied gas over a rectangular square cylinder. The main focus is on the transition between continuous flow (low Kn) and molecular flow (high Kn). The analysis involves use of a Monte-Carlo method for predicting density, velocity, temperature, pressure, skin-friction and heat transfer coefficient. Results for different Mach and Knudsen numbers are presented and compared to available data.

Jet and nozzle flows are the subject of three papers. Discharge coefficients of venturi nozzles for CO_2 and SF_6 are studied by Nakao and Takamoto. The measured coefficients are 2% higher than estimates based on isentropic flows, and the difference cannot be accounted for by real gas effects. For CO_2 the deviations can be explained assuming non-equilibrium flow, whereas for the SF_6, the reasons are not clear. Yu et al. perform numerical simulations of air flows at the exit of a nozzle and impinging on a flat plate in a pneumatic dimensional control system. Their objective is to optimize the nozzle efficiency, which they achieve with a divergent nozzle design. Ouellette and Hill use RANS with κ-ε stress model to simulate transient gaseous jets as natural gas is injected into a diesel engine. The model reproduces the dependence of penetration on momentum, time and density but accuracy is improved when one of the κ-ε coefficients is modified. Simulations are then used to determine the effects of turbulence, injection duration and wall contact.

A variety of multiphase flow problems are also being addressed. Murai and Matsumoto perform numerical simulations of the behavior and microscale characteristics of a 3-D bubble plume and the surrounding flow. A Lagrangian-Eulerian model is formulated and spatial structures, such as swaying and swirling, are identified. The results agree with experimental observations. Numerical predictions of gas-liquid flow in a right-angle bend, using Eulerian-Eulerian, two-fluid model is the subject of a paper by Graf and Neti. They show that centrifugal forces cause stratification — large void fraction in the inner part of the bend. Their predictions of pressure drop agree with measured data. Fluerenbrock derives a theory and equations for a one dimensional, three-phase flow to determine pressure gradients, choking and sonic velocity of a steam-water-solids mixture in a pipe. These mixtures are formed while processing ore slurries at elevated temperatures and pressures. He concludes that quasi choking may occur when the flow changes from sub-cooled to flashing conditions. Viscous, laminar, gravitationally driven thin film flows at moderate Reynolds numbers are modeled by Ruschak and Weinstein. They show that including a boundary layer in the model has little effect on the thickness profile and that the results are similar to profiles obtained using finite-element solutions of the Navier-Stokes Equations. However, the success of the model depends on the flow geometry. Finally, a paper by Friedman and Katz examines the rise height of negatively buoyant fountains and penetration depth of negatively buoyant jets impinging on interfaces. Using data from a wide range of systems, including air jets impacting on liquids as well as miscible and immiscible liquid-liquid systems, they show that the penetration depth is only a function of the Richardson number scaled with the jet spreading factor. For turbulent jets, the Reynolds and Webber numbers do not affect the penetration depth.

Cavitation and explosions are being investigated in several papers. Chan et al. study the interaction between explosion bubbles and structures (a disk and a sphere). They show that the shape of the structure affects the pressure loading, jetting and collapse phenomena, whereas the impact of gravitation depends on the jet direction. Bunnel and Heister use 3-D steady viscous simulations of the flow in a plain-orifice pressure atomizer fed by a manifold with a cross-flow. Their geometry replicates conditions in liquid rocket and diesel engine injectors. Both cavitating and non-cavitating conditions are considered. They show that cavitation affects the discharge coefficient, inhibits vorticity transport and limits the injection to a sector of the orifice. Linear stability analysis of cavitation in flat-plate cascades is performed by Horiguchi, et al. They conclude that in a steady flow analysis, alternate blade cavitation occurs in impellers with even number of blades. For 2 and 4 bladed impellers, there are no additional destabilizing modes to those found in previous analysis assuming inter-blade phase differences. Shi et al. perform observations on the formation and collapse of ‘‘super cavitation.’’ This phenomenon occurs during water entry of a projectile that is shot from a rifle at 342 m/s (!). They examine the cavity closure near the surface, subsequent cavity breakup below the surface and formation of bubbly flows.

New instruments and measurement techniques for multiphase flows are introduced in two papers. Kigger and Pan discuss a new Particle Image Velocimetry (PIV) method for studying solid-liquid, two-phase flows. They use a 2-D media filter to separate images of the two phases. Their approach is validated for different filters and particle sizes. Errors introduced by the filter become negligible for ratio of particle diameters (dispersed phase vs. tracers) exceeding three. Klausner et al. introduce a conductance-based instrument that measures the solid concentration in slurry pipelines ranging from 50–150 cm in diameter. Data on the concentration distribution is provided in real time and agreement with other methods is demonstrated.

Two additional papers focus on uncommon subjects. Gutman analyzes the equilibrium of a flexible cable in water flow when the cable is loaded with an arbitrarily distributed load. An optimal load, which provides maximum deflection of the cable, is defined. Gibson focuses on turbulent mixing, viscosity, diffusion and gravity in the formation of cosmological structures, the fluid mechanics of dark matter. His model includes fluid mechanics, gravity, density and gravitational diffusion at critical scales.

Joseph Katz
Technical Editor

Geometric Parameters Influencing Flow in an Axisymmetric IC Engine Inlet Port Assembly: Part I—Valve Flow Characteristics

Andreas Maier
Research Engineer

Terry H. Sheldrake
Research and Development Manager

Dennis Wilcock
Emeritus Professor of Engineering

School of Computing,
Engineering and Technology,
University of Sunderland,
Sunderland, United Kingdom

Discharge characteristics in an IC engine inlet port and the dependency on geometrical parameters are examined for two valves having seat angles of 40 and 45 deg. The characteristics were established under steady-state conditions over a range of valve lifts up to $L/D=0.25$ and pressure differentials up to 100 mm H_2O. The detailed boundary layer characteristics, indicating flow separation and reattachment on the valve seats, were established with the aid of heat transfer data using the transient liquid crystal technique. Details of the experimental methods for obtaining discharge coefficients and heat transfer coefficients are presented. The discharge and heat transfer data established the expected sequential progression, with lift through the four flow regimes for the valve with a 45 deg seat angle. For the valve with a 40 deg seat angle the four flow regimes were not present. The results demonstrate the extreme sensitivity of the valve flow and boundary layer state to small changes in valve geometry. [S0098-2202(00)00504-6]

Introduction

Today's internal combustion (IC) engine designs demand low emissions, fuel economy, and reliability with maximum volumetric efficiency and, therefore, high power output. These high design standards for more efficient and environmentally clean IC engines result in the need for detailed fluid flow data around the valve and port regions.

The flow through an inlet port discharges over the valve into the cylinder as a jet, which separates from the sealing faces of valve and seat for specific lift conditions producing shear layers with large velocity gradients. Such areas of flow separation inside the valve gap have to be reduced for optimum volumetric efficiency.

The presence of flow separation in the valve passage and the occurrence of different flow patterns has previously been identified in a number of investigations of different valve geometries. In the extensive work carried out by Tanaka in 1929 [1], it was observed that discontinuities in the flow occurred when investigating the flow quantity across the valve for different valve lifts. These discontinuities in flow were represented by change over points in the slope of the graph when plotting mass flow rate or discharge coefficients versus valve lift. From these results Tanaka postulated four flow regimes in the valve passage, illustrated in Fig. 1, to explain the discontinuities of the mass flow rate with a variation of valve lift. The four *flow regimes* were described as follows: In *flow regime I*, occurring at low valve lifts, the flow is attached to both sealing faces of valve head and seat. A vena-contracta occurs at entry into the passage and due to viscous entrainment, the flow after the vena-contracta is able to expand again and to fill the whole passage. Discharge coefficients are generally high during this flow regime and may decrease slightly for increasing lifts. A decrease in discharge coefficient in the low lift range may be a result of the steady enlargement of the separation areas formed at the entry into the passage as the lift is increased. With further increase of valve lift, a first transition in the flow pattern takes place, as the flow is fully detached from the valve seat. The effective flow area is further reduced by flow separation and the discharge coefficient decreases. This state of flow is known as *flow regime II*. The shape of the valve head diverts the flow in an outward direction and the velocity just upstream of the valve passage influences the flow in the passage. Further increase in valve lift causes the flow to break away from the port seat face giving rise to *flow regime III*. A vena-contracta is formed downstream of the geometrical minimum area limited by the valve head and the seat. For high valve lifts, the valve head is assumed to exert less influence on the flow since the flow is directed downwards and reattaches to the valve face. This final state of flow is commonly denoted as *flow regime IV*. Discharge into the cylinder is not affected by any reduction in flow area and the only influence on the discharge coefficient is assumed to be surface friction on the valve sealing face.

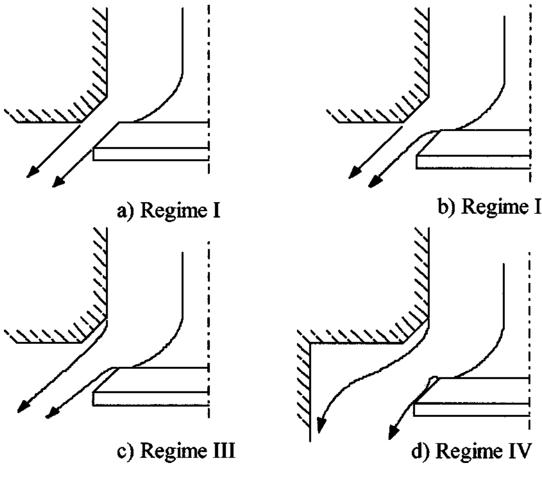

Fig. 1 The four flow regimes

Contributed by the Fluids Engineering Division for publication in the JOURNAL OF FLUIDS ENGINEERING. Manuscript received by the Fluids Engineering Division January 11, 2000; revised manuscript received June 6, 2000. Associate Technical Editor: D. Williams.

Tanaka [1] was first to verify the above flow regimes by conducting static pressure measurements along the valve and seat wall at different lift conditions. Visualization of the valve passage flow in a transparent model displayed the four flow configurations and confirmed the observation of the pressure measurements described.

Kastner et al. [2] also identified the four flow regimes on the basis of discharge coefficient measurements. An attempt was conducted to verify the characteristics of the four flow regimes in a two-dimensional valve port model by measuring the pressure distribution in the valve passage to indicate regions of flow separation from the boundary walls. Subsequently, Vafidis and Whitelaw [3] reported on flow measurements at the exit plane of the valve passage using Laser-Doppler Anemometry (LDA) with the aim to quantify the four flow regimes over a practical lift range for a typical intake valve. Prior to the detailed flow measurements, the authors conducted discharge coefficient measurements over the full range of lifts to identify the transition points in the flow regimes and therefore to define the lift conditions of interest for closer examination. Steady-state measurements of radial and axial mean velocity were then conducted at four nondimensional lift conditions to indicate the direction of the discharge jet into the cylinder and the recirculation areas in the valve passage.

Weclas et al. [4] presented a comprehensive investigation into flow separation in the inlet valve passage using measurement techniques such as discharge coefficient measurements, surface flow visualization using an oil streak technique and detailed flow measurements using LDA. Their study concentrated on the flow characteristics of two intake port geometries (an idealized directed port of a research engine and a helical port of a direct injection Diesel engine) and the effect of two different valve geometries on flow characteristics in the valve passage. The detailed flow measurements at the valve exit plane and the surface flow visualization showed the flow separation in the valve passage and identified its distribution around the valve periphery for generic inlet port geometries.

Despite such a large number of papers examining the flow through the intake valve, the flow separation phenomenon and its dependence on geometrical parameters remains poorly analyzed. However, one should be aware that a systematic variation of all the influencing factors is not feasible because of the diversity of geometries applied in real engine configurations.

The current work investigated the influence of valve geometry on the passage flow characteristics by varying incrementally the key parameters

- fillet radius
- cone angle
- seat angle

of the valve geometry which are illustrated in Fig. 2.

In the present investigation, the initial interpretation of the flow regimes in the valve passage was made from the discharge coefficients. As with previous investigations it was felt necessary to obtain corroborating evidence from another source. Flow visualization and LDA methods were not practical because of the nature of the equipment and oil streak techniques would have been extremely time consuming as the rig would need to be stripped down to gain access to the valve. A measurement indicating the state of the boundary layer at the seat surface would give a direct indication of separated and attached flows. This could then be used with the discharge data to determine the flow regime. As the experimental facility was also being used to obtain detailed spatial distribution of heat transfer coefficients over the seat faces it was determined that the same heat transfer data would be sufficient corroborating evidence and hence give a high degree of confidence in determining the flow regime (Ireland [5]).

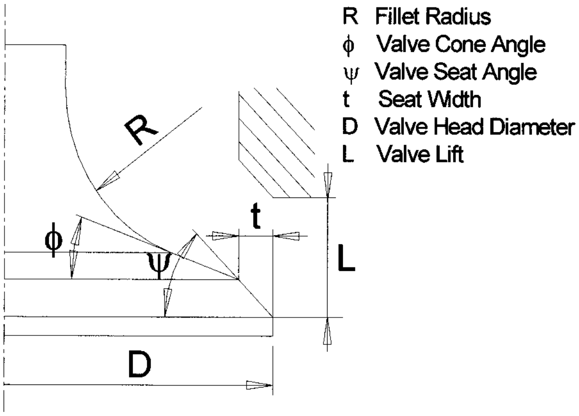

	Valve I	Valve II
Fillet Radius R/D	0.20	0.20
Valve Cone Angle	0°	0°
Valve Seat Angle	45°	40°

Fig. 2 Valve geometry

This paper establishes the measurement techniques of the present work to identify the boundary layer flow inside the valve passage and examines the flow characteristics of two valve geometries varying in their seat angle (details of the geometry are given in Fig. 2) to illustrate the sensitivity of the inlet port flow to small variations in valve geometry. The results shown in this paper form part of a parametric investigation of the influence of valve geometry on valve flow characteristics, which will be presented in Part II of this paper.

Experimental Equipment

The flow into the combustion chamber of a four-stroke internal combustion engine is pulsatory and time-dependent. Therefore, investigations in an actual engine under real operational conditions are practically limited to measurements of engine performance, operational characteristics, and emission levels. However, such test conditions are not suitable to investigate the detailed mechanism of valve flow characteristics. The investigations of inlet valve flow, described above, have therefore been conducted in mainly steady-flow tests and the conclusions on flow characteristics have been drawn on the basis of a ''quasi-static'' assumption for the induction process. The basis for this approximation is the assumption that the flow responds almost instantaneously to changes in valve lift and pressure difference across the valve passage. The inlet valve and the piston move at maximum speeds of approximately 8–15 m/s under normal engine operating conditions. The speed of the moving components is therefore significantly lower than the sonic velocity, at which the perturbations of the flow travel, so that dynamic effects would become negligible. The values for valve flow and performance characteristics obtained from steady flow experiments are hence considered representative for the dynamic flow behavior of the valve in an operating engine.

Kastner et al. [2] conducted an investigation to evaluate valve and port performance characteristics under conditions closely similar to real engine conditions and compared the findings to performance data obtained under steady flow. The results showed that the performance of an inlet valve and port, operating under actual engine conditions, can be derived with reasonable accuracy from discharge coefficient data obtained from static experiments. Fukutani and Watanabe [6] also attempted to correlate the dynamic discharge coefficient C_{Dd} to the static coefficient C_D by making use of a velocity coefficient $(v_a/\overline{v_v})$. For values of $(v_a/\overline{v_v}) \geqslant 100$, the static and dynamic discharge coefficients become approximately the same. Since this value is usually exceeded in production engines, the authors concluded that the influence of the valve motion on the flow in the valve gap is negligible and the static coefficient C_D provides a good indication of the valve performance under actual operating conditions.

Those investigations tested the validity of the ''quasi-steady'' assumption on the basis of comparing a cycle averaged static and dynamic discharge coefficient. However, no verification is provided from those results to correlate detailed flow characteristics in and around the valve and port under static and reciprocating conditions. Evidence that steady-flow results can also be used to characterize inlet port flow under actual engine conditions has therefore been obtained by investigating the detailed flow characteristics at the exit plane of the valve passage during the induction stroke using measuring techniques such as LDA and HWA (Hot-Wire Anemometry). Bicen and Whitelaw [7] conducted an investigation of the air-flow through an intake valve in a model engine under both steady and unsteady conditions. The engine was operated at 200 rpm and LDA measurements of the velocity field at the valve exit plane were taken at a number of fixed lift conditions. Similar measurements were carried out by Vafidis and Whitelaw [3] and Bicen et al. [8]. The latter authors extended the investigation and included the effects of valve operation. The profiles of the mean velocity at the valve exit plane showed close qualitative and quantitative agreement under steady and unsteady flow conditions. The investigation therefore concluded that the mean velocity distribution at the exit plane can be accurately estimated from steady-flow experiments, at least in a low speed engine. Höfler et al. [9] presented a comparison of the inlet valve flow arranged in a helical port under steady-state and operating engine conditions. The investigation aimed to justify the use of steady-flow data as inlet conditions for CFD modeling of engine cylinder flow. Measurements of the flow at the valve exit plane using LDA were taken between 40 deg CA and 170 deg CA (valve opening period was from 10 deg BTDC to 220 deg ATDC) at a fixed valve lift under motored conditions. The flow velocity profiles from the steady-flow measurements showed good qualitative and quantitative agreement around the valve periphery with those measured in the operating engine when the instantaneous mass flow rate was congruent for both experimental conditions.

These works clearly indicate the validity of using steady-flow data to model inlet port flow characteristics under operating engine conditions.

The parametric investigation of the various valve geometries of the present work was therefore conducted in the steady-state flow field of an axisymmetric engine valve test facility, which was used for flow and heat transfer measurements. This configuration was aimed at investigating the detailed characteristics of the flow phenomena in and around the inlet valve in isolation from the complex flow structure of an actual inlet port and the processes of a real engine. Such a simplified engine port model therefore allowed easy change of the flow parameters for the detailed comparative investigation.

The actual test section of the experimental rig is shown in Fig. 3 in a cross-sectional view and displays the axisymmetric arrangement of valve and port. Ambient air enters a bellmouth intake for flow measurement. It then passes a heater section, which imparts a near step change to the air stream temperature, prior to flowing through the valve and port. The high differential pressures across the valve were produced by a centrifugal blower, which is located downstream of the test section. The valve lift was adjusted from outside the port by a linear traverse, which was controlled by a lead-screw on both sides of the traverse. The valve position was measured using two linear variable differential transducers attached to either side of the traverse. The size of the test rig was designed so that the valve models were in the range of 3 times the scale of a medium sized production engine valve in order to improve the spatial resolution when applying the transient liquid crystal technique for the heat transfer measurements. This resulted in a valve head diameter of 123.9 mm with an inlet port bore diameter of 108.0 mm, a parallel passage and a seat width of $t/D=0.063$. The valves were characterized with sharp corners between valve head and the valve seat face.

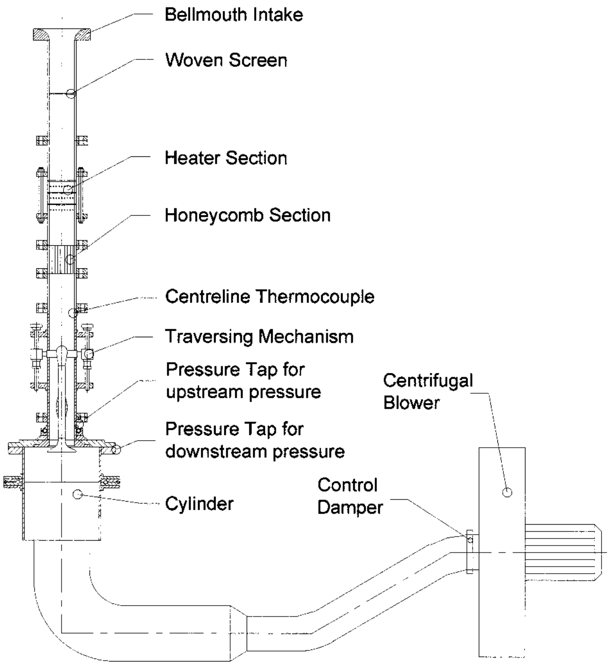

Fig. 3 Cross-sectional view of test section

Flow Measurements

The flow characteristics of the valve and seat geometries were examined under steady-flow conditions by measuring the discharge coefficients for various pressure differentials across the cylinder head. The discharge coefficient is a nondimensional measure of the valve/port performance and defined as the ratio of the actual (measured) flow to the theoretical flow through the aperture of the valve for the same pressure drop

$$C_D=\frac{\dot{m}}{\dot{m}_{\text{theor.}}}$$

The theoretical flow $\dot{m}_{\text{theor.}}$ is calculated using the analysis of a one-dimensional isentropic flow from a reservoir through a restriction at subsonic conditions including compressibility effects and expressed by the following equation

$$\dot{m}_{\text{theor.}}=A\times\sqrt{2p_0\rho_0\frac{\gamma}{\gamma-1}\left(\frac{p}{p_0}\right)^{2/\gamma}\left[1-\left(\frac{p}{p_0}\right)^{(\gamma-1)/\gamma}\right]}$$

where p_0 and ρ_0 are the stagnation conditions for pressure and density respectively and γ is the specific heat ratio. The reference area A was taken as the valve curtain area

$$A=\pi\times D\times L$$

since this area varies linearly with valve lift and is, furthermore, easier to determine than the minimum flow area used in other analysis (i.e., Vafidis and Whitelaw [3]).

The upstream pressure was measured at approximately one inlet bore diameter from the cylinder head. The pressure p at the throat was taken as the pressure at passage exit, which was taken the same as the pressure measured in the cylinder head plane.

Discharge coefficients were measured for nondimensional valve lifts L/D between 0.02 and 0.24 with an estimated uncertainty $\Delta L/D$ of $\pm1.6\times10^{-3}$ for the adjusted valve lift. After adjusting the pressure drop with the sliding gate valve, a reading of the pressure upstream and the pressure drop across the bellmouth in-

Table 1

	Exp. Cond.	Conf. Interval
$\dot{m}$	$L/D=0.02-0.24$	±1.1%
C_D	$L/D=0.02-0.24$	±3.6%
HTC	$L/D=0.06$, 0.12, 0.18, 0.23	±10.2%

take was taken using a micro-manometer. Confidence intervals and the test conditions for the mass flow rate and discharge coefficient measurements are summarized in Table 1.

Heat Transfer Measurements

The transient liquid crystal technique was applied to determine local convective heat transfer coefficients on the valve seat. A comprehensive overview of the liquid crystal technique can be found in Baughn [10]. The valve and seat were coated with micro-encapsulated thermochromic liquid crystals to indicate the surface temperature change during the transient heat transfer experiment. Convective heat transfer coefficients were then calculated based on the transient conduction into a semi-infinite model using the following relationship (Schultz and Jones [11]):

$$\frac{T_{\text{surf.}}-T_{\text{init.}}}{T_{\infty}-T_{\text{init.}}}=1-\exp\left(\frac{h^2t}{\rho c_p k}\right)\operatorname{erfc}\left(\frac{h\sqrt{t}}{\sqrt{\rho c_p k}}\right)$$

The liquid crystal color change was recorded using a monochrome CCD camera to resolve the time temperature relationship for the surface temperature history to compute heat transfer coefficients. The recorded images were digitally processed using the full intensity history of the liquid crystal color change (Wang et al. [12]) to obtain a full heat transfer coefficient map of the surface area investigated. Confidence intervals for the measured heat transfer coefficient and the test conditions are presented in Table 1.

Results and Discussion

Valve flow and performance characteristics were identified from discharge coefficient measurements for a range of fixed valve lifts for steady-flow conditions. The discharge coefficient characteristic was determined from the measured and the calculated theoretical mass flow rates for nondimensional valve lifts L/D ranging from 0.02 to 0.24 which covered the range of practical valve operations (Heywood [13]). The static pressure differential was varied from 20 mm H_2O to 100 mm H_2O to investigate a variation of port flow velocity on valve performance. Results for mass flow rate and discharge coefficient characteristics are presented for two valve geometries, denoted as valve I and II (Fig. 2) in the following discussion. The valves only differed in the valve seat angle which was 45 deg for valve I and 40 deg for valve II, respectively.

The mass flow rate and the discharge coefficient characteristic based on the valve curtain area are presented in Fig. 4 and Fig. 5, respectively, for valve I. The results showed that a variation of pressure drop had no influence on the general discharge coefficient characteristic. However, a small influence was observed on the magnitude of discharge coefficients with increasing valve lifts. For small valve lifts, discharge coefficients slightly increased as the pressure drop and therefore flow velocity inside the passage increased. The flow velocity was relatively low and viscosity effects were assumed to be dominant in the passage, which would result in the observed small increase in discharge coefficients for higher differential pressures at low lifts. In the medium lift range $(0.05<L/D<0.15)$, with transitions in flow regimes taking place, indicated by a change in slope in the mass flow rate in Fig. 4, discharge coefficients decreased as the pressure drop was increased. The characteristic may be explained on the basis that discharge coefficients are proportional to the effective flow area in the valve passage and are consequently determined by flow separation. For increasing flow velocities, the separation area in the valve passage would be enlarged and hence the effective flow area reduced, which resulted in a decrease in discharge coefficients in the region of flow transition. At high lifts $(L/D>0.20)$, discharge coefficients were found to be almost independent of pressure drop suggesting that the flow in the valve passage was highly turbulent and viscosity effects had no effect on the boundary layer flow. This finding agreed with the investigations carried out by Tanaka [1], who concluded that discharge coefficients were approximately constant and therefore independent of the pressure drop at a particular lift condition. Vafidis and Whitelaw [3] presented results for discharge coefficient measurements carried out for pressure drops ranging from 50 mm H_2O to 200 mm H_2O. They found that an increase in pressure drop increased discharge coefficients and its influence was shown to be stronger at small lifts and low pressure drops as a result of the increased contribution of viscous effects under these conditions. However, the authors stated that

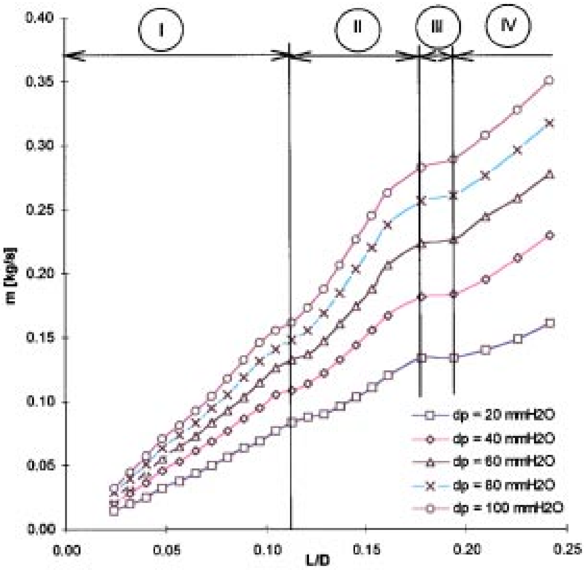

Fig. 4 Mass flow versus lift; valve I

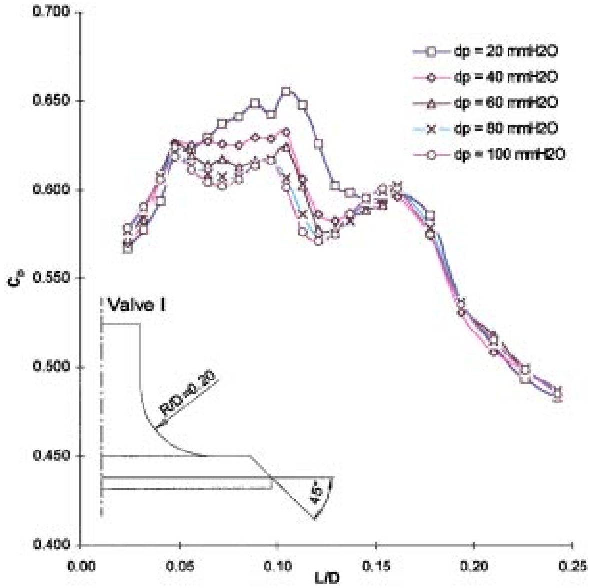

Fig. 5 Discharge coefficient characteristic versus lift; valve I

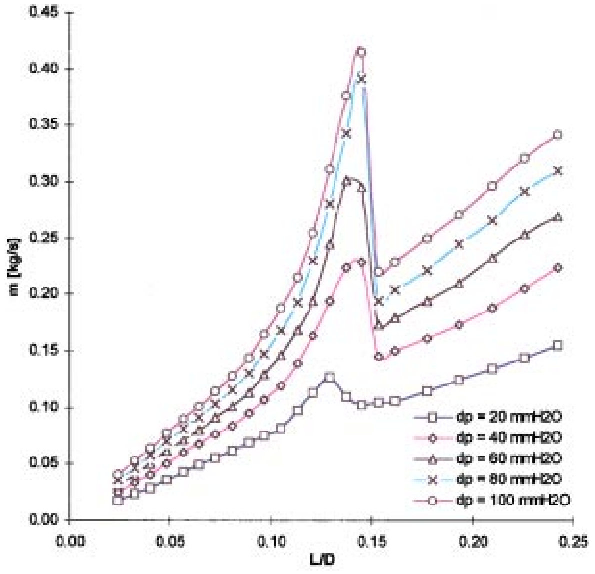

Fig. 6 Mass flow versus lift; valve II

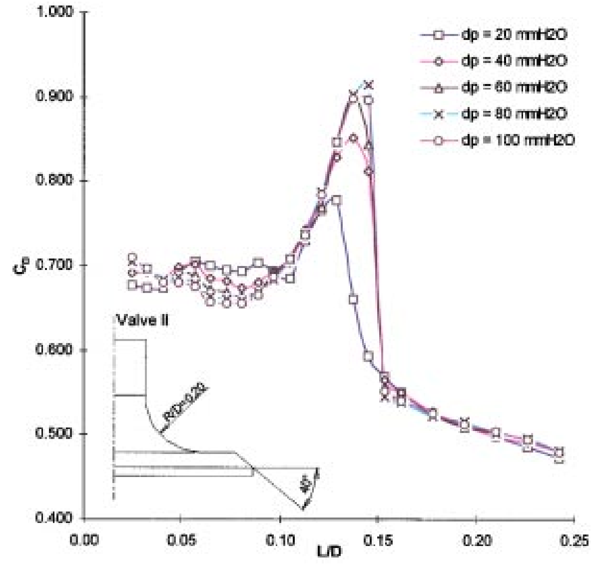

Fig. 7 Discharge coefficient characteristic versus lift; valve II

for even higher pressure drops, for which results were only partly presented, the discharge coefficient curves almost collapsed into one. This result was reflected in the present investigation for the highly turbulent flow at high valve lifts.

An analysis of the mass flow rate versus valve lift plot showed three changes in slope, illustrated in Fig. 4, from which transition points in the valve flow characteristic and the four flow regimes were identified. For $L/D<0.11$, the flow was assumed to be in its first flow regime. The boundaries of the passage are very close and the flow is forced to attach to both sealing faces as illustrated in Fig. 1(*a*). Discharge coefficients, presented in Fig. 5, increased at low lifts as a result of the pronounced influence of Reynolds number and viscosity effects in this range of lifts ($L/D<0.05$). This was continued by slightly decreasing or approximately constant discharge coefficients as the lift was increased up to $L/D=0.08$. The latter characteristic was due to a recirculation area formed at the passage entry which was enlarged as a result of the radially directed flow and the steep angle of the 45 deg seat face as the valve lift was increased.

At $L/D=0.11$, a first transition point in the flow took place and for $0.11<L/D<0.18$, the flow was thought to be separated from the valve seat face. For $L/D=0.18$, the flow was assumed to detach from the seat face and hence to form a free discharge jet. A vena-contracta was therefore formed inside the passage as a result of the recirculation area formed on either side of the discharge jet with a corresponding reduction in discharge coefficients.

In the transition at $L/D>0.20$, the flow started to reattach to the valve face since the flow was directed in downward direction at high valve lifts. The flow was therefore in its final mode (flow regime IV). Discharge coefficients were steadily falling in this range of lifts as a result of growing frictional effects as the flow velocity increased for increasing valve lifts.

Due to the continuous change in slope of the mass flow rate curves, presented in Fig. 4, the transition process between the flow patterns in the valve passage were thought to be produced by steadily increasing separation areas from the valve and seat sealing faces which eventually extended to the passage exit plane.

The results for the mass flow and discharge coefficient characteristics for valve II, presented in Fig. 6 and Fig. 7, respectively, showed a similar behavior in the low to medium lift range as identified for valve I with discharge coefficients approximately constant up to $L/D=0.09$, with the flow being assumed in flow regime I. A peculiar characteristic was observed in the low to medium lift range up to $L/D=0.14$ with a sharp increase and sudden drop in discharged coefficients as the lift was increased. This sharp increase in discharge coefficients in the medium lift range with values of C_D approaching 0.9 results in a very efficient flow performance in the medium to high lift range, which could be of significant interest for actual engine valve designs. This characteristic of valve II was attributed to a delayed flow separation from the seat face as a result of the flat valve shoulder inducing a large radial momentum to the flow. At $L/D=0.14$, a sharp drop in mass flow rate occurred with the flow assumed to enter its final mode. At lift conditions higher than $L/D=0.14$ the passage flow was presumably in flow regime IV and discharge coefficients matched those observed of valve I for lifts larger than $L/D=0.20$.

Those interpretations of the flow characteristics for the different lift ranges can only be inferred from the discharge coefficient measurements. Therefore the behavior of the flow in the valve passage was analyzed and verified in detail from the boundary layer flow interpretations obtained from heat transfer experiments using the transient liquid crystal technique. Measurements of the detailed distributions of heat transfer coefficients on the seat sealing faces were conducted at four lift conditions and four Reynolds number conditions for the inlet port flow. Distributions of heat transfer coefficients are shown in Fig. 8(*a*,*b*) on the valve seat and seat sealing face of valve I for the lowest lift condition and the four Reynolds number conditions investigated.

Points of flow reattachment generally correspond to peaks in local heat transfer coefficients as a result of the high turbulence intensity of the locally impinging flow which is illustrated in Fig. 8(*a*,*b*). Boundary layer separation is always associated with the formation of small vortices, which is reflected in a decrease of heat transfer coefficients toward the leading edge of the valve seat face (Fig. 8(*a*)) as a result of the lower velocities in the separation region. A similar pattern with a peak heat transfer coefficient at approximately mid-face position in the passage was shown in the heat transfer results for the seat sealing face and decreasing coefficients toward the trailing edge of the passage (Fig. 8(*b*)). The characteristic of decreasing heat transfer coefficients downstream of the reattachment position was as a result of a growing boundary layer after the flow reattached to the valve surface where a local thinning of the boundary layer occurred.

As the Reynolds number was increased, the separation area from the valve seat face was shown to grow which was reflected in the peak heat transfer coefficient moving in a downstream direction (illustrated in Fig. 8(*a*)). This effect was reversed on the

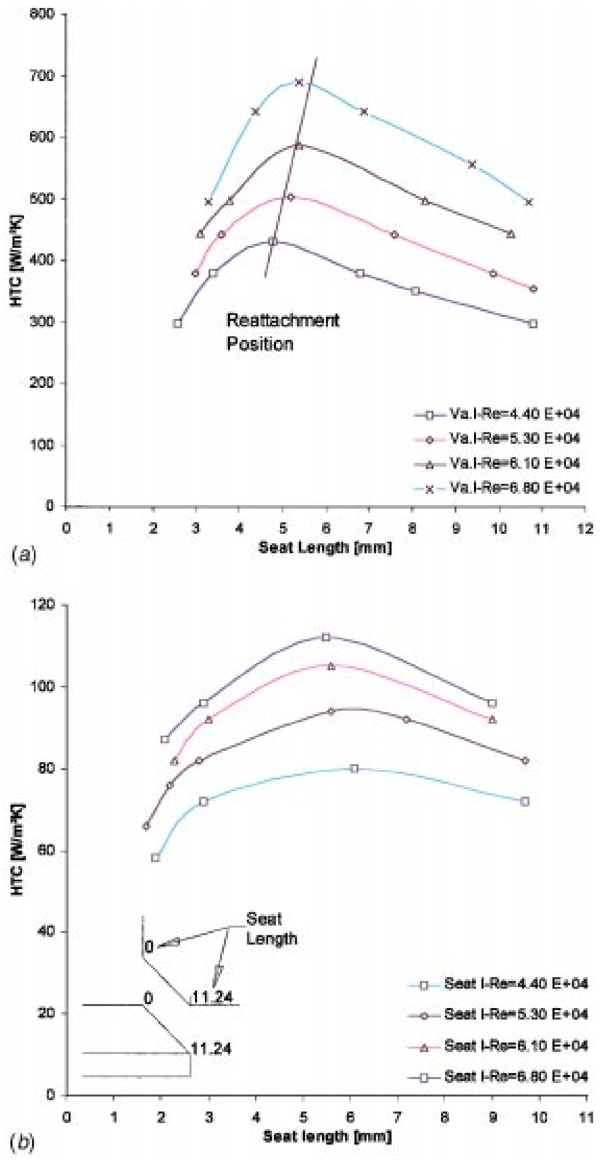

Fig. 8 (*a*) Heat transfer coefficient versus lift; valve seat I; $L/D=0.06$; (*b*) Heat transfer coefficient versus lift; port seat I; $L/D=0.06$

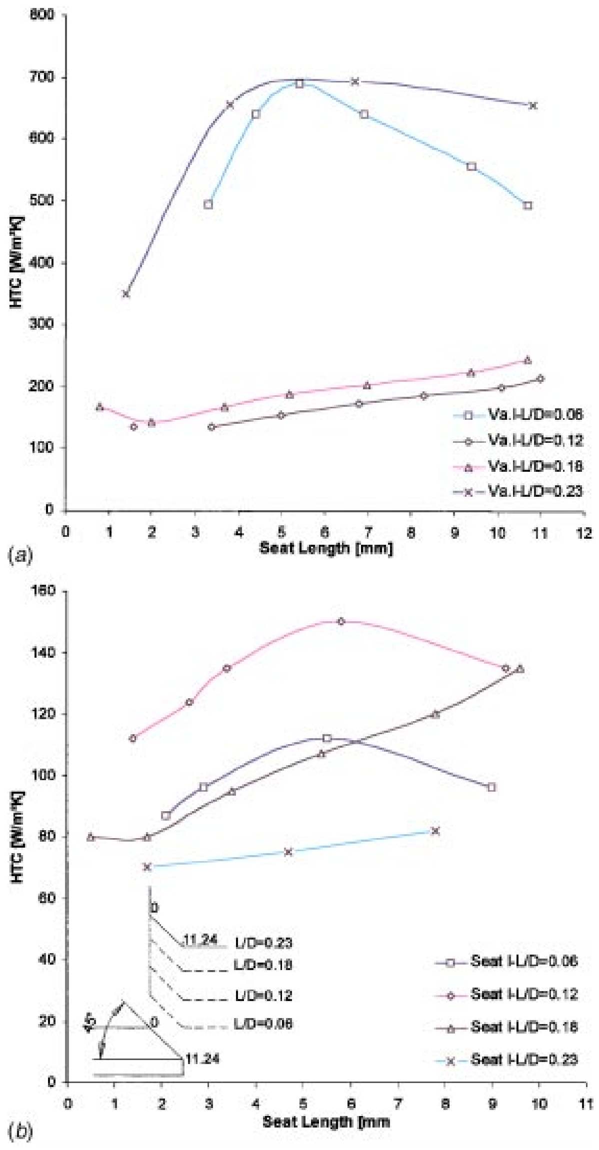

Fig. 9 (*a*) Heat transfer coefficient versus lift; valve seat I; (*b*) Heat transfer coefficient versus lift; port seat I

seat sealing face with the location of the peak heat transfer coefficient moving toward the leading edge of the seat face (shown in Fig. 8(*b*)). The characteristic was a result of the separation area from the port seat face being suppressed by the increased separation area from the valve seat face. The latter was attributed to the increased inertia of the flow in radial direction for a flat valve shoulder at low lifts. The results therefore clearly reflect an influence of port flow Reynolds number and therefore pressure differential across the valve on the separation area. This was already indicated in the varying discharge coefficients for increasing pressure differentials in the transition region of flow regimes.

Heat transfer coefficient distributions in the valve passage for the four lift conditions and the highest Reynolds number investigated are shown in Fig. 9(*a,b*) for valve I. At the lowest lift condition ($L/D=0.06$), the flow separated from the sharp corners leading into the passage and reattached to both sealing faces inside the passage as detailed above. This characteristic corresponds to flow regime I with the flow fully attached to the seat sealing faces at passage exit and a small separation bubble formed at entry into the passage. Therefore, in flow regime I, the flow is either continuously attached, or separates and reattaches, to both sealing faces of valve head and seat. This latter point was not identified in previous studies (i.e., Tanaka [1]) and results from the superior experimental techniques used in this investigation. At the lift condition $L/D=0.12$, the low heat transfer coefficients and the liquid crystal pattern during the transient heat transfer experiment indicated separated flow from the valve seat face (Fig. 9(*a*)). Flow separation and reattachment on the seat sealing face were shown by a local peak in heat transfer coefficients with the reattachment point being at approximately 6.2 mm into the passage. The inertia of the flow in radial direction at this lift condition therefore caused the flow to fully separate from the valve seat face with the separation area only slightly increased on the seat sealing face for this lift condition. The flow was in regime II in agreement with the flow interpretations from the discharge coefficient measurements. For an increased valve lift ($L/D=0.18$), the reattachment position on the seat sealing face moved considerably downstream with a locally high heat transfer coefficient observed at the trailing edge of the seat sealing face. The flow therefore separates from the seat sealing face at $L/D=0.18$ and a transition takes place from flow regime II to III verifying the interpretations of the passage flow from the discharge coefficient measurements at this

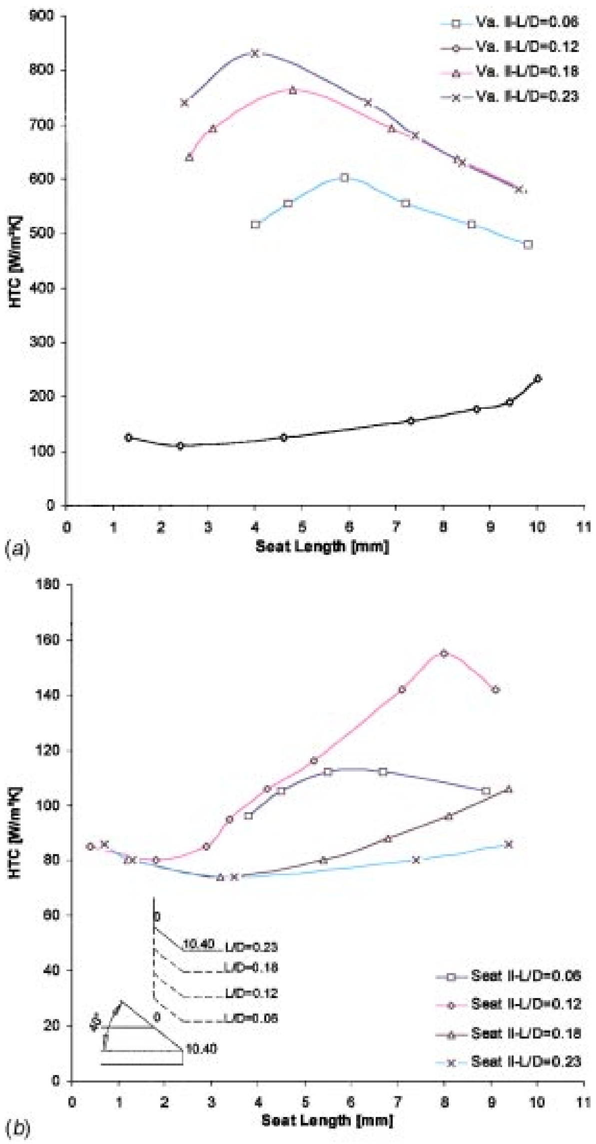

Fig. 10 (***a***) **Heat transfer coefficient versus lift; valve seat II; (*b*) Heat transfer coefficient versus lift; port seat II**

lift condition. For increasing lifts, the passage flow formed a free discharge jet with a recirculation area formed on either side of the jet.

At the highest lift condition ($L/D=0.23$), the liquid crystal data showed a very broad band of relatively high heat transfer coefficients in the lower part of the valve seat face, illustrated in Fig. 9(*a*). This characteristic reflected reattaching flow on the valve seat face and would indicate that the transition from flow regime III to IV is not a sudden process but a continuous one, which is also indicated in the smooth change in slope in the mass flow rate plot illustrated in Fig. 4.

The complete analysis for the four lift conditions resolved in detail the complex mechanism of inlet valve flow and showed the occurrence of the four flow regimes.

The heat transfer characteristic of valve II, presented in Fig. 10(*a,b*) for the valve seat and seat sealing face, respectively, showed a similar characteristic as valve I at the lowest lift condition ($L/D=0.06$). The flow separated from the sharp corners leading into the passage and reattached at approximately mid-position on both seat sealing faces indicated by a locally high heat transfer coefficient. This heat transfer pattern reflects flow regime I in agreement with the flow interpretation from the discharge coefficient measurements at this lift condition. The liquid crystal results at $L/D=0.12$ showed that the reattachment position on the seat sealing face moved downstream with the flow being fully separated from the valve seat face indicated by low heat transfer coefficients which slightly decreased toward the leading edge of the passage. At the lift condition $L/D=0.18$, the flow was reattached to the valve seat face with the reattachment position at approximately mid-position into the passage. The seat results indicated fully separated flow from the seat sealing face with the flow being in its final mode.

The characteristic at $L/D=0.18$ with the flow being reattached to the valve seat face together with the flow behavior on the seat sealing face at $L/D=0.12$ probably explains the sharp increase in flow performance observed for $L/D<0.14$. Transition from flow regime II at $L/D=0.12$ was therefore presumably back to the effective mode of flow regime I explaining the high discharge coefficients in the medium lift range. This was continued by a direct transition from flow regime I to IV, reflected in the heat transfer data at $L/D=0.18$, which resulted in the sudden steep drop in flow performance. At the lift condition $L/D=0.23$, the heat transfer data on the seat sealing faces for valve II indicated attached flow on the valve seat face. The reattachment position moved in upstream direction as compared with $L/D=0.18$ as a result of the now mainly axially directed flow. The flow on the port seat face was fully separated flow. The passage flow therefore prevailed in flow regime IV at lift larger than $L/D=0.14$ in agreement with the discharge coefficient data.

The detailed resolution of the boundary layer flow inside the passage clearly identified the four flow regimes for valve I. Valve II having a 40 deg seat resulted in a peculiar discharge coefficient characteristic showing a high flow performance in the medium lift range. The analysis of the modes of flow for this valve geometry indicated that the progress in flow regimes is not from I, II, III, to IV and the four modes of flow did not occur in sequence with valve lift for this valve geometry. The present results therefore clearly indicate the sensitivity of valve flow characteristics to small modifications in valve geometry. A detailed parametric study of the influence of inlet valve on flow characteristics is presented in Part II of this paper.

Conclusions

The detailed flow characteristics of inlet valve flow were analyzed on the basis of discharge coefficient measurements for two valve geometries from which the different regimes for the passage flow were identified. The detailed boundary layer flow was then verified from heat transfer measurements applying the transient liquid crystal technique. The heat transfer data for the various flow and lift conditions were applied to resolve in detail flow separation and the positions of flow reattachment inside the passage.

The heat transfer data shown for the low lift conditions showed that the separation areas at the leading edge of both seat sealing faces interact with each other making the flow separation in the valve passage a complex process dependent on flow conditions and valve lift.

The results presented for the two valve geometries illustrated in detail the sensitivity of flow characteristics on changes in valve geometry. For valve I, having a 45 deg seat, the heat transfer data for the four lift conditions verified the occurrence of the four flow regimes. The data for the 40 deg seat geometry indicated that the flow regimes did not occur in sequence with valve lift and the small modifications in valve geometry resulted in a significant difference in flow characteristics.

The influence of valve geometry will therefore be scrutinized in the parametric investigation presented in Part II of this paper.

The present work introduced a methodology to analyze in detail the flow characteristics in and around an IC engine inlet valve, which was applied to a parametric study to investigate the influence of valve geometry on port flow characteristics and inlet valve heat transfer.

Nomenclature

A = area
ATDC = after top dead center
BTDC = before top dead center
CA = crank angle
C_D = discharge coefficient
C_{Dd} = dynamic discharge coefficient
c_p = specific heat capacity at constant pressure
D = valve head diameter
D_p = inlet port diameter
h, HTC = heat transfer coefficient
k = thermal conductivity
L = valve lift
$\dot{m}$ = mass flow rate
μ = kinematic viscosity
p = pressure
R = valve fillet radius
Re = Reynolds number $\{\rho D_p v_a/\mu\}$
t = time, seat width
T = temperature
v_a = velocity of inlet flow
$\overline{v}_v$ = average valve velocity
γ = ratio of specific heats
ρ = density

Subscripts

0 = property at stagnation point
theor. = theoretical condition
surf. = condition at surface
init. = initial condition
∞ = final condition

References

[1] Tanaka, K., 1929, ''Airflow Through Suction Valve of Conical Seat,'' Aeronautical Research Institute Report, Tokyo Imperial University, Part 1, p. 262; Part 2, p. 361.
[2] Kastner, L. J., Williams, T. J., and White, J. B., 1963–1964, ''Poppet Inlet Valve Characteristics and their Influence on the Induction Process,'' Proc. Inst. Mech. Eng., **178**, Part 1, No. 36, pp. 955–975.
[3] Vafidis, C., and Whitelaw, J. H., 1984, ''Steady and Pulsating Air Flow Through a Stationary Intake Valve of a Reciprocating Engine,'' Imperical College, Mech. Eng. Dept. Report, No. FS/84/04.
[4] Weclas, M., Melling, A., and Durst, F., 1998, ''Flow Separation in the Inlet Valve Gap of Piston Engines,'' Prog. Energy Combust. Sci., **24**, No. 3, pp. 165–195.
[5] Ireland P. T., 1987, ''Internal Cooling of Turbine Blades,'' D. Phil. thesis, University of Oxford, UK.
[6] Fukutani I., and Watanabe E., 1982, ''Air Flow through Poppet Inlet Valves-Analysis of Static and Dynamic Flow Coefficients,'' SAE Paper 820154, pp. 1–9.
[7] Bicen, A. F., and Whitelaw, J. H., 1983, ''Steady and Unsteady Flow Through an Intake Valve,'' Imperial College, Mech. Eng. Dept. Report, No. FS/83/11.
[8] Bicen A. F., Vafidis C., and Whitelaw J. H., 1984, ''Steady and Unsteady Air Flow Through an Intake Valve of a Reciprocating Engine,'' Proc. Symp. of Flows in IC Engines, pp. 47–55.
[9] Höfler, T., Pitcher, G., and Wigley, G., 1993, ''Comparison of Diesel Engine Inlet Valve Flows under Steady State and Motoring Conditions,'' Proc. SPIE, **2052**, pp. 737–744.
[10] Baughn, J. W., 1995, ''Liquid Crystal Methods for Studying Turbulent Heat Transfer,'' Int. J. Heat Fluid Flow, **16**, No. 5, pp. 365–375.
[11] Schultz, D. L., and Jones, T. V., 1973, ''Heat Transfer Measurements in Short Duration Hypersonic Facilities,'' AGARD Report AG-165.
[12] Wang Z., Ireland P. T., and Jones T. V., 1993, ''An Advanced Method of Processing Liquid Crystal Video Signals from Transient Heat Transfer Experiments,'' ASME Paper 93-GT-282, pp. 1–7.
[13] Heywood J. B., 1988, Internal Combustion Engine Fundamentals, McGraw-Hill, New York.

Geometric Parameters Influencing Flow in an Axisymmetric IC Engine Inlet Port Assembly: Part II—Parametric Variation of Valve Geometry

Andreas Maier
Research Engineer

Terry H. Sheldrake
Research and Development Manager

Dennis Wilcock
Emeritus Professor of Engineering

School of Computing,
Engineering and Technology,
University of Sunderland,
Sunderland, United Kingdom

The influence of inlet valve geometry on IC engine port flow characteristics was investigated systematically by varying the key valve geometric parameters of fillet radius, cone angle, and seat angle. The analysis of flow through the port was measured for 36 valves having geometries determined by $R/D=0.20-0.30$, cone angle 0–20 deg and seat angle 30–45 deg. Discharge coefficients were measured to gain an understanding of the general flow performance. These were used in conjunction with heat transfer data to gain a clear understanding of the state of the boundary layer on the valve and port seats for varying lifts and pressure drops. This established the presence or otherwise of the four flow regimes within the valve passage. The results demonstrate that the cone and seat angle have major effects on valve flow performance and enable engine designers to choose more readily the valve characteristics they desire. [S0098-2202(00)00404-1]

Introduction

In an internal combustion engine, volumetric efficiency, and therefore power output, could be increased with improvements to the design of the inlet port and particularly the inlet valve. Part I of this paper clearly identified the sensitivity of valve flow characteristics to small changes in valve geometry by presenting data for two valve geometries varying in only their valve seat angle. The present work conducted a parametric investigation into the influence of valve geometry on valve flow characteristics by testing a range of inlet valve geometries.

Previous studies paid much attention to testing specific valve geometries with respect to their flow performance. Luke [1] was the first to indicate that the geometry of valve and port plays a significant role in determining the performance characteristics of the induction system. Although no geometrical details were given, the so-called ''conical-seated'' valve showed a performance superior to that of the ''flat-seated'' valve. Lewis and Nutting [2] investigated the arrangement of valves in pairs as compared with single ones and valves of different sizes. Aspects of valve geometry and its influence on the performance of the valve/port assembly were extensively investigated by Tanaka [3]. The study focused on the influence of fillet radius, valve head angle, seat width, and seat angle. The valve models were tested under steady flow conditions in an axisymmetric port/cylinder arrangement. The effects of varying parameters defining the valve geometry were examined by scrutinizing the variation in mass flow rate through the valve passage for different lift conditions at a fixed pressure differential across the port. Generally, the fillet radius did not have a significant effect on the flow quantity, but a large fillet radius was found to have a rather bad influence on flow characteristics. The effect of valve cone angle was investigated on the basis of four valve cone angle geometries ranging from 0 to 45 deg. The study showed a pronounced effect of the upper valve face corner on flow separation, which was delayed to higher lifts for a larger valve cone angle. The investigation of the seat width revealed that a wide overlap gave better flow performance. Seat angle variations were examined using four seat geometries between 0 and 60 deg to quantify its effect on valve flow characteristics. The 45 deg seat angle valve showed a distinct transition between the four flow regimes observed for various valve lifts. The valve with a 30 deg seat angle showed the transition between the different flow pattern less clearly.

In the subsequent investigations of Wood et al. [4] and Kastner et al. [5], attempts were made to reduce the tendency of the flow to separate from the sealing faces of the valve passage.

Wood et al. [4] described various attempts to reduce the flow resistance by rounding the sharp corners of the valve and seat faces, by varying the radius of the port elbow and by varying the fillet radius of the valve head in order to approach the performance of a perfect venturi nozzle. Kastner et al. [5] also reported on a range of modifications to the valve and port to improve its flow performance. The modifications included a tapered port to avoid abrupt area changes reducing wall separation and shaping the passage to a converging-diverging nozzle. Although these attempts produced considerable improvements in discharge coefficient C_D, which were however mostly in the low lift range ($L/D=0-0.10$) with values exceeding unity, the modifications resulted in complex geometrical configurations, which might prove impractical for production engine designs. Annand [6] further investigated the effects of seat width, fillet radius, and seat angle on discharge coefficients C_D with an isolated valve and results mainly agreed with the findings of Tanaka [3]. Valves with a 45 deg seat angle clearly showed the transition between the different flow regimes whereas the 30 deg seat indicated the transition points less distinctly. However, Annand recommended taking into account mechanical considerations proposed by Pope [7] for the final choice of the appropriate seat angle.

An extensive study of the flow structure at the valve exit plane and of the flow field in the cylinder was carried out by Bicen and Whitelaw [8] and Vafidis and Whitelaw [9] who measured discharge coefficients and the detailed velocity distribution using LDA for various valve geometries.

Vafidis and Whitelaw [9] investigated a 45 deg seat angle valve with and without rounded inner corners of the valve and seat

---

Contributed by the Fluids Engineering Division for publication in the JOURNAL OF FLUIDS ENGINEERING. Manuscript received by the Fluids Engineering Division January 11, 2000; revised manuscript received June 6, 2000. Associate Technical Editor: D. Williams.

sealing faces upon their effect on flow transition. The results suggested that only the valve with sharp corners exhibited the four flow regimes.

Bicen et al. [10] presented a summary of the work reported by Bicen and Whitelaw [8] and Vafidis and Whitelaw [9] in comparing discharge coefficients for the 45 and 60 deg seat angle valves and additionally the detailed flow characteristic at the exit of the valve passage. The results showed that the performance of the 45 deg seat was generally superior to the 60 deg seat over the range of lifts tested $(L/D<0.26)$.

Gosman and Ahmed [11] subsequently reported on the measurements of discharge coefficients, mean velocity and turbulent stress fields obtained by Hot-Wire Anemometry (HWA) at various valve lifts in an axisymmetric valve/port assembly with a valve geometry (45 deg seat angle and rounded corners) similar to the one investigated by Bicen et al. [10].

Weclas et al. [12] presented a comprehensive investigation into the flow separation in the inlet valve passage. Their study concentrated on the flow characteristics of two intake port geometries: an idealized directed port of a research engine and a helical port of a direct injection Diesel engine. Furthermore the investigation considered the effect of a variation in valve geometry. Two valves with a 45 deg valve seat angle that differed in the fillet radius and the valve head angle were examined for their discharge characteristics in the directed port.

Those studies identified that the inlet valve flow is clearly dependent on valve geometry with the general flow characterized by the four flow regimes (Tanaka [3]). The occurrence of the four flow regimes and the transition points were found to be influenced by the valve and port geometry. The investigations showed that with certain geometrical modifications the transition points can be altered leading to improvements in the valve flow characteristic and therefore the performance of the inlet port. However, the investigations described were mostly limited to specific valve geometries and did not provide a complete analysis of the flow through the intake valve, the flow separation phenomenon and its dependence on geometrical parameters.

No comprehensive and systematic data exist about the influence of valve and port geometries on discharge coefficients. Neither has there been any previous detailed investigation into the various flow regimes that influence flow performance. The present work therefore investigated in detail the influence of valve geometry on the passage flow characteristics by varying incrementally the key parameters

- fillet radius
- cone angle
- seat angle

of the valve geometry using discharge coefficient measurements and heat transfer data from the transient liquid crystal technique to resolve the boundary layer flow in the valve passage.

The Valve Models

To carry out the parametric investigation, a relevant range for a variation of the valve geometry had to be developed to cover practical inlet valve designs. Apart from having a very good flow performance, the overall design requirements of an engine inlet valve can be summarized as follows:

- Adequate seating area (contact area between valve head and seat) to improve cooling of the valve during the valve closing period.
- Shape of the valve to keep thermal stresses to a minimum.
- Valve head as light as possible since it is an accelerated mass and therefore exerts high forces on the valve train; it is possible that for high engine speeds the resonant frequency of the valve train is approached.
- Valve shapes that are not subject to engine deposits and wear.

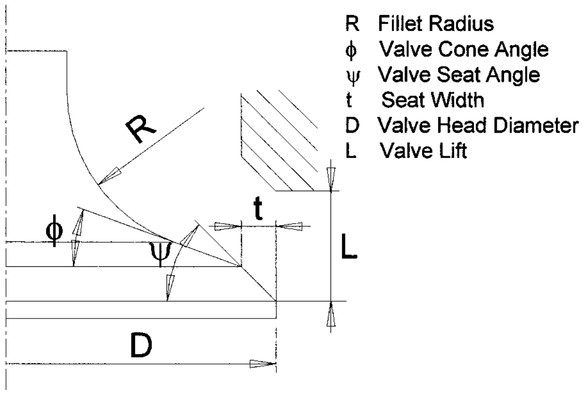

Fig. 1 Valve geometry

Those criteria clearly identify that practical valve design may differ from the recommendations for optimum flow performance. A parametric study was therefore designed to investigate the behavior of valve flow with the limits of the geometry variation taken from general design criteria for the inlet valve within the automotive industry (TRW Automotive Systems Ltd [13]). The three most influential valve parameters, which are illustrated in Fig. 1, determining valve flow were varied as follows:

Geometrical Parameter	Range	Incremental Change
Fillet Radius R/D	0.20–0.30	0.05
Valve Cone Angle	0–20 deg	10 deg
Valve Seat Angle	30–45 deg	5 deg

This resulted in a total number of 36 valve geometries to form the present parametric study.

Results and Discussion

The magnitude of discharge coefficients, transition in flow regimes, and the various flow patterns occurring in the valve passage are dependent on the valve geometry as Part I of this paper clearly identified. The combination of the geometrical parameters valve fillet radius, cone angle, and seat angle and their influence on the valve flow characteristics in terms of discharge coefficients was investigated for the full range of 36 valve geometries designed for the present investigation. Measurements were carried out for lift conditions ranging from $L/D=0.02$ to 0.24 at pressure differentials across the valves between 20 mm H_2O and 100 mm H_2O in incremental steps of 20 mm H_2O.

The detailed behavior of the boundary layer in the passage was resolved using heat transfer data from the transient liquid crystal technique. The measurement techniques and the data interpretation applied for the present parametric study were established in Part I of this paper. The results in this paper are presented and discussed on the basis of the largest pressure differential investigated since it was found that the pressure drop across the passage had no influence on the discharge coefficient characteristic. The measurements showed good repeatability with the differences well within the estimated uncertainty of ±3.6 percent for the discharge coefficient results.

Influence of Valve Cone Angle

The effect of the valve cone angle on discharge coefficient characteristic was examined for the various seat geometries investigated. Results of the mass flow rate and discharge coefficient characteristics for the three valve cone angles for a 45 deg seat geometry are presented in Fig. 2(*a*,*b*), respectively, and reflect the pronounced effect of valve cone angle on valve flow characteristics which were consistent for all the other seat geometries investigated.

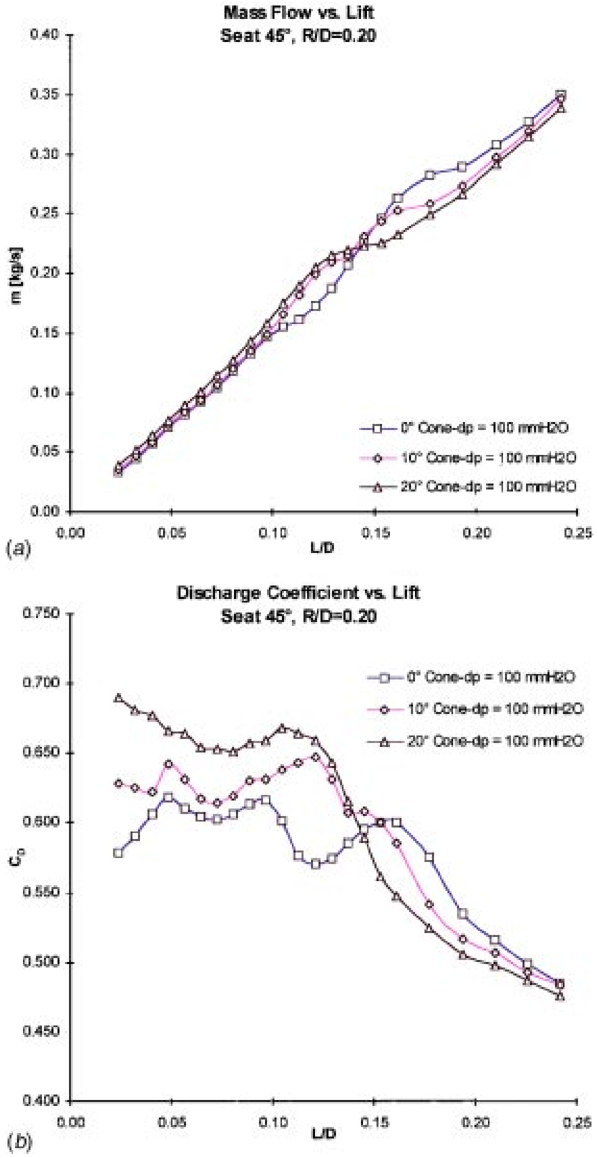

Fig. 2 (***a***) **Mass flow rate versus lift; variation of valve cone angle;** (***b***) **discharge coefficients versus lift; variation of valve cone angle**

A flat valve shoulder (0 deg cone angle in Fig. 2) showed a first change in slope at about $L/D=0.11$ in the mass flow rate versus valve lift plot (Fig. 2(*a*)) with a corresponding reduction in the C_D value, indicating a transition in flow regime, whereas the 10 and 20 deg cone angle continued the effective mode of flow regime I up to $L/D=0.14$. However, the 10 deg cone angle showed an immediate change in slope again at $L/D=0.16$. This would suggest that the flow separated from the valve seat face at $L/D=0.14$, with the effective flow area remaining constant over a small range of valve lifts, resulting in a small recovery in discharge coefficient, which was followed immediately by the flow also detaching from the seat face (transition from flow regime II to III). The latter was assumed to have produced the continuous drop in discharge coefficients at $L/D=0.16$ as shown in Fig. 2(*b*). At $L/D=0.19$, the flow was thought to reattach to the valve face, which was consistent with flow regime IV.

The results for a 20 deg valve cone angle suggested that the separation process from valve and seat face was a continuous one in the lift range between $L/D=0.125$ and 0.16. Tanaka [3] and Annand [6], however, concluded that a 20 deg cone angle in combination with a 45 deg seat would not show flow regime II and III and transition was assumed to be directly from flow regime I to IV in the medium lift range. The assumed steady increase in the flow separation would therefore be restricted to the seat face which may be a result of the increased axial flow momentum induced by a large cone angle.

The cone angle of the valve therefore affected the discharge characteristic over the full range of lifts. A large cone angle was thought to direct the flow in a more axial direction resulting in high discharge coefficients in the low lift range. This influence had the opposite effect in the medium to high lift range with a small cone angle resulting in earlier transition to flow regime II and latter transition to flow regime IV. A small valve cone angle was assumed to direct the flow toward the plane of the cylinder head, which suppressed flow separation from the seat face and resulted in a superior flow performance in the medium to high lift range.

The influence of the valve cone angle on the passage flow characteristics was examined by means of heat transfer coefficient data, which was used to resolve the detailed behavior of the boundary layer inside the valve passage. Distribution of heat transfer coefficients on the valve seat and seat sealing face is presented in Fig. 3(*a*,*b*) and Fig. 4(*a*,*b*) for the lift conditions $L/D=0.06$ and $L/D=0.18$, respectively. For the low lift condition the heat transfer data indicated that the flow separated and reattached to the seat sealing faces for all three cone angle configurations, reflected by a local peak in heat transfer coefficient in Fig. 3(*a*,*b*). The passage flow was therefore in regime I for all three cone angle geometries at this lift condition. The heat transfer results on the valve seat and seat sealing face clearly illustrated the effect of the valve cone angle on the flow direction into the valve passage. A 0 deg valve cone angle directed the flow in a more radial direction and produced the largest separation area from the valve seat face. This influence of valve cone angle on flow direction into the passage resulted in a reversed characteristic on the seat sealing face with a small valve cone angle suppressing the flow separation area.

At $L/D=0.18$, those influences of the valve cone angle were continued. The results on both seat sealing faces reflected the significance of the valve cone angle on flow direction into the passage with the flow being fully separated from the valve seat face for the 0 deg valve cone angle configuration and separating and reattaching for the 10 and 20 deg cone angle geometries. The liquid crystal data indicated that the separation area on the valve seat face was decreased with an increase in valve cone angle. This effect was reversed on the seat sealing face with the separation area being increased with a larger valve cone angle. The 10 and 20 deg cone angle geometries showed fully separated flow from the seat sealing face with the passage flow being in regime IV for these cone angle configurations. For the 0 deg cone angle geometry, the flow reattached at the trailing edge of the seat sealing face which reflects transition to flow regime III for this valve geometry as concluded from the discharge coefficient measurements.

The influence of valve cone angle on passage flow characteristics can therefore be summarized as follows. A large cone angle suppresses flow separation from the valve seat face resulting in an improved flow performance in the low lift range. This influence of cone angle is reversed in the medium to high lift range since a small cone angle directs the flow toward the plane of the cylinder head, suppressing flow separation from the seat face. The flow performance of a small valve cone angle was therefore superior in the medium to high lift range as compared with a large valve cone angle. This behavior was consistent for all seat angles investigated. However, the effect became more significant as the valve seat angle was increased in that the flow separation from the valve seat face was most pronounced for large seat angle configurations.

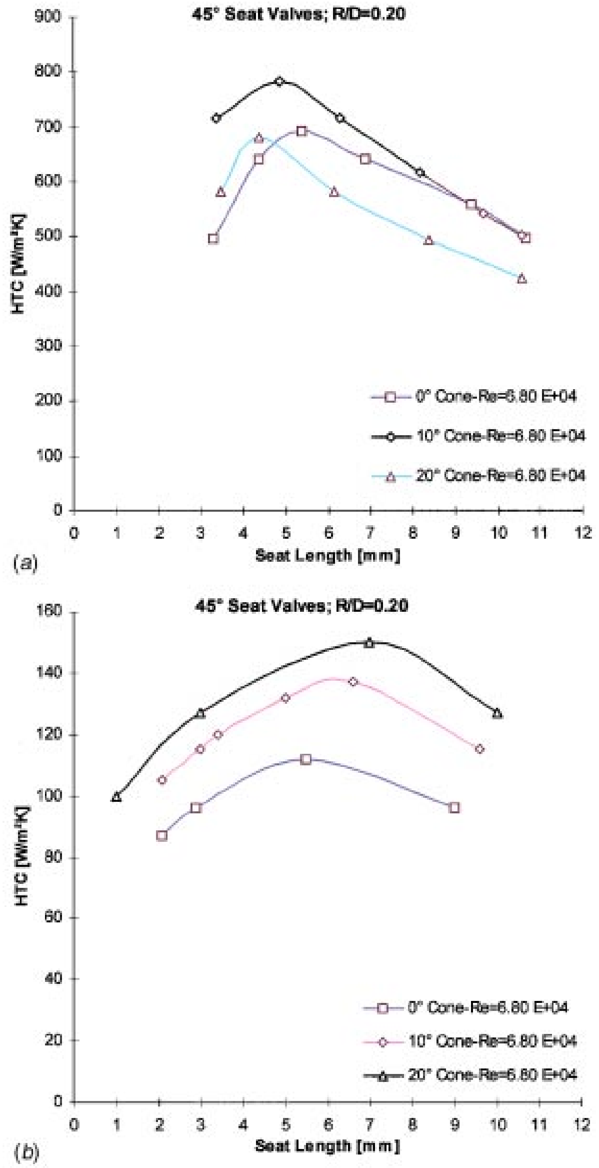

Fig. 3 (***a***) **Heat-transfer coefficient versus lift; valve seat;** $L/D = 0.06$; (***b***) **heat transfer coefficient versus lift; port seat;** $L/D = 0.06$

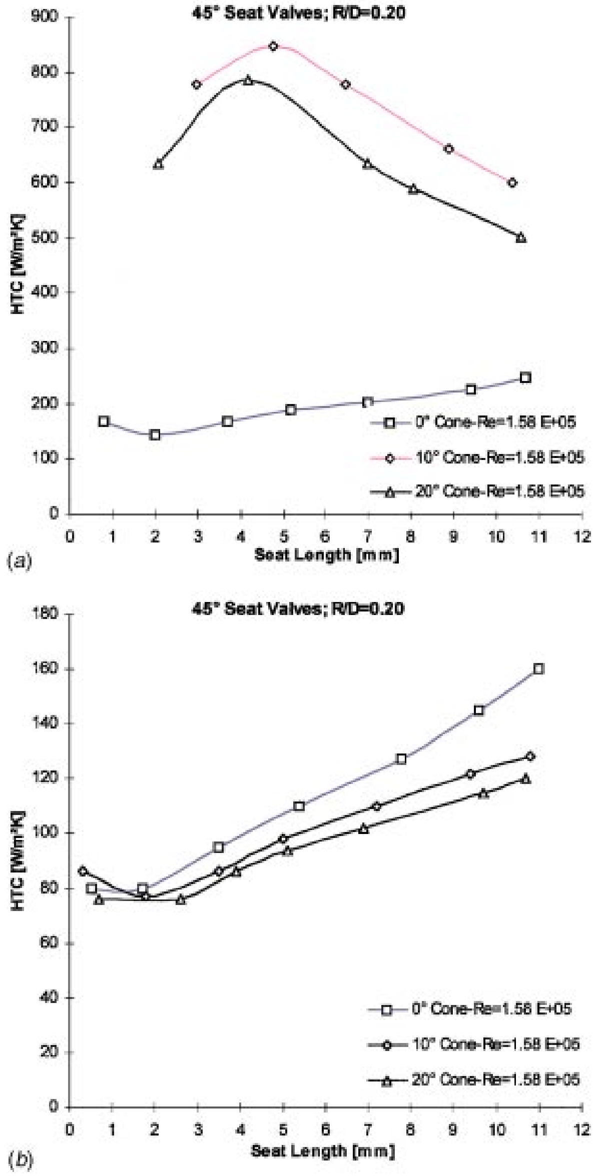

Fig. 4 (***a***) **Heat transfer coefficient versus lift; valve seat;** $L/D = 0.18$; (***b***) **heat transfer coefficient versus lift; port seat;** $L/D = 0.18$

Influence of Fillet Radius

Three fillet radius ratios ($R/D = 0.20$, 0.25, and 0.30) were investigated and their influence on the flow behavior was examined for the various valve seat and valve head configurations. Results for the discharge coefficients are presented in Fig. 5 and Fig. 6, respectively, for a 35 and 45 deg seat angle geometry, which reflect the general behavior of the influence of fillet radius on valve flow.

The results for the 35 deg seat angle, shown in Fig. 5, suggested that there was almost no influence of the fillet radius on the general discharge characteristics over the full range of lifts investigated. However, a small influence of the fillet radius was shown in the low lift range ($L/D < 0.08$) and therefore in the region where flow transitions were assumed for this geometry. A larger fillet radius resulted in slightly higher discharge coefficients since it was assumed to direct the flow in a more downward direction suppressing flow separation from the valve seat face at low lifts which results in slightly higher discharge coefficients. In the medium to high lift range, where the flow was attached to the valve seat face, the effect of fillet radius for the 35 deg seat valves was found to be insignificant and discharge coefficient curves almost matched for the various fillet radii investigated.

As was observed for the valve cone angle, the effect of fillet radius was most pronounced for the 45 deg valve seat geometries presented in Fig. 6 for a 0 deg valve cone angle geometry. For this geometry, a large fillet radius resulted in an improved flow performance in the lift range smaller than 0.05 with the influence almost diminishing in the medium to high lift range $0.12 < L/D < 0.25$. It was reasoned that a large fillet radius would not induce as much radial momentum in the flow as a small fillet radius, resulting in a decreased flow separation area from the upper valve face corner and consequently producing higher discharge coefficients in this range of lifts. The investigation of Vafidis and Whitelaw [9] showed that for a 45 deg seat geometry a small separation area was formed at the upper valve face corner at low lifts. The present results would suggest that the fillet radius had some influence on the flow separation from the upper valve seat face corner, which would therefore explain its pronounced effect

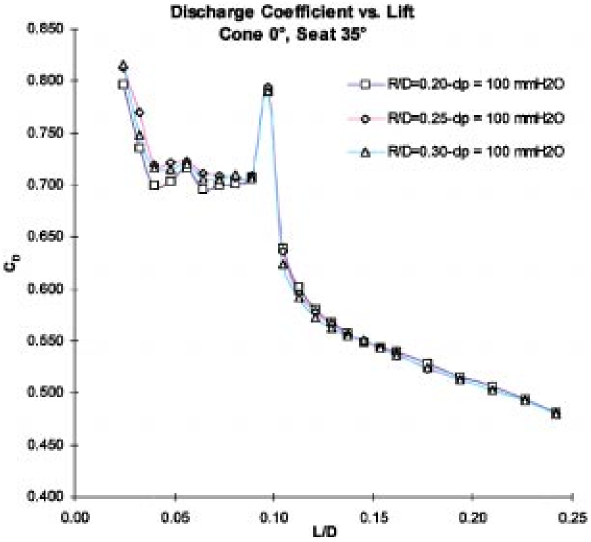

Fig. 5 Discharge coefficients versus lift; variation of fillet radius

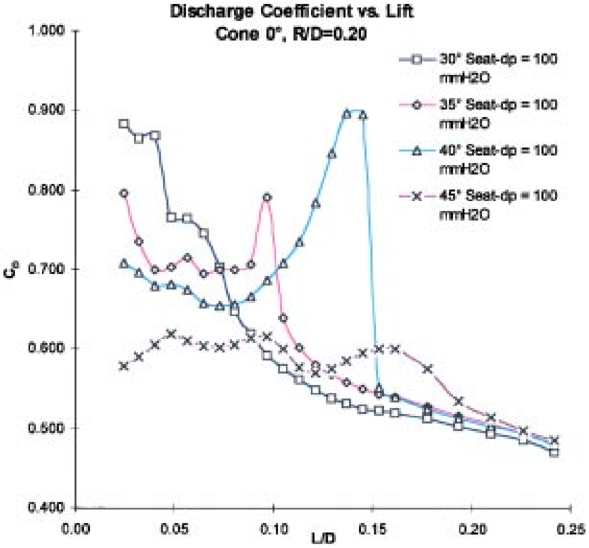

Fig. 7 Discharge coefficients versus lift; variation of seat angle

in the low lift range for only the 45 deg seat geometry. The small separation area formed at the upper corner of the valve seat face was therefore suppressed by the axially directed flow for a larger fillet radius resulting in an improved flow performance in the low to medium lift range for that valve configuration. In the high lift range, however, the differences for the various fillet radii were shown to be insignificant within the experimental error band.

Influence of Valve Seat Angle

The seat angle was varied between 30 and 45 deg in incremental steps of 5 deg in the present parametric study and results for discharge coefficients are shown in Fig. 7 and Fig. 8 for a 0 and 20 deg valve cone angle respectively.

A 30 deg seat angle generally showed very high discharge coefficients at low lifts (i.e., Fig. 8). In this lift range, the valve shoulder and the 30 deg seat formed the passage similar to a nozzle shape, which resulted in high discharge coefficients at low lifts as compared with the other seat geometries. Furthermore, it was assumed that any flow separation area formed at the upper valve face corner was decreased or suppressed for the 30 deg seat geometry as the cone angle was increased. This characteristic of the 30 deg seat geometry resulted in an improved flow performance at low lifts. A sudden drop in discharge coefficients occurred at a relatively low lift for a 30 deg seat ($L/D=0.05$ in Fig. 8), which was assumed to be caused by early flow separation from the shallow seat face. This transition point from flow regime I to IV was the only discontinuity observed in the discharge coefficient versus lift plot for a 30 deg seat as shown in Fig. 7 and Fig. 8 and hence the only change in flow pattern in the valve passage for this seat geometry. This characteristic resulted in a poor flow performance in the medium to high lift range for this valve configuration. The present findings would therefore support the recommendations of Tanaka [3] and Annand [6] to use a 30 deg valve seat angle for valves that are predominantly operated at low

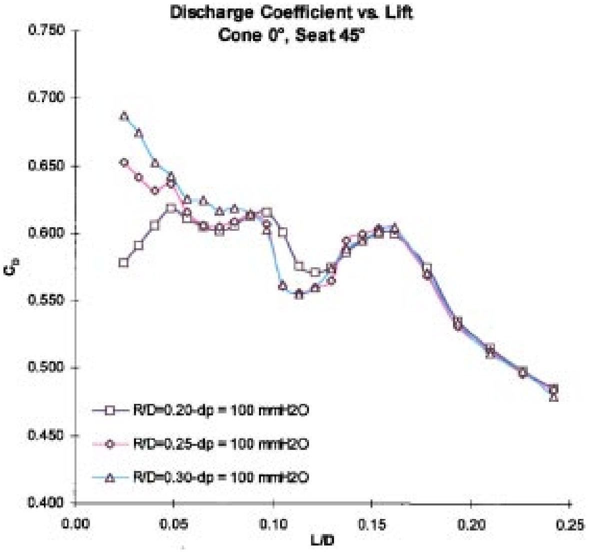

Fig. 6 Discharge coefficients versus lift; variation of fillet radius

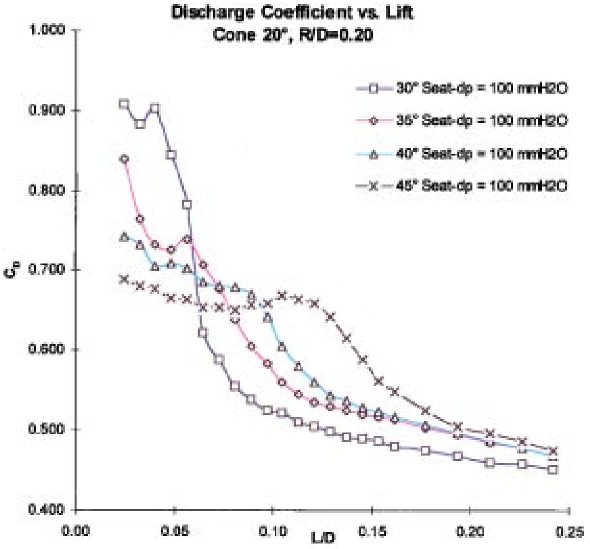

Fig. 8 Discharge coefficients versus lift; variation of seat angle

lifts due to their superior performance in this region, even though the range of effective operation for a 30 deg seat configuration was very small according to the current results.

For a 35 deg seat angle, the sudden drop in C_D observed for the 30 deg valve seat geometry at around $L/D=0.06$ was diminished and resulted in a sharp but continuous decrease in discharge coefficients for increasing valve lifts, as shown in Fig. 8 for a 20 deg valve cone angle. This characteristic was further relaxed as the seat angle was increased to 40 and 45 deg, which may be explained by the fact that the early separation from the seat face for the 30 deg seat angle was a sudden one and resulted in a sharp decrease in discharge coefficients, whereas for a larger seat angle this separation process was delayed and produced a continuous decrease in flow performance. The latter characteristic was indicated in Fig. 8 in that the transition from flow regime I to presumably IV for a 20 deg valve cone angle was considerably delayed as the valve seat angle was increased.

The recovery in discharge coefficient, which occurred at approximately $L/D=0.04$ for the 30 deg seat geometry having a flat valve shoulder, was also reflected for the 35 deg seat geometries with a 0 and 10 deg valve cone angle at $L/D=0.06$ as shown i.e., in Fig. 7 for a 0 deg valve cone angle. However, this temporary improvement in discharge coefficients at relatively low lifts was decreased for a 40 deg valve seat angle. The recovery in flow performance was assumed to be produced by an increased radially diverted flow in case of a small valve cone angle suppressing flow separation from the seat face which resulted in the effective flow area remaining constant over a small range of valve lifts. The effect was consequently most pronounced for a shallow seat and continuously decreased as the seat angle was increased.

The large increase in discharge coefficients in the medium lift range was observed for only the 35 deg and 40 deg seat angle geometries having a flat valve shoulder (0 deg valve cone angle), shown in Fig. 7, with valves for C_D exceeding 0.9 in case of a 40 deg seat angle, which could be of significant interest for practical inlet valve designs. This peculiar characteristic was therefore a combined effect of valve shoulder and valve seat angle and it was explained in Part I of this paper as a result of a delayed flow separation from the seat face leading to a significant pressure recovery in the valve passage and consequently high flow performance. However, the steep rise was followed by a sharp drop in flow performance with discharge coefficients being similar to the other seat geometries investigated at high lifts ($L/D>0.16$).

The 45 deg seat angle valve had a generally inferior performance in the low lift range and showed the transition to the four flow regimes as outlined in Part I of this paper for a 0 and 10 deg valve cone angle (see Fig. 7 for a 0 deg valve cone angle). The transition from flow regime I to II was delayed for the 10 deg valve cone angle as a result of suppressed flow separation from the valve seat face caused by the larger valve cone angle. The change to flow regime II was immediately followed by a further transition presumably to flow regime III at $L/D=0.14$ and continued to $L/D=0.18$ where the final state of flow was reached for this valve geometry.

The 20 deg cone angle showed only one clear transition for the 45 deg seat geometry (shown in Fig. 8 at $L/D=0.15$) in agreement with the findings of Tanaka [3]. The transition was therefore assumed to be from flow regime I to IV with suppression of flow regime II and III, which resulted in a smooth change in the slope of the discharge coefficient graph for increasing valve lifts.

The occurrence of the different flow regimes was verified from heat transfer data in the valve passage which are presented for the lift condition $L/D=0.12$ and $L/D=0.18$ in Fig. 9(*a*,*b*) and Fig. 10(*a*,*b*), respectively, for a 0 deg valve cone angle. The heat transfer results clearly reflected the pronounced effect of the valve seat angle on flow separation and the location of flow reattachment at low lifts. The results at the lift condition $L/D=0.12$ clearly illustrated that the reattachment location on the valve seat face moved in downstream direction for an increase in valve seat angle with the flow being fully separated for the 40 and 45 deg seat angle configuration, respectively. This effect of the seat geometry on flow separation was the opposite on the seat sealing face with the flow for the 30 and 35 deg being fully separated and therefore in flow regime IV for these seat configurations, which was in agreement with the flow interpretation from the discharge coefficient measurements. For the 40 and 45 deg seat geometry, the passage flow was in regime II and attached to the sealing face at passage exit at this lift condition. The 40 and 45 deg seat geometries represented the only seat configuration indicating flow regime II in the present investigation.

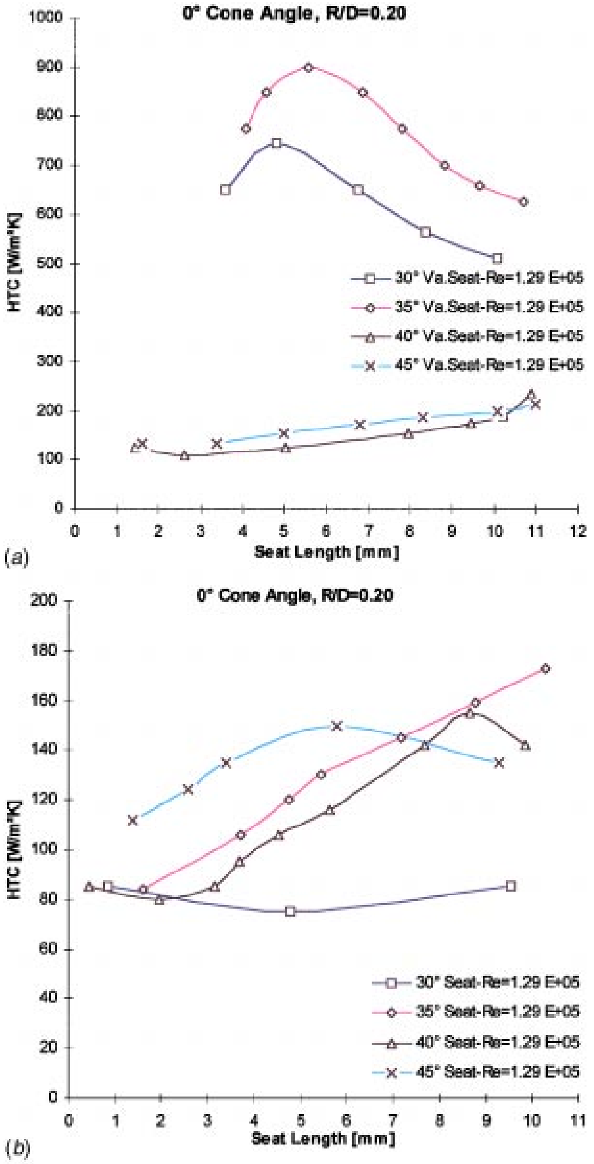

Fig. 9 (***a***) **Heat transfer coefficient versus lift; valve seat; *L*/*D* =0.12; (*b*) heat transfer coefficient Fig. versus lift; port seat; *L*/*D*=0.12**

The data presented for the lift configuration $L/D=0.18$ in Fig. 10(*a*,*b*) continued this trend of the influence of valve seat angle on flow separation. The reattachment location on the valve seat face moved in downstream direction as the seat angle was increased with the flow being fully separated from the valve seat face for the 45 deg seat configuration at this lift condition. The heat transfer coefficient distribution on the seat sealing face indicated fully

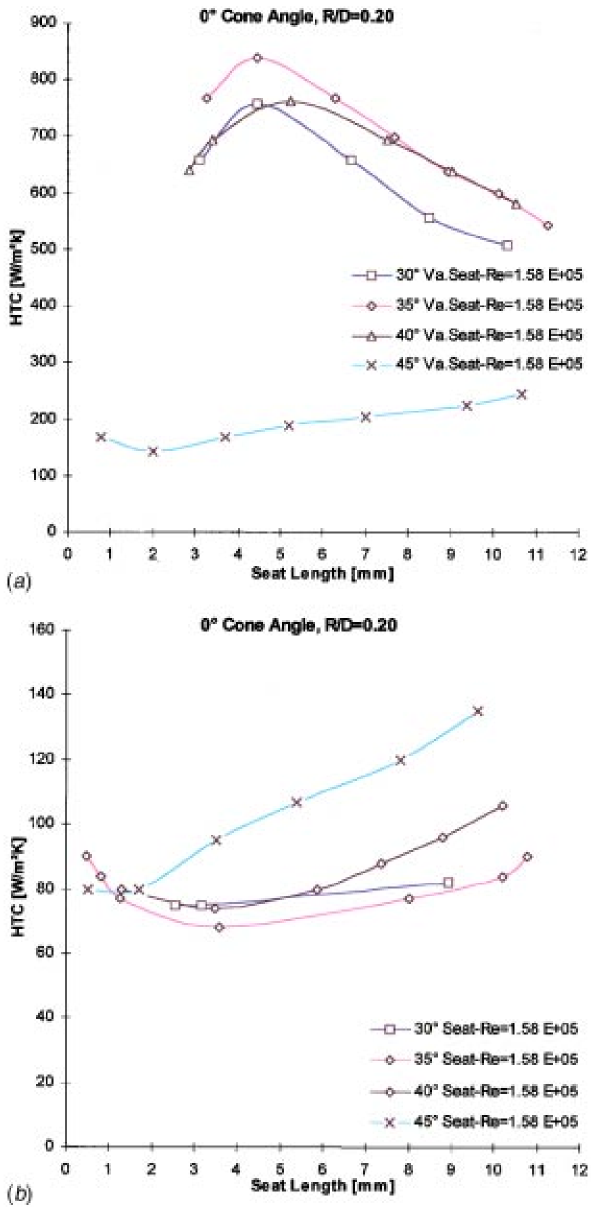

Fig. 10 (*a*) Heat transfer coefficient versus lift; valve seat; $L/D=0.18$; (*b*) heat transfer coefficient versus lift; port seat; $L/D=0.18$

separated flow for the 30, 35, and 40 deg seat geometries with the flow reattaching to the trailing edge for the 45 deg seat configuration.

The liquid crystal data therefore confirmed an early transition to flow regime IV for the 30 and 35 deg seat geometry with the flow being fully separated from the seat sealing face, which resulted in the inferior performance in the medium to high lift range for these seat configurations.

The variation in seat angle had the most pronounced effect on the discharge characteristic of all three valve parameters varied in the present investigation. In the low lift range discharge coefficients steadily decreased as the valve seat angle was increased from 30 to 45 deg, which was reversed in the high lift range (flow regime IV) when the flow started to reattach to the valve seat but was fully separated from the seat face. The four flow regimes were thought to be exhibited only by the 45 deg seat geometry having a 0 and 10 deg cone angle. Three discontinuities in the mass flow characteristic were solely observed for these seat geometries indicating the transition points to the four modes of flow. For the other valve geometries investigated in the current study, flow regime II and III were suppressed.

Conclusions

The present parametric study of the influence of valve geometry on inlet port flow showed that a variation of valve cone angle defined the flow into the passage over the full range of valve lifts with its influence decreasing towards high valve lifts. A small valve cone angle directed the flow radially, which suppressed flow separation from the seat sealing face in the medium to high lift range but enhanced the tendency of the flow to separate from the valve seat face. This influence resulted in a reversed effect at low lifts. A large valve cone angle induced an increased axial momentum in the flow and guided it into the passage, which resulted in high discharge coefficients in this lift region.

The fillet radius was found to have a minor influence on the flow characteristics for 30, 35, and 40 deg seat geometries. Some influence of the fillet radius was observed at low valve lifts and was most pronounced for a 45 deg seat geometry.

The influence of the valve seat angle on the valve performance characteristics was most significant of all the geometrical parameters varied. In the low lift range, discharge coefficients continuously decreased as the valve seat angle was increased. In the medium to high lift range this effect was shown to be reversed with a 45 deg seat geometry becoming the best performing geometry.

An interesting characteristic was observed for the 35 and 40 deg valve seat geometries having a flat valve shoulder with the discharge coefficients rising to relatively high values in the medium lift conditions making these geometries of significant interest for actual engine valve designs.

The current study presented the first large scale investigation of the valve geometry effects on port flow characteristics by combining experimental data from flow and heat transfer measurements to obtain highly detailed information about the influence of the geometrical parameters on the flow characteristics in and around the valve passage.

Nomenclature

C_D = discharge coefficient
d, Δ = differential
D = valve head diameter
D_p = inlet port diameter
h, HTC = heat transfer coefficient
L = valve lift
μ = kinematic viscosity
P = pressure
R = valve fillet radius
Re = Reynolds number $\{\rho D_p v_a/\mu\}$
v_a = velocity of inlet flow

References

[1] Luke, C. E., 1906, ''The Pressure Drop through Poppet Valves,'' Trans. ASME, **27**, pp. 232–301.
[2] Lewis, G. W., and Nutting, E. N., 1918, ''Airflow through Poppet Valves,'' NACA Report, No. 24.
[3] Tanaka, K., 1929 ''Airflow Through Suction Valve of Conical Seat,'' Aeronautical Research Institute Report, Tokyo Imperial University, Part 1, pp. 262; Part 2, p. 361.
[4] Wood, G. B., Hunter, D. U., Taylor, E. S., and Taylor, C. F., 1942, ''Air Flow through Intake Valves,'' Trans. of SAE, **50**, p. 212.
[5] Kastner, L. J., Williams, T. J., and White, J. B., 1963–1964, ''Poppet Inlet Valve Characteristics and their Influence on the Induction Process,'' Proc. Inst. Mech. Eng., **178**, Part 1, No. 36, pp. 955–975.
[6] Annand, W. J. D., 1969, ''Engine Breathing,'' Auto. Eng., **7**, pp. 50–55.
[7] Pope, J. A., 1967, ''Techniques Used in Achieving a High Specific Airflow for High-Output, Medium-Speed Diesel Engines,'' ASME J. Eng. Power, **89**, pp. 265–275.
[8] Bicen, A. F., and Whitelaw, J. H., 1983, ''Steady and Unsteady Flow through an Intake Valve,'' Imperial College, Mech. Eng. Dept. Report, No. FS/83/11.
[9] Vafidis, C., and Whitelaw, J. H., 1984, ''Steady and Pulsating Air Flow

Through a Stationary Intake Valve of a Reciprocating Engine,'' Imperial College, Mech. Eng. Dept. Report, No. FS/84/04.

[10] Bicen A. F., Vafidis C., and Whitelaw J. H., 1984, ''Steady and Unsteady Air Flow through an Intake Valve of a Reciprocating Engine,'' Proc. Symp. of Flows in IC Engines., pp. 47–55.

[11] Gosman A. D., and Ahmed A. M. Y., 1987, ''Measurement and Multidimensional Prediction of Flow in an Axisymmetric Port/Valve Assembly,'' SAE Technical Paper 870592.

[12] Weclas, M., Melling, A., and Durst, F., 1998, ''Flow Separation in the Inlet Valve Gap of Piston Engines,'' Prog. Energy Combust. Sci., **24**, No. 3, pp. 165–195.

[13] TRW Automotive Systems Ltd, 1997, private correspondence.

Measurements and Predictions of a Highly Turbulent Flowfield in a Turbine Vane Passage

R. W. Radomsky[1]

K. A. Thole
e-mail: thole@vt.edu

Mechanical Engineering Department,
Virginia Polytechnic Institute and State University,
Blacksburg, VA 24061-0238

As highly turbulent flow passes through downstream airfoil passages in a gas turbine engine, it is subjected to a complex geometry designed to accelerate and turn the flow. This acceleration and streamline curvature subject the turbulent flow to high mean flow strains. This paper presents both experimental measurements and computational predictions for highly turbulent flow as it progresses through a passage of a gas turbine stator vane. Three-component velocity fields at the vane midspan were measured for inlet turbulence levels of 0.6%, 10%, and 19.5%. The turbulent kinetic energy increased through the passage by 130% for the 10% inlet turbulence and, because the dissipation rate was higher for the 19.5% inlet turbulence, the turbulent kinetic energy increased by only 31%. With a mean flow acceleration of five through the passage, the exiting local turbulence levels were 3% and 6% for the respective 10% and 19.5% inlet turbulence levels. Computational RANS predictions were compared with the measurements using four different turbulence models including the k-ε, Renormalization Group (RNG) k-ε, realizable k-ε, and Reynolds stress model. The results indicate that the predictions using the Reynolds stress model most closely agreed with the measurements as compared with the other turbulence models with better agreement for the 10% case than the 19.5% case.
[S0098-2202(00)00804-X]

Introduction

As highly turbulent flow exiting the combustor of a gas turbine engine passes through a downstream airfoil passage, this flow experiences high rates of strain as a result of acceleration and streamline curvature. Airfoil surface heat transfer measurements, particularly on the pressure side, have local convection coefficients for a highly turbulent flow as much as two times that for low turbulence conditions (Ames [1] and Radomsky and Thole [2]). One of the goals for the turbine industry is to predict heat loads on the turbine airfoils through the use of either a boundary layer or a full Reynolds-averaged Navier-Stokes (RANS) code. Prior to making boundary layer and, ultimately, heat transfer predictions, it should be proven that the core flow inside the passage can be accurately predicted since it would provide an external boundary condition for the boundary layer calculations.

Although predicting these turbulence levels might be thought of as a first step, there is a lack of experimental data used for verifying these computational predictions. This scarceness in quality benchmark data is particularly evident at turbulence levels relevant to those exiting a gas turbine combustor, which can be as high as 20 to 30% (Goldstein et al. [3]). This paper presents both experimental measurements and computational predictions of a highly turbulent flow convecting through a turbine vane passage at inlet turbulence levels of 0.6%, 10%, and 19.5%. In the passage the flow encounters strong streamline curvature and an acceleration where the exit velocities are five times faster than the inlet velocities. The experimental measurements include all three components of mean and fluctuating velocity quantities measured with a laser Doppler velocimeter. RANS calculations were completed using four different turbulence models including the following: standard k-ε, RNG k-ε, realizable k-ε, and Reynolds stress model.

Past Studies

The effect of streamline curvature on the structure of the turbulent boundary layer flows was extensively discussed in a review by Bradshaw [4]. In this discussion, Bradshaw noted that eddy viscosity models tend to underestimate the effects of the secondary strain on the Reynolds stresses since the coefficients of the primary and secondary strains are modeled to be equal. Bradshaw [4] noted that extra rates of strain, such as streamline curvature, had a large impact on the Reynolds stresses and suggested that a multiplier of ten be placed in front of the extra strain rate term to account for the increased turbulent stress.

Launder et al. [5] performed an analysis on a boundary layer flow over a curved surface using a full Reynolds stress closure model. By combining the effects of the generation as well as the pressure-strain effects Launder et al. [5] showed an eight fold amplification of the secondary strain term, which is close to the multiplier of ten suggested by Bradshaw [4]. Their analysis suggests that the full Reynolds stress closure models give a better representation of the effects of extra rates of strain, such as streamline curvature.

Durban and Speziale [6] examined the assumption of local isotropy in the presence of mean strain. Analysis of the transport equation for the dissipation tensor showed that for the local isotropy to be a valid assumption, the ratio of the turbulent time scales to the mean rate of strain should be small, $Sk/\varepsilon \ll 1$. This ratio is rarely satisfied for many applications and particularly for turbomachinery flows where both high levels of turbulence and streamline curvature are present.

Lakshminarayana's [7] review on computation of turbomachinery flows is in agreement with the above discussion in that for flows with high streamline curvature a full Reynolds stress closure model should give improved results over two-equation k-ε models. Lakshminarayana [7] suggested that the isotropic assumptions in the two-equation models do not allow accurate flowfield predictions when there is streamline curvature. Lou and Lakshminarayana [8] predicted the effects of streamline curvature on wall turbulence for flow in 90 and 180 deg ducts. Their results showed the standard k-ε model failed to predict the damping of the turbu-

---

[1] Current address: United Technologies Research Center, 411 Silver Lane, East Hartford, CT 06108.

Contributed by the Fluids Engineering Division for publication in the JOURNAL OF FLUIDS ENGINEERING. Manuscript received by the Fluids Engineering Division August 30, 1999; revised manuscript received July 10, 2000. Associate Technical Editor: P. Bearman.

lence near the convex wall and failed to predict the enhancement of the turbulence near the concave wall. The Reynolds stress model, with the standard transport equation for dissipation, was able to predict the suppression of the turbulence near the convex wall but still somewhat underestimated the increased turbulence near the concave wall.

With respect to streamline curvature, flow through a turbine vane passage can be compared to that through a curved duct. The difference between these two flows, however, is that there is an added strain due to the flow acceleration through the passage in the case of a turbine vane. Another difference is that higher inlet turbulence levels are being considered for the turbine vane case as compared to those in curved wall simulations. These differences warrant an evaluation of the various turbulence models for high turbulence flows through a turbine vane passage.

Experimental Facility and Instrumentation

For these studies, a first stage gas turbine vane geometry was scaled up by a factor of nine to allow for high measurement resolution. The vane test section is shown schematically in Fig. 1. Although the inlet Reynolds number was matched for the engine operating at altitude conditions, the Mach number was not matched. Prior to predicting the more complicated case of compressible flow, however, assessing turbulence models at incompressible conditions is needed.

The construction and development of the scaled-up stator vane test section have been previously documented by Kang et al. [9], Kang and Thole [10] and Radomsky and Thole [11]. The test section consists of a central vane with leading edges of two adjacent vanes to give two vane passages. The initial portion of the outer sidewall exactly matches the profile of an adjacent vane. At the point where an adjacent vane geometry stops for the outer vane, the flexible wall was positioned such that the pressure distribution on the central vane matched an inviscid pressure distribution numerically predicted for a two-dimensional periodic cascade at low-speed conditions. As will be shown later in this paper, tailboards and sidewall bleeds insured periodic flow in the two passages surrounding the central vane. The thickness of each endwall boundary layer at one chord upstream of the vane was 9% of the total span. A description of the turbine vane geometry and operating conditions is given in Table 1.

An active-grid turbulence generator, described in detail by Bangert et al. [12], was placed at 1.9 chords upstream of the vane stagnation. The turbulence generator used high velocity jets blowing in both the upstream and downstream directions to generate turbulence levels between 10% and 20% measured at 0.33 chords upstream of the vane stagnation location. The integral length scale at 0.33 chords upstream for the 10% and 20% cases were $\Lambda_x/P = 0.11$ and 0.12, respectively, and were uniform across the span to within 4%.

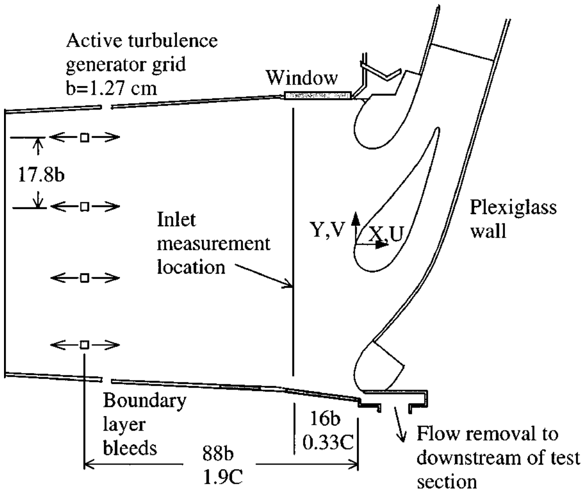

Fig. 1 Schematic of stator vane test section

Table 1 Geometrical and flow conditions for the stator vane geometry

Scaling factor	9
Scaled-up chord length	59.4 cm
Pitch / chord	0.77
Span / chord	0.93
Re_{in}	2.30×10^5
Inlet and exit angles	0° and 78°

For the results reported in this paper, the velocity field measurements were taken at the vane mid-span from mid-pitch to mid-pitch around the central vane. A Cartesian coordinate system, with the origin at the flow stagnation point, as shown in Fig. 1, was maintained for all measurements. Flowfield measurements, which included all three velocity components and rms velocities, were made with a two-component laser Doppler velocimeter (LDV) with digital burst correlator processors. For the 0.6% freestream turbulence experiments, 10,000 data points were taken for the mean and rms statistics. For the 10% and 19.5% freestream turbulence experiments, 25,000 data points taken in coincidence mode were averaged to determine the mean, rms values, and Reynolds shear stress. The measured velocities were corrected for bias errors using the residence time weighting correction scheme. Autocorrelation length scales were measured with a single sensor hot-wire having a length of 1.5 mm, and diameter of 4 microns. A complete description of the measurement techniques is given in Radomsky and Thole [11].

The uncertainty estimates were made using the procedures outlined by Moffat [13]. The precision uncertainties for the 10% and 20% inlet turbulence levels were estimated using a 95% confidence interval. The precision uncertainty for the mean velocities was 0.8% for both the 10% and 20% turbulence levels while the bias uncertainty for both was estimated to be 1%. The precision uncertainty for the rms of the velocity fluctuations was 2.0% for the 20% inlet turbulence case while the uncertainties in the measured Reynolds shear stress was estimated to be 12%. The precision uncertainty for the rms of the velocity fluctuations was 2.2% for the 10% inlet turbulence case while the uncertainties in the measured Reynolds shear stress was estimated to be 11%. For the hot-wire measurements, the precision uncertainty for the 20% case for the mean and rms velocities were 3.5% and 4.8%, respectively, while the uncertainty in the integral length scale was estimated to be 12.4%.

Computational Methods and Turbulence Models

The RANS calculations were performed using a pressure-based flow solver whereby the pressure and velocity are coupled using the Semi-Implicit Method for Pressure-Linked Equations (SIMPLE) algorithm (Patankar [14]). Second-order discretization was used for the turbulence and RANS equations. The solver chosen for this study was from the commercial package FLUENT/UNS (FLUENT 5 [15]) providing solution adaptive grid capabilities and offered a number of different turbulence models for comparisons.

The two-dimensional computational domain used in this investigation is illustrated in Fig. 2. The inlet boundary condition was placed one chord length upstream of the vane stagnation where the incoming velocity field is unaffected by the presence of the vane. The outlet boundary location, determined through a number of CFD studies to insure that the location did not affect the calculations, was placed at one and a half chord lengths downstream of the trailing edge of the vane. Periodic boundary conditions, whereby the domain was split at the flow stagnation location, were used everywhere except for the inlet, outlet, and vane sur-

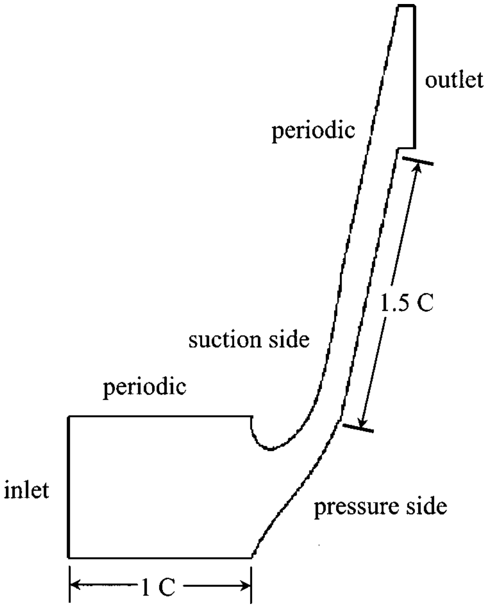

Fig. 2 Computational domain modeling a single passage of a vane cascade

face. The inlet boundary condition was set to a uniform velocity to match the turbine inlet Reynolds number given in Table 1. The boundary condition at the exit was specified as an outflow boundary condition, which assumes that the flow gradients are small. A no-slip boundary condition was imposed at the vane surface.

A hybrid-meshing scheme, available in GAMBIT (FLUENT 5, Inc., 1998) was used in which quadrilateral cells were placed near the surface of the vane and tetrahedral cells were used in the freestream region. The near-wall region, which was not the focus of this study, was modeled in all of the stator vane simulations using non-equilibrium wall functions given by Kim and Choudhury [16]. The near-wall cell was located between $30 < y^+ < 60$ to insure proper usage of the wall functions. A grid sensitivity study was performed in which a series of increasingly finer meshes were examined. Figure 3 shows the normalized total velocity, $|U|/U_{\mathrm{inlet}}$, and turbulent kinetic energy, k/U_{inlet^2}, at a location just downstream of the flow stagnation location at $X/P = 0.06$ for grid sizes ranging in size from 12,000 to 154,000. Very little difference is observed in either the total velocity or turbulent kinetic energy for the cases with greater than 31,000 cells. The results presented in this paper for all the turbulence models are for the larger mesh with 154,000 cells. Convergence for the cases presented in this paper was typically achieved after 6000 iterations. Numerical uncertainty, in terms of the convergence criteria, was assessed by comparing the lift coefficient for what was considered to be a converged case and comparing that with a case with more iterations. The lift coefficient was determined by integrating the vertical force around the airfoil. The difference in lift coefficients between these two cases was 0.07% for over 600 iterations.

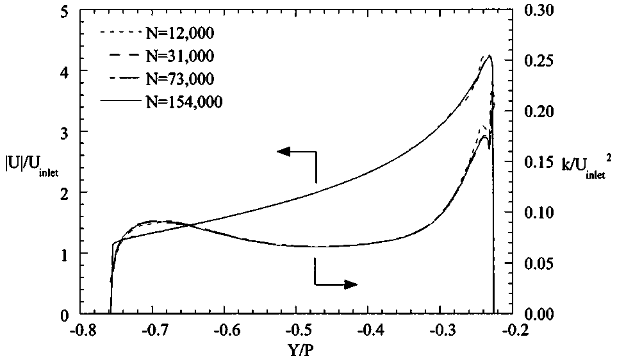

Fig. 3 Normalized total velocity, $|U|/U_{\mathrm{inlet}}$, and turbulent kinetic energy, k/U^2_{inlet}, for different grid sizes at $X/P=0.06$ for the 19.5% case

As discussed earlier, several turbulence models were compared for predicting the high turbulence convecting through the turbine vane passage. The turbulence models used were the k-ε model (Launder and Spalding [17]), RNG k-ε model (Yahkot et al. [18]), realizable k-ε model (Shih et al. [19]), and the Reynolds stress model (Launder et al. [5]).

The standard k-ε, RNG k-ε, and realizable k-ε models are similar in that the models use an eddy viscosity and mean velocity gradients to calculate the Reynolds shear stress as in the following equation

$$-\rho\overline{u_i' u_j'}=\mu_t\left(\frac{\partial U_i}{\partial x_j}+\frac{\partial Uj}{\partial x_i}\right)-\frac{2}{3}\left(\rho k+\mu_t\frac{\partial U_i}{\partial x_j}\right)\delta_{ij} \tag{1}$$

The eddy viscosity is calculated for both the k-ε model and the RNG k-ε model at high Reynolds models using the following relation

$$\mu_t=\rho C_\mu\frac{k^2}{\varepsilon} \tag{2}$$

where C_μ is a constant value of 0.09 for the k-ε model and 0.0845 for the RNG k-ε model. Note that no changes were made to any of the model constants when using these models for the predictions presented in this paper. At low Reynolds number conditions an additional differential equation is solved for the turbulent viscosity. The difference between the k-ε and RNG k-ε model is that for the RNG k-ε model the constants were optimized to give improved performance. In addition, the RNG k-ε model has a higher order expansion term in the transport equation for the turbulent dissipation rate, defined below

$$R=\frac{C_\mu\rho\eta^3(1-\eta/\eta_0)}{1+\beta\eta^3}\frac{\varepsilon^2}{k} \tag{3}$$

In Eq. (3), η is the ratio of the time scales, $\eta\equiv S\,k/\varepsilon$, previously discussed. This additional term affects the amount of destruction of dissipation in the transport equation. For small values of η, $R\rightarrow 0$, but for large values of η, η will exceed η_0, and the R term becomes negative increasing the overall dissipation rate and decreasing the turbulent viscosity. Since the Reynolds stress is computed using Eq. (1), it should then be expected that in regions of high strain rates the RNG k-ε model would predict lower Reynolds stresses than would the k-ε model.

The realizable k-ε model used in this study, developed by Shih et al. [19] also calculates the Reynolds shear stress based on a turbulent viscosity and the mean velocity gradients. The difference for this model is that there are imposed constraints such that the normal stress is always positive ($\overline{u'^2}>0$) and that the Schwarz inequality is not violated. From Eq. (1) it can be easily seen that when a large strain rate occurs a negative normal stress can result. To satisfy these constraints, a variable form of C_μ that is a function of the mean strain rate, turbulent kinetic energy and dissipation rate was developed. Shih et al. [19] also used a different form of the dissipation equation that was developed from the dynamic equation of the mean-square vorticity fluctuation at large turbulent Reynolds numbers. In this formulation, the production of dissipation is proportional to the mean rate of strain. The form of the dissipation transport equation used in the realizable k-ε model is thought to provide a better representation of the spectral energy transfer.

The Reynolds stress model used in this study is in the form given by Launder et al. [5]. To reduce numerical instabilities, the turbulent diffusion term, D_{ij}^T, was modeled following the suggestion of Lien and Leschziner [20]. The pressure strain term was modeled using a second order technique suggested by Speziale et al. [21] since it was suggested to be more accurate for streamline curvature flows. The final term requiring modeling is the dissipation tensor, which is modeled assuming the dissipative motion is isotropic. The dissipation transport equation used for the Reynolds stress model is the same as that used in the standard k-ε model.

Computational Benchmark in a 180 Degree Duct

As a validation of the computational code used in the present study, simulations of flow through a 180 deg duct were compared to experimental data by Monson and Seegmiller [20] at a $\mathrm{Re}_{\mathrm{inlet}} = 1\times10^5$. This particular benchmark served to validate the computational models for a flow having strong streamline curvature. To be consistent with the stator vane simulations, a hybrid-meshing scheme was employed. To accurately resolve the separation region near the end of the turn, however, the first grid point near the wall was located at $y^+=1$ and a two-layer zonal model was used (Wolfstein [23]). Note that no separation occurs for the turbine vane case. The inlet boundary condition was specified at four channel widths upstream of the turn. The inlet conditions used were tabulated mean and turbulence values reported by Monson and Seegmiller [22] from their experimental measurements. The outflow boundary condition was located twelve channel widths downstream of the end of the turn. After performing grid sensitivity studies, the resulting mesh contained 210,000 cells. Results from these simulations are shown in Figs. 4(*a*) through 4(*c*).

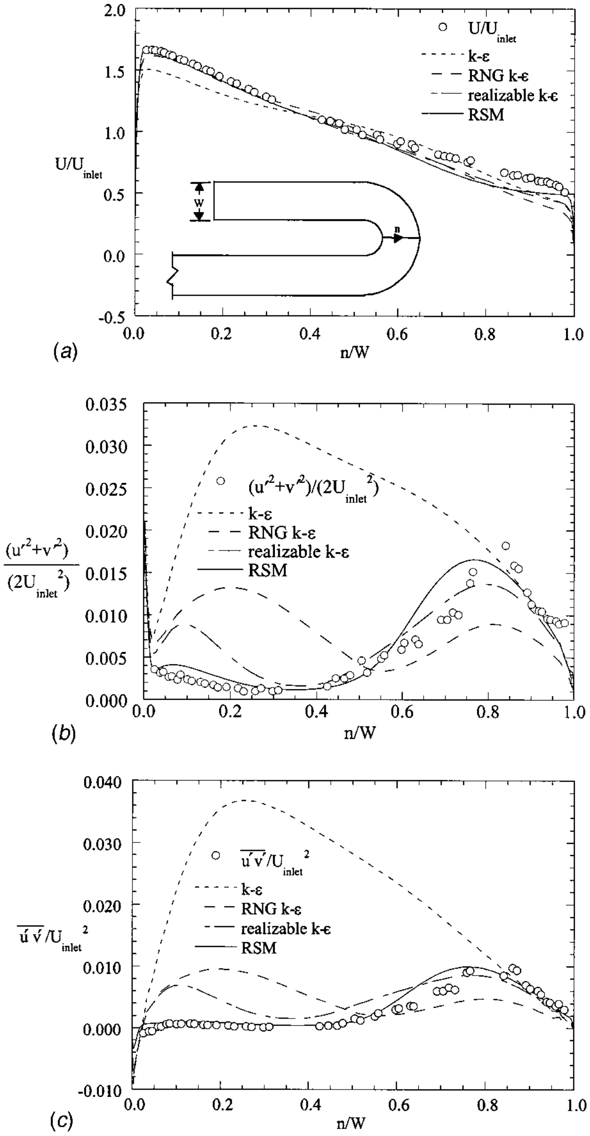

Fig. 4 (*a*) **Comparison of measured and predicted streamwise velocity profiles, U/U_{inlet}, (Monson and Seegmiller [22]) at the 90 degree location in the turn; (*b*) comparison of measured and predicted normalized turbulent kinetic energy, $(u'^2+v'^2)/U_\infty^2$ (Monson and Seegmiller [22]) at the 90 degree location in the turn; (*c*) comparison of measured and predicted normalized Reynolds shear stress, $\overline{u'v'}/U_{\mathrm{inlet}}^2$ (Monson and Seegmiller [22]) at the 90 degree location in the turn**

Figure 4(*a*) shows the mean component of the streamwise velocity taken at the 90 deg location, which is halfway through the turn. Note that n/W is the normal coordinate measured outward from the inner convex wall. As can be seen, with the exception of the standard k-ε model, the turbulence models are able to predict the high velocity region near the inner wall. The mean velocity near the outer wall is underpredicted by each of the turbulence models, which is similar to the results by Lou and Lakshminarayana [8] who also performed simulations on the U-duct but at a higher Reynolds number. The difference between measurements and predictions near the outer wall may be the result of three-dimensional effects in the experimental measurements that are not being modeled in these two-dimensional predictions.

Figures 4(*b*) and 4(*c*) show the measured and predicted turbulent kinetic energy and Reynolds shear stress at the 90 deg location. The standard k-ε model greatly over-predicts the magnitude of both the turbulent kinetic energy and shear stress. The RNG k-ε model fails to predict the damping of both the turbulent kinetic energy and Reynolds shear stress near the convex inner wall and underestimates the turbulence increase near the outer concave wall. The realizable k-ε model results do indicate a suppression and an increase of the turbulent kinetic energy for the convex and concave wall, respectively. As shown in other studies, the Reynolds stress model was able to accurately predict both the damping near the inner wall as well as the enhancement near the outer wall. Figures 4(*a*)–4(*c*) give validation that the code used in this study predicts results similar to that already published for flows with streamline curvature alone. The next step is to determine whether the turbulence models can adequately predict the turbulence for flow with the additional strain of flow acceleration, as in the turbine vane passage.

Inlet Conditions for the High Turbulence Turbine Vane Studies

The inlet turbulence conditions for the computations at one chord upstream were determined from measured values at one-third chord upstream (optical access for the measurements was not available at one chord). The turbulent quantities, ε and k, were set at one-chord upstream by performing trial-and-error simulations until the predicted values at one-third of a chord upstream matched the experimental measurements.

The dissipation rate was determined from measured energy spectra of the streamwise velocity fluctuations. Typical energy spectra for the streamwise fluctuations, measured at one-third chord upstream at both turbulence levels, are shown in Fig. 5 along with a comparison to the von Karman spectra and the unified relation given by Mayle et al. [24]. The measured spectra agree well with both correlations and show the existence of a well-defined inertial subrange. The inertial subrange region was used to calculate the dissipation rate by performing a curve fit to the following formula (Hinze [25] and Ames [1])

$$E_1(\kappa_1)=1.62(18/55)\varepsilon^{2/3}\kappa_1^{-5/3} \tag{4}$$

Table 2 gives the measured and predicted turbulent kinetic energy

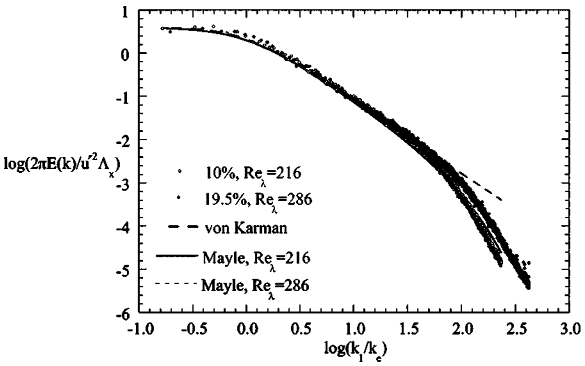

Fig. 5 Comparison of measured and predicted one-dimensional energy spectra at one-third chord upstream of the vane stagnation

values and dissipation rates at one chord ($X/C=-1$) and one-third chord. ($X/C=-0.33$) upstream of the vane for both 10% and 19.5% inlet turbulence levels.

To determine the turbulent kinetic energy (k), measurements were taken across the entire pitch of the two flow passages surrounding the central vane. Figure 6(a) shows the normalized rms levels of the streamwise (u'/U_{inlet}), cross-stream (v'/U_{inlet}), and the spanwise (w'/U_{inlet}) velocity fluctuations as well as the normalized turbulent kinetic energy measured at one-third chord upstream of the vane stagnation for the high turbulence case. The average turbulence level at this location is 19.5%. All three rms levels are close to the same value with only slightly lower spanwise fluctuations, w'/U_{inlet}. The maximum deviations relative to the average for the streamwise, cross-stream, and spanwise fluctuations were 7.5%, 10%, and 6.9%, respectively. The maximum deviation of the streamwise rms velocities to the average value across the vertical span of the turbine vane was 2.8% for the 19.5% case. Figure 6(a) also illustrates that the rms levels of the streamwise fluctuations measured using a hot-wire agree well with the LDV measurements. The turbulent kinetic energy levels given as the inlet boundary conditions at one chord upstream for all of the turbulence models are reported in Table 2. Figure 6(a) shows that for the given ε and k value at one chord upstream, the predicted k value for all of the models agrees with that measured at 0.33 chords upstream. Figure 6(b) shows the same information as in Fig. 6(a) but for the lower turbulence level case of 10%. Again, it can be seen that the measured and predicted turbulent kinetic energy agrees well at this location.

A comparison between the measured and predicted normalized turbulent kinetic energy and dissipation rate approaching the vane stagnation are illustrated in Figs. 7(a) and 7(b) for the 19.5% turbulence case. Although the initial conditions specified for the turbulence models at one chord upstream are higher than at the 0.33 chord location, the majority of the reduction occurs well

Table 2 Measured and predicted inlet turbulence conditions

	$X/C=-1$	$X/C=-0.33$
Measured 10% inset	No optical access	$k/U_{\text{inlet}}^2=0.015$ $\varepsilon C/U_{\text{inlet}}^3=0.0098$
Predicted 10% inlet	$k/U_{\text{inlet}}^2=0.026$ $\varepsilon C/U_{\text{inlet}}^3=0.027$	$k/U_{\text{inlet}}^2=0.015$ $\varepsilon C/U_{\text{inlet}}^3=0.0098$
Measured inlet 19.5%	No optical access	$k/U_{\text{inlet}}^2=0.0584$ $\varepsilon C/U_{\text{inlet}}^3=0.0519$
Predicted 19.5% inlet	$k/U_{\text{inlet}}^2=0.134$ $\varepsilon C/U_{\text{inlet}}^3=0.245$	$k/U_{\text{inlet}}^2=0.0584$ $\varepsilon C/U_{\text{inlet}}^3=0.0519$

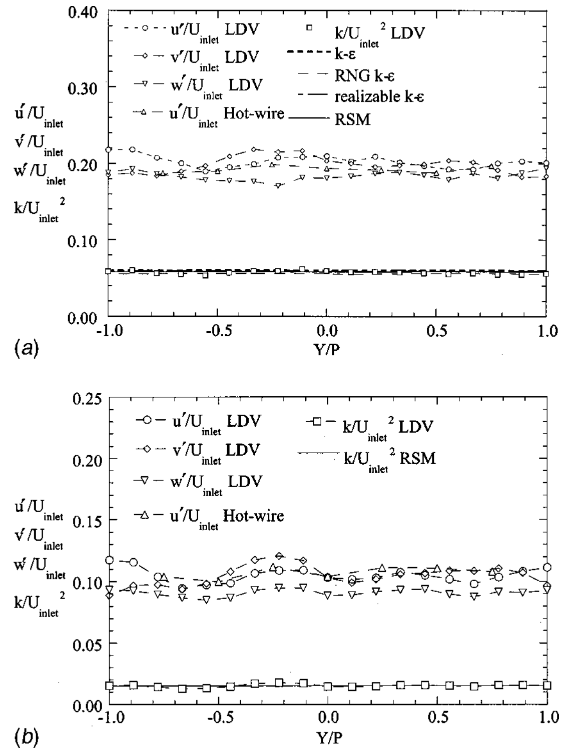

Fig. 6 (a) RMS levels of the velocity fluctuations in addition to the computed and predicted normalized turbulent kinetic energy distribution, k/U_{inlet}^2, at the inlet to the test section at $X/C=-0.33$ for the 19.5% case; (b) RMS levels of the velocity fluctuations in addition to the computed and predicted normalized turbulent kinetic energy distribution, k/U_{inlet}^2, at the inlet to the test section at $X/C=-0.33$ for the 10% case

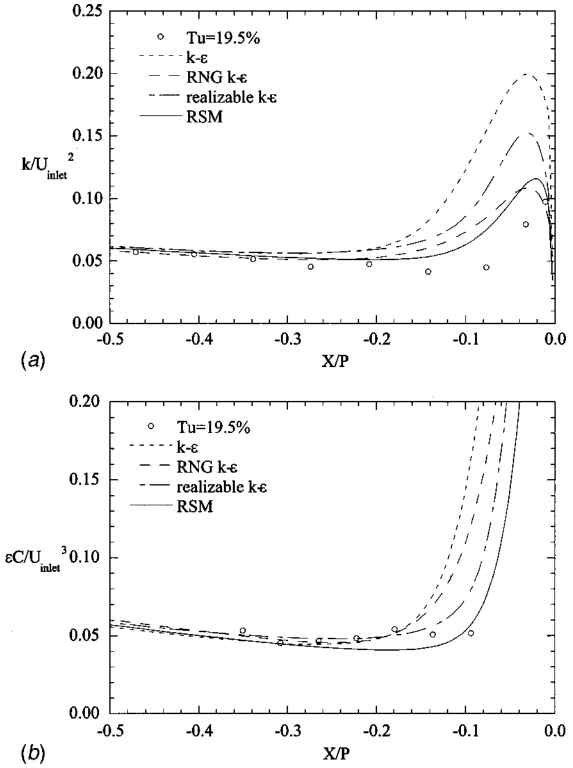

Fig. 7 (a) Comparison of measured and predicted normalized turbulent kinetic energy, k/U_{inlet}^2, approaching the vane stagnation for the 19.5% case; (b) comparison of measured and predicted dissipation rate, $\varepsilon C/U_{\text{inlet}}^3$, approaching the vane stagnation for the 19.5% case

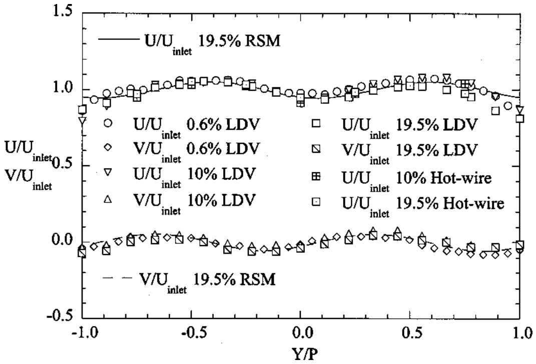

Fig. 8 Profiles of normalized streamwise, U/U_{inlet}, and pitchwise, V/U_{inlet}, velocity at the inlet to the test section at $X/C=-0.33$

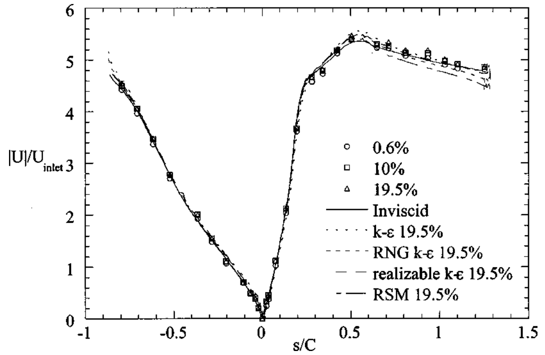

Fig. 9 Measured and predicted normalized freestream velocity, $|U|/U_{\mathrm{inlet}}$, around the vane at several turbulence levels

upstream of the test section. At 0.33 chords, both the turbulent kinetic energy and dissipation rate are relatively flat but increase when approaching the vane. Note that the dissipation rates are only reported up to $X/P=-0.2$ because the velocity is quickly decreasing and the turbulence levels are very high making the hot-wire measurements invalid. All four turbulence models predict a rapid increase in the turbulent kinetic energy, but with varying peak levels. The RNG k-ε and Reynolds stress turbulence models predict more realistic peaks when comparing with the experimental measurements. Both experimental measurements and predictions show that the dissipation rate is essentially constant up to $X/P=-0.2$. Closer to the stagnation point, all four turbulence models overpredict the kinetic energy and predict a dramatic increase in the dissipation rate.

Figure 8 shows the streamwise and pitchwise mean velocity profiles at low and high freestream turbulence levels across the two flow passages around the central vane. Even though the generated turbulence levels from the active-grid are very high, the mean flowfield is unaffected. Figure 8 also shows the predicted mean velocity profiles using the Reynolds stress model. Although not shown, at this streamwise location, all of the turbulence models agree well with each other and the experimental measurements. Near the edges of the test section, the measurements deviate slightly from the predictions due to the development of boundary layers on the sides of the test section. This measurement location is upstream of a suction slot that is designed to remove the upstream boundary layer. Figures 6–8 show that at the inlet, good agreement has been achieved for both the mean and turbulent conditions between the experiment and CFD simulations. The following sections will discuss the results for the highly turbulent flowfield in the core region surrounding the stator vane.

Comparison of Experimental Data With Predictions From the Turbulence Models

The inviscid velocity distribution around the vane surface, calculated from the total and local static pressure measurements, as compared with the inviscid and viscous predictions is given in Fig. 9. The measured distribution on the pressure surface ($s/C<0$) agrees well with the inviscid prediction as well as on the suction surface ($s/C>0$) indicating that the outer wall placement was correct. The only difference between the inviscid and viscous predictions occurs on the trailing edge of the suction side with the viscous models predicting slightly lower velocities than observed in the measurements. This can be attributed to the flow slowing down in the wake region for the viscous cases whereas in the inviscid simulations, no wake occurs.

Figures 10(*a*)–(*d*) compare the normalized total velocity contours between experimental measurements at 0.6% and 19.5% and the CFD predictions at the 19.5% turbulence level. The flowfield measurements were performed between the mid-pitch of the two passages surrounding the central vane. To allow for an easier comparison with predictions, the pitch (Y/P) position for the data was numerically shifted to show contour levels between two adjacent vane stagnation points. The smoothness of these contours indicates the good periodicity between the two passages. The measured total velocity contours at an inlet turbulence level of 19.5% (Fig. 10(*b*)) is similar to that of the low inlet turbulence condition (Fig. 10(*a*)) with the exception that there is a larger high speed region on the suction side of the airfoil for the high turbulence. This larger high speed region is due to the transition of the boundary layer occurring earlier when the turbulence level is higher causing a thickening of the boundary layer and a higher speed inviscid region. Figures 10(*c*) and 10(*d*) show total velocity contours for the k-ε and Reynolds stress models for the 19.5% case. The total velocity contours for the RNG k-ε and realizable k-ε models are very similar to that of the k-ε model predictions. All four turbulence models predict the low speed region near the stagnation region as well as the acceleration as the flow enters the

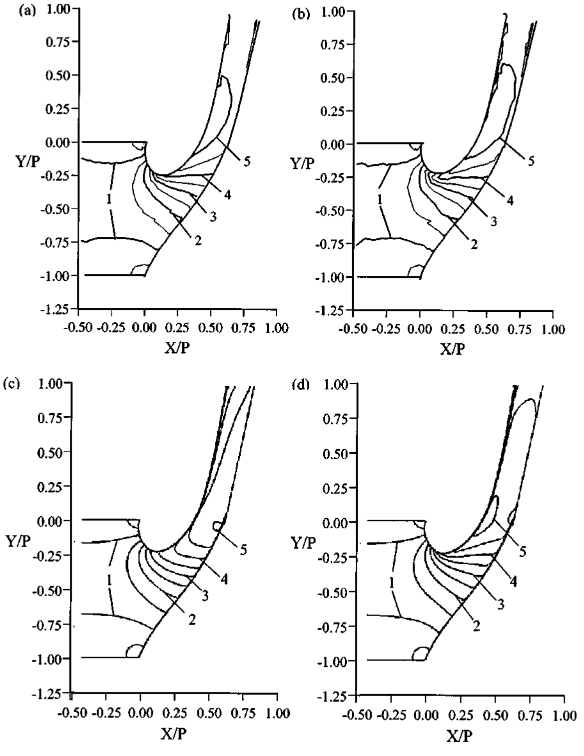

Fig. 10 Comparison of normalized total velocity, $|U|/U_{\mathrm{inlet}}$, contours between (*a*) 0.6% experiment, (*b*) 19.5% experiment, (*c*) 19.5% k-ε, and (*d*) 19.5% RSM

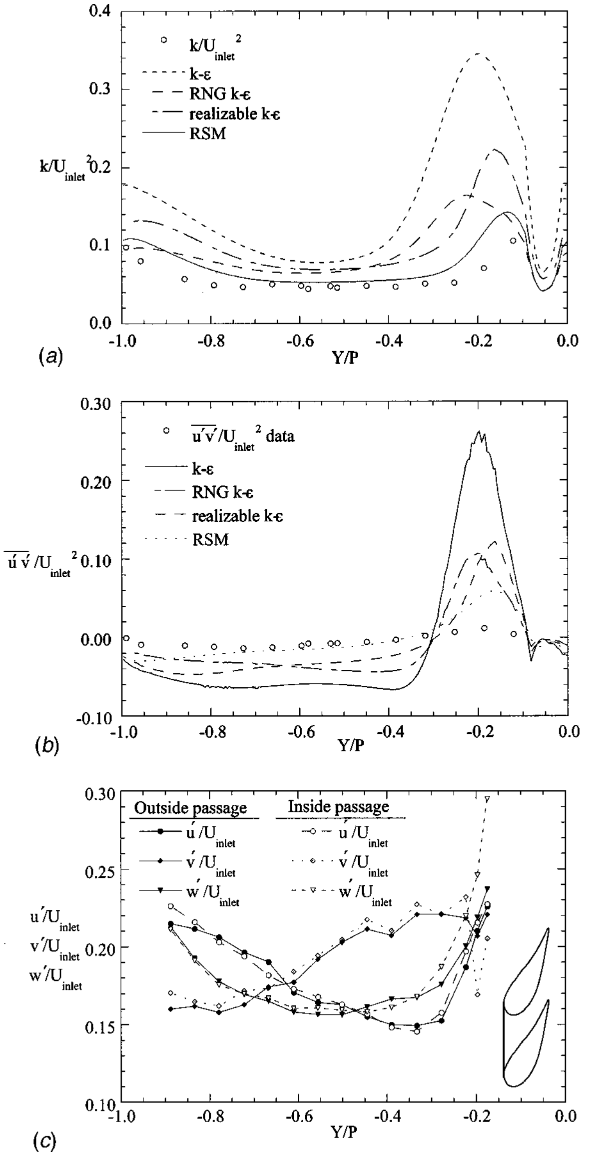

Fig. 11 (*a*) **Normalized turbulent kinetic energy, k/U_{inlet}^2, at a line at the geometrical stagnation for the 19.5% case; (*b*) normalized Reynolds shear stress, $\overline{u'v'}/U_{inlet}^2$, at a line at the geometrical stagnation for the 19.5% case; (*c*) comparison of streamwise, u'/U_{inlet}, pitchwise, v'/U_{inlet}, and spanwise, w'/U_{inlet}, turbulence levels at a line between geometrical stagnation points for the 19.5% case**

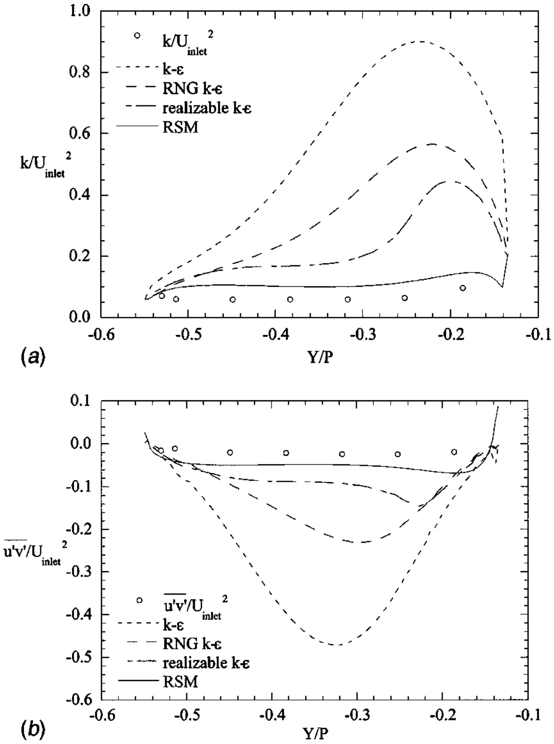

Fig. 12 (*a*) **Comparison between measured and predicted normalized turbulent kinetic energy, k/U_{inlet}^2, at $X/P=0.295$ for the 19.5% case; (*b*) comparison between measured and predicted normalized Reynolds shear stress, $\overline{u'v'}/U_{inlet}^2$, at $X/P=0.295$ for the 19.5% case**

passage. Downstream of the vane shoulder, however, the three eddy viscosity models predict that the high speed fluid moves away from the suction side of the vane. In the experimental measurements, as well as the Reynolds stress model, the highest speed fluid remains adjacent to the suction side of the vane.

Figures 11(*a*)–11(*b*) compare normalized turbulent kinetic energy (k/U_{inlet^2}) and Reynolds shear stress ($\overline{u'v'}/U_{inlet^2}$) across the pitch at the geometrical stagnation location ($X/P=-0.011$). The geometrical stagnation location is the farthest upstream axial position of the vane. At this location, the Reynolds stress model adequately predicts the levels of turbulent kinetic energy in the center of the passage whereas the eddy viscosity models greatly overpredict the levels. Similar to the curved channel, there is an overprediction of the turbulent kinetic energy near the surfaces of the turbine vanes ($Y/P\sim-1$ and -0.2) due to the acceleration along the pressure side. Although it is not shown here, the predictions for the low freestream turbulence case of 0.6% indicated very high turbulence levels for the *k*-ε and the RNG *k*-ε models. These high levels of turbulence result from the high straining rates and are in disagreement with the experimental measurements for the 0.6% turbulence case. As discussed previously, the *k*-ε and the RNG *k*-ε eddy viscosity models use a Boussinesq approximation for calculating the normal stresses from the turbulent kinetic energy. This approximation gave negative values of the streamwise normal stresses ($\overline{u'^2}$) because of the high turbulent viscosity and high strain rates. These unrealistic values demonstrate the limitations of the standard *k*-ε and RNG *k*-ε models for turbomachinery flows. The realizable *k*-ε model, developed to insure positive values for the Reynolds stresses, performed only slightly better than the other eddy viscosity models. The Reynolds stress model overpredicts the peak in the turbulent kinetic energy by approximately 20%.

Figure 11(*b*) compares measured and predicted normalized Reynolds shear stresses ($\overline{u'v'}/U_{inlet^2}$) across the pitch at the geometrical stagnation location. All four models overpredict the region of positive shear stress near the suction surface ($Y/P=-0.2$), with the standard *k*-ε model showing the largest disagreement with the measurements and the Reynolds stress model showing the closest agreement with the measured values. The three eddy viscosity models predict negative shear stress values in the middle of the passage where the experiments and Reynolds stress model show very low positive values of $\overline{u'v'}/U_{inlet^2}$.

Figure 11(*c*) shows the measured normalized rms levels of the streamwise, u'/U_{inlet}, pitchwise, v'/U_{inlet}, and spanwise, w'/U_{inlet}, fluctuating velocities at the geometrical stagnation point for the 19.5% turbulence case. At this location, the strong flow acceleration has caused considerable anisotropy in the rms levels of the fluctuating velocities. The streamwise acceleration near the suction surface causes a decrease in the streamwise fluc-

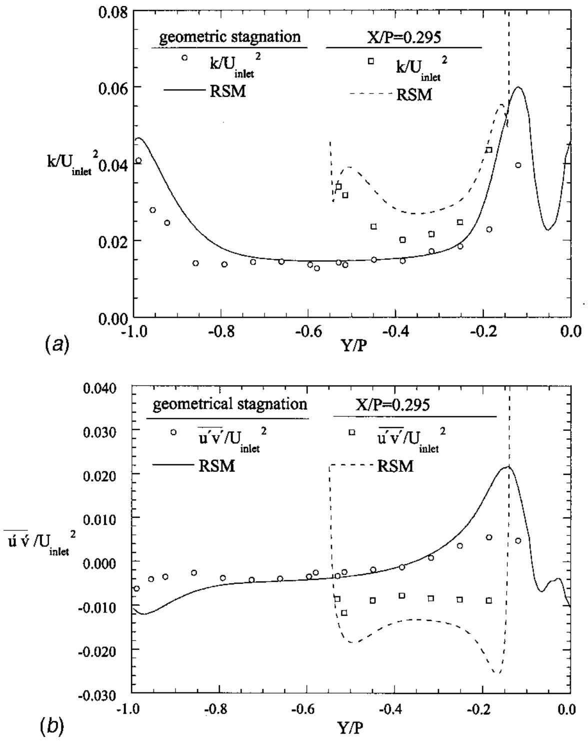

Fig. 13 (*a*) Comparison between measured and predicted normalized turbulent kinetic energy, k/U_{inlet}^2, at the geometric stagnation and $X/P=0.295$ for the 10% case; (*b*) comparison between measured and predicted Reynolds shear stress, $\overline{u'v'}/U_{\mathrm{inlet}}^2$, at the geometric stagnation and $X/P=0.295$ for the 10% case

tuations. A redistribution of the turbulent energy results in increase in the pitchwise fluctuations at the same location. An increase in the spanwise fluctuations is observed near the vane surfaces.

Figures 12(*a*) and 12(*b*) show the comparisons of turbulent kinetic energy and shear stress at a location of $X/P=0.295$ for the 19.5% case. Again, the Reynolds stress model provides the best agreement with the measurements. As in Figs. 11(*a*)–11(*b*), all of the eddy viscosity models greatly overpredict the magnitude of the turbulent kinetic energy and Reynolds shear stress.

A comparison of the measured and predicted turbulent kinetic energy, k/U_{inlet^2}, and Reynolds shear stress, $\overline{u'v'}/U_{\mathrm{inlet}^2}$, for the 10% case at the vane geometric stagnation location ($X/P=-0.011$) and at $X/P=0.295$ are shown in Figs. 13(*a*) and 13(*b*). As with the 19.5% case, good agreement with experimental measurements is observed in the middle of the passage at the geometrical stagnation point. The Reynolds stress model slightly overpredicts the turbulent kinetic energy and Reynolds shear stress near the vane surface. Farther into the vane passage, the Reynolds stress model overpredicts the magnitude of both the turbulent kinetic energy and Reynolds shear stress. However, the agreement between computation and experiment is better for the 10% case than it was for the 19.5% case.

Comparison of 10% and 19.5% Turbulence Levels

Examination of Figs. 11–13 show that all of the eddy viscosity models (k-ε, RNG k-ε, and the realizable k-ε) overpredict the turbulent kinetic energy and Reynolds shear stress. The largest overprediction occurs near the convexly-curved suction surface of the airfoil, similar to the overpredictions for the convexly-curved wall for the U-duct simulations. It is also evident that the Reynolds stress model provides much better agreement with the experimental measurements than either of the eddy viscosity models.

Figures 14(*a*)–14(*d*) compare the measured and predicted normalized Reynolds shear stress, $\overline{u'v'}/U_{\mathrm{inlet}}^2$, for the 10% and 19.5%, respectively. Comparison of the experimental measurements and predictions at the different inlet turbulence levels show that although the magnitudes are different, the sign of the Reynolds stress are in agreement. Positive values of the Reynolds shear stress are found near the geometrical stagnation location on the suction side of the vane, while negative values of shear stress occur further downstream in the passage center. The lower turbulence level of 10% has much lower values of the Reynolds stress as compared to the 19.5% case. The lower values of Reynolds stress can be explained by examining the production term for $\overline{u'v'}$ given as

$$P(\overline{u'v'})=u'^2\left(-\rho\frac{\partial V}{\partial X}\right)+v'^2\left(-\rho\frac{\partial U}{\partial Y}\right) \tag{5}$$

Equation (5) shows that for this two-dimensional flowfield the production of the Reynolds shear stress has two terms that are functions of mean velocity gradients and normal stresses. The nearly identical mean flowfield between the 10% and 19.5% cases indicate that the derivates of the velocity field should be nearly identical. Thus, the difference in production between these two cases is caused by different magnitudes of the velocity fluctuations. Equation (5) shows that the lower turbulence levels will result in less production of Reynolds shear stress for the lower turbulence condition. Both terms in Eq. (5), indicate that near the geometrical stagnation point on the suction side of the vane, production of positive Reynolds stress occurs due to the flow turning down and around the suction surface. Moving into the passage, both terms in Eq. (5) show that negative Reynolds stress will be produced as the flow is being turned up through the passage. Near the trailing edge of the vane, only small mean velocity gradients

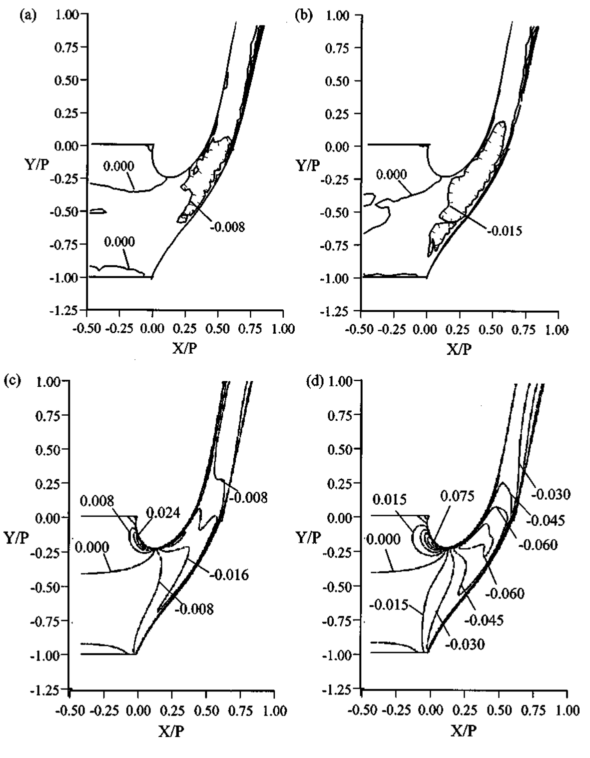

Fig. 14 Comparison of normalized Reynolds shear stress contours, $\overline{u'v'}/U_{\mathrm{inlet}}^2$, between (*a*) 10% experiment, (*b*) 19.5% experiment, (*c*) 10% RSM, and (*d*) 19.5% RSM

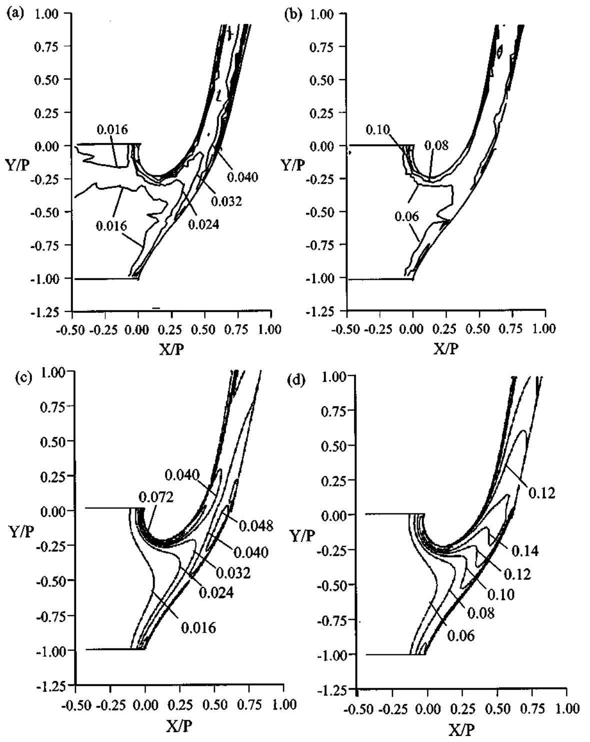

Fig. 15 Comparison of normalized turbulent kinetic energy contours, k/U_{inlet}^2, between (*a*) 10% experiment, (*b*) 19.5% experiment, (*c*) 10% RSM, and (*d*) 19.5% RSM

exist and the production of Reynolds shear stress reduces to zero. The Reynolds stress model predictions, shown in Figs. 14(*c*) and 14(*d*), indicate the same sign but larger magnitudes as compared with the experiments for both the 10% and 19.5% cases.

Figures 15(*a*)–15(*d*) compare the normalized turbulent kinetic, k/U_{inlet^2}, between experimental measurements and the Reynolds stress model predictions at 10% and 19.5%, respectively. Significant differences exist between the development of the turbulent kinetic energy at the different turbulence levels. The experimental measurements for the 19.5% case show that the turbulent kinetic energy levels increase by as much as 31% in the vane passage. At the lower inlet turbulence level of 10%, the turbulent kinetic energy through the passage increases by 130%, which is significantly higher than for the 19.5% case. Although the turbulent kinetic energy is significantly increasing through the passage, it is important to recognize that the mean velocity has accelerated up to five times the inlet velocity. This means that the turbulence level at the passage exit has decreased to approximately 3% for the 10% inlet turbulence case and 6% for the 19.5% inlet turbulence case.

The difference in the measured turbulent kinetic energy contours between the two turbulence levels can be explained by examining the mechanism for turbulent kinetic energy production given as

$$P(k)=u_{\text{rms}}^2\left(-\rho\frac{\partial U}{\partial X}\right)+\overline{u'v'}\left(-\rho\frac{\partial U}{\partial Y}-\rho\frac{\partial V}{\partial X}\right)+v_{\text{rms}}^2\left(-\rho\frac{\partial V}{\partial Y}\right) \tag{6}$$

As a result of the identical mean flow field and geometry, the ratio of turbulent kinetic energy production between the two high turbulence cases can be examined by comparing the measured Reynolds stresses. The gradients in Eq. (6) were evaluated from the CFD solution, which is a reasonable assumption given the good agreement between measurements and predictions, at locations where direct measurements of the Reynolds stresses were taken. The CFD solution was used because of the higher resolution thereby giving more accurate gradients than the experimental measurements. Figures 16(*a*) and 16(*b*) show contours of turbulent kinetic energy production for the 10% and 19.5% using the CFD mean velocities and the measured Reynolds stresses. For both these cases the largest production occurs near the shoulder of the vane passage in the high acceleration region. Over the majority of the flowfield, the 19.5% case has nearly three times the production as compared to the 10% case. The measurements indicate, however, that the 19.5% case has only a 31% increase in the turbulent kinetic energy through the vane passage, while the 10% case has a much larger increase at 131%. This difference can be explained by the fact that the dissipation at the inlet for the 19.5% case was about six times that for the 10% case. The higher value of the dissipation appears to counteract the higher production rates causing only a slight rise in the turbulent kinetic energy in the vane passage for the 19.5% case as compared to the 10% case.

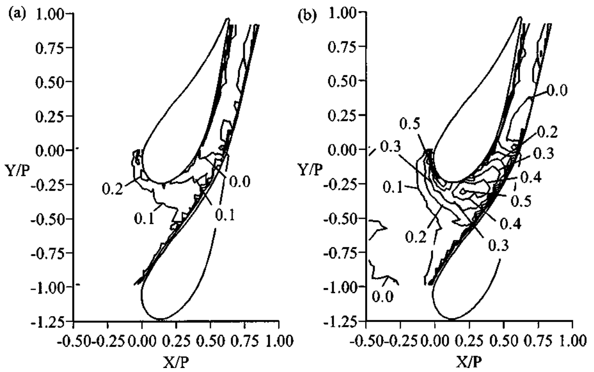

Fig. 16 Comparison of normalized turbulent kinetic energy production, $P(k)C/\rho U_{\text{inlet}}^3$, contours between (*a*) 10% experiment and (*b*) 19.5% experiment

The Reynolds stress model predictions shown in Fig. 15(*d*) for the 19.5% case give an overprediction of the turbulent kinetic energy in the vane passage by as much as 125%. At the lower turbulence level of 10%, shown in Fig. 15(*c*), the turbulent kinetic energy in the passage is overpredicted by only 25%. The Reynolds stress model predictions indicate a 160% and 125% increase in turbulent kinetic energy through the vane passage as compared to the measured 130% and 31% increase for the 10% and 19.5% cases, respectively.

Although the Reynolds stress model performed better than the eddy viscosity models, the levels of turbulent kinetic energy and shear stress were overpredicted. One possible explanation is that the Reynolds stress model used in this investigation used the same transport equation for the dissipation rate as the standard k-ε model. The limitations of this transport equation for the dissipation rate have been discussed in Lou and Lakshminarayana [26] and Shih et al. [19]. In this transport equation, the production of dissipation is set equal to the production of turbulent kinetic energy. Figures 17(*a*) and 17(*b*) show contours of a normalized dissipation rate for the 19.5% turbulence case. In the transport equation for the dissipation rate used in the realizable k-ε model, the production of dissipation is proportional to the mean strain rate of the flow. Comparisons of dissipation contours between the realizable k-ε and Reynolds stress model showed that the Reynolds stress model had dissipation levels much less than the realizable k-ε prediction. The use of a different transport equation for the dissipation rate, such as the one used in the realizable k-ε model, could produce better agreement with the experimental measurements.

Another possible reason for the over prediction of the turbulent kinetic energy involves the constants used in the RSM. These constants were evaluated for flows not too far removed from simple shear flows. The validity of these constants for flows with

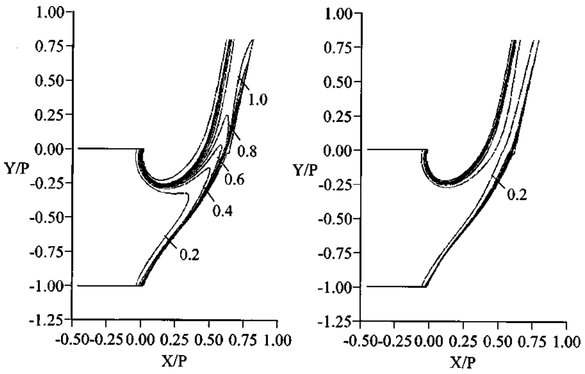

Fig. 17 Comparison of normalized dissipation rates, $\varepsilon C/U_{\text{inlet}}^3$, at 19.5% between (*a*) realizable *k*-ε model and (*b*) RSM

high freestream strain rates at elevated turbulence levels is not known. Supporting this reason is the fact that the results from the 10% case do indicate much better agreement with the measurements than the 19.5% case.

Conclusions

Experimental measurements in a stator vane passage at high freestream turbulence levels of 10% and 19.5% were compared to RANS predictions using a variety of turbulence models. The experimental measurements indicated increases in the turbulent kinetic energy of the flow as the flow convected through the turbine vane passage with much larger increases for the 10% turbulence case as compared with the 19.5% case. This difference was attributed to the fact that the dissipation was much higher for the 19.5% case.

The eddy viscosity models greatly overpredicted the turbulent kinetic energy in the vane passage as a result of the overproduction of turbulent kinetic energy in the high acceleration region resulting in additional strain. On the suction side of the airfoil where the surface is convex, the standard *k*-ε and RNG *k*-ε model produced physically unrealistic negative values for the streamwise normal stresses. The realizable *k*-ε model, developed to insure positive values of the normal stresses, performed slightly better than the other eddy viscosity models. The Reynolds stress model provided the best agreement with the experimental measurements; however, the Reynolds stress model overpredicted the turbulent kinetic energy by 125% for the 19.5% case. Considerably better agreement was achieved between measurements and predictions for the lower turbulence case of 10%. At this turbulence level, the Reynolds stress model overpredicted the turbulent kinetic energy by only 25%.

The relatively poor predictions, particularly at the high turbulence levels, may be the result of several issues. First, the current transport equation in the RSM gave very low values for the dissipation rate in the vane passage as compared to the realizable *k*-ε model. The use of a Reynolds stress model with an improved transport equation for the dissipation rate, such as the one used in the realizable *k*-ε model, may give results closer to the experimental measurements. Second, the constants used in the RSM model were evaluated from simple shear flows not too far removed from equilibrium. The better agreement for the 10% case as compared with the 19.5% case supports this reasoning.

Acknowledgments

The authors would like to thank the Department of Energy's Advanced Gas Turbine Systems Research Program for supporting this work and Dr. Lawrence Golan for serving as the contract monitor. The authors would also like to thank Pratt & Whitney, Florida for supplying the turbine vane geometry and the National Science Foundation (CTS-9996224) for their support.

Nomenclature

C = true chord length
$E_1(\kappa_1)$ = spectra for streamwise fluctuations
f = frequency
k = turbulent kinetic energy, $k=0.5(u'^2+v'^2+w'^2)$
n = distance normal to the convex curved surface
P = turbine vane pitch
R = radius of curvature for a streamline
rms = root-mean-square of the fluctuations
$\mathrm{Re}_{\mathrm{in}}$ = Reynolds number based on chord length and incident velocity
S = freestream strain rate
U_{inlet} = upstream incident velocity
$\overline{u'v'}$ = Reynolds shear stress
u, v, w = local mean velocities along a streamline
U, u' = mean and rms of fluctuating velocity in the *X*-direction
V, v' = mean and rms of fluctuating velocity in the *Y*-direction
w' = rms of fluctuating velocity in the *Z*-direction
W = passage width for the curved channel simulation
X = fixed coordinate parallel with the inlet flow where origin is at the flow stagnation
Y = fixed coordinate in the cross-pitch direction
Z = fixed coordinate in the spanwise direction
ε = turbulent dissipation obtained from Eq. (1)
κ_1 = wavenumber, $\kappa_1=2\pi f/U$
Λ_x = streamwise integral length scale
λ = Taylor microscale
ν = kinematic viscosity
σ = Stefan-Boltzman constant
η = timescale ratio

References

[1] Ames, F. E., 1995, ''The Influence of Large-Scale High-Intensity Turbulence on Vane Heat Transfer,'' ASME J. Turbomach., **119**, pp. 23–30.
[2] Radomsky, R. W., and Thole, K. A., 1998, ''Effects Of High Freestream Turbulence Levels and Length Scales on Stator Vane Heat Transfer,'' ASME Paper No. 98-GT-236.
[3] Goldstein, R. J., Lau, K. Y., and Leung, C. C., 1983, ''Velocity and Turbulence Measurements in Combustion Systems,'' Exp. Fluids, **1**, pp. 93–99.
[4] Bradshaw, P., 1973, ''Effects of Streamline Curvature on Turbulent Flow,'' AGARDograph 169.
[5] Launder, B. E., Reece, J. C., and Rodi, W., 1975, ''Progress in the development of a Reynolds-stress Turbulence Closure,'' J. Fluid Mech., **68**, pp. 537–566.
[6] Durbin, P. A., and Speziale, C. G., 1991, ''Local Anisotropy in Strained Turbulence at High Reynolds Numbers,'' ASME J. Fluids Eng., **113**, pp. 707–709.
[7] Lakshminarayana, B., 1991, ''An Assessment of Computational Fluid Dynamic Techniques in the Analysis and Design of Turbomachinery-The 1990 Freeman Scholar Lecture,'' ASME J. Fluids Eng., **113**, pp. 315–352.
[8] Luo, J., and Lakshminarayana, B., 1997, ''Prediction of Strongly Curved Turbulent Duct Flows with Reynolds Stress Model,'' AIAA J., **35**, No. 1, pp. 91–98.
[9] Kang, M., Kohli, A., and Thole, K. A., 1999, ''Heat Transfer and Flowfield Measurements in the Leading Edge Region of a Stator Vane Endwall,'' ASME J. Turbomach., **121**, No. 3, pp. 558–568.
[10] Kang, B., and Thole, K. A., 1999, ''Flowfield Measurements in the Endwall Region of a Stator Vane,'' ASME J. Turbomach., **122**, pp. 458–466.
[11] Radomsky, R. W., and Thole, K. A., 1999, ''Flowfield Measurements for a Highly Turbulent Flow in a Stator Vane Passage,'' accepted for ASME J. Turbomach.
[12] Bangert, B., Kohli, A., Sauer, J., and Thole, K. A., 1997, ''High Freestream Turbulence Simulation in a Scaled-Up Turbine Vane Passage,'' ASME Paper No. 97-GT-51.
[13] Moffat, R. J., 1998, ''Describing Uncertainties in Experimental Results,'' Experimental and Fluid Science, **1**, pp. 3–17.
[14] Patankar, S. V., 1980, *Numerical Heat Transfer and Fluid Flow*, Hemisphere, Washington D.C.
[15] FLUENT User's Guide, 1998, Release 5.0, Fluent Inc., Lebanon, N. H.
[16] Kim, S. E., and Choudhury, D., 1995, ''A Near-Wall Treatment Using Wall Functions Sensitized to Pressure Gradient,'' ASME FED Vol. 217, Separated and Complex Flows, ASME.
[17] Launder, B. E., and Spalding, D. B., 1974, ''The Numerical Computation of

Turbulent Flows,'' Comput. Methods Appl. Mech. Eng., **3**, pp. 269–289.

[18] Yakhot, V., and Orszag, S. A., 1992, ''Development of Turbulence Models for Shear Flows by a Double Expansion Technique,'' Phys. Fluids A, **4**, No. 7, pp. 1510–1520.

[19] Shih, T. H., Liou, W. W., Shabbir, A., Yang, Z., and Zhu, J., 1995, ''A New k-ε Eddy Viscosity Model for High Reynolds Number Turbulent Flows,'' Comput. Fluids, **24**, No. 3, pp. 227–238.

[20] Lien, F. S., and Leschziner, M. A., 1994, ''Assessment of Turbulent Transport Models Including Non-Linear RNG Eddy Viscosity Formulation and Second-Moment Closure for Flow Over a Backward-Facing Step,'' Comput. Fluids, **23**, No. 8, pp. 983–1004.

[21] Speziale, C. G., Sarkar, S., and Gatski, T. B., 1991, ''Modelling the Pressure-Strain Correlation of Turbulence: An Invariant Dynamical Systems Approach,'' J. Fluid Mech., **227**, pp. 245–272.

[22] Monson, D. J., and Seegmiller, H. L., 1992, ''An Experimental Investigation of Subsonic Flow in a Two-Dimensional U-duct,'' NASA Contract Report 103931.

[23] Wolfstein, M., 1969, ''The Velocity and Temperature Distribution of One-Dimensional Flow with Turbulence Augmentation and Pressure Gradient,'' Int. J. Heat Mass Trans., **12**, pp. 301–318.

[24] Mayle, R. E., Dullenkopf, K., Schulz, A., 1998, ''The Turbulence That Matters,'' ASME J. Turbomach., **114**, pp. 707–714.

[25] Hinze, J., 1975, *Turbulence*, 2nd Edition, McGraw-Hill, New York.

[26] Luo, J., and Lakshminarayana, B., 1997, ''Analysis of Streamline Curvature Effects on Wall-Bounded Turbulent Flows,'' AIAA J., **35**, No. 8, pp. 1273–1279.

[27] Gibson, M. M., and Rodi, W., 1981, ''A Reynolds-Stress Closure Model of Turbulence Applied to the Calculation of a Highly Curved Mixing Layer,'' J. Fluid Mech., **103**, pp. 161–182.

Investigation of the Flopping Regime of Two-, Three-, and Four-Plate Arrays

D. W. Guillaume
Assistant Professor,
Department of Mechanical Engineering,
California State University, Los Angeles,
Los Angeles, CA 90032

J. C. LaRue
Professor,
Department of Mechanical
and Aerospace Engineering,
University of California, Irvine,
Irvine, CA 92697

The variation of the base pressure coefficient (Cp) and the characteristics of the power spectra of the velocity for arrays of two-, three- and four-plates aligned normal to the flow are presented. The wakes downstream of the plates in the array are shown to exhibit behavior that varies between stable modes, flopping and quasi-stable behavior depending on the s/t distance (where s is the spacing between the top and bottom surfaces of adjacent plates and t is the thickness of the plate). For the two and three-plate arrays with $s/t=0.25$, peaks in the power spectra of about 48.2 and 98.1 Hz which correspond to Strouhal numbers of 0.06 and 0.11 are observed. For the four-plate array with $s/t=0.192$, no clear peaks are visible. Probability density functions of uncalibrated hot-wire signals show that the peaks in the power do not correspond to continuously periodic fluctuations. [S0098-2202(00)00604-0]

1 Introduction and Background

Adjacent bluff bodies or plates are often present in many flow field applications. Thin plates, or vane arrays, are commonly used to condition or alter flow fields. For example, arrays of flat vanes placed in ducts are used to either straighten or aid in turning the flow. Electro-mechanical components or mechanical support structures often take the general shape of thicker plates or rectangular bluff bodies. All of these rectangular objects can generate wakes that can alter the downstream flow field in an adverse manner. For example, unstable wakes downstream of combustor swirl vanes may produce reaction instabilities by altering the shape of the recirculation zone.

The characteristics of the flowfield about a vane or plate depend on the aspect ratio c/t where c is the chord, i.e., the dimension of the plate in the flow direction, and t is the dimension of the plate normal to the flow and on the spacing ratio s/t where s is the shortest distance between adjacent sides of plates. These parameters also affect the magnitude and temporal variation of the base pressure coefficient ($Cp=(P-P\infty)/1/2\rho U\infty^2$), which is always negative. For simplicity in the following discussion, since *Cp* is always negative, only the magnitude of *Cp* is used when comparing the effect of plate spacing on the average *Cp* value behind a plate in the plate array. Hence hereafter, the phrase ''higher *Cp*'' refers to a more negative *Cp* magnitude while the phrase ''lower *Cp*'' refers to a less negative *Cp* magnitude.

For a two-plate array, when s/t is very large, the near wake of each plate in the array is expected to be similar to that found downstream of a single plate placed in a flow. Conversely, as s/t is reduced to nearly zero ($s/t\approx 0$), the two-plate array is expected to have the same flow characteristics as a thick single plate in that a single wake will be observed after a very short downstream distance.

Although no studies of this transition from multiple independent wakes to a single wake have been performed for plates, the transition has been thoroughly studied for arrays of two cylinders. For example, Bearman and Wadcock [1] show that, for a two-cylinder array, when the cylinder spacing-to-diameter ratio (s/d) is set equal or greater than four, the near wake of each cylinder in the array is similar to that found downstream of a single cylinder. Far downstream, the individual wakes amalgamate to form a single wake which is also similar to that of a single cylinder. They also show that within a critical spacing-to-diameter ratio, $0.1\leqslant s/d\leqslant 1.3$, the average *Cp* of each cylinder varies in time and takes on two different values. Kim and Durbin [2] describe this as the ''flopping regime.'' They suggest that flopping occurs spontaneously when the wake behind each cylinder alternates between a wide wake with a low magnitude *Cp*, and a narrow wake with a high *Cp*.

Since past studies have shown that the wakes of closely spaced bluff bodies may interact in several different ways it is useful to define terms that describe three types of wake interactions: quasi-stable behavior, spontaneous flopping, and forced flopping.

- Quasi-stable behavior is the wake behavior observed downstream of the plate array in which different *Cp* values exist behind each plate. The *Cp* values do not vary with time. A large amplitude flow perturbation can cause the average *Cp* values to change, but the *Cp* values remain at the new values until another large perturbation is applied.
- Spontaneous flopping is the behavior observed downstream of a plate array where the average *Cp* values are observed to alternate over time between relatively high and low values, even when no large perturbation is applied to the flow field.
- Forced flopping is the behavior observed downstream of the plates in which initially stable wakes exhibit flopping as a result of a large, one-time perturbation. After the initial large perturbation is applied and flopping occurs, there is no observable difference between the wake and *Cp* value variations for forced and for spontaneous flopping.

Kim and Durbin [2] present the first statistical analysis of the time interval for each period that the average *Cp* value remains relatively high combined with the time for each period that the average *Cp* value remains relatively low. They find that the probability density function for the time intervals has a zero event Poisson distribution and that the time duration between transitions decreases as velocity increases.

Hayashi et al. [3] with $0\leqslant s/t\leqslant 2.75$, $0.014\leqslant c/t\leqslant 0.114$, and $6\times 10^3\leqslant \mathrm{Re}\leqslant 1.9\times 10^4$ find quasi-stable behavior and forced but not spontaneous flopping with two-plate arrays. Only quasi-stable behavior is observed for three, and four-plate arrays. Specifically, they find forced flopping to occur only with the two-plate array when $s/t=1.75$. Flow visualization behind the two, three, and four-plate arrays show narrow and wide wakes that exchange positions as a function of time. They also present results that show average *Cp* trends over specific ranges of s/t. Specifically, they

---

Contributed by the Fluids Engineering Division for publication in the JOURNAL OF FLUIDS ENGINEERING. Manuscript received by the Fluids Engineering Division September 13, 1999; revised manuscript received June 1, 2000. Associated Technical Editor: P. Bearman.

find that, for $0<s/t<0.75$, the value of *Cp* increases as s/t increases. Further, for $0.75<s/t<2.5$, the difference in *Cp* values for individual plates in the array becomes very large. Finally, for $s/t>2.5$, quasi-stable behavior is not observed.

For a two-plate array with $s/t<2$ and $0.014\leqslant c/t\leqslant 0.114$, Hayashi et al. [3] show two values of the Strouhal number downstream of a two-plate array. The higher value corresponds to the narrow wake, i.e., higher average *Cp*, and the lower value corresponds to the wide wake, i.e., lower average *Cp*. With the three-plate array, since only one peak is observed in the power spectra, only one corresponding Strouhal number is shown. They suggest that this Strouhal number corresponds to a narrow wake behind a plate. Hence, they suggest that the plate with the narrow wake, i.e., higher average *Cp*, shows regular vortex shedding whereas the plate with the wide wake shows no regular vortex shedding. Neither power spectra nor Strouhal numbers are presented for the four-plate array. Since they find a relationship between the existence of a Strouhal number, i.e., the presence of regularly shed vortices, and the change in wake size behind a plate, they conclude that the origin of the quasi-stable behavior is strongly related to the vortex shedding of the plates.

Miau et al. [4] study the flow downstream of a two-plate array with $0.4\leqslant s/t\leqslant 2.0$, $c/t=0.150$, and $1.3\times 10^3\leqslant \mathrm{Re}\leqslant 1.2\times 10^4$ and find both spontaneous flopping and quasi-stable behavior. They find periodic vortex shedding near the plate with the narrow wake. When a wide wake exists behind the same plate, turbulent fluctuations are found downstream of the plate, but no periodic shedding is detected. Further, they find that for $1.5\leqslant s/t\leqslant 1.85$, spontaneous flopping occurs and the rate of flopping increases with increasing s/t. The time interval between one transition from wide-wake to narrow-wake, and the subsequent transition from wide-wake to narrow-wake, appears to follow a zero-event Poisson distribution.

Miau et al. [5] with $1.4\leqslant s/t\leqslant 2.1$, $6.6\times 10^3\leqslant \mathrm{Re}\leqslant 1.8\times 10^4$, and $c/t=6.66$ appear to be the first to add grid turbulence to the freestream flow and study flopping behind plate arrays. They position a two-plate array with $c/t<3.2$ and vary the turbulent intensity from 0.23 percent–7.12 percent and the integral length scale from $0.32t$ to $0.84t$ and use flow visualization and hot-wires to determine the effects of free stream turbulence on spontaneous flopping. They find that an increase in turbulent intensity shortens the time interval between one transition from wide-wake to narrow-wake, and the subsequent transition from wide wake to narrow-wake with $1.4\leqslant s/t\leqslant 1.9$ and has indiscernible effects with $1.9\leqslant s/t\leqslant 2.1$.

In summary, quasi-stable behavior and forced and spontaneous flopping have been observed for two, three, and four-plate arrays with $c/t<3.2$ and the effects of spacing and velocity on flopping have been determined. Only quasi-stable behavior has been observed for plate arrays with three or more plates. However, no studies of the effect of spacing on flopping and quasi-stable behavior have been presented for arrays of more than two plates with $c/t>3.2$ which describe the plate array characteristics typical in engineering applications. Further, the flow characteristics for $c/t>3.2$ can be significantly different than the behavior observed with $c/t<3.2$. Hence, the purpose of this study is to determine the flow characteristics that exist for $0.04\leqslant s/t\leqslant 2$ different for planar two, three, and four-plate arrays with $c/t=4$.

2 Facilities and Approach

The large UCI closed-return windtunnel was used for all the experiments. The test section had a length of 6.71 m, a cross-section of 61 by 91 cm, and was preceded by a contraction section with an area reduction from 5.15 m^2 to 0.55 m^2 (a contraction ratio of 9.36). For the velocity range of 3 to 24 m/s, the mean velocity in the central portion of the test section (outside the wall boundary layer) was constant to within 1 percent, and the freestream turbulence intensities at both the entrance and exit of the test section for a centerline velocity of 10 m/s was, respectively, 0.17 percent and 0.22 percent. The temperature in the windtunnel was maintained to within ±1.0°C for each data collection period.

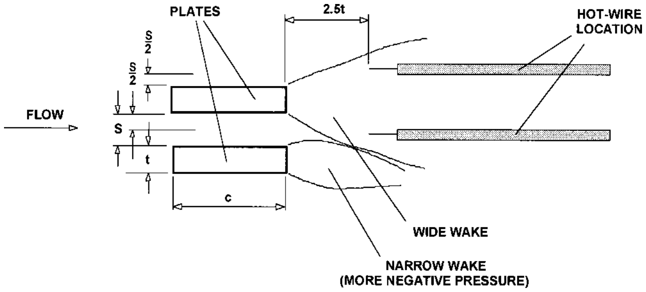

Fig. 1 Schematic illustration of forced or spontaneous flopping downstream of the plate array. The other mode is the opposite in that the wide wake is on the bottom and the narrow wake is on the top.

For all test plates used in this study, $t=1.27$ cm, $c=5.08$ cm, and the length in the spanwise direction was 0.30 m. The plates are mounted at each end to identical 1.27 cm diameter, 0.62 m high rods that were attached to chemistry stands (Fig. 1). The vertical rods were placed 0.29 m apart and mounted so that the rods passed vertically through the center of the chord of the plates at the two spanwise ends of the plates. Each plate array was mounted parallel to the floor of the tunnel and centered between the floor and the ceiling of the tunnel. The base of each stand had an approximate width of 16 cm, a length of 27 cm, and a height of 2.54 cm. The leading edge of the base was directly below the leading edge of the plate array. The downstream coordinate, x, and the vertical coordinate y, had their origins at the trailing edge of the plate that is third from the bottom of the six-plate array. From the results obtained from cylinder arrays using a geometrically similar setup (cf. Guillaume and LaRue [6]), three-dimensional effects were believed to be negligible.

A 0.01 mm diameter pressure port was located at the rear of each plate at the center plane of each plate. The port intercepted a 0.48 cm diameter passage that was drilled along the centerline of the plate in the spanwise direction. The passage was blocked at one end of the plate and the other end was connected to a Setra (Model 339-1) differential pressure transducer by means of a 2.5 m long silicone tube with an inner diameter of 1.8 mm. The output of the Setra transducer was connected to a filter, to a Computer Boards Inc. (CBI) SSH-16 sample and hold board and a CBI CIO-AD16F 12 bit analogue to digital converter which were controlled by a PC clone. The pressure signal was sampled at 10 samples/s for a three-hour time period and filtered at 5 Hz.

Flow visualization, using smoke which was illuminated with a laser light sheet, was used to obtain flow images. The nominal 0.8 mm thick laser sheet was produced by passing a 2 W argon-ion beam through a cylindrical lens. The smoke was produced using mineral oil and was injected at the leading edge of the plates through four equally spaced holes. Images were collected with a Sony video camera (Model CCD-V101) at a shutter speed of 1/1000 s. The images were digitized with ''frame grabbing'' hardware and software. The use of a video camera has two advantages: first, since the allowable shutter speed was much faster than traditional cameras, a continuous light source could be used; second, the images could be viewed immediately.

The single hot-wire sensor, that was used to obtain the frequency spectra, was made by soldering a 2 mm long, 0.00508 mm diameter, Wollaston wire to a TSI-1210 sensor holder. The sensor holder was connected to a traverse that is located 45 cm downstream of the hot-wire sensor and had a resolution of 0.1 mm in the vertical direction. The hot-wire sensor was connected to a TSI Model 1050 constant temperature anemometer and then to the same acquisition system used to obtain the pressure data. The data were collected at a sample rate of 2000 samples/s and filtered at

1000 Hz for a time period of five minutes. The sensor was positioned in the flow so that the hot-wire was parallel to the horizontal plane and perpendicular to the air flow.

Three methods were used to apply external perturbations to the flow field. The first was to simply turn off and on the windtunnel fan. The second was to open and close a door in the test section of the windtunnel near the plate array. The third was to block the flow slightly upstream from the plates with a 25 cm wide and 15 cm long plate and then quickly remove it. All three lead to flopping behavior after the initial perturbation. For the results reported herein, the third technique was used.

Uncertainties of the velocity measurements were estimated to the 95 percent confidence using techniques of Kline and McClintock [7]. The combination of the uncertainty of windtunnel velocity and measured wake pressure led to an uncertainty of ± 0.02 in *Cp* value.

3 Results

In the first part of the results, the *Cp* behavior is presented for two, three, and four-plate arrays with $0.040 < s/t < 2.000$ and $c/t = 4.0$. Examples of *Cp* time-series are presented along with corresponding flow visualizations. In the second part of the results, uncalibrated hot-wire power spectra and autocorrelations obtained downstream of the arrays and the probability density functions (pdf) of the time lengths between *Cp* transitions are compared during flopping for a two, three, and four-plate arrays.

Figure 2 shows a sample *Cp* time-series that is exhibiting flopping for a two-plate array with $s/t = 0.25$ and $U = 11.08$ m/s. Each time the *Cp* value behind one of the plate rises, the *Cp* value behind the other plate falls. Specifically, when the *Cp* value behind the top plate is about -0.74 while the *Cp* values behind the bottom plate is about -0.59. Alternatively, when the *Cp* value behind the top plate is about -0.59, the *Cp* value behind the bottom plate is about -0.74.

A summary of the average values of *Cp* for the two-plate array with $0.040 \leqslant s/t \leqslant 2.000$ and $U = 11.08$ m/s is shown in Table 1. Specifically, for $0.040 \leqslant s/t \leqslant 0.100$, the average *Cp* values of the two plates are nearly equal and neither spontaneous nor forced flopping is observed. No other quasi-stable mode can be produced within this range even when a large external perturbation is applied. Hence, the flow is stable. For $0.100 \leqslant s/t \leqslant 0.644$, forced flopping is sometimes observed for the two-plate array. When forced flopping does not occur, one of two quasi-stable modes is observed. In one of the quasi-stable modes, the average *Cp* value of the top plate remains high, and the average *Cp* value of the bottom plate remains low. In contrast, for the other quasi-stable mode, the average *Cp* value of the top plate remains low and the average *Cp* value of the bottom plate remains high. For $0.644 \leqslant s/t \leqslant 2.000$, neither forced nor spontaneous flopping is observed. As with $0.040 \leqslant s/t \leqslant 0.100$, only one stable mode is observed where, after any large applied perturbation, the average *Cp* values of the two plates remain nearly equal.

Table 1 Modes of stability of a two-plate array for various spacing ranges ($U = 11.14$ m/s, $t = 1.27$ cm)

s/t	MODES	Cp	
RANGE		PLATE 1	PLATE 2
0.040-0.100	Cp of plates equal	-0.66	-0.66
0.100-0.644	spontainous flopping between plates	-0.80 or -0.62	-0.62 or -0.80
0.644-2.000	Cp of plates equal	-0.66	-0.66

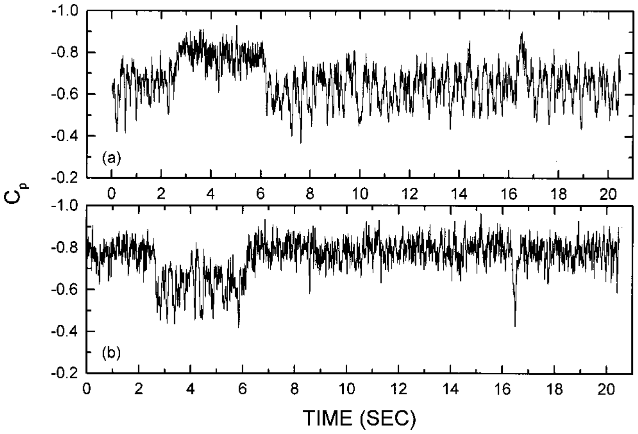

Fig. 2 Base pressure coefficient, *Cp*, as a function of time for a two-plate array with $U = 11.08$ m/s and $s/t = 0.25$. Figure 1(*a*) corresponds to the top plate and Fig. 1(*b*) corresponds to the bottom plate.

Results for a three-plate array with $s/t = 0.50$ and $U = 11.08$ m/s show that the average *Cp* value behind the middle plate remains relatively constant at a higher average *Cp* value than the highest average *Cp* value found behind either of the outer plates. Specifically, the average *Cp* value behind the middle plate is -0.84 while the average *Cp* values behind the outer plates are about -0.59 or -0.74.

Table 2 shows a summary of the average values of *Cp* for the three-plate array with $0.040 \leqslant s/t \leqslant 2.000$ and $U = 8.96$. Specifically, for $0.040 \leqslant s/t \leqslant 0.100$, a stable mode occurs and the average *Cp* values of the two outer plates are nearly equal and high, and the average *Cp* value of the center plate is relatively low. For $0.100 \leqslant s/t \leqslant 0.375$, a different stable mode occurs in which the average *Cp* values of the two outer plates are nearly equal and relatively low, and the average *Cp* value of the middle plate is relatively high. For $0.375 \leqslant s/t \leqslant 0.625$, spontaneous flopping between the top and bottom plates is observed. For $0.625 \leqslant s/t \leqslant 2.000$, only one mode is observed, where, after any large applied perturbation, the average *Cp* values of the two outer plates remains relatively equal and low and the center plate has an average *Cp* value of -0.84.

To present the results of the *Cp* values for the four-plate array, the plates are distinguished as follows: plate 1 is the top plate of the array; plate 2 is the upper-middle plate of the array; plate 3 is the lower-middle plate of the array; and plate 4 is the bottom plate of the array. Figure 3 shows a sample time-series of *Cp* with $s/t = 0.50$ and $U = 11.08$ m/s. Within this c/t range, flopping is not observed between any specific pairs of plates, but appears to randomly occur between different pairs of plates over time. For example, as shown in the time series of Fig. 3, the average *Cp* value behind plate 1 changes from -0.88 to -0.57 at about 8.2 s, which is the same time that the average *Cp* value behind plate 2 changes from -0.56 to -0.80. Also, at about 16 s, the average *Cp* value behind plate 1 changes from -0.57 to -0.88 and the average *Cp* value behind plate 3 changes from -0.80 to -0.56. Likewise the *Cp* values change behind plates 1 and 4 at about 11 s, behind plates 2 and 3 at about 16 s, behind plates 2 and 4 at about 5.5 s, and behind plates 3 and 4 at about 19.5 s.

A summary of the average values of *Cp* for each plot in the four-plate array is shown in Table 3 with $0.040 \leqslant s/t \leqslant 2.000$ and $U = 11.08$ m/s. Specifically, for $0.040 \leqslant s/t \leqslant 0.070$, a stable mode occurs and the average *Cp* values behind all four plates are relatively equal. For $0.070 \leqslant s/t \leqslant 0.108$, a different stable mode occurs in which the average *Cp* values of the outer plates, i.e., plates 1 and 4, are nearly equal and high, and the average *Cp* values of the center plates, i.e., plates 2 and 3, are relatively lower.

Table 2 Modes of stability of a three-plate array for various spacing ranges ($U = 8.96$ m/s, $t = 1.27$ cm)

s/t	MODES	Cp		
RANGE		PLATE 1	PLATE 2	PLATE 3
0.040-0.100	outer plates equal, center plate high	-0.81	-0.63	-0.81
0.100-0.375	outer plates equal, center plate low	-0.71	-0.84	-0.71
0.375-0.625	spontaneous flopping	-0.74 to -0.59	-0.84	-0.59 to -0.74
0.625-2.000	outer plates equal, center plate high	-0.71	-0.84	-0.71

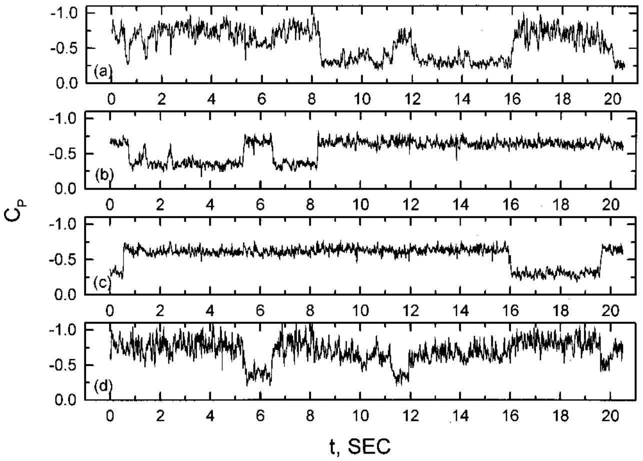

Fig. 3 Base pressure coefficient, *Cp*, as a function of time for a four-plate array with $U=11.08$ m/s and $s/t=0.192$. Figure 3(*a*) corresponds to the top plate, Fig. 3(*b*) corresponds to the upper middle plate, Fig. 3(*c*) corresponds to the lower middle plate, and Fig. 3(*d*) corresponds to the bottom plate.

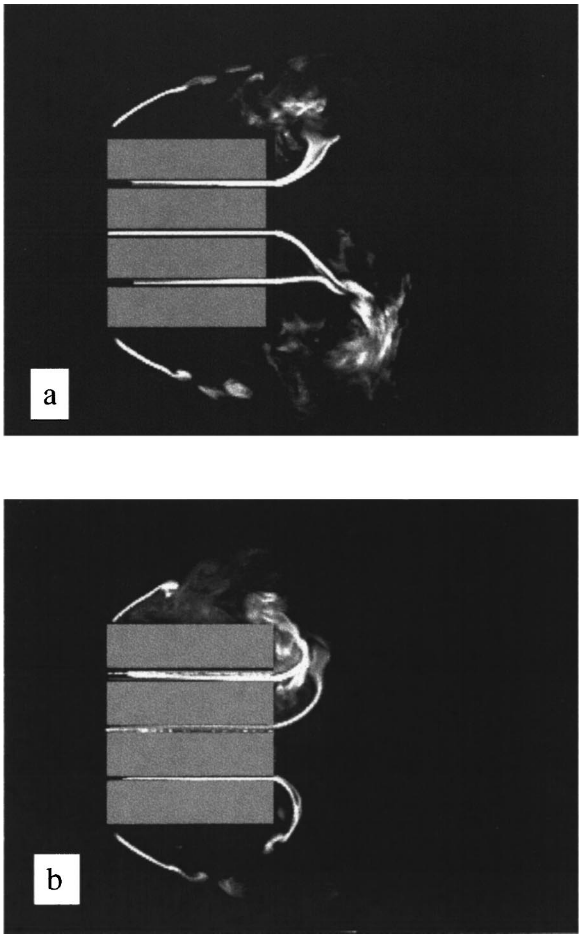

Fig. 4 Smoke visualization showing spontaneous flopping of the wakes downstream of the four-plate array with $U=11.08$ m/s and $s/t=0.192$. Figures 4(*a*) and 4(*b*) show example flow patterns before and after flopping.

For $0.108 \leq s/t \leq 0.176$, spontaneous flopping between the center plates, i.e., plates 2 and 3, is observed. The *Cp* values behind the outer plates, i.e., plates 1 and 4, are nearly equal and constant at higher average *Cp* values than the highest average *Cp* value found behind either of the center plates. For $0.176 \leq s/t \leq 0.262$, spontaneous flopping between all four plates is observed.

For $0.262 \leq s/t \leq 0.528$, spontaneous flopping between the outer plates, i.e., plates 1 and 4, is observed. The *Cp* values behind the inner plates, i.e., plates 2 and 3, are relatively equal and constant at higher average *Cp* values than the highest average *Cp* value found behind either of the outer plates. For $0.528 \leq s/t \leq 2.000$, a stable mode occurs in which the average *Cp* values of the inner plates, i.e., plates 2 and 3, are nearly equal and high, and the average *Cp* values of the outer plates, i.e., plates 1 and 4, are nearly equal but relatively lower than the *Cp* values for the inner plates.

The flow visualization of Fig. 4(*a*) shows narrow wakes downstream of plates 1 and 3 while wide wakes are observed downstream plates 2 and 4. Consistent with the time series of pressure coefficient shown in Fig. 3, a new mode can be observed spontaneously after flopping has occurred. The flow visualization of Fig. 4(*b*) shows a second mode in that narrow wakes are observed downstream of plates 1, 2, and 4 and a wide wake is observed downstream of plate 3.

The flow visualization of Figs. 5(*a*) and 5(*b*) show examples of two other modes of spontaneous flopping observed downstream of the four-plate array. In Fig. 5(*a*), narrow wakes are observed downstream of plates 2, 3, and 4 while wide wakes are observed downstream of plate 1. In Fig. 5(*b*), narrow wakes are observed downstream of plates 1, 2, and 3 while a wide wake is observed downstream of plate 4.

In order to determine the probability density function (pdf) of the time interval between *Cp* transitions, a threshold is set to delineate between the high and low *Cp* values. The length of time for each period that the average *Cp* magnitude remains relatively high or low for the top plate in each plate array is determined and, with these data, two probability density functions are created as shown in Fig. 6. The solid line represents the zero event Poisson distribution, $P(t/T) \approx e^{-t/T}$, where T is the mean interval between transitions. This agrees with the measured pdf. Hence, consistent with the observation of Kim and Durban [2] for two-cylinder arrays, the duration of time intervals at both high and low *Cp* values for two, three, and four-plate arrays follow a zero-event Poisson distribution.

Table 3 Modes of stability of a four-plate array for various spacing ranges ($U=11.08$ m/s, $t=1.27$ cm)

s/t	MODES	Cp			
RANGE		PLATE 1	PLATE 2	PLATE 3	PLATE 4
0.040-.070	Cp of all plates equal	-0.63	-0.63	-0.63	-0.63
0.070-0.108	centers equal and low, outer plates equal and high	-1.02	-0.88	-0.88	-1.02
0.108-0.176	flopping between center plates	-0.85	-0.80 to -0.56	-0.56 to -0.80	-0.85
0.176-0.262	flopping between all plates	-0.88 to -0.57	-0.80 to -0.55	-0.55 to -0.80	-0.57 to -0.88
0.262-0.528	flopping between outer plates	-0.74 to -0.65	-0.90	-0.90	-0.65 to -0.74
0.528-2.000	centers equal and high, outer plates equal and low	-0.74	-0.92	-0.92	-0.74

Figure 7 shows the pdf of the time intervals between one transition from low to high *Cp* value and the subsequent transition from low to high *Cp* value for the top plate in the two, three, and four-plate arrays. The solid line represents the one-event Poisson distribution, $P(t/T_i) \approx (t/T_i) e^{-t/T_i}$, where T_i is the flopping period. Although the distribution for all plate arrays is very similar, the measured pdf and one-event Poisson distribution are clearly dissimilar. Hence, flopping for two-, three-, and four-plate arrays is not a Poisson process.

Figure 8 shows the power spectra of an uncalibrated hot-wire signal for two, three, and four-plate arrays with $U=11.08$ m/s, which are measured in the downstream plane at $x/t=2.5$ from the trailing edge of the plates in the array. Specifically, Fig. 8(*a*) shows the power spectra for a two-plate array with $s/t=0.25$ measured on the centerplane of the array and Fig. 8(*b*) show the power spectra for the same array measured at s/2 above the upper surface of the upper plate. Peaks in the power spectra that is obtained on the plane between the upper and middle plates are shown at 48.2 Hz and 98.1 Hz which correspond to Strouhal numbers of 0.06

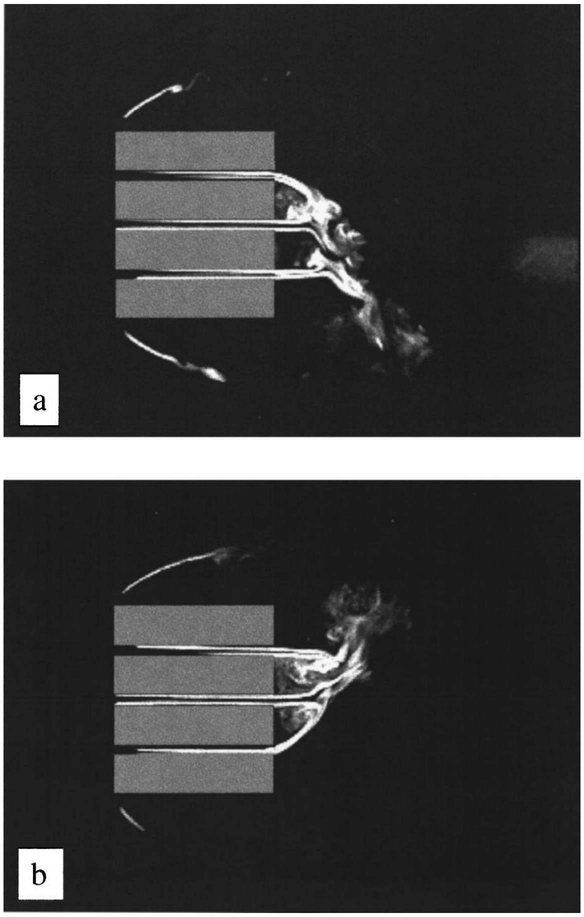

Fig. 5 Smoke visualization showing spontaneous flopping of the wakes downstream of the four-plate array with $U=11.08$ m/s and $s/t=0.192$. Figures 5(*a*) and 5(*b*) show example flow patterns before and after flopping.

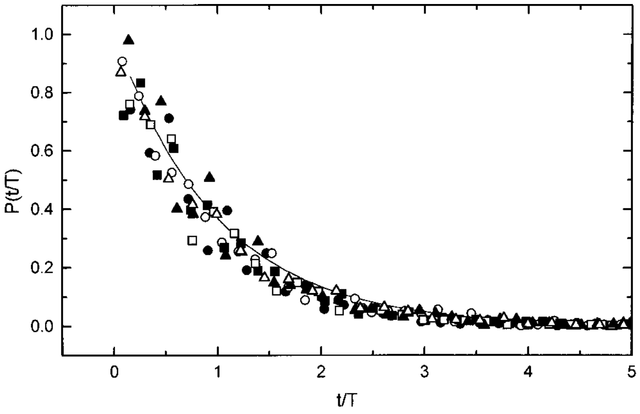

Fig. 6 Probability density function for the time duration of high average and low average *Cp* values with $U=11.08$ m/s. Symbols: zero-event Poisson distribution, —; high average *Cp* values (two-plate array, $s/t=0.25$), ●; low average *Cp* values (two plate array, $s/t=0.25$), ○; high average *Cp* values (three plate array, $s/t=0.5$), ■; low average *Cp* values (three plate array, $s/t=0.5$), □; high average *Cp* values (four-plate array, $c/t=0.192$), ▲; and; low average *Cp* values (four-plate array, $s/t=0.192$), △.

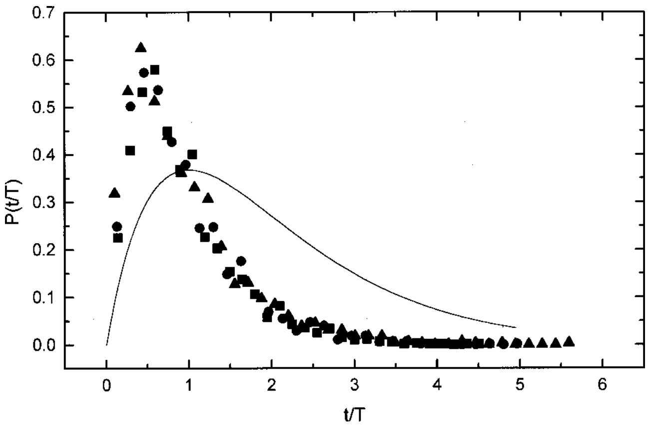

Fig. 7 Probability density function for the time intervals between one transition from low to high *Cp* and the subsequent transition from low to high *Cp* with $U=11.08$ m/s. Symbols: one event Poisson distribution, —; pdf for the two-plate array with $s/t=0.25$, ●; pdf for the three plate array with $s/t=0.5$, ■; and, pdf for the four plate array with $s/t=0.192$, ▲.

and 0.11. The Strouhal number of 0.11 is fairly consistent with the Strouhal number of 0.14 observed by Nakamura [8]. Thus the peak observed at 98.1 Hz is also observed of single plates. The power spectra measured at s/2 above the plate show the peak at 48.2 Hz but not the peak at 98.1 Hz. Although the peaks in the power spectra show average dominant frequencies, the informa-

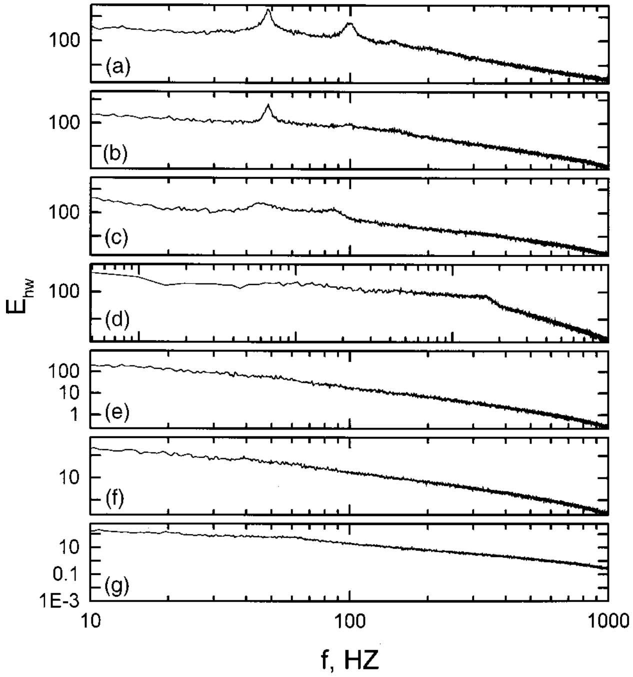

Fig. 8 Power spectra of the hot-wire signal, E\-(hw), with $U=11.08$ m/s and $x/t=2.5$. Fig. 8(*a*) measured on the centerplane of the two-plate array; Fig. 8(*b*) measured at $s/2$ above the upper plate of the two-plate array; Fig. 8(*c*) measured in the plane between the center plate and the upper plate of the three-plate array; Fig. 8(*d*) measured at $s/2$ above the upper plate of the three-plate array; Fig. 8(*e*) measured on the centerplane of the four-plate array; Fig. 8(*f*) measured between plate$_1$ and plate$_2$ of the four-plate array; and, Fig. 8(*g*) measured at $s/2$ above the plate$_1$ of the four-plate array.

tion gained from the pdf shows that wake fluctuations that correspond to these peak frequencies are random, and do not correspond to continuously periodic fluctuations.

Figure 8(*c*) shows the power spectra for a three plate array with $s/t = 0.50$ measured on the plane between the middle plate and the upper plate of the array and Fig. 8(*d*) show the power spectra for the same array measured at s/2 above the upper surface of the upper plate. Again, peaks in the power spectra that is obtained on the plane between the upper and middle plates are shown at 48.2 Hz and 98.1 Hz. No clear peaks are visible on the plane at s/2 above the upper surface of the top plate. Further testing shows that no peaks in the power spectra are found at s/2 above the top plate with downstream positions ranging from $x/t = 1.5$ to 6.5.

Figure 8(*e*) shows the power spectra for a four-plate array with $s/t = 0.192$ measured on the centerplane of the array, i.e., between plates 2 and 3. Figure 8(*f*) shows the power spectra for the same array measured on the plane between plate 1 and plate 2, and Fig. 8(*g*) shows the power spectra for the same array measured at s/2 above the upper surface of the upper plate. No clear peaks are visible at any of these locations on this plane of $x/t = 2.5$. Further tests show that no peaks in the power spectra are present at any of the three locations over an x/t range of 1.5 to 6.5.

4 Summary

This study shows that when plates with a chord-to-thickness ratio of 4:1 are placed in an array normal to the flow, the pressure fields generated around the plates may interact and cause the average magnitude of the *Cp* values in the wakes of the plates to be unequal. Depending on the separation distance between the plates, this interaction results in flow field behavior that is either quasi-stable or flopping. These behaviors produce two distinct peaks in the power spectra. The frequencies of the wake fluctuations that correspond to these peaks do not exhibit continuously periodic behavior.

Acknowledgments

The authors gratefully acknowledge the valuable assistance of Graham W. Clark in constructing the apparatus and performing the tests. This project is part of a larger research project and we wish to acknowledge the helpful suggestions of Professor G. S. Samuelsen, and Dr. S. R. Vilayanur. This work is supported by the US Department of Energy, Morgantown Energy Technology Center, Contract Number DE-FC21-92MC29061 and the Southern California Gas Company, Contract SCG-19596.

References

[1] Bearman, P. W., and Wadcock, A. J., 1973, ''The Interaction Between a Pair of Circular Cylinders Normal to a Stream,'' J. Fluid Mech., **61**, pp. 499–511.
[2] Kim, H. J., and Durbin, P. A., 1988, ''Investigation of the Flow Between a Pair of Circular Cylinders in the Flopping Regime,'' J. Fluid Mech., **196**, pp. 431–448.
[3] Hayashi, M., Sakurai, A., and Ohya, Y., 1986, ''Wake Interference of a Row of Normal Flat Plates Arranged Side by Side in a Uniform Flow,'' J. Fluid Mech., **164**, pp. 1–25.
[4] Miau, J. J., Wang, H. B., and Chou, J. H., 1992, ''Intermittent Switching of Gap Flow Downstream of Two Flat Plates Arranged Side by Side,'' J. Fluid Struct., **6**, pp. 563–582.
[5] Miau, J. J., Wang, H. B., and Chou, J. H., 1996, ''Flopping Phenomenon of Flow Behind Two Plate Place Side-by-Side Normal to the Flow Direction,'' Fluid Dyn. Res., **17**, pp. 311–328.
[6] Guillaume, D. W., and LaRue, J. C., 1999, ''Investigation of the Flopping Regime of Two-, Three-, and Four-Cylinder Arrays,'' Exp. Fluids, **27**, pp. 137–144.
[7] Kline, S. J., and McClintock, F. A., 1953, ''Describing Uncertainties in Single-Sample Experiments,'' Mech. Eng. (Am. Soc. Mech. Eng.), **75**, pp. 3–9.
[8] Nakamura, Y., Ohya, Y., and Tsuruta, H., 1991, ''Experiments on Vortex Shedding from Flat Plates with Square Leading and Trailing Edges,'' J. Fluid Mech., **222**, pp. 437–447.

H. Huitenga
Research Engineer,
Siemens AG/KWU,
45470 Mülheim, Germany

N. K. Mitra[1]
Professor,
Institut für Thermo- und Fluiddynamik,
Ruhr-Universität Bochum,
44780 Bochum, Germany

Improving Startup Behavior of Fluid Couplings Through Modification of Runner Geometry: Part I—Fluid Flow Analysis and Proposed Improvement

For the use as a startup device the characteristic of a hydrodynamic coupling has to be steep at the nominal high speed operation condition and flat in the range of lower speed ratios. The economical design of the runner requires that the mass and the volume of the coupling should be as small as possible. The flow field in a starting configuration is simulated and a detailed analysis of the three-dimensional flow field is performed to deduce constructional modifications which meet both requests. The analysis shows that several modifications on pump and turbine runner seem to be successful. The consequences of the variation of the runner geometries will be discussed in detail in Part II of this paper. [S0098-2202(00)02104-0]

Introduction

Fluid or hydrodynamic couplings belong to the group of hydraulic gears. The coupling consists of a pump impeller and a turbine runner with radial vanes which are aligned face to face in a single casing which also rotates with the pump (Fig. 1). Generally, the impeller and the runner are of symmetrical structure with nearly the same number of blades ($\Delta Z = 1-3$), which have no profile and are not twisted in radial direction. The working fluid is usually an oil of low viscosity. The pump is driven by a prime mover. The working fluid flows in the blade channel, leaves the pump at the tip, enters into the blade channel of the turbine, and moves toward the hub where the fluid moves back to the pump. Momentum exchange between the fluid and the turbine blades makes this wheel turn in the same direction as the pump. The circulation of the fluid moving from the pump to the turbine, for which a speed difference or slip is the necessary condition, transports the torque. Under steady operating conditions the inertia of the fluid need not be considered, since no other intermediate element such as a stator as in a torque converter is present. So the torque of the turbine runner is equal to that of the pump, see Formanski [1].

The advantage of hydrodynamic couplings over mechanical clutches lies in their ability to absorb shocks and isolate torsional vibrations and to cut the power transmission by draining the coupling while the prime mover is running. No-load motor startup is possible and the driven machine is accelerated smoothly by filling the coupling. In contrast to mechanical clutches, they have no losses due to friction when accelerating to the operating conditions. Hydrodynamic couplings are used for driving conveyors, propellers of icebreaking ships, heavy earth-moving and agriculture machineries. The transmitted torque M for hydrodynamic couplings is given by:

$$M = |M_T| = |M_P| = \dot{m} \cdot (r_{c_u}|_A - r_{c_u}|_E)$$

where $\dot{m}$ is the circulating mass flow and $(r_{c_u}|_A - r_{c_u}|_E)$ is the specific moment of momentum.

Thus, the torque increases with increasing $\Delta(r \cdot _{c_u})$ and so it becomes maximum for the stopped turbine. Obviously, the amount of fluid in the working enclosure determines the torque transport. In a partially filled coupling a two phase flow system consisting of a liquid and a gas (air) appears. The torque is generally represented by the efficiency number $\lambda = M/(\rho \cdot \omega_P^2 \cdot D^5)$ in nondimensional form. The transmission behavior is a function of the ratio of the rotational speed ω_T/ω_P between the turbine and the pump. This characteristic depends on the flow structure which depends on the geometry. An experimental determination of the detailed flow field in order to study the effect of the geometry is prohibitively expensive and probably not possible. The other alternative is a numerical investigation of the flow field. To this purpose the authors developed a code in the body-fitted rotating coordinates in order to solve Reynolds averaged Navier-Stokes equations with k-ε turbulence model. This code has been used to analyze the flow field in a standard coupling, see Bai et al. [2] and industrial couplings, see Huitenga et al. [3]. Bai et al. [4] have compared the coupling characteristics with experiments in order to validate the code.

This work focuses on the fluid flow analysis to gain understanding of the time averaged and the time dependent effects. This knowledge serves as a basis for geometrical modifications which lead both to improved startup behavior as well as more economical design. The characteristic of a coupling with good startup

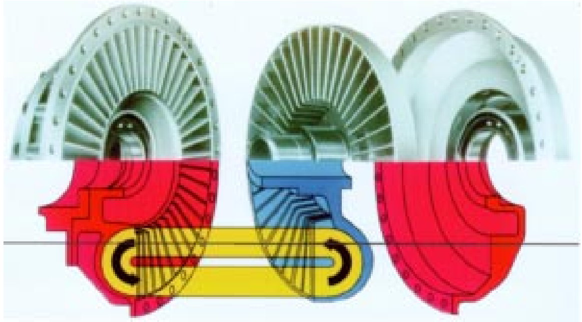

Fig. 1 Elements of a hydrodynamic coupling and schematic flow path

---

[1] Deceased.

Contributed by the Fluids Engineering Division for publication in the JOURNAL OF FLUIDS ENGINEERING. Manuscript received by the Fluids Engineering Division December 4, 1998; revised manuscript received July 10, 2000. Associate Technical Editor: M. Dhavbhadel.

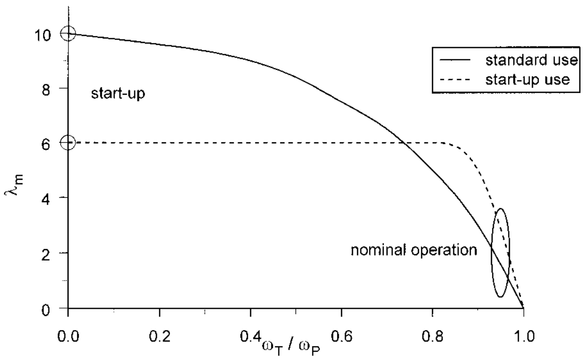

Fig. 2 Operation characteristic for a standard coupling and a special start-up device

behavior should run horizontal for small speed ratios, see Fig. 2. This means a constant difference between the torque transmitted through the coupling and the one provided by the motor so that the acceleration of the load is constant also. The characteristic should also have a steep gradient at the nominal point of operation. This allows the driven to turn with nearly constant speed while the torque may vary in a wide range. This means also a small difference of speed between the two runners in order to minimize the power dissipating into heat. The modifications of the runner wheels should result in lower mass and construction volume in order to enable higher loading capacity and compact machinery.

Basic Equations

In the present study the coupling is assumed to be completely filled so that a single phase flow can be considered. Furthermore, constant properties of the fluid i.e., constant viscosity and density are assumed. The fluid flow can be described by the three-dimensional unsteady Reynolds averaged Navier-Stokes equations in conjunction with the eddy viscosity concept, which is realized here through the k-ε model, Bai et al. [2]. Since the fluid flow area in industrial couplings is quite irregular, see Huitenga et al. [3], the numerical solution method is suited for nonorthogonal, contour-fitted grids. Cartesian velocity components are used, so that the conservation laws are spatially invariant and the momentum equations are in strong conservation form see Perić [5]. The mathematical model is discussed in detail by Bai et al. [2]. The general transport equation for a specific variable Φ can be expressed in contour fitted coordinates ξ_j with cartesian velocity components:

$$\frac{\partial \Phi}{\partial t}+\frac{1}{J}\frac{\partial}{\partial \xi_j}(C_j\Phi+D_j^{\Phi})=S_{\Phi} \quad \text{for} \quad \Phi=u,v,w,k,\varepsilon.$$

The convective, diffusive, and source term C_j, D_j^{Φ}, and S_{Φ}, respectively, vary for mass, momentum, turbulent kinetic energy, and turbulent kinetic diffusion equation.

Method of Solution

The finite volume scheme is applied and all dependent variables are defined at the center of each control volume (non-staggered grid). The discretization in time is second-order accurate (Schönung [6]). The deferred correction procedure of Khosla and Rubin [7] is used to discretize the convective fluxes. The diffusive parts are obtained by assuming linear variation of the variables.

The coupled equation system is solved through several iterations (sequential solution method). In the present method, the coupling between pressure and velocities is achieved by the SIMPLEC algorithm, see van Doormal and Raithby [8]. In order to avoid an oscillatory pressure field due to the nonstaggered variable arrangement a special interpolation has been used to determine the mass fluxes through control volume faces from adjacent control volume centered quantities, see Rhie [9]. Constant values for all flow variables are given as initial conditions. A stationary solution for every relative position is reached after five passages of the turbine blade through the computational domain. The computational domain is limited by walls in axial and radial direction. Because the coordinate system is fixed to the pump these walls do not move, whereas the ones in the turbine turn with the difference of the circumferential speed against the sense of rotation. Wall functions are employed to describe the boundary conditions along the walls of pump and turbine impeller, see Launder and Spalding [10] and Bai et al. [4]. Since the geometric form of the blades is simple, it is possible to use one grid block for calculation. The blades of the turbine runner are treated as internal obstacles moving relatively to the computational domain (Kost et al. [11]). This procedure is suitable to avoid problems arising from matching grids that move relatively to each other, see Rai [12]. But it is not suitable for turbo-machines with complex geometrical forms.

Periodic boundary conditions are prescribed at the circumferential surfaces of the computational domain (Kost et al. [13]). Since the matrices that arise from discretizing the Navier-Stokes equations are symmetric and sparse, an incomplete lower-upper decomposition method, the strongly implicit procedure is applied, to solve the equation system, see Stone [14]. Details of the flow equations and of the computational scheme can be found in Bai et al. [2].

Analysis of Flow Field

The torque transport between the pump and the turbine wheels is achieved by the circulating mass flow. This primary flow is superimposed with strong secondary flows, which are caused by the centrifugal and the Coriolis forces in radial direction and by the flow not aligned to the blades. The area of the secondary flows is strongly dependent on the working condition and the relative position of the wheels to each other.

The basic geometry has a rectangular shape of the working circuit with inner to outer diameter $d/D=0.28$ and blade-width to outer diameter $B/D=0.33$. The number of blades for the flow analysis is $Z=24$ and $Z=48$ for later modifications (Part II).

Time Averaged Flow Field

Figure 3 shows the velocity components in a section along the coupling axis. The flowfield is averaged first in time for all relative positions of pump and turbine and secondly in circumferential direction. The primary flow is directed clockwise in the blade channel. Only the corners of the geometry show small dead water areas and secondary eddies. At nominal operation ($s=0.03$) the center (neutral point) of the circulating flow is fixed in the gap between the two runners. The radial position of the neutral surface is situated in such a way that the segment of the circular ring bounded by the two blades and the hub and tip is divided into two equal areas. This results in equal average axial velocity in the two parts.

At the outer diameter the fluid flows from the pump to the turbine parallel to the outer wall. The alteration toward the hub is forced by the back wall because the centrifugal force acts against it. The reduced area toward the coupling axis leads to an increase of the axial components of velocity and a flow toward the pump. Immediately after entering the pump the velocity vectors show increasing radial components because of the increasing centrifugal forces. The magnitude of the vectors changes only slightly although the free flow cross section increases toward the outer diameter. This can be explained by the superposition of the circumferential velocity due to the secondary flow on the axial velocity. Velocity components in pure radial direction are found only near the back wall whereas the velocity vectors near the gap are diagonally directed.

A change of the operation condition ($s=0.50$) leads to a change of the flow structure. The radial position of the neutral

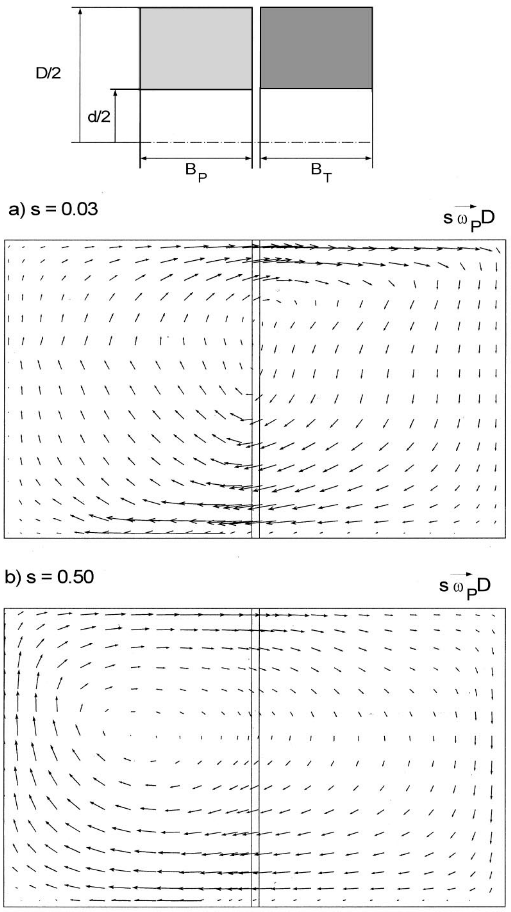

Fig. 3 Flow field averaged in time and circumferential direction in a meridional cross section

point sinks down to half the blade height and moves in axial direction from the gap into the middle of the pump. It is interesting to see that the area reaching from the neutral point to the gap and a quarter of the blade height radially outwards shows actually no flow at all. Thus, the circulating mass flow is fixed to a small area at the back wall.

In Fig. 4 several sections through the machine axis from the pump over the gap and toward the turbine are presented side by side to elucidate the spatial flow structure. The flow field is again time averaged and the vectors represent the relative velocity so that pump and turbine wheel do not move relative to the flow. The shaded areas represent the axial components of the relative velocity in the corresponding section. Areas with negative sign imply a mass flow from the turbine to the pump and are outlined by dashed lines. The line of view is along the rotating axis.

In the pump the pressure side is on the front of the blade and the suction side is on the back. The flow structure below the neutral point can be described by a frictionless relative flow in a rotating radial channel (Fig. 4(*a*) I . . . III). This results from a superposition of a throughflow while the wheel is standing still and a circulating flow without throughflow (relative channel vortex). The last one is characterized by a homogeneous velocity distribution along the whole channel which results from the assumptions of the one dimensional theory of streamlines. The circulating flow consists of a vortex and shows the same angular velocity like the wheel but in the opposite direction. For inviscid fluid the total rotation of the system (wheel and fluid) should be zero. This can be achieved only by the fluid having a motion in the opposite direction as the wheel.

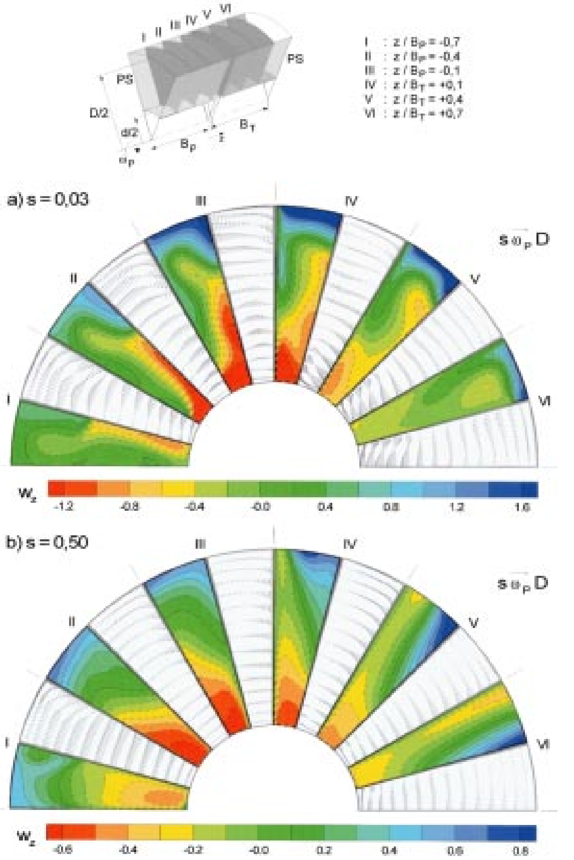

Fig. 4 Spatial distribution of flow components for two different points of operation

Because the velocities of the relative channel vortex are directed against the throughflow on the front of the blade (pressure side) only small velocities are there. They influence the flow structure at small slip so that local backflow (Fig. 4(*a*) I . . . II) appears at the blade root which is no longer visible when the massflow increases (Fig. 4(*b*) I . . . II).

With increasing radius the influence of the friction leads to higher velocities in the middle of the channel opposed to the near wall region (Fig. 4(*a*) III). They cause higher Coriolis forces which result in a pressure gradient toward the pressure side. The forces transport fluid from the middle of the channel to the blade front so that the flow profile is shifted. The casing defines the channel in radial direction and the fluid is transported in the boundary layer there from pressure to suction side. This mechanism in conjunction with the deflection toward the blade root makes the flow roll up at the blade tip (passage vortex). Because the rotation of the vortex is equal to the one of the wheel the velocities of the particles involved into the vortex are directed against the circulating mass flow.

In contrast to the pump where the pressure field is impressed from outside it follows in the turbine as a reaction. Therefore the suction side develops at the front of the blade and the pressure side at the back. The effects acting on the flow field are equal to the ones in the pump but opposite conditions result from the different flow directions. Above the neutral point higher velocities are found on the suction side and lower velocities along the pressure side because of the superposition of the circulating flow and the relative channel vortex (Fig. 4(*a*) IV . . . VI). The Coriolis force shifts the flow profile to high velocities on the pressure side. A secondary eddy develops between the blade roots and causes a fluid transport in the boundary layer at the hub.

The distribution of the axial flow components shows that the entering and leaving mass flows are divided by an inclined plane (Fig. 4(*a*) I . . . VI). It starts on the front of the blade near the hub and ends on the back of the blade at 0.3 of the blade height beneath the casing. The exact radial position on the blade suction side is defined through the stagnation point and shifts outwards from the gap to both wheels back wall. Therefore, the pressure side shows an area where the velocities are distributed against the entering massflow. In addition to that, the area in the pump shows no radial components, so the mass flow is blocked here.

The axial velocities are maximum at the hub between the gap and the middle of the pump, whereas they are maximum along the blade tip and the back wall of the turbine. The distribution of the radial flow components changes from pump to turbine because of the alternating flow direction, but are constant for each runner. In contrast the axial velocities decrease towards the back wall. With increased slip the flow through the pump is now mainly aligned to the back wall (Fig. 4(*b*) I). The flow profile is more homogeneous but is again influenced by the Coriolis force. The increased velocities in contrast to nominal operation dissolve the deadwater region on the pressure side (Fig. 4(*a*) I . . . II) and the circulating mass flow is divided into incoming and out going parts in axial direction through a radial plane. The location of this plane is given by the stagnation line of the passage vortex, whose size is reduced in circumferential direction (Fig. 4(*b*) I . . . III).

The mostly axial flow along the first 40% of the blade length makes the passage vortex more significant. Radial components are restricted to this secondary flow, so that the mass flow is directed toward the hub. The stagnation point indicating the separation plane between positive and negative axial velocities drops to half the blade height near the hub. Because the direction of rotation of the passage vortex is identical to that of the wheels, the reorganization from the gap to the turbine is continuous.

Figure 5 shows the passage from one wheel to the other in two corresponding levels. The line of view is from the tip to the root of the blades. Points of operation differing only slightly from nominal operation show all the same structure and are therefore represented here by $s = 0.50$. Strong secondary flows are present in both points of operation and reduce the cross-section in circumferential direction.

At small slip the entrance region of the pump shows an extended vortex along the pressure side, which forces the mass flow toward the suction side (Fig. 5(*a*)). This can be led back to the action of the centrifugal forces in the meridional cross section. Due to the boundary layer at the blades the velocities along the center of the flow channel become higher. This results in a stagnation point at the center of the back wall and fluid transportation along the blade walls toward the gap. These structures are typical for pipe elbows with two symmetrical vorticies, indeed. Due to the rotation of the whole blade segment and the resulting pressure and suction sides the fluid is led away to the blade back, so that only one secondary vortex persists. The secondary flow between the tips of the turbine blades develops for identical reasons as it does in the pump.

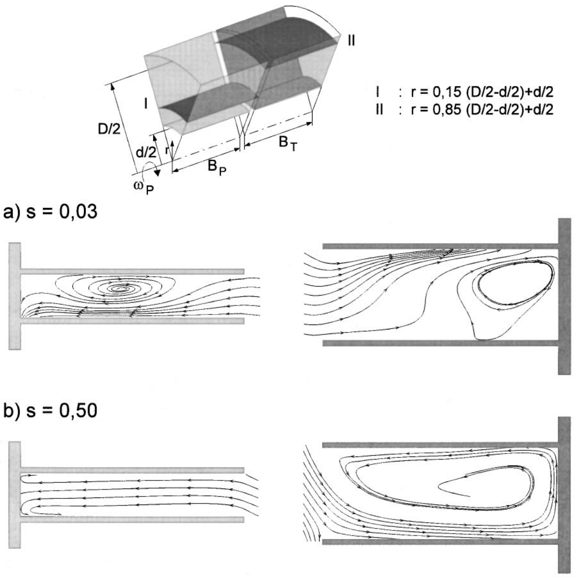

Fig. 5 Flow path along two different cylinder sections

At higher slip ($s = 0.5$) the circulating mass flow increases, so that the vortex in the pump vanishes completely (Fig. 5(*b*)). Because of the higher axial flow components the fluid flows over the whole length of the turbine blades. The large difference between the speed of the wheels makes the flow detach at the leading edge, so that this wheel shows velocities directed against the circulating mass flow over half the channel width in circumferential direction.

Time Dependent-Periodic Flow Procedures

Figure 6 shows the influence of the blade movement on the pressure field. In both wheels, 4 reference points were chosen to show the static pressure difference Δp_s on the blades in the course of one flow period. The resulting forces from this pressure difference outweigh all other terms and thus represent the significant part of the torque transmission. Besides the influence of the relative movement it shows which part of the blade takes part in torque transmission.

The amplitudes of the pressure changes are maximum in the pump at the blade tip and are smoothed with increasing axial extension (Fig. 6(*a*) I). The flow proceeding along the pump pressure side into the other wheel is modified by the pressure field belonging to the turbine blade. With increasing distance between these two blades the boundary layer of the turbine front side re-

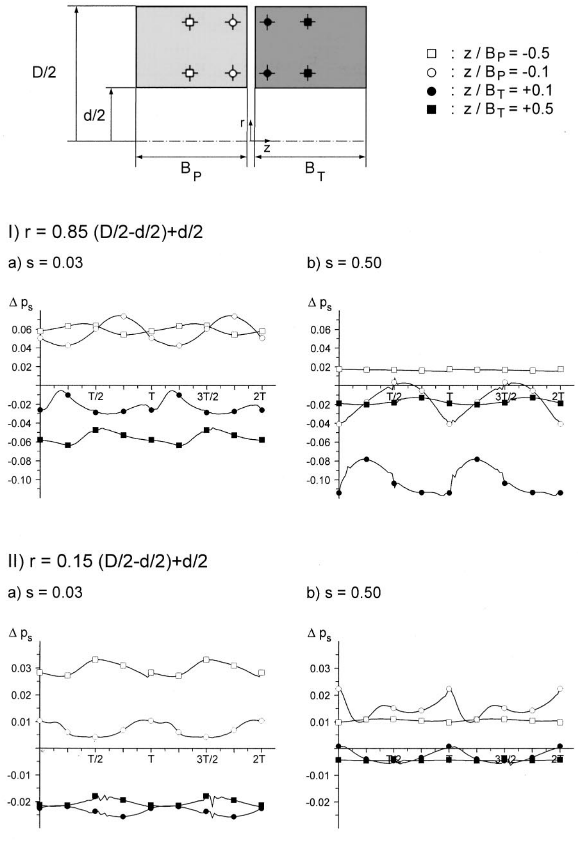

Fig. 6 Variation of static pressure difference on the blades for two different points of operation

duces, so that the axial velocities in the pump reach their maximum at $t=1/4\,\mathrm{T}$ and the pressure increases. The approach of the two pressure sides causes the flow to dam up on the pump front side so that the pressure difference is maximum at $t=3/4\,\mathrm{T}$ because the pressure level on the pump blade back is not influenced due to the steady spatial position of the passage vortex. Immediately near the gap the turbine wheel shows at time $t=1/4\,\mathrm{T}$ equal static pressure on both sides of the blade tip resulting from high axial velocities which show only insignificant change of direction. In the course of time the pressure on the front side decreases, so that the difference swings to half the absolute level as in the pump. Similar pressure history takes place in the turbine middle with a phase lag. The mean values are reduced by half in the turbine blade root region in relation to the casing (Fig. 6(*a*) II). The passage vortex stabilizes the flow structure here, so that at both reference points only small variations are visible. The encounter of the circulating mass flow out of the turbine with the velocity components toward the gap resulting from the secondary flow inside the pump (cf. Fig. 5) leads to a local stagnation point on pump pressure side. At $t=0$ it is directly aligned to the turbine suction side, so that it is fixed immediately in the gap and the pressure difference increases. Through the relative movement the pressure field of the turbine shifts the stagnation point in axial direction to the wheel ground. This leads at time $t=1/2\,\mathrm{T}$ to maximum results in the middle of the blade.

The effects of the relative movement are limited directly to the gap at higher slip (Fig. 6(*b*) I+II). The amplitudes of the oscillations have doubled at the turbine blade tip and the pump blade root. The pressure difference is limited in the turbine to a small area on the tip near the gap. This area widens at blade front position at $t=0$ from the turbine pressure side to pump suction side, so that negative pressure differences are found here (Fig. 6(*b*) I). The dimension of the pressure bubble in circumferential direction is so large that it embraces the leading edges at $t=1/2\,\mathrm{T}$, so that the pressure difference becomes zero.

The oscillations in the turbine result from changes on the suction side. The widening distance between the blade leading edges in timespan $t=0$ to $t=1/2\,\mathrm{T}$ lower the axial velocities along the blade front side, resulting to static pressure maximum at $t=1/4\,\mathrm{T}$. At the hub of the turbine, the absolute of the pressure difference falls of to one forth of the values at the casing (Fig. 6(*b*) II), which means that the momentum transport is limited to the blade tip. The pressure oscillations in the course of time happen in the pump for the same reasons as in the turbine.

Torque Transmission

The transmitted torque follows from a balance between the time dependent change of the moment of momentum of the mass inside the control volume and the torque acting on the mass through outer forces.

$$\vec{M}=\frac{D\vec{L}}{Dt}=\frac{\partial}{\partial t}\int_{v}\vec{x}x(\rho\vec{c})dV+\int_{A}\vec{x}x(\rho\vec{c})d\dot{V}$$

The moment of momentum $\vec{L}$ results from the movement of a fluid element ρdV with velocity $\vec{c}$ relative to reference point with distance $\vec{x}$. The material derivation follows from a local change and a convective transport of the moment of momentum over the free surface of the control volume. The vector equation (3) has to be evaluated only for the component in machine axis direction and gives the nondimensional torque transmission coefficient.

Because of the relative movement of the blades the calculated torque is time dependent over one flow period. The consequences on torque transmission behavior can be analyzed in more detail by dividing the material derivation into the convective transport over the free flow area and the local, time dependent part. For laminar and turbulent simulations this is documented by Bai et al. [4] and more parameter analysis is done by Formanski et al. [1]. Here, it should only be hinted that with increasing slip the time dependent part shows a phase change against the convective part and increases its importance. Because of the periodicity in circumferential direction the mean value of the time dependent part is zero over one flow period.

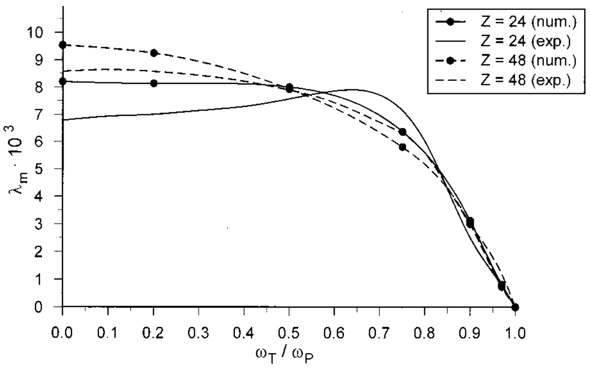

Fig. 7 Simulated and experimental operation characteristic

The operating characteristic follows from simulation of different points of operation. Figure 7 shows the calculated in comparison to measured values for the two basic geometries, which differ only in the number of blades. The difference between the values is for slip $s=0$ to $s=0.4$ lower than 10% and increases to 20% for blocked turbine, so that the results of the following parameter studies are transferable to industrial hydrodynamic couplings.

Conclusions

The significant points of understanding which follow from the foregoing flowfield analysis are summarized below along with the deduced modifications of the geometry that influence the secondary flows with the aim to improve the start up behavior of the coupling. In Part II of this paper some of these modifications will be investigated.

1 At high slip the pump shows from the gap to the middle of the wheel only axial velocity components. The energy transformation is limited to the wheel ground.

⇒ *Reduction of wheel width to half.*

2 A secondary flow forms between the blade tips in the pump and extends in circumferential direction over half the channel width.

⇒ *Fragmented blades fixed at the hub.*

3 Along the pump pressure side a dead water area is visible at nominal operation which extends from the hub to half the blade height.

⇒ *Fragmented blades fixed at the casing.*

4 At nominal operation the fluid is transferred along the turbine blade tips from the pressure to suction side.

⇒ *Gap at the back wall.*

5 In the turbine a secondary flow forms between the root of the blades, which extends at nominal operation over half the channel width.

⇒ *Fragmented blades fixed at the casing.*

6 At the turbine casing the axial and radial velocities increase with different gradients when leaving nominal operation.

⇒ *Reduction of number of blades.*

7 Departing from nominal operation means that maximum pressure differences are at the corner between blade tip and gap in the turbine.

⇒ *A reduction of blade length as well as height is of disadvantage.*

Acknowledgment

We thank DFG for financial support through SFB 278 Project B1 and Prof. M. Fiebig for his interest in this work.

N. K. Mitra—In Memorium

Professor N. K. Mitra died unexpectedly in October, 1999, at the age of 60. During my time at Ruhr University, I got to know and came to appreciate him as a kindly and reserved person. He was a wonderful teacher of mathematical techniques and their relationships to physical problems, especially in developing algorithms into numerical procedures. He gave to me not only professional guidance in my work, but also personal friendship during my graduate school career. The death of Dr. Mitra is therefore both a loss of an outstanding scientist, and also a painful personal loss.

References

[1] Formanski, T., Huitenga, H., Mitra, N. K., and Fiebig, M., 1995, ''Numerical investigation of 3D flow and torque transmission in fluid couplings under unsteady working conditions,'' *International Gas Turbine and Aeroengine Congress and Exposition*, 95-GT-81.

[2] Bai, L., Fiebig, M., and Mitra, N. K., 1997, ''Numerical Analysis of turbulent flow in fluid couplings,'' ASME J. Fluids Eng., **119**, pp. 569–576.

[3] Huitenga, H., Formanski, T., Mitra, N. K., and Fiebig, M., 1995, ''3D flow structures and operating characteristic of an industrial fluid coupling,'' *International Gas Turbine and Aeroengine Congress and Exposition*, 95-GT-52.

[4] Bai, L., Kost, A., Mitra, N. K., and Fiebig, M., 1994, ''Numerical investigation of unsteady incompressible 3D turbulent flow and torque transmission in fluid couplings,'' *International Gas Turbine and Aeroengine Congress and Exposition*, 94-GT-69.

[5] Perić, M., 1985, ''A finite volume method for the prediction of three-dimensional fluid flow in complex ducts,'' Ph.D. thesis, University of London.

[6] Schönung, B. E., 1990, *Numerische Strömungsmechanik*, Springer, Berlin.

[7] Khosla, P. K., and Rubin, S. G., 1974, ''A diagonally dominant second-order accurate implicit scheme,'' Comput. Fluids, **2**, pp. 207–209.

[8] van Doormal, J. P., and Raithby, G. D., 1984, ''Enhancement of the SIMPLE method for predicting incompressible fluid flows,'' Numer. Heat Transfer, **7**, pp. 147–163.

[9] Rhie, C. M., 1981, ''A numerical study of the flow past an isolated airfoil with separation,'' Ph.D. thesis, University of Illinois.

[10] Launder, B. E., and Spalding, D. B., 1974, ''The numerical computation of turbulent flows,'' Comput. Methods Appl. Mech. Eng., **3**, pp. 269–289.

[11] Kost, A., Mitra, N. K., and Fiebig, M., 1994, ''Computation of unsteady 3D flow and torque transmission in hydrodynamic couplings,'' *International Gas Turbine and Aeroengine Congress and Exposition*, 94-GT-70.

[12] Rai, M. M., 1987, ''Navier-Stokes simulations of rotor/stator interaction using patched and overlaid grids,'' J. Propulsion, **3**, pp. 387–396.

[13] Kost, A., Bai, L., Mitra, N. K., and Fiebig, M., 1992, ''Calculation procedure for unsteady incompressible 3D flows in arbitrarily shaped domains,'' Notes Num. Fluid Mech., **35**, pp. 269–278.

[14] Stone, H. L., 1968, ''Iterative Solution of Implicit Approximations of Multidimensional Partial Differential Equations,'' SIAM J. Num. Anal., **5**, pp. 530–558.

Improving Startup Behavior of Fluid Couplings Through Modification of Runner Geometry: Part II—Modification of Runner Geometry and Its Effects on the Operation Characteristics

H. Huitenga
Research Engineer,
Siemens AG/KWU,
45470 Mülheim, Germany

N. K. Mitra[1]
Professor,
Institut für Thermo- und Fluiddynamik,
Ruhr-Universität Bochum,
44780 Bochum, Germany

In Part I of this paper, we analyzed the turbulent flow structure and the torque transport characteristics of a fluid coupling. The results suggested certain modifications of the geometry which can improve the start-up behavior and reduce at the same time the material costs. In Part II we perform the numerical simulation of the flow in the modified geometry and investigate the influence of the modification on the performance.
[S0098-2202(00)02204-5]

Introduction

The numerical analysis of the flow structure in a hydrodynamic coupling with a chosen base design was carried out in Part I of this work. The basic equations, boundary conditions and the computational scheme are summarized in Part I and can be found detailed in Bai et al. [1].

Typical flow phenomena which affect pump and turbine in different ways are aligned to each point of operation. The following paragraphs will focus on three of the suggested six modifications. The missing three are discussed in detail by Huitenga [2]. These variations represent the first step in the line of improvement, because only one of the coupling wheels is modified. The difference between the original and the new geometry is analyzed locally by means of the flow field and over the whole operation field by means of the operating characteristic. The second step of improvement is done by reinforcing the single effects through a combined modification of pump and turbine, using only the most useful alterations.

Improvement No. 1: Reduction of Pump Wheel Width to Half

Figure 1 compares a hydrodynamic coupling of standard configuration with a modified one, where the pump wheel width is reduced by half. Because this modification affects all blades, its effects are analyzed through the distribution of the dimensionless static pressure difference Δp_s on the blades. The pictures on the right show the pressure in the original geometry and the ones on the left show the pressure in the coupling with the modified pump wheel. The dashed lines around the shaded areas indicate negative values of the pressure difference.

The original geometry shows at operation point $s=0.03$ in the pump the maximum pressure differences, which reach from the center of the blade to the back wall, while expanding to equal parts in radial direction. The pressure level decreases weakly along the region where the passage vortex shows velocity components directed toward the hub. At the blade base negative pressure differences are visible following from the secondary flow fields there. The minimum pressure in the turbine reaches over the whole blade width. It is limited toward the hub by a line parallel to the axis and toward the tip by a diagonal line ending in the corner between back wall and outer casing. Following this structure the pressure differences decrease in direction of the outer and inner diameters.

It becomes evident that the modification of the pump wheel has nearly no effect on the turbine. The structure of the pressure distribution is identical to the one in the base geometry, though the values lie beyond them. The distribution in the pump is similar to that in the original geometry from the middle of the blade to the

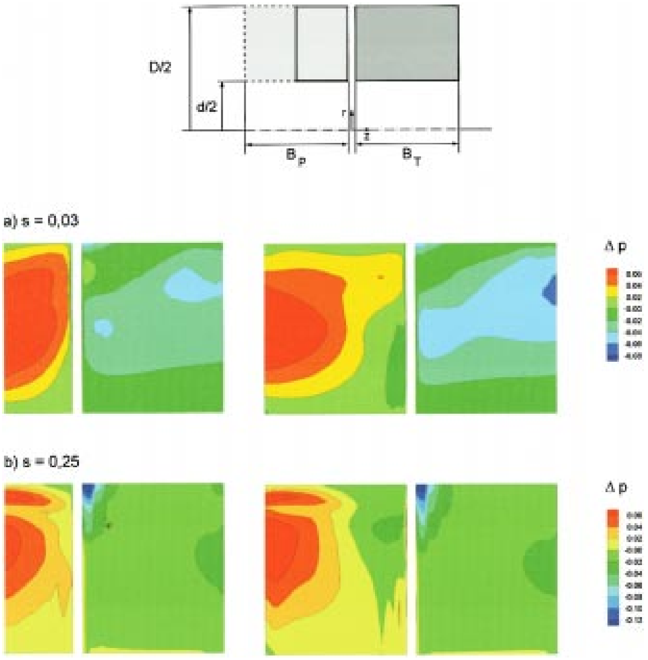

a) s = 0,03

b) s = 0,25

Fig. 1 Static pressure distribution on modified and standard coupling

---

[1] Deceased.

Contributed by the Fluids Engineering Division for publication in the JOURNAL OF FLUIDS ENGINEERING. Manuscript received by the Fluids Engineering Division December 4, 1998; revised manuscript received July 10, 2000. Associate Technical Editor: M. Dhavbhadel.

back wall. The maximum of the pressure difference extends in radial direction toward the hub as well as to the casing.

With increasing slip the maximum along the back wall of the pump falls into two pieces, because the circulation mass flow increases so that the passage vortex moves outwards. Thus, the stagnation point on the suction side shifts to the blade tip and the resulting pressure differences decrease. The outwardly directed throughflow occurs mainly along the back wall, so that the effects of the secondary flows are visible only to the middle of the wheel. Beyond that, the pressure on the blade front increases more slowly than on the back, which results in an area of negative pressure differences. The nonaligned flow to the blades due to the higher speed difference becomes noticeable through the detached vortex in the turbine due to impact. This results in a stagnation point between tip and leading edge of the blade with high static pressure, respectively, pressure difference minimum.

The modified coupling shows again no difference regarding the pressure distribution in the turbine. The pump shows the splitted maximum as in the base geometry but is lacking most of the negative pressure differences. The resulting operating characteristic for this coupling is compared to the original one in Fig. 4.

Improvement No. 3: Fragmented Blades in the Pump Fixed at Casing

Figure 2 shows a hydrodynamic coupling with a modified pump wheel where every second blade has a gap of 20% of the blade height between the root and the blade foot so that it ends inside the middle of the deadwater area described in Part I.

As a function of the relative position of the blades to each other the axial velocity profile in the pump is presented for $s=0.03$ for the original $(s_u/D=0)$ and the modified geometry $(s_u/D=0.07)$. The sectional plane is placed midway between the root of the modified blade and the hub.

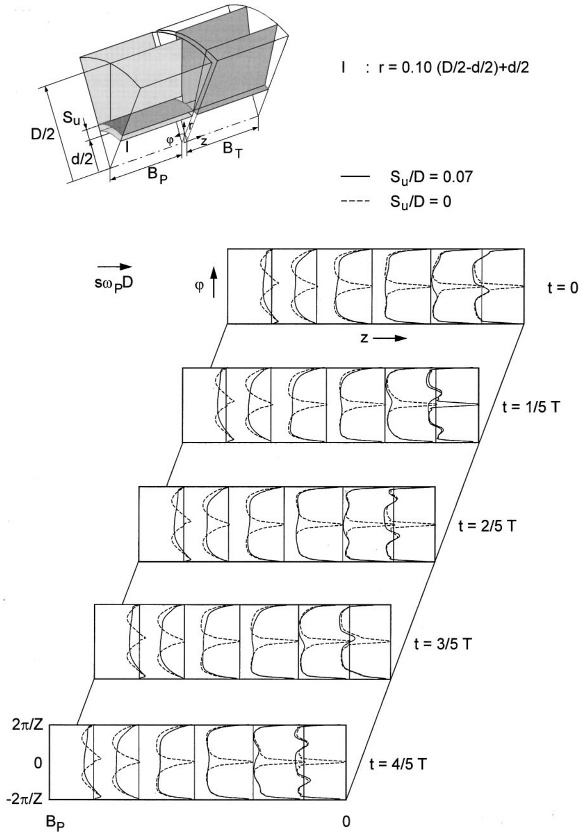

Fig. 2 Influence of relative motion on axial flow field

At point $t=0$ the blades in both wheels face each other. Because the axial guiding of the fluid along the blades vanished for the modified coupling, at all times two parts of the flow coming from the turbine mix inside the pump. This incident is distinguished by the minimum in the velocity profile as a typical wake. Because of the relative movement of the blades the wake moves toward the pump's blade front side during one period. The pressure gradient in circumferential direction shifts the mixture area inside the channel toward the suction side, so that the velocity maximum at point $t=0$ on the blade back moves to the middle of the channel at $t=2/5$ T to the blade front at $t=4/5$ T. Because of the largely homogeneous influx from the turbine the extension of the mixture zone is equal at all times, so that unrelated to the relative position the process of mixing is completed at 1/2 B_P.

The velocity profile in the modified geometry nearly covers the one of the basic geometry, whereby the deviations on the pressure side increase faster than on the suction side. Because of the missing development of a boundary layer in the middle of the channel more mass can be carried through. The expected massive influence on the dead water area is not obtained, because the dimensions are reduced by the increased number of blades already (see Part I). The effect on the operating characteristic is shown in Fig. 4.

Improvement No. 4: Gap at the Turbine Back Wall

The next modification focuses on the turbine wheel. A gap at the wheel ground of 20% of the blade width allows fluid to flow around the blade in axial direction from pressure to suction side. In Fig. 3 the flow process into the turbine is presented through the

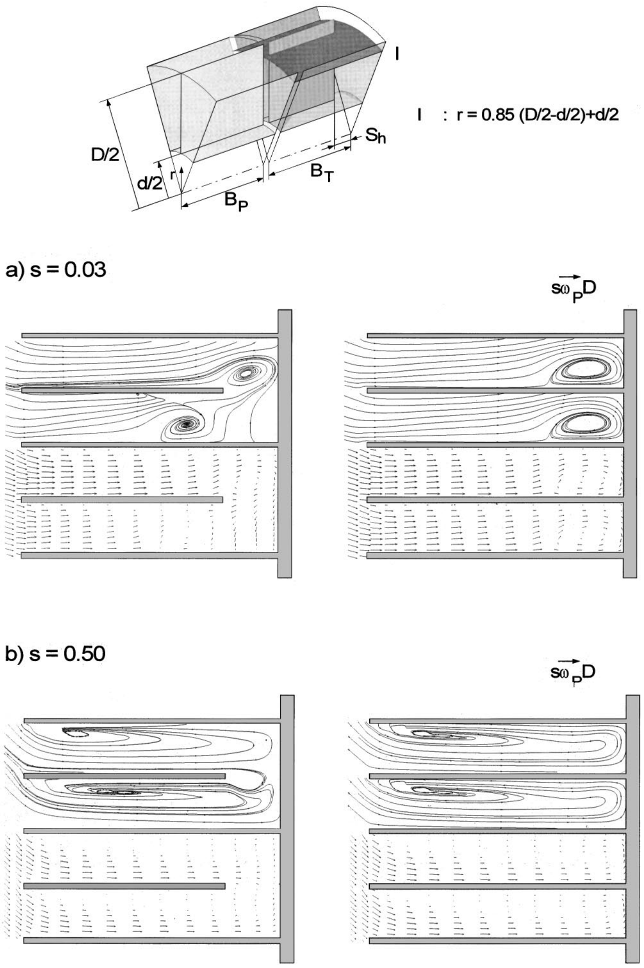

Fig. 3 Time averaged velocity vectors and streamlines

time averaged flow field for two different operational conditions. The cross section is placed near by the casing and shows the projected velocity vectors together with the calculated streamlines. Again, the modified coupling is presented on the left side, the original one on the right.

Figure 3(*a*) represents the nominal point of operation. It becomes clear that the reduction of the blade length does not lead to a dissolution of the secondary flow at the back wall. The axial extend of the vortex in the second channel, looking in the direction of rotation, is now determined by the gap itself. The limited extension in axial direction is combined with a smaller one in circumferential direction. The flow process into the turbine causes considerable effect on the velocity field in the first channel. The secondary flow field is shifted from the wheel ground toward the gap. The diagonal toward the blade directed velocities from the second channel lead to a stagnation point on the suction side. The axial flow through the first channel is tied up completely after half the channel length, so that the mass flow in the second channel is higher than in the first.

An increase of the speed difference between the two runners causes the circulating mass flow to increase as well as the mismatching flow towards the blades. The inflow concentrates mostly on the pressure side and shows along the whole blade width no velocity deceleration. Therefore the vortex found at nominal operation is displaced and the flow structure along the whole channel is dominated by the detaching vortex. At the wheel ground the fluid is guided toward the suction side unrelated to the design of the blades. Only a small amount of mass flows over from the second channel into the first one, so that neither the order of magnitude of the velocity vectors nor the dimension of the dead water area differ from the basic geometry. Figure 4 presents the resulting operation characteristic.

Pump **Turbine**

1. Reduction of wheel width *4. Gap at back wall*

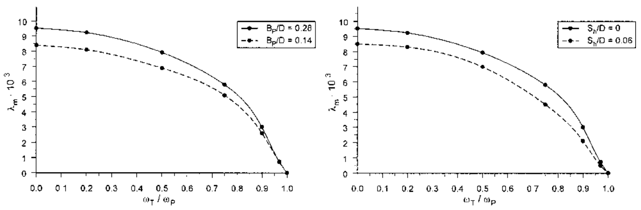

2. Fragmented blades fixed at hub *5. Fragmented blades fixed at casing*

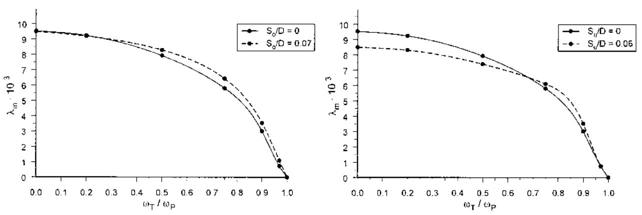

3. Fragmented blades fixed at casing *6. Reduction of number of blades*

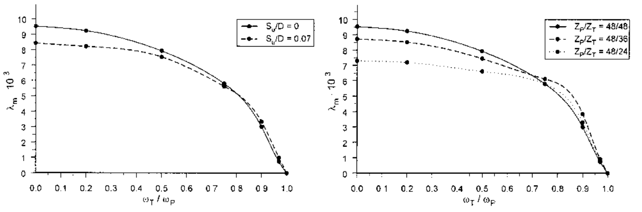

Fig. 4 Comparison of different pump and turbine modifications

Evaluation of the Effects on the Operation Characteristic

The effects on the operational characteristic from the modification of the runner geometries are presented for all 6 variants (see Part I) in Fig. 4, where the left-hand side deals with the pump and the right-hand side with the turbine modifications.

The effects on the flow field were discussed for the first variant by means of the pressure distribution on the blades (cf. Fig. 1). The characteristic of the modified coupling reaches the same torque level at nominal operation as the basic geometry does (Fig. 4(*a*)), because here the pump blade showed negative pressure differences near the gap, which don't show up in the new coupling. The degree of stiffness (DST) reduces about 10% and the transported torque decreases to about 95% of that of the starting geometry independent from slip.

The intention to modify the coupling with a gap between blade tip and casing, was to influence the passage vortex, which was found to be dominant at nominal operation. The extension of the secondary flow is reduced in the blade channel being second in the rotational sense. At the same time, the axial velocity is increased, so that the torque is raised by 51% and the degree of stiffness by 18% (Fig. 4(*b*)). With increasing slip the high radial velocities work against the direct flow around the blade tip from pressure to suction side. So both variants transport the same torque from $\omega_T/\omega_P = 0.3$ to the blocked turbine.

The dead water area at the blade front is influenced by the blade height reduction near the hub. The effects were discussed looking at the axial velocity distribution (cf Fig. 2). The torque at nominal operation exceeds the one of the basic geometry by 35% (Fig. 4(*c*)). With increasing speed the difference between the characteristics decrease, so that the lines cross each other at $\omega_T/\omega_P = 0.8$.

The gap at every second turbine blade along the wheel back wall leads to a severe flow around the blade tail (cf. Fig. 3). Therefore, the first blade channel is choked and the torque falls to about 70% of the initial one (Fig. 4(*d*)). With increasing slip the velocity fields in both channels equalize, so that the difference in torque transport minimizes. Nevertheless, the torque reaches only 90% of the original value at turbine standstill.

The fractional blades fixed at the casing cause the mass to flow with high circumferential velocities from the second to the first channel. This results in a common single secondary flow area at the hub. Additionally, the axial velocities are not affected, so that the torque is 3% higher at nominal operation (Fig. 4(*e*)). The positive effects intensify until $\omega_T/\omega_P = 0.9$ where an increase of torque transmission of 17% is found. With the turbine wheel slowing down the modified geometry reaches at $\omega_T/\omega_P = 0.7$ just the same value and runs nearly parallel to the basic geometry until $\omega_T/\omega_P = 0.0$.

The transition from nominal operation to braking causes, in conjunction with the detaching vortex in the turbine, low velocity gradients in the circumferential direction. While increasing the opening angle between the blades this structure can be used to increase the circulating mass flow. Two different kinds of blading are tested. It is obvious that having the number of blades reduces the start-up torque by 24% and the characteristic runs nearly horizontal until $\omega_T/\omega_P = 0.7$ (Fig. 4(*f*)). The nominal torque is slightly influenced by an increase of 7%, while the DST increases about 11%. With a blade ratio of $Z_P/Z_T = 48/36$ the tendency is reversed. Here the torque is increased at nominal operation by 26% and the DST by 29%. The whole partial operation shows values of about 7% beneath the ones of the starting configuration.

The reduction of mass comes to 3% for shortened blade runners and to 5% and 9%, respectively, for the modification with reduced number of blades in the turbine. Halving the pump wheel leads to 25% reduction of mass and is of interest since, simultaneously, the coupling volume becomes smaller.

All characteristics in Fig. 4 represent the modifications of one single basic geometry. Additional experimental data were ob-

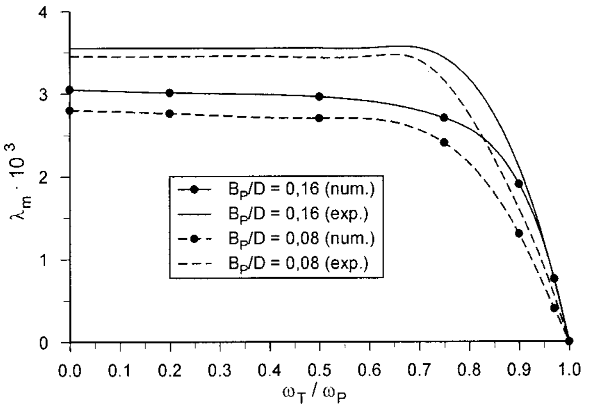

Fig. 5 Reduced pump wheel width for $Ek = 4.7 \cdot 10^{-6}$, $Z = 45$, $d/D = 0.40$

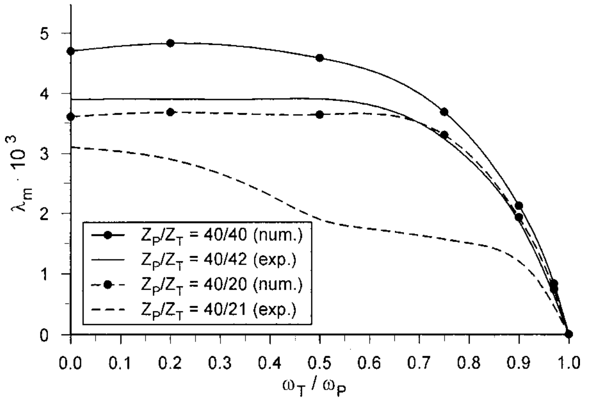

Fig. 6 Reduced number of blades for $Ek = 2.5 \cdot 10^{-6}$, $B/D = 0.17$, $d/D = 0.49$

a) Optimisation of start-up behaviour

⇨ **Pump with fragmented blades fixed at hub,**
Turbine with reduced number of blades

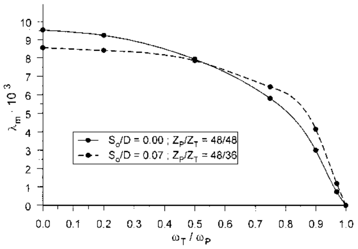

torque (nominal):	+ 63%
degree of stiffness:	+ 29%
torque (start-up):	− 10%
mass:	− 8%

b) Reduction of mass

⇨ **Pump with half wheel width,**
Turbine with reduced number of blades

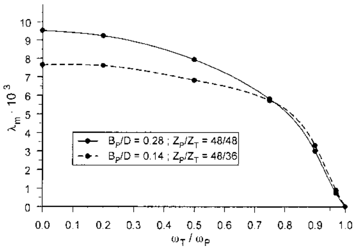

torque (nominal):	+ 22%
degree of stiffness:	+ 7%
torque (start-up):	− 20%
mass:	− 30%

Fig. 7 Optimization of start-up behavior and reduction of mass

tained from two hydrodynamic couplings which were tested under different operational conditions (see Fister [3]). In both cases, the calculations again agree well with the experiments.

One geometry was tested with a reduced length of the pump runner. In Fig. 5 the calculated torque transport is 25% less than the experimental value over the whole range of slip. But the calculated and measured characteristics of the modified coupling run both only 10% beneath the original one, so that the tendency predicted by the presented numerical results is confirmed.

The reduction of the number of blades in the turbine by half has also been compared with experiments. Although the coupling was not completely filled with the working fluid, leading to a severely different operation characteristic, it was found that the experimental and numerical data indicate a reduction of start-up torque by 10% (Fig. 6). On the other hand, the torque at nominal operation and the degree of stiffness slightly increase, so that this examination again confirms the results above.

Conclusion

For the optimization of the transmission behavior it is necessary to combine a pump wheel with fractional blading and a turbine wheel with 36 blades (Fig. 7(*a*)), because the reduced pump wheel width will at any rate lead to a lower start-up torque, which has to be compensated. It can be seen that the operational features of both variants superimpose at low slip, so that the torque at nominal operation raises about 63% and the DST about 29%. The clear increase in torque transmission until $\omega_T/\omega_P = 0.5$ results together with the 90% reduced start-up torque to an operational characteristic which allows the hydrodynamic coupling to be used for start-up application. The mass of the coupling is reduced by 8% from the basic geometry.

If the development focuses on the mass and volume reduction, a half-width pump runner combined with a turbine runner with 36 blades is suitable. With this wheel combination it is also possible to increase the torque at nominal operation by 22% and the DST by 7% (Fig. 7(*b*)). Because the start-up torque sinks to 80% the operational characteristic has an even expiration. Besides the good adaptation of the operational condition the mass can be reduced by 30%.

Acknowledgment

We thank DFG for financial support through SFB 278 Project B1 and Prof. M. Fiebig for his interest in this work.

Nomenclature

A = surface area of blade channel
C_j = convective term, $j = 1,2,3$
D = outer diameter
D_j^{Φ} = diffusive term, $j = 1,2,3$
DST = degree of stiffness, $\mathrm{DST} = d\lambda / d(\omega_P/\omega_T)|_{s=0.03}$
$\underset{\sim}{J}$ = Jacobian
$\underset{\sim}{\mathbf{L}}$ = moment of momentum
$\underset{\sim}{\mathbf{M}}$ = torque
S_{Φ} = source term
V = control volume
Z = number of blades
$\vec{\mathbf{c}}$ = velocity vector in relative system
k = turbulent kinetic energy
$\dot{\mathbf{m}}$ = circulating mass flow
r = distance between fluid element and rotational axis
s = slip, $s = (\omega_P - \omega_T)/\omega_P$
t = time
u,v,w = velocity vector components in relative system
$\vec{x}$ = distance between fluid element and reference point
Δp = dimensionless static pressure difference, $\Delta p = (p_{\mathrm{Front}} - p_{\mathrm{Back}})/(\varrho \omega_P(\omega_P - \omega_T)D^2)$
ε = dissipation rate
λ = nondimensional torque

ξ_j = generalized coordinates, $j=1,2,3$
ϱ = density
Φ = conserved intensive property
ω = angular velocity

Indices

A = exit
E = entrance
P = pump
T = turbine
m = meridional direction
u = circumferential direction

References

[1] Bai, L., Fiebig, M., and Mitra, N. K., 1997, ''Numerical Analysis of turbulent flow in fluid couplings,'' ASME J. Fluids Eng., **119**, pp. 569–576.
[2] Huitenga, H., 1997, *Verbesserung des Anlaufverhaltens hydrodynamischer Kupplungen durch Modifikation der Kreislaufgeometrie*, VDI, Düsseldorf.
[3] Fister, M., 1993, *Experimentelle Untersuchung an hydrodynamischen Kupplungen mit verstellbaren Kanälen*, Ph.D thesis, Bochum.

Mustafa Tutar
Makine Muhendisligi Bolumu,
Mersin Universitesi,
Ciflikkoy 33160, Mersin, Turkey
e-mail: m.tutar@mersin.edu.tr

Arne E. Holdø
Aeronautical, Civil and Mechanical
Engineering Department,
University of Hertfordshire,
Hatfield Herts, AL 10 9 AB U.K.

Large Eddy Simulation of a Smooth Circular Cylinder Oscillating Normal to a Uniform Flow

Results of a numerical evaluation of transitional flow around a circular cylinder forced to oscillate in a direction normal to a uniform flow are presented. The cylinder is considered to be a representative of a single riser exposed to a steady current. Numerical simulations were carried out using the LES method in 2-D and 3-D with a near-wall approach that was developed without using a ''law of the wall'' for a finite element code (FEM). The 3-D simulations were compared with the 2-D results and experimental data in order to assess the relative performance of the 3-D LES simulations. The results show that 3-D LES gives more realistic flow field predictions and can further remove overconservatism in the prediction of hydrodynamic force coefficients. [S0098-2202(00)01103-2]

1 Introduction

Offshore risers are essential parts of modern offshore technology. The risers may be many hundred meters long and have diameters of around 0.5 meters. The present work is an initial framework for the use of Computational Fluid Dynamics (CFD) in the modeling of the hydrodynamic forces on risers connected to floating oil and gas production systems. Due to the dimensions of typical risers it is difficult to model them in laboratory scale at realistic Reynolds numbers, thus the application of CFD to such studies may be very useful for future offshore projects. While risers experience higher Reynolds numbers and different oscillatory frequencies to those reported here, there is little experimental data available for these situations. On the other hand, it is necessary to compare the simulation results with experimental values that are available in the literature.

The early experimental studies conducted by Tritton [1] and Achenbach [2] show that even at a relatively low Reynolds number the flow around a circular cylinder becomes turbulent and the boundaries of the flow regimes are directly influenced by the change in the Reynolds number. Bearman and Currie [3] emphasize the effect of cylinder oscillation frequency and/or amplitude on the flow as well as that of Reynolds number. The extensive experimental study of Sarpkaya [4] shows that for rough cylinders, force coefficients depend also on the surface roughness and differ significantly from corresponding to the smooth cylinder. On the other hand, Williamson [5] indicates that three dimensionality plays a role in the wake flow dynamics of the cylinder motion. The conclusion from these well-known experiments is that oscillatory frequency and/or amplitude, three dimensionality, surface roughness, and Reynolds number are the main governing parameters that significantly affect the hydrodynamic forces on the cylinder.

In recent years, there have been a number of numerical studies to examine these governing parameters and hence to predict their effects on the flow around a bluff body. The numerical representation of the cylinder movement in the computational domain and the modeling of turbulence have been important considerations. In tackling cylinder oscillation and simulating the effect of cylinder movement on the flow, Hurlburt et al. [6] and Chilikuri [7] use a noninertial Eulerian grid system that is fixed to the cylinder oscillating normally to a uniform laminar flow. They modify Navier-Stokes equations with acceleration terms. Sun et al. [8] use an inertial Eulerian fixed grid system in which cylinder oscillation is represented by sinusoidal slip velocity boundary conditions. In contrast, Namura [9] and Wei et al. [10] carry out successful Arbitrary Lagrangian and Eulerian (ALE) solutions in which the mesh is moved in the vicinity of the cylinder surface while being fixed in the far field. Although ALE formulation in these studies seems promising, it is computationally expensive and time consuming as it requires a great number of mesh points to be transformed to their new position in the computational domain. There is also a chance for meshing errors. In pointing out this fact, Tutar and Holdǿ [11] suggest that for small cylinder displacements, a flow problem defined with the ALE formulation in a moving domain can be remodeled in a fixed inertial Eulerian grid system by adding a new body force term to the governing equations which are valid in a fixed Eulerian grid system.

Numerical modeling of turbulence is the another issue to be tackled. Since the time and space scales of turbulent motion are so small, the large number of grid points and small size of the time steps required makes direct computation of turbulent flow still impractical. Therefore, in order to accomplish the complete solution of the flow field equations for bluff body, some simplification of the flow system by using an appropriate turbulence model is needed. Numerical simulations carried out by Majumdar and Rodi [12] suggest that the widely used Reynolds-averaged Navier-Stokes equations (RANS) based standard two-equation turbulence models ($k-\varepsilon$ and $k-l$) are incapable of accurately predicting turbulent flows where the local isotropy of the turbulent stress play an important role. However, the nonlinear RNG $k-\varepsilon$ model and the anisotropic eddy viscosity model of Launder [13] used by Tutar et al. [14] improve the resolution of the turbulent flow and hence the calculation of dynamic loading on a stationary cylinder. Furthermore, the Large Eddy Simulation (LES) of turbulent flows based on the Smagorinsky Sub-Grid Scale (SGS) turbulence model is shown to yield far more realistic flow results than those obtained by traditional two-equation turbulence models due to Tutar et al. [14]. Zhang and Dalton [15], Wang and Dalton [16] and Lu et al. [17] also perform SGS based 2-D LES simulations for flow around a circular cylinder in order to investigate the fluid-cylinder interactions within different modes of oscillatory motion.

Contributed by the Fluids Engineering Division for publication in the JOURNAL OF FLUIDS ENGINEERING. Manuscript received by the Fluids Engineering Division September 21, 1999; revised manuscript received May 5, 2000. Associate Technical Editor: F. Wasden.

It is also concluded that LES-based simulations are not overly expensive in terms of computing time when compared with realistic two-equation based simulations.

The present work deals with the CFD modeling of the hydrodynamics of a smooth circular cylinder forced to oscillate transversely at a Reynolds number representative of an actual riser of small diameter (Re=10,000 to 100,000). At such Reynolds numbers it is necessary to include a turbulence model in order to simulate the effects of turbulence on the flow. Using the conclusion of their previous work, for this the authors have used the LES simulation of those flows based on a Smagorinsky Sub-Grid Scale turbulence model.

It is frequently suggested that 2-D simulations can yield adequate results for predicting the load on a riser. The aim of the present work was to compare typical 2-D results with those obtained from limited 3-D simulations in order to understand any benefits of 3-D simulations and any limitations of 2-D simulations.

2 Governing Equations

For the present isothermal, incompressible, viscous flow conditions, the flow could be represented by the Navier-Stokes equations. However, as the flow was at a sufficiently high Reynolds number to become turbulent, it was also necessary to include a model to cater for the effects of turbulence on the flow field. Previous work by Tutar et al. [14] using various turbulence models demonstrated that models based on RANS were inadequate for this type of flow. Instead the work showed that Large Eddy Simulations (LES) gave an improved simulation of the flow. LES is based on the idea that the large turbulent eddies are resolved by the computational grid, while the eddies which can not be resolved or smaller than the grid size need to be modeled. We use the time-averaged Navier-Stokes equations, with the subgrid scale stress term

$$\tau_{ij}=\widehat{u_i u_j}-\hat{u}_i\hat{u}_j \tag{1}$$

and its anisotropic part is represented by an eddy viscosity like model

$$\tau_{ij}=-v_t\left(\frac{\partial \hat{u}_i}{\partial x_j}+\frac{\partial \hat{u}_j}{\partial x_i}\right) \tag{2}$$

In the above equation, the relationship for the eddy viscosity is obtained in a similar fashion to that of the commonly used viscosity model for the Reynolds stress. A natural length scale for the small eddies is provided by the width of the cell (Δx_i). Only one time scale is required and the natural choice is a velocity derivative. This leads to the following model due to Smagorinsky [18]

$$v_t=(C_s\Delta)^2(2\hat{S}_{ij}\hat{S}_{ij})^{1/2} \tag{3}$$

In the present work, Δ is a characteristic length scale related to the local average grid size. In the 2-D case and 3-D case the values are as follows

$$\Delta=f(\Delta x_1\Delta x_2)^{1/2} \quad \text{or} \quad \Delta=g(\Delta x_1\Delta x_2\Delta x_3)^{1/3} \tag{4}$$

respectively.

The flows in the boundary layer near the cylinder walls need careful modeling. This is because of the high velocity gradients in these regions and the increased anisotropy of the turbulent fluctuations as the wall is approached. There is also a transition from the near wall laminar sublayer through the buffer layer and all these mechanisms affect separation and the separation point which are vital for the prediction of the flow around the cylinder.

Wall effects were taken into account by introducing a damping term in the calculation of length scale in the vicinity of the cylinder surface up to 8 percent of the cylinder diameter. This distance was considered to be an approximate wall effective layer thickness in the present turbulence flow. The damping term ensured that the length scale near the wall would become zero at the cylinder surface and had an alternative form of the van Driest damping function [19] as follows

$$D_\tau=1-\exp\left[-\left(\frac{y^+}{A^+}\right)^2\right] \tag{5}$$

where y^+ is the inner law variable that is considered to be the dimensionless normal distance from the cylinder surface and A^+ is an empirical damping constant which assumes a value of about 26 for the present study owing to the fact that cylinder has smooth surface. Consequently, the Smagorinsky model was rewritten in the near wall region of the cylinder with

$$l_s=C_s\Delta D_\tau \tag{6}$$

Another crucial issue was the choice of an optimum value for the length scale parameter, C_s (also called Smagorinsky constant) in the above equation. In most applications to flow with mean shear smaller values of C_s are found necessary to avoid excessive damping of the resolved structures. McMillan et al. [20] show that C_s must decrease with increasing strain rates. Mason and Callen [21] find that the a value $C_s=0.20$ gives good predictions if the resolution is sufficiently fine, and conclude that lower values of C_s are required only if the grid resolution is sufficient. Piomelli et al. [22], on the other hand, claim that the optimum value of C_s to be around 0.10 even with meshes much finer than those used by Mason and Callen [21]. In conclusion, there is not much agreement on the value of C_s. Values ranging from 0.060 to 0.30 have been claimed to be optimum by different authors, depending upon the unclear correlation with the flow conditions, the grid size, and the numerical methods employed. In the present work, since the values higher than 0.20 and lower than 0.10 caused excessive damping of large-scale fluctuations and convergence problem respectively, the optimum value for was then chosen to be 0.15 for all calculations.

3 Problem Formulation

In order to simulate the effect of cylinder oscillations, a major issue to address is the treatment of the moving interface between the fluid and the oscillating rigid body. In the present work, the moving boundary was treated in a noninertial Eulerian grid system which is fixed relative to the oscillating cylinder. This was carried out by a noninertial coordinate transformation from the stationary Eulerian frame system to a noninertial Eulerian frame system moving with the cylinder. If primitive variables are used, it is clear that Navier-Stokes equations as generally used by CFD software are only applicable in an inertial fixed Eulerian reference system. These equations need to be modified with additional terms in a new noninertial Eulerian frame system.

For an oscillating cylinder in the transverse direction with an amplitude A and an oscillation frequency $2\pi f_c$ the motion is given as

$$\lambda(t)=-A\cos 2\pi f_c t \tag{7}$$

where $\lambda(t)$ gives the cylinder displacement in the transverse direction. The noninertial coordinate transformation in the transverse direction enables the time dependent deforming interface to be treated as a stationary nondeforming new interface. The initial transformation can be carried out in the y-direction as follows

$$\overline{y}=y-\lambda(t) \tag{8}$$

Due to the transformation, the velocity and pressure components in the x and y direction are transformed as follows

$$\begin{aligned}\overline{u}&=u,\\ \overline{\nu}&=\nu-\frac{\partial\lambda(t)}{\partial t},\\ \overline{P}&=P\end{aligned} \tag{9}$$

The constraining of the cylinder motion is only in the y direction and there is thus no relative velocity change between the flow and the cylinder in the x direction (or z direction in 3-D simulations). In the new noninertial coordinate system the cylinder appears as a stationary cylinder. The governing equations can now be transformed to a new accelerating frame that is fixed relative to the cylinder and are spaced averaged as follows

$$\frac{\partial \hat{\overline{u}}_i}{\partial t}+\frac{\partial}{\partial x_j}\hat{\overline{u}}_i\hat{\overline{u}}_j=-\frac{1}{\rho}\frac{\partial \hat{\overline{P}}}{\partial x_i}+\frac{\partial}{\partial x_j}\left[\nu\left(\frac{\partial \hat{\overline{u}}_i}{\partial x_j}+\frac{\partial \hat{\overline{u}}_j}{\partial x_i}\right)-\tau_{ij}\right]+A_i(t) \tag{10}$$

$$\frac{\partial \hat{\overline{u}}_i}{\partial x_j}=0$$

In the above equation $\hat{\overline{u}}_i$ is the spaced averaged relative velocity component, the term $A_i(t)$ is the extra term resulting from the noninertial coordinate transformation from the frame of reference (x,y,z) to a new frame $(\overline{x},\overline{y},\overline{z})$ that moves with the harmonically oscillating cylinder. This term here was treated as an additional body force per unit mass for the flow field defined in a fixed Eulerian method and is given as follows

$$A_i=-\frac{\partial^2\lambda(t)}{\partial t^2}=-(2\pi f_c)^2A\cos 2\pi f_c t \tag{11}$$

4 Computational Principles

4.1 Solution Method. All simulations were carried out by using the FIDAP finite element code [23]. The dimensionless time step (Ut/D) was 0.03 for all simulations.

The computational domain and boundary conditions used for the 2-D models are given in Fig. 1 while Fig. 2 displays the 3-D boundary conditions and computational domain. The domain was extended laterally to minimize the effects of the boundaries on the flow around the cylinder. The blockage ratio of the cylinder within the computational domain was 0.071, less than the value 0.08 needed to eliminate blockage effects on the flow following the study of Ramamurthy and Ng [24]. In the present case there were also no boundary layers on the side walls of the domain (boundary layers are of course present on wind tunnel walls) due to the free-slip boundary conditions; thus effects of blockage would be less than for a typical experimental case. The domain extended far enough downstream so that a vortex street with several vortices could be attained. The calculations were carried out with a non-uniformly spaced grid with 21,864 and 34,804 nodes for the simulations in 2-D to study mesh sensitivity. The LES simulations contain high a number of nodes because the LES method is based on the concept of space averaging, and requires resolving the larger turbulent eddies in the flow by the grid.

For the 3-D case the grid was extended in the direction of the cylinder axis. The total number of grid points for this mesh was 108,624 and the domain was extended $4D$ along the cylinder axis or z-direction. The length of computational domain in the z-direction was not very large, so that the arguments about the 3-D structures hereafter would be limited to the eddies that were small compared to the diameter of the cylinder. Since the primary interest here was to simulate the effects of smaller eddies better called secondary eddies in the free shear layer and to show the existence of three dimensionality in the wake, the length of $4D$ along the cylinder axis was sufficient. Alternatively, the imposition of periodic boundary conditions would also simulate the infinite cylinder and contribute to the three dimensionality. In the 3-D case the following boundary conditions in a noninertial Eulerian frame were applied:

1 No slip velocity boundary conditions on the cylinder surface $(u=v=w=0)$

2 Uniform flow at the inlet $(u=U,\ v=w=0)$

3 Free outflow boundary conditions

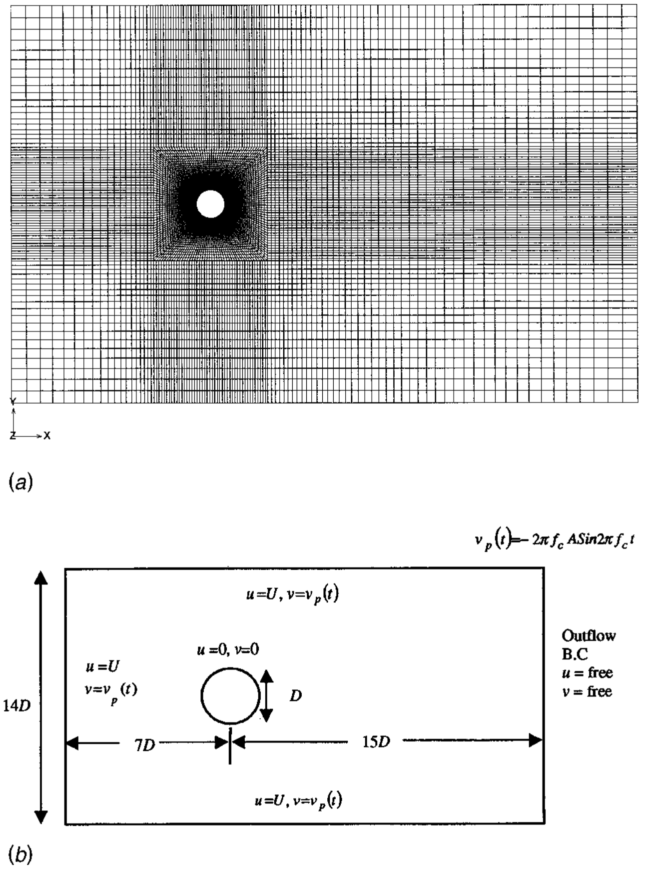

Fig. 1 Computational domain and the imposition of boundary conditions for 2-D LES simulations for a cylinder transversely oscillating in a uniform flow at Re=2.4×10^4 and A/D=0.11; (a) Global mesh (34,804 nodes); (b) Imposed boundary conditions

4 Oscillatory velocity boundary conditions in the y-direction and uniform flow in the x-direction at the upper and lower side face of the computational domain $(v=-2\pi f_c A\sin(2\pi f_c t),\ u=U,\ w=0)$

5 Periodic boundary conditions at the top and bottom surfaces in order to simulate an infinite cylinder.

5 Results

The results are presented both as primitive variable plots as well as integrated values. While the primitive variables can be obtained directly from the simulation, the integrated values need to be obtained by manipulation.

The total force acting on the cylinder (in both 2-D and 3-D) was determined from integrating the pressure and shear stress contributions. The total drag and transverse force coefficients were then calculated as follows

$$C_D=\frac{F_x}{\frac{1}{2}\rho U^2 D}$$
$$C_{tf}=\frac{F_y}{\frac{1}{2}\rho U^2 D} \tag{12}$$

The lift force (coefficient) was corrected for cylinder acceleration by taking the inertia effects into account in the following formulas:

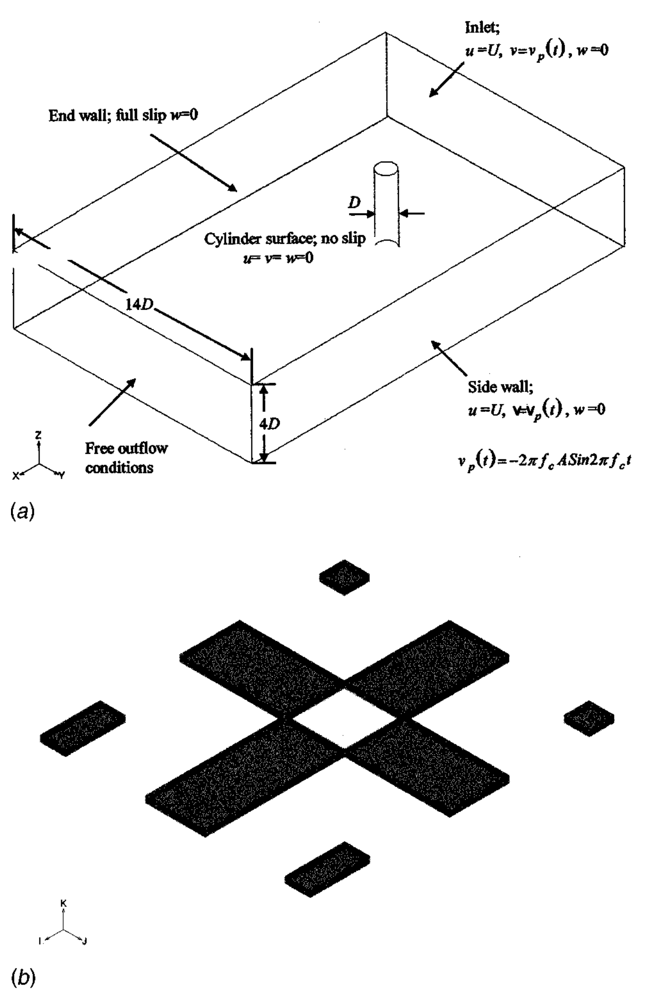

Fig. 2 Computational setup for 3-D LES simulation for transversely oscillating circular cylinder; (a) Size of domain and imposition of boundary conditions; (b) Logical description of the 3-D model

$$C_{tf}=C_L+\left(\frac{\pi D}{2U^2}\right)C_A\frac{d^2\lambda(t)}{dt^2} \tag{13}$$

In the above equation the choice of the added mass coefficient C_A was critical. The added mass coefficient for a fixed cylinder as suggested by Lipsett and Williamson [25] may be expressed as $C_A=C_M-1$, where C_M is the inertia coefficient. An extensive study for the determination of C_M was conducted by Sarpkaya [26] who investigated the variation of the value of C_M depending upon the Keulegan-Carpenter number [27], K ($K=2\pi A/D$ for harmonic oscillation), Re number and viscous parameter, β ($\beta=\mathrm{Re}/K$). Sarpkaya [26] shows that over a large range of β with measurements carriout out for circular cylinders in a planar oscillatory flow of small amplitude, C_M has the theoretical value $C_M=2$ due to the formulation of Wang [28] in the range of $0<K<4$. However, for K larger than about 4 there is a significant deviation from the value $C_M=2$ and the determination of C_M needs careful investigation. With this in mind, since the present work was conducted at relatively low amplitude-to-diameter ratio of 0.11, C_M assumed to have a value of and hence C_A had a value of 1. The drag coefficient on the other hand was not affected by inertia forces due to transverse oscillations.

5.1 Results From 2-D Simulations. The 2-D case was first tested for mesh sensitivity. Previous work suggested that mesh systems based on 21,864 and 34,804 nodes should be studied, Tutar [29]. First a study for a stationary cylinder at a Reynolds number of 1.4×10^5 was carried out. The results were compared with the experimental work of Cantwell and Coles [30]. An illustration of the findings is shown in Fig. 3. Here the time averaged centerline velocity behind the cylinder is compared for different cases. It is seen that when the number of nodes is increased to 34,804 then there is a better agreement with the experimental results. The time averaged recirculation length is increased by 9 percent, which is in better agreement with the experimental data. An increase in the application of the damping term of the length scale from 2 percent of the cylinder diameter to 8 percent also improves the prediction of the time averaged velocity distribution. This indicates that the turbulence length scale is not only required to be reduced in the boundary layer but also in the near wall region of the separated flow. On the other hand, Fig. 4 illustrating the turbulence levels obtained at $x/D=1$ for the two mesh resolutions suggest that the higher mesh resolution and longer turbulence length scale damping range gives better agreement with experimental results. Remainder of the work was carried out with 34,804 nodes mesh nodes.

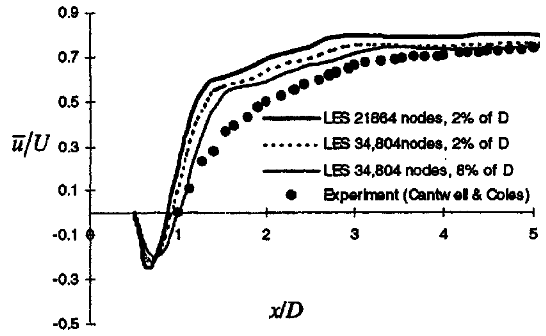

Fig. 3 Time averaged velocity distribution along the centerline of a stationary circular cylinder at a Re=1.4×10^5 for LES simulations containing different mesh resolutions and application range of damping term

The next 2-D simulation was carried out for a cylinder oscillating for a range of values of reduced velocities (U/f_cD) at an amplitude to diameter ratio (A/D) of 0.11. Due to the limited amount of experimental data available, the test case was based on the results of Bearman and Currie [3]. The data were obtained at a Reynolds number of 2.4×10^4 and a stationary cylinder test for the Reynolds number of 2.0×10^4 was also carried out and compared with the data due to Yokuda and Ramaprian [31]. Typical 2-D results from this test series is seen in Fig. 5(a)–(c). The instantaneous vorticity contours for each transverse simulation case

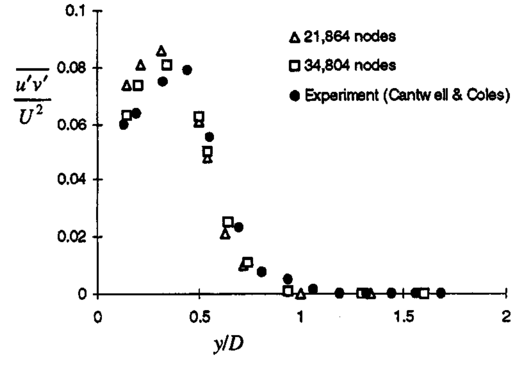

Fig. 4 The comparison of global time averaged shear stress distribution for LES simulations with different mesh resolutions and experimental data of Cantwell and Coles [30] due to turbulence at $x/D=1.0$ for a stationary cylinder in a uniform flow at Re=1.4×10^5

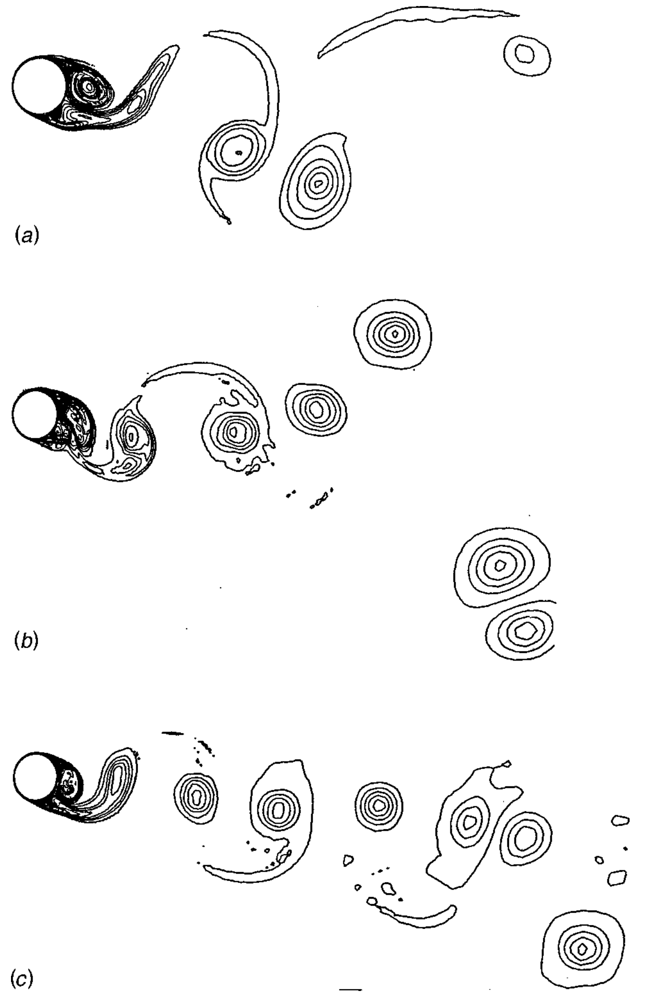

Fig. 5 Instantaneous vorticity contours taken with a constant contour value for 2-D LES simulation for a cylinder transversely oscillating in a uniform flow at Re=2.4×10^4 and A/D =0.11 with varying reduced velocity U/f_cD; (a) $U/f_cD=3$; (b) $U/f_cD=5.4$; (c) $U/f_cD=9.0$

when the cylinder is at its extreme upper position at the end of the fourth oscillation cycle. An interesting finding is that the two-vortex row does not persist in the wake due to its instability. It is clear that the ratio of the lateral to longitudinal vortex spacing is much larger than the limit for the stable von Karman vortex street which contains negative and positive vorticies. For the low reduced velocities there is a strong near wake vorticity which causes the formation length to decrease and this leads to higher lift and drag forces experienced by the cylinder.

When comparing the 2-D oscillating cylinder results with the experimental values of pressure distribution (Yokuda and Ramaprian [31]), it is seen from Fig. 6 that while there is good agreement between the predictions and the experimental results on the streamwise side of the cylinder there are differences on the leeward side especially in terms of time averaged base pressure. Returning to Fig. 5, all the results indicate that the manner by which the vorticies are formed at the early stage of the vortex street development shows similarities regardless of the cylinder oscillation frequency. However, the asymmetry in the flow develops differently owing to the cylinder oscillation frequency and causes the cylinder to experience varying unsteady forces. The secondary eddies have an important role in terms of the determination of some important features such as the location of the separation point, transition of the flow regime in the separated shear layer and small scale fluctuations which are associated with the three-dimensional nature of the flow. It is also noticed that the vortices are dissipated quickly into the wake.

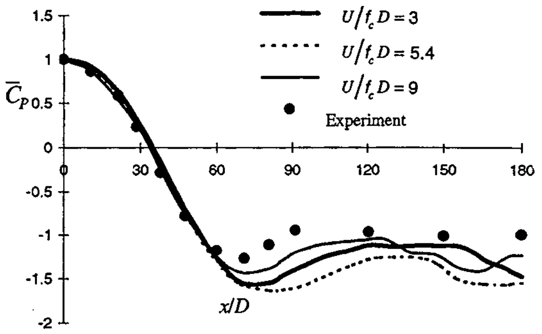

Fig. 6 Time averaged pressure distribution over two oscillation cycles for all 2-D LES simulations for different values of U/f_cD for a cylinder transversely oscillating in a uniform flow at Re=2.4×10^4 and A/D=0.11. Experimental data is for a stationary cylinder at Re=2.0×10^4 (Yokuda and Ramaprian [31]).

5.2 Results From 3-D Simulations. 3-D simulations were carried out at Reynolds number of 2.4×10^4 and were based on the experiments of Bearman and Currie [3] for a transversely oscillating cylinder at an $A/D=0.11$ and $U/f_cD=5.4$. A few different presentations of the results of this simulation are shown in Fig. 7. The boundary layer separates at about time averaged separation angle of 75 deg from the front stagnation point of the cylinder and the fluid is also separated from the main flow in the near wake. The flow departs from two dimensionality at station 3 and this suggests a development of a 3-D wake zone behind the cylinder. This is qualitatively in agreement with Roshko [32,33] who observed that the 2-D vortex wake undergoes transition to three dimensionality at a Reynolds number of 180. The transition was observed in the form of irregularities in the wake velocity fluctuations and different forms of streamwise vorticity in the wake.

5.3 Comparison Between 2-D and 3-D Simulation Results. Instantaneous vortex plots obtained from the 2-D and 3-D simulations are compared with each other when the cylinder is at $Ut/D=10.8$. These are shown in Fig. 8. It can easily be noticed that the space between the vortices in the transverse and streamwise directions and the width of the vortex formation length change considerably when the simulation dimension is changed from two to three. 2-D simulation generates a shorter vortex formation length and hence larger lateral spaces of the vorticies compared with those of the 3-D simulations. The elongation of the vortex formation region in 3-D simulation causes a decrease in drag. On the other hand, when the vorticity plots presented for two different spanwise locations are compared with each other (3-D simulation) there is not a noticeable difference in terms of vortex strength and vortex elongation in the wake.

The three dimensionality in the near wake of the flow of interest was further assessed by investigating the spanwise variation of some unsteady quantities related to the vortex shedding frequency, such as the fluctuating pressures. The profiles of the spanwise correlation coefficient of the streamwise and transverse velocity components and pressure in the near wake are illustrated in Fig. 9. There is a reduction in correlation coefficient toward the center of the cylinder in the spanwise direction. The value of the correlation coefficient of transverse velocity component is reduced to 0.85 indicating a 15 percent reduction toward the center of the spanwise direction. The correlation coefficient of those

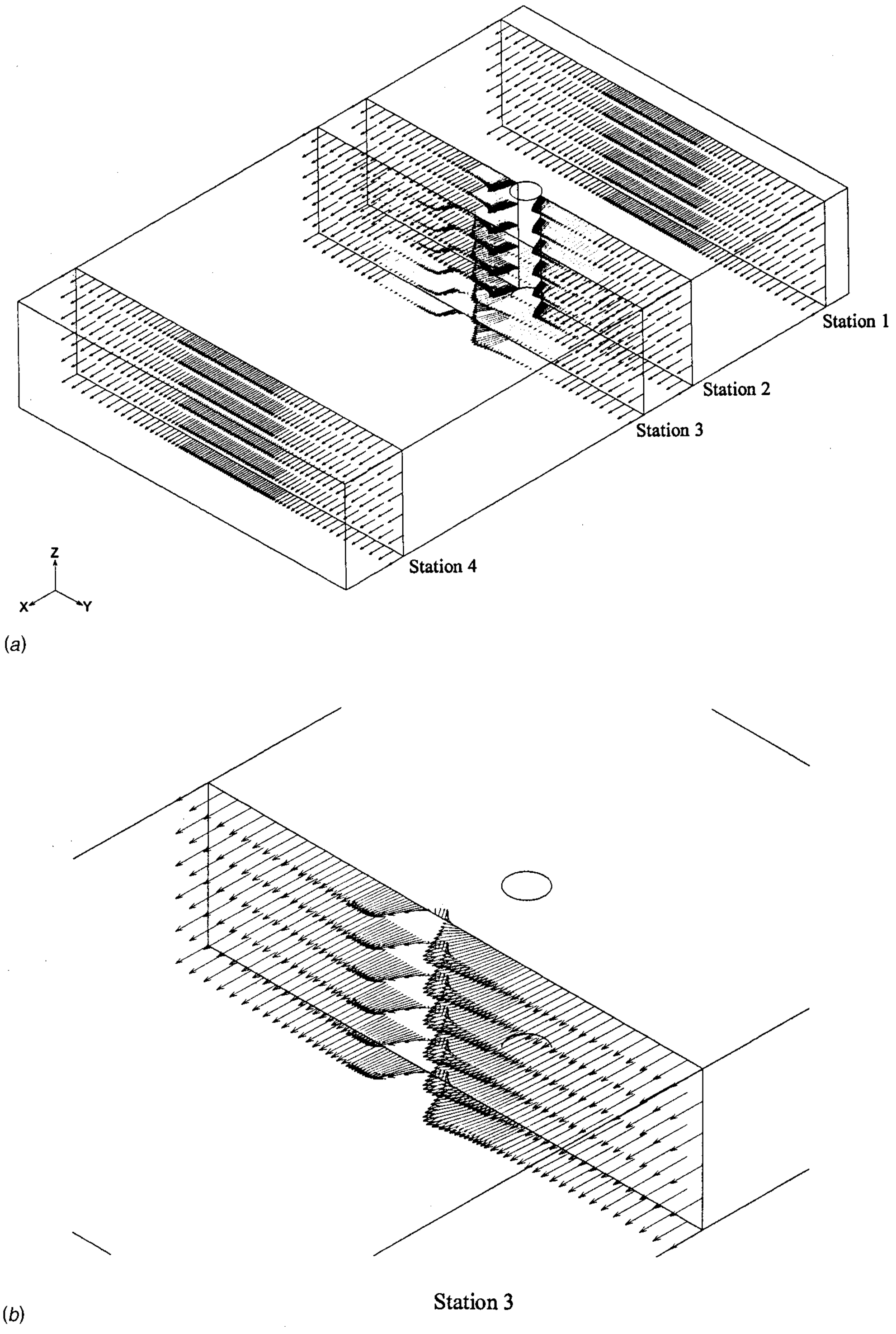

Fig. 7 Instantaneous velocity fields obtained from 3-D simulation at selected planes along the flow domain at $Ut/D=10.8$. Cylinder oscillates in the transverse direction in a uniform flow at $U/f_cD=5.4$ (Re$=2.4\times10^4$ and $A/D=0.11$).

quantities along the cylinder length changes symmetrically about the mid-length position due to the use of periodic boundary conditions. This observation emphasize spanwise flow structures and hence the three dimensionality which is also observed in Fig. 10(a)–(c). This figure gives typical instantaneous velocity fields obtained by 2-D and 3-D simulations at two different spanwise locations at the same nondimensional time of $Ut/D=10.8$. The phase shift between the timings of first vortex being shed from the cylinder for both simulations can also be observed in Fig. 10. The figure clearly shows that 3-D simulation predicts a relatively larger room for vortices to develop behind the cylinder compared to 2-D simulation. This leads 3-D model to produce more elongated and slightly weaker vortices growing in size and hence a longer recirculation length. Finally a summary is presented in Table 1. Again, there are clearly improvements in the results from the 3-D simulation.

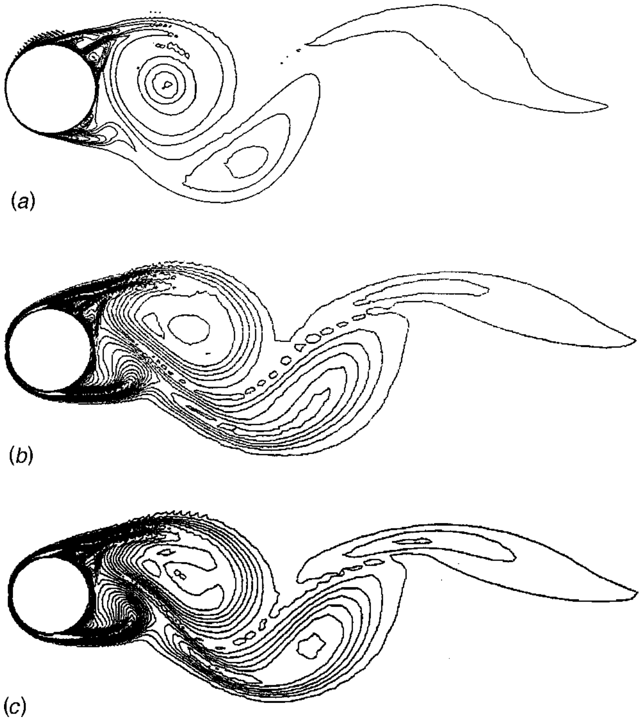

Fig. 8 Instantaneous vorticity plots taken with constant contour values at $U/f_cD=5.4$ and at $Ut/D=10.8$. Cylinder oscillates in the transverse direction in a uniform flow ($Re=2.4\times10^4$ and $A/D=0.11$).

6 Discussion

The present results show that the LES simulation based turbulence model gives reasonable results in terms of forces and flow structure when compared with experimental values. It is clear from the limited experimental results that even though the experiments are limited in scope that there exists three dimensionality in the flow around the transversely oscillating cylinder. The results that most readily illustrate this are the correlation values which for even a very short axial distance $(2D)$ are reduced to a value of 0.75. The fluid dynamic mechanisms for this reduction in correlation are not so clearly seen, but they are present and the results from these CFD simulations can aid the understanding of the mechanisms. One observation toward this goal is illustrated by the comparison between the streamwise vorticity plots in Fig. 8. The space between the vorticies in the transverse and streamwise directions and the width of the vortex is different for 2-D and 3-D simulations. This is further reinforced by viewing velocity vectors in Fig. 10. The figure also shows that there is a phase shift between the timing at which the first vortex is being shed from the cylinder for both simulations.

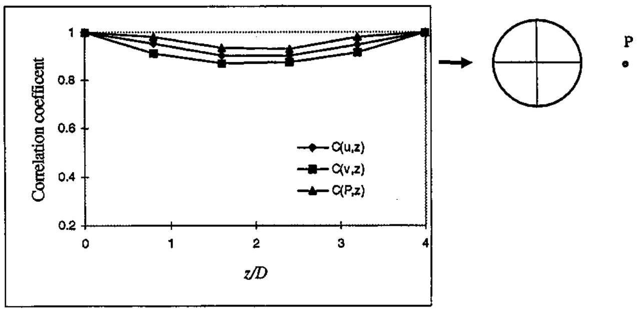

Fig. 9 Correlation coefficients from 3-D LES simulation for velocity components and pressure at $P(x, y)=(8D, 9D)$ for a transversely oscillating cylinder at $U/f_cD=5.4$ ($Re=2.4\times10^4$ and $A/D=0.11$)

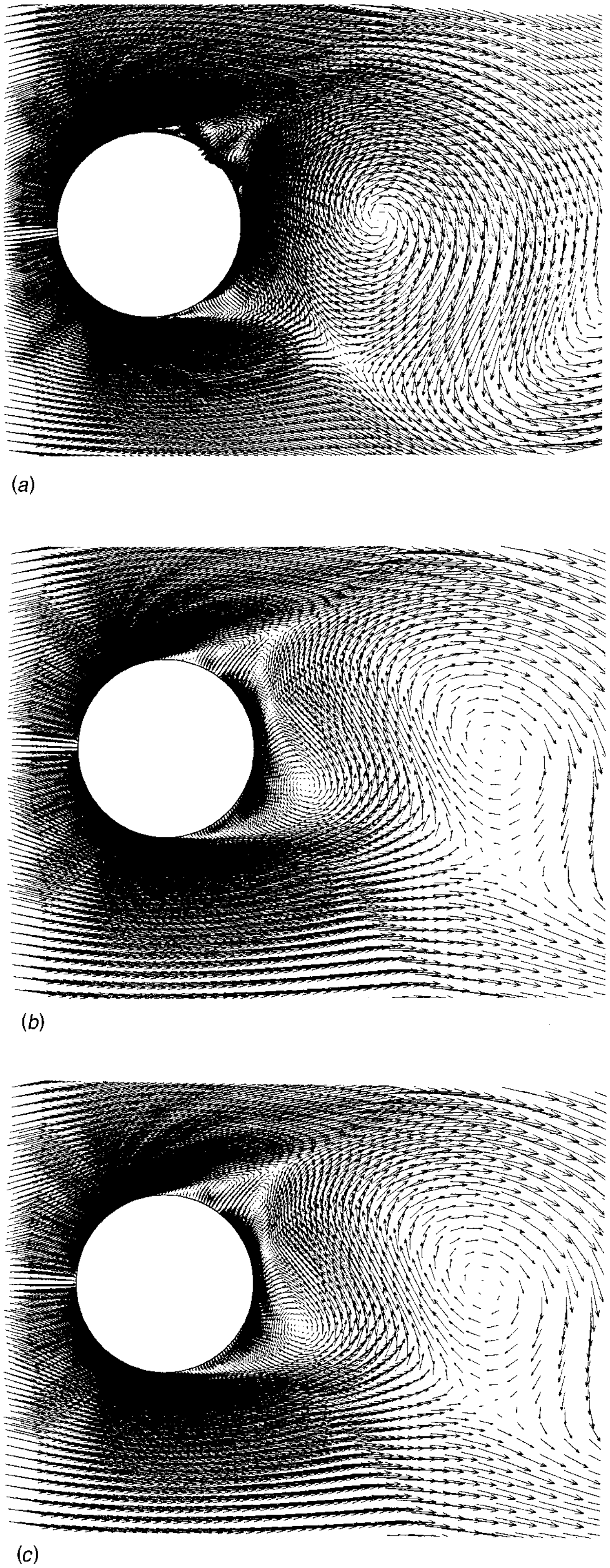

Fig. 10 Instantaneous velocity vector fields obtained from 2-D and 3-D LES simulations at $U/f_cD=5.4$ and at $Ut/D=10.8$; (a) 2-D LES; (b) 3-D LES at $z=2.4D$; (c) 3-D LES at $z=0.8D$

Table 1 Summary of flow parameters predicted by the present LES simulations and experimental values of Bearman and Currie [3] for the transversely oscillating circular cylinder in a uniform flow at $U/f_cD=5.4$ ($\mathrm{Re}=2.4\times10^4$ and $A/D=0.11$)

Models	St	$-\overline{C}_{Pb}$	$C_{Pr.m.s}$	$\overline{C}_D$	$\overline{C}_{L\max}$
2-D Simulation	0.177	1.55	0.85	1.322	0.63
3-D Simulation	0.191	1.37	0.71	1.26	0.71
Experiment	0.1852	-	0.622	-	-

7 Conclusions

Following conclusions can be drawn from the present work:

- 3-D LES simulation for a transversely oscillating cylinder gives longer time averaged recirculation length than 2-D simulations at a reduced velocity of 5.4.
- A slight phase difference in the calculation of timing of the initial vortex being shed from the cylinder between 2-D and 3-D LES simulations was observed.
- 3-D simulations produced 7.5 percent smaller rms pressure values in the separated region than 2-D simulations and were found to be in better agreement with experimental data.
- The time averaged values of drag coefficient and the absolute base pressure for 3-D simulation were also found to be smaller than the corresponding values of 2-D simulation. The deviations between 2-D and 3-D results indicate the existence of three dimensionality in the near wake flow.

Acknowledgments

The authors acknowledge Mersin University, Turkey for its financial support and the Computational Fluid Dynamics Group at the University of Hertfordshire for its help and support.

Nomenclature

A = cylinder displacement amplitude
A_i = body force term due to noninertial coordinate transformation
$\overline{b}_i$ = body force term
$\overline{C}_D$ = time averaged drag coefficient
$\tilde{C}_L$ = periodic lift coefficient
$\overline{C}_{Pb}$ = time averaged base pressure coefficient
$C_{P\mathrm{rms}}$ = rms fluctuating pressure coefficient
C_s = Smagorinsky constant
D = cylinder diameter
D_T = damping term
f_c = cylinder oscillation frequency
l = length scale
P = pressure
Re = reynolds number
$\hat{S}_{ij}$ = resolvable strain rate
St_ν = nondimensional vortex shedding frequency
t = time
u = x-component velocity
U = freestream velocity
u_i = u, ν, and w for $i=1$, 2, and 3, respectively
$\overline{u}_i$ = relative velocity for components u, ν, and w in a noninertial frame
$\hat{u}_i$ = space averaged velocity for components u, ν, and w
ν = y-component velocity
w = z-component velocity
ρ = fluid density
Δ = the averaged grid size
μ = laminar dynamic viscosity
v_t = subgrid scale eddy viscosity
y^+ = nondimensional distance
τ_{ij} = subgrid scale stress term

References

[1] Tritton, D. J., 1959, ''Experiments on the Flow Past Circular Cylinder at Low Reynolds Number,'' J. Fluid Mech., **6**, pp. 547–567.
[2] Achenbach, E., 1968, ''Distribution of Local Pressure and Skin Friction around a Circular Cylinder in a Cross Flow up to $\mathrm{Re}=5\times10^6$,'' J. Fluid Mech., **34**, pp. 625–635.
[3] Bearman, P. W., and Currie, I. G., 1979, ''Pressure Fluctuation Measurements on an Oscillating Circular Cylinder,'' J. Fluid Mech., **91**, pp. 661–667.
[4] Sarpkaya, T., 1977, ''In-line and Transverse Forces on Cylinders in Oscillatory Flow at High Reynolds Number,'' J. Ship Res., **21**, No.4, pp. 200–216.
[5] Williamson, C. H. K., 1988, ''The existence of Two Stages in Transition to Three Dimensionality of a Cylinder Wake,'' Phys. Fluids, **31**, pp. 3165.
[6] Hurlbut, S. E., Spaulding, M. L., and White, F. M., 1982, ''Numerical Solution for a Laminar two Dimensional Flow About a Cylinder Oscillating in a Uniform Stream,'' ASME J. Fluids Eng., **104**, pp. 104–120.
[7] Chilikuri, R., 1987, ''Incompressible Laminar Flow Past a Transversely Vibrating Cylinder,'' ASME J. Fluids Eng., **109**, pp. 166–171.
[8] Sun, J., Li, J., and Roux, B., 1993, ''Flow Regimes and Frequency of a Cylinder Oscillating in an Upstream Cylinder Wake,'' Int. J. Numer. Methods Fluids, **26**, pp. 915–929.
[9] Namura, T., 1993, ''A Numerical Study on Vortex Excited Oscillations of Bluff Cylinders,'' J. Wind Eng. Ind. Aerodyn., **90**, pp. 75–84.
[10] Wei, R., Sekine, A., and Shimura, M., 1995, ''Numerical Analysis of 2d Vortex Induced Oscillations of a Circular Cylinder,'' Int. J. Numer. Methods Fluids, **21**, pp. 993–1005.
[11] Tutar, M., and Holdǿ, A. E., 1999, ''Application of Differing Forcing Function Models on the Flow Past an Oscillating Cylinder in a Uniform Low Reynolds Number Flow,'' Int. J. Comput. Fluid Dynam., **11**, Nos. 3–4, pp. 223–235.
[12] Majumdar, S., and Rodi, W., 1985, ''Numerical Calculations of Flow Past Circular Cylinder,'' *Proceedings of 3rd Symposium on Numerical and Physical Aspects of Aerodynamic Flows*, Long Beach CA.
[13] Launder, B. E., 1993, ''Lecture Notes on Turbulence Modelling in Industrial Flows,''Les Hauches Summer School on Computational Fluid Dynamics.
[14] Tutar, M., Holdǿ, A. E., and Lewis, A. P., 1998, ''Comparative Performance of Various Two Equation Models and LES on Simulated Flow Past a Circular Cylinder in Subcritical Flow Regime,'' *Proceedings of ASME Fluids Eng. Summer Meeting on Finite Element Applications in Fluid Dynamics*, Washington, D.C.
[15] Zhang, J., and Dalton, C., 1996, ''Interactions of Vortex-Induced Vibrations of a Circular Cylinder and a Stead Approach Flow at a Reynolds number of 13,000,'' Comput. Fluids, **25**, No. 3, pp. 283–294.
[16] Wang, X., and Dalto, C., 1991, ''Oscillating Flow Past a Rigid Circular Cylinder: A-Finite Difference Calculation,'' ASME J. Fluids Eng., **113**, pp. 377–383.
[17] Lu, X., Dalton, C., and Zhang, J., 1997, ''Application of Large Eddy Simulation to Flow past a Circular Cylinder,'' J. Offshore Mech. Arct. Eng., **119**, pp. 219–225.
[18] Smagorinsky, J., 1963, ''General Circulation Experiment with the Primitive Equations: Part 1. The Basic Experiment,'' Mon. Weather Rev., **91**, pp. 99–152.
[19] Van Driest, E. R., 1956, ''On the Turbulent Flow Near a Wall,'' J. Aeronaut. Sci., **23**, pp. 1007–1011.
[20] McMillan, O. J., Ferziger, J. H., and Rogallo, R. S., 1980, ''Tests of New Subgrid Scale Models in Strained Turbulence,'' AIAA Paper, No. 80-1339.
[21] Mason, P. J., and Callen, N. S., 1986, ''On the Magnitude of the Subgrid Scale Coefficient in Large Eddy Simulation of Turbulent Channel Flow,'' J. Fluid Mech., **162**, pp. 439–462.
[22] Piomelli, U., Moin, P., and Ferziger, J. H., 1988, ''Model Consistency in Large-Eddy simulation of Turbulent Channel Flows,'' Phys. Fluids, **31**, No. 7, pp. 1884–1891.
[23] FDI (Fidap Dynamics International), Fidap Users Manual, 1993.
[24] Ramamurthy, A. S., and Ng., C. P., 1973, ''Effect of Blockage on Steady Force Coefficients,'' Proc. ASCE. EM4, pp. 755–772.
[25] Lipsett, A. W., and Williamson, I. D., 1994, ''Response of Fluids and Structures,'' J. Fluids Struct., **8**, pp. 681–709.
[26] Sarpkaya, T., 1986, ''Force on a Circular Cylinder in Viscous Oscillatory Flow at Low Keulegan-Carpenter Numbers,'' J. Fluid Mech., **165**, pp. 61–71.
[27] Keulegan, G. H., and Carpenter, L. H., 1958, ''Forces on Cylinders and Plates in an Oscillating Fluids,'' Journal of Research of hte National Bureau of Standards, **60**, No. 5, pp. 423–440.
[28] Wang, C. Y., 1968, ''On High-frequency Oscillating Viscous Flows,'' J. Fluid Mech., **32**, pp. 55–68.

[29] Tutar, M., 1998, ‘‘Computational Modelling of Vortex Shedding From Offshore Risers,’’ Ph.D. thesis, University of Hertfordshire.

[30] Cantwell, B., and Coles, D., 1983, ‘‘An Experimental Study of Entrainment and Transport in the Turbulent Wake of a Circular Cylinder,’’ J. Fluid Mech., **136**, pp. 321–374.

[31] Yokuda, S., and Ramaprian, B. R., 1990, ‘‘The Dynamics of Flow around a Circular Cylinder at Subcritical Reynolds Numbers,’’ Phys. Fluids A, **2**, No. 2, pp. 784–791.

[32] Roshko, A., 1954, ‘‘On the Development of Turbulent Wakes from Vortex Street,’’ NASA Report, No. 1191.

[33] Roshko, A., 1955, ‘‘On the Wake and Drag of Bluff Bodies,’’ J. Aeronaut. Sci., **22**, pp. 124–132.

S. Lu[1]
Graduate Student

Ö. F. Turan
Associate Professor
e-mail: ofturan@dingo.vu.edu.au

School of the Built Environment-Mechanical Engineering,
Victoria University of Technology,
P.O. Box 14428 MC,
Melbourne, Victoria 8001,
Australia

Numerical Prediction of Flow Fields Around Circular Cylinders: Forced Motion and Dynamic Response Cases

At Re=2000, the predicted flow field around a circular cylinder in forced transverse oscillation is verified with experimental results. For coupled torsional and transverse oscillation cases, the numerical results indicate that lock-in depends on the relative phase between torsional and translational oscillations. The dynamic response of an elastically mounted circular cylinder in cross flow, obtained by solving the structural equations simultaneously with the Navier-Stokes equations, is in reasonable agreement with experimental data. The dynamic response results indicate that the change of wake pattern from 2S to 2P with increased frequency ratio, is not always simultaneous with the change in the relative phase between lift force and cylinder displacement. [S0098-2202(00)02003-4]

I Introduction

Toward predicting the wind-induced oscillation of transmission conductors, a numerical model is developed to study the flow fields around moving circular cylinders. Coupled with wind tunnel tests, a detailed understanding gained through numerical modeling is expected to lead to modified damper designs. Among different types of wind-induced oscillation of structures, ''galloping'' refers to high-amplitude (5–300 conductor diameters) and low-frequency (0.1–3 Hz) aeroelastic oscillations at wind speeds of 6–25 m/s (Pon et al. [1]). Several electrical transmission line and transmission tower failures have been caused by galloping of conductor cables and guy wires, especially after freezing rain storms. With ice accretion, cables lose their approximately circular cross sections, and the resulting shapes can have aeroelastic instability. Due to very high replacement costs of such lines and towers, conductor cable and guy wire galloping has been widely studied since the early work of Den Hartog [2]. In the existing analytical and numerical models for galloping analysis, the assumption of a quasi-steady flow field has been widely used (Blevins [3]). According to this assumption, the fluid force on the structure is determined solely by the instantaneous relative velocity and angle of attack of the flow. However, this assumption is not valid for many observed field galloping cases (Zdero et al. [4]).

In this study, the time dependent Navier-Stokes equations are solved to obtain the instantaneous force coefficients, coupled with the solution of the appropriate equations of motion for the structure, thus eliminating the need for a quasi-steady assumption. After verification with limited experimental results, the numerical results have provided more detailed information on the flow structure than available from experiments. The details of the code are given in the next section. As indicated in Section 3, the results of the code have been compared first with benchmark experimental data of flow fields around stationary circular cylinders at Re =100, 1000, and 2000. Subsequently, the controlled transverse oscillation cases were verified with experimental results, and the flow fields around circular cylinders in controlled translational, torsional and combined translational and torsional oscillations were studied in detail. The forced motion results are summarized in Section 4. The dynamic response of a spring-mounted circular cylinder in cross-flow was also examined, along with the details of the flow field. These results are given in Section 5. The conclusions are summarized in Section 6.

II Numerical Scheme

Flow fields around vibrating circular cylinders have been studied numerically, but mostly at Reynolds numbers of less than 1000 (Chang and Sa [5], Chilukuri [6], Hulbert et al. [7], Lecointe and Piquet [8], to name a few). The reason is that the wake is fully turbulent at higher Reynolds numbers, and accurate prediction becomes more difficult due to problems associated with turbulence modeling and resolution of the numerical grid. The results presented here were obtained from solutions without a turbulence model at a Reynolds number of 2000 for comparison with the forced-motion experimental results of Zdero et al. [4].

A FORTRAN code is developed based on the framework of the TEACH code, and a two-step time dependent solution is incorporated coupling the flow and structural equations. For the flow solution, the continuity and Navier-Stokes equations are discretized using a finite volume method (Patankar [9]). The computational domain is divided into cells, or control volumes, by a set of radial lines and concentric circles in polar coordinates. For grid independence, 100 radial cells and 120 circumferencial cells are used in most cases, with the computational domain extending 40 cylinder diameters radially. The size of the cells is distributed nonuniformly in the radial direction, with high concentration near the cylinder surface to resolve the boundary layer. Two layers of cells are used radially with different linear expansion coefficients. From the cylinder surface to a distance of 0.4 radius, 20 live cells are used, with an expansion coefficient of 1.12, and for the rest of the domain, the expansion coefficient is 1.06. The variables are stored on a staggered arrangement proposed by Patankar [9]. The value of the velocity components at the control volume faces is interpolated using a bounded form (Gaskell and Lau [10]) of QUICK originally devised by Leonard [11], arranged in the upwind form (Hayase et al. [12]). The discretized equations are then solved with the SIMPLE-C algorithm (Van Doormaal and Raithby [13]). Implicit time marching and tridiagonal matrix method are used with alternate sweep direction.

Since the mesh is fixed relative to the cylinder in the numerical solution, the translational motion of the cylinder is transformed into the time dependent boundary condition at the outer boundary of the computational domain and no-slip condition on the cylinder

---

[1] Now with the University of California, Berkeley.

Contributed by the Fluids Engineering Division for publication in the JOURNAL OF FLUIDS ENGINEERING. Manuscript received by the Fluids Engineering Division; revised manuscript received February 8, 2000. Associate Technical Editor: G. Erlebacher.

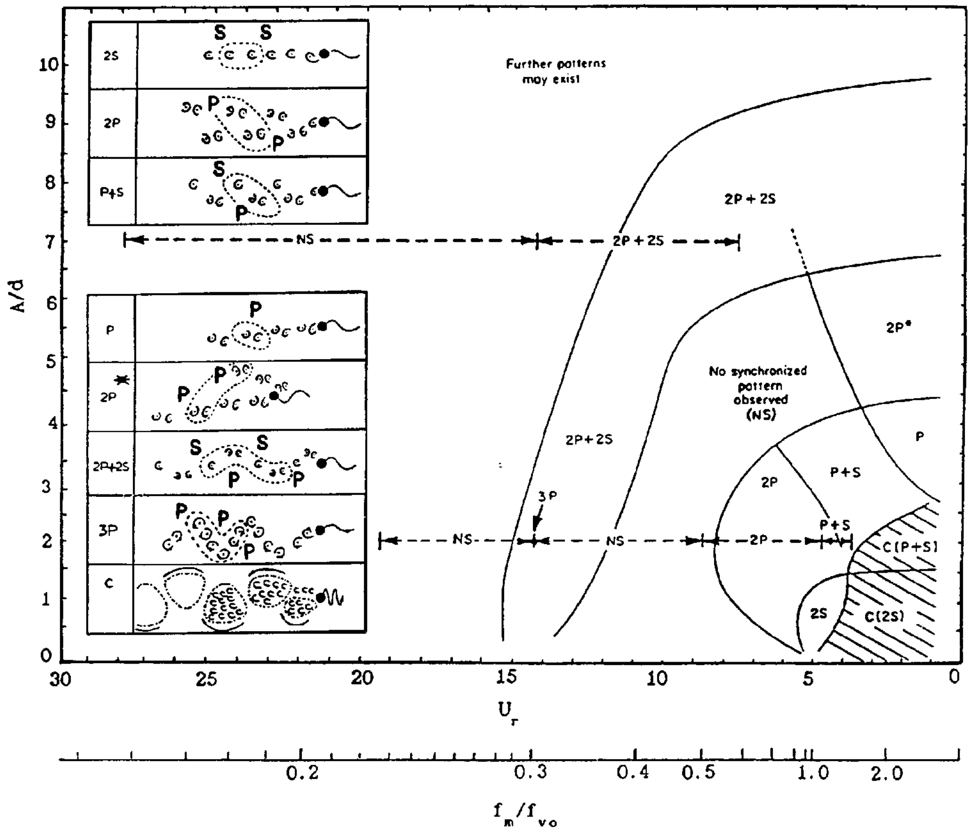

Fig. 1 Regions of vortex synchronization patterns given by Zdero et al. [4] based on a map given by Williamson and Roshko. The flow visualization results of Zdero et al. are shown by the dashed lines corresponding to $A/d=2$ and 7. The details of the synchronized wake regions are given in the inset where vortices shed per motion cycle are enclosed by dotted lines (S, single vortex; P, vortex pair; C, coalescence).

surface, as well as an inertial force acting on the fluid. Taking a_x and a_y as the longitudinal and transverse accelerations, respectively, of the cylinder in Cartesian coordinates, the inertial terms $(-a_x \sin\theta - a_y \cos\theta)$ and $(a_x \cos\theta - a_y \sin\theta)$ are added to the momentum equations. Hence, these terms contribute to the source terms in the discretized equations.

Due to the difficulty of defining an outflow condition, a time dependent boundary condition is prescribed along the whole outer boundary. This approach is validated by the fact that it gives the same result as using an outflow condition for a stationary cylinder. At each time step, the boundary condition is updated for a moving cylinder. Taking dV_x and dV_y as the velocity increments of the cylinder during one time step, the radial and circumferencial velocity increments at the outer boundary are $(dV_x \cos\theta - dV_y \sin\theta)$ and $(-dV_x \sin\theta - dV_y \cos\theta)$, respectively. This change in the boundary velocity violates the continuity condition temporarily, and it takes a number of iterations for the boundary information to propagate to the cylinder.

In order to reduce the number of iterations for convergence, an inviscid flow field is also calculated from the incremental radial and azimuthal cylinder velocities. This correction velocity is added to the velocity field of the last time step to provide an initial guess for the present time step. The resulting velocity field is already a good approximation in the inviscid region considering the continuity equation. However, the no-slip condition is not satisfied with this velocity field, and as a result, more sweeps are needed close to the wall. The program is designed to perform more sweeps in the boundary layer region. This method was found to accelerate convergence considerably, because the continuity equation is satisfied even when the boundary velocity is changed. A dimensionless mass residual of 1×10^{-6} is used for convergence.

The present implementation allows three degrees of freedom for the cylinder: two translational and one torsional. The calculation of the dynamic response of an elastically mounted cylinder is achieved through the coupling of the Navier-Stokes equations with the corresponding structural equations of motion. The total fluid force exerted on the structure including fluid damping and inertial forces, are calculated from surface pressure and skin friction as a result of the flow solution. Although better accuracy could have been achieved by using the Runge-Kutta method for the solution of the structural equations, a direct explicit approach is used here, because the time step as dictated by the solution of the flow field, is small. For most cases, 500 time steps were used per period of the cylinder motion to obtain a flow field that is independent of the time step.

At each time step, the flow field is updated first, and the force coefficients are computed. The fluid forces are then fed into the structural equations to update the response of the cylinder. Next, the results are used to update the boundary conditions, preparing to move to the next time step. The details of the program as well as a users' manual are given by Lu and Turan [14].

III Stationary Circular Cylinder Cases: Benchmark Comparisons

To validate the numerical implementation, detailed comparisons were made with benchmark experimental and some numeri-

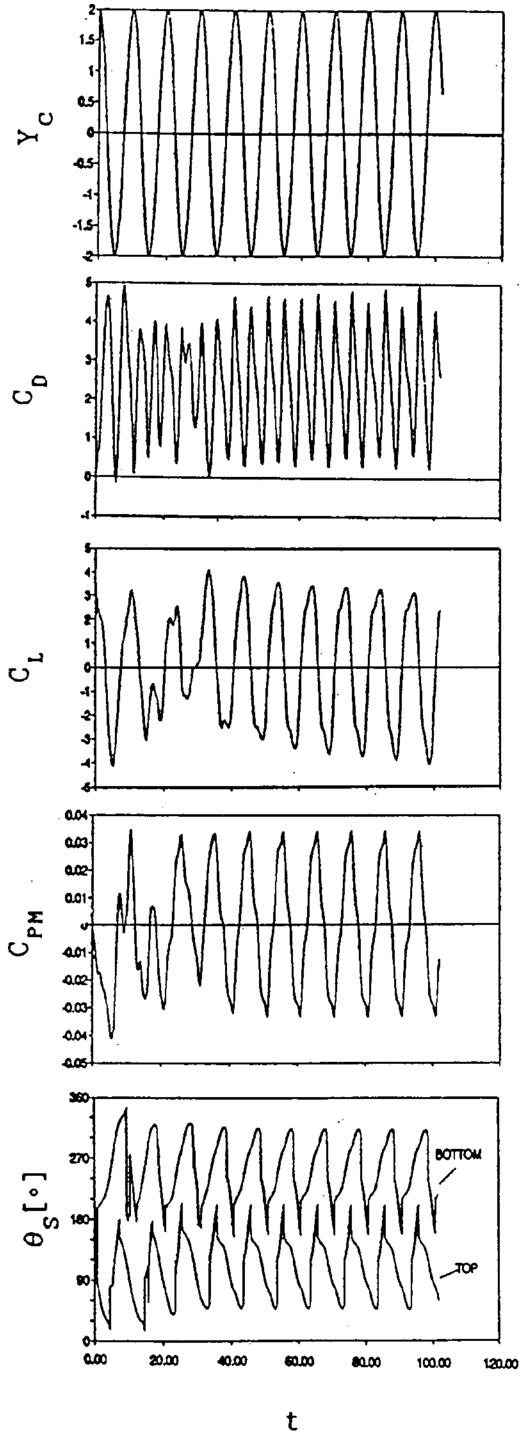

Fig. 2 Cylinder displacement, force coefficient and separation point histories for $f_m/f_{v0}=0.83$, Re=2000

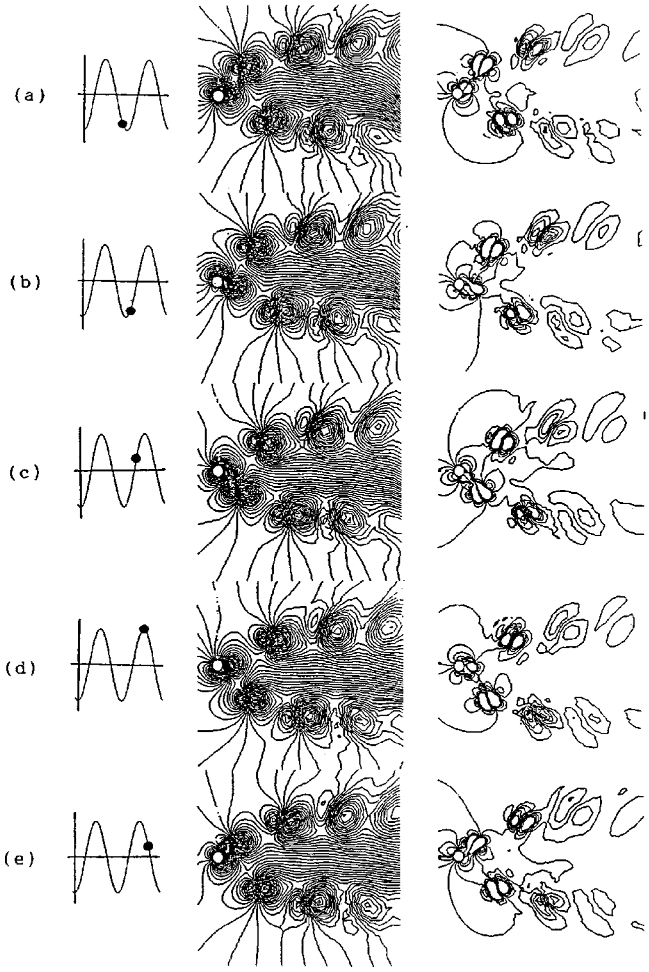

Fig. 3 Streamline and vorticity contours for $f_m/f_{v0}=0.83$, Re =2000

cal results of the flow fields around stationary circular cylinders. These comparisons are summarized in this section. The first stationary case is vortex shedding from a circular cylinder at a Reynolds number of 100, where the wake is laminar. Numerical results were obtained from a mesh with 90 circumferencial and 70 radial cells. The computational domain extended to 40 cylinder diameters. A mean drag coefficient of 1.3 and a Strouhal number of 0.16 were computed, in agreement with the classical experimental data. Here, the drag coefficient is defined as, $C_D = D/(\rho U_0^2 a l)$, where D is the drag force on cylinder; U_0 is the free-stream velocity; ρ is the fluid density; a and l are the cylinder radius and length, respectively. The Strouhal number is defined as, $\mathrm{St}=2af_{v0}/U_0$, where f_{v0} is the frequency of vortex shedding from a stationary cylinder.

All other cases employ a mesh with 120 circumferencial cells and 100 radial cells in order to fully resolve the boundary layer at a higher Reynolds number. The evolution of near wake structure at a Reynolds number 1000 is similar to that given by Braza et al. [15]. The present results give a mean drag coefficient of 1.4 and a Strouhal number of 0.23, higher than the experimental values of 1.2 and 0.21, respectively. This difference must be due to the two-dimensionality imposed in the simulation, and it is consistent with the numerical results of Lecointe and Piquet [8] which give a Strouhal number of 0.24 at Re=875. The seemingly good agreement with experimental data in earlier results (Jordan and Fromm [16], Braza et al. [15]) is probably due to insufficient mesh resolution in the boundary layer and the use of lower order (such as central difference) schemes.

From a comparison of the numerically predicted von Karman vortex street formation with the experimental one (Batchelor [17]) at Re=2000, it is observed that the global vortex structure compares well with flow visualization, while the computed drag coefficient and Strouhal number values, $C_D=1.5$ and $\mathrm{St}=0.24$, are higher than the experimental values of 1.2 and 0.21, respectively.

From the test cases above, it is seen that the present code gives results comparable with experiments at Re=100. For Re>1000, quantitative differences occur, although the qualitative flow field is still in close agreement with the experimental results. As indicated earlier, these differences are expected to be mostly due to the two-dimensional solution, along with the lack of a turbulence model and possibly not enough resolution of the flow field next to the cylinder surface. With further comparison of the numerical predictions with the experimental results for moving cylinders, it was possible to use the same code to obtain qualitative pictures of the flow field.

IV Controlled Transverse and Torsional Oscillation Cases

In this section, forced-oscillation results are presented, starting with transverse oscillation cases, followed by the cases of torsional oscillation, and combined transverse and torsional oscillations. In Fig. 1, Fig. 5 of Zdero et al. [4] is given, which is a variation of the vortex synchronization map of Williamson and Roshko [18], with the dashed lines showing the experimental results of Zdero et al. In this figure, $U_r = U_0/2af_m$ is the reduced

Fig. 5 Streamline and vorticity contours for $f_m/f_{v0}=0.50$, Re $=2000$

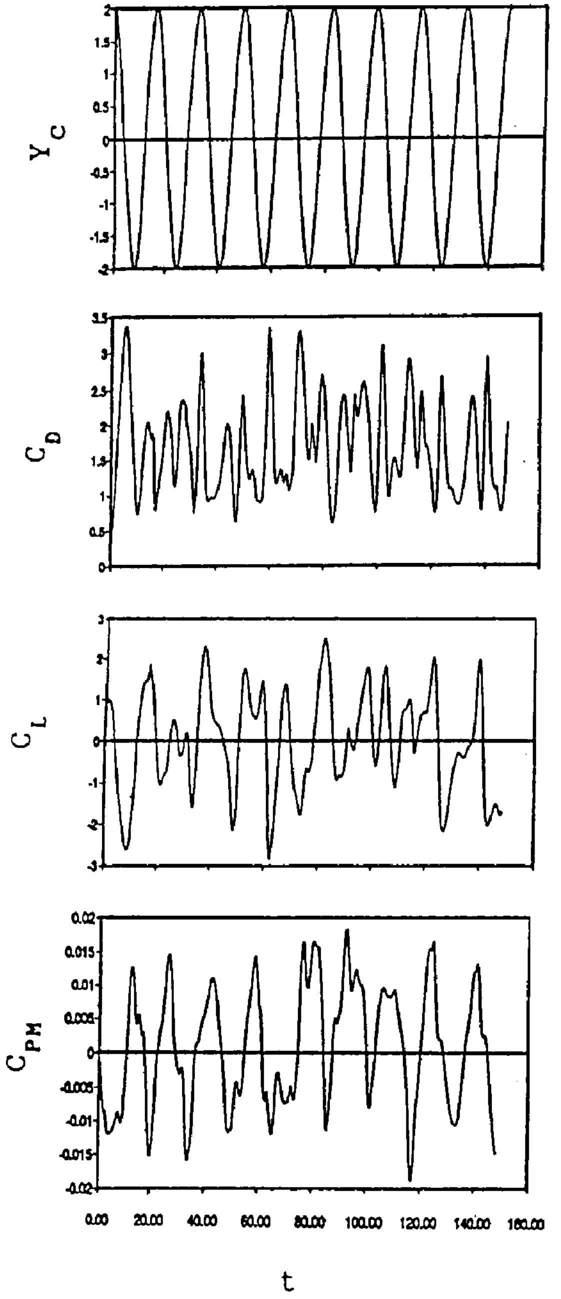

Fig. 4 Force coefficient histories for $f_m/f_{v0}=0.50$, Re=2000

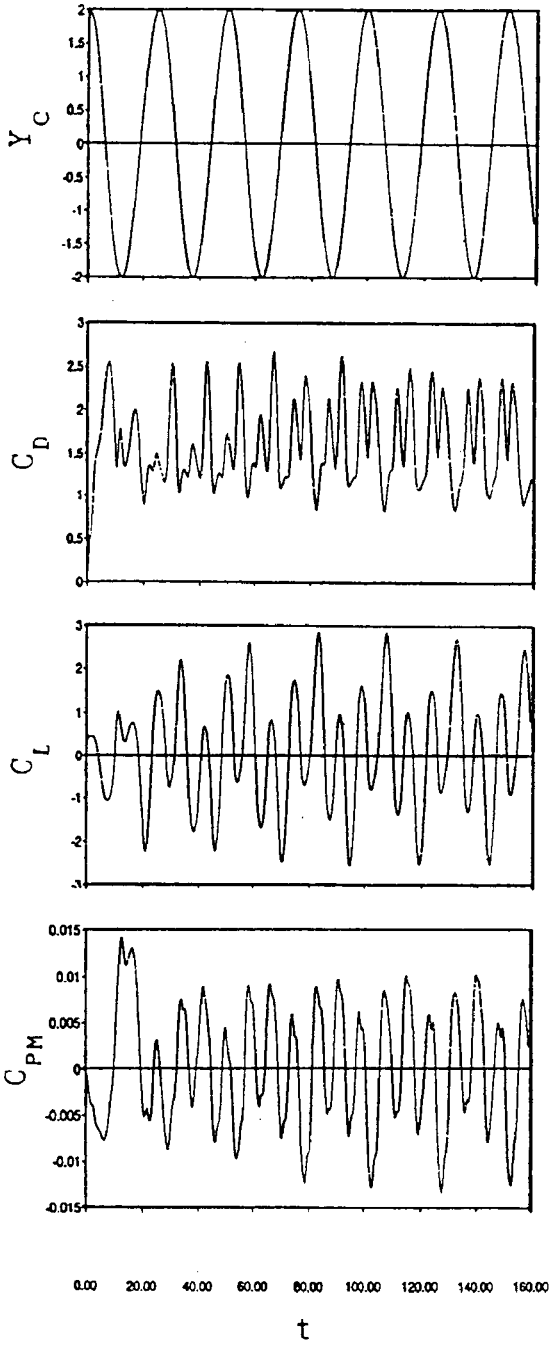

Fig. 6 Force coefficient histories for $f_m/f_{v0}=0.33$, Re=2000

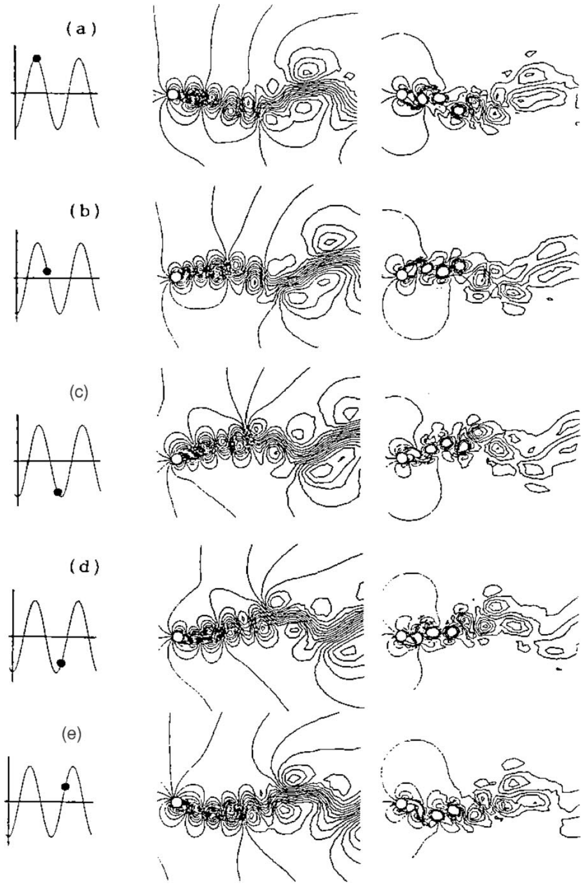

Fig. 7 Streamline and vorticity contours for $f_m/f_{v0}=0.33$, Re $=2000$

velocity, A is the peak to peak transverse oscillation amplitude, and d is the cylinder diameter. The transverse controlled-motion results given in this section are compared with the experimental results given in Fig. 1. The Reynolds number is 2000, and the peak to peak amplitude is 2 cylinder diameters for the transverse oscillation cases $(A/d=2)$ summarized next. The experimental results of Zdero et al. indicate that stranding does not affect the flow field at this Reynolds number; and therefore, the numerical results presented below also hold for stranded cases. The ratios of the transverse motion frequency to stationary vortex shedding frequency, f_m/f_{v0}, used in the calculations are: 0.33, 0.36, 0.5, 0.83, 0.91, and 1.07.

When a cylinder oscillates transversely at a frequency f_m near its stationary vortex shedding frequency f_{v0}, the vortex shedding process may become synchronized with the cylinder motion, and ''lock-in'' occurs. It could also occur when the motion frequency is near a harmonic $(f_m/f_{v0}=2,3,\ldots,n)$ or subharmonic $(f_m/f_{v0}=1/2,1/3,\ldots,1/n)$ of the stationary vortex shedding frequency. The latter is more relevant in the study of cable galloping where the frequency is low. At other frequency ratios, the vortex shedding frequency may be different from the motion frequency of the cylinder. These cases are classified as nonsynchronized, NS, modes.

The cylinder displacement and force coefficient histories for the case of $f_m/f_{v0}=0.83$ are given in Fig. 2. Also shown in this figure is the fluctuation of the top and bottom separation points, located at approximately 124 and 234 deg, respectively, within ±81 deg. The time axis in this figure and in other histories to come, is non-dimensionalized with a/U_0. It can be seen that periodic motion was obtained after several periods of vibration, indicating that the vortex shedding frequency is locked onto motion frequency.

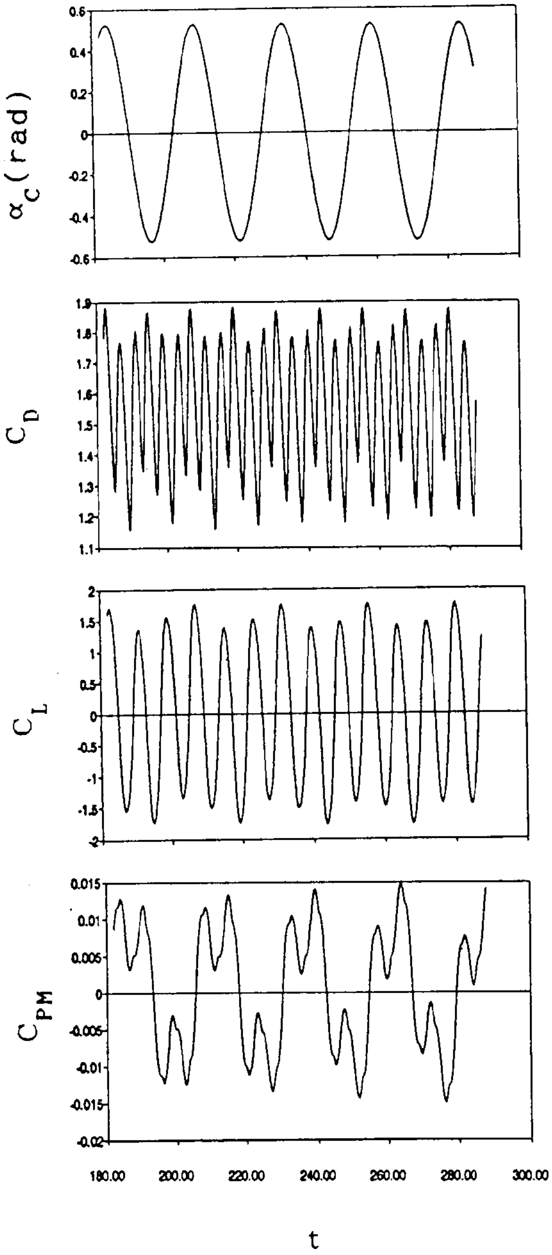

Fig. 8 Force coefficient histories for $f_t/f_{v0}=0.36$, Re$=2000$

The lift and pitching moment coefficients and the top and bottom separation points fluctuate at the same frequency as the transverse oscillations; while the drag coefficient fluctuates at twice this frequency. The corresponding Lissajous figures, which illustrate the relative phase between the force coefficients, do not conform to a standard form, because the force coefficients are not strictly harmonic. The evolution of streamlines and vorticity contours in approximately one period of cylinder motion for the case of $f_m/f_{v0}=0.83$ is given in Fig. 3. It can be observed that two pairs of vortices are shed in one period of motion, the 2P mode. The in-line spacing between pairs of vortices appears narrow as a result of over-prediction of the Strouhal frequency. Each opposite-signed pair of vortices is convected away from the centerline while moving downstream, thus creating two rows of alternative vortices and a wide ''dead area'' near the centerline. The fluctuation of velocity and pressure in the dead area is weak, as observed from the velocity and pressure histories at several diameters from the rear stagnation point of the cylinder. Similar fundamental

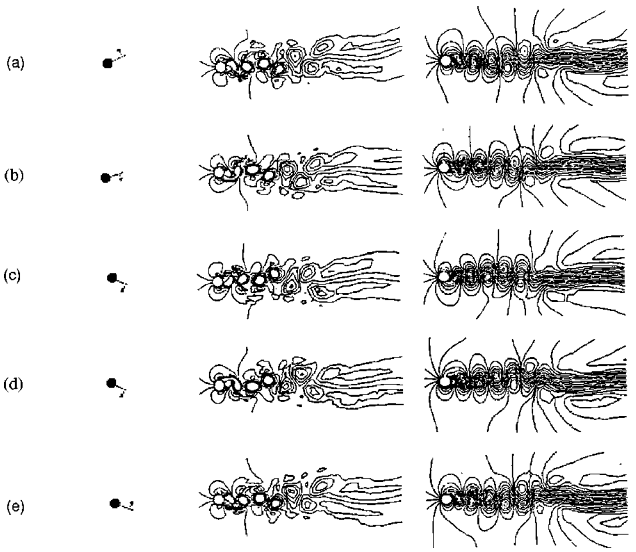

Fig. 9 Streamline and vorticity contours for $f_t/f_{v0}=0.36$, Re $=2000$

lock-in was also found for $f_m/f_{v0}=0.91$ and 1.07. The presence of the 2P mode for $f_m/f_{v0}=0.83$, 0.91 and 1.07 is in agreement with the experimental results given in Fig. 1.

The force coefficient histories for the case $f_m/f_{v0}=0.5$ is given in Fig. 4. An example of the corresponding streamline and vorticity patterns is shown in Fig. 5. No periodicity is observed for this case, as seen from the force coefficient histories. The instantaneous streamline and vorticity contour plots suggest that the vortices are shed in pairs but not at fixed points within the motion cycle (the phase of shedding changes over time). This nonsynchronized pattern is in agreement with the results of Williamson and Roshko [18]. Zdero et al.'s results indicate that $f_m/f_{v0}=0.5$ is the boundary of the 2P mode, as shown in Fig. 1. For the case of $f_m/f_{v0}=0.36$, a nonsynchronized flow field was obtained, in agreement with Zdero et al.'s flow visualization results, although Williamson and Roshko observed the 2P+2S mode in their flow visualization at a lower Reynolds number.

As shown in Fig. 6, for the case $f_m/f_{v0}=0.33$, the lift and pitching moment histories have the motion frequency, and the drag coefficient twice the motion frequency, as the fundamental frequency component over which higher frequencies are imposed due to vortex shedding. In fact, six peaks exist per period of the lift and pitching moment histories, and per two periods of the drag history. The streamline and vorticity plots in Fig. 7 suggest that six alternative, equally spaced vortices are shed per motion period. Hence, this is virtually the same structure as what was called 3P mode by Zdero et al. as shown in Fig. 1.

Following the favorable comparison between the numerical and experimental results of forced translational oscillation cases, several cases were run to see the effect of torsional oscillations. The results obtained for six cases of torsional oscillations are summarized next. The first case is of torsional oscillations alone with a peak-to-peak amplitude of 60 deg and torsional frequency ratio, f_t/f_{v0}, of 0.91. The second case is of combined torsional and in-phase transverse oscillations. The third case is of combined torsional and out-of-phase transverse oscillations. For the second and third cases, $f_t/f_{v0}=f_m/f_{v0}=0.91$. In the remaining three cases, the parameters are the same as in the first three cases, except that the frequency ratio is set at 0.36.

The force coefficient histories of the case of torsional oscillations alone at $f_t/f_{v0}=0.91$ had a strong component of the motion frequency. The streamline and vorticity contour plots displayed the synchronized 2S mode. When the torsional motion was coupled with in-phase transverse motion, $f_t/f_{v0}=f_m/f_{v0}=0.91$, lock-in was present with a sudden drop in the fluctuating amplitude of the pitching moment. The wake pattern had the 2P mode, and it was similar to the previous lock-in cases. As the cylinder moved downward, it also rotated counter-clockwise shedding a strong clockwise vortex and a weakened counter-clockwise vortex, and vice versa. When the torsional motion was coupled with out-of-phase transverse motion, still keeping $f_t/f_{v0}=f_m/f_{v0}=0.91$, all synchronization was lost. The force coefficient histories indicated a long term of quasi-periodic evolution. The streamlines and vorticity contour plots displayed little organization.

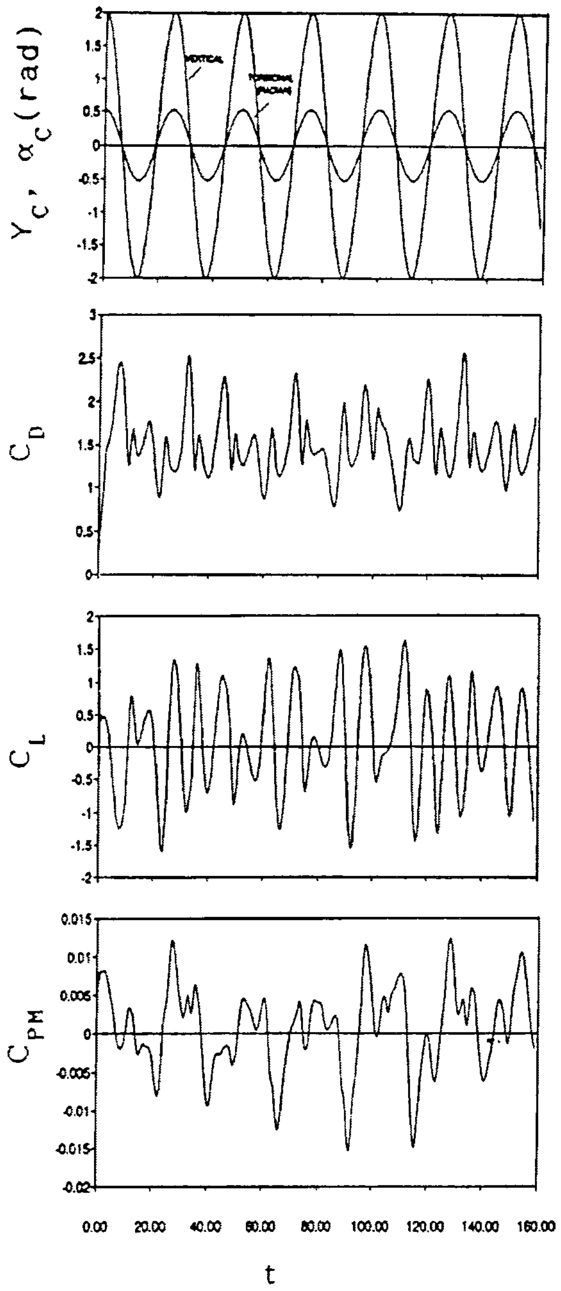

Fig. 10 Force coefficient histories for $f_t/f_{v0}=f_m/f_{v0}=0.36$, in-phase torsional and transverse oscillations, Re=2000

At $f_t/f_{v0}=0.36$, the force coefficients are periodic, as seen in Fig. 8. Similar to the histories in Fig. 6 for $f_m/f_{v0}=0.33$, the lift and pitching moment coefficient histories display the torsional oscillation frequency, and the drag coefficient twice the torsional frequency, as the fundamental one. In all three histories, higher frequencies are imposed on the fundamental frequency. Both the

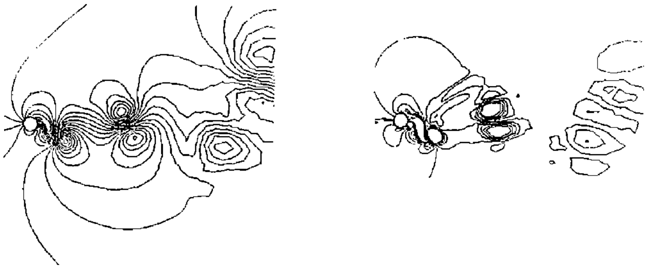

Fig. 11 Streamline and vorticity contours for $f_t/f_{v0}=f_m/f_{v0}=0.36$, in-phase torsional and transverse oscillations, Re $=2000$

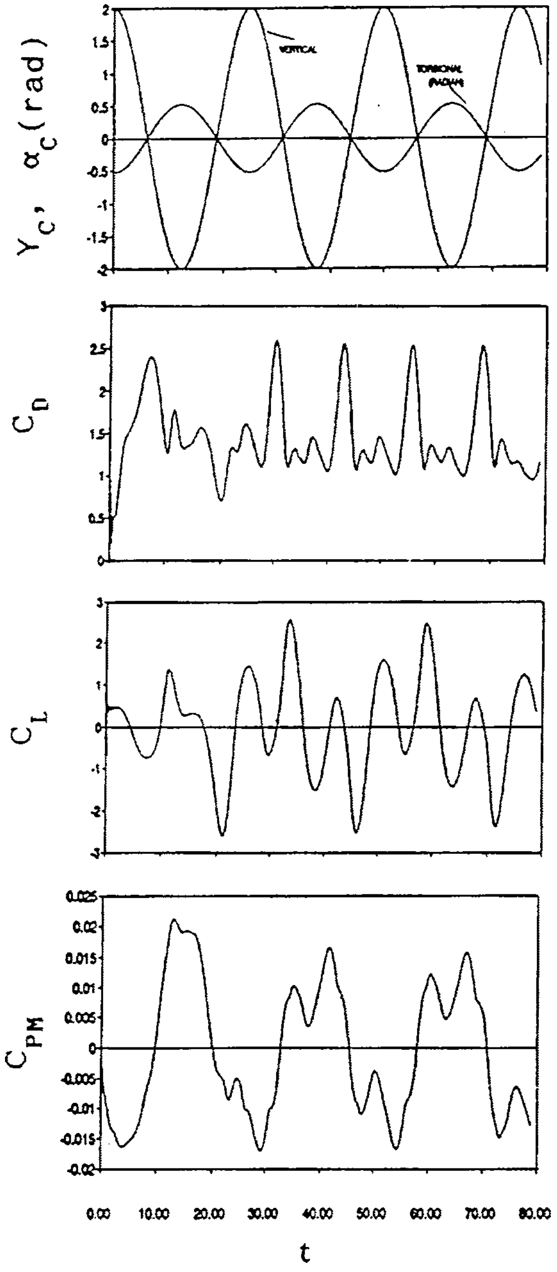

Fig. 12 Force coefficient histories for $f_t/f_{v0}=f_m/f_{v0}=0.36$, out-of-phase torsional and transverse oscillations, Re $=2000$

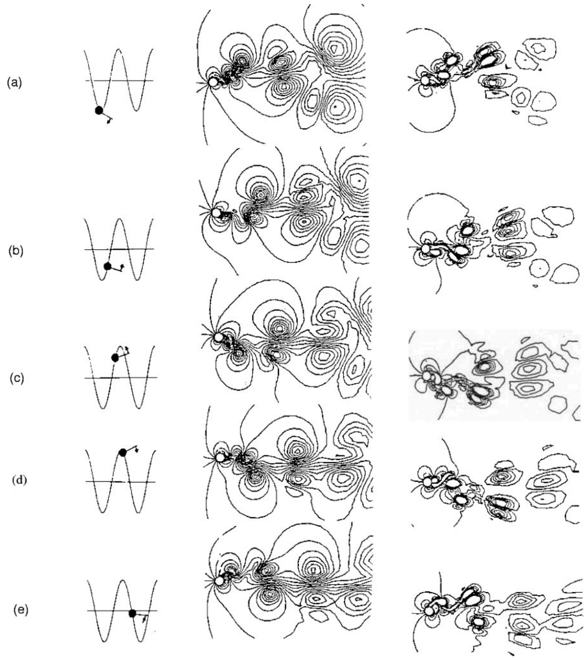

Fig. 13 Streamline and vorticity contours for $f_t/f_{v0}=f_m/f_{v0}=0.36$, out-of-phase torsional and transverse oscillations, Re $=2000$

Table 1 Summary of vortex modes for forced motion cases at Re $=2000$

cases with vertical motion alone							
$f_m/f_{v\circ}$	1.07	0.91	0.83	0.5	0.36	0.33	0.41
A/d	2	2	2	2	2	2	7
vortex mode	2P	2P	2P	NS	NS	6S	NS
cases with torsional (and vertical, A/d=2) motion, ±30°							
$f_m/f_{v\circ}$		0.91	0.91		0.36	0.36	
$f_t/f_{v\circ}$	0.91	0.91	0.91	0.36	0.36	0.36	
phase		in phase	out of phase		in phase	out of phase	
vortex mode	2S	2P	NS	6S	NS	2P+2S	

lift and drag coefficient histories have six distinct peaks per period. As illustrated in Fig. 9, six alternate vortices are shed during one period of torsional motion. When combined with in-phase vertical motion, $f_t/f_{v0}=f_m/f_{v0}=0.36$, the periodicity in the force coefficient histories is lost, as seen in Fig. 10, and the flow pattern depicted in Fig. 11 is not synchronized. Interestingly, when the torsional motion is combined with out-of-phase vertical motion at $f_t/f_{v0}=f_m/f_{v0}=0.36$, the force coefficient histories in Fig. 12 become almost periodic, and the vortex pattern 2P+2S emerges, as illustrated in Fig. 13. One vortex is shed whenever the cylinder is near or past the maximum displacement to form a pair, and a single vortex is shed whenever the cylinder passes the equilibrium point.

The forced translational, torsional and combined oscillation cases are summarized in Table 1.

V Dynamic Response Cases

Following the prediction of forced motion cases, the dynamic response of an elastically mounted cylinder is discussed next. By solving the flow equations with the structural equations, onset and development of galloping can be predicted if the shape of the cylinder is aerodynamically unstable. In the case of a circular cylinder, a stable cross section, vortex induced vibration results.

Unlike the controlled motion cases, the vibration amplitude may take long to build up in the calculations, especially when the fluid density is low.

Several experimental results from elastically mounted circular cylinders are reported in the literature. A hysteresis was reported by Feng [19] in his experiments on a lightly damped circular cylinder. The amplitude achieved a higher peak when the reduced velocity was increased than when it was decreased over the same range. Similarly, when the reduced velocity was increased, the 2S mode continued for a longer range of reduced velocities than when it was decreased. In other words, the 2P mode switched to the 2S mode at a lower reduced velocity when the reduced velocity was decreased than when it was increased. Bishop and Hassan [20] observed a similar hysteresis in their lift and phase measurements with a cylinder in controlled motion, but it occurred over a somewhat lower range of reduced velocities. Griffin and Ramberg [21] compared the free vibration experiments on circular cylinders in air and water. No hysteresis was reported in these experiments. Hence, it is not clear over what range of damping and mass ratios hysteresis occurs in the dynamic response of a spring-mounted circular cylinder. A plausible guess based on Feng's experiments is that it may occur when the damping and fluid to structure mass ratios are both low. Williamson and Roshko [18], on the other hand, explained the jump in the lift and phase measurements by the change of wake pattern, namely, between 2S and 2P modes. As described below, the present results indicate that the change in the phase difference between lift and displacement at the motion frequency may not always be simultaneous with the change of vortex mode.

The mass ratios $m/2\rho a^2 = 1.57$ and 7.6 were used in the present simulations, with the latter matching the mass ratio in Dean et al.'s experiment in water given by Griffin and Ramberg [21] (where m is the structural mass per unit length, ρ is the fluid density, and a is the radius of the cylinder). The lower mass ratio corresponds to equal mass densities of the cylinder and fluid. Critical damping ratios of 0 and 0.051 were used with the higher mass ratio, to represent undamped and light damping cases, respectively, the light damping being the same as in Dean et al.'s experiment. The lower mass ratio cases were run as undamped, only. Here, the critical damping ratio is defined as, $\xi_y = c_y/2(mk_y)^{1/2}$, where c_y and k_y are the damping and stiffness coefficients, respectively, in the transverse direction. The corresponding natural frequency is, $\omega_y = (k_y/m)^{1/2}$.

In Fig. 14, the amplitude ratio calculated for the dynamic cases is plotted against the frequency ratio f_{v0}/f_n. Dean et al.'s experimental results in water are given in the same figure. The choice of the frequency ratio f_{v0}/f_n as the horizontal coordinate, instead of the reduced velocity, U_r, is discussed first ($U_r = U_0/2af_n$, where f_n is the natural frequency of the cylinder in fluid). The computed stationary Strouhal number, St, is 0.24 at Re=2000 instead of being about 0.21. As a result, the predicted resonance range would be different from the experimental one, if the reduced velocity were used in Fig. 14. In order to match the two scales, computational and experimental, the frequency ratio f_{v0}/f_n is employed, where $f_{v0} = U_0 \mathrm{St}/d$ is the vortex shedding frequency of the stationary circular cylinder, St=0.24 for the numerical cases and St=0.21 for the experimental cases. f_n was measured in still water in the experiments; while for the numerical results, it is obtained by adding the mass of the fluid displaced by the circular cylinder to that of the structure, $f_n = f_{n0}[m/(m+\pi\rho a^2)]^{1/2}$, where f_{n0} is the natural frequency in air. Using the new parameter, f_{v0}/f_n, the response peak appearing near a reduced velocity of 6 in the experiments occurs at a frequency ratio of 1.2 both computationally and experimentally. This figure is discussed further with respect to the three sets of computational results below.

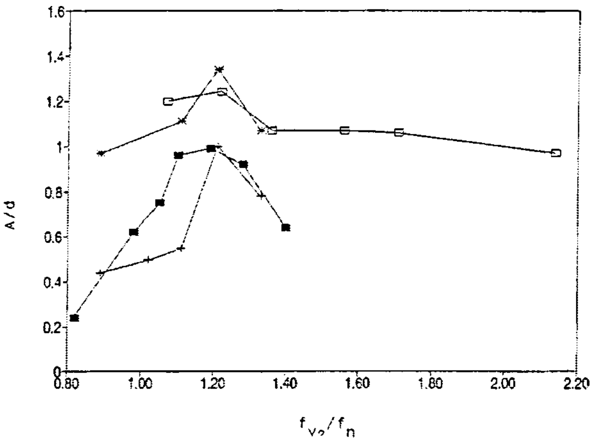

Fig. 14 Response amplitudes of a spring-mounted circular cylinder in cross flow. Present results: □, $m/2\rho a^2 = 1.57$, $\xi_y = 0$; *, $m/2\rho a^2 = 7.6$, $\xi_y = 0.$; +, $m/2\rho a^2 = 7.6$, $\xi_y = 0.051$); experimental results (Griffin and Ramberg [21]): ■, $m/2\rho a^2 = 7.6$, $\xi_y = 0.051$.

At a mass ratio of $m/2\rho a^2 = 1.57$, the dynamic response of the cylinder was computed at frequency ratios of $f_{v0}/f_n = 1.07$, 1.22, 1.36, 1.56, 1.71, and 2.14. The response amplitudes shown in Fig. 14 demonstrate wide resonance, with the maximum amplitude ratio of 1.25. The wake pattern was the 2P mode for all these six cases, and it is illustrated for $f_{v0}/f_n = 1.36$ in Fig. 15 with the streamline and vorticity contours.

Bearman [22] concluded from a compilation of experimental results that the Reynolds number may not be an important parameter for oscillating circular cylinders away from boundary layer transition. Therefore, the Reynolds number was fixed at 2000 in the present computations for convenience, while the natural frequency of the cylinder was varied to change the frequency ratio.

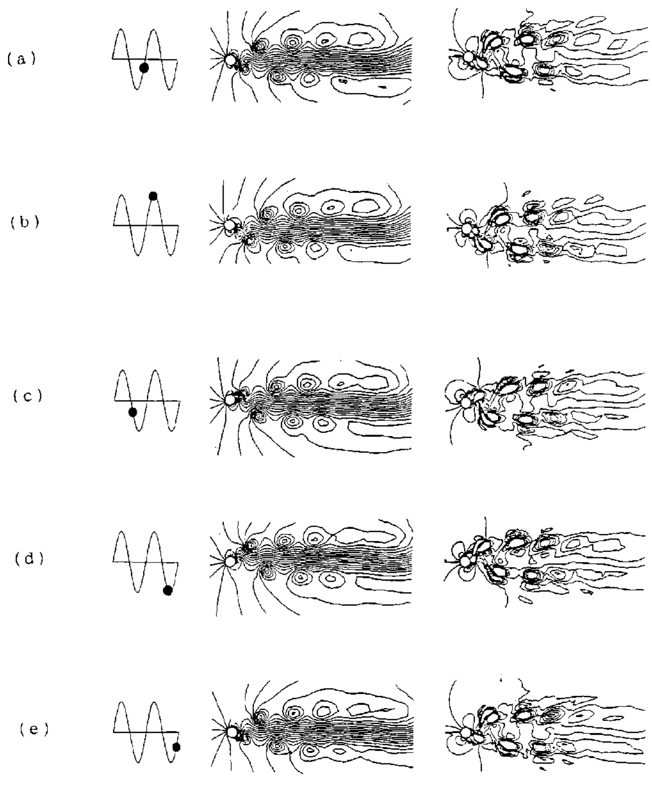

Fig. 15 Streamline and vorticity contours for $f_{v0}/f_n = 1.36$, $m/2\rho a^2 = 1.57$, $\xi_y = 0.$, Re=2000

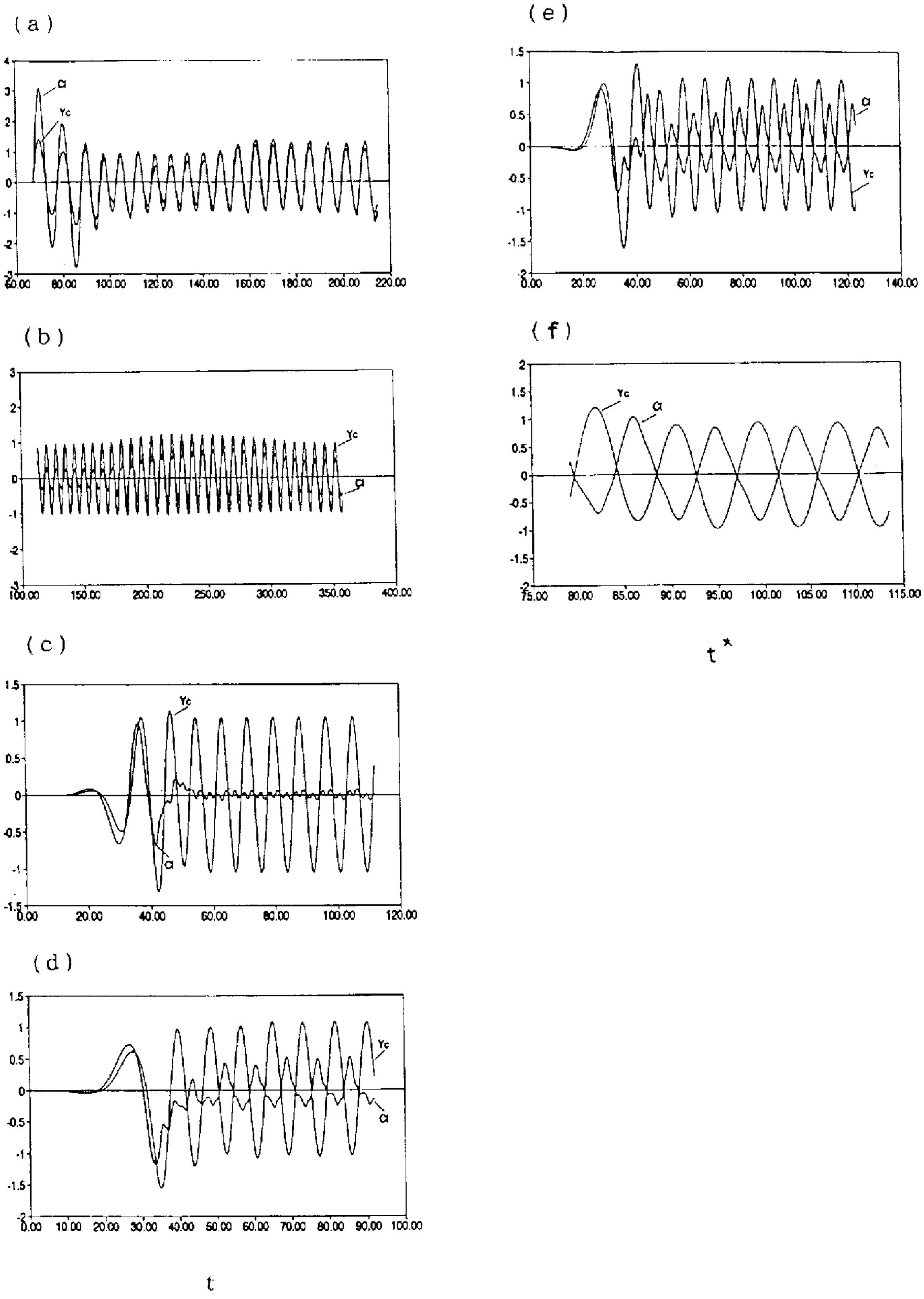

Fig. 16 Relative phase between lift and displacement for $f_{v0}/f_n=(a)$ 1.07, (b) 1.22, (c) 1.36, (d) 1.56, (e) 1.71 and (f) 2.14 at $m/2\rho a^2=1.57$, $\xi_y=0.$, Re=2000

In the experiments, the flow speed was adjusted, thus changing vortex shedding frequency of the stationary cylinder and the frequency ratio as a consequence, along with the Reynolds number.

The force coefficient histories for $f_{v0}/f_n=1.07$, 1.22, 1.36, 1.56, 1.71, and 2.14 at $m/2\rho a^2=1.57$ show some asymmetry, especially in the lift coefficient, although the displacement is nearly symmetrical. The lift amplitude drops to almost zero at a frequency ratio of 1.36, with high frequency fluctuation. This case is the transitional one from the lift force being in phase with the displacement to out of phase, as illustrated in Fig. 16. With the displacement plotted together with lift coefficient, the change in the lift coefficient is clearly visible, from being in-phase to out-of-phase with displacement. The wake pattern obtained in the range of the frequency ratios investigated is basically the 2P mode, while the lift is in phase with displacement for $f_{v0}/f_n=1.07$ and 1.22; during transition at $f_{v0}/f_n=1.36$; and while the lift is out of phase with displacement for $f_{v0}/f_n=1.56$, 1.71 and 2.14. Close inspection of the vortex formation process in all these cases indicates that it is virtually identical to the flow pattern during one period of the cylinder motion given in Fig. 15 for $f_{v0}/f_n=1.36$. The vorticity contours clearly show that the 2P mode wake is also similar to those found in forced motion cases discussed in the previous section. The only difference is that at higher frequency ratios $f_{v0}/f_n=1.71$ and 2.14, the vortex in each pair away from the center line is weakened so that the pairs do not form closed vortices in the streamline plots. This set of results indicate that the change of vortex mode from 2S to 2P does not always occur simultaneously with the change of the lift from in-phase to out-of-phase with the displacement. The next two sets of results confirm this conclusion further.

Next, the mass ratio is increased to $m/2\rho a^2=7.6$, and the frequency ratios of $f_{v0}/f_n=0.89$, 1.11, 1.21, and 1.33 are used. The relative phase between the lift and displacement is illustrated in Fig. 17 for this mass ratio. The time histories especially for the case $f_{v0}/f_n=0.89$ contain significant beat, while the flow pattern indicated the presence of a 2S vortex pattern. The lift is in-phase with the displacement for this frequency ratio, as seen in Fig. 17(*a*). At frequency ratios of 1.11 and 1.21, the lift patterns are in the transition process, from being in-phase with displacement to out-of-phase, and appear to have twice the vortex shedding frequency, as shown in Fig. 17(*b*) and 17(*c*), respectively. The corresponding wake patterns for these two frequency ratios have already changed to the 2P mode. The lift becomes out-of-phase with the displacement for $f_{v0}/f_n=1.33$ as shown in Fig. 17(*d*). The wake pattern for this case is also the 2P mode. Both the 2S and 2P modes were identical to those of the forced motion cases.

The maximum amplitude ratio of 1.34 is obtained at $f_{v0}/f_n=1.21$ and $m/2\rho a^2=7.6$, as shown in Fig. 14. This value is lower than the limit values obtained from simplified mathematical models such as the wake oscillator and correlation models (Blevins [3]), which give limit amplitude ratios greater than 2.0 for an elastically mounted rigid circular cylinder. In this case, the maximum amplitude is greater than that obtained at the mass ratio of 1.57, although a fully steady amplitude was not secured in the latter case, as shown in Fig. 16(*b*).

The cases discussed above for $m/2\rho a^2=1.57$ and 7.6 do not have any structural damping. In the cases that follow, a damping ratio of 0.051 is applied to match the value measured in Dean et al.'s experiment (Griffin and Ramberg [21]), while the mass ratio was kept at 7.6. The frequency ratios used are $f_{v0}/f_n=0.89$, 1.02, 1.11, 1.21, and 1.33. With light damping, the response amplitudes drop significantly from the undamped case, as seen in Fig. 14. The maximum amplitude compares well with the experimental value, although the resonance peak obtained is narrower than the experimental one. The discrepancy between the present results and experimental data may have resulted from lacking a turbulence model and imposed two-dimensionality in the computations. The relative phase between lift and displacement is plotted in Fig. 18. For $f_{v0}/f_n=0.89$, 1.02, 1.11, and 1.21, the vortex shedding was in the 2S mode, while the lift remained in phase with the cylinder displacement, as shown in Fig. 18(*a*) to 18(*d*). At $f_{v0}/f_n=1.33$, the vortex mode became 2P, and the lift became almost out of phase with displacement, according to Fig. 18(*e*). The result from an FFT analysis of the lift and displacement histories indicated that the lift now actually lead the displacement by 145 deg. The departure of phase difference from 180 deg provided energy to the cylinder to maintain a constant amplitude in the presence of viscous damping. The 2S and 2P modes were again identical to the forced motion patterns.

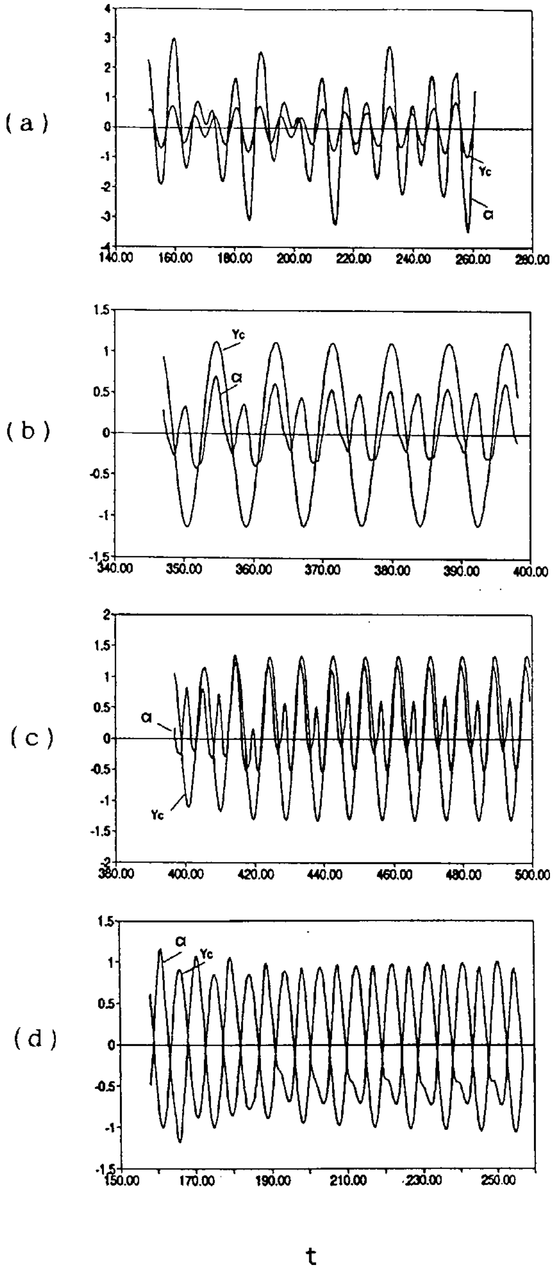

Fig. 17 Relative phase between lift and displacement for $f_{v0}/f_n=$(*a*) 0.89, (*b*) 1.11, (*c*) 1.21, and (*d*) 1.33 at $m/2\rho a^2=7.6$, $\xi_y=0.$, Re=2000

In Fig. 19, the dimensionless response frequency, f/f_n, is plotted against the dimensionless stationary vortex shedding frequency, f_{v0}/f_n. The results in this figure indicate that at the low mass ratio of 1.57, the response frequency is locked on to the stationary vortex shedding frequency rather than the natural frequency of the cylinder, as it is usually obtained in experiments with high structure to fluid mass ratio. Hence, high amplitude resonance is predicted over a wide range of reduced velocities or frequency ratios for a light structure, in which the response frequency may be controlled by stationary vortex shedding frequency (inverse lock-in). When the mass ratio is increased moderately to 7.6, the response frequency remains between the natural frequency of the structure and the stationary vortex shedding frequency. It is interesting to note that adding light viscous damping

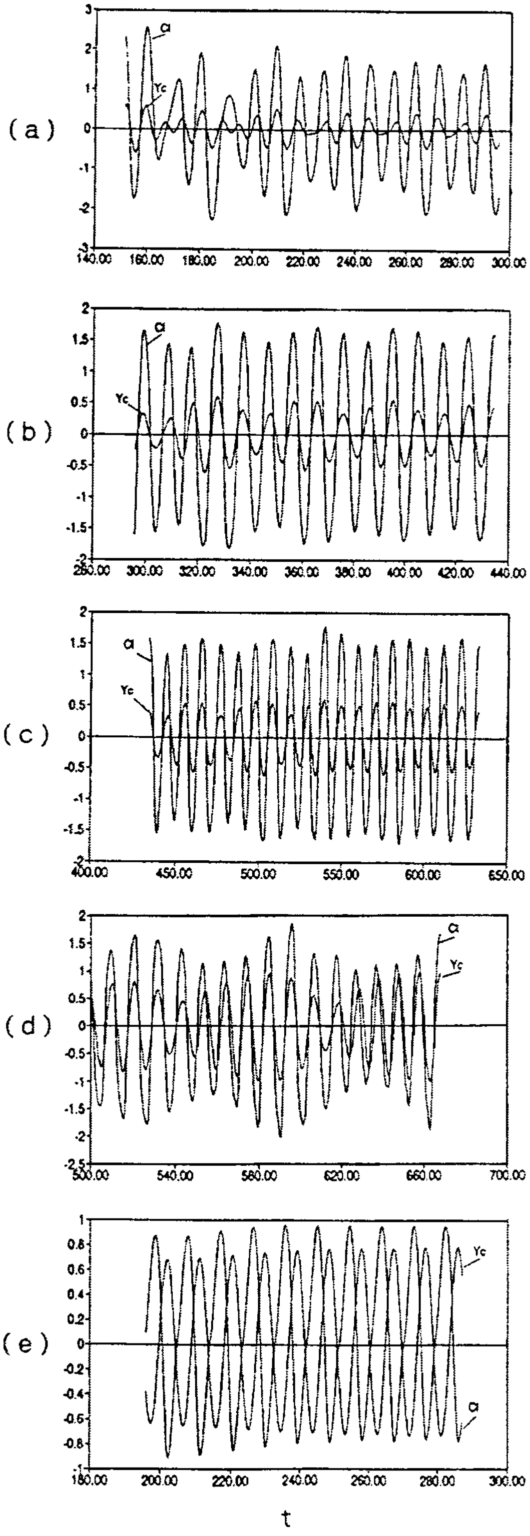

Fig. 18 Relative phase between lift and displacement for f_{v0}/f_n=(*a*) 0.89, (*b*) 1.02, (*c*) 1.11, (*d*) 1.21, and (*e*) 1.33 at $m/2\rho a^2$=7.6, ξ_y=0.051, Re=2000

affects the response frequency as a result of nonlinear interaction, while viscous damping has little effect on the natural frequency in a linear spring-mass system at similar damping levels.

A summary of the vortex modes and lift phases is given in Table 2 for the three sets of dynamic cases.

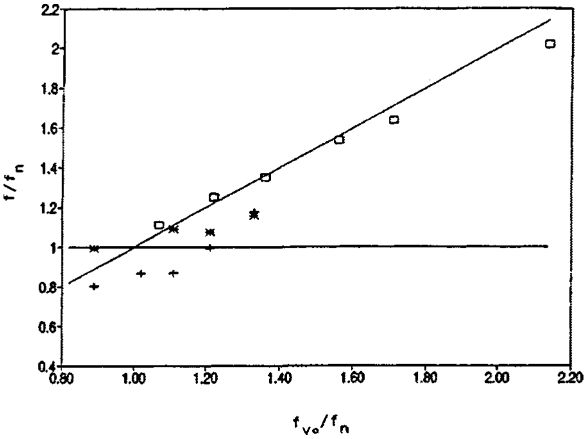

Fig. 19 Response frequency, *f*, of a spring-mounted circular cylinder. □, $m/2\rho a^2$=1.57, ξ_y=0; *, $m/2\rho a^2$=7.6, ξ_y=0.; +, $m/2\rho a^2$=7.6, ξ_y=0.051.

Table 2 Summary of vortex modes and the relative phase between lift force and cylinder displacement for dynamic response cases at Re=2000

$m/2\rho a^2$ = 1.57, ξ = 0						
f_{vo}/f_n	1.07	1.22	1.36	1.56	1.71	2.14
vortex mode	2P	2P	2P	2P	2P	2P
phase	in phase	in phase	transition	out of phase	out of phase	out of phase
$m/2\rho a^2$ = 7.6, ξ = 0						
f_{vo}/f_n	0.89	1.11	1.21	1.33		
vortex mode	2S	2P	2P	2P		
phase	in phase	transition	transition	out of phase		
$m/2\rho a^2$ = 7.6, ξ = 0.051						
f_{vo}/f_n	0.89	1.02	1.11	1.21	1.33	
vortex mode	2S	2S	2S	2S	2P	
phase	in phase	in phase	in phase	in phase	out of phase	

VI Conclusions

The numerical predictions of the flow fields around stationary and transversely oscillating circular cylinders, as well as of the dynamic response of a spring-mounted circular cylinder, have been found to be in reasonable agreement with the available experimental data. The predictions were obtained with a FORTRAN code developed using the SIMPLE-C algorithm with the QUICK scheme.

From the results of the controlled motion cases, it can be seen that when torsional motion is coupled with the vertical oscillation, the lock-in of the vortex shedding is possible, but it depends largely on the relative phase between the torsional and translational oscillations. With torsional motion alone, the flow field may not be modified significantly.

The numerical simulation of the dynamic cross flow response of a spring-mounted circular cylinder confirm the phase change, namely, from the lift force being in-phase with the cylinder displacement to out-of-phase, with increased frequency ratio, as well as the change of wake pattern from 2S to 2P. However, the change of wake pattern does not always occur simultaneously with the change of the relative phase between the lift force and displacement.

Acknowledgment

Financial support for this project was provided by NSERC (Natural Sciences and Engineering Research Council) Canada, Ontario Hydro, Canada, and Victoria University of Technology, Australia. The authors are grateful to D. G. Havard of Ontario Hydro for many helpful discussions. A shorter version of this paper was presented at the 1996 ASME Fluids Engineering Division Conference (Turan and Lu, 1996) in San Diego, California.

References

[1] Pon, C. J., Havard, D. G., Currie, I. G., and MacDonald, R., 1989, Aeolian Vibration of Bundle Conductors, CEA REPORT 117-T-510, March.

[2] Den Hartog, J. P., 1932, ''Transmission Line Vibration due to Sleet,'' AIEE Trans., **51**, No. 4, pp. 1074–1086.

[3] Blevins, R. D., 1977, *Flow-Induced Vibration*, Van Nostrand Reinhold, New York.

[4] Zdero, R., Turan, Ö. F., and Havard, D. G., 1995, ''Galloping: Near Wake Study of Oscillating Smooth and Stranded Circular Cylinders in Forced Motion,'' Exp. Therm. Fluid Sci., **10**, pp. 28–43.

[5] Chang, K. S., and Sa, J. Y., 1992, ''Patterns of Vortex Shedding from an Oscillating Circular Cylinder,'' AIAA J., **30**, No. 5, pp. 1331–1336.

[6] Chilukuri, R., 1987, ''Incompressible Laminar Flow Past a Transversely Vibrating Cylinder,'' ASME J. Fluids Eng., **109**, pp. 166–171.

[7] Hulbert, S. E., Spaulding, M. L., and White, F. M., 1982, ''Numerical Solution of the Time Dependent Navier-Stokes Equations in the Presence of an Oscillating Cylinder,'' ASME J. Fluids Eng., **104**, pp. 201–206.

[8] Lecointe, Y., and Piquet, J., 1990, Computation of Unsteady, Laminar, Incompressible, Viscous Flows Using the Vorticity Streamfunction Formulation, Computational Methods in Viscous Aerodynamics, Murthy, T. K. S., and Brebbia, C. A., eds., Elsevier and Computational Mechanics, pp. 77–116.

[9] Patankar, S. V., 1980, *Numerical Heat Transfer and Fluid Flow*, McGraw-Hill, New York.

[10] Gaskell, P. H., and Lau, A. K. C., 1988, ''Curvature-Compensated Convective Transport: Smart, A New Boundedness Preserving Transport Algorithm,'' Int. J. Numer. Methods Fluids, **8**, No. 6, pp. 617–641.

[11] Leonard, B. P., 1979, ''A Stable and Accurate Convective Modelling Procedure Based on Quadratic Upstream Interpolation,'' Comput. Methods Appl. Mech. Eng., **19**, pp. 59–98.

[12] Hayase, T., Humphrey, J. A., and Greif, R., 1992, ''A Consistently Formulated QUICK Scheme for Fast and Stable Convergence Using Finite-Volume Iterative Calculation Procedures,'' J. Comput. Phys., **98**, pp. 108–118.

[13] Van Doormaal, J. P., and Raithby, G. D., 1984, ''Enhancement of the SIMPLE Method for Predicting Incompressible Fluid Flows,'' Numer. Heat Transfer, **7**, pp. 147–163.

[14] Lu, S., and Turan, Ö. F., 1996, ''A FORTRAN Code to Simulate Flow Fields around Oscillating Conductors,'' Departmental Report, MET9608, Mech. Eng. Dept., Victoria University of Technology, Melbourne.

[15] Braza, M., Chassaing, P., and Ha Minh, H., 1986, ''Numerical Study and Physical Analysis of the Pressure and Velocity Fields in the Near Wake of a Circular Cylinder,'' J. Fluid Mech., **165**, pp. 79–130.

[16] Jordan, S. K., and Fromm, J. E., 1972, ''Oscillatory Drag, Lift, and Torque on a Circular Cylinder in a Uniform Flow,'' Phys. Fluids, **15**, No. 3.

[17] Batchelor, G. K. 1967, *An Introduction to Fluid Dynamics*, Cambridge University Press.

[18] Williamson, C. H. K., and Roshko, A., 1988, ''Vortex Formation in the Wake of an Oscillating Cylinder,'' J. Fluids Struct., **2**, pp. 355–381.

[19] Feng, C. C., 1988, ''The Measurement of Vortex Induced Effects in Flow past Stationary and Oscillating Circular and D-section Cylinders,'' M.Sc. thesis, University of British Columbia, Vancouver.

[20] Bishop, R. E. D., and Hassan, A. Y., 1964, ''The Lift and Drag Forces on a Circular Cylinder Oscillating in a Flowing Fluid,'' Proc. R. Soc. London, Ser. A, **277**, pp. 51–75.

[21] Griffin, O. M., and Ramberg, S. E., 1982, ''Some Recent Studies of Vortex Shedding with Application to Marine Tubulars and Risers,'' ASME J. Energy Resour. Technol., **104**, pp. 2–13.

[22] Bearman, P. W., 1984, ''Vortex Shedding from Oscillating Bluff Bodies,'' Annu. Rev. Fluid Mech., **16**, pp. 195–222.

[23] Turan, Ö. F., and Lu, S., 1996, ''Numerical prediction of Flow Fields around Circular Cylinders: Forced Motion and Dynamic Response Cases,'' ASME Fluids Engineering Division Conference, FED-Vol. 237, pp. 647–652.

Image Singularity System to Represent Two Circular Cylinders of Different Diameter

D. K. Lee
Professor,
School of Transportation Systems Engineering,
University of Ulsan,
Ulsan 680-749, Korea

The singularity system to represent two circular cylinders poised under different ambient flow fields is considered in the present research. The singularity system, composed of a series of singularities, has to be truncated for numerical calculations. A rational criterion to determine how many terms of this series should be retained to maintain the prescribed accuracy is provided through analysis of the converging property of the series. A particular emphasis is put on how to deal with the discrete vortex model of a boundary layer, this possibility being the basis for the development of a tool to simulate vortex shedding from a structure composed of two circular cylinders. The principle in obtaining the present singularity system can be applied to more-than-two-cylinders structures. Only the series becomes more complex with an increase in the number of cylinders.
[S0098-2202(00)01704-1]

1 Introduction

When a single circular cylinder is present in the two-dimensional irrotational flow field, the complex potential is defined and the singularity system representing the cylinder can be readily found. The circle theorem (Milne-Thomson [1]) proves to be an efficient tool in this process, if used with some care.

However, when there is more than one circular cylinder in the flow field, the singularity system representing each cylinder cannot be obtained so easily due to the interactions between the cylinders. The circle theorem can still be applied for one cylinder at a particular stage but the result accompanies violation of the boundary condition on the other cylinder. This fact makes it more convenient to compose the singularity system with the concept of image singularity than with the help of the circle theorem.

Only the case of two circular cylinders has been considered in the present study. The method proposed herein can be applied without alteration to other cases with more circular cylinders. However, the complexity of the singularity system grows rapidly with an increase of the number of the cylinders.

The method of calculating potential flow around multiple cylindrical bodies is useful in connection with several contexts. The potential flow itself perturbed due to the bodies in a given basic ambient flow is of some interest for its own sake or as the basis for further theoretical and/or numerical analysis as can be found in the study by Müller [7] who dealt with the dipole system to represent two circular cylinders in a uniform ambient flow. Another field of applications can be found in the techniques to simulate viscous flow through the frame of potential flow with embedded vortices, as can be found for instance in the series of papers by Sarpkaya [2]. The investigations by Lewis and Porthouse [3], Fink and Soh [4], and Mook and Dong [5] among many others may also be referred to to see some variations of the technique. In these kinds of flow simulations, commonly referred to as the discrete vortex method, the vorticity in the wake region is represented by a large number of point vortices, all of which have been released in a step-by-step fashion from the body and convected downstream in the flow field. The wall boundary condition being of the Neumann type is usually satisfied through the use of the concept of image vortex if the body cross section is circular. When there is only one cylinder this task offers no particular complexity but when there are more than one it is not so simple owing to the interaction effects between the cylinders and requires some remedies such as considered in this paper. The possibility of this application has in fact been the motivation of the present investigation.

2 The Complex Potentials

Let us consider the flow situation depicted in Fig. 1 in which the vortex of the strength Γ is supposed to be shed from a particular cylinder, say the greater one. An image dipole is needed at the center of each cylinder to satisfy the boundary condition on the cylinder surface in connection with the free-stream velocity. Since the dipole within the greater cylinder is an external singularity when viewed from the smaller cylinder, an image dipole is to appear in the smaller cylinder against this external dipole, and similarly an image dipole is also to be employed in the greater cylinder as well. These second step image dipoles bring in further image dipoles in both cylinders. This process continues indefinitely to compose the whole image dipole system.

As for the shed vortex, an image vortex immediately responds within the cylinder from which the vortex has been shed. Then each of these two vortices calls for respective image vortices

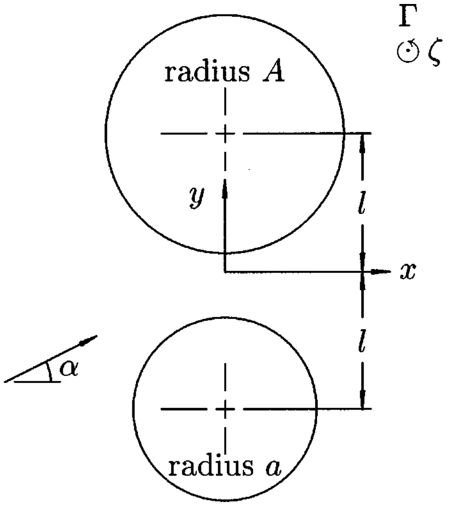

Fig. 1 Uniform flow with a vortex

Contributed by the Fluids Engineering Division for publication in the JOURNAL OF FLUIDS ENGINEERING. Manuscript received by the Fluids Engineering Division May 30, 2000; revised manuscript received June 23, 2000. Associate Technical Editor: D. P. Telionis.

within the other cylinder and these latter two image vortices bring another two image vortices in the first cylinder and so on.

In this process of determining the image singularity system, the Milne-Thomson's circle theorem can be used, except for the first step, to determine the immediate image vortex corresponding to the shed external one. Here, only one image vortex at the inverse point is chosen to bring the total circulation together with the shed vortex to zero.

The resulting complex potential when nondimensionalized with respect to the radius of the major cylinder and the magnitude of the free-stream velocity is as follows:

$$\varphi(z)=e^{-i\alpha}z+\varphi_d(z)+\varphi_v(z). \tag{1}$$

$\varphi_d(z)$ standing for the series of the image dipoles can be obtained through repeated use of the circle theorem and takes the following form:

$$\varphi_d(z)=\mu_{10}\frac{e^{i\alpha}}{z-\xi_{10}}+\mu_{11}\frac{e^{-i\alpha}}{z-\xi_{11}}+\cdots+\mu_{20}\frac{e^{i\alpha}}{z-\xi_{20}}+\mu_{21}\frac{e^{-i\alpha}}{z-\xi_{21}}+\cdots \tag{2}$$

where

$$\mu_{1k}=\mu_{2(k-1)}\frac{1}{(|\xi_{2(k-1)}-is/2|)^2}, \tag{3}$$

$$\mu_{2k}=\mu_{1(k-1)}\frac{r^2}{(|\xi_{1(k-1)}+is/2|)^2}, \tag{4}$$

$$\xi_{1k}=\frac{1}{\xi_{2(k-1)}+is/2}+i\,\frac{s}{2}, \tag{5}$$

$$\xi_{2k}=\frac{r^2}{\xi_{1(k-1)}-is/2}-i\,\frac{s}{2}, \tag{6}$$

$$\mu_{10}=1,\quad \mu_{20}=r^2,$$

$$\xi_{10}=is/2,\quad \xi_{20}=-is/2,$$

$$s=2l/A,\quad r=a/A.$$

$\varphi_v(z)$ represents the complex potential due to the shed vortex and the series of the image vortices and can be expressed as follows:

$$\varphi_v(z)=-\frac{i\Gamma}{2\pi}\log(z-\zeta)+\frac{i\Gamma}{2\pi}[\log(z-\zeta_{11})-\log(z-\zeta_{12})+\cdots]+\frac{i\Gamma}{2\pi}[\log(z-\zeta_{21})-\log(z-\zeta_{22})+\cdots] \tag{7}$$

where

$$\zeta_{1k}=c_{1k}+is/2,\quad \zeta_{2k}=c_{2k}-is/2, \tag{8}$$

ζ; dimensionless position of the shed vortex,
Γ; dimensionless strength of the shed vortex.

ζ_{1k} and ζ_{2k} denote the position of the image vortices within cylinder 1 and cylinder 2, respectively, and c_{1k} and c_{2k} represent the complex position vectors of each of these image vortices relative to the center of the respective cylinder it belongs to and are given by:

$$c_{1k}=\frac{1}{\zeta_{2(k-1)}+is/2},\quad c_{2k}=\frac{r^2}{\zeta_{1(k-1)}-is/2} \tag{9}$$

with

$$\zeta_{10}=\zeta_{20}=\zeta.$$

It is interesting to see that each term of φ_d or φ_v takes the form of a continued fraction. Although some properties of continued fraction are available, as can be found in Abramowitz and Stegun [6], it might be fruitful to take this problem as the physical model in investigating further properties of that intriguing mathematical entity.

When there are N_1 and N_2 vortices in the flow field shed, respectively, from cylinder 1 and cylinder 2, the complex potential would be given as

$$\varphi(z)=e^{-i\alpha}z+\varphi_d(z)+\sum_{j=1}^{2}\sum_{k=1}^{N_j}\varphi_v(z;(\Gamma)_{jk},(\zeta)_{jk}) \tag{10}$$

in which $\varphi_v(z;(\Gamma)_{jk},(\zeta)_{jk})$ is just $\varphi_v(z)$ of Eq. (7) with Γ and ζ replaced, respectively, by $(\Gamma)_{jk}$ and $(\zeta)_{jk}$. This expression may be taken for the discrete vortex model for the boundary layer and the wake created around a two-cylinder structure located in the uniform stream.

3 Truncation of the Infinite Series

3.1 Truncation of the Series for φ_d. For this purpose, it would be sufficient to consider the series of μ's rather than φ_d itself and, moreover, only the series of μ's within either series. Let this series be denoted by S_μ, that is,

$$S_\mu=\mu_0+\mu_1+\cdots+\mu_{m-1}+R_{\mu m} \tag{11}$$

where

$$R_{\mu m}=\mu_m+\mu_{m+1}+\cdots, \tag{12}$$

$$\mu_k=\mu_{1k}\ \text{ or }\ \mu_k=\mu_{2k}.$$

It can be recognized without difficulty that this series converges slowest when the two cylinders have the same radius, i.e., when $r=1$. If so, μ's are expressed as

$$\mu_k=\prod_{j=1}^{k}g_j^2\quad \text{for } k=1,2,\ldots\quad \text{with } \mu_0=1 \tag{13}$$

where

$$g_j=\frac{h_1}{s-}\,\frac{h_2}{s-}\cdots\frac{h_{j-1}}{s-}\,\frac{h_j}{s} \tag{14}$$

and

$$h_1=h_2=\cdots=h_j=1.$$

If the cylinders are not in contact, s is greater than 2 and hence

$$g_k<g_{k+1}<\frac{1}{s-1}\quad \text{for } k=1,2,\ldots. \tag{15}$$

From these inequalities, we can deduce that

$$R_{\mu m}<\frac{1}{[(s-1)^2-1](s-1)^{2(m-1)}}. \tag{16}$$

Equating the right-hand side of this expression to a certain prescribed small number ϵ_μ, we can fix the number of terms M_d to be retained to keep the sum of the neglected terms within the desired error bound as shown below:

$$M_d-1<1-\frac{\log[\epsilon_\mu s(s-2)]}{2\log(s-1)}\leq M_d. \tag{17}$$

3.2 Truncation of the Series for φ_v. Consider the series for $\varphi_v(z)$ excluding the external vortex term and the two leading image vortex terms. The remaining series $\varphi_v'(z)$ can be expanded as the following:

$$\begin{aligned}\varphi_v'(z) = -\frac{i\Gamma}{2\pi}&\left\{\left[\frac{\Delta\zeta_{12}}{z-\zeta_{12}}+\frac{(\Delta\zeta_{12})^2}{2(z-\zeta_{12})^2}+\cdots\right]\right.\\ &\left.+\left[\frac{\Delta\zeta_{14}}{z-\zeta_{14}}+\frac{(\Delta\zeta_{14})^2}{2(z-\zeta_{14})^2}+\cdots\right]+\cdots\right\}\\ -\frac{i\Gamma}{2\pi}&\left\{\left[\frac{\Delta\zeta_{22}}{z-\zeta_{22}}+\frac{(\Delta\zeta_{22})^2}{2(z-\zeta_{22})^2}+\cdots\right]\right.\\ &\left.+\left[\frac{\Delta\zeta_{24}}{z-\zeta_{24}}+\frac{(\Delta\zeta_{24})^2}{2(z-\zeta_{24})^2}+\cdots\right]+\cdots\right\} \qquad (18)\end{aligned}$$

where

$$\begin{aligned}\Delta\zeta_{1k}&=\zeta_{1(k+1)}-\zeta_{1k},\\ \Delta\zeta_{2k}&=\zeta_{2(k+1)}-\zeta_{2k}.\end{aligned} \qquad (19)$$

The inverse points ζ_{1k} and ζ_{2k} in Eq. (7) and the above equations have the following properties:

$$\zeta_{1k}\in\Omega_{(k-1)} \quad \text{and} \quad \zeta_{2k}\in\omega_{(k-1)} \qquad (20)$$

where Ω_k; the image region of the region $\omega_{(k-1)}$,
ω_k; the image region of the region $\Omega_{(k-1)}$,
Ω_0; the inner region of the cylinder 1,
ω_0; the inner region of the cylinder 2,

the image region of a region being defined as the set of inverse points of all the points in the region. Since a subregion will be mapped into a sub image region, it is not difficult to see that

$$\Omega_k\subset\Omega_{(k-1)}, \quad \omega_k\subset\omega_{(k-1)} \qquad (21)$$

and, hence, the absolute values of $\Delta\zeta_{1k}$ and $\Delta\zeta_{2k}$ are smaller than unity.

Now, for determination of the truncation position of the series Eq. (18) it may be sufficient to consider the following series only,

$$S_{1v}=\Delta\zeta_{12}+\cdots+\Delta\zeta_{1(2m)}+R_{1v(2m)} \qquad (22)$$

where

$$R_{1v(2m)}=\sum_{k=1}^{\infty}\Delta\zeta_{1(2m+2k)} \qquad (23)$$

in view of the fact that the series comprised of the first-order terms converges most slowly. We may think of only S_{1v} because, in fact, the same conclusion is obtained from the consideration of the series composed of $\Delta\zeta_{2k}$. The relative importance of the remainder of this series would become more evident when the first term is made unit value by dividing both sides of Eq. (22) by $\Delta\zeta_{12}$.

c_{1k} and c_{2k} as defined by Eq. (9) take a form of continued fraction. Inserting Eq. (8) into Eq. (19) and making use of a property of continued fractions, we have, after some manipulation,

$$\frac{\Delta\zeta_{1(2k)}}{\Delta\zeta_{12}}=\prod_{j=1}^{2(k-1)}[c_{1(3+j)}\overline{c}_{2(2+j)}/r] \quad \text{for } k=2,3,\ldots. \qquad (24)$$

The properties in Eq. (21) imply that

$$|c_{1k}|_{\max}>|c_{1(k+1)}|_{\max} \quad \text{and} \quad |c_{2k}|_{\max}>|c_{2(k+1)}|_{\max}. \qquad (25)$$

$|c_{1k}|$ and $|c_{2k}|$ become greatest either when $\zeta=(s/2-1)i$ or when $\zeta=-(s/2-r)i$ and we have the maximum values for $|c_{12}|$ and $|c_{22}|$

$$|c_{12}|_{\max}=\frac{1}{s-r}, \quad |c_{22}|_{\max}=\frac{r^2}{s-1}. \qquad (26)$$

The inequalities shown by Eq. (25) affirm that

$$\left|\frac{R_{1v(2m)}}{\Delta\zeta_{12}}\right|<\sum_{k=m}^{\infty}\left[\frac{r}{(s-r)(s-1)}\right]^{2k}. \qquad (27)$$

Suppose a certain small number ϵ_v is specified to the right-hand side of the above equation, that is,

$$\left[\frac{r}{(s-r)(s-1)}\right]^{2m}\frac{1}{1-[r/(s-r)(s-1)]^2}=\epsilon_v. \qquad (28)$$

The truncation position $2m$ can be determined from this equation as the smallest even number just greater than the value satisfying the equation. In view of the definition of $\Delta\zeta_{1k}$, let us denote $2m$ so obtained plus 1 by M_v. Then M_v is determined as the smallest odd number satisfying the following inequality

$$\frac{\log\{\epsilon_v(1-[r/(s-r)(s-1)]^2)\}}{\log[r/(s-r)(s-1)]}+1\le M_v. \qquad (29)$$

4 The Truncated Complex Potential

The exposition of the previous section allows us to truncate Eq. (1) as follows

$$\begin{aligned}\varphi(z)=e^{-i\alpha}z+\sum_{j=1}^{2}\sum_{k=0}^{M_d}\mu_{jk}\frac{1}{z-\xi_{jk}}e^{(-1)^k i\alpha}-\frac{i\Gamma}{2\pi}&\left\{\log[z-(\zeta)_p]\right.\\ &\left.+\left[\sum_{j=1}^{2}\sum_{k=1}^{M_v}(-1)^k\log(z-\zeta_{jk})\right]+\log[z-\zeta_{(3-p)(M_v+1)}]\right\}\end{aligned} \qquad (30)$$

where p; 1 or 2 according to the cylinder from which the vortex is shed.

The last term in the curly bracket is required, because the image vortices appear in pairs at all the stages so that the total circulation vanishes.

5 Calculated Examples

Streamlines obtained from the present investigation are shown in the following figures for a number of different flow situations. In each case, the plotted region is covered by a grid system and the value of the complex potential is calculated at every nodal point. Then the streamlines are generated by tracing the contours of constant value of the stream function.

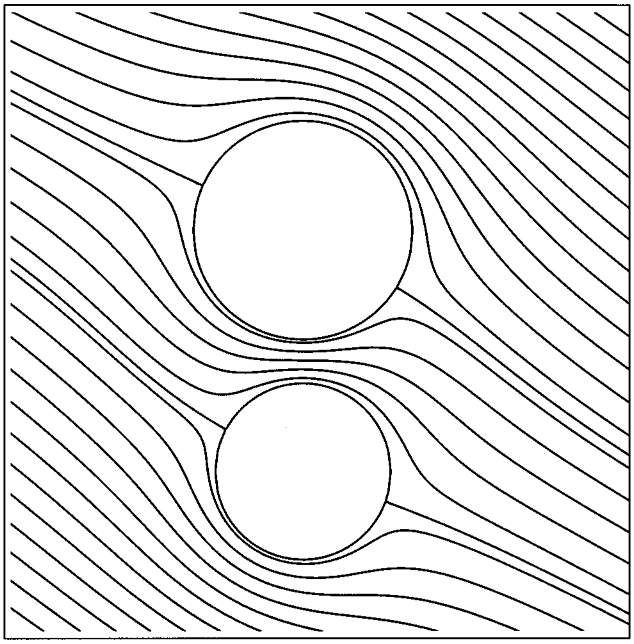

$r=0.8 \quad s=2.2 \quad \alpha=-30°$

Fig. 2 Uniform flow

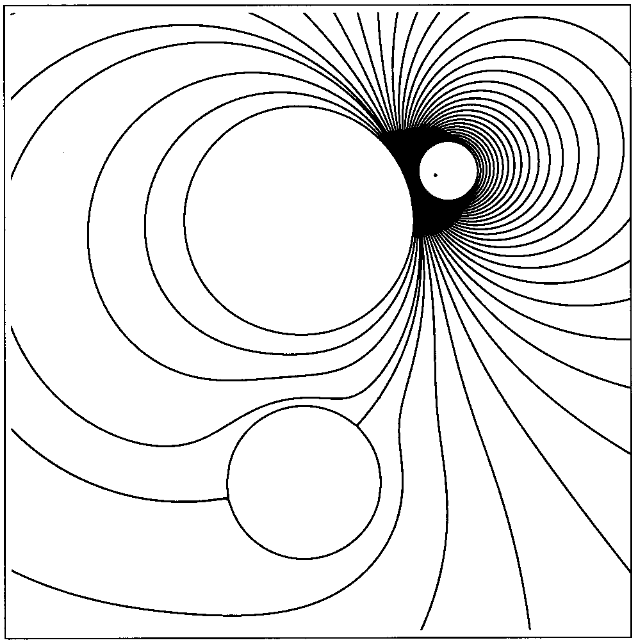

Fig. 3 Two cylinders with a single vortex

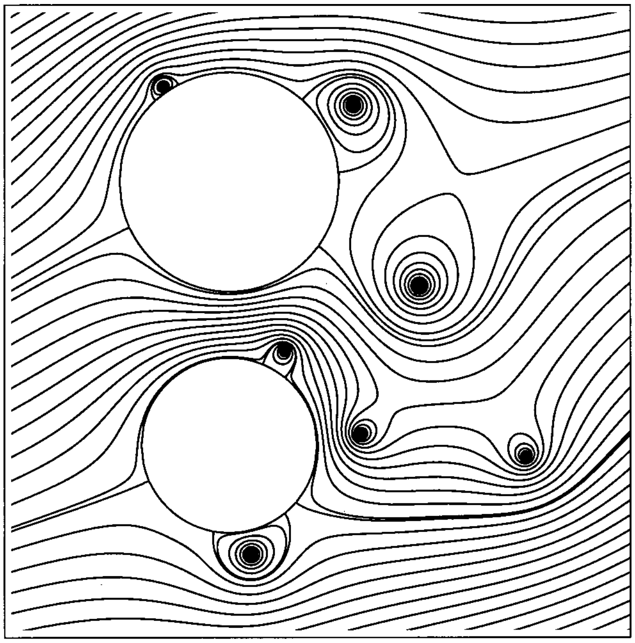

Fig. 5 Uniform flow with some shed vortices

The employed mesh size is typically 0.02 in both x- and y-direction but with more dense nodes at the adjacent region of the cylinders. The series were truncated using 0.0001 as the truncation parameter for both ϵ_μ and ϵ_v. The streamlines are chosen so that difference of the stream function between any two neighboring streamlines is fixed.

Figure 2 shows the streamlines of a uniform stream approaching the cylinders at an angle of $\alpha = -30$ deg. The number of terms to be retained in each series of the dipole potential φ_d was $M_d = 28$. Of course the vortex potential does not exist. Figure 3 shows the streamlines when there is a single vortex at the position (1.2,1.6) with the center of the major cylinder at (0,1.2). In this case, the stream function was nondimensionalized with respect to the vortex strength. The other parameters are shown in the figure. Figure 4 shows the case of two cylinders introduced in the flow field that has been created by a vortex. This is the situation stipulated by the Milne-Thomson's circle theorem. The computational parameters have the same values as those of Fig. 3. In both the cases of Fig. 3 and Fig. 4, no dipole potential comes into existence and that part of Eq. (30) representing the vortex potential was determined with $M_v = 9$. When a uniform flow with the approaching angle $\alpha = 20$ deg is superposed with a number of flows of the nature shown by Fig. 3, we have the streamline distribution shown in Fig. 5. In the diagram the upper three vortices are supposed to be shed from the major cylinder while the other four from the smaller one. The strengths are arbitrarily chosen between 2.4 and 3.2, and so are the locations. These strengths are rather great compared with those normally encountered in a numerical simulation by the discrete vortex method and are chosen so as to exaggerate streamlines around the vortices. M_d and M_v were 15 and 11, respectively. The same value of M_v applies to all the shed vortices since it depends only on ϵ_v, r, and s. The degree of violating the exact boundary condition is given theoretically as a simple addition of that of each single vortex. This calculation demonstrates that the case shown in Fig. 3 plays the role of the basic building block for a vortex shedding simulation with a large number of discrete vortices.

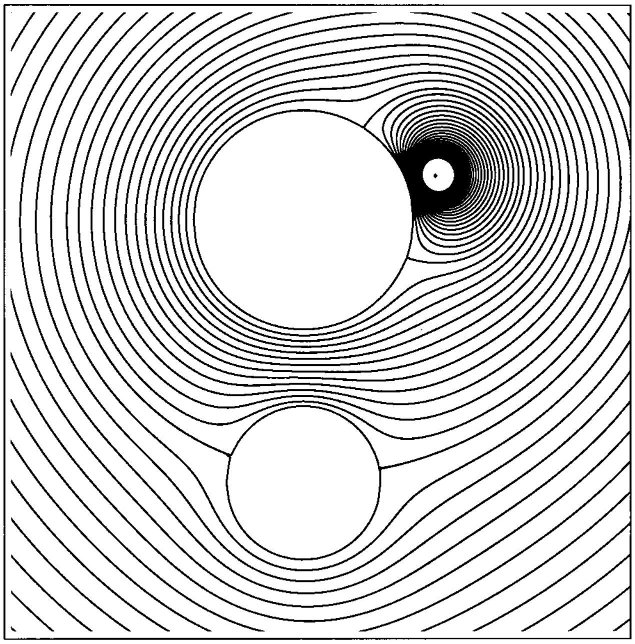

Fig. 4 Flow by a vortex

6 Conclusions

The calculated streamlines seem to provide sufficient ground to believe that the present way of tackling the problem is truly reliable.

Treatment of the series in connection with determining the truncation position might have at first sight appeared rather rough. If the converging property of the series was in question, rigor is, of course, a crucial factor to be maintained. But to find the truncation position only, it seems to be justifiable that the present treatment is adequate. In fact, the comment may be added that an appreciable margin is expected if the suggested way of truncation is used to acquire the accuracy in mind.

The same principle of building up the image singularity system can be extended to the situation of more than two circular cylinders placed in any arbitrary fashion. From a practical point of view, only the complexity grows almost prohibitively with an increase of the number of cylinders. However, if the image singularity system is sought through analytical means there can be no alternative other than the present way of approaching the problem.

Acknowledgments

The author wishes to acknowledge the financial support of the Korea Research Foundation made in the program year of 1997.

References

[1] Milne-Thomson, L. M., 1968, *Theoretical Hydrodynamics*, 5th ed., Macmillan, New York.

[2] Sarpkaya, T., 1989, ''Computational Methods With Vortices—The 1988 Freeman Scholar Lecture,'' ASME J. Fluids Eng., **111**, pp. 5–52.

[3] Lewis, R. I., and Porthouse, D. T. C., 1983, ''Recent Advances in the Theoretical Simulation of Real Fluid Flows,'' Trans. NECIES, **99**, pp. 88–104.

[4] Fink, P. T., and Soh, W. K., 1974, ''Calculation of vortex sheets in unsteady flow and applications in ship hydrodynamics,'' *Proc. 10th Symp. Naval Hydro.*, MIT, Cambridge, pp. 463–491.

[5] Mook, D. T., and Dong, B., 1994, ''Perspective: Numerical Simulation of Wakes and Blade-Vortex Interaction,'' ASME J. Fluids Eng., **116**, pp. 5–21.

[6] Abramowitz, M., and Stegun, I. A., 1972, *Handbook of Mathematical Functions*, Dover, New York.

[7] von Müller, W., 1929, ''Systeme von Doppelquellen in der ebenen Strömung, insbesondere die Strömung um zwei Kreiszylinder,'' Z. Angew. Math. Mech., **9**, No. 8, pp. 200–213.

DSMC Analysis of Rarefied Gas Flow Over a Rectangular Cylinder at All Knudsen Numbers

Chin-Hsiang Cheng
Professor
e-mail: <cheng@ttu.edu.tw>

Feng-Liang Liao
Graduate Student

Department of Mechanical Engineering,
Tatung University,
40 Chungshan N. Rd., Sec. 3,
Taipei, Taiwan 10451
R.O.C.

The present study is concerned with the flow behavior of the rarefied gas over a rectangular square cylinder. Attention has been focused on the transition regime between the continuous flow (at low Knudsen number) and the molecular flow (at high Knudsen number). The direct simulation Monte Carlo method (DSMC) is employed for predicting the distributions of density, velocity, and temperature for the external cross-flow. Meanwhile the pressure, skin friction, and net heat transfer coefficients on the surfaces of the cylinder are also evaluated. The length (l) and width (h) of the cross-section of the cylinder are both fixed at 0.06 m. The Mach number (Ma) ranges from 0.85 to 8, and the Knudsen number (Kn) is in the range 0.01≤Kn≤1.0. Results for various parameter combinations are presented. For some special cases, the numerical predictions are compared with existing information, and close agreement has been found. [S0098-2202(00)01404-8]

Introduction

A gas flow may be modeled at either the macroscopic or the microscopic level. The macroscopic model regards the gas as a continuous medium, and the continuity and Navier–Stokes equations provide a conventional mathematical model for analyzing the flow field. On the other hand, the microscopic (or molecular) model recognizes the particulate structure of the gas as a myriad of discrete molecules and provides information for the position, velocity, and state of every molecule at any instant. One of the major mathematical models at this level is constructed by using the Boltzmann equation. In addition, the Monte Carlo method is an alternative method, which has proven to be useful when applied to the microscopic model analysis.

The degree of rarefaction of a gas is generally expressed in terms of the Knudsen number (Kn) which is defined by the ratio of the mean free path of the gas (λ) to the characteristic dimension of the considered problem (l). A higher Knudsen number may result from either a larger mean free path or a smaller characteristic dimension. Larger mean free path is usually a consequence of a lower gas density. The lower-gas-density flows, which are termed ''rarefied gas flows,'' are encountered in the fields ranging from hypersonic fluid dynamics to vacuum technology.

Generally, when the Knudsen number exceeds 0.1, the continuum model is not able to provide accurate results and hence, the molecular model ought to be adopted instead. However, according to the existing information, it seems to be rather difficult to obtain analytical solutions of the Boltzmann equation. Therefore, the direct simulation Monte Carlo method (DSMC) proposed by Bird [1] offers a valuable tool for predicting the flow behavior, instead of seeking solution of the Boltzmann equation. The DSMC method adopts a probabilistic procedure which is based on the assumption that the gas molecules are in a situation of molecular chaos. Hence, the DSMC method is particularly suitable for predicting the dilute-gas flows.

The DSMC method has been applied to the analysis of a number of engineering problems in the past several decades. For example, Bird [1] first calculated the drag forces, heat transfer rates, and flow fields for a hypersonic rarefied gas flow over several kinds of objects, including sphere, circular cylinder, and flat plate. Numerical solutions presented by Dahlen et al. [2], Cuda and Moss [3], and Wetzel and Oertel [4] for flows over blunt bodies, by Jain [5], Dogra et al. [6], and Liu et al. [7] for flow past spheres, by Harvey et al. [8] for hypersonic flows over a flat-ended circular cylinder, by Stefanov and Cercignani [9] and Golshtein and Elperin [10] for convective instabilities of rarefied gases within a horizontal parallel-plate channel, and more recently by Mavriplis et al. [11], Wong et al. [12], and Liou and Fang [13] for flows in microchannels all exhibit the performance of the applications of the DSMC method for rarefied-gas flow analysis. Meanwhile, experimental validation for the DSMC method has been performed by many authors, such as Dahlen, et al. [2], Shufflebotham et al. [14], Dankert et al. [15], and Allegre et al. [16].

The present study is concerned with the flow behavior of the rarefied gas over a rectangular cylinder at all Knudsen numbers. The analysis of the flow over a rectangular cylinder is one of the major concerns to the researchers related to gas dynamics since it is frequently encountered in a number of practical engineering systems. For example, Tai and Muller [17] made a micro beam of 6 microns in width and 150 microns in length by surface micromachining. The rectangular-cylinder structure of the micro beam can be used as a hot-wire probe for flow field research when surface micromachining is combined with bulk micromachining (Jiang et al. [18]). However, although the external rarefied gas flows over an object have been widely considered in the literature, problems associated with the external flow over a rectangular cylinder have been considered by relatively few authors. Therefore, theoretical information regarding the rarefied-gas flow fields about the rectangular cylinder is still insufficient, not to mention the data for the micro hot-wire probe, especially for the transition regime between the continuous and the molecular flows.

Under these circumstances, in this study the DSMC method is employed for predicting the flow behavior within the transition regime. Results for the flows ranging from subsonic to supersonic areas are presented.

Physical model of the present problem is shown in Fig. 1. A rectangular cylinder with a cross section of $l \times h$ is placed horizontally in a uniform incoming air stream. The incoming air velocity and the ambient air temperature are denoted by u_∞ and T_∞, respectively. At the far fields, a free-stream condition is specified. In this study, the length (l) and the width (h) of the cross-section are both fixed at 0.06 m. Two major parameters are considered in the analysis. The Mach number (Ma) ranges from 0.85 to 8. The

---

Contributed by the Fluids Engineering Division for publication in the JOURNAL OF FLUIDS ENGINEERING. Manuscript received by the Fluids Engineering Division August 10, 1999; revised manuscript received July 13, 2000. Associate Technical Editor: P. Bearman.

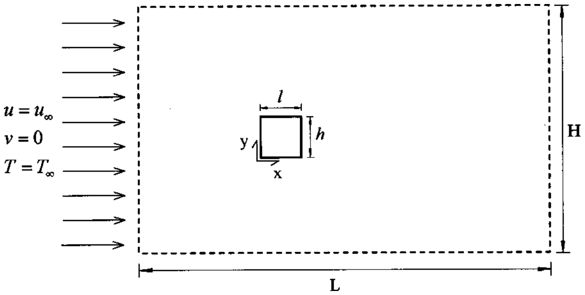

Fig. 1 Rarefield air flow over a rectangular cylinder

second parameter, the Knudsen number (Kn), is in the range $0.01 \leqslant \text{Kn} \leqslant 1.0$. Note that the range of the Mach number covers the subsonic and the supersonic flow regimes, and the transition behavior between a continuous (low Kn) and molecular (high Kn) flow can be observed within $0.01 \leqslant \text{Kn} \leqslant 1.0$.

Numerical Methods

The DSMC method is a numerical simulation technique which modeling a real gas flow by at least thousands of simulated molecules. Each simulated molecule represents a lump behavior of a group of real molecules. The data of velocity and position of the simulated molecules at any instant are traced. These molecules could be in collision with other molecules, or experience boundary interactions in the simulated physical space. The VHS model proposed by Bird [19] incorporates the hard-sphere scattering law for collisions, and treats the cross-section of the molecules as a function of the relative translational energy during the collision. Therefore, it is adopted to determine real diameter of gas molecule (d) and the total collision cross-section (σ_T). An evaluation of various intermolecular collision models has been made by Davis et al. [20]. Further information can be found in this report.

The calculations have been performed for air in which rotational energy exchange has been included. However, in this study the vibration mode is assumed to be negligible. For a nonreacting air flow at a temperature that are not comparable with the characteristic temperature of vibration, the coupling between the vibration mode and the rotational and transitional modes are very weak (Bird [19], Harvey et al. [8]); therefore, the assumption is acceptable.

The determination of the rotational collision number (Z_{rot}) is based on the model developed by Pullin [21] and Davis et al. [20], in which the exchange restriction factor ϕ_{rot}, representing the fraction of energy elastically scattered during each collision, is given by

$$\phi_{\text{rot}} = 0.148 + 1.018 e^{-0.001722(E_{cm}/2k)} \tag{1}$$

where E_{cm} is the center-of-mass energy and k is the Boltzmann's constant. Then, the rotational collision number Z_{rot} is predicted by $Z_{\text{rot}} = C/\phi_{\text{rot}}$, where C is set equal to 1.736, as suggested by Pullin [21].

The sampling routine is extended to cover the rotational energies, and hence the output includes both the translational and the rotational temperatures (T_{tr} and T_{rot}). The translational and the rotational temperatures are equal for the equilibrium gas and the common value may represent the thermodynamic temperature of the gas. However, for the nonequilibrium gas considered in the present study, the gas temperature (T) is represented by an overall temperature which is a weighted mean of T_{tr} and T_{rot} as

$$T = (3T_{tr} + \varsigma T_{\text{rot}})/(3 + s) \tag{2}$$

where ς denotes the number of internal degrees of freedom.

The physical region of interest is divided into a network of spatial cells in the DSMC computation. There can be at least thousands of cells and grid points as well. Each cell is divided into four subcells of equal area. The principle of setting the cell size Δr is that the macroscopic flow properties are not allowed to experience significant variations within a cell. The variations of properties are caused by the intermolecular collisions; therefore, the cell size ought to be in the same order as the mean free path or even smaller. In addition, an essential feature of the DSMC method is that the molecular motion and collisions are actually uncoupled over the period of a specific time step. All the molecules are moved after a time step, and predictions of the new positions of the molecules as well as the resulting boundary interactions are followed by the selection of a set of possible intermolecular collisions that are appropriate during the time step. In general, the time step ought to be sufficiently small in comparison with the mean collision time. The mean collision time (τ_0) is the inverse of the collision rate. That is

$$\tau_0 = 1/\nu_0 = \frac{1}{4 d_{\text{ref}}^2 n (\pi k T_{\text{ref}}/m)^{1/2} (T/T_{\text{ref}})^{1-\omega}} \tag{3}$$

where T_{ref} and d_{ref} are reference temperature and reference diameter of the molecules, respectively, and ν_0 is the intermolecular collision rate. With the help of Eq. (3), one can determine a suitable time step for numerical simulation.

The computation starts with a uniform, equilibrium gas condition which agrees with the free stream conditions in the physical space. It is assumed that the molecules inside each cell are of equal number at the beginning of the simulation procedure. The velocity of a simulated molecule is assumed to be a linear combination of the thermal velocity $\boldsymbol{c}'$ and the free stream velocity $\boldsymbol{c}_0$. That is, $\boldsymbol{c} = \boldsymbol{c}' + \boldsymbol{c}_0$. At the initial state, in the absence of the free-stream velocity, a simulated molecule ought to be moving only with the thermal velocity.

For rarefied gas, the flow is actually subject to a slip-condition at the solid surface. The velocity of a reflected molecule is determined by a model involving the gas-surface interaction. Two widely used models for the gas-surface interaction are the diffuse and the specular reflection models. The diffuse model, which is actually a more commonly used model than the specular model, assumes that the incident and reflected molecules may have different temperatures due to the boundary interaction. An indication of the extent to which the reflected molecules have their temperature adjusted toward the surface temperature is given by a thermal accommodation coefficient (a_c), which is defined as

$$a_c = (q_i - q_r)/(q_i - q_w) \tag{4}$$

where q_i and q_r are the incident and reflected energy fluxes, respectively, and q_w is the reflected energy flux when $T_r = T_w$. In this study, the accommodation coefficient is assigned to be unity.

The pressure coefficient C_p, the skin friction coefficient C_f, and the net heat transfer coefficient C_h can then be defined in terms of the incident and the reflected flow properties. A flux is regarded as positive if it is directed toward the surface. The definitions of these three quantities are:

$$C_p = \frac{P - P_\infty}{\frac{1}{2}\rho_\infty u_\infty^2} = \frac{(P_i + P_r) - nkT_\infty}{\frac{1}{2} n m u_\infty^2} \tag{5a}$$

$$C_f = \frac{\tau}{\frac{1}{2}\rho_\infty u_\infty^2} = \frac{(\tau_i + \tau_r)}{\frac{1}{2} n m u_\infty^2} \tag{5b}$$

$$C_h = \frac{q}{\frac{1}{2}\rho_\infty u_\infty^3} = \frac{(q_i + q_r)}{\frac{1}{2} n m u_\infty^3} \tag{5c}$$

Table 1 Properties of air

m [kg]	μ_{ref} [N-s/m^2]	T_{ref} [K]	d_{ref} [m]	s	ω	c [m/s]
4.81×10^{-26}	1.719×10^{-5}	273	4.19×10^{-10}	2	0.77	347.21

Table 2 Studied cases

Case	n_∞ [l/m^3]	l [m]	h [m]	u_∞ [m/s]	T_∞ [K]	P_∞^* [Pa]	ρ_∞^+ [kg/m^3]	Ma	Kn	Remark
1	2.137×10^{19}	0.06	0.06	2777.655	300	0.0885	1.028×10^{-6}	8	1	supersonic
2	2.137×10^{20}	0.06	0.06	2777.655	300	0.8851	1.028×10^{-5}	8	0.1	supersonic
3	2.137×10^{21}	0.06	0.06	2777.655	300	8.8512	1.028×10^{-4}	8	0.01	supersonic
4	2.137×10^{19}	0.06	0.06	1736.035	300	0.0885	1.028×10^{-6}	5	1	supersonic
5	2.137×10^{20}	0.06	0.06	1736.035	300	0.8851	1.028×10^{-5}	5	0.1	supersonic
6	2.137×10^{21}	0.06	0.06	1736.035	300	8.8512	1.028×10^{-4}	5	0.01	supersonic
7	2.137×10^{19}	0.06	0.06	694.414	300	0.0885	1.028×10^{-6}	2	1	supersonic
8	2.137×10^{20}	0.06	0.06	694.414	300	0.8851	1.028×10^{-5}	2	0.1	supersonic
9	2.137×10^{21}	0.06	0.06	694.414	300	8.8512	1.028×10^{-4}	2	0.01	supersonic
10	2.137×10^{19}	0.06	0.06	295.126	300	0.0885	1.028×10^{-6}	0.85	1	subsonic
11	2.137×10^{20}	0.06	0.06	295.126	300	0.8851	1.028×10^{-5}	0.85	0.1	subsonic
12	2.137×10^{21}	0.06	0.06	295.126	300	8.8512	1.028×10^{-4}	0.85	0.01	subsonic

$^*P_\infty = n_\infty k T_\infty$
$^+\rho_\infty = n_\infty m$

where pressure P is the sum of the normal momentum fluxes of both the incident and the reflected molecules at each time step, shear stress τ is the sum of the tangential momentum fluxes of both the incident and the reflected molecules at each time step, and net heat transfer q is the sum of the translational and rotational energies of both the incident and the reflected molecules. The subscripts "i" and "r" are used to denote the incident and reflected molecular streams, respectively. Note that for a free-molecule flow, the pressure, skin friction, and net heat transfer coefficients on a surface element associated with the incident molecules at incidence α are derived by Bird [19] as

$$C_p=\frac{2kT_\infty}{mu_\infty^2}\left\{\left[\pi^{-1/2}s\sin\alpha+\frac{1}{2}\left(\frac{T_r}{T_\infty}\right)^{1/2}\right]\exp(-s^2\sin^2\alpha)+\left[\left(\frac{1}{2}+s^2\sin^2\alpha\right)+\frac{1}{2}\left(\frac{T_r}{T_\infty}\right)^{1/2}(\pi^{1/2}s\sin\alpha)\right]\times[1+erf(s\sin\alpha)]\right\} \tag{6}$$

$$C_f=\frac{2kT_\infty}{mu_\infty^2}(\pi^{-1/2}s\cos\alpha)\{\exp(-s^2\sin^2\alpha)+(\pi^{1/2}s\sin\alpha)[1+erf(s\sin\alpha)]\} \tag{7}$$

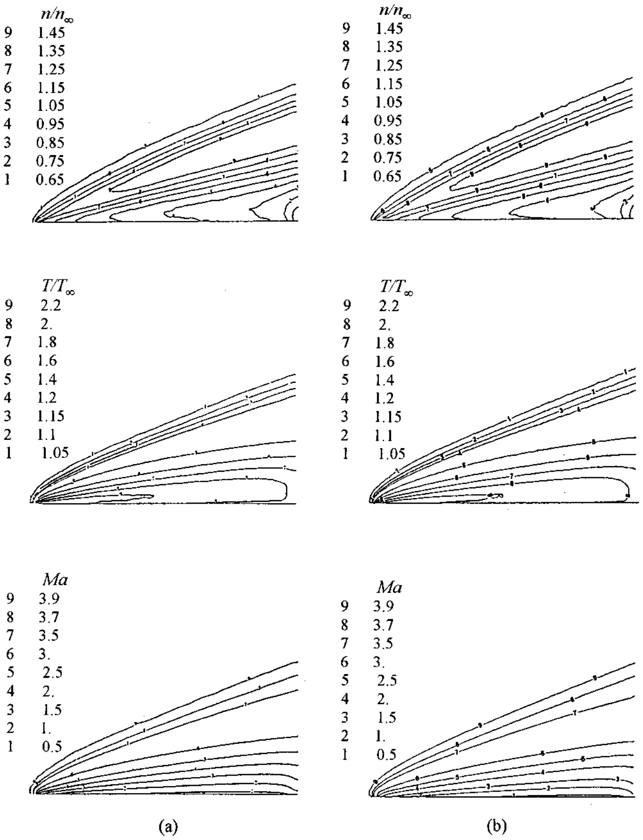

Fig. 2 Contours of number density, temperature, and Mach number for flat-plate flow at Ma=4 and Kn=0.0143, compared with the data of Bird [19]. (*a*) Data provided by Bird [19], (*b*) present predictions

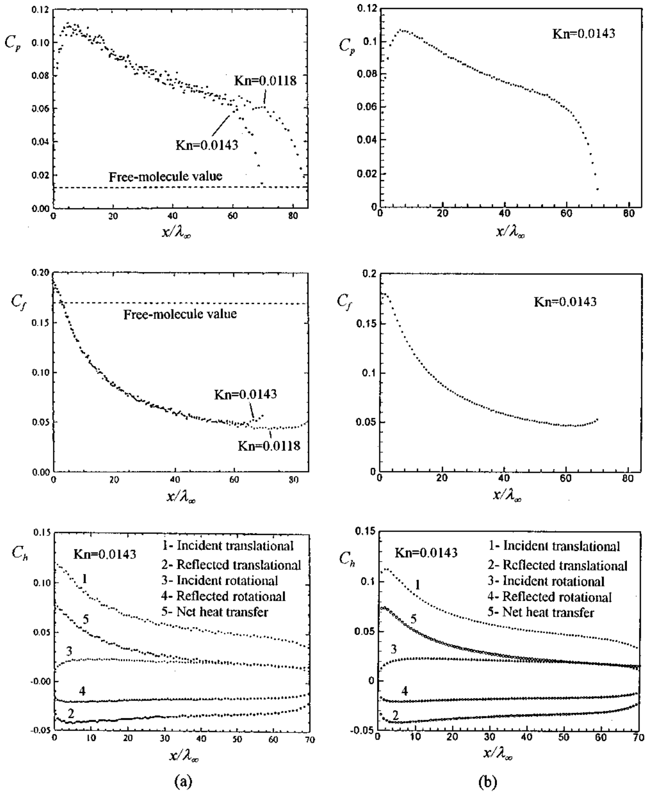

Fig. 3 Distributions of pressure, skin friction, and heat transfer coefficients along a horizontal flat plate at Ma=4 and Kn =0.0143, compared with the data of Bird [19] (*a*) Data provided by Bird [19], (*b*) present predictions

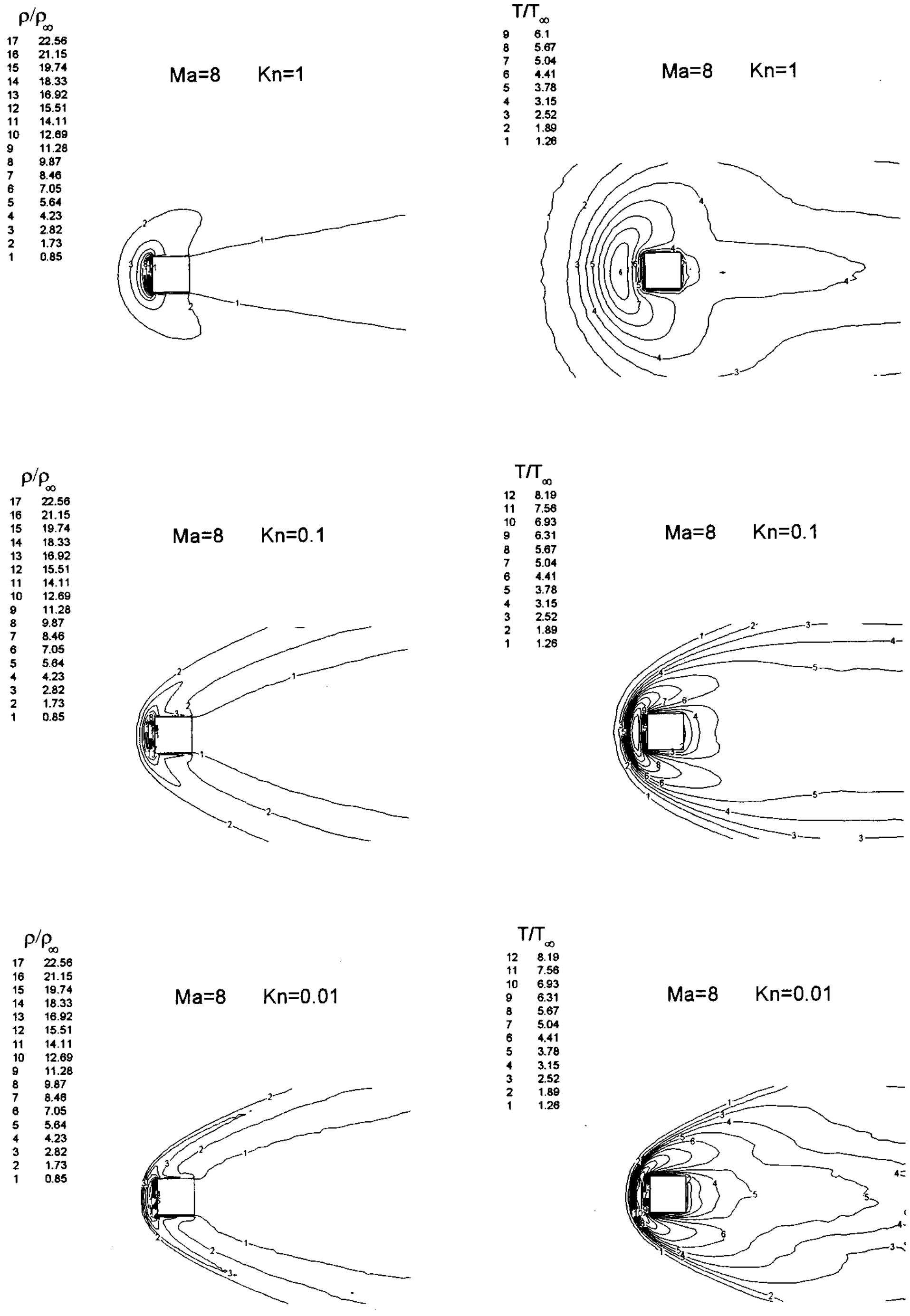

(a) (b)

Fig. 4 Flow over a rectangular cylinder for various Knudsen numbers at Ma=8 (cases 1 to 3). (*a*) Contours of number density, (*b*) contours of temperature (*c*) velocity-vector plot, (*d*) contours of Mach number.

$$C_h=\frac{1}{2\beta^3u_\infty^3}(\pi^{-1/2})\left[\left\{s^2+\frac{\gamma}{\gamma-1}-\frac{1}{2}\left(\frac{\gamma+1}{\gamma-1}\right)\left(\frac{T_r}{T_\infty}\right)\right\}\times\{\exp(-s^2\sin^2\alpha)+\pi^{1/2}s\sin\alpha[1+erf(s\sin\alpha)]\}-\frac{1}{2}\exp(-s^2\sin^2\alpha)\right] \tag{8}$$

Numerical solutions for the case at infinite Knudsen number may be compared with the values from Eqs. (6)–(8).

In the present study, typically a uniform 100×60 grid is adopted. Each individual grid cell contains four subcells inside. Far field boundaries are subject to the freestream condition, with which the incoming molecules are prescribed with undisturbed freestream velocity. And, the outgoing molecules across the

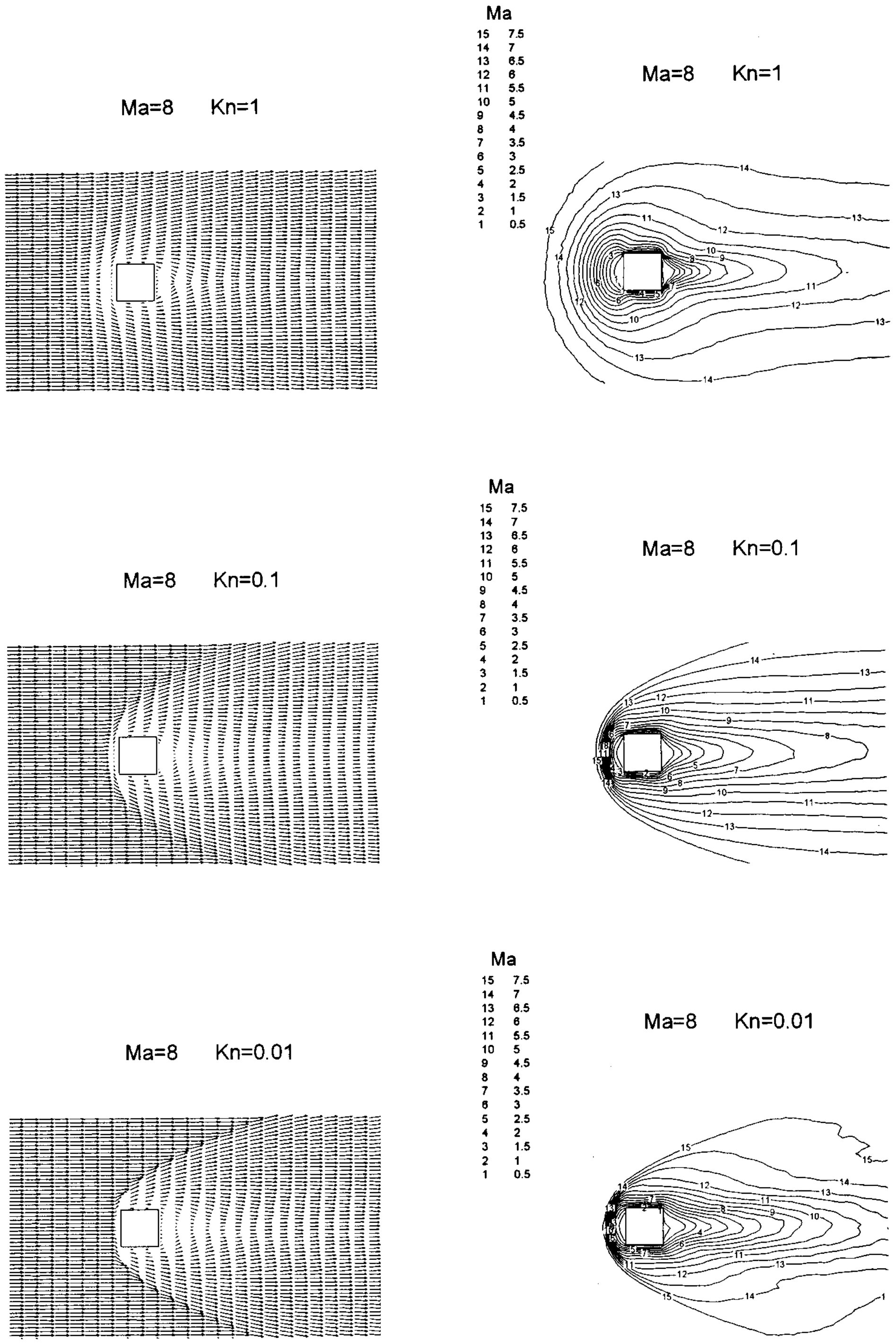

(c) (d)

Fig. 4 (***Continued***).

boundaries are actually discarded. The working fluid considered is air, of which the number density is 2.687×10^{25} m^{-3} at standard air conditions, 1 atm and 0°C. Table 1 gives the properties of air required by the DSMC method. The physical and geometric conditions for all the studied cases are displayed in Table 2. These studied cases range from subsonic to supersonic flows so that the effects of air speed on the rarefied gas flow behavior may be evaluated. Note that the temperature on the cylinder surface is maintained at 300 K for all cases considered.

Results are presented basically in dimensionless form. Figures showing the contours of the Mach number, temperature, and number density are provided. In addition, to illustrate the flow patterns, the velocity-vector plots are also presented. The solutions for temperature and velocity enable the distributions of C_p, C_f, and C_h on the surfaces of the cylinder to be further evaluated. Computation time required to complete a typical case is approximately 80 to 90 hours on a Pentium-200 MHz personal computer.

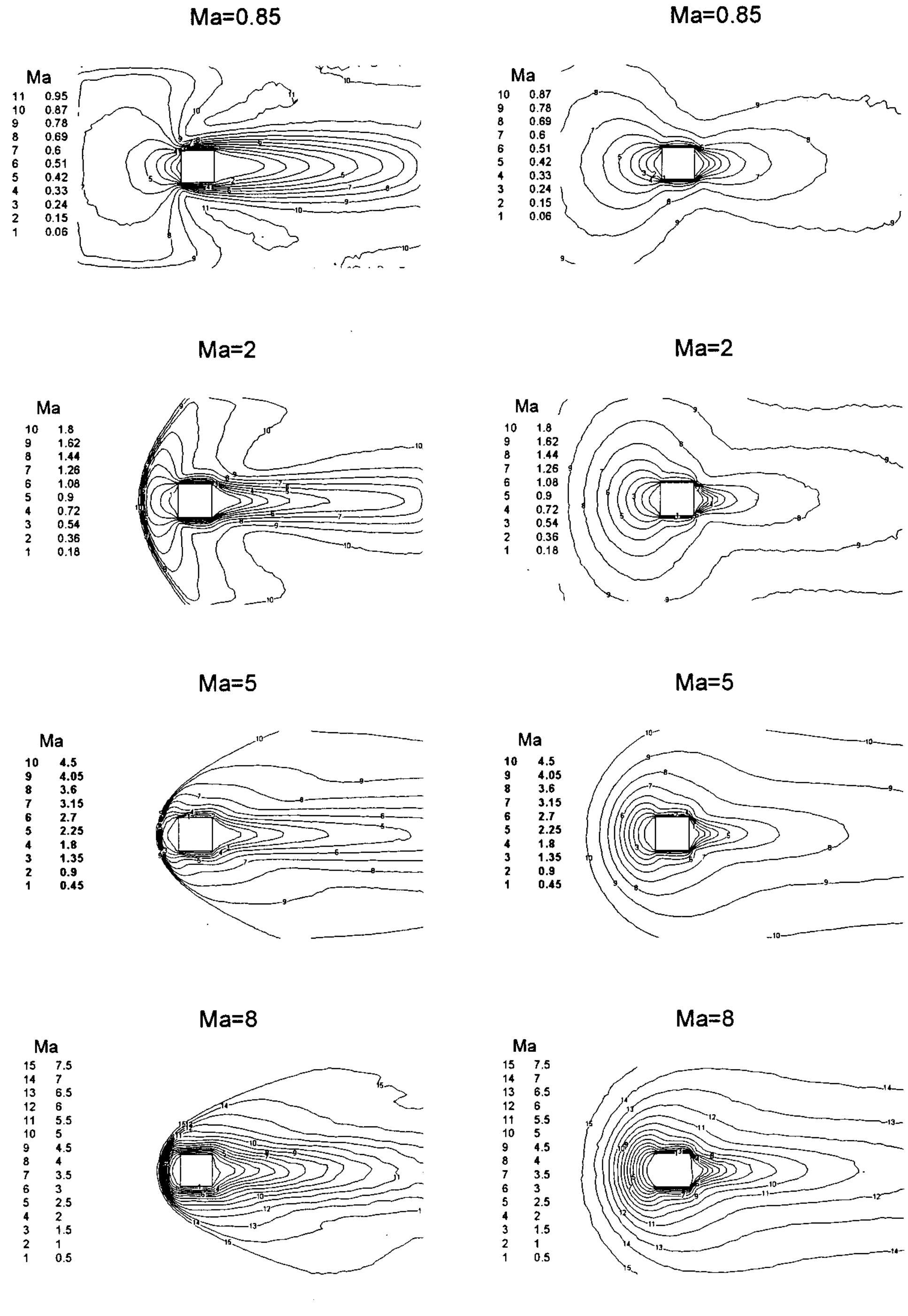

(a) (b)

Fig. 5 Contours of Mach number for various Knudsen numbers (cases 1, 3, 4, 6, 7, 9, 10, and 12). (*a*) Kn=0.01, (*b*) Kn=1

Numerical Checks. In order to check the validity of the simulation program, a comparison between the obtained results and the existing information has been made. For a supersonic external flow over a horizontal flat plate of finite length, the results presented by Bird [19] regarding the flow and temperature fields can be used for verification. Information for the case is given in the following:

Working fluid: nitrogen
Mach number: 4
Knudsen number: 0.0143
Length of flat plate: 0.9 m (approximately 70 times the mean free path)
Temperature of flat plate: $1.67T_\infty$

Comparisons between the two sets of data for the test problem are shown in Figs. 2 and 3. Presented in the left and the right portions of Fig. 2 are the data of Bird [19] and the present study, respectively, and contours of n/n_∞, T/T_∞, and the Mach number are plotted. Figure 3 shows the distributions of pressure, skin friction, and heat transfer coefficients along the horizontal flat plate. Visual inspection shows a good agreement between the two sets of data. Notice that the values of C_p and C_f for the free-molecule flow are also given in Fig. 3(a) for validation.

Results and Discussion

Figure 4 shows the flow over a rectangular cylinder for various Knudsen numbers at Ma=8. Results for cases 1 to 3 are presented in this figure. It is found that a strong normal shock is developed in front of the rectangular cylinder at Kn=0.01. However, the normal shock is gradually smeared when the Knudsen number is increased. Note that the case at Kn=0.01 is close to the continuous flow, and the case at Kn=1 approaches the molecular flow. It is seen that the structure of the shock is not visible at Kn=1. Also note that the air experiences remarkable temperature and density increases in the stagnation zone. The maximum temperature and density reached in the stagnation zone is obviously decreased by an increase in the Knudsen number. The temperature increase is attributed to compression heating in the stagnation zone. This figure shows that when a continuous flow is converting to a molecular one, the smearing of a shock wave is accompanied by a reduction in the compression heating. Meanwhile, according to the velocity-vector plot shown in Fig. 4(c), it is obvious that the velocity field experiences a discontinuous drop across the shock wave. However, the discontinuity of velocity field is not observed at Kn=1.

Contours of Mach number at various Knudsen numbers and free-stream Mach numbers are shown in Fig. 5. The flows at Kn =0.01 and Kn=1 are investigated. The results tend to confirm the expectation that at Kn=0.01, the normal shock takes place in front of the rectangular cylinder as Ma is changed within the range between 2 and 8; however, at Kn=1.0 the shock wave structure is not observed for Mach number varying within the same range. When the Mach number is reduced to 0.85, which is associated with a subsonic flow, a rather different flow behavior is seen. As shown in Fig. 5, the flows with cases 10 and 12 do not display a shock-wave structure at all Knudsen numbers, and the local Mach number is less than unity throughout the domain.

Figure 6 shows the distribution of pressure coefficient C_p along each surface of the rectangular cylinder for cases 4–6. The effects of the Knudsen number at Ma=5 are considered. The solutions are basically symmetric with respect to the central line of y/h =0.5. Due to the stagnation effects in front of the rectangular cylinder, in general the pressure coefficient is greater on the front surface than on other three surfaces. At Kn=1, the pressure coefficient on the front surface is nearly a constant value of 1.97, and the magnitude of pressure coefficient on this surface decreases with the Knudsen number. However, an inverse trend is observed on the bottom and the top surfaces. The pressure coefficient on these two surfaces is basically increased by a decrease in Kn. On the bottom and top surfaces, the distribution of the pressure coefficient for the case at Kn=1 is more uniform than those for Kn =0.1 and 0.01. A local maximum value is observed at approximately $x/l=0.15$ for the curves for Kn=0.1 and 0.01. In general, the curves for all Knudsen numbers display a trend of slow descent on the bottom and the top surfaces. In addition, on the rear surface, it is found that the pressure coefficient becomes negative and is uniformly distributed. To sum up, the distribution of pressure coefficient is more uniform at each surface with a large Knudsen number. That is, when a flow approaches the molecular flow regime, the distribution of C_p will become uniform. This observation exactly agrees with the behavior of the free-molecule flow, in which the pressure coefficient is constant on each surface.

Figure 7 shows the distributions of skin friction coefficient C_f along each surface of rectangular cylinder at different Knudsen numbers for the same cases. On the front surface, the distributions of C_f for all Knudsen numbers are nearly identical. The range of C_f is between −0.3 and 0.3 on the front surface, and zero C_f occurs at the stagnation point ($y/h=0.5$). On the rear surface, the distributions of C_f for all Knudsen numbers are also identical, but the distributions are uniform and close to zero along the surface. The value of C_f appreciably increases with Knudsen number on the top and bottom surfaces. On these surfaces, the value of C_f becomes more uniform at larger Knudsen numbers.

Distributions of net heat transfer coefficient C_h along each surface of rectangular cylinder for different Knudsen numbers are shown in Fig. 8. The net heat transfer coefficient C_h represents the

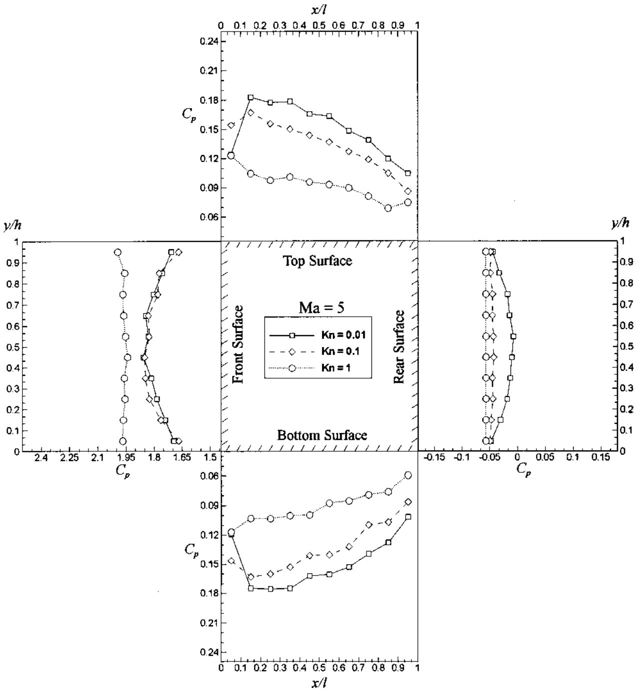

Fig. 6 Distribution of pressure coefficient C_p along each surface of rectangular cylinder for various Knudsen numbers at Ma=5 (cases 4–6)

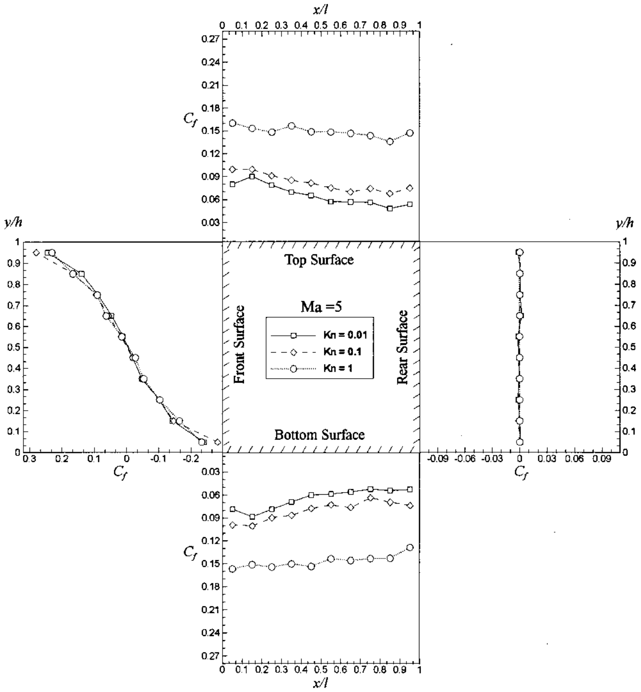

Fig. 7 Distribution of skin friction coefficient C_f along each surface of rectangular cylinder for various Knudsen numbers at Ma=5 (cases 4–6)

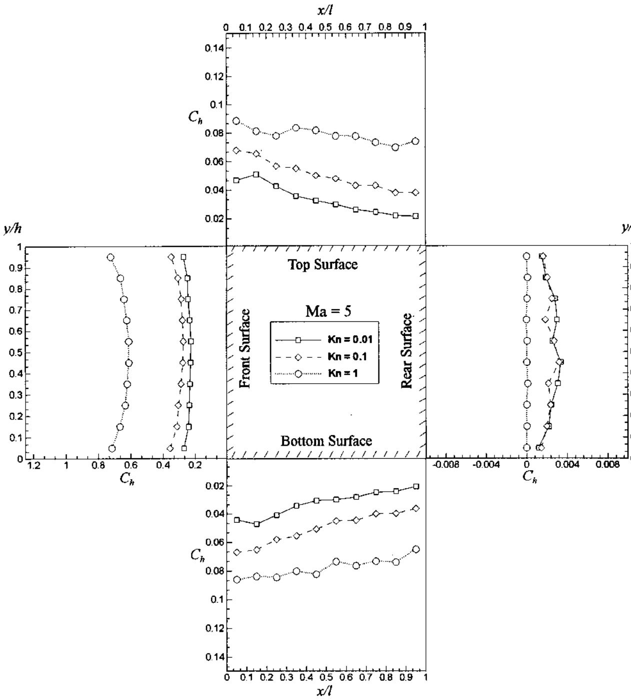

Fig. 8 Distribution of net heat transfer coefficient C_h along each surface of rectangular cylinder for various Knudsen numbers at Ma=5 (cases 4–6)

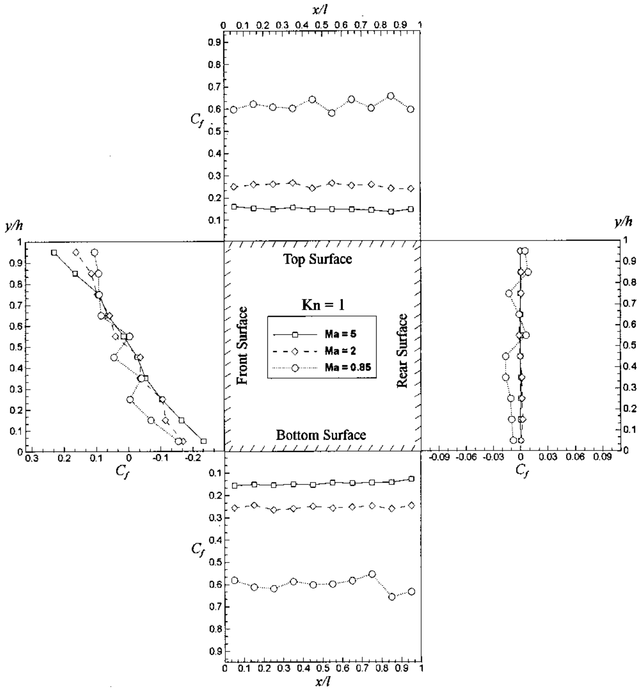

Fig. 10 Distribution of skin friction coefficient C_f along each surface of rectangular cylinder for various Mach numbers at Kn=1 (cases 4, 7, and 10).

ratio of the sum of translational and rotational energies of both incident and reflected molecules to the term $1/2\rho u_{\infty}^{3}$, as defined in Eq. (5). On the front surface, the net heat transfer coefficient C_h increases with the Knudsen number significantly. On the top and the bottom surfaces, the trend of the distributions of net heat transfer coefficient is basically similar to that of the skin friction coefficient shown in Fig. 7. A nonzero but small value of C_h is observed on the rear surface as Kn=0.1 or 0.01; however, at Kn=1, C_h is found to be zero nearly on the rear surface. This again shows the features of the free-molecules regime.

Figures 9, 10, and 11 provide the distributions of C_p, C_f, and C_h for different Mach numbers at Kn=1. In Fig. 9, it is found that

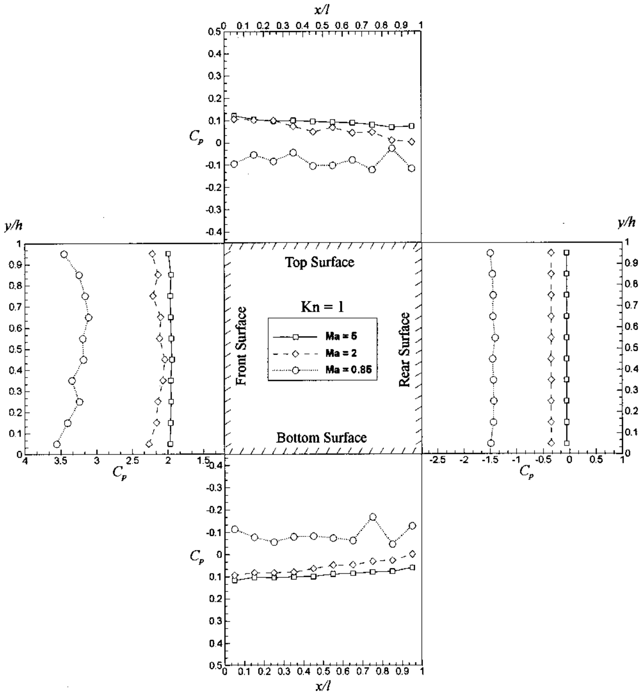

Fig. 9 Distribution of pressure coefficient C_p along each surface of rectangular cylinder for various Mach numbers at Kn=1 (cases 4, 7, and 10)

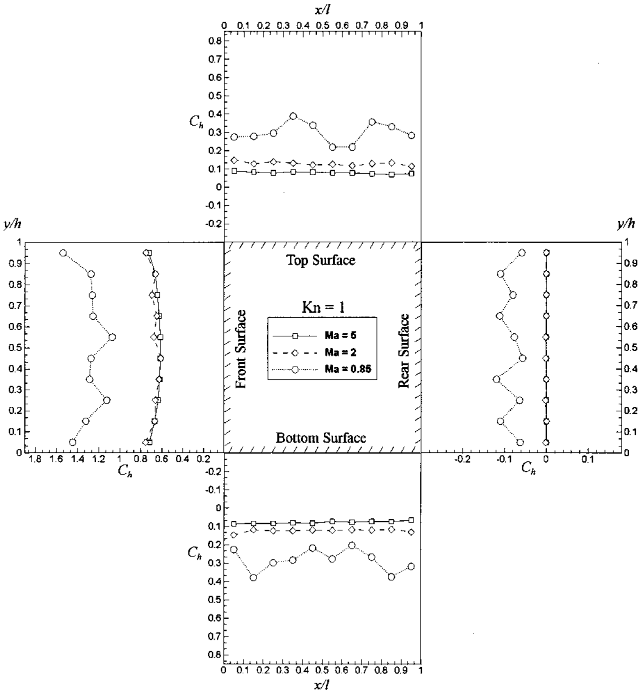

Fig. 11 Distribution of net heat transfer coefficient C_h along each surface of rectangular cylinder for various Mach numbers at Kn=1 (cases 4, 7, and 10)

the magnitude of C_p is decreased by an increase in the Mach number on the front surface, while it tends to increase with the Mach number of the rear one. Note that on the top and the bottom surfaces the value of C_p becomes negative for the subsonic flow at Ma=0.85. Significant difference in C_p between the supersonic (Ma=5 and Ma=2) and the subsonic flows (Ma=0.85) is seen on each surface of the rectangular cylinder.

Distributions of skin friction coefficient C_f along the surfaces are displayed in Fig. 10. On both the front and the rear surfaces, the distribution of C_f is not sensitive to the Mach number. However, on the top and bottom surfaces, the value of C_f significantly increases as the Mach number is decreased, and the distribution of C_f is uniform along the surface for each Mach number.

Figure 11 shows the distributions of net heat transfer coefficient C_h. The distributions of C_h for Ma=5 and Ma=2 are nearly identical, and the values are approximately 0.7 and 0 on the front and the rear surfaces, respectively. However, C_h for Ma=0.85 displays an oscillatory feature, and the average magnitude of C_h for this subsonic flow is larger than those for the supersonic flows (Ma=5 and Ma=2) on all surfaces.

Concluding Remarks

The flow behavior of the rarefied gas over a rectangular cylinder at all Knudsen numbers is investigated. The solution method based on the DSMC method has been developed. Effects of air speed on the flow and thermal fields for wide ranges of parameters are investigated. The Mach number is varied from 0.85–8, and the Knudsen number ranges between 0.01 and 1.0. Cases considered in this study cover the subsonic and the supersonic flow regimes. Numerical predictions for some special cases have been compared with existing information for validation, and good agreement has been found.

For the supersonic flows, a normal shock wave is formed in front of the rectangular cylinder only when the Knudsen number is sufficiently small. The shock wave is gradually smeared by an increase in the Knudsen number. It is noted that for the flow at Kn=1, the shock wave is not observed even though the Mach number is elevated to 8. This implies a great discrepancy in the flow behavior between the continuous and the rarefied gas flows. Furthermore, when a continuous flow converts to molecular flow due to the increase in Knudsen number, the smearing of the shock wave is accompanied by a reduction in the compression heating effects in the stagnation zone. However, the results tend to confirm the previous finding that the strength of the shock wave as well as the compression heating are both significantly increased with the Mach number. But for the subsonic flow at Ma=0.85, it is found that no shock wave exists in the entire solution domain.

Results for the distribution of C_p, C_f, and C_h along the surfaces of the rectangular cylinder for various combinations of the Knudsen and the Mach numbers are provided. It is observed that when a flow approaches the molecular flow regime with a large Knudsen number, the distributions of these coefficients become uniform on each surface. This observation exactly agrees with the behavior of the free-molecule flow.

Acknowledgment

The financial support of this study by National Science Council, Republic of China, under grant NSC 89-2212-E-036-001, is gratefully acknowledged.

Nomenclature

a_c = accommodation coefficient, see Eq. (4)
c = speed of sound
$\boldsymbol{c}$ = molecular velocity vector
$\boldsymbol{c}_0$ = macroscopic velocity vector
C_f = skin friction coefficient, see Eq. (5*b*)
C_h = net heat transfer coefficient, see Eq. (5*c*)
C_p = pressure coefficient, see Eq. (5*a*)
d = molecular diameter
E_{cm} = total center-of-mass energy
h = the height of rectangular cylinder
k = Boltzmann constant, $k=1.380622\times 10^{-23}$ J/K
Kn = Knudsen number, $\mathrm{Kn}=\lambda/l$
l = the length of rectangular cylinder
m = molecular mass
Ma = Mach number, $\mathrm{Ma}=u_\infty/c$
n = number density
P = pressure
q = energy flux
R = gas constant
s = speed ratio, $s=c_0\beta$
t = time
T = overall temperature
u = velocity component in the *x*-direction
v = velocity component in the *y*-direction
Z_{rot} = rotational collision number
α = angle of incidence
β = reciprocal of the most probable molecular speed, $\beta=(2RT)^{-1/2}$
ϕ_{rot} = exchange restriction factor
γ = specific heat ratio, $\gamma=(\varsigma+5)/(\varsigma+3)$
ς = number of internal degrees of freedom
λ = mean free path
μ = kinetic viscosity
ν_0 = collision rate, see Eq. (3)
ρ = density
σ_T = total collision cross-section
τ = viscous stress
τ_0 = mean collision time
ω = empirical coefficient, $\omega=0.77$

Subscripts

i = inward or incident molecule
r = reflected molecule
rot = rotational mode
ref = reference quantity
tr = translational mode
w = surface of rectangular cylinder
∞ = freestream

References

[1] Bird, G. A., 1966, ''Aerodynamic Properties of Some Simple Bodies in the Hypersonic Transition Regime,'' AIAA J., **4**, pp. 55–60.
[2] Dahlen, G. A., Macrossan, M. N., Brundin, C. L., and Harvey, J. K., 1984, ''Blunt Cones in Rarefied Hypersonic Flow: Experiments and Monte-Carlo Simulations,'' *Proceedings of the 14th International Symposium on Rarefied Gas Dynamics*, Vol. 1, pp. 229–240.
[3] Cuda, V., Jr., and Moss, J. N., 1986, ''Direct Simulation of Hypersonic Flows over Blunt Slender Bodies,'' AIAA paper no: 0146-3705.
[4] Wetzel, W., and Oertel, Jr., H., 1990, ''Monte Carlo Simulation of Hypersonic Flows Past Blunt Bodies,'' J. Thermophys. Heat Transfer, **4**, pp. 157–161.
[5] Jain, A. C., 1987, ''Hypersonic Merged-Layer Flow on a Sphere,'' J. Thermophys. Heat Transfer, **1**, pp. 21–27.
[6] Dogra, V. K., Moss, J. N., Wilmoth, R. G., and Price, J. M., 1994, ''Hypersonic Rarefied Flow Past Spheres Including Wake Structure,'' J. Spacecr. Rockets, **31**, pp. 713–718.
[7] Liu, H. C. F., Beskok, A., Gatsonis, N., and Karniadakis, G. E., 1998 ''Flow Past a Micro-Sphere in a Pipe: Effects of Rarefaction,'' ASME DSC-Vol. 66, pp. 445–452.
[8] Harvey, J. K., Celenligil, M. C., and Dominy, R. G., 1992, ''Flat-Ended Circular Cylinder in Hypersonic Rarefied Flow,'' J. Thermophys. Heat Transfer, **6**, pp. 35–43.
[9] Stefanov, S., and Cercignani, C., 1992, ''Monte Carlo Simulation of Benard's Instability in a Rarefied Gas,'' Eur. J. Mech. B/Fluids, **11**, pp. 543–554.
[10] Golshtein, E., and Elperin, T., 1996, ''Convective Instabilities in Rarefied Gases by Direct Simulation Monte Carlo Method,'' J. Thermophys. Heat Transfer, **10**, pp. 250–256.
[11] Mavriplis, C., Ahn, J. C., and Goulard, R., 1997, ''Heat Transfer and Flowfields in Short Microchannels Using Direct Simulation Monte Carlo,'' J. Thermophys. Heat Transfer, **11**, pp. 489–496.
[12] Wong, C. C., Hudson, M. L., Potter, D. L., and Bartel, T. J., 1998, ''Gas Transport by Thermal Transpiration in Micro-Channels—A Numerical Study,'' ASME DSC-Vol. 66, pp. 223–228.

[13] Liou, W. W., and Fang, Y., 1999, ''Heat Transfer in Microchannel Devices using DSMC,'' *Proceedings of the Heat Transfer and Fluid Mechanics Institute*, California State University, pp. 31–45.

[14] Shufflebotham, P. K., Bartel, T. J., and Berney, B., 1995, ''Experimental Validation of a Direct Simulation by Monte Carlo Molecular Gas Flow Model,'' J. Vac. Sci. Technol. B, **13**, pp. 1862–1866.

[15] Dankert, C., Danckert, A., Gundlach, G., and Lehmkoester, K., 1995, Measurement of Rotational Temperature Near Surfaces in Hypersonic Flow,'' *International Congress on Instrumentation in Aerospace Simulation Facilities*, pp. 38.1–38.7.

[16] Allegre, J., Bisch, D., and Lengrand, J. C., 1997, ''Experimental Rarefied Density Flowfields at Hypersonic Conditions Over 70-Degree Blunted Cone,'' J. Spacecr. Rockets, **34**, pp. 714–718.

[17] Tai, Y. C., and Muller, R. S., 1988, ''Polysilicon Bridge as a Flow Meter,'' Sens. Actuators, **15**, pp. 63–75.

[18] Jiang, F., Tai, Y. C., Ho, C. M., Karan, R., and Garstenauer, M., 1994, ''A Theoretical and Experimental Studies of Micromachined Hot-Wire Anemometers,'' Tech. Dig. Int. Electron Devices Meet., San Francisco, CA, pp. 264–267.

[19] Bird, G. A., 1994, *Molecular Gas Dynamics and the Direct Simulations of Gas Flows*, Oxford, London.

[20] Davis, J., Dominy, R. G., Harvey, J. K., and Macrossan, M. N., 1983, ''An Evaluation of Some Collision Models Used for Monte Carlo Calculations of Diatomic Rarefied Hypersonic Flows,'' J. Fluid Mech., **135**, pp. 355–371.

[21] Pullin, D. I., 1979, ''Kinetic Models for Polyatomic Molecules with Phenomenological Energy Exchange,'' Phys. Fluids, **21**, pp. 209–216.

Discharge Coefficients of Critical Venturi Nozzles for CO_2 and SF_6

Shin-ichi Nakao
Senior Research Scientist,
e-mail: nakao@nrlm.go.jp

Masaki Takamoto
Group Leader
e-mail: takamoto@nrlm.go.jp

Flow Measurement Section,
National Research Laboratory of Metrology,
1-4, Umezono-1, Tsukuba, Ibaraki, Japan

The discharge coefficients of critical Venturi nozzles were measured for CO_2 and SF_6 on the Reynolds number range from 3×10^3 to 2×10^5. The results showed that the measured discharge coefficients for both gases were about 2 percent larger than the theoretical estimation based on the assumption of isentropic flow of a perfect gas and this large deviation could not be reduced even by introducing real gas effects. The experimental results also showed that the large deviation for CO_2 could be explained through the assumption of a nonequilibrium flow at the throat. On the other hand, the reason of the deviation observed for SF_6 has not been clear yet, but one possible explanation would be the inadequate estimation of the boundary layer at the throat because the theory is based on the laminar boundary layer of a perfect gas. [S0098-2202(00)02004-6]

1 Introduction

Many kinds of gases are used as process gases in semiconductor industries or as calibration gases for instruments used in environmental measurements and so on. Presently, a thermal type mass flow controller (MFC) is mainly used to control and measure gas flow rates in these fields. However, when a gas flow rate is measured by a MFC, which is not calibrated by that gas, the output of the MFC must be corrected with a questionable correction factor. Thus, the reliability and accuracy of flow measurements is questionable in such cases. Therefore, the development of a highly accurate flow measurement technique independent of the kind of gas is required.

National Research Laboratory of Metrology (NRLM) has developed the flow measurement technique using the critical Venturi nozzles to transfer the standard of small mass flow rates of gases (Nakao and Takamoto [1]) to accreditation laboratories. Ishibashi et al. [2] designed super-fine manufactured critical Venturi nozzles, which have exactly the same shape as the nozzle used in the theoretical analyses of Geropp [3], and found that the measured discharge coefficients of these nozzles were within ±0.03 percent of the theoretical estimation which was developed by Ishibashi and Takamoto [4] based on the analysis of Hall [5] and Geropp [3]. The theoretically determined discharge coefficient is described by two parameters determined under the assumptions that a core flow is isentropic and a perfect gas, which are a function of the specific heat ratio and the nozzle shape. Thus, if a gas is close to the perfect gas state, the discharge coefficient of the critical Venturi nozzle for that gas can be theoretically determined using these two parameters. Nakao et al. [6] measured the discharge coefficients of the critical Venturi nozzle for ten gases including CO_2 and SF_6. And the results showed that the measured discharge coefficients for the gases tested, except CO_2 and SF_6, were within ±0.6 percent of the theoretical estimation developed by Ishibashi [4]. However, the results of CO_2 and SF_6 were 2 percent larger than the theoretical estimation.

This paper describes the results of the discharge coefficients for CO_2 and SF_6 measured for the four critical Venturi nozzles with different throat diameters, and the behaviors of the two parameters describing the discharge coefficient were investigated and the flow fields at the throat were discussed to explain the large deviations found in these gases.

2 Theoretical Estimation of the Discharge Coefficient of a Critical Venturi Nozzle

The discharge coefficient of a critical nozzle, C_d, is defined by

$$C_d = Q_m / Q_{mth} \tag{1}$$

where Q_m is the actual mass flow rate and Q_{mth} is the theoretical mass flow rate calculated from the throat condition and is written as

$$Q_{mth} = A \times \rho^* \times c^*, \tag{2}$$

where A is the throat area, ρ is the density of gas, and c is the sound speed. The theoretical Reynolds number, $\mathrm{Re}_{\mathrm{th}}$, is given by

$$\mathrm{Re}_{\mathrm{th}} = Q_{mth} \times D / (A \times \mu_0) \tag{3}$$

where D is the throat diameter and μ_0 is the viscosity of gas at the stagnation condition. The superscript "*" refers to the throat condition. The throat condition is determined from the stagnation condition using the isentropic relation of a perfect gas. Thus, the throat condition can be calculated from the measurements of the upstream pressure and temperature of a critical nozzle.

When the boundary layer at the throat is laminar, the discharge coefficient can be generally described as follows (ISO 9300 [7]);

$$C_d = a - b / (\mathrm{Re}_{\mathrm{th}})^{0.5}. \tag{4}$$

The two parameters in Eq. (4), "*a*" and "*b*", can be determined theoretically on the assumption of a perfect gas isentropic flow. The details of the theoretical analyses are described in Hall [5] and Geropp [3]. Therefore, only brief explanations of the results are given here.

2.1 Determination of "*a*".

"*a*" reflects the defect of the mass flow rate through the nozzle due to the distortion of a velocity profile at the throat, which is caused by the acceleration flow from the entrance region to the throat. Hall [5] calculated analytically the velocity components near the throat using the expansions in inverse powers of the radius of curvature of the nozzle wall at the throat, R. In his calculations, he assumed axially symmetric irrotational flow and used the isentropic relations of a perfect gas. Finally, "*a*" is written using the first three terms of the series solution as follows

$$a = 1 - (\gamma+1)/K^2 \times [1/96 - (8\gamma+21)/(4608K) + (754\gamma^2 + 1971\gamma + 2007)/(552960K^2) - \ldots] \tag{5}$$

where $K = R \times 2/D$, D is the throat diameter and γ is the specific heat ratio of gas.

Contributed by the Fluids Engineering Division for publication in the JOURNAL OF FLUIDS ENGINEERING. Manuscript received by the Fluids Engineering Division January 10, 2000; revised manuscript received August 17, 2000. Associate Technical Editor: P. Bearman.

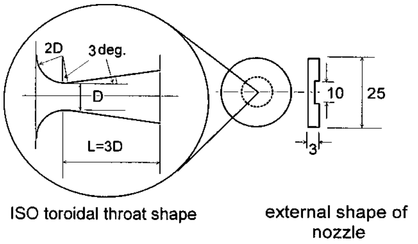

nozzle name	throat diameter (mm)
B1	2.360
B3	1.185
A1	0.594
A3	0.295

Fig. 1 Schematic diagram of the ISO type toroidal throat Venturi nozzle and their throat diameters

2.2 Determination of "*b*". Another parameter influencing the mass flow rate through a nozzle is the displacement thickness of a laminar boundary layer developing at the throat, which reduces the effective area of the throat. Geropp [3] and Tang and Fenn [8] obtained analytically the exact solution of the Prandtl boundary layer equation for axially symmetric flow with an appropriate boundary condition, which gives a nozzle profile. They also used the assumption of isentropic flow and a perfect gas. Finally, "*b*" is written as follows

$$b = 4/m \times [(\gamma+1)/2]^{1/(2(\gamma-1))} \times (3\sqrt{2} - 2\sqrt{3} + (\gamma-1)/\sqrt{3}) \quad (6)$$

where the nozzle shape m is defined by

$$m = [8/(K(\gamma+1))]^{1/4} \times [(\gamma+1)/2]^{(2\gamma-1)/(2(\gamma-1))} \quad (7)$$

As found from Eqs. (5) and (6), the parameters, "*a*" and "*b*," are functions of the specific heat ratio and the nozzle shape. The nozzles used in the present paper have a similar shape and K is equal to 4 because the radius of curvature of the throat is twice D as shown in Fig. 1. Thus, "*a*" and "*b*" become functions of only the specific heat ratio, and consequently, the discharge coefficient of the critical Venturi nozzle can be theoretically determined using Eq. (5) and Eq. (6) with Eq. (7).

3 Experimental Results

The discharge coefficient of the critical Venturi nozzle was determined by the gravimetric calibration facility of NRLM (Nakao and Takamoto [1]). When the test gas was changed, the whole facility was purged with the new test gas for two whole days. As the vapor rate included in the bottled gases used here was less than 0.01 percent, the vapor effect on the gas density was neglected. The critical nozzles used here are an ISO type toroidal throat Venturi nozzle as shown in Fig. 1. The radius of curvature at the throat is twice D, and the diffuser with a half angle of 3 degrees is three times D in length. The throat diameters of the critical Venturi nozzles used here are listed in Fig. 1. The critical nozzles were manufactured at the center of the disk by the machining technique and the throat diameter was measured along four different diameters by the profile projector with the resolution of 1 μm and the averaged value of the four measurements was used as the throat diameter.

The Reynolds number dependency of the discharge coefficient was investigated for each gas by changing the upstream pressure of the critical nozzle from 30 kPa to 300 kPa. The results are shown in Fig. 2, in which the symbol "×" is the result of the gases in Nakao et al. [6], that is, N_2, Ar, He, H_2, O_2, CH_4, C_2H_2, and C_2H_6. It is found from this figure that the discharge coefficients strongly depend on the kind of gas and the smaller the Reynolds number, the stronger the Reynolds number dependency of the discharge coefficient. The transverse axis of this figure is the theoretical Reynolds number defined in Eq. (3). The results in Fig. 2 are plotted in Fig. 3 versus the square root of the inverse of the theoretical Reynolds number. The symbol "×" is also the results of Nakao et al. [6]. Figure 3 shows that the linear relation of Eq. (4) can be applied to all gases tested. The maximum standard deviation of the residual between the experimental results and the fitted curve determined by the least square method from the data in Fig. 3 was 0.05 percent for SF_6. It should be noticed that the results for CO_2 and SF_6 are quite different from other gases.

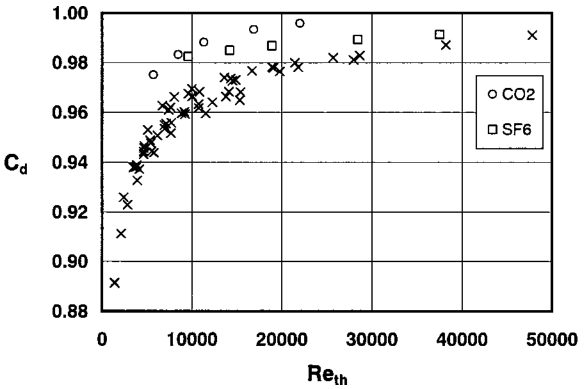

Fig. 2 The variations of the discharge coefficients versus the theoretical Reynolds number (×: from Nakao et al. [6])

The uncertainty of the discharge coefficient consists of the components summarized in Table 1. The standard uncertainty of the calibration facility, by which the discharge coefficient of the critical nozzle is determined, depends on the flow rate and the kind of gas, and the maximum values for N_2, CO_2, and SF_6 on the present flow rate range are listed in Table 1. The repeatability of the measurement, which is determined from the measurements of the upstream pressure and temperature of the nozzles, was 0.043 percent under the present experimental conditions. Another important component is the uncertainty of the throat diameter, which depends on the resolution of the measuring tool. The throat diameter of the critical nozzle was measured by the measuring tool with the resolution of 1 μm. Therefore, the relative standard

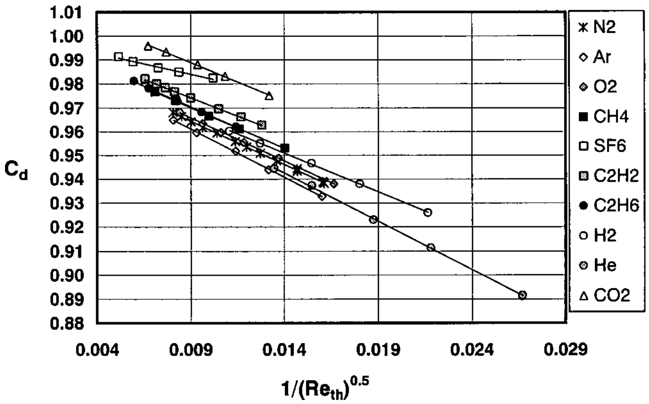

Fig. 3 The linear relation between the discharge coefficient and the inverse of the square root of the theoretical Reynolds number

Table 1 The sources and magnitude of the uncertainties of the A1 sonic nozzle for gases

Components of C_d	Value (%)		
	N_2	SF_6	CO_2
maximum uncertainty of calibration facility (at 50kPa)	0.02	0.004	0.01
repeatability of calibration facility	0.043 (at 50kPa)		
Cross sectional area of the throat ($=D^2 \times \pi/4$)	0.08 (B1 nozzle) – 0.68 (A3 nozzle)		
thermophysical properties	±0.03		
standard deviation of the residuals between the experimental results and Eq.(4)	±0.03	±0.04	±0.02
combined standard uncertainty	0.1 – 0.68	0.1 – 0.68	0.1 – 0.68

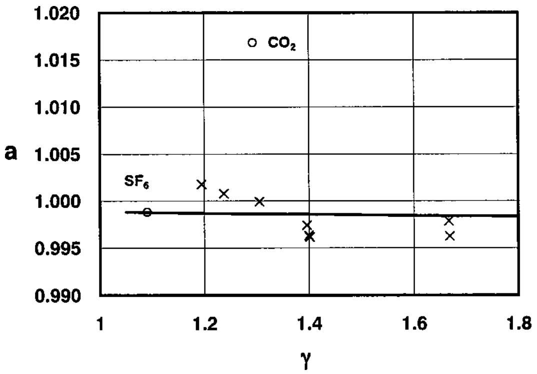

Fig. 4 The variation of "*a*" with specific heat ratio (×: from Nakao et al. [6])

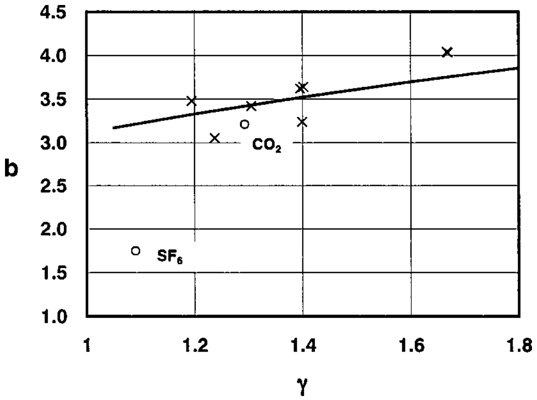

Fig. 5 The variation of "*b*" with specific heat ratio (×: from Nakao et al. [6])

uncertainties of the throat diameters were 0.04 percent for the B1 nozzle, and 0.34 percent for the A3 nozzle. The thermophysical properties like a specific heat ratio were given by polynomial functions of the pressure and the temperature, which were determined from the tables of JSME Data Book [9]. The standard deviations of the curve fit residuals were less than ±0.03 percent in each thermophysical property. Finally, the combined standard uncertainties of the discharge coefficients of the nozzles were 0.1 percent for the largest nozzle and 0.68 percent for the smallest nozzle as shown in Table 1.

The ''*a*'' and ''*b*'' values of Eq. (4) were derived from the fitted curve for each gas in Fig. 3. The theoretical results calculated from Eq. (5) and Eq. (6) are also indicated by the solid lines in these figures. The variations of ''*a*'' versus the specific heat ratio are shown in Fig. 4, which includes the results of Nakao et al. [6] (symbol ''×''). The result for CO_2 deviates from the theoretical value by more than 2 percent, but that of SF_6 is very close to the theoretical estimation. The behavior of ''*b*'' versus the specific heat ratio is shown in Fig. 5. The results show that the displacement thickness of a laminar boundary layer becomes thinner as the specific heat ratio decreases, and the result of SF_6 is rather smaller than the theoretical value, but that of CO_2 is close to the theoretical one. This suggests that the large deviations between the theoretical estimations and the experimental results for CO_2 and SF_6 are caused by different reasons; the wrong estimations of the defect of the mass flow in the core flow in CO_2 and the boundary layer thickness at the throat in SF_6.

4 Discharge Coefficients of CO_2 and SF_6

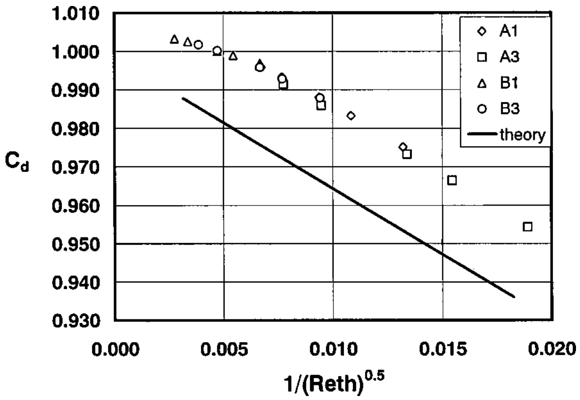

Fig. 6 The discharge coefficients of the four nozzles for CO_2 versus the inverse of the square root of the theoretical Reynolds number

As the theoretical analyses of Hall [5] and Geropp [3] are based on the assumption of isentropic flow of a perfect gas, the discharge coefficients for CO_2 and SF_6 were recalculated introducing real gas effects according to Johnson's method (Johnson [10]). By doing this, the differences were decreased by about 0.5 percent. The results were slightly improved, but this correction did not bring any essential changes to the results. Therefore, the discharge coefficients of the four critical Venturi nozzles with different throat diameters were measured for CO_2 and SF_6 to investigate how the characteristics of their discharge coefficients were changed by the nozzle size.

The discharge coefficients of the four critical Venturi nozzles for CO_2 are shown in Fig. 6. The transverse axis is the square root of the inverse of the theoretical Reynolds number and the solid line indicates the theoretical estimation. All of the experimental results are on the same curve, which is slightly curved in the range of large theoretical Reynolds numbers. Thus, the two parameters of the discharge coefficient, ''*a*'' and ''*b*'' were determined for each nozzle by the least square method. The variations of ''*a*'' in CO_2 versus the throat diameter of a critical nozzle are shown in Fig. 7. The figure indicates that ''*a*'' decreases toward the theoretical value as the throat diameter increases. This means that the mass flow defect in the core flow depends on the throat diameter (i.e., the size of the flow field).

When a flow property such as pressure or temperature is changed, a gas redistributes its internal energy to a new flow condition exchanging the energy between translational, rotational, and vibrational modes through the collisions between molecules. In a nozzle flow, the gas temperature of the core flow quickly decreases toward the throat so that the gas is about to redistribute the internal energy to a new flow condition. However, when the flow passage is short and narrow like the present nozzle, the time that the flow passes through the passage is shorter than the relaxation time of the energy mode, and thus the gas will be unable to

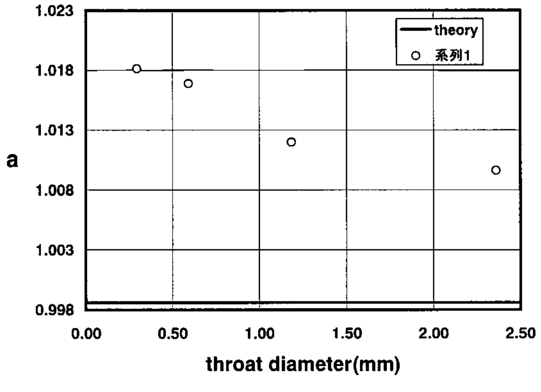

Fig. 7 The variation of "*a*" versus the throat diameter for CO_2

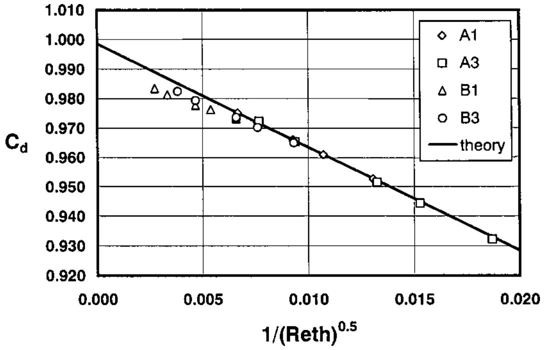

Fig. 8 The comparison of the measured discharge coefficients and the theoretical discharge coefficients with $\gamma=1.38$ under a nonequilibrium flow condition for CO_2

have enough collision number to relax that energy mode (Levine and Bernstein [11]). As a result, that energy mode is considered to be unable completely to recover to the equilibrium condition. Generally, the relaxation time for vibrational mode is quite longer than that for translational and rotational modes, and that of CO_2 is about 10^{-5} s at the present experimental condition (Simpson et al. [12]). And as the time that the flow passes through the present nozzles is from 10^{-5} s to 10^{-6} s, it is the same order as the relaxation time for vibrational mode of CO_2.

Another important parameter to determine the flow condition, equilibrium or nonequilibrium, is the characteristic temperature of vibrational mode, θ_v. The vibrational temperature which determines the vibrational motion is a function of the characteristics temperature of vibrational mode. In a nozzle flow, the gas temperature decrease largely toward the throat, but the vibrational temperature changes slightly in the case of the gases with the high characteristics temperature, for example in N_2 ($\theta_v=3340$ K) (Leipmann and Roshko [13]). On the other hand, in the gases with the low characteristics temperature, for example in CO_2 ($\theta_v=954$ K: this is the lowest value.) (Leipmann and Roshko [13]), the vibrational temperature has a large increase. In this case, if the relaxation time for vibrational mode is longer compared with the time that the gas passes through a nozzle, the vibrational temperature will be unable to recover to the value of the equilibrium condition, that is, the flow will be in nonequilibrium. A gas under nonequilibrium condition must have a specific heat ratio between an equilibrium flow and a frozen flow. In nonequilibrium flow, the specific heat ratio is related to the internal freedom, and it becomes larger in a nonequilibrium flow, in which the internal freedom reduces.

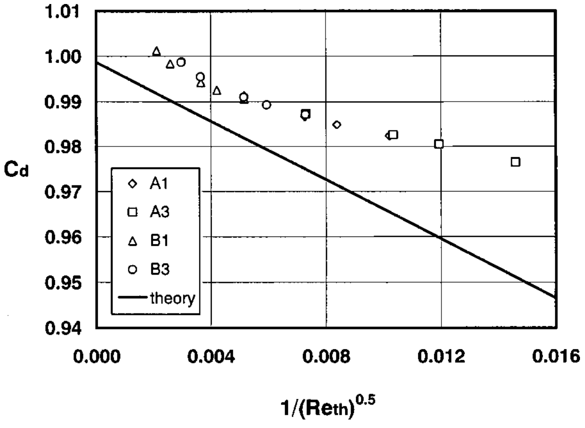

Fig. 9 The discharge coefficients of the four nozzles for SF_6 versus the inverse of the square root of the theoretical Reynolds number

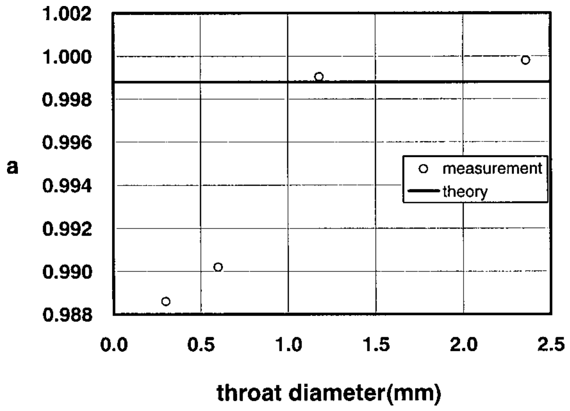

Fig. 10 The variation of "*a*" versus the throat diameter for SF_6

The discharge coefficients for CO_2 were recalculated from both the actual mass flow rates experimentally determined and the new theoretical mass flow rates calculated with the specific heat ratio of $\gamma=1.38$, the value between an equilibrium flow and a frozen flow. Next, the discharge coefficients for CO_2 were theoretically determined from Eq. (5) and Eq. (6) with $\gamma=1.38$, that is, the discharge coefficients for a fictitious perfect gas which has the same viscosity and the same molecular weight as CO_2, but the specific heat ratio of 1.38. The specific heat ratio is actually not the same for the four nozzles because the level of nonequilibrium is different in the different nozzles. However, the same value was used for the four nozzles in the above calculations because there is no way to determine the specific heat ratio of a nonequilibrium flow. Both results shown in Fig. 8 are in very good agreement. This suggests that the large deviation between the theoretical estimation based on Eq. (5) and Eq. (6) and the experimental results for CO_2 is explained by assuming that the flow at the throat is nonequilibrium. This estimation that the flow is nonequilibrium at the throat is supported by the reasons that CO_2 has the low characteristic temperature for vibrational mode and the time that the gas passes through the nozzle is the same order as the relaxation time of vibrational mode.

The results of the discharge coefficients of the four critical Venturi nozzles for SF_6 are shown in Fig. 9. All experimental results make the line gradually curved over the whole range and here the solid line indicates the theoretical estimation. The deviation between the theoretical and the experimental results is larger than 2 percent in the lower Reynolds number range. As in CO_2, the two parameters of the discharge coefficient for each nozzle were determined from the data of Fig. 9. The results of "*a*" are shown in Fig. 10. In this figure, "*a*" seems to increase with increasing a throat diameter, but the change of "*a*" is very small, the order of the measurement uncertainty. Therefore, it is likely that "*a*" is independent of the throat diameter and the mass flow defect in the core flow for SF_6 must be estimated accurately by the theoretical analyses. From the results that the standard deviations of the residual between the fitted curve and the experimental results were around 0.1 percent in the four nozzles, it is suggested that the linear relation of Eq. (4) based on a laminar boundary layer cannot be applied to SF_6, that is, Eq. (6) cannot be used to estimate the boundary layer thickness at the throat for SF_6.

5 Discussion and Conclusion

The measured discharge coefficients for CO_2 and SF_6 were about 2 percent larger than the theoretical estimation based on the assumption of isentropic perfect gas, although those of any other gas tested were within 0.6 percent of the results theoretically estimated. The large deviations for CO_2 and SF_6 could not be explained even by introducing real gas effects.

Therefore, the discharge coefficients of the four critical nozzles with different throat diameters were measured for CO_2 and SF_6 to investigate how the discharge coefficients are changed. The results for CO_2 showed that the narrower the flow field, the larger the discharge coefficient deviates from the theoretical value. This suggests that the flow is nonequilibrium at the throat because the gas cannot completely redistribute the internal energy to a new flow condition due to a short and narrow flow field. The discharge coefficients theoretically recalculated with the specific heat ratio between an equilibrium flow and a frozen flow were in good agreement with the experimental results. Yokogawa and Nishioka [14] carried out the numerical simulations of nonequilibrium nozzle flow for CO_2 on the basis of N-S equation using TVD scheme and showed that the results were within 0.5 percent of the experimental results for the four critical Venturi nozzles. And Johnson et al. [15] confirmed numerically the influence of nonequilibrium flow on the discharge coefficients for CO_2 and they also investigated the nonequilibrium effects in vibrational mode on the discharge coefficient by the experiments using mixtures of CO_2 and water vapor.

On the other hand, the large deviation between the theoretical estimation and the experimental results found in SF_6 may be explained by the wrong estimation of the boundary layer thickness at the throat, not by the mass flow defect in the core flow. Back [16] reported in his paper that the laminar boundary layer becomes much thinner when the boundary layer develops on the strongly cooling wall in an acceleration flow. Meanwhile, a nozzle flow is accelerated from the entrance to the throat and the temperature drop in the boundary layer at the throat is considered to be fairly large as the gas temperature decreases largely toward the throat. However, as such a temperature drop in the boundary layer is realized for other gases, it would be difficult to explain the results of SF_6 from the analogy the Back's study. Further study about the boundary layer of SF_6, maybe from the viewpoint of the heat transfer, will be required. And also the possibility of nonequilibrium flow like in CO_2 may have to be discussed when considering the fact that the characteristics temperatures of some vibrational modes are comparable with that of CO_2.

References

[1] Nakao, S., and Takamoto, M., 1999, ''Development of the Calibration Facility for Small Mass Flow rates of Gases and the Sonic Venturi Nozzle Transfer Standard,'' JSME, Series B, **42**, pp. 667–673.

[2] Ishibashi, M., Takamoto, M., and Nakao, Y., 1994, ''Precise Calibration of Critical Nozzles of Various Shapes at the Reynolds Number of $0.8-2.5 \times 10^5$,'' FLOMEKO'94, Glasgow, Session 6.

[3] Geropp, D., 1971, ''Laminare Grenzschichten in ebenen und rotationssymmetrischen Lavalduesen,'' Deutsche Luft und Raumfahrt Forschungsbericht (in Germany).

[4] Ishibashi, M. and Takamoto, M., 1997, ''Very Accurate Analytical Calculation of the Discharge Coefficients of Critical Venturi Nozzles with Laminar Boundary Layer,'' Proceedings of FLUCOME, Japan.

[5] Hall, I. M., 1962, ''Transonic Flow in Two Dimensional and Axially Symmetric Nozzles,'' Q. J. Mech. Appl. Math., **15**, pp. 487–508.

[6] Nakao, S., Hirayama, T., Yokoi, Y., and Takamoto, M., 1997, ''Effects of Thermalphysical Properties of Gases on the Discharge Coefficients of the Sonic Venturi Nozzle,'' *Proc. 1997 ASME FED Summer Meeting*, Vancouver, Canada.

[7] International Standard ISO 9300, 1990, ''Measurement of gas flow by means of critical flow Venturi nozzles,'' p. 8.

[8] Tang, S. P., and Fenn, J. B., 1978, ''Experimental Determination of the Discharge Coefficients for Critical Flow Through as Axisymmetric Nozzle,'' AIAA J., **16**, pp. 41–46.

[9] JSME Data Book, 1986, *Thermophysical Properties*, edited by Japan Society of Mechanical Engineers (in Japanese).

[10] Johnson, R. C., 1964, ''Calculations of Real-Gas Effects in Flow Through Critical-Flow Nozzles,'' ASME J. Basic Eng., Series D, **86**, Sept., pp. 519–526.

[11] Levine, R. D., and Bernstein, R. B., 1974, *Molecular Reaction Dynamics*, Oxford University Press (1997: translated in Japanese).

[12] Simpson, C. J. S. M., Bridgman, K. B., and Chandler, T. R. D., 1968, ''Shock-Tube Study of Vibrational Relaxation in Carbon Dioxide,'' J. Chem. Phys., **49**, pp. 513–522.

[13] Liepmann, H. W., and Roshko, A, 1960, *Elements of Gasdynamics*, Wiley, New York (1983: translated in Japanese).

[14] Yokogawa, A., and Nishioka, M., 1999, ''Numerical Studies on the Sonic Nozzle for Mass Flow Calibration,'' Ms. thesis, Univ. of Osaka-prefecture (in Japanese).

[15] Johnson, A., Wright, J., Nakao, S., Merkle, C. L., and Moldover, M. R., 1999, ''The Effect of Vibrational Relaxation on the Discharge Coefficient of Critical Flow Ventur,'' Flow Meas. Instrum., **11**, pp. 315–327.

[16] Back, L. H., 1970, ''Acceleration and Cooling Effects in Laminar Boundary layers-Subsonic, Transonic, and Supersonic Speeds,'' AIAA J., **8**, pp. 794–802.

Numerical Simulation on the Flow Structure Around the Injection Nozzles for Pneumatic Dimensional Control Systems

S. C. M. Yu
Senior Lecturer

H. J. Poh
Graduate Student

C. P. Tso
Associate Professor

Thermal and Fluids Engineering Division,
School of Mechanical and Production Engineering,
Nanyang Technological University,
Singapore 639798

A numerical simulation on the airflow exiting from a nozzle in a pneumatic dimensional control system has been conducted using computational fluid dynamics code FLUENT (V. 4.3), which solves finite-difference equations. The important changes occurring in the velocity and pressure fields in the vicinity of the nozzle, as the air exiting from the nozzle and impinging on a flat plate, are the prime objectives of the present studies. Simulation studies were first focus on examining the flow characteristics of the system with the conventional nozzle geometry design. Some comparisons with the experimental results previously obtained by Crnojevic et al. (Crnojevic, C., Roy, G., Bettahar, A., and Florent, P., ''The Influence or the Regulator Diameter and Injection Nozzle Geometry on the Flow Structure in Pneumatic Dimensional Control Systems,'' ASME J. Fluids Eng., **119**, *pp. 609–615) were also made. Further simulation studies were conducted with particular attention to a more efficient nozzle geometry. It was found that a divergent type of nozzle design could effectively eliminate the flow separation regions within the nozzle head. By allowing the divergent angle of the nozzle head (α) to vary (from zero to about 25 degrees), a more extensive and sensitive measurement range can be achieved at a given pressure regulator diameter to nozzle diameter ratio.* [S0098-2202(00)02404-4]

Introduction

Many industrial metrology applications employ pneumatic dimensional control for various calibration and manufacturing processes. The principle behind the method is in fact relatively simple. As shown in Fig. 1, air under a constant supplied pressure (P_{al} = constant) flows through two orifices, A and B, arranged coaxially and in series and separated by a large chamber. The pressure rise in the chamber between the two orifices is a function of their area ratio (Wattebot [1]). If the areas of the two orifices are fixed, and the exit of nozzle B is situated at a small distance (δ) from a nearby flat plate positioned perpendicularly to the nozzle axis, the chamber pressure is also a function of δ. Through detailed calibration, the magnitude of chamber pressure can be used to measure or control δ. Depending on the supply pressure, it is possible to have any one of the following four flow regimes: subsonic at both A and B, subsonic at A and sonic at B, sonic at A and subsonic at B, or sonic at both A and B.

If the absolute pressure inside the chamber is P_1 and the size of the chamber is much larger than the size of the exiting nozzle, the flow condition at the exit of the nozzle relative to the chamber can be approximated as

$$P_1 \cong P_2 + \frac{1}{2}\rho U_2^2 \tag{1}$$

where $U_2 \gg U_1$. As the flow exiting from the nozzle enters the gap laterally, Eq. (1) can be written as

$$P_1 \cong P_2 + \frac{1}{2}\rho U_2^2 = P_3 + \frac{1}{2}\rho U_3^2 \tag{2}$$

Consider the mass continuity between stations 2 and 3, i.e.,

$$\begin{aligned} m &= \rho U_2 A_2 = \rho U_3 A_3 \\ &= \rho U_2 \pi r_s^2 = \rho U_3 2\pi r_3 \delta \end{aligned} \tag{3}$$

Substitute Eq. (3) into Eq. (2), after simplifying, the following expression can be obtained.

$$\begin{aligned} P_1 &= P_3 + \frac{1}{2}\rho\left[\frac{U_2 r_2}{2\delta}\right]^2 \\ &= P_3 + \rho\frac{U_2^2 r_2^2}{8\delta^2} \end{aligned} \tag{4}$$

Since P_3 equals to the atmospheric condition, the gauge pressure at the chamber becomes

$$P_{1g} \alpha \rho \frac{U^2}{\delta^2} \tag{5}$$

From the above expression, the chamber gauge pressure varies inversely with the square of the gap height. At sonic condition, compressibility effect would also have an important influence to the above correlation. Experimentally (Crnojevic et al. [2]), it was found that a region of linear relationship existed between P_{1g} and δ, when the gap height approaches zero. This range of linearity is rather narrow. For a typical dimensional control system, i.e., $D/d = 0.5$ and 2 bar $< P_{al} <$ 3 bar, the linearity range is within 60 μm $< \delta <$ 200 μm. It is obvious that the effective range of the system is to be increased at value lower than 60 μm and higher than 200 μm.

In typical pneumatic dimensional control applications (i.e., 50 μm $< \delta <$ 400 μm), as the air flows through the gap between nozzle head and flat plate, flow separation occurs in several regions in the vicinity of the nozzle head. This was marked by the annular deposit of oil and dirt on the flat plate surface as well as at regions near the lips of the nozzle. It was also found that some restrictions to the air flow through the gap (δ) appears over a period of time as a result of the deposits built-up. This may eventually lead to the wrong interpretation on the displacement δ at a given chamber

---

Contributed by the Fluids Engineering Division for publication in the JOURNAL OF FLUIDS ENGINEERING. Manuscript received by the Fluids Engineering Division October 8, 1998; revised manuscript received August 3, 2000. Associate Technical Editor: D. Telionis.

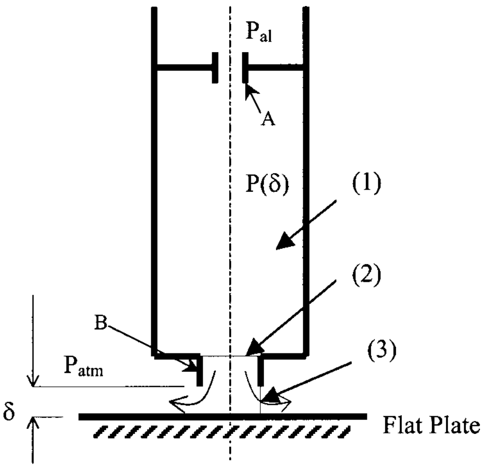

Fig. 1 Schematic of the pneumatic dimensional control system

pressure. Thus, the principal objective of the present study is to numerically visualize the flow field in the vicinity of the injection nozzle which reveals the distributions of velocities, pressure, and any possible flow separation regions.

Due largely to the experimental difficulties associated with the small size of the nozzle head, previous experimental investigations onto this topic are rare (Roy et al. [3] and Crnojevic et al. [2]). Only some comparisons between the simulation results with the pressure measurements on the flat plate of Crnojevic et al. [2] can be made here. After establishing the detailed flow characteristics of the system with the existing nozzle design. Further simulation studies will then focus on obtaining the most optimum nozzle design which would be able to avoid some of the adverse effects encountered in the existing design.

Physical System and Computational Analysis

The system considered here is similar to that of Crnojevic et al. [2]. As shown in Fig. 2, air flows from compressed air source towards a chamber with internal diameter of 8 mm. The chamber inlet has a regulator of diameter (D) 0.2 mm, 1 mm, or 2 mm while the nozzle exit has an internal diameter (d) of 2 mm and external diameter (D_s) of 4 mm. There is a converging shape before the end of nozzle exit, so that any unwanted recirculations at the corresponding region can be eliminated.

The air is assumed to obey ideal gas law, $\rho=(P+P_0)/RT$ where P_{atm} is the atmospheric pressure. The dynamic viscosity (μ) of air is 1.72×10^{-5} kg/m.s.

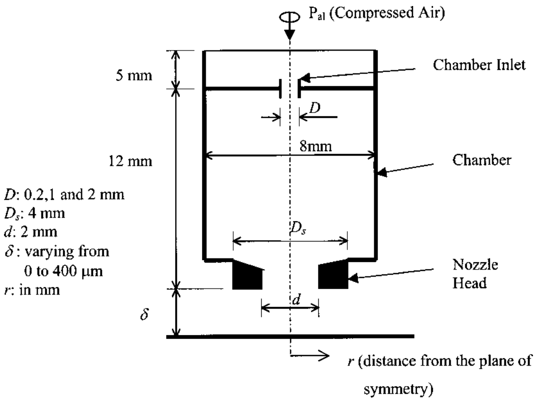

Fig. 2 Geometry of the pneumatic dimensional control system and the coordinate system adopted in the present simulation

Assumptions for the physical model used are:

- axis-symmetric flow (about the center axis at $r=0$),
- compressible and steady flow,
- turbulence is described by a two equation k-ε model,
- the wall is considered as adiabatic,
- upstream of the flow is assumed to have constant total gauge pressure of 2–3 bar and
- downstream of the flow (exit of nozzle head, lateral surface parallel to external diameter nozzle head, D_S) is at atmospheric pressure.

FLUENT (V4.3) is a two-part program consisting of a preprocessor preBFC, and a main module. The preBFC was used to define geometry and a structured grid for our model. Subsequently, the grid information was transferred from preBFC to FLUENT via a grid file (FLUENT User Manual [4]). FLUENT solves the governing partial differential equations for the conservation of mass, momentum, energy and chemical species in a general form which can be written in Cartesian tensor notation as

$$\frac{\partial}{\partial t}(\rho\phi)+\frac{\partial}{\partial x_i}(\rho u_i\phi)=\frac{\partial}{\partial x_i}\left[\Gamma_\phi\frac{\partial\phi}{\partial x_i}\right]+S_\phi \tag{6}$$

where ϕ is the conserved quantity and terms are the convection (LHS), diffusion, and source terms. The equations are reduced to their finite difference analogs by integration over the computational cells into which the domain is divided. A second-order upwind scheme is used for interpolation between grid points and to calculate derivatives of the flow variables. The numerical solutions for velocities (u,v), enthalpy (h) and pressure (P) were solved using a semi-implicit iterative scheme.

The truncation errors could be assessed by grid independence tests and comparison with experimental data. Four options of grid density have been assessed: 41(r) by 81(z), 61(r) by 151(z), 81(r) by 193(z), and 101(r) by 251(z). No significant difference is discovered for the results between the grid density of 81(r) by 193(z) and 101(r) by 251(z). Therefore, the grid independent or grid convergent results had been established. In view of the cost effective of computation run, the grid density of 81(r) by 193(z) is used for the analysis of the computational model.

The numerical solutions are validated by comparisons with experimental results obtained by Crnojevic et al. [2]. This is the only

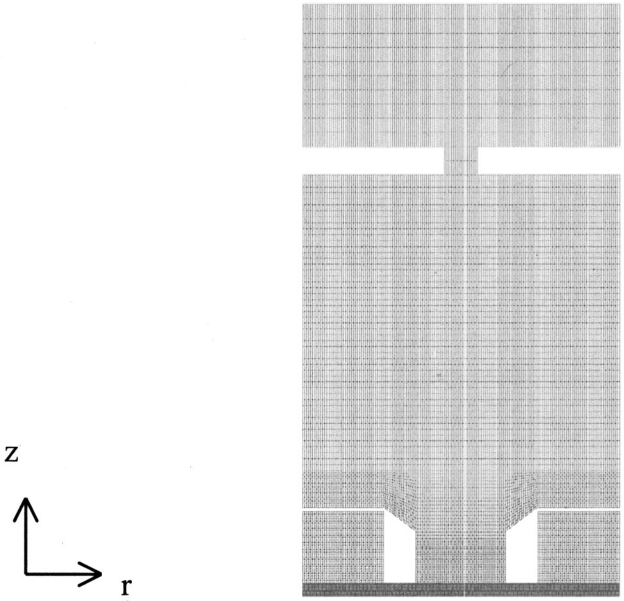

Fig. 3 Grid generated for the pneumatic dimensional control system (81(r) by 193(z))

set of measurements available for comparison in literature. Good agreement between simulated results and measurements are obtained and are shown in Figs. 5 and 6 (they will be elaborated further later). As a result of the above tests, the truncation errors arise from the discretization of the governing equations are expected to be very small.

Figure 3 shows the grid distribution (81×193) that was being applied in the numerical simulation. Grid density is higher at the region between the nozzle head and flat plate, as that is the region of interest. Constant pressure and enthalpy were applied at both inlet and outlet boundary conditions. Zero velocity with no slip conditions at solid wall boundary were used. For turbulent flow, the standard wall function was applied at the solid wall boundary.

The Reynolds numbers of the flow investigated, based on the nozzle exit diameter and the volume flow rate ($\mathrm{Re}=4V/\pi\nu d$) at the nozzle exit plane was within the range of $1400<\mathrm{Re}<3000$. The range of the gap height investigated was of $10\ \mu\mathrm{m}<\delta<400\ \mu\mathrm{m}$. The range of the orifice diameter ratio was $1<D/d<0.1$. All the computations were run on a IBM PC with Pentium processor platform and the converged solutions were obtained until the residual level reached 10^{-4} after 3000 iterations.

Results and Discussion

(a) General Features of the Flow With the Conventional Nozzle Design

(i) Pressure Distribution on the Flat Plate. Initial studies were performed by the simulation under different flow conditions and turbulence models. Figure 4 shows the comparison of pressure distribution obtained by simulation and experiments (Crnojevic et al. [2]) along the flat plate at $\delta=400\ \mu\mathrm{m}$ and $P_{al}=3$ bar. If laminar incompressible flow model was being used in the simulation, no pressure drop at the stagnation point (at $r=0$, relative to the supply pressure, P_{al}) could be found as the gap distance δ increased from 100 to 400 μm. On the other hand, using incompressible flow assumption together with turbulence k-ε model, the expected trend of the pressure drop at the stagnation point as δ increased could be captured correctly. However, the best agreement with measurements was obtained when the compressible flow assumption together with turbulence k-ε model was applied. It appears that the incompressible flow assumption had overestimated the magnitude of the flow acceleration before entering the gap and this in turn gave rise to higher-pressure loss (from $r=0.5$ mm to 1 mm) at the corresponding region.

Using the compressible turbulence flow equations as the basis, simulations were further carried out by varying the distance δ from 5 μm to 400 μm and the P_{al} from 1–3 bar. More comparisons of wall static pressure distribution on the flat plate can then be made between the simulated results and the experimental results of Crnojevic et al. [2]. As the wall pressure distribution in the experiments was determined by a 0.2 mm diameter tap (connecting to a pressure transducer) drilled on a movable flat plate, the estimated positional accuracy should be within the range of ±0.1 mm.

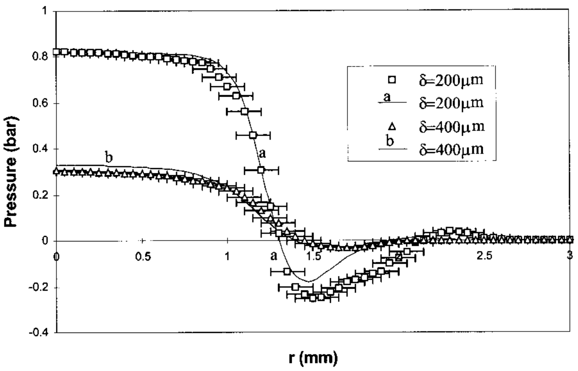

Fig. 5 Comparison between experiment and simulation on the wall static pressure distribution at $P_{al}=2$ bar

Figures 5 and 6 show good agreement between experiments and simulation for the supply pressure of 2 and 3 bars, respectively. For each pressure distribution curve, an almost uniform region appears from the center ($r=0$) to the entrance of the gap ($r=1$ mm). This is followed by a rapid decrease in static pressure from the entrance to about the middle section of the gap ($r=1.5$ mm). The rapid decrease in pressure indicates a corresponding acceleration of the velocities. The pressure recovers quickly back to atmospheric conditions as the flow reaches the end of the gap. Thus, a low pressure region ($<P_{\mathrm{atm}}$) is found to exist at around $1.2\ \mathrm{mm}<r<2.2\ \mathrm{mm}$ for both values of δ. This low pressure region, however, would disappear when δ is less than 150 μm (Fig. 7).

(ii) Flow Separation Regions. Within the range of gap dimensions ($10\ \mu\mathrm{m}<\delta<400\ \mu\mathrm{m}$) and supplied pressure investigated ($1\ \mathrm{bar}<P_{al}<3\ \mathrm{bar}$), three flow separation regions were generally found in the vicinity of the nozzle, as shown in the schematic sketch of Fig. 8. The first region (S1) appeared at the gap ceiling, as may have been expected from the pressure distribution in Figs. 5 and 6. As the air exiting from the injection nozzle hit the flat plate and changes its direction laterally, the flow would accelerate through the gap due to a reduction in the cross-sectional area. The area ($A_3=d\pi\delta$) at the entrance (e-e′) of the gap is very much smaller than the nozzle exit area ($A_2=\pi d^2/4$, where $d=2$ mm). As the change in the flow direction was rather rapid near the entrance of the gap, the flow was not able to follow the contour of the gap closely and hence gave rise to the flow separation at the gap ceiling (S1).

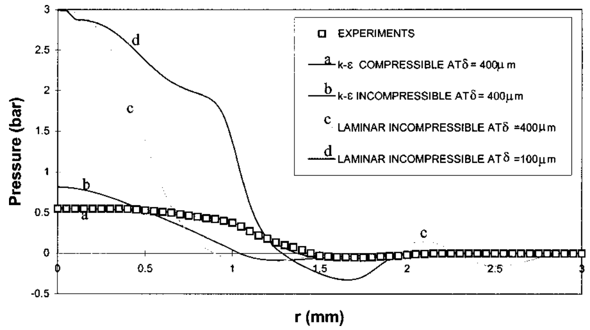

Fig. 4 Comparison between experiment and simulation using different flow models

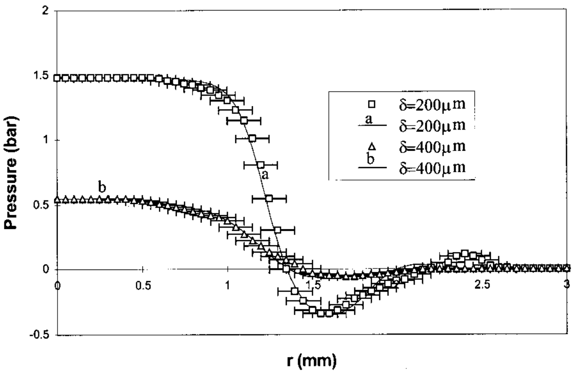

Fig. 6 Comparison between experiment and simulation on the wall static pressure distribution at $P_{al}=3$ bar

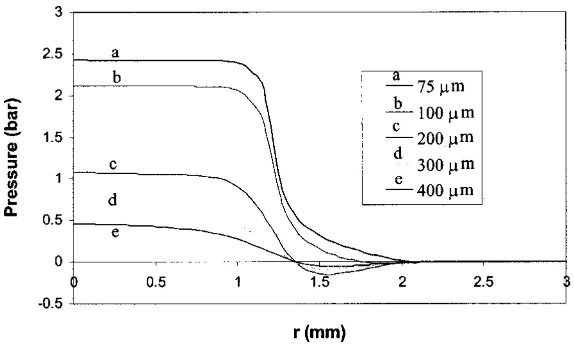

Fig. 7 Pressure distribution on the flat plate at $P_{al}=3$ bar and at different δ

The magnitude of the velocities along the centerline of the gap, as shown in Fig. 9, shows further that the flow accelerated even before entering the gap. A maximum increase of more than six times for the velocities appeared within the range of 1.25 mm $<r<1.35$ mm, depending on the gap height. The location where this maximum velocity appeared is known as critical section and is denoted by the radial coordinate r^* (e.g., $r^*=1.25$ mm for $\delta=400$ μm) and the corresponding effective gap height is denoted as δ^*. After the critical section, as the distance r continues to increase, the velocity would decrease correspondingly. Due to the presence of the flow separation region (S1), the flow did not occupy the entire area between the top and bottom surfaces of the gap. Hence, in order to maintain mass continuity through the gap, flow acceleration must appear underneath the separation bubble. The velocity variation along the $\delta/2$ plane in Fig. 9 clearly shows that the flow through the gap resembled closely to the convergent-divergent compressible nozzle flow characteristic when $\delta>100$ μm. The flow accelerates until the critical (minimum cross-sectional area at r^*) section. The air velocity at the critical section achieves a maximum value corresponding to the local speed of sound. From Fig. 9 and for the case of $\delta<100$ μm, the flow was found to accelerate even after reaching the critical section and it thus exhibited supersonic flow characteristic, until it encountered atmospheric pressure at section s-s′.

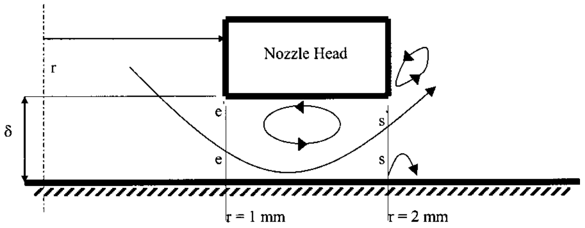

Fig. 8 Schematic of the streamlines between nozzle frontal area and flat plate

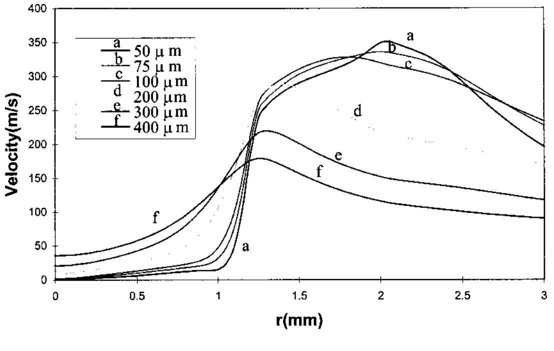

Fig. 9 Velocity along the $\delta/2$ plane

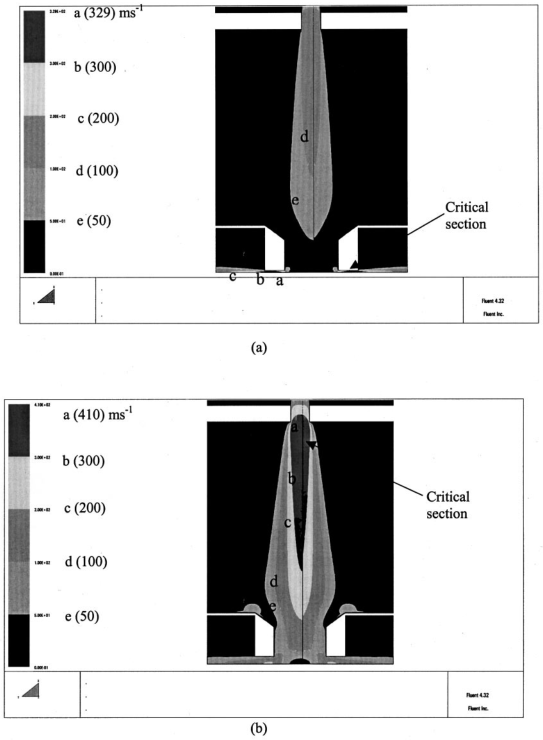

Fig. 10 Critical section for (*a*) $\delta=100$ μm and (*b*) 400 μm

Within the range of δ investigated here, no shock wave was found. It should also be noted that the locations of the maximum velocity within the gap shifted towards the exit of the gap as δ approached zero. As the distance (δ) increases further (>220 μm), the maximum velocity region moves upstream into the chamber because its cross-sectional area becomes the same as the minimal area section i.e., $A^*=D^2\pi/4<r^*\pi\delta^*$. Figure 10 shows clearly the critical section r^* was inside the gap when $\delta=100$ μm, and it shifts upstream to the inlet chamber when δ increased to 400 μm. Under this situation, the flow is subsonic after orifice A (c.f. Fig. 1). Hence, δ would no longer vary linearly with the chamber pressure (c.f. Eq. (1) when the variation of the density became negligible). Thus, the results shown in Fig. 10 confirm the speculations of Crnojevic et al. [2].

At the exit section of the gap at around $r=2$ mm, a sudden expansion in cross-sectional area was encountered where atmospheric pressure conditions exist. Since the airflow cannot follow closely to the sudden sharp change of the nozzle contour, a separation bubble was formed on the flat plate (S2) (c.f. Fig. 8). The circulation bubble on the flat plate (S2) is relatively small and would quickly disappear when δ is greater than 400 μm.

(iii) Measurement Range and Sensitivity. The volume flow rate through the gap was obtained and compared with experimental results. The measurement accuracy for volume flow rate was estimated to be ±5 percent, as shown by the error bar in Fig. 11. There are good agreements between the simulation and the experimental results. Two distinct regions can be observed from the graph. From 0 to about 220 μm, the volume flow-rate increases almost linearly with the distance δ. Sonic flow occurs in region between the nozzle and flat plate. Beyond $\delta=220$ μm, the flows would be choked (c.f. Fig. 9), sonic flow occurs in the chamber inlet and the flow-rate could not increase any further, even by increasing the gap height δ. This is outside the pneumatic control

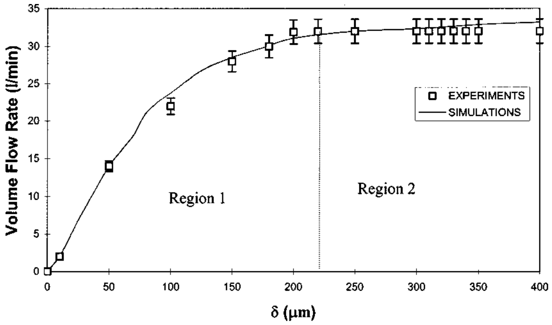

Fig. 11 Comparison between experiment and simulation for the volume flow rate as a function of δ for $D/d=0.5$ and $P_{al}=3$ bar

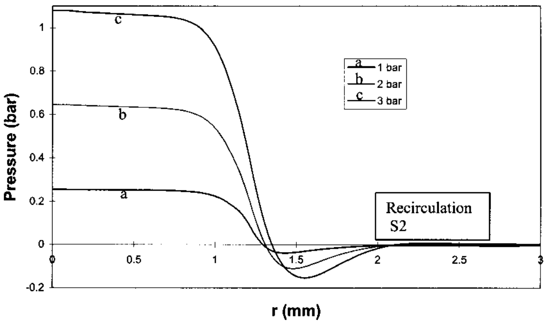

Fig. 14 Wall pressure distribution on the flat plate at different supply pressure for $\delta=200$ μm and $D/d=0.5$

range. However, by increasing the D/d ratio, it is possible to increase the effective range of the system. For example, compare the cases for $D/d=1.0$ and 0.1 in Fig. 12.

The simulation results on the variation in stagnation point pressure on the flat plate as a function of the distance δ for different D/d ratio is shown in Fig. 13. There are three distinct regions for $D/d=0.5$. Zone 1 (60 μm$<\delta<$220 μm) corresponds to the linear pressure drop region, with a pressure gradient of 0.01091 bar/μm. This value is an important parameter to define the pneumatic sensitivity ($s=\partial p/\partial\delta$) of the setup. As for zone (220 μm$<\delta<$330 μm), the pressure curve is also relatively linear (0.00385 bar/μm) but is not as sensitive as zone 1.

It is interesting to note that there was a pressure discontinuity exists outside the pneumatic dimensional control range at zone 3 ($\delta\approx$330 μm). It is in the form of sharp increase, occurring over very short distance (0$<\delta<$5 μm). The existence of this ''jump'' was first noted by Markow [5] and subsequently, Crnojevic et al. [2]. The present numerical studies prove further that the ''jump'' is caused by an oblique shock wave created at the exit section near the flat plate. This flow phenomenon, however, did not affect the operating range of the pneumatic system.

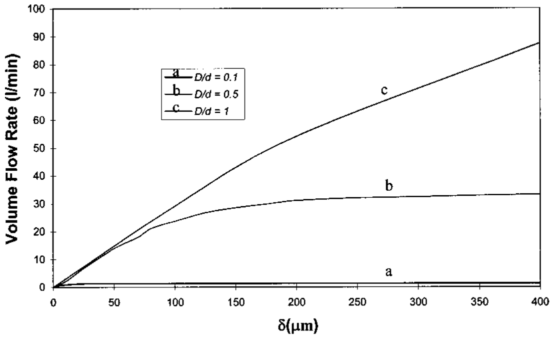

Fig. 12 Volume-flow rate as a function of δ for different ratio of D/d with $P_{al}=3$ bar

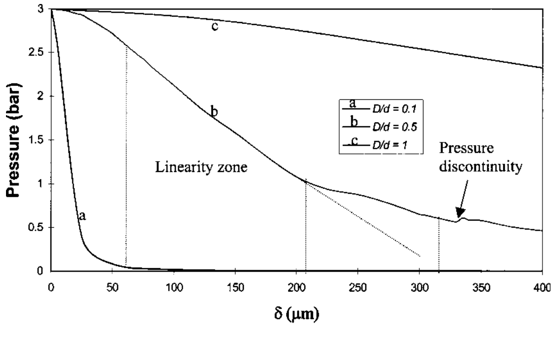

Fig. 13 Stagnation pressure as a function of δ for different ratio of D/d with $P_{al}=3$ bar

As pointed out in the preceding paragraph, it is possible to increase the effective range of the system by increasing the D/d ratio. However, as shown clearly in Fig. 13, the sensitivity would be reduced significantly if the ratio D/d became too high. For example, for the case of $D/d=1.0$, the operating range can be increased but the sensitivity was reduced by about almost 100 percent when comparing to case of $D/d=0.5$. It appears that a compromise between the two factors is required for a particular range of application.

(b) Flow Features for the New Nozzle Design. It is very likely that the existence of the circulation bubbles (S1 and S2) can cause the accumulation of oil and dirt. If they are being unattended over a period of time, they will eventually affect the accuracy of the gap measurements. Therefore, they should be avoided in a good nozzle design for dimensional control applications. Furthermore, the pressure drop from the supply pressure to the stagnation point should also be maximized (as δ increased) so as to increase the sensitivity of the system (c.f. Fig. 13). Based on the preceding analysis on the conventional nozzle design, the three important factors affecting the efficiency of the control system are

(i) the supply pressure
(ii) the injection nozzle geometry, and
(iii) D/d ratio

Wall pressure distribution shown in Fig. 14 are for the cases of $\delta=200$ μm with $P_{al}=1$, 2 and 3 bar, respectively. It can be seen from the figure that there is a small region of negative pressure from $r=2$ to 2.5 mm. This corresponds to the small recirculation region of S2 in Fig. 8 (Although it will disappear when $\delta>400$ μm, it is outside the range of the pneumatic control system.) The recovery of the pressure from negative to atmospheric condition provided an adverse pressure gradient against the flow close to the wall causing it to separate (at region S2). In addition, at a fixed value of δ, the variation of the supply pressure had little effects on this region of negative pressure.

Injection nozzle geometry, by contrast, may have greater influence on the flow development and wall pressure distribution. As shown in the preceding sections, the separated flow regions around the vicinity of the nozzle head were essentially caused by sudden change of the flow direction as the air exiting from the nozzle. The situation may be rectified through the modification on the nozzle head geometry, for example, a bevelled nozzle. Based on this proposition, several different types of nozzle head had been designed and analyzed numerically in order to match the requirements for the above mentioned good nozzle design. The shapes and names of the nozzle heads are tabulated in Fig. 15. They can basically be divided into two categories, i.e., the con-

NOZZLE HEAD	DESCRIPTION
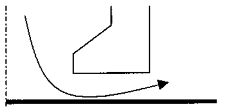	(a) Name: NS Standard nozzle
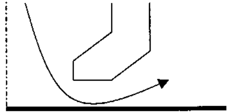	(b) Name: N1 Bevelled edge nozzle (45^0) with small frontal area
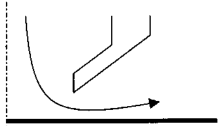	(c) Name N2 Bevelled edge nozzle (45^0) without any frontal area
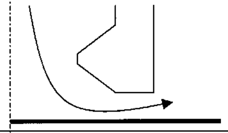	(d) Name: INV N1 Divergent shaped outlet (45^0) with small frontal area
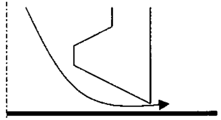	(e) Name: INV N2 Divergent shaped outlet (45^0) without any frontal area
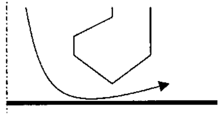	(f) Name: TIP Divergent shaped outlet and bevelled edge nozzle (45^0) without any frontal area

Fig. 15 Schematic of different nozzle designs

vergent nozzle type (b and c) and the divergent nozzle type (d, e, and f). The conventional nozzle design is denoted as the NS type in Fig. 15.

(i) Pressure and Velocity Distribution in the Vicinity of the Nozzle Heads. Comparing the first three (i.e., convergent type) nozzle head designs (at $P_{al}=3$ bar and $\delta=200$ μm), i.e., NS, N1 and N2, N2 nozzle head is able to eliminate the low-pressure region on the flat plate, see Fig. 16. As the design changes from a converging shape (i.e., N1 and N2) to a diverging shape (INV N1, INV N2, and TIP) of nozzle inlet in Fig. 17, the pressure distribution along the flat plate for INV N2 is always greater than the atmospheric pressure. By examining carefully the best nozzle design from both groups, i.e., the N2 and INV N2, respectively, in Fig. 18, certain important observation can be summarized below. First, both types of nozzle design can minimize the low pressure region. Second, it was noted that the vectors in the vicinity of the gap for the N2 case (Fig. 19) were not parallel to the wall and appeared to be the effects of the large divergent angle. For the vectors distribution in case INV N2, the converging shape of the nozzle accelerated the flow such that it exited from the nozzle in a direction almost parallel to the wall. Although the recirculation at the vertical lip of the nozzle head cannot be eliminated completely, the built-up of the oil and dirt deposit at the corresponding region should not have any significant effects to the effective operation of the system.

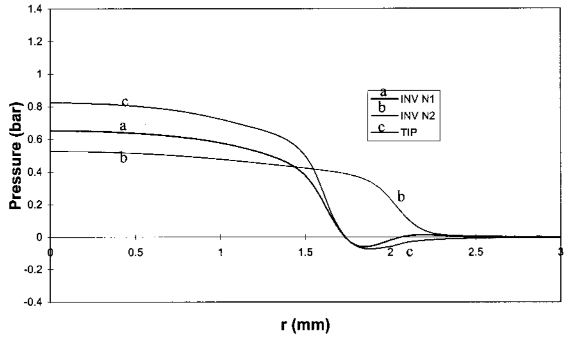

Fig. 17 Wall pressure distribution for divergent type of nozzle inlet at δ=200 μm, $D/d=0.5$ and $P_{al}=3$ bar

It should be noted that the pressure drop at the stagnation point on the flat plate for the divergent type (INV N2) is far greater than that of the convergent type (N2). As it will be shown later, the former will be more effective in enhancing the sensitivity of the system.

(ii) Measurement Range and Sensitivity. The angle of divergence (α) in Fig. 20 is a key factor to the effective application of the divergent shaped nozzle (INV N1, INVN2, and TIP). The sensitivity curves for the cases of NS and N2 are shown in Fig. 21. The N2 nozzle basically has the same sensitivity range as the conventional design.

On the other hand, for the INV N2 nozzle, more sensitive response can be found by varying α, as shown in Fig. 22. However, the linearity range is relatively shorter than that of the conventional design. The NS (α=0) has a linear range from 60 μm to about 200 μm. When α increased to 5 deg, the sensitivity (gradient of the curve) will be improved by 50 percent, but the linearity range would be reduced and shifted to the lower end (from 10 μm to 110 μm). For α=22.5 and 45 deg, better sensitivity can be obtained, but the linearity zone will be reduced further from 10 μm to 80 μm. Based on the results obtain from Fig. 22, it may be advisable to have nozzle head design of variable divergent angle so that a wider range of measurements with acceptable sensitivity can be obtained.

Figure 23 shows the sensitivity curve at different D/d ratio. As already shown in Fig. 14 that at $D/d=1.0$ and $P_{al}=3$ bar, the

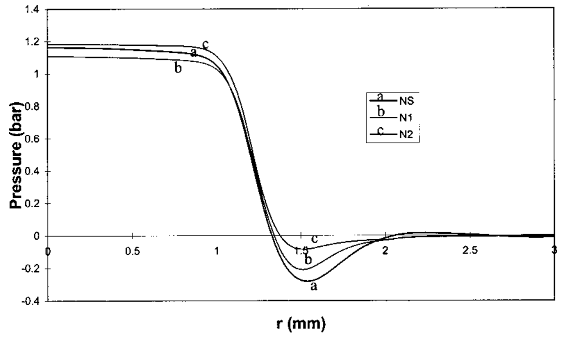

Fig. 16 Wall pressure distribution for convergent type of nozzle inlet at δ=200 μm, $D/d=0.5$ and $P_{al}=3$ bar

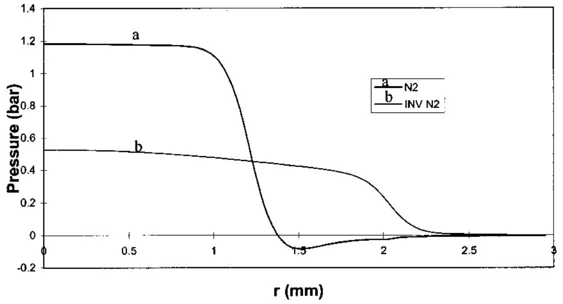

Fig. 18 Wall pressure distribution for N2 and INV N2 nozzle at δ=200 μm, $D/d=0.5$ and $P_{al}=3$ bar

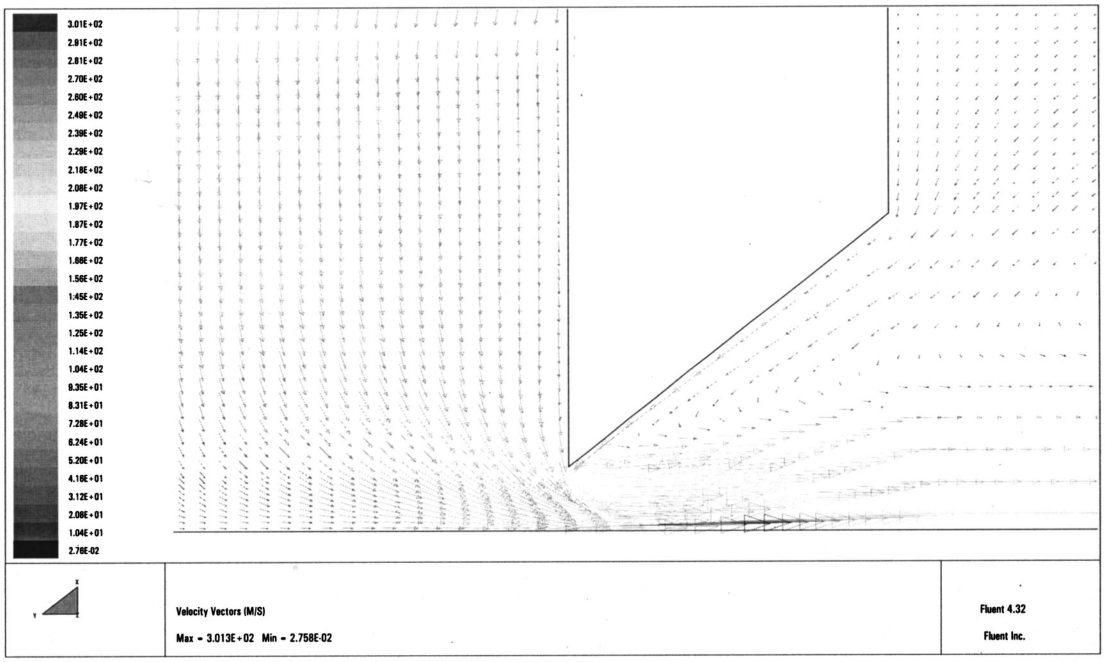

(a) N2

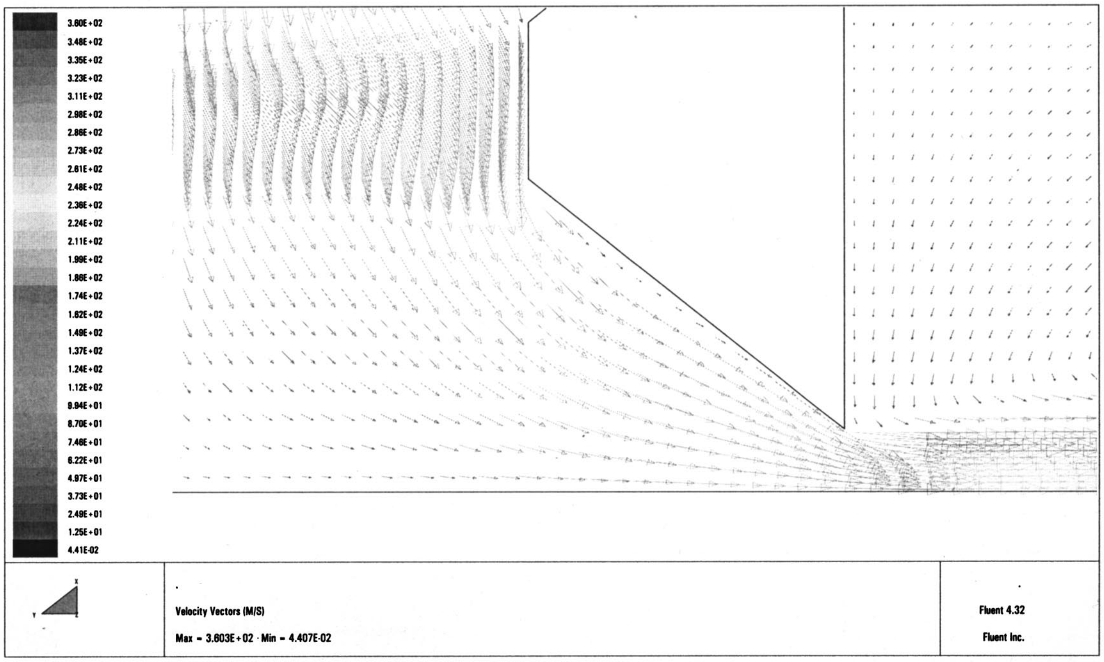

(b) INV N2

Fig. 19 Velocity vector for N2 and INV N2 nozzle, with P_{al}=3 bar, D/d=0.5 and δ=200 μm

operating range is from 100 μm to 400 μm, but the sensitivity is rather low (0.00016 bar/μm). Hence, an alternate solution is to increase the angle α, so that a more extensive and sensitive measurement can be obtained. From Fig. 23, using the INV N2 nozzle at $\alpha=5$ deg can effectively increase the sensitivity to 0.00024 bar/μm, while for $\alpha=22.5$ deg, the sensitivity can be increased further to 0.003 bar/μm (a increase of 10 fold) and it is still able to maintain the range of linearity. Thus, the simulated results shown the INV N2 nozzle design would be useful for increasing the operation range at both the lower and higher ends, in conjunction with the value of D/d ratio.

Concluding Remarks

The numerical simulation results presented in the present paper on the studies of the flow in a pneumatic dimensional control system lead to the following conclusions:

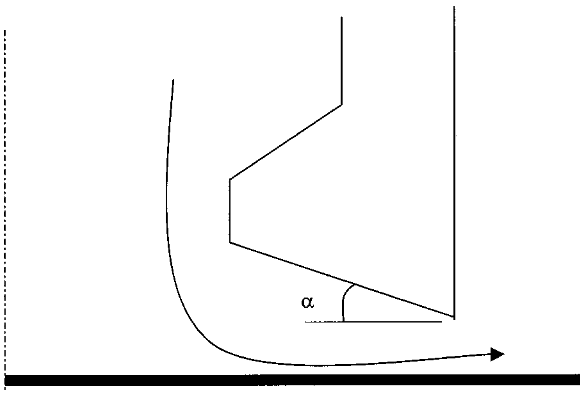

Fig. 20 Angle variation for INV N2 nozzle

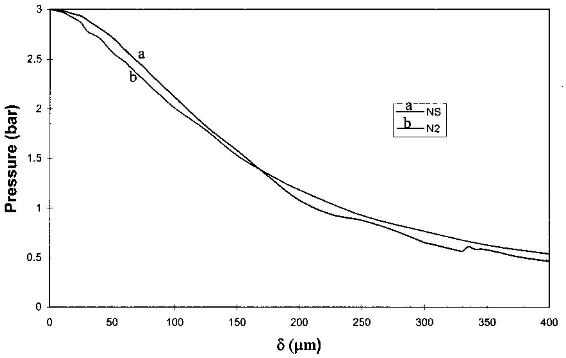

Fig. 21 Variation of stagnation pressure for nozzle NS and N2 with $D/d=0.5$ and $P_{al}=3$ bar

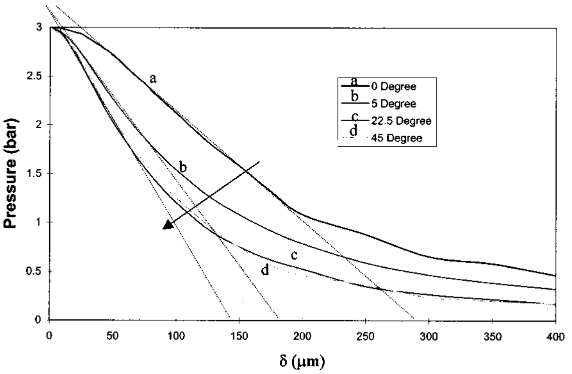

Fig. 22 Variation of stagnation pressure at various α for INV N2 nozzle with $D/d=0.5$ and $P_{al}=3$ bar

(i) Flows in the vicinity of a nozzle head in a pneumatic dimensional control system is best modeled by using a k-ε turbulence model together with the compressible flow equations.

(ii) Two flow separation regions were found in the conventional nozzle design within the range of the flow conditions investigated here. The first one appeared at the gap ceiling. The second appeared on the flat plate just outside the nozzle head. They will have significant effects on the long term performance of the system, due to possible oil and dirt built-up over a period of time.

(iii) By varying the convergent shaped nozzle head at various angles, N2 is able to eliminate the two separation regions mentioned in (ii) but the sensitivity range of the system cannot be improved.

(iv) The divergent shaped nozzle head, INV N2, is able to eliminate the first two separation regions mentioned in (ii) and the sensitivity range of the nozzle can also be improved. For example, at $P_{al}=3$ bar and $D/d=0.5$, the operating range becomes from 10 μm to 80 μm at sensitivity 0.02 bar/μm while that for the conventional design is 60 μm to 220 μm at much lower sensitivity 0.01 bar/μm. Hence, a controllable divergent angled nozzle thus offer the advantages of a larger dynamic measurement range.

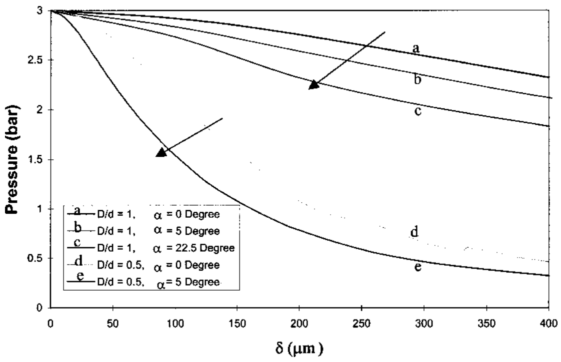

Fig. 23 Variation of stagnation pressure for nozzle at different α and D/d ratio for $P_{al}=3$ bar

(v) Furthermore, the divergent shaped nozzle head can also improve the operating range for the case of large D/d ratio. For example, at $P_{al}=3$ bar and $D/d=1$, the operating range is between 100 to 400 μm but with very low sensitivity. Incorporating the divergent shaped nozzle can improve the sensitivity by 50 percent at the same operating conditions.

Nomenclature

A = area
A^* = minimal cross-section area
P_{al} = supply gauge pressure
P = static gauge pressure
P_{atm} = atmospheric pressure
δ = distance separating nozzle and flat plate
δ^* = effective gap height at the critical position
d = injection nozzle inner diameter
D = regulator diameter
D_s = nozzle external diameter
r = radial coordinate
r^* = position of critical section
ρ = density
α = angle variation for INV N2 nozzle
m = mass flow rate
Re = Reynolds number
V = volume flow rate
μ = dynamic viscosity

Subscripts

1 = upstream
2 = downstream

Superscripts

$*$ = value at the critical cross-sectional area

References

[1] Wattebot, L., 1937, ''Principles of the Pneumatic Amplification,'' J. Mech. (in French), pp. 70–72.
[2] Crnojevic, C., Roy, G., Bettahar, A., and Florent, P., 1997, ''The Influence of the Regulator Diameter and Injection Nozzle Geometry on the Flow Structure in Pneumatic Dimensional Control Systems,'' ASME J. Fluids Eng., **119**, pp. 609–615.
[3] Roy, G., Crnojevic, C., Bettahar, A., Florent, P., and Vo-Ngoc, D., 1994, ''Influence of Nozzle Geometry in Radial Flow Applications,'' *Proc. International Conference on Fluid and Thermal Energy Conversion*, Vol. 1, Bali, Indonesia, pp. 363–368.
[4] *FLUENT*, *User's Manual*, Version 4.3, Fluent Inc, 1991–1993.
[5] Markow, B. N., 1971, ''Pneumatic Dimensional System with the Measuring Nozzle,'' Feineratetechnik (in German), **20**, Jg.Helt 4, pp. 160–161.

P. Ouellette
Westport Research Inc.,
1691 West 36th Avenue,
Vancouver, British Columbia,
Canada, V6N 2P9

P. G. Hill
Department of Mechanical Engineering,
University of British Columbia,
2324 Main Mall,
Vancouver, British Columbia,
Canada, V6T 1Z4
e-mail: hill@mech.ubc.ca

Turbulent Transient Gas Injections

Compressible transient turbulent gaseous jets are formed when natural gas is injected directly into a diesel engine. Multi-dimensional simulations are used to analyze the penetration, mixing, and combustion of such gaseous fuel jets. The capability of multi-dimensional numerical simulations, based on the k-ε turbulence model, to reproduce the experimentally verified penetration rate of free transient jets is evaluated. The model is found to reproduce the penetration rate dependencies on momentum, time, and density, but is more accurate when one of the k-ε coefficients is modified. The paper discusses other factors affecting the accuracy of the calculations, in particular, the mesh density and underexpanded injection conditions. Simulations are then used to determine the impact of chamber turbulence, injection duration, and wall contact on transient jet penetration. The model also shows that gaseous jets and evaporating diesel sprays with small droplet size mix at much the same rate when injected with equivalent momentum injection rate. [S0098-2202(00)02304-X]

Introduction

The prospect of reducing emissions from heavy-duty diesel engines, while retaining their inherently high fuel economy, drives continuing research on direct injection of natural gas in diesel engines (Hodgins et al. [1], Nylund [2], Willi and Richards [3], Meyers et al. [4]). When a gaseous fuel is directly injected in a diesel engine, it forms transient turbulent jets that are typically underexpanded. Under free conditions, the penetration of these jets obeys a linear dependency with the square root of time, and scales with the 1/4 power of the ratio of momentum injection rate to chamber density. This dependency is described in Hill and Ouellette [5] and is briefly reviewed in the following. In engines, however, the jets are submitted to various conditions that may affect these experimentally observed characteristics. For example, the jets are of finite injection duration, they propagate in chambers where turbulence levels and swirl may be significant, they may be in contact with either the top or piston wall, and finally, but not least, they at some point ignite and burn. In an effort to understand the injection and combustion of directly injected gaseous fuel in diesel engines and to help establish the optimum injection characteristics, multi-dimensional numerical simulation was undertaken. The ultimate purpose of the simulation is to include all phenomena, including piston motion, swirl and combustion. This paper, however, concentrates on transient turbulent gas injection into a large chamber with no bulk fluid motion.

The first objective of this paper is to show that multi-dimensional numerical simulations of transient jets using the k-ε turbulent model and performed over grids typical of those used in engine simulations today are compatible with experimentally confirmed relationships. A second objective is to establish, using the numerical model, the effects of finite injection duration, engine combustion chamber turbulence levels and wall contact on the penetration rate of the jet. A third objective is to relate the penetration and mixing of gaseous jets and that of evaporating sprays of small droplet size. The mesh and injection boundary conditions for underexpanded jets present particular challenges, which are the focus of discussions in the paper.

Experimental Knowledge of Transient Jets

Miyake et al. [6], Chepakovich [7], and Ouellette [8] have measured the penetration rates of gaseous jets under conditions similar to those prevailing in direct injection engines. These experimental observations showed that the penetration of the fuel jets obeys a linear dependency on the square root of time. These jets are therefore of the transient type rather than of the puff jet type, which obey a 1/4 power dependency on time (Hill and Ouellette [5]). The observed jets had Reynolds number of the magnitude of 5×10^5, and are therefore fully turbulent. The jets are also typically underexpanded, that is the pressure at the exit of the nozzle is greater than the chamber pressure, and the gas velocity is sonic.

Rizk [9] measured the penetration rate of incompressible jets. His photographs reveal that the jets reach a self-similarity expressed by a constant ratio of the jet maximum width (D) to jet penetration length (z_t). This ratio is found to reach a value D/z_t of 0.25 ± 0.05. This observation is corroborated by the compressible data of Miyake et al. In Hill and Ouellette [5], this self-similarity observation is used in conjunction with a momentum conservation argument to establish that the penetration of jets can be expressed by

$$\frac{z_t}{(\dot{M}_n/\rho_a)^{1/4}t^{1/2}}=\Gamma \tag{1}$$

where z_t is the jet penetration, $\dot{M}_n$ is the momentum injection rate at the nozzle, ρ_a is the density in the chamber, t is the time from the beginning of injection, and Γ a constant whose value is 3.0 ±0.1 for turbulent jets issued from round nozzles. To derive Eq. (1), the mass entrainment rate correlation of Ricou and Spalding [10] was used. The jet penetration measurements of Rizk [9], Witze [11], Miyake et al., Chepakovich, and Ouellette all have a slope in agreement with a Γ value of 3.0 ± 0.1 when scaled with the above ratio of momentum injection rate to chamber density. The data of Miyake et al. for 2 different nozzle diameters are presented as an example in Fig. 1. As the above-cited experimental data cover incompressible and compressible jets, including underexpanded, sonic and subsonic ones, the above expression has a wide range of applicability. The expression is valid for distances greater than about 20 nozzle diameters, for free jets (no wall contact), for jet Reynolds number greater than 3×10^4 and for times shorter than the injection duration. The expression states that the penetration is not directly dependent on the injection pressure, velocity or nozzle diameter, but strictly on the momentum injection rate. Equation (1) can be transformed directly to the following form, which is often cited (for example, in Abraham et al. [12]), showing the similarity length and time scales employed:

$$\frac{z_t}{d_{eq}}=\Gamma\left(\frac{\pi}{4}\right)^{1/4}\left(\frac{tU_n}{d_{eq}}\right)^{1/2} \tag{2}$$

where the equivalent diameter d_{eq} is equal to $d_n(\rho_n/\rho_a)^{1/2}, d_n$ is the nozzle diameter, and ρ_n and U_n are the density and velocity of the injected gas at the nozzle.

Contributed by the Fluids Engineering Division for publication in the JOURNAL OF FLUIDS ENGINEERING. Manuscript received by the Fluids Engineering Division July 13, 1999; revised manuscript received July 18, 2000. Associate Technical Editor: D. Telionis.

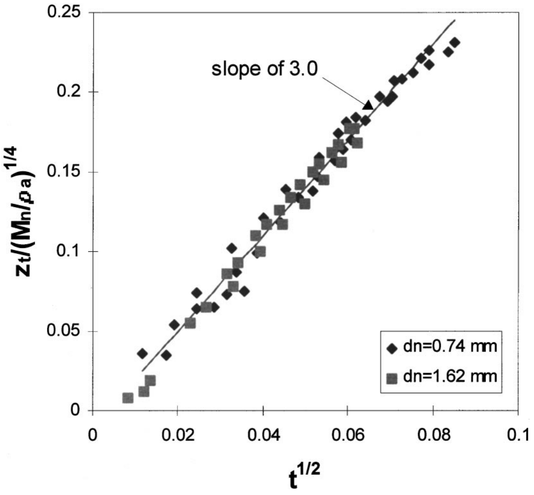

Fig. 1 Nondimensional penetration rate of turbulent methane jets issued from round nozzles of 2 different diameters. $U_n = 409$ m/s, $\rho_n/\rho_a = 3.2$. Data from Miyake et al. [6]. Both axis have units in [$s^{1/2}$].

The above relationships provide a simple understanding of the influence of many engine operating parameters on the penetration of gaseous jets. For examples, the effect on penetration of chamber pressure and temperature, of injection pressure and of nozzle diameter can all be understood with Eq. (1).

Modeling of Transient Jets

Kuo and Bracco [13] modeled transient incompressible jets using a finite difference solution to the equations of motion including the k-ε turbulence model. Their results compared well with experimental data, but comparison was presented only for the early stages of the jet development. Their results pertained to incompressible turbulent jets with Reynolds number between 8650 and 135,100. They provided a correlation similar to Eq. (2), but included a Reynolds number dependency, as the lower Reynolds number jets were not fully turbulent. Assuming a Reynolds number of 1×10^5 in their correlation leads to a value of Γ of 2.75. The comparison is, however, uncertain because of the Reynolds number dependency, which should disappear at Reynolds number greater than 3×10^4.

Gaillard [14] used a similar model to predict the penetration of transient turbulent jets. Gaillard noted the known inadequacy of the k-ε model in reproducing the spreading rate of steady-state jets issued from round nozzles and proposed different coefficients for the turbulent kinetic energy dissipation equation.

As noted by Gaillard, it is well known that for steady-state round jets, the k-ε turbulent model leads to an overestimate of the spreading rate. Malin [15] and Hanjalic and Launder [16], among others, reported that the k-ε turbulent model leads to an overestimation of the spreading rate (ratio of the jet half-width, i.e., the radius at which the velocity is half of that at the axis, to the distance from nozzle) of steady-state turbulent jets. For round free jets of air into air, the turbulence model is reported to predict a spreading rate of 0.11, while the accepted experimental value is 0.085–0.09. The reason for the inaccuracy is related to the assumption of isotropy in modeling the turbulence. The assumption apparently does not hold for jets, in which strains normal to the jet axis differ from aligned ones.

Algebraic corrections have been proposed (Hanjalic and Launder, and Malin) for steady-state turbulent jet modeling, but the corrections require knowledge of the jet centerline position and velocity. This may be difficult to obtain in complex, varying volume geometry such as engine combustion chambers.

Changing the coefficients in the modeled transport equation for the turbulent kinetic energy dissipation ε is reported to improve the situation, though this means giving up the idea that the established coefficients are universals. Pope [17] reported an improvement of the steady-state prediction by changing $C_{\varepsilon 1}$ from 1.44 to 1.6. Gaillard adjusted the model coefficients to better reproduce the mass entrainment rate in steady-state jets. Using the optimized coefficients ($C_{e1} = 1.52$ instead of 1.44, and $C_{e2} = 1.89$ instead of 1.92) in the ε equation, the spreading rate of simulated steady-state jets, $r_{1/2}/z$, was reported to be 0.08. Despite the improvement, the penetration constant Γ of the jets modeled by Gaillard is about 2.5, which is lower than the expected value of 3.0. Mesh density effects may be the cause of this low value.

Abraham [18] and Abraham et al. [12] noted that the equivalent diameter as used in Eq. (2) is a valid length scale for the scaling of calculated transient jets that differ in density from the surrounding fluid. They also reported the square-root dependency on time. Abraham [18] used the standard k-ε turbulent model to calculate the mass entrainment rate in transient jets. The calculations included jets of different densities but did not discuss underexpanded jets.

Johnson et al. [19] modeled hydrogen jets and found that the jet penetration was severely under-predicted when computed over a three-dimensional cylindrical mesh. They attributed the discrepancy to increasing mesh coarseness in the radial direction. This coarseness induces unrealistic turbulent length scales, resulting in too large diffusion. They proposed a solution by limiting the magnitude of the turbulent length scales within the cone of the jet. Although the approach gives good results, it may be equally difficult to implement in an engine situation, where the jet location is affected by piston motion, wall effect and swirl.

The Numerical Model

The KIVA-II code (Amsden et al. [20]), developed for engine-based modeling, was modified to include gaseous jet injection capabilities and was used in this study. KIVA-II offers a solution for gas phase flows and for the propagation of a liquid evaporating spray (liquid phase) within a chamber. The gas phase flow modeling is a finite-volume solution to the unsteady equations of motion for compressible turbulent chemically reactive flows in two- or three-dimensions. An arbitrary number of species can be specified, and are treated as ideal gases. The equations are Navier-Stokes equations for a mixture of gases. The k-ε model used in this work is the standard one (Launder and Spalding, as referred to in Amsden et al.), corrected only for compression effects. The equations are not modified, and a complete description can be found in Amsden et al.

Injection Boundary Conditions. There are a number of possible strategies for representing specific experimental conditions. One is to include the details of the nozzle flow in the computations. This is the method followed by Zhang et al. [21]. In engines, the length scale difference between the nozzle and the chamber dimension is of the order of 100. To resolve the details of the velocity profile at the nozzle exit, one must compute at scales maybe 10 times smaller than the nozzle diameter, such that a difference in scale of 1000 would be required. Because of this difference in scale, only codes which have a multi-grid scale capability can be practically used to resolve both nozzle and chamber flows. The computations of nozzle flow details remain time-consuming.

Another method is to use specific, detailed computations to establish the velocity and gas flow parameters at the nozzle, and then use the computed profile in a coarser computation. This is the method proposed by Johnson et al. [19]. When the chamber conditions are changing, as they are in a reciprocating engine, the boundary conditions are also changing in time, such that a large number of preliminary computations may be required to handle, for example, a study of injection timing.

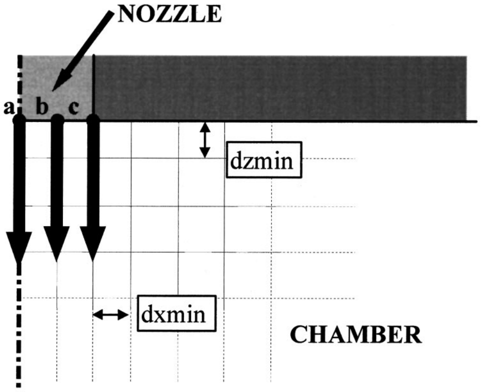

Fig. 2 Injector/nozzle interface for 2-d computational mesh

A third method, which is used in this work, is based on the observation that far from the nozzle (at $z_t/d>20$), the jet penetration is predominantly dependent on the nozzle momentum injection rate, as expressed by Eq. (1), and not on the details of the conditions at the nozzle. In this work, the momentum at the nozzle is estimated for each experimental condition and an equivalent momentum is imposed at the injector/chamber interface. The momentum may be calculated from provided experimental conditions, such as velocity and discharge coefficient, or can be calculated from one-dimensional flow with friction when the pressure ratio across the nozzle is known. Compressibility effects may be taken into consideration when significant.

The velocity, temperature, and density of the incoming gas were accordingly set at the computational cells lying at the injector/chamber interface. Figure 2 shows the injector/chamber interface for an axisymmetric grid with downward injection originating from the center of the top wall, at the symmetry axis. The chamber in this case would have the shape of a cylinder, with the jet propagating along its axis, as can be seen in Fig. 3. The velocity and temperature must be provided at the vertices within the nozzle/chamber interface (**a**, **b**, and **c**). The density, internal energy, turbulent length scale, and turbulent kinetic energy flux across the cell faces (**a-b**,**b-c**) in the interface region must also be provided. The specifications of the temperature, velocity, and density are inputs to the solution and are discussed further. The internal energy is obtained from the JANAF tables once the temperature has been calculated. The influx of specific turbulent kinetic energy and of the turbulent length scale must also be specified. In this work the specific turbulent kinetic energy influx was set at 10 percent of the nozzle flow specific kinetic energy, while the turbulent length scale was set at 50 percent of the nozzle diameter. These values are similar to those used by Gaillard [14] and MacInnes and Bracco [22]. The sensitivity to these choices was assessed in Ouellette [8] for turbulent transient jets, and it was found that the jet rapidly creates its own turbulence properties and numerical simulations were not sensitive to the above choices in the downstream region of the jet.

Jet Penetration Definition. When computing the penetration of a transient jet, the definition of penetration must be established. Figure 4 shows the details of the methane mass fraction value along the axis of the chamber and in the region of the jet tip corresponding to Fig. 3. It may be seen that the jet forefront is well defined but not absolutely sharp because of the grid resolution. An appropriate penetration definition may be to take the point of intersection of a tangent to the steepest part of the forefront with the axis (point B). But at large distances from the nozzle, the steepness of the front is not as easily defined as that shown in Fig. 4 and it becomes difficult to determine the forefront. The change of slope that identifies the beginning of the jet head (point A on Fig. 4) remains on the other hand obvious at all times for the cases studied. This point however is not at the forefront but rather at some point near the back of the vortex head. Here the jet tip was taken as half way between points A and B. For the jet travel distance of interest here, from about 20 to 100 nozzle diameters, the half way point between A and B corresponded to a mass fraction of methane of roughly 3 percent.

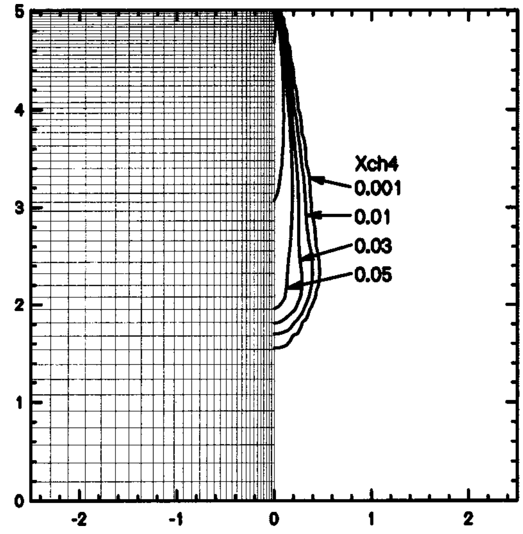

Fig. 3 Mesh and methane mass fraction for axisymmetric transient jet study

Grid Size Effect. The effect of mesh density on the jet penetration was investigated in this work, particularly the maximum grid size in the chamber and the grid size in the nozzle area. In all computations, the number of cells in the nozzle exit area and the size of the cell immediately adjacent to the nozzle are specified; the grid is geometrically expanded from the nozzle to the wall, in both the axial and radial directions, as may be seen in Fig. 3. For each case, the jet penetration was calculated then expressed in terms of Eq. (1), and the corresponding value of Γ is established.

The number of cells within the nozzle was increased from 2–4, with a modest reduction of 1 percent in the value of Γ. The maximum grid size in the chamber was increased from a maximum of 1 mm (2 nozzle diameters) to 2 mm, with a change of only 0.5 percent in the value of Γ. However, the size of cell adjacent to the nozzle has a more significant effect and is reported in Table 1. The parameters $\mathbf{dx}_{\min}$ and $\mathbf{dz}_{\min}$ denote the size of the cell adjacent to the nozzle area, as illustrated in Fig. 2. For all cases, the maxi-

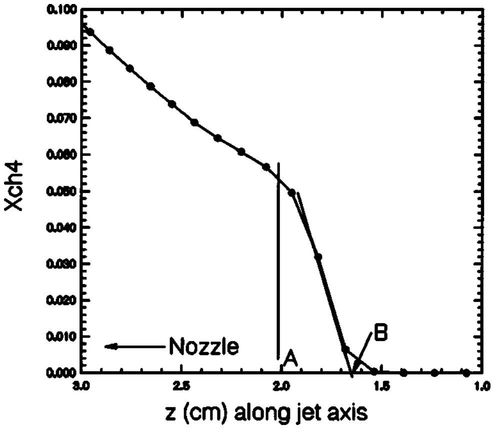

Fig. 4 Axial methane mass fraction at the jet forefront, corresponding to jet in Fig. 3

Table 1 Effect of grid size in vicinity of nozzle, penetration constant based on an average forefront definition (free jet)

Dx_{min} , dz_{min}	Γ	% Change
1.0d (0.5 mm)	2.94	
0.75d (0.375 mm)	2.80	4.8
0.5d (0.25 mm)	2.67	4.6
0.25d (0.125 mm)	2.60	2.6

mum cell size in the chamber (at the outside and bottom walls) was kept at 1.5 mm, resulting in more cells being used as the adjacent cells size was reduced in size.

Table 1 reveals that the calculated value of the constant Γ decreases further from the experimental value of 3.0 as the mesh density is increased, and furthermore that although the change is small between the two last cases, grid independence is not yet reached with a cell sized corresponding to 1/4 diameter. It should be noted that in these simulations, the chamber turbulence was set to zero and that the jets created their own turbulence.

When modeling an engine, a cylindrical three-dimensional mesh is used; this offers another challenge as the size of the cells in the circumferential direction is increasing with the radius. It was found necessary to use at least two cells in the nozzle area in the circumferential direction while performing three-dimensional computations. A comparison was made between the penetration of round jets computed in two-dimensions (axisymmetric) and in three-dimensions. The three-dimensional mesh consisted of a 60 deg portion of a cylindrical chamber divided into 30 axial cells, 32 radial cells and of 12 circumferential cells. The cylindrical chamber was 6.1 cm in radius and 2.5 cm high. When modeling engine cycles, the injection boundary injections are placed on the side of a protruding injector tip, as depicted in Fig. 5. The nozzle was recessed further in the chamber such that wall effects would be avoided in this comparison. The same adjacent cell sizes were kept. The test showed that three-dimensional simulations resulted in a value of Γ 7.5 percent smaller when compared to two-dimensional simulations. Furthermore, because of the increase in cell size in the circumferential direction, the linear dependency with the square root of time was not as good at further distances from the nozzle. Early tests and literature data indicate that further to the grid density requirement in the nozzle area, three-dimensional cylindrical calculations also require that r-z planes (where r is the radial axis and z the axial axis) be spaced every 2 to 3 degrees.

Adjustment of k-ε Coefficients. The k-ε model used in KIVA-II is the standard one (Launder and Spalding, as stated in Amsden et al.), only corrected for compression-induced turbulence. It therefore yields an inaccurate steady-state jet spreading rate, as discussed above. This was demonstrated by performing axisymmetric calculations and identifying the half radius from the quasi-steady-state stem of transient jets. A value of 0.10 was obtained, which compares to experimentally determined values between 0.085 and 0.09. This inaccuracy translates into a jet width-to-penetration ratio of 0.30, compared with the value of 0.25 ± 0.05 as observed in Rizk [9] and Miyake et al. [6], and in an under-predicted penetration rate, with a slope of 2.7 instead of 3.0 as illustrated in Fig. 6.

Following Pope [17] and Gaillard [14], the coefficients $C_{\varepsilon 1}$ and $C_{\varepsilon 2}$ of the turbulent kinetic energy equation were modified to best reproduce transient jets and their quasi steady-state stem. Computations using cell sizes in the nozzle area of 1/2 diameter (0.25 mm) were performed with the coefficients change proposed by Pope and Gaillard, and the corresponding values of Γ and $r_{1/2}$ are presented in Table 2. Other coefficient changes were also considered as indicated. There is an improvement of the penetration constant as $C_{\epsilon 1}$ is increased from 1.44 to 1.52. It appears also that the value of $C_{\epsilon 2}$ is best unchanged (at 1.92) for the current model and for the mesh density used. The effect of this coefficient change will need to be assessed when considering engine flow.

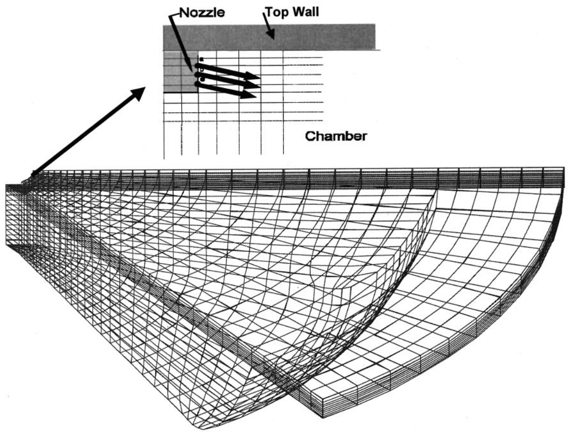

Fig. 5 Three-dimensional chamber and chamber-nozzle interface

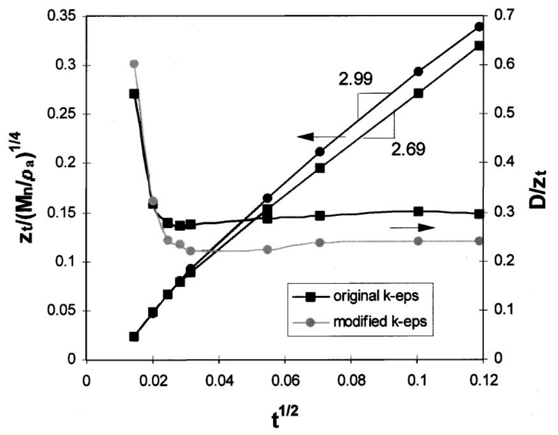

Fig. 6 Nondimensional penetration rate and ratio of head vortex to jet tip for uncorrected and corrected turbulent model (simulations)

Underexpansion and Virtual Nozzle Injection. When considering the direct injection of a gaseous fuel in a compression ignition engine, the resulting jet may be underexpanded, that is the nozzle exit pressure is higher than the chamber pressure. Underexpansion of natural gas occurs when the upstream-to-chamber pressure ratio is greater than approximately 1.85 (assuming perfect gas behavior of methane). At underexpanded conditions, the flow chokes at the exit of the nozzle. Underexpansion is a complex adjustment process involving expansion and compression waves, which form a barrel-shaped shock pattern. Figure 7 shows a schematic of the expansion process outside the nozzle.

Table 2 Effect of change in the value k-ε coefficients, as obtained in this study with a grid density of 1/2 d in nozzle area

	$C_{\varepsilon 1}$	$C_{\varepsilon 2}$	$r_{1/2}$	Γ
Original k-ε Amsden [20]	1.44	1.92	0.100	2.69
Pope [17]	1.60	1.92	0.066	3.42
Gaillard [14]	1.52	1.89	0.078	3.15
This study #1	1.50	1.92	0.083	2.94
This study #2	1.52	1.92	0.084	2.99

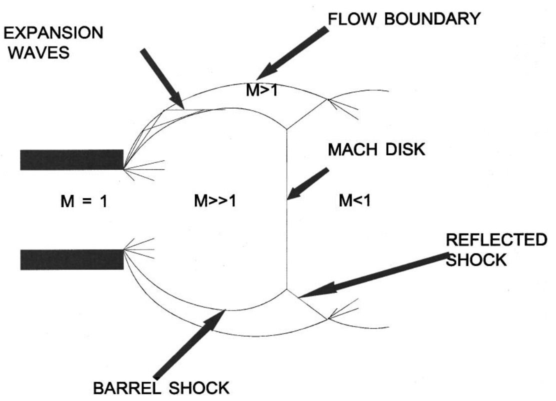

Fig. 7 Underexpansion process (from Ewan and Moodie [23])

KIVA-II solves compressible equations of motion, and can in principle handle the underexpansion. Since the expansion process outside the nozzle involves some shocks, it is doubtful that the predicted flow field near the nozzle will be accurate unless a very fine grid is used. It was decided to evaluate methods of avoiding the computations of this expansion process.

One method consists in using Eq. (1) as the basis to provide a correctly expanded nozzle with equivalent momentum injection rate. Equation (1) states that the penetration will be the same as long as the momentum injection rate is duplicated for a given chamber density. The assumption is made that no mixing takes place over the expansion region. To satisfy momentum conservation, the corrected diameter must then satisfy

$$\frac{d_c}{d_n}=\left(\frac{\rho_n}{\rho_c}\right)^{1/2}\frac{U_n}{U_c} \tag{3}$$

where the subscript *c* refers to a nozzle which provides a correctly expanded jet and *n* to the real nozzle exit conditions. Fixing arbitrarily the corrected diameter's Mach number at Mc, and since the Mach number at the nozzle exit is unity, the corrected diameter becomes, under the assumption of perfect gas law:

$$\frac{d_c}{d_n}=\left(\frac{\rho_n}{\rho_c}\right)^{1/2}\frac{\sqrt{\gamma R_{CH4}T_n}}{\mathrm{M_c}\sqrt{\gamma R_{CH4}T_c}}=\frac{1}{\mathrm{M_c}}\left(\frac{\rho_n T_n}{\rho_c T_c}\right)^{1/2} \tag{4}$$

The gas density at the nozzle ρ_n is $P_n/R_{CH4}T_n$, and the density at the corrected nozzle must be taken at chamber pressure P_a and is $P_a/R_{CH4}T_c$. Replacing in Eq. (4) leads to

$$\frac{d_c}{d_n}=\frac{1}{\mathrm{M_c}}\left(\frac{P_n}{P_a}\right)^{1/2} \tag{5}$$

The nozzle pressure can be readily calculated assuming perfect gas law and having unity Mach number at the nozzle:

$$P_n=P_o\bigg/\left(1+\frac{(\gamma-1)}{2}\mathrm{M_n^2}\right)^{\gamma/\gamma-1}=0.546P_o \tag{6}$$

where P_o is the pressure in the reservoir, and taking γ to be 1.3. Replacing into Eq. (6) leads to:

$$\frac{d_c}{d_n}=\sqrt{\frac{0.546}{\mathrm{M_c^2}}\frac{P_o}{P_a}} \tag{7}$$

which is valid under the assumption of perfect gas law. The correction is equivalent to providing a nozzle with lower stagnation pressure but same momentum. The validity of this scaling is further supported by the fact that Ewan and Moodie [23] scaled underexpanded steady-state jets generated by pressure ratios as large as 70 using Eq. (7) with $\mathrm{M_c}$ equal to 1. This observation is further discussed in the paper by Hill and Ouellette.

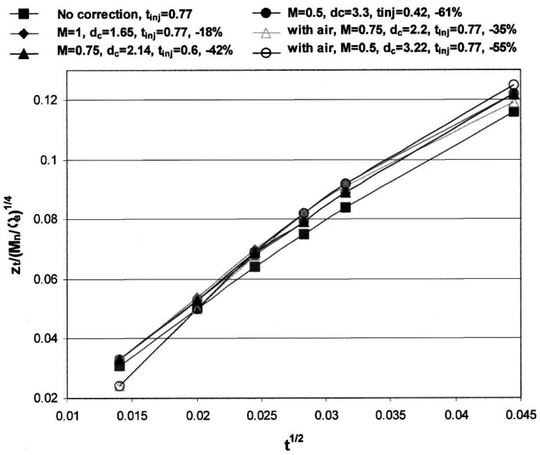

Fig. 8 Nondimensional jet penetration for different underexpansion treatments. $P_o/p_a=5$. T_{inj} is the injection duration and d_c is the corrected diameter. The percentage value indicates the reduction in computing time. Units of both axis in [$s^{1/2}$].

For the corrected diameter to reproduce not only the momentum injection rate at the nozzle but also the mass injection rate, the corrected diameter's injection velocity U_c must be the same as the nozzle injection velocity U_n. Under the assumption that no mixing takes place during the expansion process, the stagnation temperature T_o remains constant, and the Mach number $\mathrm{M_c}$ is equal to $\mathrm{M_n}$, which is unity. If a subsonic velocity is chosen to speed up calculations, the mass injection rate is no longer the same as that of the actual nozzle. For example, if a corrected nozzle Mach number of 0.75 is chosen, the corrected nozzle diameter is $d_c/d_n=\sqrt{.971P_o/P_a}$ and the associated drop in velocity yields a mass injection rate reduced by 23 percent.

When using a correction for underexpansion in numerical simulations, the nozzle conditions are first calculated (temperature, density, velocity), then the corrected diameter is calculated with Eq. (7), while the temperature, density and velocity are calculated as

$$T_c=T_o\bigg/\left(1+\frac{(\gamma-1)}{2}\mathrm{M_c^2}\right),$$

$$\rho_c=\frac{P_a}{RT_c},\quad U_c=\mathrm{M_c}\sqrt{\gamma RT_c}$$

Figure 8 shows the predicted penetration rate obtained with different assumptions for a nozzle operated at a pressure ratio of 5. In the first case, underexpanded conditions were set at the injection boundary conditions (no corrections). In the second, third and fourth cases, equivalent diameters with Mach numbers of 1, 0.75, and 0.5 were provided. The mass injection rate differs from that of the original case for subsonic Mach numbers, but the same total mass of methane is injected, such that the injection duration differs, as indicated. The reduction in computing time is also indicated in percentage in the legend.

It may be seen that all corrected cases predict a somewhat larger penetration than that of the uncorrected case, by about 5 percent, despite the identical momentum injection rate. This could be explained by the fact that a much denser grid would be required to treat the pressure adjustment of the underexpanded case. For the two corrected cases with Mach numbers of 1 and 0.75, the penetration is nearly identical, despite the difference in injection duration and rate. This observation re-enforces the momentum dependency of the jet penetration. The two corrected cases lead to a reduction in computing time of 18 percent and 42 percent, respectively (for the $\mathrm{M_c}=0.75$ case, the reduction is linked to a 22 percent shorter injection duration). For the Mach 0.5 case, the computing time is reduced by 60 percent (injection duration 45 percent shorter), but the penetration is not as well reproduced, particularly in the early stages. The potential core, the region of the jet near the nozzle where the injected fluid has not mixed with the surrounding, extends further downstream for a larger nozzle, which may explain the early difference.

To compensate for the difference in mass injection rate, another correction strategy can be followed. A subsonic jet of equal momentum and methane mass injection rate can be obtained if a mixture of methane and air is initially injected. This corresponds in essence to replacing nozzle boundary conditions by averaged conditions existing a few diameters downstream of the nozzle. For a desired Mach number, a percentage of air can be found that provides equal momentum and methane mass injection rate. Two such cases are presented in Fig. 8, with Mach numbers of 0.75 and 0.5, and corresponding air fractions of 19 and 41 percent. Again the predicted penetration rate for the case of Mach 0.75 is equivalent and equal to that predicted by the pure methane injection at the same speed. The reduction in computational time is 35 percent this time. The small distance over which the mixing would really take place was not considered in the penetration of Fig. 8.

Which of the above methods is best to use depends somewhat on the application. For engine modeling, it can be argued that reproducing the mass injection rate is important to reproduce the combustion rate following the end of injection. In that respect a corrected diameter with unity Mach number that provides a match for both the mass and momentum injection rate is a better choice and has been used in the current work.

Results

Comparison With Penetration Formula. Numerical simulations were performed to evaluate the capability of reproducing transient jet characteristics. Methane was injected at a velocity of 50 m/s and at a density of 19.3 kg/m^3 through a nozzle of 0.5 mm in a chamber filled with air at a density of 34.8 kg/m^3. The Reynolds number was then approximately 50,000. The methane was injected in a chamber of 25 mm in radius and 50 mm in length. In these simulations, a square velocity profile was imposed at the nozzle, and the momentum calculated accordingly. The new coefficient $C_{\varepsilon 1}$ equal to 1.52 was used. Figure 6 shows the penetration rate of a simulated jet, rendered dimensionless according to Eq. (1). The square root of time dependency is well reproduced by the simulations. The slope is 2.99 which compares well with the experimentally confirmed value of the value of 3.0 ± 0.1 presented in Eq. (1).

Direct Comparison With Experimental Data of Witze [11]. To further verify the proper implementation of injection boundary conditions and estimate the capability of KIVA-II to reproduce transient jets, a computational case was compared with the experimental data of Witze [11]. Witze took hot wire measurements on the centerline of a suddenly started air jet. For the case considered here, the nozzle was 1.2 mm in diameter and steady-state nozzle velocities of 53 and 103 m/s were tested. These jets are essentially incompressible, but not fully turbulent as the Reynolds numbers are approximately 6000 and 12,000.

The nozzle conditions were reproduced in KIVA-II, and air was injected in a cylindrical chamber of radius 25 mm and length 100 mm. These dimensions were chosen to minimize wall effects over the time period considered. An axisymmetric calculation was performed over a mesh of 100 axial cells and 30 radial cells. For this particular case, the penetration definition of Witze was used; the penetration time is obtained at one location when the axial velocity is 70 percent of the steady-state velocity at that location. Figure 9 shows the results of the comparison between the experimental penetration data of Witze (reported in Kuo and Bracco [13]) and those obtained with KIVA-II. The agreement is fair, although there is a penetration difference in the early stages.

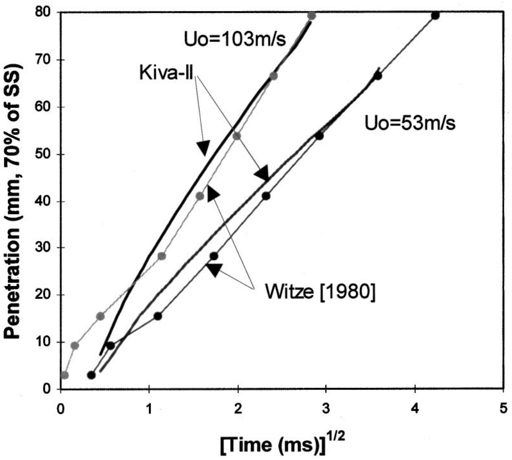

Fig. 9 Comparison of predicted penetration rate with experimental data of Witze [11]. Incompressible air jet into air, $d_n = 1.2$ mm.

Direct Comparison With Experimental Data of Ouellette [8]. Simulations were also compared to flow visualization studies presented in Ouellette [8] and Hill and Ouellette [5]. The flow visualization experiments consisted of schlieren photographs of transient methane jets issued from the round nozzles of a gaseous injector used in engine. The injection took place in a pressurized optically accessible chamber 18 by 18 cm wide and 5 cm in height. The injector tip protrudes from the center of the top wall, as in an engine, and the gas was injected at an angle of 10 deg from the top wall. The chamber was pressurized at 1.5 MPa, and injection pressures of 2.3, 3.7, 6, and 8.1 MPa were used, corresponding to nozzle to chamber gas density ratios of 0.63, 0.86, 1.44, and 2.01. The nozzle diameter was 0.5 mm. The penetration rate was measured from the photograph with an accuracy of 0.1 ms on time. The jet penetration measurements had a standard deviation of approximately 1 mm. Figure 10 shows the penetrating jet at different times.

Because of the geometry and the observed contact with the top wall, the simulation of these experiments required three-dimensional computations performed in cylindrical coordinate system. Although the chamber used in the experiments was square, a cylindrical chamber was used in the simulations. The

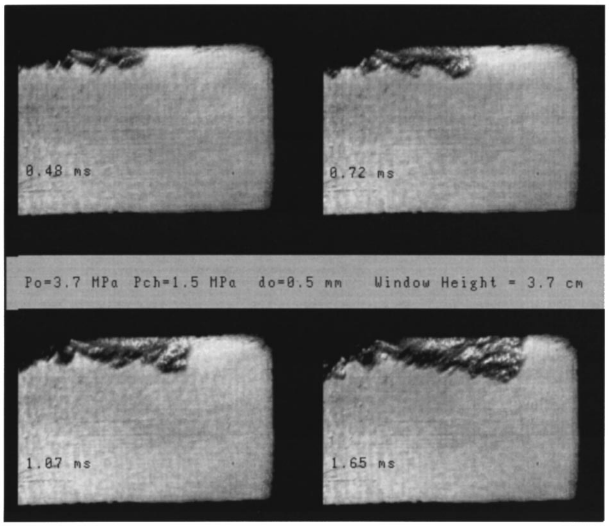

Fig. 10 Schlieren photographs of jet in fixed volume chamber

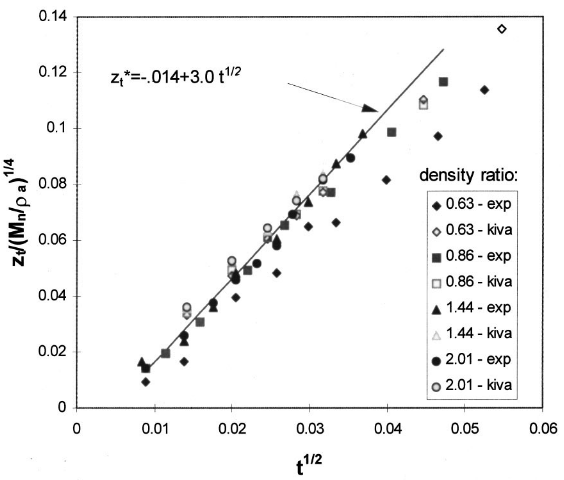

Fig. 11 Comparison between experimental data and computations

diameter of the chamber was the same as the width of the chamber. The volume differed, but the pressure rise in the chamber due to gas injection was negligible and would not impact the jet penetration. The simulations were performed over a 60 deg sector as seen in Fig. 5. There was no contact with the chamber walls other than with the top wall. Injection boundary conditions were established on the side of a protruding injector tip, as illustrated in Fig. 5. The mesh consisted of 30 axial cells, 32 radial cells and 12 circumferential cells. The cells in the nozzle area had sizes smaller or equal to the nozzle diameter. Grids of higher density were considered in Ouellette et al. [24], and it was found that within 90 diameters from the nozzle, which is the range considered here, the penetration changed only by 4 percent when going from the grid used here to a grid nearly twice as dense.

The injection boundary conditions (velocity, temperature, and density) were calculated based on the measured injection and chamber pressures. It was found that both friction and real gas effects affected the flow inside the nozzle, and thus were considered in determining the nozzle exit momentum and mass flow rates. The real gas behavior is significant for the conditions considered, with a compressibility factor of 0.88 at the highest injection pressure. The calculated momentum from one-dimensional flow considering real gas behavior and friction differed by less than 2.5 percent from that made using perfect gas assumption with friction, but the mass injection rate differed by as much as 8 percent. Details of the nozzle flow conditions estimate can be found in Ouellette [8]. For the three higher injection pressures, the nozzle flow was underexpanded, and a corrected diameter was calculated, based on Eq. (7) and with a unity corrected Mach number.

Figure 11 shows the results of the comparison between the simulations and the experimental results. The experimental data collapse close to the slope of 3, indicating that there is close agreement with the scaling of Eq. (1), although the two lowest density ratio cases deviate substantially at later times from the linear dependency because of the wall effect. The experimental case with density ratio ρ_n/ρ_a of 0.63 lies somewhat below the other data points, yet has much the same slope in the region unaffected by the wall, indicating that the initial jet development differs from the other cases. It is possible that the injector needle opening time has some dependency on the injection pressure.

The computational results scale well with the momentum-to-density ratio and compare relatively well with the numerical results. The slope of the computational data is still lower than expected at approximately 2.65. This lower value of Γ is due both to the circumferential grid expansion in three-dimensional cylindrical computations and to the wall contact. By comparing with three-dimensional computations of a jet propagating without touching the wall, it was found that the wall contact reduces the value of Γ by approximately 5 percent.

Table 3 Simulation conditions for studies of turbulence and injection duration

Chamber dimensions	Radius: 20 mm Length: 90 mm
Grid	25 radial, 100 axial dxmin, dzmin: 0.5d
Injection pressure and temperature	$P_o = 15$ MPa, $T_o = 350$ K
Chamber pressure and temperature	$P_a = 5$ MPa, $T_a = 850$ K
Wall temperature	$T_w = 450$ K
Nozzle diameter	$d_n = 0.5$ mm
Injected mass	3.5 mg
Turbulence level	1.5 m^2/s^2

The Effect of Turbulence and Finite Injection Duration on Jet Penetration. The dependency described by Eqs. (1) and (2) does not take into consideration certain engine conditions that may affect the penetration of gaseous jets. Numerical simulations were performed to verify the validity of the dependency established by Eq. (1) for: i) jets of finite duration, and ii) jets propagating in chambers where the turbulence level is increased to values found in diesel engines, as discussed below. Realistic chamber conditions, summarized in Table 3, were set in a two-dimensional axisymmetric chamber.

Effect of Turbulence. It should be noted that all simulations above were done in quiescent chambers where the turbulence levels were set to zero. The jets created their own turbulence. In engines at top-dead-center, turbulent fluctuations are of the order of 1/2 the mean piston speed (Heywood [25]). For the engine considered here, the mean piston speed varies between 2 and 8 m/s. The turbulent fluctuations may be of the order of 1 to 4 m/s, corresponding to a turbulent kinetic energy of 1.5 m^2/s^2 to 20 m^2/s^2. Figure 12 shows three cases with three different initial turbulence levels; 0, 0.5 and 5 m^2/s^2. As may be seen, increasing turbulence reduces the penetration as defined by a 3 percent mass fraction contour line. The case with 0.5 m^2/s^2 initial turbulent kinetic energy is accompanied by a reduction of 5 percent in penetration. The subsequent 10 fold increase reduces the penetration by another 2 percent. The corresponding values of Γ are 2.92, 2.79, and 2.74. The decrease in penetration is accompanied by an increase in lateral spreading.

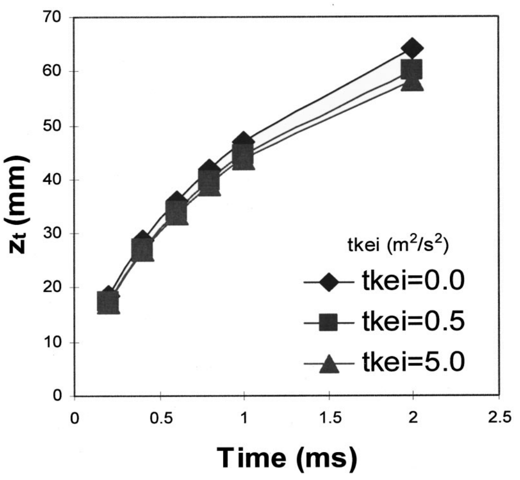

Fig. 12 Effects of chamber turbulence on jet penetration (tkei is the initial turbulence kinetic energy in the chamber)

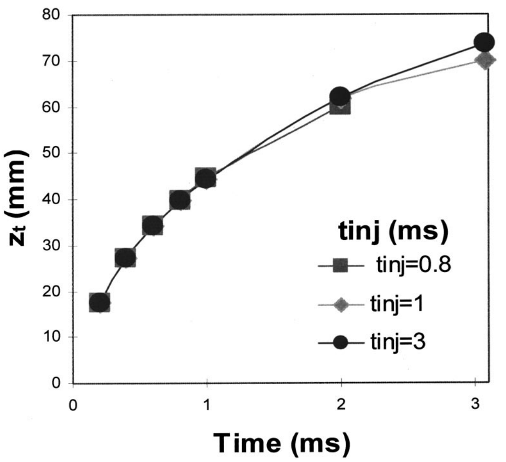

Fig. 13 Effects of injection duration on jet penetration (tinj is the injection duration)

Effect of Injection Duration. Figure 13 shows three injections with same conditions, but with different injected masses. In the first case, 5 mg of fuel are injected, with a corresponding injection duration of 1 ms, while in the second case the injection is continuous. It is seen that the penetration rate of the interrupted jet remains the same as that of the continuous jet for up to twice the injection duration (until 2 ms in Fig. 13).

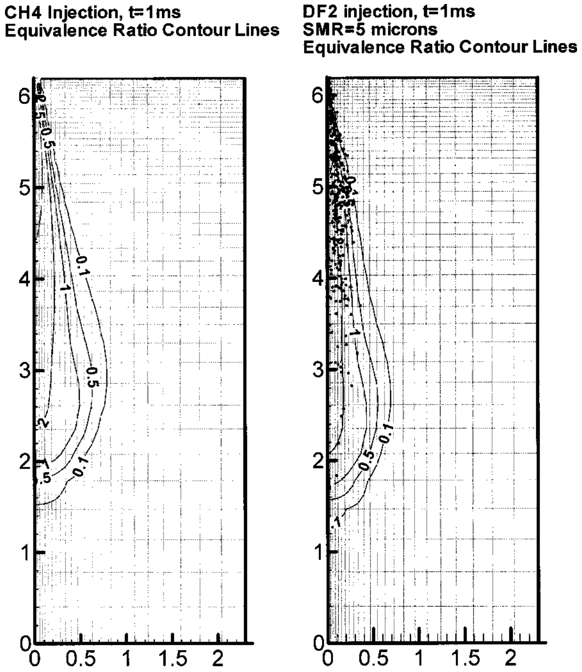

Fig. 14 Mesh and equivalence ratio contour lines for gaseous jet (left) and for a diesel spray (right) for an equivalent momentum injection rate (dimensions in cm, df2 is diesel #2)

Comparison Between Jet and Spray Penetration and Mixing. In the continuing effort to reduce emissions from diesel engines, much research has been done on the injection rate and configuration of sprays. In that respect, it is of interest to know whether gaseous jets behave much like sprays. Kuo and Bracco [13] compared the penetration of liquid sprays and gas jets. Their work indicates that for sprays in general it is not enough to say, as we have shown (Hill and Ouellette [5]) for turbulent gas jets, that the penetration rate depends only on time and the ratio of nozzle exit momentum flow rate to chamber density. Their evidence indicates that spray penetration may also depend on liquid-to-gas density ratio, length-to-diameter ratio of the nozzle and the parameters which control atomization and vaporization rate. This is reasonable since these latter parameters affect droplet size and one would expect large droplets to have a strong effect on momentum transfer between fuel and air, and thus strongly affect spray mixing and penetration. However, for the case of vanishingly small droplets, one would expect spray behavior to be essentially identical to that of the turbulent gas jet.

The particular question considered in the following is whether, under typical diesel chamber conditions, penetration of turbulent impulsively injected gas jets is essentially the same as that of sprays if the typical droplet is small, i.e., of the order of a few microns. In the absence of experimental data comparing sprays and gas jets with the same momentum-to-chamber-density ratio, numerical simulation was employed to investigate the question. Though it is recognized, as we outlined in this paper, that numerical simulation is limited in absolute accuracy due to grid size effects and to approximations in modeling turbulence, we postulate that much the same limitations will appear in calculations of both jets and sprays if the droplet size in the latter is small.

Two-dimensional axisymmetric numerical simulations of sprays and gaseous jets with equivalent momentum injection rate were performed using KIVA-II. The spray model incorporated in KIVA-II (Taylor Analogy Breakup, Amsden et al.) was used to calculate spray penetration and evaporation. The spray model was only modified to ensure that the momentum injection rate was identical to that of the gaseous jet. In order to control the spray cone angle, fine droplets of a specified Sauter mean radius were injected within a specified cone angle (another option is to inject larger droplets and to use the aerodynamic droplet break-up submodel included in KIVA-II, but this offers less control on the spray angle).

Liquid diesel fuel sprays were compared to a gaseous jet, all injected in air at 17.42 kg/m^3 and 1200 K. The initial turbulence level in the chamber was set at 3600 cm^2/s^2, corresponding to a turbulent fluctuation of approximately 0.5 m/s. 5 mg of fuel were injected in each case at the same momentum injection rate. The calculations were performed over a mesh made of 23 radial cells for a radius of 23 mm, and of 45 axial cells for a length of 62 mm. At the nozzle, the cells had the dimension of the gas nozzle radius, 0.25 mm, and were expanding geometrically in the radial and axial direction, as seen in Fig. 14.

The first spray was specified to have a cone angle of 26 deg, which is the approximate spreading angle of the gaseous jet, and droplets of Sauter mean radius of 5 μm. The simulated diesel nozzle was 0.13 mm in diameter, such that the grid to diesel orifice radius ratio was about 4. This is within the range used in the literature as reported by Abraham [26]. Methane was injected through a 0.5 mm diameter nozzle at an injection pressure of 150 bar.

Figure 14 shows the grid, along with the methane and diesel equivalence ratio for the case of 5 micron droplets injected within a cone of 26 deg at 1 ms after the beginning of injection. It may be seen that the penetrations and fuel distributions are very similar. Figure 15 shows the corresponding mixing rate based on mixture strength. A mixture equivalence ratio below 0.5 was arbitrarily considered lean, while a mixture equivalence ratio above 2.0 was considered rich. It may be seen that the flammable and lean mixture formation rates are nearly identical for the gaseous jet and this controlled spray. The rich mixture formation is different, since only the vapor was considered when calculating the amount of fuel within each region.

Increasing the droplet Sauter-mean-radius to 10 μm resulted in an increase in fuel vapor in the lean mixture, but in a decrease in vapor in the flammable mixture. There is now little fuel within rich regions, as more fuel is left within the droplets. It seems that larger droplets overall reduced the mixing of the diesel vapor with

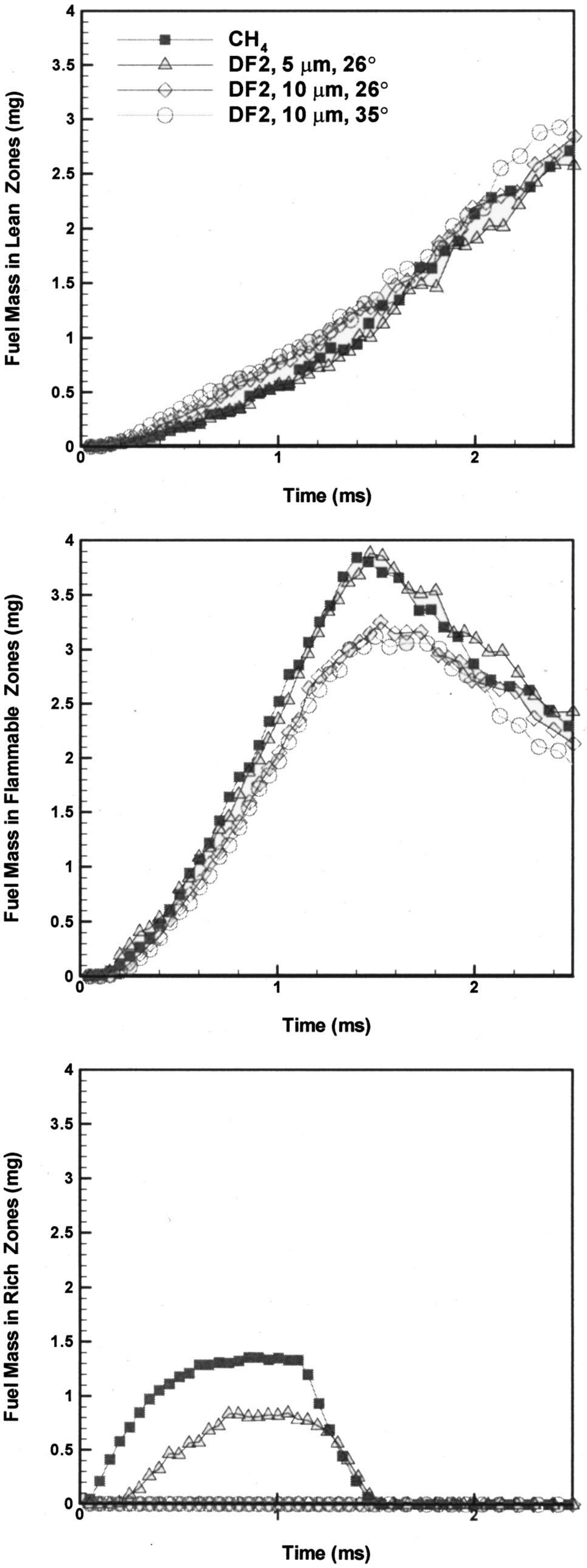

Fig. 15 Mixing rate of a gaseous jet and different sprays. Equivalence ratios of 0.5 and 2 were used to discriminate between lean, flammable and rich mixtures.

the air. Reducing the droplet size would most likely provide a mixing rate even closer to that of the gaseous jet. To simulate the effect of a different nozzle, the cone angle was changed to 35 deg with the main effect of broadening the spray while reducing its penetration. This was not found to affect the mixing significantly as shown in Fig. 15.

Thus numerical calculations indicate that for droplet sizes of the order of a few microns, and with injection into air of typical diesel chamber density, the penetration and mixing of sprays will be essentially the same as those of impulsively injected gaseous jets as long as the momentum injection rate is the same. For droplets of a few microns the spray cone angle specified in the simulation had apparently little effect on the calculated mixing rate.

It should be noted that, in practice, achieving the same momentum injection rate is not a major difficulty. The natural gas density at the nozzle may be 15–20 times less than that of diesel fuel, but this is easily compensated by using larger holes. Since the diesel holes are typically less than 0.15 mm, an area 15 times greater calls for holes of the order of 0.6 mm. Diesel fuel injection requires small holes to facilitate atomization, a requirement which is not existent for natural gas.

Conclusions

The following conclusions pertain to transient turbulent gas injections in quiescent chambers and issued from round nozzles with Reynolds number above 3×10^4 and which are possibly underexpanded.

- With small modification of coefficients, and small grid size near the nozzle, the k-ε turbulence model can correctly represent experimental data on jet penetration at distances greater than 10–20 diameters from the nozzle.
- Near grid independence requires spacing near the nozzle of the order of 1/4 of the nozzle diameter for two-dimensional axisymmetric flows. For three-dimensional simulations performed on a cylindrical coordinate mesh, a further requirement is that r-z planes be spaced at less than 2–3 degrees.
- The downstream penetration of underexpanded jets can be satisfactorily calculated with the use of a corrected nozzle diameter which provides the same momentum injection rate as the actual nozzle but at completed expansion to chamber pressure.
- With jet Reynolds number (based on nozzle exit velocity and diameter) greater than 10^5, increasing engine chamber turbulence intensity from 0 to 0.5 percent (ratio of fluctuation to nozzle exit velocity) affected the jet penetration rate only slightly.
- With constant rate of injection, the jet penetration is approximately independent of the injection duration for times less than twice the injection duration.
- Simulations and measurements show that wall contact affects the penetration rate of turbulent jets, with lower momentum jets being more sensitive. The scaling remained however largely valid in the region of interest for jets in contact with the wall for jets with higher momentum.
- Comparative numerical simulations of sprays and impulsively injected turbulent gas jets with the same momentum injection rate, same chamber air density and over the same grid configuration show that the penetration and mixing rates are closely similar as long as the spray droplets diameter is less than about 5 μm.

References

[1] Hodgins, K. B., Hill, P. G., Ouellette, P., and Hung, P., 1996, ''Directly Injected Natural Gas Fueling of Diesel Engines,'' SAE Paper 961671.
[2] Nylund, I., 1993, ''Latest Achievements in Gas Diesel Technology and the Experience from some Power Plant Operation,'' Transactions of the Institution of Diesel and Gas Turbine Engineers.
[3] Willi, M. L., and Richards, B. G., 1996, ''Design and Development of a Directly Injected Glow Plug Ignition Assisted, Natural Gas Engine,'' ASME, ICE-Vol. 22, p. 31.
[4] Meyers, D. P., Bourn, G. D., Hedrick, J. C., and Kubesh, J. T., 1997, ''Evalu-

ation of Six Natural Gas Combustion Systems for LNG Locomotive Applications,'' SAE 972967.
[5] Hill, P. G., and Ouellette, P., 1999, ''Transient Turbulent Gaseous Fuel Jets for Diesel Engines,'' ASME J. Fluids Eng., **121**, pp. 93–101.
[6] Miyake, M., Biwa, T., Endoh, Y., Shimotsu, M., Murakami, S., and Komoda, T., 1983, ''The Development of High-Output, Highly Efficient Gas Burning Diesel Engines,'' CIMAC Paper D11.2.
[7] Chepakovich, A., 1993, ''Visualization of Transient Single- and Two-Phase Jets Created by Diesel Engine Injectors,'' M.A.Sc. thesis, University of British Columbia.
[8] Ouellette, P., 1996, ''Direct Injection of Natural Gas for Diesel Engine Fueling,'' Ph.D. thesis, Department of Mechanical Engineering, University of British Columbia.
[9] Rizk, W., 1958, ''Experimental studies of the mixing process and flow configurations in two-cycle engine scavenging,'' Proc. I. Mech., **17**, pp. 417–424.
[10] Ricou, F. P., and Spalding, D. B., 1961, ''Measurements of entrainment by axisymmetrical turbulent jets,'' J. Fluid Mech., , **11**, pp. 21–32.
[11] Witze, P., 1980, ''The Impulsively Started Incompressible Turbulent Jet,'' SAND80-8617, pp. 3–15.
[12] Abraham, J., Magi, V., MacInnes, J., and Bracco, F. V., 1994, ''Gas versus Spray Injection: Which Mixes Faster?'' SAE Paper 940895.
[13] Kuo, T. W., and Bracco, F. V., 1982, ''On the Scaling of Transient Laminar, Turbulent, and Spray Jets,'' Society of Automotive Engineers, SAE Paper 820038.
[14] Gaillard, P., 1984, ''Multidimensional Numerical Study of the Mixing of an Unsteady Gaseous Fuel Jet with Air in Free and Confined Situations,'' SAE Paper 840225.
[15] Malin, M. R., 1989, ''Modelling the Effects of Lateral Divergence on Radially Spreading Jets,'' Comput. Fluids, **17**, No. 3, pp. 453–465.
[16] Hanjalic, K., and Laundner, B. E., 1980, ''Sensitizing the Dissipation Equation to Irrotational Strains,'' Trans. ASME, **102**, p. 34.
[17] Pope, S. B., 1978, ''An Explanation of the Turbulent Round-Jet/Plane-Jet Anomaly,'' AIAA J., **16**, No. 3, p. 279.
[18] Abraham, J., 1996, ''Entrainment Characteristics of Transient Gas Jets,'' Numer. Heat Transfer, Part A, **30**, pp. 347–364.
[19] Johnson, N. L., Amsden, A. A., Naber, J. D., and Siebers, D. L., 1995, ''Three-Dimensional Computer Modeling of Hydrogen Injection and Combustion,'' Los Alamos Report LA-UR-95-210.
[20] Amsden, A. A., O'Rourke, P. J., and Butler, T. D., 1989, ''KIVA-II: A Computer Program for Chemically Reactive Flows with Sprays,'' Los Alamos report LA-11560-MS.
[21] Zhang, J., Fraser, R. A., and Strong, A. B., 1994, ''Modelling Diesel Engine Natural Gas Injection: Injector/Cylinder Boundary Conditions,'' SAE Paper 940329.
[22] MacInnes, J. M., and Bracco, F. V., 1990, ''Computation of the Spray from an Air-Assisted Fuel Injector,'' SAE Paper 902079.
[23] Ewan, B. C. R., and Moodie, K., 1986, ''Structure and Velocity Measurements in Underexpanded Jets,'' Combust. Sci. Technol., **45**, pp. 275–288.
[24] Ouellette, P., Mtui, P. L., and Hill, P. G., 1998, ''Numerical Simulations of Directly Injected Natural Gas and Pilot Diesel Fuel in a Two-Stroke Compression Ignition Engine,'' SAE Paper 981400.
[25] Heywood, J. B., 1988, *Internal Combustion Engine Fundamentals*, McGraw-Hill, New York.
[26] Abraham, J., 1997, ''What is Adequate Resolution in the Numerical Computations of Transient Jets?'' SAE Paper 970051.

Discussion: ''Turbulent Gas Injections'' (Ouellette, P., and Hill, P. G., 2000, ASME J. Fluids Eng., 122, pp. 743–752)

John Abraham
School of Mechanical Engineering, Purdue University,
West Layfayette, IN 47907

It has been established during the last 2–3 years that spray computations that employ the Lagrangian-Drop-Eulerian-Fluid (LDEF) model, as in KIVA-II, do not show grid independence (Abraham [1], Iyer and Abraham [2], Aneja and Abraham [3], Subramaniam [4]). This difficulty arises, in part, because the LDEF approach assumes that the droplets are uniformly distributed in the computational cells where droplets are present. In representing a Diesel spray, this assumption is rarely valid. The droplets stay close to the axis of the spray (Aneja and Abraham [1], Siebers [5]), where typical numerical cells sizes are limited to a minimum value of about twice the orifice diameter. Such grids do not resolve the core region of the spray near the orifice. As explained by Aneja and Abraham [2], this would imply that as the grid resolution is changed, the number density and, hence, the collision frequency and the coalescence rate of the drops would show dramatic changes. This effect is seen for all drop sizes. Furthermore, it has been shown that for transient gas jets and sprays, when relatively coarse grid resolution is employed, typically where the grid size is greater than the radius of the orifice, the computed results become very sensitive to the specified initial values of k and ε (Abraham [1], Iyer and Abraham [2]). In the case of gas jets, it is possible to employ relatively high resolution as the authors have done in this paper but not for sprays. The result is that one can get arbitrary results for sprays, dependent on the selection of grid resolution and on the specification of initial values of k and ε. Hence, computational approaches that compare spread rates or penetration of gas jets and sprays, using the LDEF approach, are not meaningful. It may be possible to compare computed gas jets, where adequate resolution can be employed, with measured sprays, when the same mass and momentum flow rates are used for the two. This has been reported by Iyer and Abraham [2] and it has been shown that they penetrate at about the same rate under Diesel conditions. Ultimately, even for gas jets there are challenges in reproducing the spreading rates with the standard k-ε model constants. Pope [6] reported a spreading rate value of 0.125. The authors report a value of 0.1. Pope [6] modified the k-ε model constants to obtain a spreading rate of 0.09. The authors employed these modified constants. However, since the spreading rate was 0.1 prior to changing the constants, whereas it was 0.125 for Pope [6], it is possible that the modified constants may reduce the spreading rate to values less than the desired 0.085−0.09. The value of 0.1 obtained in the computations by the authors when employing the standard model constants, rather the value of about 0.12 generally reported for round jets (Wilcox [7]), is also likely to be an indication of inadequate grid resolution even in the gas jet computations. Conclusions that may be drawn from such computations would have to be qualitative and problem dependent.

References

[1] Abraham, J., 1997, ''What is Adequate Resolution in the Numerical Computations of Transient Jets?'' SAE Trans., **106**, No. 3, pp. 141–155.
[2] Iyer, V., and Abraham, J., 1997, ''Penetration and Dispersion of Transient Gas Jets and Sprays,'' Combust. Sci. Tech., **130**, pp. 315–334.
[3] Aneja, R., and Abraham, J., 1998, ''How Far Does the Liquid Penetrate in a Diesel Engine: Computed Results vs. Measurements?'' Combust. Sci. Tech., **138**, pp. 233–255.
[4] Subramaniam, S., 1999, ''Statistical Representation and Modeling of Sprays: II The Droplet Distribution Function,'' Los Alamos Laboratory Report, LA-UR-99-3665.
[5] Siebers, D. L., 1998, ''Liquid-Phase Fuel Penetration in Diesel Sprays,'' SAE Paper No. 980809.
[6] Pope, S. B., 1978, ''An Explanation of the Turbulent Round-Jet/Plane-Jet Anomaly,'' Technical Note, AIAA J., **16**, No. 3, p. 279.
[7] Wilcox, D. C., 1994, *Turbulence Modeling for CFD*, DCW Industries, La Cañada, CA.

Closure to ''Discussion of 'Turbulent Gas Injections' '' (2000, ASME J. Fluids Eng., 122, p. 752)

P. Ouellette and P. G. Hill

The authors thank Professor Abraham for his discussion of numerical problems in simulating jets and sprays using the KIVA code with the k-ε turbulence model. On the issue of predictinggas jets with the k-ε model, we seem to be in agreement with Prof. Abraham in noting the difficulty of identifying better k-ε constants independently from the details of the mesh. New k-ε constants are needed to alleviate the limitations associated with the isotropy assumption. Given this difficulty, it appears our results are very much in line with the work of other authors (as seen in the literature and in Prof. Abraham's discussion) and are in good agreement with reported steady-state jet spreading. Our computed transient jet penetrations with the modified k-ε constants are also in good accord with experimental measurements of transient gas jets. We feel our results not only add to this knowledge but also provide other insights not previously reported, such as 1) the equal if not greater importance of the size of the cells adjacent to the nozzle over that of the nozzle cells themselves; 2) the agreement of the simulations with the experimentally determined penetration constant for gas jets; 3) the numerical treatment of underexpansion; 4) the effect of limited jet injection period and 5) the possible impact of injection adjacent to a wall.

On the issue of whether sprays can be successfully represented by the model used in KIVA-II, we appreciate Prof. Abraham's point that there are difficulties additional to the problem of grid sensitivity. We recognize that similarity assumptions applicable to transient gas jets cannot be transferred to coarse sprays. It is clear that, in general, transient spray penetrations depend not only on time and the ratio of nozzle exit momentum to chamber density, but also on liquid droplet size, vaporization parameters and possibly other variables. Large droplets must affect turbulence levels and spreading rates. However it is not unreasonable to suppose that gas jets and sprays with vanishingly small droplet size should display similar dynamic behavior, In their discussion of sprays, we had no intention of treating the general behavior of real and computed sprays, but focused solely on the question of whether with very small droplet size the penetration and mixing of sprays and gas jets are similar for given ratio of nozzle exit momentum to chamber density. Numerical analysis using the KIVA code with the adjusted k-ε turbulence model and the properties of a typical diesel spray indicates that this similarity of behavior is obtained as long as mean droplet diameter is less than about 5μ. This finding has not yet, to our knowledge, been verified experimentally.

Y. Murai
Research Associate,
Department of Mechanical Engineering,
Fukui University,
Bunkyo 3-9-1, Fukui 910-8507, Japan
e-mail: murai@fv.mech.fukui-u.ac.jp

Y. Matsumoto
Professor,
Department of Mechanical Engineering,
The University of Tokyo,
Hongo 7-3-1, Bunkyo-ku, Tokyo
113-8654, Japan

Numerical Study of the Three-Dimensional Structure of a Bubble Plume

The whole behavior and the micro scale flow characteristics of a three-dimensional bubble plume are investigated numerically. The bubble plume drives liquid convection in a tank due to strong local two-phase interaction so that the Eulerian-Lagrangian model is formulated with emphasis on the translational motions of the bubble. In this model, each bubble motion is tracked in a bubbly mixture which is treated as a continuum. The three-dimensional numerical results reveal several particular structures, such as swaying and swirling structures of the bubble plume. These simulated flow structures show qualitatively good agreement with the experimental observations. Furthermore, the detailed behavior in the bubble plume is clarified by various analysis to discuss the dominant factors causing such the strong three-dimensionality. [S0098-2202(00)00904-4]

1 Introduction

A variety of flow structures come out in bubbly two-phase flows owing to the strong interaction between two phases and the complexities of the translational motion of a bubble. Performance of various industrial systems, such as chemical plants, nuclear power plants, and bioreactors are consequently dominated by the two-phase flow pattern. A great number of numerical investigations to establish the prediction tool for two-phase flow was done, especially for nuclear engineering research by Wijngaaden [1], Ransom [2], and Liles [3]. Their basic equations were constructed for simulating one-dimensional flows based on two fluid formulation model, i.e., two-fluid model. In the last ten years, the construction of governing equations to be applied for the multi-dimensional prediction were advanced as reported by Kataoka and Serizawa [4], Stewart and Crowe [5], and Zhang and Prosperetti [6]. However, the modeling of multi-dimensional phase interaction is still roughly treated, such as partial empirical formulation and over-ranged extrapolation. On the other hand, further microscopic simulation techniques were recently proposed by developing a new numerical method for free surface, such as Unverdi and Tryggvason [7]. Their direct numerical simulations showed a great possibility for further accurate modeling for phase interaction terms. The ''inverse energy cascade'' in a bubbly flow which is discussed based on the DNS by Esmaeeli and Tryggvason [8] indicated the importance in the simulation method for fine scale flows.

With this viewpoint, the Eulerian-Lagrangian model (hereafter, E-L Model) has much better potential to solve the detailed flow structure than the Eulerian-Eulerian models (Murai and Matsumoto [9], Druzhinin and Elghobashi [10]). The latter model moreover cannot provide correct solution for some cases that the dispersion phase does not have enough number density and spatial continuity. Therefore, the E-L model has the following advantages in principle. (1) Lagrangian description of each bubble motion has much higher spatial resolution than the Eulerian description, (2) the E-L model can treat exactly the deviation of bubble size without increasing computer's memory, (3) bubble-bubble interaction for dense cases can be treated by constructing some models, (4) boundary conditions of the bubbles at wall, free surface, and bubble injection part can be exactly expressed. In addition, equation of motion for the bubble is easily revised and examined by referring recent new information for bubble dynamics. For instance, the experiments reported by Hassan and Canaan [11], Sridhar and Katz [12], are available. Many theoretical works on the force components can also be useful, such as Ruetsch and Meiburg [13] and summarized paper of Michaelides [14].

In this study, the E-L model is applied for predicting a three-dimensional bubble plume. Controlling the bubble plume is known to be very difficult due to its strong unsteady two-phase interaction as reported by many experimental researchers (Rietema and Ottengraf [15], Hussain and Siegel [16], McDougall [17], Alam and Arakeri [18], and Iguchi et al. [19]). Measuring the liquid flow induced by the interaction is still important work as done by Leitch and Baines [20] and Gross and Kuhlman [21]. The fundamental mechanism of driving the liquid flow due to buoyant bubbles is estimated by the wake of single bubble (Bhaga and Weber [22]). While the liquid flow rate can be approximately estimated by integrating the flow generated by the single bubble, it does not agree with the integrated value when high void fraction is supplied. The reason is the energy dissipation owing to the three-dimensional structurization. The performance of substance mixing, phase separation, and chemical reaction are significantly affected by the three-dimensionality. The authors have shown its two-dimensional flow in a previous paper (Murai and Matsumoto [23]). In the present paper, its three-dimensional flow structures are shown. Detailed correlations between the motion of rising bubbles and spatial development of the liquid flow inside the bubble plume are discussed.

2 Governing Equations

The present governing equations for bubble flow are described by the Eulerian form equations for continuous phase and the Lagrangian form equations for disperse phase. The following assumptions are employed for the construction of the present set of equations: (1) Bubble size is smaller than the characteristic length of the flow. Local bubble motion in a control-volume is described by the volumetric and translational motion equations. (2) Coalescence and fragmentation of the bubbles are neglected since void fraction in the bubbly flow is less than 0.1 for the present simulation. (3) Local bubble-bubble interaction owing to the liquid flow near the bubble interface is neglected. (4) Gas inside the bubble is noncondensable and obeys the perfect gas law. Also, there is no mass diffusion of gas near bubble interface. Therefore, the amount of gas inside the bubble is constant.

Contributed by the Fluids Engineering Division for publication in the JOURNAL OF FLUIDS ENGINEERING. Manuscript received by the Fluids Engineering Division April 22, 1999; revised manuscript received June 20, 2000. Associate Technical Editor: M. Sommerfeld.

- **Gas Volume Fraction**

$$f_G=\frac{1}{V}\int_V f dV, \quad f_L=1-f_G, \tag{1}$$

here, f_G and f_L are the gas and liquid volume fractions. The kernel f is the phase indicator, i.e., $f=1$ in gas phase and $f=0$ in liquid phase. V is an averaging volume. The Lagrangian variables for gas phase is expressed by subscript k indicating each label number.

- **Equilibrium Equation of Bubble Volume**

$$p_{G0k}V_{G0k}=(p_L-C_p\rho_L|u_{Sk}|^2)V_{Gk}, \quad u_{Sk}=u_{Gk}-u_{Lk}, \tag{2}$$

here, suffix 0 indicates standard condition of gas. p_G and V_G are the pressure and the volume of the bubble. The inertial oscillation of bubble volume, which was known as Rayleigh-Plesset equations (e.g., Plesset and Prosperetti [24]) is not considered here because its time scale is enough short that it does not contribute to the whole flow structure. The viscosity of ambient liquid does not affect directly the volume change while the slip velocity of the bubble against the liquid reduces the mean pressure on the bubble interface. In Eq. (2), C_p is the pressure coefficient for a spherical bubble, which is analytically given by 1/4 according to Euler's equation. Incidentally, C_p becomes smaller in case of low Reynolds number, and $C_p=0$ for Stokes flow.

- **Conservation Equation of Liquid Mass**

$$\frac{\partial f_L\rho_L}{\partial t}+\nabla\cdot f_L\rho_L u_L=0, \rightarrow \frac{\partial f_l}{\partial t}+\nabla\cdot f_L u_L=0, \tag{3}$$

- **Conservation Equation of Total Momentum**

$$\begin{aligned}&\frac{\partial f_L\rho_L u_L}{\partial t}+\nabla\cdot(f_L\rho_L u_L u_L)+\frac{\partial f_{Gk}\rho_{Gk}u_{Gk}}{\partial t}+\nabla\cdot(f_{Gk}\rho_{Gk}u_{Gk}u_{Gk})\\ &\quad=-\nabla p-(f_L\rho_L+f_G\rho_G)g\\ &\qquad+\nabla\cdot(1+f_G)\mu_L\left\{\nabla u_L+(\nabla u_L)^T-\frac{2}{3}(\nabla\cdot u_L)I\right\}\end{aligned} \tag{4}$$

here μ_L is viscosity of liquid, g is the gravitational acceleration. The right-hand side of Eq. (4) is derived by summing the external force components for both phases. Therefore, momentum exchange terms between the two phases are eliminated because of Newton's third law. The viscous term is modeled by using continuous phase component of velocity and the effective viscosity due to the presence of dispersed bubbles. The effective viscosity is given by Einstein's theoretical formula as written by Batchelor [25].

- **Translational Motion Equation of Bubble**

$$\begin{aligned}&\frac{d}{dt}\{(\rho_{Gk}+\beta\rho_L)V_{Gk}u_{Gk}\}-\frac{D_L}{Dt}(\beta\rho_L V_{Gk}u_L)\\ &\quad=V_{Gk}\left\{-\nabla p+\mu_L\left\{\nabla^2 u_L+\frac{1}{3}\nabla(\nabla\cdot u_L)\right\}\right\}\\ &\qquad-\frac{1}{2}\rho_L\pi r_{Gk}^2 C_D|u_{Sk}|u_{Sk}-C_L\rho_L V_{Gk}\\ &\qquad\times\{u_{Sk}\times(\nabla\times u_L)\}-\rho_G V_{Gk}g,\end{aligned} \tag{5}$$

Equation (5) consists of the following force components: self inertia force, added inertia force, pressure gradient force, viscous force, drag force, lift force, and gravity force. Here, the viscous force is necessary while it has been frequently neglected in conventional models. The reason can be explained by considering an example for a pipe flow in which a small liquid tracer particle is suspended. If the viscous term is neglected, the particle moves faster than the liquid due to the pressure gradient force, which is induced by wall friction. The correct response of the particle does not have such a slip velocity since pressure gradient force and the viscous force are balanced. In other words, the drag term expresses the viscous+pressure effects which are determined by the bubble-generated local flow in the vicinity of the bubble surface. On the contrary, the viscous flow term stands for the force coming from the shear stress in the circumferential liquid flow, which is not caused by the bubble.

History force like the Basset force for the bubble can be ignored because the shape of the bubble is almost spherical and there is little vorticity generation at the bubble interface. It is also the reason that the modeling of the actual history force on the bubble has not yet been generalized in the current state.

In Eq. (5), β is added mass coefficient for a spherical bubble, C_D is drag coefficient, C_L is lift force coefficient of Auton [26] or Auton et al. [27] and these are given by

$$C_D=\max\left\{\frac{48}{\mathrm{Re}}\left(1-\frac{2.21}{\sqrt{\mathrm{Re}}}\right),\frac{16}{\mathrm{Re}}\right\}, \quad \mathrm{Re}=\frac{2r_{Gk}\rho_L|u_{Sk}|}{\mu_L}, \tag{6}$$

$$\frac{D_L}{Dt}=\frac{\partial}{\partial t}+u_L\cdot\nabla, \quad C_L=\frac{1}{2}, \quad \beta=\frac{1}{2}, \tag{7}$$

here, the drag coefficient is given by combining Moore's and Stokes theoretical results (Moore [28]). These formulas approximate well the experimental result for a spherical gas bubble without surfactant when the bubble Reynolds number is smaller than 200.

- **Tracking Equation of Bubble Position**

$$X_{Gk}(t)=X_{G0k}+\int_0^t u_{Gk}(t)dt, \tag{8}$$

here X_{G0k} is the initial position vector of the bubble.

3 Numerical Method

The set of governing equations are solved by a semi-implicit method based on the HSMAC algorithm (Hirt and Cook [29]) for incompressible viscous flow. The original HSMAC method is extended to the bubbly two-phase flow analysis using the following equation for pressure correction.

$$\delta p=\omega\varepsilon\Big/\left(\frac{\partial\varepsilon}{\partial p}\right), \quad \frac{\partial\varepsilon}{\partial p}=2\rho_L\delta t^2\left(\frac{1}{\delta x^2}+\frac{1}{\delta y^2}+\frac{1}{\delta z^2}\right)+\frac{f_G\rho_L}{p}, \tag{9}$$

where ω is a relaxation coefficient. ε is the over-estimated volume fraction given by f_L+f_G-1. δt and δx are the time step and the spatial interval for discretizing the governing equations. The derivative of ε with respect to p is derived by coupling the differentiated equations of Eqs. (2), (3), and (4).

By using this equation, the bubble-containing region and non-bubble region can be simultaneously solved provided that an adequate under-relaxation coefficient ω is adopted. Using the HSMAC algorithm makes it quite easy to develop a compact simulation code. The present numerical procedure is constructed as follows.

1. Calculate new translational velocity of bubble by Eqs. (5), (6), and (7)
2. Calculate new weight center coordinates of bubbles by using the translational velocity by Eq. (8)
3. Calculate new liquid velocity by Eq. (4)
4. Calculate new bubble volume by Eq. (2)
5. Calculate new gas volume fraction by Eq. (1)
6. Calculate new liquid volume fraction by Eq. (3)
7. Calculate the over-estimated volume fraction and pressure correction value which are described by Eq. (9)

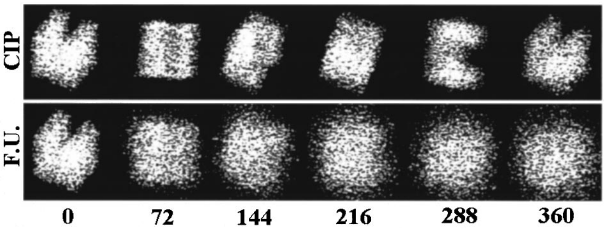

Fig. 1 Restriction of numerical diffusion by CIP scheme

8 Go to the next time step if the over-estimated volume fraction is converged enough to zero.

Using these procedures, not only the large scale interaction between two phases, but also a micro scale fluctuation can be validly simulated. A component for pseudo turbulence (Lance and Bataille [30]) is also calculated by the following numerical process: (1) a bubble with volume V enters into a grid, ε becomes positive value due to increase of the void fraction α in the grid, (2) the pressure in the grid increases according to Eq. (9), liquid flow accelerates in the outer direction from the grid due to the pressure gradient against the surrounding grids, (3) when the bubble goes out of the grid, the inverse phenomenon happens.

The mapping method of physical variables between Eulerian and Lagrangian phases is as follows. Liquid velocity component around a bubble is calculated by second-order interpolation using the data of surrounding grids. The velocity gradient tensor needed for solving Eq. (5) is given by this interpolated profile. Pressure gradient is given by differential pressure between two grids surrounding the bubble. The effect of the bubble on the liquid flow is reflected in each grid by variation of the local void fraction. The maximum time step is determined by the CFL conditions for advection terms: $\delta t < \delta x / U_L$ (here, U_L is maximum liquid velocity), and viscosity stability: $\delta t < \delta x^2 (2 v)^{-1}$ (here, v is kinematic viscosity of liquid phase) the same as conventional explicit-type solvers. In the present study, the tolerated value of ε, and the relaxation coefficient ω are set 10^{-6} and 0.95, respectively. The differencing schemes for convective terms are mentioned in the next section.

High Resolution Scheme. In the conventional numerical analysis for two-phase flow, numerical viscosity is frequently added in the discretized equations in order to restrict the numerical instability which is caused by strong nonlinearity of the system equations. However, the numerical diffusion is serious for the prediction of flow instability and micro scale flow. The CIP (Cubic Interpolated Propagation) scheme (Takewaki and Yabe [31]) is applied in the present analysis for liquid phase advection terms, and has been confirmed to have almost no numerical diffusion. For instance, the performance of the CIP scheme is shown in Fig. 1. Here, a scalar distribution whose initial shape is like ''U'' is rotated in three-dimensional space by using an advection equation without any diffusion term. The number of grids used is $20\times 20 \times 20$. It is confirmed with the results that the CIP keeps the initial shape clearly after one rotation while the first order upwind difference (F.U.) obtains a diffused one. Moreover, it is known that the CIP does not produce any numerical oscillation because the spatial gradient of the variable is also tracked by the third-order spline function. Consequently, it is one of the most suitable schemes, for convective terms to simulate the local unsteady 3-D structure of the bubble plume.

4 Three-Dimensional Behavior

The three-dimensional two phase flow structure of a bubble plume is numerically simulated. A rectangular tank is employed as a boundary of the flow because of the convenience in finite difference method using Cartesian coordinates and experimental visualization. The simulation conditions are summarized in Table 1. Added pressure on the upper free surface is set to 101.3 kPa. 10 percent of standard deviation for bubble radius is taken into account by Gaussian distribution according to the experimental results. Non-slip and free-slip conditions are adopted to the wall boundary and the top free surface boundary conditions, respectively.

Table 1 Simulation conditions

Liquid density $\rho_L = 960$ kg/m^3	Height of liquid $H = 0.400$ m
Gas density $\rho_G = 1.2$ kg/m^3	Bubble injection area 25×25 mm^2
Tank size (horizontal) $L = 0.1$ m	Bubble injection part=bottom
Total liquid volume=0.004 m^3	Number of needles $5\times 5 = 25$
Kinematic viscosity of liquid $v_L = 5\times 10^{-6}$ m^2/s	
Void fraction at bubble injector α=0.01 to 0.10	
Grid division number for Euler phase=$40\times 40\times 160 = 256{,}000$	

Figure 2 shows the starting structure of bubble plume. Bubbles accumulate into the core of a starting ring vortex in the case of a small bubble. More diffused structure appears in a large bubble case due to larger rising velocity of the bubble than the vortex-rising velocity. As the flow develops, a thin bubble plume with high number density near the axis is generated in the case of small bubble due to surrounding entrainment flow. A three-dimensional meandering phenomenon appears owing to the increase of buoyancy gradient and strong vorticity generation beside the bubble plume. This phenomenon is considered to be the three-dimensional case of the sinuous instability (Alam and Arakeri [18]).

Figure 3 represents the numerical results and experimental photograph in the case of $R = 1.0$ mm. The experiment is done by stereo-photographing using a mirror. The bubble plume is straight for large bubble case but has a swirling structure for high void fraction case. Simulated results have qualitatively good analogy with the photographs. Here, the bubble distribution itself is not changed by using a more rough grid resolution ($20\times 20\times 80$), so that the numerical convergence is confirmed. Strictly speaking, the grid resolution is limited in the E-L model because of limited spatial resolution of averaged equations. The authors' idea is that the ratio of the grid volume to the bubble volume must be larger

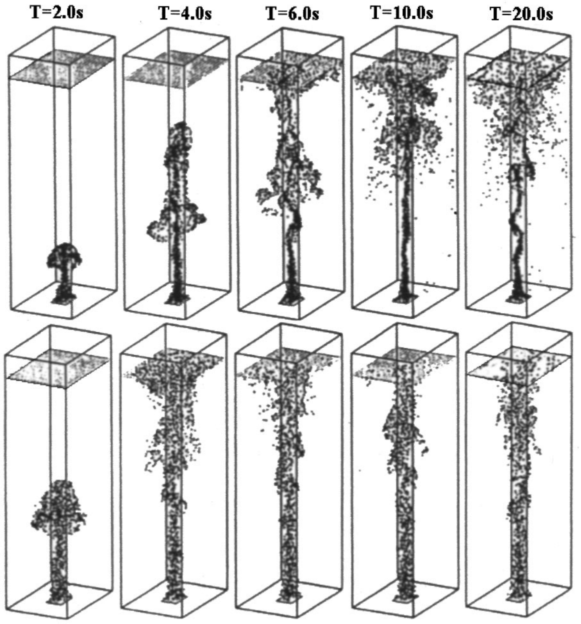

Fig. 2 Starting structures of bubble plumes (top: $R = 0.2$ mm, bottom: $R = 0.5$ mm)

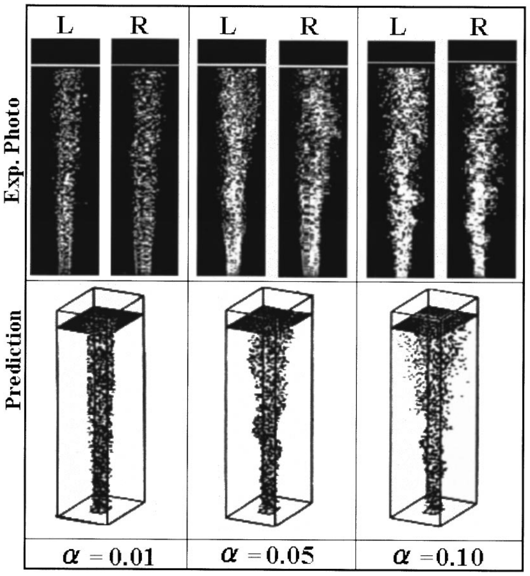

Fig. 3 Three-dimensional behavior of bubble plume (prediction and experiment)

than 10. For instance, the liquid flow in the vicinity of the bubble surface cannot be simulated even if further small grid is adopted.

Figure 4 shows the structure of the bubble plume which is represented by center of gravity of the bubbles. The center of gravity is calculated by averaging the *x-y* coordinates of the bubbles, which belong to each control volume with a thickness of 20 mm in vertical direction. The bottom side in Fig. 4 shows the top view of the center of gravity. Two experimental results are also inserted in Fig. 4. The experimental data are obtained by 3-D image processing. The following matters are recognized by these results: (1) width of the swirling structure expands with increase of the void fraction, (2) wave number of the swirling structure in the vertical direction seems to range from 3–5, (3) radius and orientation of the swirl changes locally, (4) the orders of the width, the wavenumber, and the complexity of the swirling structures in simulated results correspond well with the experimental results.

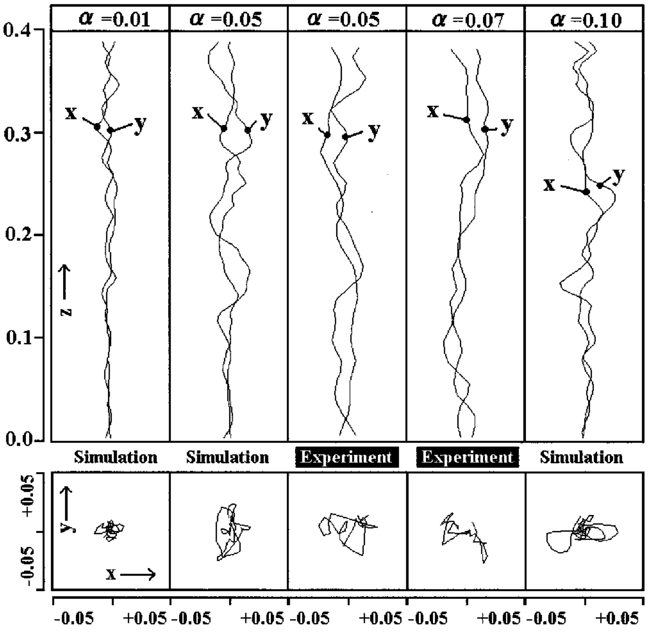

Fig. 4 Instantaneous structure of center of gravity of the bubble plume (simulation and experiment): measurement uncertainty is estimated 0.01 m due to accuracy of image processing

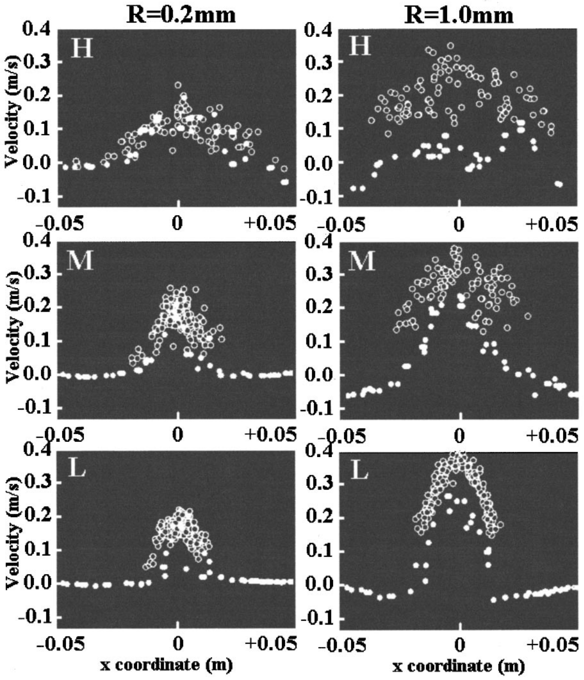

Fig. 5 Rising velocity profile of two phases in the bubble plume (open circle: bubble, closed circle: particle)

The mechanism of generating the swirling structures is not easy to explain. At least, the dynamic stability of the swirling state can be related to the following matters: (1) the trigger of the swirling motion comes from the asymmetric component of liquid in-flow to the bubble injection area, whose mechanism partially resembles a tornado (Snow et al. [32]), (2) static pressure is lower inside the bubble plume than surrounding region. This pressure distribution aligns with the pressure decrease of the core region due to the swirling flow, (3) the flow induced by the bubble plume is a kind of natural convection so that the steady flow pattern is determined by balancing the buoyancy supply and the momentum dissipation due to viscosity. The generation of swirling structure is one balancing mechanism against the increase of buoyancy supply. Furthermore, as mentioned in the later section, the characteristics of bubble's translational motion can also be the factor to intensify the swirling motion because of its very small inertial response time.

5 Features of Bubble-Generated Turbulence

Bubble Rising Velocity Profile. Figure 5 shows the simulated distribution of vertical velocity component of the bubble (drawn by open circles) and the tracer particles (drawn by closed circles) in three horizontal cross sections—0.100 m (l), 0.225 m (M), and 0.350 m (H) from the bottom plane. Here, two different conditions in bubble radius are compared. The following matters are recognized by these results. (1) The bubble rising velocity profiles are almost parabolic like laminar flows at position *L* for both conditions. (2) Since the terminal slip velocities of the bubble in quiescent liquid are estimated 0.015 m/s for $R=0.2$ mm, and 0.138 m/s for $R=1.0$ mm, it can be said that the maximum rising velocities in the bubble plume are much larger than them. (3) In the case of $R=0.2$ mm, the liquid velocity profile corresponds well with the bubble velocity profile. On the contrary,

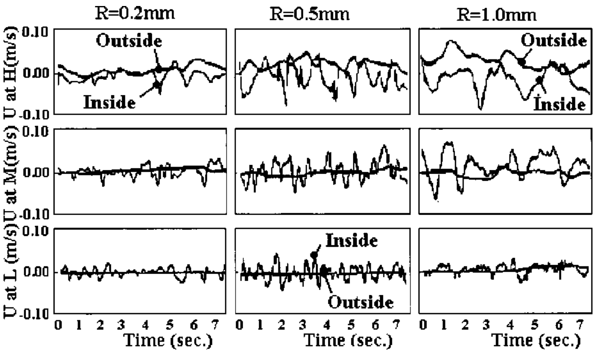

Fig. 6 Liquid velocity wave form (thick=outside, thin=inside the bubble plume)

that $R=1.0$ mm is slower than the bubble velocity. The resultant maximum liquid velocity at the position H in the case of $R=1.0$ mm is smaller than that in the case of $R=0.2$ mm. (4) The bubble rising velocity has a large deviation like turbulent flows at the position H for both cases. However, this fluctuation is not caused by ''true'' turbulence but caused by nonuniformity of the bubble number density which supplies the momentum in liquid phase. The bubble number density is governed by the motion characteristics of bubbles, so that it can be considered that the feature of the turbulent-like fluctuation is essentially different from single-phase turbulent shear flow as well as single-phase thermal plume.

Liquid Velocity Waveform. Figure 6 shows time serial wave form of the liquid phase velocity (U) inside and outside the bubble plume. The thin lines and thick lines denote the ones obtained at the two-phase region on the center position of the tank, and at the liquid single phase region on the position which is 20 mm from the tank side wall. Index L, M, and H are the measurement positions the same as Fig. 5. The following interesting matters are recognized. (1) A large fluctuation is found in the case of large bubble more than in the case of small bubble. (2) In the case of large bubble, the fluctuation frequency reduces owing to, maybe, the two-way interaction effect in which the large bubbles elongate the liquid vortices in the vertical direction. (3) Also, in the large bubble case, a very high frequency component in the liquid velocity wave form is detected. This appears because a disturbance flow is induced by the migration of a large bubble which has a large slip velocity.

Here, the high frequency component in factor (3) is of course not numerical order but a partial component of so-called pseudo turbulence (Lance and Bataille [30]). This is because the exact two-way interaction for volume or kinematic condition, which is expressed by Eq. (3), is calculated. However, the bubble-induced turbulence due to the momentum transportation through the bubble interface is not taken into account in the present governing equations. Therefore, the presently obtained component must be recognized as the ''kinematic'' pseudo turbulence. Furthermore, the calculated amplitude depends on the grid volume, because liquid velocity is defined by spatial averaged value in the grid volume.

By adapting the Eulerian-Lagrangian model, a partial component of pseudo turbulence can be detected according to the setting grid volume. This kinematic component (or velocity potential component) is estimated to have a great effect on the local pressure field beyond the grid, because the pressure fluctuation is not dissipated locally. Also, it can be an important trigger of the turbulent flow transition in bubbly flows. In the near future, the momentum transportation component of the bubble-induced turbulence is expected to be modeled and introduced to the present model.

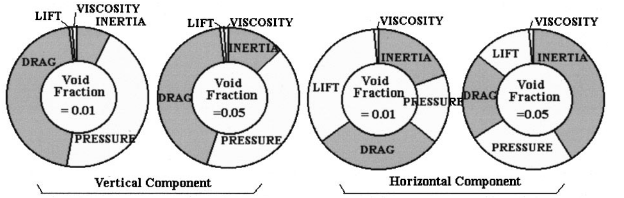

Fig. 7 Force component ratio of bubbles in the bubble plume (INERTIA=inertia+added inertia, PRESSURE=pressure gradient force, DRAG=drag, LIFT=lift, VISCOSITY=viscous stress from liquid flow)

6 Statistics of Bubble Motion

Force Components of Bubble. The force components of bubble in each direction of the bubble plume is represented in Fig. 7. This diagram is made by statistical averaging for over 30 seconds, which is long enough. In this figure, ''inertia'' means the sum of self and added inertia forces. In the vertical direction, drag and pressure forces are dominant factors. This indicates that the bubbles rise with a speed close to their terminal slip velocity. Only about 10 percent of the component is contributed by other transient force components. In the horizontal directions, four components, i.e., inertia force, pressure gradient force, drag force, and lift force are balanced at almost the same order. This indicates that the horizontal motion of the bubble is not so simple compared to that in the vertical direction. This component rate means that the translational motion of bubble depends on the surrounding liquid flow which has nonuniform velocity field with transiency. Although it has been frequently reported that the lift force of bubble is the most significant factor in multi-dimensional bubbly flow, we have to conclude that every factor of force component is important when liquid flow includes micro scale fluctuation like turbulent fluctuation.

On the Bubble-Bubble Interaction. In actual bubbly flows, the bubble-bubble interaction due to the liquid flow in the vicinity of the bubble interface is important for dense cases. However, its effect is neglected as mentioned in assumption (3) because of the following three reasons. (1) The flow field around the bubble can be considered as a fluid sphere in case of using silicone oil. Therefore, the bubble-bubble interaction is not so drastic compared to that for contaminated bubbles or solid particles. (2) The modeling methodology for the bubble-bubble interaction has not been established yet, especially for a middle Reynolds number bubble (i.e., 10 to 200). (3) The interaction between the flow around the bubble and the turbulence in surrounding liquid is quite complex.

These problems are to be set as future targets for the E-L model.

Frequency Response of Bubble. Frequency response of the translational motion of a bubble is studied analytically to clarify its traceability to the turbulent fluctuation in liquid phase. For easy understanding, here, let us consider the one-dimensional translational motion of single bubble which has no volume change in liquid single phase medium. The equation is given by

$$(\beta+\gamma)\frac{dU_G}{dt}-(1+\beta)\left(\frac{\partial}{\partial t}+U_L\frac{\partial}{\partial x}\right)U_L + \frac{3}{8}\frac{C_D}{R_G}|U_G-U_L|(U_G-U_L)=0, \qquad (10)$$

here β is added mass coefficient, γ is mass density ratio given by ρ_G/ρ_L. The drag coefficient C_D for bubble is given by $C_D=A/\mathrm{Re}$ since bubble Reynolds number Re is considered to be small. Here, A is constant in Stokes' formula. This equation can be easily derived from Eq. (5) by substituting the above defini-

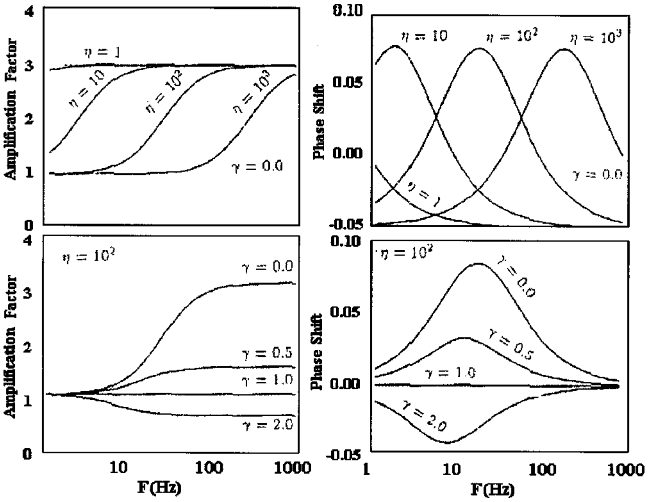

Fig. 8 Frequency response characteristics of a spherical bubble (γ=density ratio of dispersion against continuous phase, η=viscosity factor)

tions, and $V_G=\text{const}$, $r_G=R_G$, $u_L=(U_L,0,0)^T$, $u_G=(U_{\_}G,0,0)^T$, and the next relation between surface force and inertial force

$$-\nabla p+\mu_L\left\{\nabla^2 u_L+\frac{1}{3}\nabla(\nabla\cdot u_L)\right\}\rightarrow\frac{D_L u_L}{Dt}. \tag{11}$$

This relation is the Navier-Stokes equation and exact relation if the surrounding space of the single bubble is liquid single phase. As the spatial gradient of U_L is zero, Eq. (11) becomes linear equation. When periodic flow of liquid phase with frequency ω, $u_L=\sin(\omega t)$ is given, the bubble must also have periodic fluctuation; $u_G=\alpha\,\sin(\omega t+\varphi)$. Then amplification factor α and phase shift φ are derived as the following formula

$$\alpha=\sqrt{1+2\theta\,\cos(\phi)+\theta^2},\quad \theta=\frac{(1-\gamma)\omega}{\sqrt{(\beta+\gamma)^2\omega^2+\eta^2}}, \tag{12}$$

$$\tan(\phi)=\frac{\theta\,\sin(\varepsilon)}{1+\theta\cos(\varepsilon)},\quad \tan(\varepsilon)=\frac{\eta}{(\beta+\gamma)\omega},\quad \eta=\frac{3A\mu_L}{16\rho_L R_G^2}. \tag{13}$$

From this result, as shown in Fig. 8, the following matters are made clear. (1) Amplification factor α for bubble (γ=0) becomes 3.0 in the case of high frequency. (2) α for heavy particle (γ>1) decreases in the case of high frequency. (3) Bubble has a phase lead (φ>0) and heavy particle has a phase lag (φ<0). Their phase shifts have a maximum value at a particular frequency. This frequency becomes low as the dumping factor η is small. These tendencies of the translational motion of the bubble are very important in discussing the behavior of bubbles in bubbly flow with large fluctuation like turbulent flows.

To evaluate the actual response of the bubble in the bubble plume, the relation among η, α, φ, and the actual period of liquid fluctuation is shown in Table 2, where the actual period of velocity fluctuation in water or Silicone oil (5cSt in kinematic viscosity) is represented in the right side for the case of 1.00 mm radius bubble. Since these periods are the same time scale of the actual fluctuation of the bubble plume, it is expected that this phase shift has some influences on the interaction between the two phases and turbulence structure in the bubble plume.

7 Concluding Remarks

The Eulerian-Lagrangian model is applied for three-dimensional numerical prediction of a bubble plume. The set of governing equations is formulated with emphasis on the translational motions of the bubble under the condition that maximum void fraction is 0.1, and maximum bubble Reynolds number is 110. The following matters are revealed from the simulated results.

(1) Detailed three-dimensional structure of a bubble plume is numerically simulated precisely by using the Eulerian-Lagrangian model where each bubble motion is tracked in a bubbly mixture which is treated as a continuum. The simulated flow structure shows good agreement with the experimental observations. (2) Simulated results show three-dimensional swaying and swirling structures which are induced by the two-way interaction. These structures are compared with experimental data and confirmed a good agreement. (3) Local liquid flow velocity inside the bubble plume has a high frequency component due to the bubble migration. The present calculated pseudo turbulence is considered to be the ''kinematic'' component, since the momentum transportation through gas-liquid interface is not taken into account in the present grid-averaged governing equations. (4) The bubbles which rise up inside the bubble plume has the two dominant force components in the vertical direction, i.e., pressure gradient force (equivalent to buoyancy force) and drag force. To the contrary, a variety of the force components is contributed to the horizontal translational motion of the bubble.

Table 2 Frequency response of bubble

Period η	Amplitude α	Phase ψ(rad)	Actual period air-water	 air-5cSt oil
$\eta\rightarrow\infty$	1.00	0.00		
η=20.00	1.05	0.05	42.0s	8.40 s
η=0.86	1.94	0.52	1.9s	0.50 s
η=0.10	2.95	0.13	0.2s	0.05 s
η=0.00	300	0.00		

Acknowledgment

This work is supported for one of the authors, through the Grant-in-Aid for Encouragement of Young Scientists (A. No. 10750121), and for Scientific Research (C. No. 10650166) by the Ministry of Education, Science and Culture, Japan.

Nomenclature

C_D = drag coefficient
C_L = lift coefficient
f = volume fraction
g = gravity acceleration
p = pressure
r,R = bubble radius
Re = Reynolds number
t = time
u,U = velocity

Subscripts

G = gas phase
k = label of bubble
L = liquid phase
S = slip component
V = averaging volume
X = position
0 = initial condition
α = amplification factor
β = added mass coefficient
δ = discritization size
ε = overestimated volume fraction
ρ = density
∇ = spatial derivative operator
μ = viscosity coefficient
ξ = phase shift

References

[1] Wijngaaden, L., 1972, ''One-Dimensional Flow of Liquids Containing Small Gas Bubbles,'' Annu. Rev. Fluid Mech., **4**, pp. 369–395.

[2] Ransom, V. H., et al., 1985, ''RELAP/MOD2 Code Manual, Vol. 1, Code Structure, System Models, and Solution Methods,'' NUREG/CR-4312, EGG-2796.

[3] Liles, D., et al., 1986, ''TRAC-PFI/MOD1, An Advanced Best Estimate Computer Program for Pressurized Water Reactor Thermal-Hydrotic Analysis,'' NUREG/CP-3858, LA-10157-MS.

[4] Kataoka, I., and Serizawa, A., 1989, ''Basic Equations of Turbulence in Gas-Liquid Two-Phase Flows,'' Int. J. Multiphase Flow, **15-5**, pp. 843–860.

[5] Stewart, C. W., and Crowe, C. T., 1993, ''Bubble Dispersion in Free Shear Flows,'' Int. J. Multiphase Flow, **19-3**, pp. 501–515.

[6] Zhang, D. Z., and Prosperetti, A., 1994, ''Ensemble Phase-Averaged Equations for Bubbly Flows,'' Phys. Fluids, **6**, No. 9, pp. 2956–2970.

[7] Unverdi, S. O., and Tryggvason, G., 1992, ''A Front-Tracking Method for Viscous, Incompressible, Multi-fluid Flows,'' J. Comput. Phys., **100**, No. 1, pp. 25–37.

[8] Esmaeeli, A., and Tryggvason, G., 1996, ''An Inverse Energy Cascade in Two-Dimensional Low Reynolds Number Bubbly Flows,'' J. Fluid Mech., **314**, pp. 315–336.

[9] Murai, Y., and Matsumoto, Y., 1994, ''The Transient Flow Structure of Bubble Mixtured Liquid Jets,'' ASME-FED, **185**, pp. 203–208.

[10] Druzhinin, O. A. and Elghobashi, S., 1998, ''Direct Numerical Simulation of Bubble-Laden Turbulent Flows Using the Two-Fluid Formulation,'' Phys. Fluids, **10**, No. 3, pp. 685–697.

[11] Hassan, Y. A., and Canaan, R. E., 1991, ''Full-Field Bubbly Flow Velocity Measurements Using a Multiframe Particle Tracking Technique,'' Exp. Fluids, **12**, pp. 49–56.

[12] Sridhar, G., and Katz, J., 1995, ''Drag and Lift Forces on Microscopic Bubbles Entrained by a Vortex,'' Phys. Fluids A, **7**, pp. 389–402.

[13] Ruetsch, G. R., and Meiburg, E., 1993, ''On the Motion of Small Spherical Bubbles in Two-Dimensional Vortical Flow,'' Phys. Fluids A, **5**, pp. 2326–2340.

[14] Michaelides, E. E., 1997, ''Review—The Transient Equation of Motion for Particles, Bubbles, and Droplets,'' ASME J. Fluids Eng. **119**, pp. 233–247.

[15] Rietema, K., and Ottengraf, P. P., 1970, ''Laminar Liquid Circulation and Bubble Street Formation in a Gas-Liquid System,'' Trans. Inst. Chem. Eng., **48**, pp. 54–62.

[16] Hussain, N. A., and Siegel, R., 1976, ''Liquid Jet Pumped by Rising Gas Bubbles,'' ASME J. Fluids Eng. **98**, pp. 49–61.

[17] McDougall, T. J., 1978, ''Bubble Plume in Stratified Environments,'' J. Fluid Mech., **85**, pp. 655–672.

[18] Alam, M. and Arakeri, V. H., 1993, ''Observations on Transition in Plain Bubble Plumes,'' J. Fluid Mech., **254**, pp. 363–380.

[19] Iguchi, M., Okita, K., Nakatani, T., and Kasai, N., 1997, ''Structure of Turbulent Round Bubbling Jet Generated by Premixed Gas and Liquid Injection,'' Int. J. Multiphase Flow, **23**, No. 2, pp. 249–262.

[20] Leitch, A. M., and Baines, W. D., 1989, ''Liquid Volume Flux in a Weak Bubble Plume,'' J. Fluid Mech., **205**, pp. 77–95.

[21] Gross, R. W., and Kuhlman, J. M., 1991, ''Three-Component Velocity Measurements in a Laboratory Bubble Column,'' Proc. Int. Conf. Multiphase Flow '91-Tsukuba, G. Matsui et al., eds., Japan Society of Multiphase Flow, pp. 157–163.

[22] Bhaga, D. and Weber, M. E., 1981, ''Bubbles in Viscous Liquids: Shapes, Wakes, and Velocities,'' J. Fluid Mech., **105**, pp. 61–85.

[23] Murai, Y., and Matsumoto, Y., 1998, ''Numerical Analysis of Detailed Flow Structure in a Bubble Plume,'' JSME Int. J., Ser. B, **64-626**, pp. 568–574.

[24] Plesset, M. S., and Presperetti, A. 1977, ''Bubble Dynamics and Cavitation,'' Annu. Rev. Fluid Mech., **9**, pp. 587–616.

[25] Batchelor, G. K., 1967, *An Introduction to Fluid Dynamics*, Cambridge University Press, pp. 452–455.

[26] Auton, T. R., 1987, ''The Lift Force on a Spherical Body in a Rotational Flow,'' J. Fluid Mech., **183**, pp. 199–212.

[27] Auton, T. R., Hunt, J. C. R., and Prud'homme, M., 1988, ''The Force Exerted on a Body in Inviscid Unsteady Non-Uniform Rotational Flow,'' J. Fluid Mech., **197**, pp. 241–260.

[28] Moore, D. W., 1959, ''The Rise of a Gas Bubble in a Viscous Liquid,'' J. Fluid Mech., **6**, pp. 113–130.

[29] Hirt, C. W., and Cook, J. L., 1972, ''Calculating Three-Dimensional Flows Around Structures and over Rough Terrain,'' J. Comput. Phys., **10**, pp. 324–340.

[30] Lance, M., and Bataille, J., 1991, ''Turbulence in the Liquid Phase of a Uniform Bubbly Air-Water Flow,'' J. Fluid Mech., **222**, pp. 95–120.

[31] Takewaki, H., and Yabe, T., 1987, ''The CIP Method; Application to Nonlinear and Multi-Dimensional Hyperbolic Equations,'' J. Comput. Phys., **70**, pp. 345–356.

[32] Snow, J. T., Church, C. R., and Bahnhart, B. J., 1980, ''An Investigation of the Surface Pressure Fields Beneath Simulated Tornado Cyclones,'' J. Atmos. Sci., **77**, pp. 1013–1026.

Two-Phase Flow Pressure Drop in Right Angle Bends

Edward Graf
Ingersoll Dresser Pumps,
Phillipsburg, NJ 08865-2797

Sudhakar Neti
Lehigh University,
Bethlehem, PA 18015-3085

Gas-liquid two-phase bubbly flows in right angle bends have been studied. Numerical predictions of the flow in right angle bends are made from first principles using an Eulerian-Eulerian two-fluid model. The flow geometry includes a sufficiently long inlet duct section to assure fully developed flow conditions into the bend. The strong flow stratification encountered in these flows warrant the use of Eulerian-Eulerian description of the flow, and may have implications for flow boiling in U-bends. The computational model includes the finer details associated with turbulence behavior and a robust void fraction algorithm necessary for the prediction of such a flow. The flow in the bend is strongly affected by the centrifugal forces, and results in large void fractions at the inner part of the bend. Numerical predictions of pressure drop for the flow with different bend radii and duct aspect ratios are presented, and are in general agreement with data in the literature. Measurements of pressure drop for an air-water bubbly flow in a bend with a nondimensional bend radius of 5.5 have also been performed, and these pressure drop measurements also substantiate the computations described above. In addition to the global pressure drop for the bend, the pressure variations across the cross section of the duct that give rise to the fluid migration (due to centrifugal forces), and stratification of the phases are interesting in their own right. [S0098-2202(00)01004-X]

Introduction

Bubbly two-phase flows are very common in industry. Such flows occur in numerous industrial settings including turbomachinery, oil refineries, and nuclear reactors. Historically, due to a lack of understanding, the prediction of these flows and the associated transport phenomenon have been very empirical. This present work deals with the description and the prediction of such phenomenon from first principles based on some recent successes by the authors.

The presence of the second phase enhances the transport phenomenon in such flows, and quite often such flows are used to improve mixing and other processes. While the most common occurrence of bubbly flows is associated with boiling processes, the second (gas) phase is some times deliberately added to the liquid to enhance transport. The pressure drop associated with two-phase flows is usually larger than that in single-phase flows. As it turns out, even very small (mass) additions of the second phase increase the flow pressure drop substantially. For this and other reasons, measurements and prediction of pressure drop in two-phase flows are of great interest to the industrial community. Recent advances in computational fluid dynamics, along with the availability of larger and faster computer facilities, have made it possible for the numerical description of two-phase flows using Navier-Stokes equations. The present work describes the prediction of two-phase flow pressure drop in ducts and right angle bends.

The flow geometry studied here includes a sufficiently long inlet duct section to assure fully developed flow conditions into the bend. The flow in the bend is strongly affected by the centrifugal forces, and results in larger void fractions at the inner part of the bend. The strong flow stratification encountered in these flows warrants the use of Eulerian-Eulerian description of the flow, and the results may have implications for flow boiling in U-bends. The computed bubble trajectories through the vertical straight section, ninety-degree bend and the subsequent horizontal bend compared very well with high speed digital photographs that were made. However, what is more interesting is the good agreement in overall total pressure loss since this is typically the most difficult variable to accurately quantify in any numerical algorithm. The computational model used includes the finer details associated with turbulence behavior and a robust void fraction algorithm necessary for the prediction of such a flow. Numerical predictions of pressure drop for the flow with different bend radii and duct aspect ratios are presented. The mathematical modeling and numerical technique are validated by comparison with the authors' measurements of pressure drop as well as with data in the literature for straight and curved duct two-phase flows. The authors' measurements are for an air-water bubbly flow in a bend with a nondimensional bend radius of 5.5.

Review of Two-Phase Flow Techniques

Multi-phase flows are classified into the following flow regimes based on the interactions between the phases: bubbly, slug, annular, and dispersed flows. These regimes are essentially based on the topological differences in the flows. Modern approaches to the modeling of two-phase flows can be divided into two broad classes: locally homogeneous analyses and separated flow analyses. The majority of two-phase experimental data is for homogeneous flows. Homogeneous flow analysis, as well as the related experimental analysis, is probably not useful in understanding stratified flows of the kind in a bend. Separated flow analysis includes Direct Numerical Simulation, Drift Flux (mixture) models, Eulerian/Lagrangian models where the continuum is treated by Eulerian methods and the distributed phase is treated by Lagrangian methods, and the Eulerian/Eulerian (two-fluid) model where both the fluids are assumed to be part of an interpenetrating continuum. Given the processor speeds and storage capabilities of today's computers, Eulerian/Lagrangian and Eulerian/Eulerian models are the most advanced procedures that can be used to predict turbulent transport phenomena for the complex flow geometries typical of industrial problems.

Low void fraction ($\alpha < 0.1$) turbulent two-phase flows can be predicted with an Eulerian/Lagrangian scheme (the latter for bubbles) with a two-equation model to describe the turbulence (Neti et al. [1]). Such a model includes the effect of the dispersed phase on the mean continuum properties (from the Lagrangian prediction), the effect of the bubbles on the turbulence, and the effect of turbulence on the bubbles. For larger void fractions (α

Contributed by the Fluids Engineering Division for publication in the JOURNAL OF FLUIDS ENGINEERING. Manuscript received by the Fluids Engineering Division January 6, 1998; revised manuscript received June 19, 2000. Associate Technical Editor: M. Sommerfeld.

>0.1), Eulerian/Eulerian methods are more suitable, particularly for large phase density ratios and if body forces are important. A number of two-fluid two-phase one and two-dimensional computations have recently been reported. Satyamurthy et al. [2] considers a one-dimensional steady-state simulation of liquid metal vertical flows in the bubble, churn turbulent, and slug regimes. Comparisons are made with data for both void fraction profiles and total pressure drop. Graf et al. [3], have presented predictions of bubbly flow in a driven cavity with an average void fraction of 0.3 (with local levels even greater). De Ming et al. [4] have presented a computation of a two-dimensional bubbly flow in a sudden enlargement using a finite volume scheme incorporating a two-phase modified k-ε turbulence model.

We present here a robust algorithm for fully three-dimensional flows and illustrative computations. Graf [5] has presented details of the three-dimensional flow features for the basic geometries considered here, including lateral void distributions and bubble trajectories. Overall pressure loss predictions and comparisons with data in such complex flows are discussed presently.

Computational Scheme

The salient features of the computational procedures applicable for the Eulerian/Eulerian procedures are briefly described here and additional details are presented extensively elsewhere (Graf [5]). Steady, incompressible, noncondensing, two-component (e.g., water-air), turbulent, bubbly flows with no phase change are considered. Density difference between the two phases is large and thus buoyancy forces can be important. Reynolds numbers are assumed to be high and the local properties of the gaseous and liquid phases are not assumed to be the same. The differences in the individual phase velocities, and other properties, and their effect on turbulence intensity play a role in determining the overall pressure drop.

The flows in the duct and the right angle duct bend are three-dimensional in nature. The axial velocity, w is assumed to be along z direction, the primary flow direction. The u and v components of velocity (in the x and y directions) are the cross plane components. The treatment of the equations for both the phases is similar except for the source terms. The bubbles in the present model share ''their space'' with the liquid in the same control volumes. As a result, the two fluids can be thought of as interpenetrating continua.

Prediction of two-phase flows such as those described above involves the solution of several coupled partial differential equations. These include six Reynolds averaged momentum equations (three for each phase), a continuity equation for each phase, two to four for turbulence equations (for a modified isotropic k-ε model), and other equations for the scalars. This translates to the solution of thousands of coupled linear equations in the discretized domain.

The equations governing the turbulent flow through the 90 deg bend are parabolic in nature even for fairly tight bends (Humphrey [6]), and thus a marching solution with two-dimensional storage for all major variables is used. Pressure is stored as a three-dimensional variable to provide better feedback between the axial and cross plane momentum equations.

Two-phase flows with large phase density differences pose additional difficulties in computation. The lighter phase despite occupying significant space and moving with a noticeably different velocity does not contribute much mass. Thus the second phase has little impact on the mass continuity. Carver [7] has proposed ways to minimize this problem by normalizing the equations by their appropriate densities, and these ideas are used in the present computations.

Care has to be taken in the numerics to ensure that the computed void fraction is bounded $\langle 0,1 \rangle$. This latter condition is particularly important and difficult to achieve when the primary (axial) flow is small or nonexistent. Since the mass conservation for each finite volume and the whole domain in turn can only be achieved to within some required tolerance (usually larger than the gas phase contribution), unrealistically high or low void fraction results can be computed. This is especially serious in regions with little flow. Even small mass residuals result in large void changes. The analysis of two-phase flow in a two-dimensional driven cavity with a moving wall (Graf et al. [3]) was a particularly good test for evaluating this phenomenon since the flows entering and leaving the finite volumes at the core of the vortex were rather small. The solution to this was to add an effective mass residual term (S_P) resulting from the linearization of the source term. This helps the procedure since then the mass residuals are not large enough to destabilize the void fraction calculation.

The procedures used for the prediction of the bubbly flows are described in general terms above. The next few sections present details with regard to the equations solved, turbulence-modeling, effects of bubbles on turbulence, turbulence modeling of the dispersed phase, and issues pertaining to interfacial momentum transfer.

Equations and Solution Details. The steady, turbulent, incompressible, noncondensing, two-fluid, two-phase flow in the duct bend are described by a set of equations in toroidal coordinates. The governing equations are formulated in primitive variable form: i.e., the dependent velocities, u, v, w, local static pressure, p, and void fraction, α, are solved for directly. In vector form the mass conservation, void fraction, and pressure correction equations are

$$\frac{\nabla\cdot(\alpha\rho\overline{U})_1}{\rho_{1\mathrm{ref}}}-\frac{\nabla\cdot(\alpha\rho\overline{U})_2}{\rho_{2\mathrm{ref}}}=0 \tag{1}$$

$$\frac{\nabla\cdot(\alpha\rho\overline{U})_1}{\rho_{1\mathrm{ref}}}+\frac{\nabla\cdot(\alpha\rho\overline{U})_2}{\rho_{2\mathrm{ref}}}=0 \tag{2}$$

Momentum Equations are:

$$\nabla\cdot(\alpha\rho\overline{UU})_k=-\alpha_k\nabla p+\nabla\cdot\alpha_k\tau+\alpha_k\rho_k\overline{g}+\overline{M}_k=0 \tag{3}$$

where τ is the shear stress, g is the acceleration due to gravity, M_k is the interphase momentum per unit volume, and the subscript $k=1,2$, refers to the two phases. The equations for the right angle bend are in fact solved in toroidal coordinates with rectangular grids for the cross plane representations. The generalized interphase momentum transfer, M_k, can include all relevant forces, including drag, lateral lift force, virtual mass, and Basset forces. The modeling of these forces is considered in a subsequent section.

The partial differential equations described above are discretized using hybrid differencing (Patankar [8]) on a staggered grid, and the resulting set of algebraic equations is solved. This approach is useful in avoiding pressure-velocity decoupling in the computation of incompressible flows (Patankar [8]). The solution procedure consisted of solving the flow equations using the SIMPLEC algorithm (Van Doormal [9]).

One of the major challenges for a two-fluid bubbly flow model is an algorithm for computing the void fraction (volume fraction of dispersed phase). Since the two phases are of very different densities (e.g., 1000:1 for water: air), the effect of the heavier fluid would totally mask any contributions from the lighter fluid. To alleviate this, the mass conservation equations are normalized by their reference densities (Carver [7]). The Eulerian/Eulerian scheme needs special attention in handling several aspects of the second phase such as limiting of void fraction to $\langle 0,1 \rangle$, and other issues related to the use of the two continuity equations. The equation for the void fraction shown above was constructed by subtracting the continuity equations for the two phases from one another. The volume fraction of the continuous phase, denoted as phase 1, was eliminated by the relation

$$\alpha_1+\alpha_2=1 \tag{4}$$

The general form of the equation being solved for the local void fraction, α_2 can be written in the form

$$\alpha_p A_p = \alpha_e A_e + \alpha_w A_w + \alpha_n A_n + \alpha_s A_s + \alpha_u A_u + \alpha_d A_d + S_{\alpha_1} \quad (5)$$

Such an approach was found to be unstable. It violated the criterion that (Patankar [8]):

$$A_p = \sum A_{nb} \quad (6)$$

The coefficient of A_p originally did not meet the criterion above. It was necessary to subtract from the terms of A_p the sum of the two continuity equations with each normalized by its reference density in a somewhat modified form. The continuity equation contains the local void fraction. So introducing it directly would bring the void fraction at surrounding nodes (N, S, E, W, U, and D) into the coefficient for the void fraction at the point of solution (P). This would not readily permit the solution of the equation set at each node. A simplifying assumption was made (for this term only), that the local void fraction at the neighbors of P are all equal to the value at P. This is similar in logic to the approximations made in the SIMPLE and SIMPLEC algorithms. With this addition, the criterion for the coefficients of A_P described above is met.

The iterative solution procedure uses an initial estimate of the pressure field. The u, v, and w momentum equations for the continuum phase and then for the distributed phase are solved. Next, the difference between the continuity equations (normalized by the reference density) is used to determine the correction to the pressure field (Carver [6]). The u, v, and w equations are resolved until a certain convergence is achieved. The sum of the continuity equations (normalized by the reference densities) is used to determine the void fraction distribution. Finally, the equations for any transported scalars are solved and the procedure repeated until convergence.

Turbulence Modeling. Previous two-fluid algorithms in the literature have used either algebraic turbulence models or employed higher-level turbulence models only for the continuous phase. The dispersed phase turbulent eddy viscosity in these works has often been assumed proportional to the continuous phase diffusivity (i.e., a particle Prandtl number). Another approach for computing the turbulent eddy viscosity of the distributed phase is to relate it to the continuous phase turbulent viscosity by means of an algebraic equation. The theory of a particle dispersed in a turbulent flow field based on the work of Tchen [10] and Peskin [11] provides such an algebraic equation. This modeling approach has been by Mostafa et al. [12]. Turbulent flows reported in a previous work (Graf and Neti [3]) were computed both by using a constant particle Prandtl number as well as by applying a two-phase modified two-equation k-ε model to the distributed phase as well as the continuous phase. While there was some improvement noted for high void fraction simulations, in general it was concluded that the additional run-times and resources required did not warrant the inclusion of two additional PDEs.

In this work, a modified isotropic k-ε turbulence model that accounts for the presence of the bubbles by the addition of source terms is used. A turbulent viscosity is computed after solving for k, the turbulent kinetic energy, and ε, the dissipation of kinetic energy. The proposed isotropic turbulence model becomes less accurate in describing complex flows where significant anisotropic rate-of-strain components might be present (due to streamline curvature or rotation or separation, etc.). Single-phase turbulent flow computations were performed for bends of increasingly tight radius and compared with existing data. The standard k-ε turbulence model yielded reasonable predictions for normalized radius ratios as low as 2.3. Due to the segregation of the phases the two-phase bend that can adequately be computed with an isotropic turbulence model is probably not as tight as $R/D=2.3$. It was felt that the test geometry, i.e., $R/D=5.5$, would be a gentle enough bend for the application of the proposed isotropic turbulence model. We have used various algebraic curvature correction models as well as solved additional transport equations (i.e., Algebraic Reynolds Stress Models) to improve the quality of single-phase turbulent computations. It was felt that the first application of a two-phase modified turbulence model for a fully three-dimensional problem should not resort to a higher order turbulence model if it could rationally be avoided. Certainly more complex two-phase turbulence models can be tried within the framework of the present solution algorithm.

The source terms in the transport equations of the turbulence variables arise naturally from the addition of the interphase momentum term to the momentum equations. The turbulent kinetic energy transport equation is

$$\rho \overline{U} \cdot \nabla k = \nabla \cdot (\Gamma_k \nabla k) + G - \rho\varepsilon + S_k \quad (7)$$

The transport equation for ε (i.e., the rate of dissipation of k) is

$$\rho \overline{U} \cdot \nabla \varepsilon = \nabla \cdot (\Gamma_\varepsilon \nabla \varepsilon) + \frac{C_1 \varepsilon}{k} G - \frac{C_2 \rho \varepsilon^2}{k} + S_\varepsilon \quad (8)$$

These equations allow for the possibility that the distributed phase either increase or suppress the continuous phase turbulence since the bubbles interact with the continuous phase to both create and dissipate turbulence. The continuous phase turbulence has been found to be suppressed by the presence of the dispersed phase in highly turbulent flows. Simpler models that assume that the total turbulence is the sum of the wall shear-induced turbulence and the bubble induced turbulence always result in an increase in turbulence.

Nondimensionalized bubble ratios between 0.04 and 0.20 were considered. This range was chosen so as to study flows in which the bubble diameter was both smaller and larger than the integral length scale of turbulence expected for single-phase duct flow (i.e., 0.08). The interaction of the bubbles with the turbulent eddies associated with duct flow are expected to result in a break-up of eddies and an overall reduction in the turbulent length scale. A two-phase modification of the mixing length $(l=\kappa y)$ is suggested (Al Taeweel and Landau [13]), and was also used for two-phase flows by Neti and Mohammed [1]. For a flow with quality, x, and with bubble and hydraulic diameters, d and D, respectively, κ_{TP} is written as: $\kappa_{TP}=\kappa\Phi_L^2$; and $\Phi_L^2=[1-(xd/D)(\rho_g/\rho_L-1)]$. This results in a two-phase length scale that is less than it is for single-phase. Smaller bubbles are considered less likely to cause the break up of a turbulent eddy. The turbulent viscosity is finally computed as $v_t=C_\mu k^2/\varepsilon$, where C1 $(=1.44)$, C_2 $(=1.92)$, and C_μ $(=0.09)$ are the standard constants in the k-ε turbulence model.

Liquid Turbulence Modification Induced by Bubbles. The interaction of the dispersed phase (bubbles/particles) with the continuum phase fluid tends to modify the fluid turbulence. Wang et al. [14] have reported turbulence measurements in bubbly flows and have described the effects of the bubbles on the flow. Usually, the presence of the bubbles in a flow gives rise to an increase of turbulence. Consider the changes induced in the present curved duct test rig when bubbles are injected into what is originally a single-phase flow. There are strong lateral and longitudinal pressure gradients in the flow. These pressure gradients will generate different fluid and bubble accelerations due to the mass differences between the two phases. This relative acceleration between the two phases can be expected to cause additional velocity fluctuations.

The effect of the dispersed phase on mean quantities of velocity and void fraction lead to theories in which the von Karman constant is modified by the presence of the bubbles. Hino [15] and Neti and Mohammed [1] report theories in which the von Karman constant is modified to account for the local presence of the distributed phase.

In the present work a two-phase turbulence model is used that appears naturally from the derivation of the transport equations. These equations are derived from the momentum equations, which for two-phase flows include a momentum interchange force. When the transport equations are derived additional terms result, which are included as source terms for both the k and ε equations (these are denoted as S_k and S_ε, respectively). The present turbulence model as derived in this work is consistent with that given by Wang et al. [16]. This is unlikely to be the last word on two-phase turbulence transport modeling, but a plausible model that will be improved upon with further experimental and numerical studies.

The transport equations for k and ε given above include additional source terms S_k in the turbulent kinetic energy equation and S_ε in the dissipation equation. These additional terms arise in the development of the two-phase turbulent transport equations from the momentum equations. The presence of the interfacial momentum-exchange force term in the momentum equation results in these terms appearing in the turbulence model.

$$S_k = 2^*\mathrm{CNST2}(C_t - 1)k \tag{9}$$

$$S_\varepsilon = 2^*\mathrm{CNST2}(C_t - 1)\varepsilon \tag{10}$$

where, C_t, is the ratio of dispersed phase to continuous phase turbulent velocity fluctuation. It is set equal to 1.5 in this work based on Wang et al. [16].

While these expressions for the source terms are relatively simple, they permit solutions in which the turbulence is suppressed as well as incremented. Additionally, they satisfy the condition (de Bertodano et al. [17]) derived from (7) and (8) for bubbles rising in a stagnant duct:

$$S_\varepsilon = \frac{\varepsilon}{k} S_k \tag{11}$$

Turbulence Modeling for the Dispersed Phase. It is expected that for bubbly flows the turbulence in the dispersed phase will be much less important in determining the overall flow field compared to the turbulence in the continuous phase (Besnard et al. [18]). Then it might be sufficient to model the dispersed phase turbulent eddy viscosity by treating the bubbles as particles suspended in a turbulent stream. The theory of Tchen [10] and Peskin [11] as modified by Soo [19] gives a ratio of particle turbulent viscosity to the continuous phase turbulent viscosity (''particle turbulent Prandtl number'') by computing the statistics of an individual particle interacting with the turbulent eddies of the continuous phase. The particle turbulent Prandtl number depends on the ratio of particle impulse response time to the time a fluid particle remains in a velocity correlated region; this ratio is called the impulse response parameter and is denoted by K. It is similar to the momentum exchange coefficient. The ratio of the Lagrangian microscale of turbulence to the Eulerian scale (i.e., λ/λ_E) is important in determining this relationship. For a spherical particle or bubble:

$$K = \frac{\sqrt{\pi}}{18} \mathrm{Re}_{\mathrm{particle}} \frac{\rho_{\mathrm{particle}}}{\rho_{\mathrm{continuous}}} \frac{d_{\mathrm{particle}}}{\lambda} \tag{12}$$

When the ''particle'' is an air bubble in a liquid the density ratio is approximately 1/1000, and K is small. Thus the particle eddy diffusivity is seen to approach unity. The calculations in this study were carried out by setting the bubble turbulent Prandtl number equal to unity.

There is an intermediate approach between assuming a bubble turbulent Prandtl number equal to unity and solving an additional two-equation turbulence model. The theory of Tchen [10] and Peskin [11] can be incorporated into the model, so that a local bubble turbulent Prandtl number is implicitly calculated. This approach appears to be promising especially for flows where the bubble or particle density approaches (or exceeds) that of the continuous phase. Mostafa and Mongia [12] have used this approach for turbulent bubbly jet flows.

Modeling of the Interphase Momentum Transfer, $\mathbf{M}_k$. The numerical algorithm presented in the previous section can be applied to a wide variety of two-phase flow programs beyond the work reported herein, e.g., the two-phase driven cavity problem (Graf and Neti [20]). The interphase momentum transfer, M_k, must include all the relevant forces for the problem under consideration; most commonly:

$$M_k = F_{\mathrm{Drag}} + F_{\mathrm{Lateral\ Lift}} + F_{\mathrm{Virtual\ Mass}} + F_{\mathrm{Basset}} \tag{13}$$

Based on the work done at Harwell Laboratory (Jayanti and Hewitt [18]), the inter-phase friction force added to the U_i momentum equation is

$$F_{\mathrm{drag}} = \frac{3}{4} \frac{\alpha_k C_D \rho_1}{d} V_{\mathrm{rel}} (U_{i1} - U_{i2}) \tag{14}$$

The drag coefficient is:

$$C_D = \frac{24}{\mathrm{Re}_b} (1 + 0.1\,\mathrm{Re}_b^{0.75}) \tag{15}$$

The above drag coefficient is for a spherical bubble. High speed photography of all sections of the test loop showed that the fraction of bubbles distorted to aspect ratios greater than 1.1 was not large; there were, however, some bubbles with aspect ratios as high as 1.5. A distributed phase that is not spherical will have an increased average drag coefficient. Computation of the bubble distortion was not considered necessary for the present problem and would not have been straightforward. Bunner and Tryggvason [21] presented results of a direct numerical simulation of a finite number of bubbles rising in a square cross-section duct. The Reynolds number based on bubble rise velocity was eighteen. A front-tracking finite difference Eulerian/Lagrangian method was used to determine bubble shapes. This method is extremely compute intensive and limited to low Reynolds number flows.

Bubbles in the flow are subjected to shear driven lift forces. These lift forces tend to concentrate bubbles toward near wall regions. This effect is strongest at the end of the vertical section and gives rise to the so called ''chimney effect'' as reported in numerous experimental studies. Saffman [22,23] calculated these lift forces for a sphere moving through a simple shear flow, with results applicable to low Reynolds number, low shear flows. Mei and Klausner [24] extended Saffman's work for finite Reynolds numbers and finite shear rates. Saffman's theory with Mei and Klausner's corrections is implemented in the present computations to predict the movement of bubbles toward regions of larger shear rates. The implementation of the Saffman force for the determination of lateral void distributions was found to be better than the procedure used for pipe flow calculations which was based on turbulence parameters (Wang et al. [16]). Saffman [22,23] computed the lift force for a sphere moving through a simple shear flow:

$$F_{\mathrm{lateral}} = \frac{81.2}{4\pi} \frac{\mu V_{\mathrm{rel}} \left(\frac{d}{2}\right)^2 \kappa^{0.5}}{\nu^{0.5}} \quad \text{where:} \quad \kappa = \nabla \overline{V}_{\mathrm{abs}} \tag{16}$$

This result is valid only for very small Reynolds numbers and low shear rates. Mei and Klausner [24] extended Saffman's work for finite Reynolds number and finite shear rates. Their lift force reduces to Saffman's as the Reynolds number approaches zero but has a lower value elsewhere. The present algorithm properly computes the peaking of bubble concentrations at the perimeter of the duct as the flow mover vertically upwards.

A virtual mass force arises when the bubbles accelerate through the surrounding continuous phase. A bubble experiences a resisting force equal to one-half the mass of the displaced fluid times

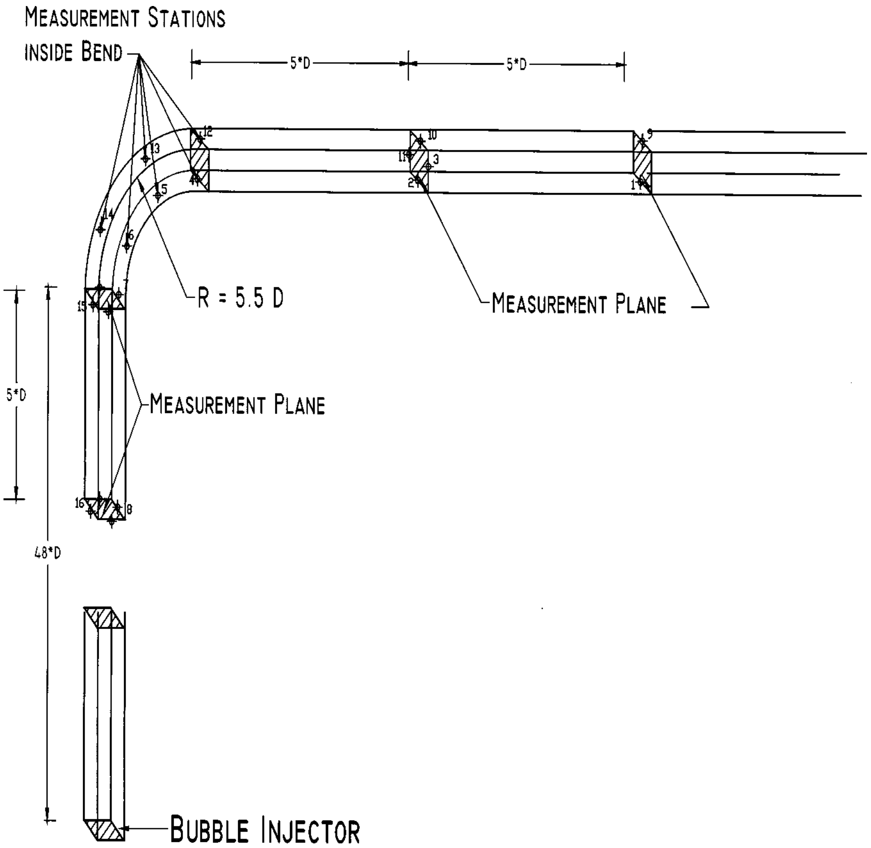

Fig. 1 Schematic of the right angle duct bend with pressure taps used in the experiments

the acceleration of the bubble. Using the model for the virtual mass force as given by Drew et al. [25] it can be shown that this force contribution can be neglected for the steady flow simulations presently being considered. However, for many flows this will not be the case, e.g., explosive flows with high spatial accelerations.

The Basset force arises from the acceleration induced changes of the viscous drag and the unsteady boundary-layer development. For the present class of problems, this force is also neglected.

Experimental Apparatus and Methods

Pressure drop measurements for a water-air bubbly flow in a right angle bend with a nondimensional bend radius of 5.5 are also included in the results presented here. The methods used for the pressure drop measurements and a description of the apparatus used are given here.

The test section was made of transparent Plexiglas and consisted of a 25-mm side vertical square duct followed by the 90 deg bend with a horizontal square duct down stream of it. The vertical duct was 48 hydraulic diameters long, and the curved duct had a mean radius to hydraulic diameter ratio of 5.5. The horizontal duct was 15 hydraulic diameters long. The test section was part of a two-phase flow loop made up of 37-mm (1.5 in.) stainless steel piping. It included a pump (1/3 HP, 10 GPM), a collection tank upstream of the pump, a water-air tank after the test section, a flow meter and the necessary flow control valves. The water flowmeter (drag type float meter) was calibrated by diverting and collecting water into a weighing tank for a measured time. Compressed air at the desired pressure could be injected through a set of tube manifolds into the water flow at the bottom of the vertical square duct. The airflow tubes had 0.5 mm diameter holes for the generation of the bubbles. The injected airflow was measured with a calibrated gas rotameter.

High-speed digital photographs were made throughout the test section. This served to quantify the change in the lateral distribution of bubbles throughout the three different sections of the test rig. The computed void distributions compared well with this flow visualization even at the exit of the bend exit where the bubbles move rapidly from the inside of the bend to the top of the horizontal duct (Graf [5]).

The test section with the right angle bend was instrumented with sixteen pressure taps. A schematic of the right angle bend used in the present experiments with the pressure taps is shown in Fig. 1. Pressure taps were located on the inside as well as the outside radius of the duct bend, and care was taken to ensure that the taps were flush inside the duct. Pressure differences were measured with a calibrated Validyne DP 15-20 reluctance type differential pressure transducer. The transducer with the diaphragm used had range of 88 mm H_2O with a resolution of 0.02 mm. The transducer output could be read with a Validyne CD379 pressure display meter and was recorded with the help of a Data Translation DT-2805 A/D board with 12 bit resolution and an IBM compatible personal computer. Pressure differences were measured by connecting the appropriate pressure taps to the transducer ports. Due to the turbulent nature of the flow, the pressure measurements were time variant with fluctuations. The data reported here are the result of averaging such fluctuating data over sufficiently long (100 data points in 10 second) periods.

Results and Discussion

Results of the computational procedure and the experiments described above for two-phase bubbly flow in a vertical duct, a right angle bend, and a horizontal square duct are described here. Two-phase pressure drop in the ducts and the bend are shown in terms of the two-phase loss multiplier, which is the ratio of two-phase pressure drop to the pressure drop that would occur if the

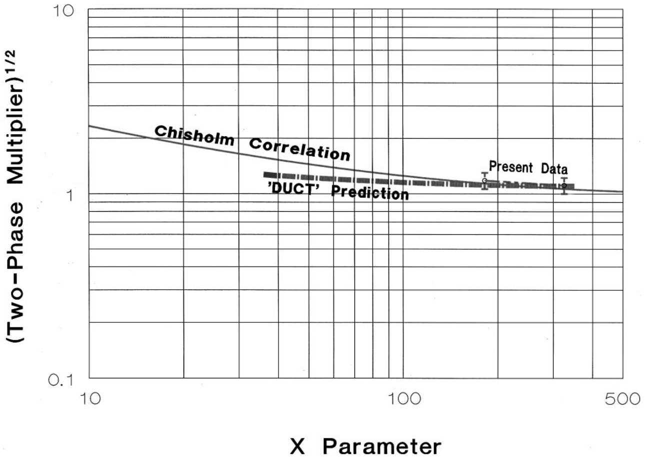

Fig. 2 Two-phase multiplier for pressure drop versus Martinelli parameter for a right angle bend

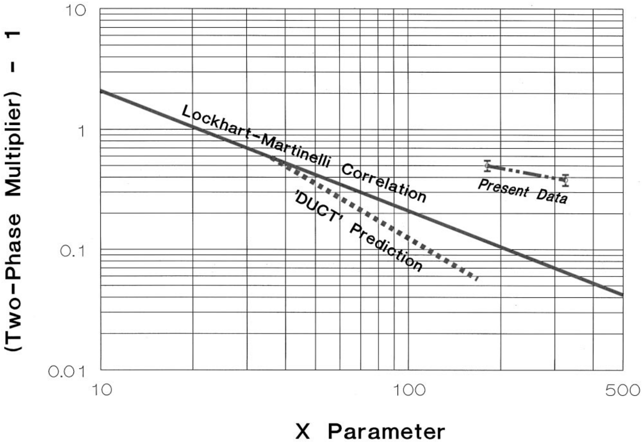

Fig. 4 Two-phase multiplier for pressure drop versus Martinelli parameter for a vertical duct

flow were liquid only. Figures 2–4 show the computationally predicted and measured values of two-phase loss multipliers along with available empirical correlations. The two-phase loss multiplier for the flow in the right angle bend is shown as a function of the Martinelli flow parameter, X, as presented by Chisholm and Laird [26].

$$X=\left(\frac{\Delta P_L}{\Delta Pg}\right)^{0.5}=\left(\frac{G_L}{G_g}\right)^{(2-n)/2}\left(\frac{\mu_L}{\mu_g}\right)^{n/2}\left(\frac{\rho_g}{\rho_L}\right)^{0.5} \tag{17}$$

This expression can be simplified if n, the power of the Reynolds number in the friction factor relation, is taken as 0.25 (i.e., turbulent flow in smooth tubes):

$$X=\left(\frac{G_L}{G_G}\right)^{0.875}\left(\frac{\mu_L}{\mu_G}\right)^{0.125}\left(\frac{\rho_G}{\rho_L}\right)^{0.5} \tag{18}$$

where, G represents the mass flow rates, ρ and μ are density and dynamic viscosity respectively, with subscripts L and g representing the liquid and gas phases. Larger amounts of the lighter phase (air) correspond to lower values of X.

The computed and experimentally measured values of two-phase loss multiplier for the duct bend are compared in Fig. 2 with the measurements of Chisholm [27] for a right angle bend in a circular pipe. Chisholm's data are for R/D values of ∞ (i.e., straight pipe), 5.02, and 2.36. A curve fit of the above data covering the above nondimensional pipe radii has been determined (Fig. 2). As per their choice, the square root of the two-phase loss coefficient is plotted as a function of the Martinelli parameter. Though the present experimental measurements are for a square duct bend and Chisholm's were for a circular pipe bend, the present pressure drop measurements seem to agree quite well with their data. The pressure drop predictions from the present computational show good agreement with Chisholm's empirical data. The empirical loss correlation depends only on the amount of the gas present in the two-phase flow. Our computed pressure drop data has at least a weak dependence on the bubble size among other things. The computational predictions plotted are for 5-mm diameter bubbles. Pressure losses are about 10 percent higher for 1 mm bubbles, and could explain discrepancies based on bubble sizes. More detailed experiments and additional computations are needed before more definitive statements can be made in this regard. The present numerical computations appear to somewhat underestimate the pressure losses for two-phase flow in a right angle bend.

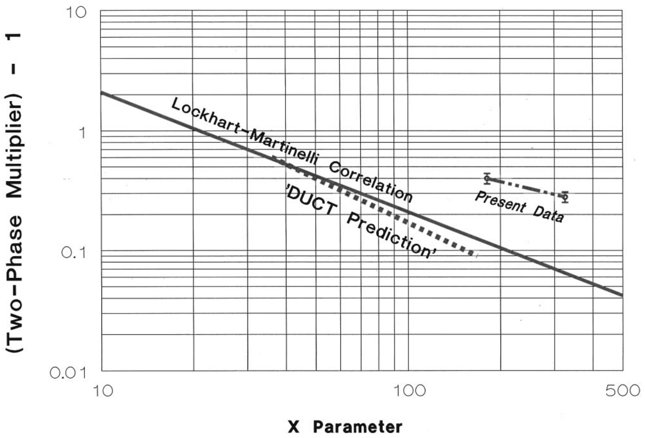

Fig. 3 Two-phase multiplier for pressure drop versus Martinelli parameter for a horizontal duct

Pressure drop in a two-phase flow consists of contributions from frictional loss, acceleration effects and gravitational influence. The hydrostatic head in vertical ducts is normally not counted as part of the pressure losses. Thus the Lockhart-Martinelli two-phase loss multiplier (Wallis [28]) is the same for horizontal as well as vertical pipes. The two-phase loss coefficient in the horizontal section down stream of the right angle bend is shown in Fig. 3. The horizontal duct after the bend is only about 15 diameters long, and the pressure drop in this duct is probably influenced by the nature of flow coming out of the bend. The measured pressure losses were larger than those based on the Lockhart-Martinelli curve as reported by Chisholm and Laird [26]. The computed pressure losses are again lower than the correlation but the trend appears to be correct. A comparison of the pressure loss coefficient for a vertical duct is shown in Fig. 4, and again the computations underpredict the correlation.

The consistent under prediction of the pressure losses by the computation could be an indication of the need for change in some basic assumptions made for the boundary conditions. The near wall velocity (and shear) are determined per the log-law wall function for the turbulent boundary layer. To accommodate two-phase flow effects, the mixing length ($l=\kappa y$) has been modified using κ_{TP}. For a flow with quality, x, and with bubble and hydraulic diameters, d and D, κ_{TP}, which is written as a function of quality, bubble and hydraulic diameters. For the bubbly flows in question, further modifications of the log-law may be necessary to predict the wall shear better.

The effect of void fraction on pressure drop in a right angle bend is shown more explicitly in Fig. 5 where the two-phase pressure loss coefficient is plotted as a function of void fraction.

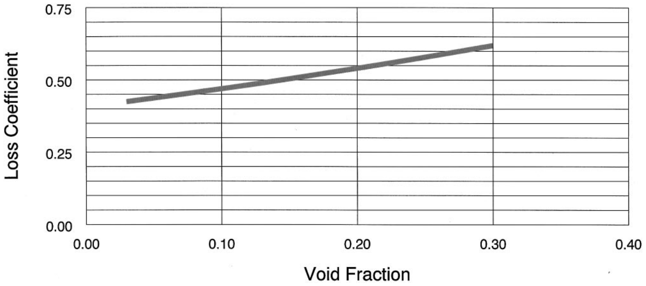

Fig. 5 Variation of pressure drop in a right angle bend with void fraction

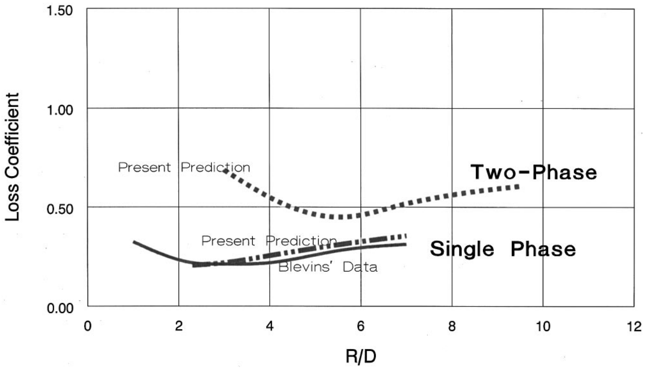

Fig. 6 Variation of pressure drop in a right angle bend with radius of the bend

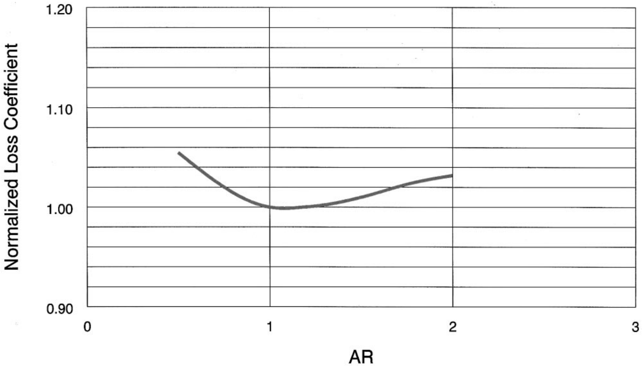

Fig. 7 Variation of pressure drop in a right angle bend with duct aspect ratio

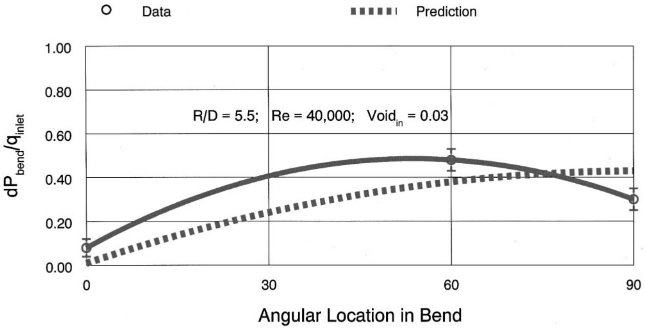

Fig. 8 Pressure variation in the cross section of a right angle bend

The loss coefficient is defined as: loss coefficient$=\Delta p/q_{\text{inlet}}$, where Δp is the pressure change and q_{inlet} is the inlet dynamic head. As expected, increase in void fraction results in increased pressure drop.

The bend radius is an important parameter in determining the flow conditions and phase segregation. Effects of bend radius on pressure drop are shown in Fig. 6. Single-phase flow typically shows a minimum loss at a dimensionless radius ratio (i.e., R/D) between two and three. Diffusion losses are the major contributor to overall losses when the radius ratio is less than two. Wall friction losses begin to predominate for flows with radius ratios greater than this. For single-phase flow, the predicted pressure drop is slightly higher than the data reported by Blevins [29]. The present parabolic predictive scheme is not suitable for computing flows in smaller radius ratio ducts where elliptic effects and flow separation may be important. The two-phase loss prediction indicates that a minimum loss occurs for a radius ratio between five and six. This is higher than that found for single-phase flow. The phase segregation that occurs with two-phase flows may be the reason for this difference. The lighter phase fills the inner part of the right angle bend. It is expected that this blockage will exacerbate the increasing pressure loss that occurs (in single-phase flow) with decreasing radius ratio and thus tends to move the minimum to a higher value.

Flows in rectangular cross-section ducts are also of interest in many typical industrial problems. Therefore computations were also performed for rectangular ducts of different aspect ratios. Pressure loss coefficient as function of aspect ratio (AR, i.e., the ratio of the duct's height in the radial direction to its base) is shown in Fig. 7. For single-phase flows, the minimum pressure loss condition was shown by Graf [5] to occur for an aspect ratio between 1.75 and two. The two-phase minimum is predicted to occur at an aspect ratio between one and 1.25. For smaller duct aspect ratios, the pair of counter-rotating vortices that forms inside the bend results in an increasingly larger percentage of the total flow being highly sheared. The loss also increases as the aspect ratio increases but not as strongly as with decreasing aspect ratio. This is possibly due to the earlier formation of multiple vortex pairs in the bend with their resulting increase in shear.

The flow in a bend results in substantial phase segregation due to the body forces. Initially the bubbles enter the vertical duct bend with peaked values near the walls, and with symmetric distribution. About half way through the bend, the bubbles are mostly concentrated at the inner radii with the outer radii of the bend filled with liquid, see computations and digital photographs in Graf [5]. The bubbles end up at the outer radii (top of the bend) near the exit of the bend. Such transport of the phases requires rather complicated cross plane distributions of pressure in the duct. These cross plane pressure differences are shown in Fig. 8. The present experimental measurements of these cross plane pressure variations and the computed gradients are in general agreement. The present data show that some lateral pressure gradient exists at the inlet to the bend (i.e., at the 0 deg plane). However, the present computational method does not predict this effect. The experimental data indicates that the maximum pressure gradient occurs at approximately 60 deg in the bend. The computations, however, predict an increasing cross plane pressure gradient from bend inlet to exit.

Conclusions

1 Numerical predictions of two-phase bubbly flows from first principles (Navier-Stokes equations) with minimal empirical input, in vertical and horizontal ducts and a right angle bend have been obtained. The computed overall total-pressure loss data are compared with both the authors' measurements and existing data in the literature.

2 Measurements of pressure drop for air-water bubbly flows in a right angle duct bend of dimensionless radius ratio 5.5 are reported.

3 The pressure drop measured in the duct bend is close to that reported by Chisholm [27] but the computations somewhat underpredict the pressure drop.

4 The increase in pressure drop (loss coefficient) that occurs with void fraction is predicted well by the present algorithm.

5 The effect of duct radius ratio on two-phase pressure drop is similar to that in a single-phase flow. However, the minimum pressure loss is predicted to occur at a higher radius ratio (between 5 and 6).

6 The effect of duct AR on pressure drop is similar to that seen with single-phase flows. However, the minimum pressure loss is expected to occur at a lower aspect ratio ($\sim$1.25) than seen in single-phase flow.

7 Cross plane variations of pressure were measured and are compared to computational predictions. The predicted level of cross plane pressure gradient is reasonable. However, the maximum in the measured pressure gradient occurring at 60 deg in the bend is predicted to occur close to the duct exit.

Nomenclature

AR = aspect ratio
C_D = drag coefficient
C_1 = turbulence model constant
C_2 = turbulence model constant
C_μ = turbulence model constant
d = bubble diameter
D = hydraulic diameter
F_D = interfacial force
G = mass flow rate
k = turbulence kinetic energy
q = inlet dynamic head
R = bend radius
Re = Reynolds number
$\overline{U}$ = velocity vector
u, v, w = velocity components corresponding to x, y, z, respectively
u', v' = fluctuating turbulence components
V_{rel} = relative velocity between phases
X = Martinelli parameter
x, y, z = Cartesian coordinates
x, y cross section plane of duct
z primary flow direction in duct
x = quality (mass fraction of gas)
α = void fraction
ΔP_L = friction pressure drop for liquid flowing alone in the duct
ΔP_g = friction pressure drop for gas flowing alone in the duct
ε = turbulence kinetic energy dissipation rate
Φ_L^2 = two-phase multiplier
Γ = transport parameter for k or ε
μ = dynamic viscosity
ρ = density
$\rho_{1\text{ref}}$ = reference density of the continuous phase (998 kg/m^3 presently)
$\rho_{2\text{ref}}$ = reference density of the distributed phase (1.21 kg/m^3 presently)
τ = shear stress
ν = kinematic viscosity

Subscripts

b = bubble
c = centerline
i = vector direction
rel = relative
ref = reference
v = vapor, lean phase
1, L = liquid, continuum phase
2, G = gas, lean, dispersed phase

References

[1] Neti, S., and Mohamed, O. E. E., 1990, ''Numerical Simulation of Turbulent Two-Phase Flows,'' Int. J. Heat Fluid Flow, **11**, pp. 204–213.

[2] Satyamurthy, P., Dixit, N. S., Thiyagarajan, T. K., Venkatramani, N., Quraishi, A. M., and Mushtaq, A., 1998, ''Two-Fluid Model Studies for High Density Two-Phase Liquid Metal Vertical Flows,'' Int. J. Multiphase Flow, **24**, pp. 721–737.

[3] Graf, E., and Neti, S., 1996, ''Computations of Laminar and Turbulent Two-phase Flow in a Driven Cavity,'' ASME Fluids Eng. Div., Vol. 236, pp. 127–135.

[4] De Ming, W., Issa, R. I., and Gosman, A. D., 1994, ''Numerical Prediction of Dispersed Bubbly Flow in a Sudden Enlargement,'' ASME Numerical Methods in Multiphase Flows, FED-Vol. 185, pp. 141–157.

[5] Graf, E., 1996, ''A Theoretical and Experimental Investigation of Two-phase Bubbly Turbulent Flow in a Curved Duct,'' Ph.D. dissertation, Lehigh University.

[6] Humphrey, J. A. C., et al. 1981, ''Turbulent Flow in Square Duct with Strong Curvature,'' J. Fluid Mech., **103**, pp. 443–463.

[7] Carver, M. B., 1982, ''A Method of Limiting Intermediate Values of Volume Fraction in Iterative Two-Fluid Computations,'' J. Mech. Eng. Sci., **24**, pp. 221–224.

[8] Patankar, S. V., 1980, *Numerical Heat Transfer and Fluid Flow*, Hemisphere Publishing, New York.

[9] Van Doormal, J. P., and Raithby, G. D., 1984, ''Enhancements of the SIMPLE Method for Prediction of Incompressible Flows,'' Numer. Heat Transfer, **7**, pp. 147–163.

[10] Tchen, C. M., 1947, Dissertation, Delft, Martinus Nijhoff, The Hague.

[11] Peskin, R. L., 1959, ''Some Effects of Particle-Particle and Particle-Fluid Interaction in Two-Phase Turbulent Flow,'' Ph.D. thesis, Princeton University, Princeton, N.J.

[12] Mostafa, A. A., Mongia, H. C., 1987, ''On the Modeling of Turbulent Evaporating Sprays; Eulerian versus Lagrangian Approach,'' Int. J. Heat Mass Transf., **30**, pp. 2583–2592.

[13] Al Taweel, A. M., and Landau, J., 1977, ''Turbulence Modulation in Two-Phase Jets,'' Int. J. Multiphase Flow, **3**, pp. 341–351.

[14] Wang, S. K., Lee, S. J., Jones, O. C., and Lahey, R. T., 1987, ''3-D turbulence and phase distribution in bubbly two-phase flow,'' Int. J. Multiphase Flow, **13**, No. 3, pp. 327–343.

[15] Hino, M., 1963, ''Turbulent Flow With Suspended Particles,'' Proceedings, American Society of Chemical Engineers, **89**, pp. 161–185.

[16] Wang, D. M., Issa, R., and Gosman, A. D., 1994, ''Numerical Prediction of Dispersed Bubbly Flow in a Sudden Enlargement,'' Fluid Engineering Division, Numerical Methods in Multiphase Flows, **185**, pp. 141–148.

[17] De Bertodano, M. L., Lahey, Jr., R. T., and Jones, O. C., 1994, ''Development of a k-ε Model for Bubbly Two-Phase Flow,'' ASME J. Fluids Eng., **116**, pp. 128–134.

[18] Besnard, D. C., Katoka, I., and Serizawa, A., 1991, ''Turbulence Modification and Multiphase Turbulence Transport Modeling,'' Fluids Engineering Division, Vol. 110, *Turbulence Modification in Multiphase Flow*, pp. 51–57.

[19] Soo, S. L., 1967, *Fluid Dynamics of Multiphase Systems*, Blasisdell Publishing Company, London, UK.

[20] Jayanti, S., and Hewitt, G. F., 1991, ''Review of Literature on Dispersed Two-phase Flow with a View to CFD Modeling,'' AEA Technology Report, AEA-APS-0099.

[21] Bunner, B., and Tryggvason, G., 1998, *American Physical Society Division of Fluid Dynamics 51st Annual Meeting*, Nov., Paper # BA.03.

[22] Saffman, P. G., 1965, ''The Lift on a Small Sphere in a Slow Shear Flow,'' J. Fluid Mech., **22**, pp. 385–400.

[23] Saffman, P. G., 1968, Corrigendum to ''The Lift on a Small Sphere in a Slow Shear Flow,'' J. Fluid Mech., **31**, p. 624.

[24] Mei, R., and Klausner, J. F., 1994, ''Shear Lift Forces on Spherical Bubbles,'' Int. J. Heat Fluid Flow, **15**, pp. 62–65.

[25] Drew, D., Cheng, L., and Lahey, Jr., R. T., 1979, ''The Analysis of Virtual Mass Effects in Two-Phase Flow,'' Int. J. Multiphase Flow, **5**, pp. 233–242.

[26] Chisholm, D., and Laird, D. K., 1958, ''Two-Phase Flow in Rough Tubes,'' Trans. ASME, **80**, pp. 276–286.

[27] Chisholm, D., 1980, ''Two-Phase Flow in Bends,'' Int. J. Multiphase Flow, **6**, pp. 363–367.

[28] Wallis, G. B., 1969, *One-Dimensional Two-Phase Flow*, McGraw-Hill, New York.

[29] Blevins, R. D., 1984, *Applied Fluid Dynamics Handbook*, Van Nostrand Reinhold Co., New York.

F. Fluerenbrock
Principal Engineer,
Kvaerner,
12657 Alcosta Blvd,
San Ramon, CA 94583

Pressure Gradient and Choking Velocity for Adiabatic Pipe Flow of a Homogeneous Steam-Water-Solids Mixture

Mixtures containing steam, water, and solids develop when processing ore slurries at elevated temperature and pressure. Based on homogeneous one-dimensional three-phase flow theory equations are derived for pressure gradient, choking velocity, and sonic velocity of a steam-water-solids mixture flowing in a pipe. It is concluded that a quasi-choking condition may occur when the flow changes from subcooled to flashing conditions. [S0098-2202(00)00104-8]

Introduction

Mixtures containing steam, water, and solids are encountered in the mining industry when processing ore by pressure oxidation or pressure leaching. In these processes ground ore is mixed with water to obtain a slurry containing up to 50 percent solids. The slurry is treated in a reaction vessel. Typical operating conditions for the reaction vessel, called autoclave in the industry, are 2500 kPa/200°C for pressure oxidation and 4500 kPa/250°C for pressure leaching. From the autoclave the slurry is discharged to a flash vessel, which in the case of single stage pressure reduction is close to atmospheric pressure. In the case of pressure reduction in two or more stages all but the last flash vessel are at an elevated pressure. The pressure reduction is accomplished by means of a control valve, or a pipe type orifice, or a control valve and a pipe orifice in a series arrangement. The devices are installed between the autoclave and the first flash vessel and between the flash vessels themselves. Due to the pressure reduction a water to steam phase change will occur in each letdown piping system and, if the number of flash stages is small, the flow is generally choked.

Control of abrasive wear in the letdown piping system is a serious challenge in the design of the system, including the sizing of the flow controlling components. A major factor determining abrasive wear is the flow velocity, which can be very high in sections where steam is present as a result of flashing. It is clear that cavitation in components such as control valves also has to be reckoned with. While there have been numerous papers on flashing water flows, among others by Benjamin and Miller [1], Allen [2], Starkman et al. [3], Moody [4], Henry and Fauske [5], little has been published on flashing water-solids systems. In this paper a set of equations is formulated and developed to give an equation for the pressure gradient that can be integrated by numerical methods to provide a one-dimensional description of the flow from inlet to exit. Equations are derived that give the choking velocity of a steam-water-solids mixture in terms of the local properties of the fluid. The general methodology employed is similar to that used in a co-authored earlier paper (Fluerenbrock et al. [6]) on the hydrogen-water-solids mixture formed during the electrochemical machining of metals.

Current State of Practice

The flow controlling components are control valves and pipe type orifices. The typical control valve is an angle valve with abrasion resistant ceramic plug and seat. Depending on system design features and operating conditions flashing may occur in this valve. Valve sizing is accomplished by one of the methods outlined in American National Standard ANSI/ISA-S75.01 ''Flow Equations for Sizing Control Valves.'' The method indicated for a vaporizing liquid may not be exact for a flashing water-solids mixture, but due to the very nature of the valve (a variable orifice) some uncertainty is tolerable.

The size of a pipe type orifice, whether operating downstream of a control valve or as the only flow restricting element, is first determined approximately, e.g., by using capacity charts for the discharge of flashing water (Moody [7]) or experience from similar plants, and then refined by trial installation of different size orifices until system performance is satisfactory.

Descriptive Equations

While the slurries processed in autoclaves are not pure water-solids mixtures, treating them as such allows for a rational approximation. The model used is that of a homogeneous three-phase fluid. The underlying assumptions include:

- Adiabatic, one-dimensional, steady flow
- Thermodynamic equilibrium
- In any cross-section pressure, temperature and velocity of the three phases are the same
- The mass fraction of the solids remains unchanged
- Change to supersonic conditions does not occur, except in convergent-divergent configurations

For a pipe component with or without area change a momentum balance over a control volume leads to an equation for the pressure gradient as

$$\frac{dp}{dx}=-\frac{V}{v}\frac{dV}{dx}-F-G \tag{1}$$

This equation can be converted to

$$\frac{dp}{dx}=-\frac{V}{v}\left(\frac{V}{v}\frac{dv}{dx}-\frac{V}{A}\frac{dA}{dx}\right)-F-G \tag{2}$$

by use of the conservation of mass equation

$$V=\dot{m}v/A \tag{3}$$

The energy equation is used in the form

$$h=e-\frac{1}{2}V^2-gz \tag{4}$$

where e is the specific energy. In the absence of the gravity term e would be equal to the stagnation enthalpy.

Contributed by the Fluids Engineering Division for publication in the JOURNAL OF FLUIDS ENGINEERING. Manuscript received by the Fluids Engineering Division February 9, 2000; revised manuscript received June 19, 2000. Associate Technical Editor: K. Zaman.

The specific volume of the mixture in terms of component specific volumes and their mass fractions is

$$v=x_g v_g+x_f v_f+x_s v_s \tag{5}$$

and, considering that

$$x_f=1-x_g-x_s \tag{6}$$

it follows from the analogous equation for the specific enthalpy that

$$x_g=\frac{h-h_f+x_s(h_f-h_s)}{h_g-h_f} \tag{7}$$

The mathematical description of the model is completed by 6 equations of state

$$h_g, h_f, h_s, v_g, v_f, v_s=f(p) \tag{8}$$

Under saturated conditions the temperature $T=T(p)$. Therefore the phase properties are a function of pressure p only.

The Pressure Gradient

Equations (3)–(8) present a system of 11 equations, in which $\dot{m}$, x_s, and e are known constants and A and z are known functions of x. This leaves 12 unknowns. If of these unknown variables the pressure p is specified, or predicted by means of Eq. (2), all other variables can be determined, though this will involve iterative methods. It follows that v may be considered to be a function of p only, which allows dv/dx to be expressed as $dv/dp{*}dp/dx$. This makes it possible to convert Eq. (2) into

$$\frac{dp}{dx}=\frac{\frac{V^2}{vA}\frac{dA}{dx}-F-G}{1+\frac{V^2}{v^2}\frac{dv}{dp}} \tag{9}$$

An expression for dv/dp is developed in the following. Differentiation of Eq. (5) with respect to p, and recognizing that $dx_s/dp=0$, results in

$$\frac{dv}{dp}=v_g\frac{dx_g}{dp}+v_f\frac{dx_f}{dp}+x_g\frac{dv_g}{dp}+x_f\frac{dv_f}{dp}+x_s\frac{dv_s}{dp} \tag{10}$$

Differentiating Eq. (7) gives

$$\frac{dx_g}{dp}=\frac{\partial x_g}{\partial h}\frac{dh}{dp}+\frac{\partial x_g}{\partial h_g}\frac{dh_g}{dp}+\frac{\partial x_g}{\partial h_f}\frac{dh_f}{dp}+\frac{\partial x_g}{\partial h_s}\frac{dh_s}{dp} \tag{11}$$

The partial derivatives in this equation are evaluated from Eq. (7) as

$$\frac{\partial x_g}{\partial h}=\frac{1}{h_g-h_f}=\frac{1}{h_{fg}} \tag{12}$$

$$\frac{\partial x_g}{\partial h_g}=-\frac{x_g}{h_{fg}} \tag{13}$$

$$\frac{\partial x_g}{\partial h_f}=-\frac{x_f}{h_{fg}} \tag{14}$$

$$\frac{\partial x_g}{\partial h_s}=-\frac{x_s}{h_{fg}} \tag{15}$$

and Eqs. (4) and (3) yield

$$\frac{dh}{dp}=-V\frac{dV}{dp}=-\frac{V^2}{v}\frac{dv}{dp} \tag{16}$$

Substituting Eqs. (12)–(16) into Eq. (11) gives

$$\frac{dx_g}{dp}=-\frac{V^2}{vh_{fg}}\frac{dv}{dp}-\frac{x_g}{h_{fg}}\frac{dh_g}{dp}-\frac{x_f}{h_{fg}}\frac{dh_f}{dp}-\frac{x_s}{h_{fg}}\frac{dh_s}{dp} \tag{17}$$

From Eq. (6) follows that

$$\frac{dx_f}{dp}=-\frac{dx_g}{dp} \tag{18}$$

Replacing dx_g/dp and dx_f/dp in Eq. (10) with these expressions, rearranging and substituting $v_{fg}=v_g-v_f$ results in

$$\frac{dv}{dp}=\frac{-\frac{v_{fg}}{h_{fg}}\left(x_g\frac{dh_g}{dp}+x_f\frac{dh_f}{dp}+x_s\frac{dh_s}{dp}\right)+x_g\frac{dv_g}{dp}+x_f\frac{dv_f}{dp}+x_s\frac{dv_s}{dp}}{1+\frac{V^2v_{fg}}{vh_{fg}}} \tag{19}$$

Equations (9) and (19) present the final form of the pressure gradient.

The Choking Velocity

Considering that dv/dp is a negative quantity, it is evident that the denominator in Eq. (9) contains a singularity. The denominator can be rewritten as $1-V^2/c^2$ by defining

$$\frac{1}{c^2}=-\frac{1}{v^2}\frac{dv}{dp} \tag{20}$$

This c is the choking velocity.

By setting the velocity V in Eq. (19) equal to zero and substituting dv/dp into Eq. (20), a quantity c_0 can be defined as

$$c_0=\frac{v}{\left\{\frac{v_{fg}}{h_{fg}}\left(x_g\frac{dh_g}{dp}+x_f\frac{dh_f}{dp}+x_s\frac{dh_s}{dp}\right)-x_g\frac{dv_g}{dp}-x_f\frac{dv_f}{dp}-x_s\frac{dv_s}{dp}\right\}^{1/2}} \tag{21}$$

This c_0 represents the choking velocity at constant enthalpy and may be called the isenthalpic choking velocity. For actual flow though choking occurs when the flow velocity is equal to the real choking velocity. Setting $V=c$ in Eq. (9), simplifying the equation by means of Eq. (21), substituting it into Eq. (20), and solving for c results in

$$c=\frac{c_0}{\left(1-\frac{c_0^2v_{fg}}{vh_{fg}}\right)^{1/2}} \tag{22}$$

The choking velocity can be calculated directly from Eqs. (21) and (22), if local pressure and composition of the mixture are known. On the other hand, if pressure and specific energy e are specified, Eqs. (3)–(8) have to be solved simultaneously to determine specific volume and mixture composition for use in Eqs. (21) and (22).

The Sonic Velocity

A more familiar form of Eq. (20) is $c^2 = dp/d\rho$, and, subject to the assumption of constant entropy, c is also known as the sonic velocity. An expression for the sonic velocity can be obtained by evaluating the derivative dv/dp in Eq. (20) for an isentropic change. The steam mass fraction in this case is given by

$$x_g = \frac{s - s_f + x_s(s_f - s_s)}{s_g - s_f} \tag{23}$$

and its derivative, for use in Eq. (10), is obtained by applying the method used previously (for Eqs. (11)–(15)) and noting that $s_{fg} = s_g - s_f$

$$\frac{dx_g}{dp} = -\frac{x_g}{s_{fg}}\frac{ds_g}{dp} - \frac{x_f}{s_{fg}}\frac{ds_f}{dp} - \frac{x_s}{s_{fg}}\frac{ds_s}{dp} \tag{24}$$

Equation (18) is valid again. Substituting dx_g/dp and dx_f/dp into Eq. (10) and combining with Eq. (20) gives the sonic velocity as

$$c = \frac{v}{\left\{\frac{v_{fg}}{s_{fg}}\left(x_g\frac{ds_g}{dp} + x_f\frac{ds_f}{dp} + x_s\frac{ds_s}{dp}\right) - x_g\frac{dv_g}{dp} - x_f\frac{dv_f}{dp} - x_s\frac{dv_s}{dp}\right\}^{1/2}} \tag{25}$$

This equation is consistent with equations given by Moody [7] and Leung [8] for steam-water. Comparison of velocities calculated by Eqs. (22) and (25) shows the results to be virtually identical for steam-water mixtures. Slight differences exist in the case of mixtures with large solids mass fractions.

Evaluation of c or c_0 demands elaboration on some of the terms in Eqs. (21) and (25). The derivatives dh_g/dp, dh_f/dp, ds_g/dp, ds_f/dp, dv_g/dp, and dv_f/dp are to be evaluated along the steam-water saturation curve. This can be done by calculating the difference quotients $\nabla h_g/\nabla p$, etc., around the pressure point of interest. They can also be determined by differentiation of the reduced enthalpy, reduced entropy and reduced volume functions given in Appendix 1 Section 9 of the ASME Steam Tables [9]. For example, for the reduced entropy σ_g the differentiation takes the form

$$\frac{d\sigma_g}{d\beta} = \frac{\partial\sigma_g}{\partial\beta} + \frac{\partial\sigma_g}{\partial\Theta}\bigg/\frac{d\beta}{d\Theta} \tag{26}$$

where β and Θ are reduced pressure and reduced temperature, respectively.

Using $dh_s = c_p dT$ gives $dh_s/dp = c_p/(dp/dT)$. Similarly it follows from $ds_s = c_p dT/T$ that $ds_s/dp = c_p/(T\,dp/dT)$. The derivative dp/dT can be obtained by differentiation of the K-function given in Appendix 1 Section 5 of the Steam Tables. Alternatively it may be evaluated by means of the Clapeyron equation of classical thermodynamics. Furthermore, $dv_s/dp = -v_s/E_s$. The modulus of elasticity E_s of the solids in the mixture is often not known. Fortunately, for a typical mixture the choking velocity is not sensitive to E_s. (For example, using values of 100 MPa and 10,000 MPa for the model mixture of Figs. 1 and 2 does not produce a difference of more than 0.1 percent in the calculated choking/sonic velocities.)

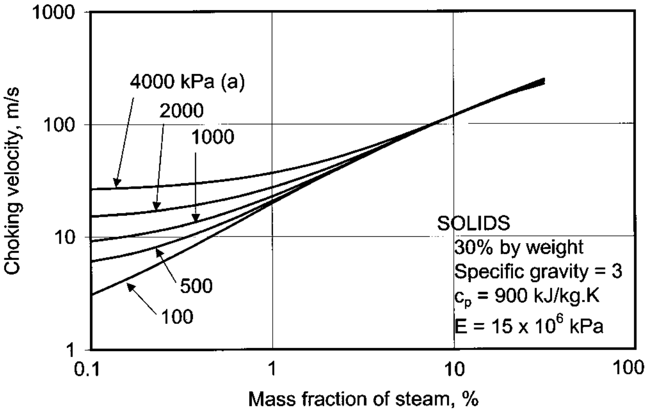

Fig. 1 Choking velocity versus steam mass fraction

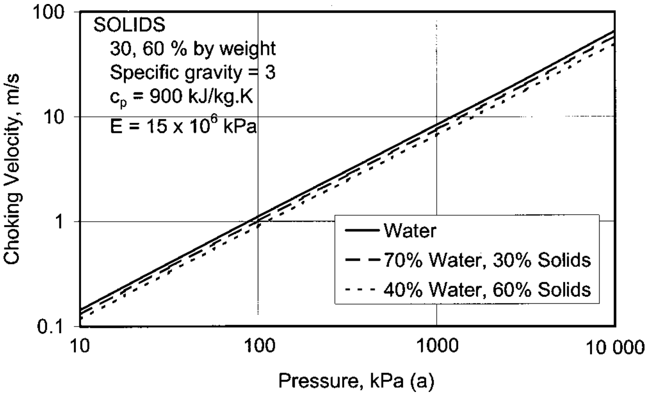

Fig. 2 Choking velocity at incipient flashing

Figure 1 shows the choking velocity for a typical steam-water-solids mixture as a function of steam mass fraction and pressure. Figure 2 presents choking velocities at incipient flashing. These were calculated from Eq. (22) and accessory Eq. (21) by setting $x_g = 0$.

The Exit Condition

The conditions that may occur at the exit are summarized in Table 1. The choking conditions identified include only cases re-

Table 1 Summary of exit conditions

Case	p_e	x_{ge}	V_e	$(dp/dx)_e$	Flow condition
1	$=p_b, >p_{sat}$	<0	$<c_{fs}$	finite	nonflashing, not choked
2	$=p_b = p_{sat}$	>0	$<c$	finite	flashing, not choked
3	$>p_b, = p_{sat}$	>0	$=c$	$\to -\infty$	flashing, choked
4	$>p_b, = p_{sat}$	$=0$	$>c_i, <c_{fs}$	finite	nonflashing, choked*
5	$=p_b = p_{sat}$	>0	$=c$	$\to -\infty$	flashing, choked
6	$=p_b = p_{sat}$	$=0$	$>c_i, <c_{fs}$	finite	nonflashing, choked*

Notes: p_{sat} is the saturation pressure corresponding to the temperature in the exit plane
c_{fs} is the choking velocity of a pure water-solids mixture
$x_g < 0$ indicates a subcooled condition

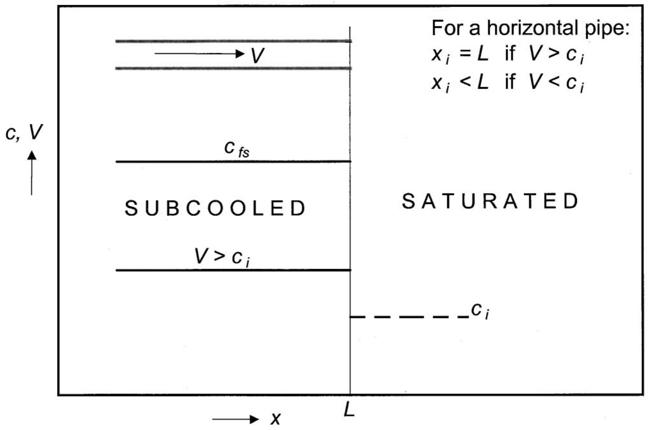

Fig. 3 Quasi-choking occurs if at the point of incipient flashing the velocity *V* is higher than the choking velocity c_i

lating to the choking velocity of a steam-water-solids mixture. It is clear that a choking condition also exists, when the exit velocity is equal to the choking velocity of a water-solids mixture c_{fs}. However, this velocity is of the order of 1500 m/s. Such cases are of little practical significance and hence are not included in the table. Cases 5 and 6 may be viewed as limits of cases 3 and 4, respectively.

The two cases marked with an asterisk (*) present a quasi-choking condition. This condition arises when upon pressure reduction from a subcooled state the saturation pressure is reached at a velocity that is higher than the choking velocity at incipient flashing c_i. A reduction in back pressure p_b and the ensuing drop of exit pressure p_e would move the point of incipient flashing from the exit plane to upstream of the exit plane. Because of the associated step drop in choking velocity, the exit velocity would now be higher than the local choking velocity. Under the stated assumption of ''no supersonic flows'' this scenario is rejected. The quasi-choking condition lacks the characteristics of the ordinary choking condition, i.e., the exit velocity is higher than the choking velocity at incipient flashing and the pressure gradient remains finite. Whereas the ordinary choking condition is the result of a singularity in the pressure gradient, the quasi-choking condition results from the step reduction in choking velocity that accompanies the change from the two-phase water-solids mixture to the three-phase steam-water-solids mixture, or, for that matter, from water to steam-water. Figure 3 may serve to illustrate the situation.

The step change in the choking velocity at incipient flashing can be summarily explained by the presence of the terms dx_g/dp and dx_f/dp in Eq. (10). Both terms are different from zero over the entire saturation range $x_g=0$ to $x_f=0$. It follows that there is a similar step change, albeit much smaller, at the boundary between the saturated and the superheated regions.

In a plot of mass flux versus terminal pressure of a depressurizing compressible fluid the maximum mass flux is usually indicated by a maximum in the curve. For a steam-water mixture accelerating from a stagnation condition of sufficient subcooling the maximum flux is represented by a sharp peak in the curve (see Moody [7]). This peak is the manifestation of a quasi-choking condition.

It has been reported many times that steam-water flows discharging under critical conditions generally exceed the mass flow rate predicted by a homogeneous equilibrium flow theory. The explanations given for this behavior include nucleation delay preventing steam-water equilibrium and departure from the homogeneous flow pattern. There is some reason to expect that for mixtures containing solids the excess flow is less than for steam-water. For one, the finely ground solid particles provide an abundance of nucleation sites, thereby reducing the deviation from equilibrium. Second, because of the higher viscosity of the mixture with solids, velocity differences between the phases should develop slower and departure from the homogeneous flow pattern is possibly delayed.

On the Integration of the Pressure Gradient

The ore processes under consideration are usually, but not always, operated at an overpressure imposed by oxygen or air. In this case the mixture consists initially of water and solids, the water being subcooled. Incipient flashing occurs downstream at the location *x*, where the pressure has been reduced to the saturation pressure. The mathematical description developed for the three-phase mixture is not valid for the two-phase mixture.

Integration of the pressure gradient can be accomplished by finite difference methods. When doing so, it may be advantageous to use the Eq. (2) form of the pressure gradient, since this equation applies to both flashing and nonflashing flows. The integration can be effected either by specifying the inlet pressure and varying the mass flow rate (or inlet velocity) or by specifying the mass flow rate and varying the inlet pressure, until the exit condition is met. Equation (2) does not reveal the singularity in the pressure gradient. Though hidden, it has not gone away and it will be necessary to monitor the velocity ratio V/c at every step.

Determination of the pressure in the exit plane is a necessary part of the integration. An accurate determination is difficult with a pressure gradient that tends towards minus infinity. The difficulty can be overcome by solving Eq. (22) iteratively to determine the pressure corresponding to $c=V$ and tracking this precursor choking pressure to the exit. As V/c approaches unity, the precursor pressure converges to the true choking pressure.

Conclusion

Homogeneous three-phase flow theory is used to develop expressions for the pressure gradient and the choking velocity of a homogeneous steam-water-solids mixture. The pressure gradient can be integrated numerically to give the pressure distribution in the piping system from inlet to exit. If the flow is choked, the underlying flow rate is the maximum flow rate for the given inlet condition.

It is concluded that there is a quasi-choking condition that occurs, when the exit flow velocity is higher than the choking velocity for flashing incipient at the prevailing exit pressure.

Nomenclature

A = area
c = choking velocity
c_p = specific heat of solids
e = total specific energy
E = bulk modulus of elasticity
F = pressure loss due to friction
g = gravitational constant
G = pressure change due to elevation change
h = specific enthalpy
L = length of pipe
$\dot{m}$ = mass flow rate
Ma = Mach number, V/c
p = pressure
s = specific entropy
T = absolute temperature
v = specific volume
V = velocity
x = mass fraction when subscripted, otherwise position variable
z = vertical distance
ρ = density

Subscripts

b = downstream of exit plane
e = exit plane
f = liquid
g = steam, vapor
i = incipient flashing
s = solids
0 = zero velocity or inlet condition

References

[1] Benjamin, M. W., and Miller, J. G., 1942, ‘‘The Flow of a Flashing Mixture of Water and Steam Through Pipes,’’ Trans. ASME, **64**, pp. 657–669.

[2] Allen, W. F., 1951, ‘‘Flow of a Flashing Mixture of Water and Steam Through Pipes and Valves,’’ Trans. ASME, **73**, pp. 257–265.

[3] Starkman, E. S., Schrock, V. E., Neusen, K. F., and Maneely, D. J., 1964, ‘‘Expansion of a Very Low Quality Two-Phase Fluid Through a Convergent-Divergent Nozzle,’’ ASME J. Basic Eng., **86**, pp. 247–256.

[4] Moody, F. J., 1965, ‘‘Maximum Flow Rate of a Single Component, Two-Phase Mixture,’’ ASME J. Heat Transfer, **87**, pp. 134–142.

[5] Henry, R. E., and Fauske, H. K., 1971, ‘‘The Two-Phase Critical Flow of One-Component Mixtures in Nozzles, Orifices, and Short Tubes,’’ ASME J. Heat Transfer, **93**, pp. 179–187.

[6] Fluerenbrock, F., Zerkle, R. D., and Thorpe, J. F., 1976, ‘‘Compressibility Effects in Electrochemical Machining,’’ ASME J. Eng. Ind., **98**, pp. 423–430.

[7] Moody, F. J., 1990, *Introduction to Unsteady Thermofluid Mechanics*, Wiley, New York, pp. 75 and 85.

[8] Leung, J. C., 1996, ‘‘On the Application of the Method of Landau and Lifshitz to Sonic Velocities in Homogeneous Two-Phase Mixtures,’’ ASME J. Fluids Eng., **118**, pp. 186–188.

[9] *ASME Steam Tables*, 1967, 3rd Edition.

Thin-Film Flow at Moderate Reynolds Number

Kenneth J. Ruschak
Senior Research Associate
e-mail: kenneth.ruschak@kodak.com

Steven J. Weinstein
Research Associate

Manufacturing Research and
Engineering Organization,
Eastman Kodak Company,
Rochester, NY 14752-3701

*Viscous, laminar, gravitationally-driven flow of a thin film over a round-crested weir is analyzed for moderate Reynolds numbers. A previous analysis of this flow utilized a momentum integral approach with a semiparabolic velocity profile to obtain an equation for the film thickness (Ruschak, K. J., and Weinstein, S. J., 1999, ''Viscous Thin-Film Flow Over a Round-Crested Weir,'' ASME J. Fluids Eng., **121**, pp. 673–677). In this work, a viscous boundary layer is introduced in the manner of Haugen (Haugen, R., 1968, ''Laminar Flow Around a Vertical Wall,'' ASME J. Appl. Mech. **35**, pp. 631–633). As in the previous analysis of Ruschak and Weinstein, the approximate equations have a critical point that provides an internal boundary condition for a bounded solution. The complication of a boundary layer is found to have little effect on the thickness profile while introducing a weak singularity at its beginning. The thickness of the boundary layer grows rapidly, and there is little cumulative effect of the increased wall friction. Regardless of whether a boundary layer is incorporated, the approximate free-surface profiles are close to profiles from finite-element solutions of the Navier-Stokes equation. Similar results are obtained for the related problem of developing flow on a vertical wall (Cerro, R. L., and Whitaker, S., 1971, ''Entrance Region Flows With a Free Surface: the Falling Liquid Film,'' Chem. Eng. Sci., **26**, pp. 785–798). Less accurate results are obtained for decelerating flow on a horizontal wall (Watson, E. J., 1964, ''The Radial Spread of a Liquid Jet Over a Horizontal Plane,'' J. Fluid Mech. **20**, pp. 481–499) where the flow is not gravitationally driven.* [S0098-2202(00)01904-0]

Introduction

The regime of flow in thin films where flow is laminar but inertial effects are significant is important in the film-coating industry. Experiments show that turbulence develops at Reynolds numbers between about 250 and 800 (Fulford [1]).

Simplified equations, attractive for ease of use, are possible when film thickness changes gradually in the flow direction. These equations are related to the classical equations for a viscous boundary layer. The nonlinear boundary-layer equation and continuity equation may be solved numerically (Cerro and Whitaker [2]), but more often a velocity profile is assumed for integrating the equations across the film and reducing the computational problem to an ordinary differential equation for the profile of film thickness.

The momentum integral approach is practical because of the relative insensitivity of the film-thickness profile to the velocity profile chosen (Anderson [3]). At low Reynolds numbers, the clear choice is a semiparabolic profile, which is the exact profile for fully developed, rectilinear flow determined by Nusselt (Wilkes and Nedderman [4]), and which arises in the limit of small capillary number in the absence of inertial effects (Landau and Levich [5], Ruschak [6]). The resulting equation will be referred to in this paper as the Nusselt film equation. A higher-order polynomial introduces additional parameters requiring auxiliary equations and can lead to less satisfactory results (Anderson [3]). Watson [7] generated a velocity profile for negligible gravitational effects from a similarity solution. Cerro and Scriven [8] used a velocity profile that is a linear combination of full and semiparabolic profiles for flow from a slot onto an incline, but their weighting of the two profiles is arbitrary.

The appropriateness of a semiparabolic profile can be questioned as the Reynolds number increases. On one hand, the momentum flux, normalized with the product of mass flow rate and average velocity, is 1.2 and differs only modestly from unity for a flat profile. On the other hand, a semiparabolic profile spans the film thickness and thereby constrains the shear rate at the wall; underestimating wall friction is potentially a larger source of error.

A way to capture higher shear rates at the wall is to follow Prandtl and consider a viscous boundary layer adjacent to the wall and a region of inviscid flow between the boundary layer and the interface with air (Schlichting [9], Watson [7], Haugen [10], Yang and Yarbrough [11]). A continuously differentiable choice for the velocity profile is semiparabolic in the boundary layer and flat in the inviscid region (Haugen [10]). Bernoulli's equation for the surface streamline supplies the additional relationship required when a boundary layer is introduced. This extended model will be referred to in this paper as the Prandtl film equation. Once the boundary-layer thickness becomes equal to the film thickness, the Prandtl film equation reduces to the Nusselt film equation. The boundary-layer model has also been solved numerically without assuming a velocity profile (Bruley [12]), but the introduction of a boundary layer is of little advantage when a partial differential equation remains.

The main objective of this paper is to demonstrate the effectiveness of the Nusselt film equation for gravity-driven flow. Flow over a round-crested weir, previously analyzed with this equation (Ruschak and Weinstein [13]), is recomputed with a boundary layer, and numerical solutions of the Navier-Stokes equation are provided. Additionally, the previously treated problems of developing flow on a vertical wall and decelerating flow on a horizontal plane are briefly revisited.

The results support the conclusion that the Nusselt film equation is accurate for gravitationally driven flow when the underlying assumptions are met. At moderate Reynolds number, boundary-layer thickness increases so rapidly that the initially high wall friction has little cumulative effect. The constraint of a critical point encountered with the approximate equations is found to be consistent with the numerical solutions of the Navier-Stokes equation obtained with standard boundary conditions.

Equations

As a previous analysis of flow over a round-crested weir (Ruschak and Weinstein [13]) is generalized to admit a boundary layer

---

Contributed by the Fluids Engineering Division for publication in the JOURNAL OF FLUIDS ENGINEERING. Manuscript received by the Fluids Engineering Division December 20, 1999; revised manuscript received July 5, 2000. Associate Technical Editor: D. Williams.

in the manner of Haugen [10] and others, the formulation of the equations can be brief. A Newtonian liquid with viscosity μ and density ρ flows over the crest of a weir that is quarter round, as in Fig. 1, or half round, as in Fig. 4, with radius R. In the former case, liquid flowing from the reservoir abruptly encounters the solid wall at the corner of the crest. With gravitational acceleration denoted G and volumetric flow rate per unit width q, the length scale for film thickness in gravitationally driven viscous flow is $h_c=\sqrt[3]{\mu q/\rho G}$. The two dimensionless groups are Reynolds number, $\mathrm{Re}=\rho q/\mu$, and a ratio of length scales, $\delta=h_c/R$. For $\delta\ll 1$, film thickness changes gradually. For $\mathrm{Re}\gg 1$, vorticity generated at the wall requires some distance downstream to diffuse across the film. Horizontal coordinate x and vertical coordinate z originate at the center of the rounded section. Additional coordinates are r, a radial coordinate, and θ, an azimuthal coordinate increasing from the crest in the flow direction. Radial distance measured outward from the rounded wall, $y=r-R$, is related to dimensionless coordinate η such that $y=h_c\eta$ and $r=R(1+\delta\eta)$. The free surface of the film is given by $y=h(\theta)=h_c\zeta(\theta)$, and η ranges from 0 at the wall to $\zeta(\theta)$ at the free surface. Dimensionless velocity components u and v are defined such that the azimuthal velocity component is qu/h_c and the radial component $\delta q v/h_c$. Pressure is given by ρGRp, where p is dimensionless, to reflect the essentially hydrostatic pressure field across the film.

Flow at the corner of the crest ($\theta=0$) is presumed inviscid, and a viscous boundary layer grows downstream. The initial velocity profile is taken to be flat, although this cannot be precisely the case because the interface over the reservoir is slightly curved. Additionally, the boundary layer is more realistically given an initial thickness because viscous boundary layers adjoin all walls. An initial thickness avoids a singularity in the solution arising from a discontinuity in velocity at the corner.

For slowly varying film flow, the boundary-layer approximation to the Navier-Stokes equation is justified (Bruley [12], Cerro and Whitaker [2], Anderson [14]). For the weir, the approximate equations are (Ruschak and Weinstein [13])

$$\mathrm{Re}\,\delta\left[u\frac{\partial u}{\partial\theta}+v\frac{\partial u}{\partial\eta}\right]=-\frac{\partial p}{\partial\theta}+(1+\delta\eta)\sin(\theta)+\frac{\partial^2 u}{\partial\eta^2}\tag{1}$$

$$0=-\frac{\partial p}{\partial\eta}-\delta\cos(\theta)\tag{2}$$

where the trigonometric terms are gravitational. The continuity equation is

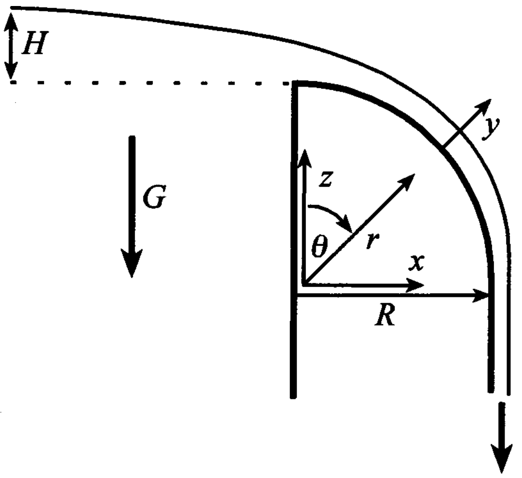

Fig. 1 Definition sketch

$$\frac{\partial u}{\partial\theta}+\frac{\partial v}{\partial\eta}=0\tag{3}$$

The surface of the film, $\eta=\zeta$, is a streamline and free of stress

$$v=u\frac{d\zeta}{d\theta};\quad \frac{\partial u}{\partial\eta}=0;\quad p=0\quad(\eta=\zeta)\tag{4}$$

Velocity is zero at the wall.

$$u=0,\quad v=0\quad(\eta=0)\tag{5}$$

Equations (1)–(5) can be directly applied to film flow, and a rectangular domain can be obtained through the von Mises transformation (Cerro and Whitaker [2]). In this transformation, the stream function replaces the cross-film coordinate, and the dependent variable is the square of the streamwise velocity component.

A simpler approach is to assume a continuously differentiable velocity profile that is semiparabolic across the viscous boundary layer ($0\leqslant\eta\leqslant\omega$) and flat in an inviscid region between the boundary layer and the surface ($\omega\leqslant\eta\leqslant\zeta$).

$$\begin{aligned}u&=U[2\eta/\omega-(\eta/\omega)^2]\quad(0\leqslant\eta\leqslant\omega)\\ u&=U\quad(\omega\leqslant\eta\leqslant\zeta)\end{aligned}\tag{6}$$

This profile is consistent with fully developed, rectilinear flow once the boundary layer spans the film ($\omega=\zeta$). The streamwise velocity component in the inviscid region, U, depends on θ. Pressure is eliminated through Eqs. (2) and (4). Equations (1) and (3) are integrated across the film and evaluated using Eq. (6) to become, respectively

$$\mathrm{Re}\,\delta\frac{d}{d\theta}\left[U^2\left(\zeta-\frac{7\omega}{15}\right)\right]=\zeta\sin(\theta)(1+\delta\zeta)-\delta\zeta\cos(\theta)\frac{d\zeta}{d\theta}-\frac{2U}{\omega}\tag{7}$$

$$U(\zeta-\omega/3)=1\tag{8}$$

A third equation needed to solve for ζ, ω, and U is provided by Bernoulli's equation for the surface streamline

$$\mathrm{Re}\,\delta U^2/2=1+H/R-(1+\delta\zeta)\cos(\theta)\tag{9}$$

where H is the head, the height of the surface of the reservoir above the crest of the weir approached as $U\to 0$ and $\theta\to-\pi/2$. Equation (9) is also a solution of Eq. (7) with $\omega=0$ and without the viscous term, the far term on the right. Writing Eqs. (8) and (9) at $\theta=0$ and identifying variables evaluated there with a subscript 0 gives

$$H/R=\delta\zeta_0+\mathrm{Re}\,\delta U_0^2/2\tag{10}$$

$$U_0(\zeta_0-\omega_0/3)=1\tag{11}$$

Furthermore, Eq. (7) can be rewritten through use of Eq. (9) as

$$d\zeta/d\theta=N/D\tag{12}$$

$$N=\sin(\theta)(1+\delta\zeta)(9\zeta-7/U)/5-2U/\omega\tag{13}$$

$$D=\delta[\cos(\theta)(9\zeta-7/U)/5-2\,\mathrm{Re}\,U^2/5]\tag{14}$$

Flow passes from subcritical in the main body of liquid to supercritical as the liquid accelerates (Ruschak and Weinstein [13]). At the critical point, $D=0$, and it follows from Eq. (12) that the slope of the film can be finite there only if $N=0$ as well. So, if $\zeta=\tilde{\zeta}$, and $\theta=\tilde{\theta}$ at the critical point, then nonlinear algebraic equations for the position of the critical point and the film thickness there are

$$N(\tilde{\zeta},\tilde{\theta})=D(\tilde{\zeta},\tilde{\theta})=0\tag{15}$$

These conditions at the critical point propagate upstream and downstream, and it is natural to integrate Eq. (12) from the critical point in both directions. With $\tilde{\zeta}$ and $\tilde{\theta}$ determined by standard methods for solving nonlinear algebraic equations, the film slope at the critical point follows as the solution to the quadratic equation

$$\frac{\partial D}{\partial \zeta}\left(\frac{d\zeta}{d\theta}\right)^2+\left(\frac{\partial D}{\partial \theta}-\frac{\partial N}{\partial \zeta}\right)\frac{d\zeta}{d\theta}-\frac{\partial N}{\partial \theta}=0 \quad (\theta=\tilde{\theta},\zeta=\tilde{\zeta}) \tag{16}$$

The final equations are solved by iteration. The initial boundary-layer thickness expressed as a fraction of initial film thickness, ω_0/ζ_0, is assigned a small but nonzero value to avoid unbounded derivatives at $\theta=0$, and the value of the initial film thickness, ζ_0, is guessed. Equation (11) then gives U_0, the initial velocity on the surface streamline. The head H follows from Eq. (10). U is then known in terms of ζ and θ from Eq. (9), and ω follows from Eq. 8. Consequently, Eqs. (15) and (16) can be solved for conditions at the critical point, $\tilde{\theta}$, $\tilde{\zeta}$, and the corresponding slope. Equation (12) is integrated from the critical point upstream to the start of the film, $\theta=0$, thereby determining new values for ζ_0 and ω_0 inconsistent with the previously assigned values. This inconsistency is eliminated in subsequent iterations by a numerical implementation of Newton's method.

If the integration were performed in the downstream direction from the start of the boundary layer, the direction in which information usually flows in boundary-layer problems, a local analysis with an initial boundary-layer thickness of zero would have been natural to use to start the integration at a position slightly downstream from the singularity at $\theta=0$. However, because of the constraints on film thickness at the critical point at Eq. (15) and the upstream flow of information in subcritical flow, the natural direction of integration in the problem at hand is from the critical point to the start of the boundary layer. While a local analysis might be used to extrapolate from a finite boundary-layer thickness at the end of the numerical integration to a boundary-layer thickness of zero, this additional step was not attempted because the numerical results were not sensitive to the initial boundary layer thickness for the conditions studied.

With flow to the critical point resolved, Eq. (12) is integrated from the critical point downstream until the boundary-layer thickness equals the film thickness ($\omega=\zeta$). From that point onward the velocity profile is semiparabolic, Eq. (8) simplifies to $U\zeta=3/2$, and the integration is continued with Nusselt film equation,

$$\delta\frac{d\zeta}{d\theta}=\frac{(1+\delta\zeta)\sin(\theta)-3/\zeta^3}{\cos(\theta)-6\ \mathrm{Re}/5\zeta^3} \tag{17}$$

The counterparts of the above equations for the separate problems of developing flow on a vertical wall and decelerating flow on a horizontal wall are similarly derived. With θ_w the angle of the wall from horizontal and with $h_c\xi$ distance along the wall in terms of a dimensionless coordinate ξ, the above equations can be converted by dropping the term $\delta\zeta$ and by replacing $\sin(\theta)$ with $\sin(\theta_w)$, $\cos(\theta)$ with $\cos(\theta_w)$, and $\delta d\zeta/d\theta$ with $d\zeta/d\xi$. For these problems initial film thickness is specified, and iterative solution is not required.

The Navier-Stokes equation was solved for flow over a round-crested weir and for developing flow on a vertical wall by the finite-element method as previously described (Ruschak [15]). The velocity is piecewise linear and the pressure piecewise constant in triangular elements. The resulting nonlinear, algebraic equations for the velocity components at nodes and the pressures in elements were solved by Newton's method.

The result of Cerro and Whitaker [2] for developing flow on a vertical wall obtained by numerical solution of the boundary-layer equation was found to disagree with the finite-element solution of the Navier-Stokes equation, and so the problem of Cerro and Whitaker was solved again. The flow domain was mapped to a semi-infinite strip by the von Mises transformation, which replaces the variable y with the streamfunction ψ, $0\leqslant\psi\leqslant 2/3$. The transformed equation was solved by finite differences and the method of lines. A new variable ϑ is defined that places more mesh points near the wall, specifically $\vartheta=[\log(\psi+\varepsilon)-\log(\varepsilon)]/[\log(2/3+\varepsilon)-\log(\varepsilon)]$, $0\leqslant\vartheta\leqslant 1$. The interval for ϑ was divided into 100 segments, and ε was set to 10^{-6}. The resulting set of first-order, nonlinear differential equations in the streamwise coordinate was solved in MATLAB by solver ODE15S, which employs a variable-order implicit method.

Results

For flow over a weir, the calculation for the Prandtl film equation assumes as the extreme case a virtually flat velocity profile at the crest, $\omega_0/\zeta_0=0.01$. Film profiles are shown in Fig. 2 for Re $=300$ and $\delta=0.00616$. For this Reynolds number, the critical point is very near the crest of the weir at $\tilde{\theta}=3.4$ deg. Also shown is the profile according to the Nusselt film equation, for which the position of the critical point is shifted to $\tilde{\theta}=0.5$ deg. The profiles do not differ much because boundary-layer thickness increases rapidly, and the cumulative effect of increased wall friction is small. The purely inviscid solution is also shown, for which the position of the critical point is $\tilde{\theta}=0$ deg. The viscous profiles depart significantly from the inviscid profile.

The free-surface profile from the Prandtl film equation is compared with that from the Navier-Stokes equation in Fig. 3 for Re=50 and $\delta=0.0282$. For the finite-element computation, 437 elements were employed, and a semiparabolic velocity profile was imposed at the inlet. The computations were found to be insensitive to the precise geometry and boundary conditions imposed in the reservoir, and in Fig. 3 a horizontal solid boundary was added.

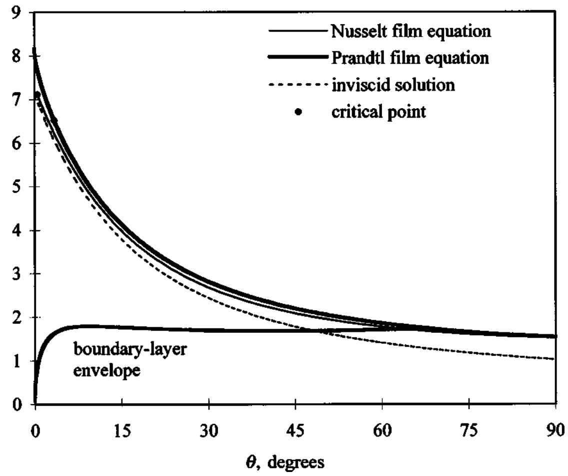

Fig. 2 Film profiles for flow over a quarter-round weir for Re =300, δ=0.00616, and ω_0/ζ_0=0.01. The envelope of the boundary layer is additionally shown for the case of the Prandtl film equation.

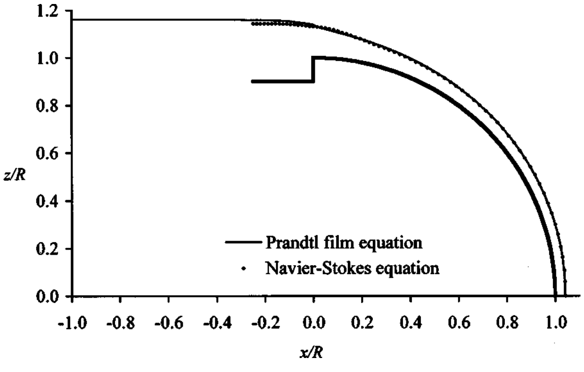

Fig. 3 Film profiles for flow over a quarter-round weir for Re=50 and δ=0.0282. The horizontal solid boundary was added for the solution of the Navier-Stokes equation.

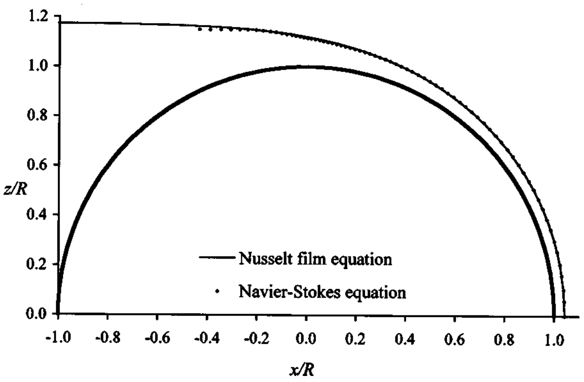

Fig. 4 Film profiles for flow over a half-round weir for Re=50 and δ=0.0286

The profile for the Nusselt film equation was also computed but is so close to the others that it is not shown for clarity. The Nusselt film equation gives a slightly thinner profile near θ=0 deg, and the profile from the Prandtl film equation tracks that from the Navier-Stokes equation better there. The velocity profile from the finite-element solution is not flat at the vertical cross section through the corner at the crest, but instead resembles that shown below in Fig. 7. Although the solutions for the Nusselt film equation and Prandtl film equation arise from a critical point internal to the flow, that for the Navier-Stokes equation involves only standard boundary conditions. The approximate equations are therefore more revealing.

For the half-round weir treated by Ruschak and Weinstein [13], changes in the flow are everywhere gradual, and there is no need to introduce a boundary layer. Profiles from the Nusselt film equation and from the Navier-Stokes equation for 348 elements are shown in Fig. 4 for Re=50 and δ=0.0286, and agreement is excellent.

Developing flow on a vertical wall, being gravitationally driven, is closely related to the weir flow. Results for developing flow on a vertical wall were converted to the dimensionless variables of Cerro and Whitaker [2] to facilitate comparisons. Specifically, the Reynolds number differs from that defined above by a factor of 3/2 and has the value 263 corresponding to Re=175. Film thickness is normalized with that reached asymptotically downstream, h_∞. The streamwise coordinate is made dimensionless with the product of the redefined Reynolds number and h_∞ and denoted X. The initial film thickness, where the velocity profile is taken to be flat, is 2.63 times the final film thickness.

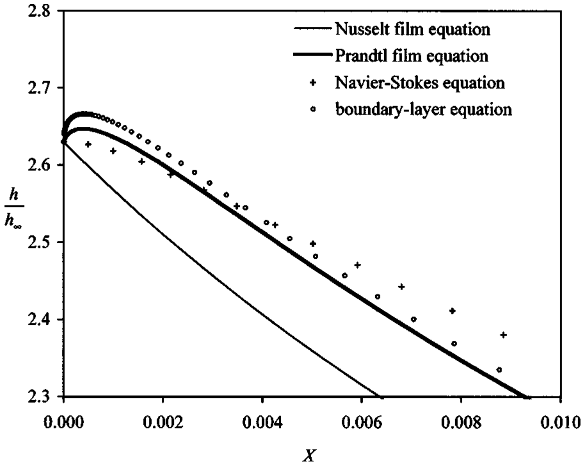

Fig. 6 Film profiles near the origin for developing flow on a vertical wall for Re=175

Figure 5 is a plot of h/h_∞ versus X and corresponds to Fig. 11 of Cerro and Whitaker. Profiles from the Prandtl film equation, the boundary-layer equation, and the Navier-Stokes equation are nearly indistinguishable at this scale. The Nusselt film equation gives a slightly thinner profile as a consequence of underestimating the wall shear stress; this curve has the analytical expression given by Anderson [14]. These results are consistent with the curves in Fig. 11 of Cerro and Whitaker corresponding to the analyses of Bruley [12] and Haugen [10]. However, the solution of the boundary-layer equation by means of the von Mises transformation does not agree with that of Cerro and Whitaker; the agreement of the present solution with that of the Navier-Stokes equation supports the conclusion that the computation of Cerro and Whitaker is in error. Moreover, the curve of Hassan [16] in Fig. 11 of Cerro and Whitaker, also differing from present results, is known to be in error (Anderson [14]).

The discontinuous velocity at the inlet for all cases but the Nusselt film equation introduces a weak singularity in the profiles that is evident in Fig. 6, a magnified view of the start of the profiles. The solution to the Navier-Stokes equation, because of its streamwise viscous terms, is less singular than the solutions to the boundary-layer equation or the Prandtl film equation. Figure 7 shows dimensionless velocity profiles very near the inlet. That from the Navier-Stokes equation shows near the wall a local increase in velocity over the initial value, an effect not captured by the solution to the boundary-layer equation.

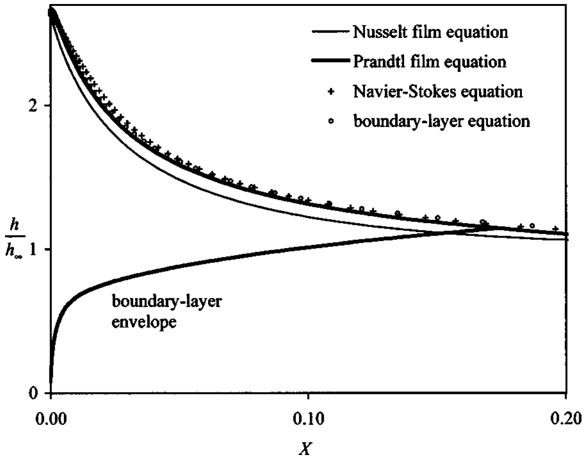

Fig. 5 Film profiles for developing flow on a vertical wall for Re=175

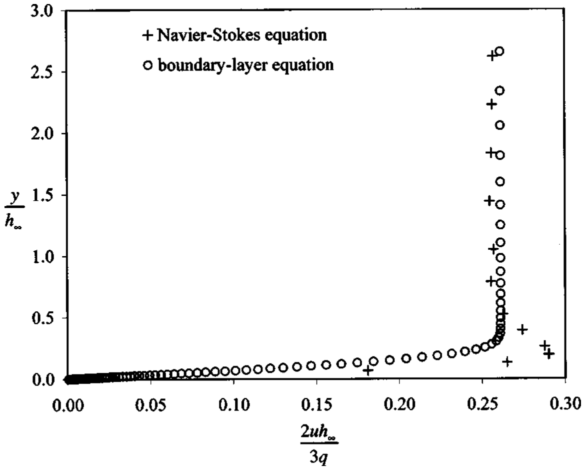

Fig. 7 Velocity profiles at X=0.001 for developing flow on a vertical wall for Re=175

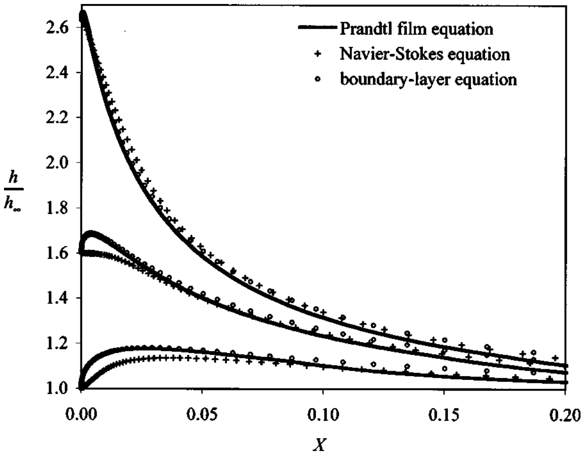

Fig. 8 Film profiles for developing flow on a vertical wall for Re=175 for initial-to-final film-thickness ratios of 2.63, 1.6, and 1.0

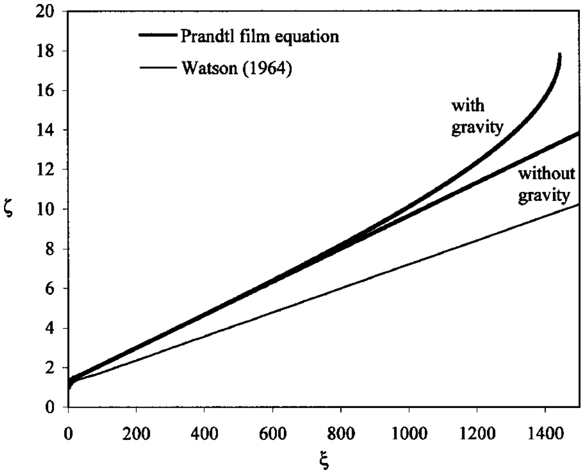

Fig. 9 Film profiles for decelerating flow on a horizontal plate for Re=300 and $\zeta_0=0.4$. Profiles computed with and without gravity are shown for the Prandtl film equation.

Profiles for two additional initial-to-final film-thickness ratios, 1.0 and 1.6, are shown in Fig. 8. In each case the profile for the Prandtl film equation closely tracks the profile for the boundary-layer equation. The profile for the Navier-Stokes equation is initially flatter.

Finally, the Prandtl film equation is applied to decelerating flow on a horizontal wall. Flow is momentum driven, and the momentum is gradually dissipated by wall friction. Watson [7] neglected gravity and constructed a viscous boundary layer that grows to encompass the film. Watson furthermore obtained a similarity solution for the fully viscous flow downstream of the boundary layer. This similarity solution is in fact a limiting case of Jeffery-Hamel flow, an exact similarity solution of the Navier-Stokes equation for radially diverging streamlines (Rosenhead, [17], Ruschak [18]); as such, Watson's results should be accurate. Profiles from Watson's analysis and from the Prandtl film equation for Re=300 and $\zeta_0=0.4$ are shown in Fig. 9. The linear increase in film thickness along the wall in the fully viscous flow with gravity negligible has a slope of 1.81/Re by Watson's analysis and 2.5/Re by the Nusselt film equation, and so the semiparabolic profile over predicts wall friction. Eventually, gravity becomes important, and the solution to the Nusselt film equation ends at a point of infinite slope, likely the approximate location of a hydraulic jump.

Conclusion

In slowly varying laminar flow of a thin film driven by gravity, incorporating a viscous boundary layer and an adjacent region of inviscid flow in approximate equations for film flow is tractable but does not substantially change the film profile or the conditions at a critical point. The increased wall shear stress generated by the boundary layer thickens the film initially and thereby improves agreement with the Navier-Stokes equation. However, the cumulative effect is not great because the boundary layer thickens rapidly. Furthermore, the Navier-Stokes equation generates a velocity profile near the start of the boundary layer that solutions based on the boundary-layer equation do not match. Finally, the stress singularity at the wall at the start of the boundary layer gives rise to a weak singularity in the film profile not exhibited by the profile from the Navier-Stokes equation. So, in the weir flow, there is a discontinuity in slope at the start of the boundary layer. However, at moderate Reynolds number, an initially flat velocity profile, the source of the singularity, is not realistic. So, the incorporation of a boundary layer achieves mixed results and entails a significant penalty in computational effort and complexity. Therefore, even when a boundary layer can be expected, the film equation arising from a semiparabolic velocity profile represents an attractive choice in practice. However, less accurate results are obtained with this velocity profile if flow is not gravitationally driven, and one based on Watson's analysis is preferable.

The singularity at the critical point is not removable in all problems. In that event the approximate equations fail and must be altered. A proposal for generalizing the Nusselt film equation will be reported in the near future.

Acknowledgment

Kam Ng of Eastman Kodak Company's Research Laboratories solved the boundary-layer equation for flow on a vertical wall.

References

[1] Fulford, G. D., 1964, ''The Flow of Liquids in Thin Films,'' Adv. Chem. Eng., **5**, pp. 151–210.
[2] Cerro, R. L., and Whitaker, S., 1971, ''Entrance Region Flows With a Free Surface: the Falling Liquid Film,'' Chem. Eng. Sci., **26**, pp. 785–798.
[3] Anderson, H. I., 1987, ''The Momentum Integral Approach to Laminar Thin-Film Flow,'' Proc. ASME Symposium on Thin Films, Vol. 48, pp. 7–13.
[4] Wilkes, J. O., and Nedderman, R. M., 1962, ''The Measurement of Velocities in Thin Films of Liquid,'' Chem. Eng. Sci., **17**, pp. 177–187.
[5] Landau, L., and Levich, B., 1942, ''Dragging of a Liquid by a Moving Plate,'' Acta Physicochim. URSS, **17**, pp. 42–54.
[6] Ruschak, K. J., 1976, ''Limiting Flow in a Pre-Metered Coating Device,'' Chem. Eng. Sci., **31**, pp. 1057–1060.
[7] Watson, E. J., 1964, ''The Radial Spread of a Liquid Jet Over a Horizontal Plane,'' J. Fluid Mech., **20**, pp. 481–499.
[8] Cerro, R. L., and Scriven, L. E., 1980, ''Rapid Free Surface Flows. An Integral Approach,'' Ind. Eng. Chem. Fundam., **19**, pp. 40–50.
[9] Schlichting, H., 1979, *Boundary-Layer Theory*, 7th edition, McGraw-Hill, New York, pp. 157–158.
[10] Haugen, R., 1968, ''Laminar Flow Along a Vertical Wall,'' ASME J. Appl. Mech., **34**, pp. 631–633.
[11] Yang, T. M. T., and Yarbrough, D. W., 1973, ASME J. Appl. Mech., **40**, pp. 290–292.
[12] Bruley, D. F., 1965, ''Predicting Vertical Film Flow Characteristics in the Entrance Region,'' A.I.Ch.E. Journal, **11**, No. 5, 945–950.
[13] Ruschak, K. J., and Weinstein, S. J., 1999, ''Viscous Thin-Film Flow Over a Round-Crested Weir,'' ASME J. Fluids Eng., **121**, pp. 673–677.
[14] Anderson, H. I., 1984, ''On Integral Method Predictions of Laminar Film Flow,'' Chem. Eng. Sci., **39**, No. 6, pp. 1005–1010.
[15] Ruschak, K. J., 1980, ''A Method for Incorporating Free Boundaries With Surface Tension in Finite Element Fluid-Flow Simulators,'' Int. J. Numer. Methods Eng., **15**, pp. 639–648.
[16] Hassan, N. A., 1967, ''Laminar Flow Along a Vertical Wall,'' ASME J. Appl. Mech., **34**, pp. 535–537.
[17] Rosenhead, L., 1940, ''The Steady Two-Dimensional Radial Flow of Viscous Fluid Between Two Inclined Plane Walls,'' Proc. R. Soc. London, **175**, pp. 436–467.
[18] Ruschak, K. J., 1974, ''The Fluid Mechanics of Coating Flows,'' Ph.D. thesis, University of Minnesota.

Rise Height for Negatively Buoyant Fountains and Depth of Penetration for Negatively Buoyant Jets Impinging an Interface

P. D. Friedman
Department of Mechanical Engineering,
The United States Naval Academy,
Annapolis, MD 21402

J. Katz
Department of Mechanical Engineering,
The Johns Hopkins University,
Baltimore, MD 21218

A vertical jet or fountain, whose velocity is opposite to the direction of its buoyant force, reverses direction after reaching a maximum penetration depth. This penetration depth is measured from the jet exit or, if present, the location of the undisturbed interface. This paper shows that the penetration depth is only a function of a Richardson number divided by a jet spreading factor. If no interface is present, the spreading factor is one; otherwise the spreading factor is only a function of distance between the jet exit and the interface. As long as the jet is fully turbulent, the penetration depth is independent of Reynolds and Weber numbers. These trends are applicable to a broad range of fluid systems including air jets impacting liquids as well as miscible and immiscible liquid-liquid systems with only slight density differences. [S0098-2202(00)00304-7]

Introduction

Jets and fountains with negative buoyancy occur in numerous situations including oxygen jets directed into molten metal furnaces, refueling compensated fuel tanks on naval vessels and the negatively buoyant overshoot stage of a smokestack discharging into a stratified atmosphere. In this paper, we develop a universal correlation for the maximum penetration depths for two related flows. For the flow in Fig. 1(*a*), the jet travels through an identical fluid before reaching a sharp density interface (density difference $\Delta\rho$), where negative buoyancy slows it down until the jet reaches a maximum penetration depth, h. In this case, the penetration depth is measured from the elevation of the undisturbed interface. In Fig. 1(*b*), a fountain is injected directly into a fluid with a different density (in essence, $l=-\infty$) and the penetration depth is measured from the jet exit. When $l<0$, the magnitude of l has no significant effect and h has the same value it does when $l=0$. While numerous technical papers have analyzed the jet and fountain penetration depth, only correlations for narrow data ranges have been published (a number of these are compared later). For simplicity, all the discussions assume a heavy fluid directed upward into a lighter fluid. However, the results are equally valid for a jet directed downward into a denser fluid. Data for both the upward and downward cases are compared.

Analysis and Data

Friedman and Katz [1] show that for $l=0$ the dimensionless penetration is governed by the following relationship:

$$\frac{h}{D_P}=\phi\left(\mathrm{Re}_P,\mathrm{Ri}_P,\mathrm{We}_P,\frac{l}{D_P}\right) \tag{1}$$

where

$$\mathrm{Re}_P=\frac{\rho_j U_P D_P}{\mu_j},\quad \mathrm{Ri}_P=\frac{g\Delta\rho D_P}{\rho_j U_P^2},\quad \mathrm{We}_P=\frac{\rho_j U_P^2 D_P}{\sigma}$$

The parameters σ, ρ, μ, and U are interfacial tension, density, viscosity and velocity, respectively. The ''j'' subscript refers to the jet fluid and the ''P'' subscript refers to parameters at the exit of the jet. It is also shown that the effect of We_P is negligible in most flows of concern; a conclusion supported in the present paper by collapsing data collected from various sources, over a wide range of We_P, to a single line. Friedman et al. [2] show that the viscosity of the penetrated fluid is also an important parameter that must be considered in the characteristics of droplets formed; however, for the purposes of the present discussion concerning penetration by the jet, it is not relevant. This results because the impacted fluid has relatively little flow apart from interfacial mixing. Friedman and Katz [1] demonstrate that the Re_P effect is limited to laminar jets and can be accounted for with the proper definition of velocity. Similarly, Cresswell and Szczepura [3] conclude that for fully turbulent flow, Re has little effect on the mean motion. Reynolds number effects for laminar jets are quantitatively discussed later. Thus for the flow of Fig. 1(*a*) when $l=0$ or for the flow of Fig. 1(*b*), h is a function of Ri_P only. Friedman and Katz [1] experimentally demonstrate a power law for $l=0$ over a broad range of Ri_P:

$$\frac{h}{D_P}=\frac{C_n}{\mathrm{Ri}_P^n} \tag{2}$$

where n varies between 1/3 and 1 and C_n depends on n. For jet exits that are separated from the interface $(l>0)$, spreading causes a velocity reduction and consequent increase in interfacial Richardson number, Ri_i,

$$\mathrm{Ri}_i=\frac{g\Delta\rho D_i}{\rho U_i^2}$$

where the ''i'' subscript refers to properties at the interface.

Assuming that the only effect of $l>0$ is to reduce jet velocity, Eq. (2) can be modified with a velocity decay factor,

$$\frac{h}{D_P}=\frac{C_n}{(\mathrm{Ri}_P/F^2)^n} \tag{3}$$

where $F=U_i/U_P$ varies with l/D_P. For fountain flow of Fig.

Contributed by the Fluids Engineering Division for publication in the JOURNAL OF FLUIDS ENGINEERING. Manuscript received by the Fluids Engineering Division January 11, 2000; revised manuscript received June 22, 2000. Associate Technical Editor: D. P. Telionis.

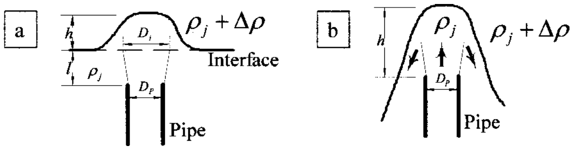

Fig. 1 (*a*) Fluid below the interface, which is the same as jet fluid, is separated from the upper fluid by a sharp density interface. Flow exits the jet at velocity and diameter (U_P, D_P), and spreads to (U_i, D_i) when it reaches the position of the undisturbed interface. (*b*) Fountain rises to a maximum height and reverses.

1(*b*) or for an interface located within the near field or potential core of a jet, $F=1$. In the far-field or fully self-similar region, the centerline velocity decays linearly with the distance from a virtual origin (White [4]),

$$F=\left[\frac{D_P K_2}{l-x_o}\right] \tag{4}$$

Here K_2 is an empirical coefficient and x_o is the downstream position of the virtual origin, normally $-7<x_o/D_p<-4$. Commonly cited values of K_2 range from 5.1 to 7.7 (Banks and Chandrasekhara [5]). For this paper we choose values of $x_o/D_P=-5$ and $K_2=6.7$. For a more detailed treatment of the centerline velocity decay see Papadopoulos and Pitts [6].

Figure 2 summarizes the measured penetration depths from various sources: Chatterjee and Bradshaw [7] (air jet impacting a water interface), Cheslak et al. [8] (air impacting wet cement, which is allowed to harden during deformation), Cresswell and Szczepura [3] (hot water fountain directed into cold water), Friedman and Katz [1] (water impacting diesel fuel), Qian et al. [9] (air impacting water), Shy [10] (acid impacting a miscible base) and Turner [11] (Saltwater fountain directed into freshwater). Except for very shallow penetrations with the jet exit close to the interface (Friedman and Katz data at $\mathrm{Ri}_P/F^2>2$), all data collapse to a narrow band. We will return to the shallow penetration anomaly later. Figure 2 also contains 3 power law relationships in the form of Eq. (2), where $n\in\{\frac{1}{3},\frac{1}{2},1\}$.

The $n=1$ trend has been explained in two ways. A number of studies (e.g., Shy [10]) use a balance of kinetic and potential energy to derive the trend to within an empirical constant.

$$\frac{h}{D_i}=\frac{C_1}{\mathrm{Ri}_i} \quad \text{or} \quad \frac{h}{D_P}=\frac{C_1}{\mathrm{Ri}_P/F^2} \tag{5}$$

Friedman and Katz [1] use a momentum balance and derive a similar expression with $C_1=1$ (the trend shown in Fig. 2). Except for the shallow penetration anomaly where the pipe exit is in close proximity to the interface (i.e., $l/D_P\ll 1$), data from Qian et al., [8] show that the $n=1$ trend continues to very high Ri_P/F^2.

Banks and Chandrasekhara [5] propose a methodology to extend the energy argument for deep cavities, but as shown below their approach is not satisfactory for low values of Ri_P/F^2. They argue that a stagnation point occurs where the loss in kinetic energy is balanced by the increase in potential energy. Further, they propose that the kinetic energy should be based on the centerline velocity of a free jet, which decays through spreading to the location $l+h$. This argument has been widely used, most recently by Qian et al. [9]. In order to test this theory, some of the data of Fig. 2 are replotted on Fig. 3, but in this case the jet spreading factor is $F=D_P K_2/(l+h-x_o)$. A substantial deviation and divergence between data sets occur for low Ri_P/F^2. This divergence is relatively insensitive to the choices of K_2 and x_o/D_P.

As shown in Fig. 2, several papers, including Turner [11], on negatively buoyant fountains propose a better correlation than that of Banks and Chandrasekhara [5]. Turner argues that the penetration depth is proportional to the length scale $M^{3/4}B^{-1/2}$

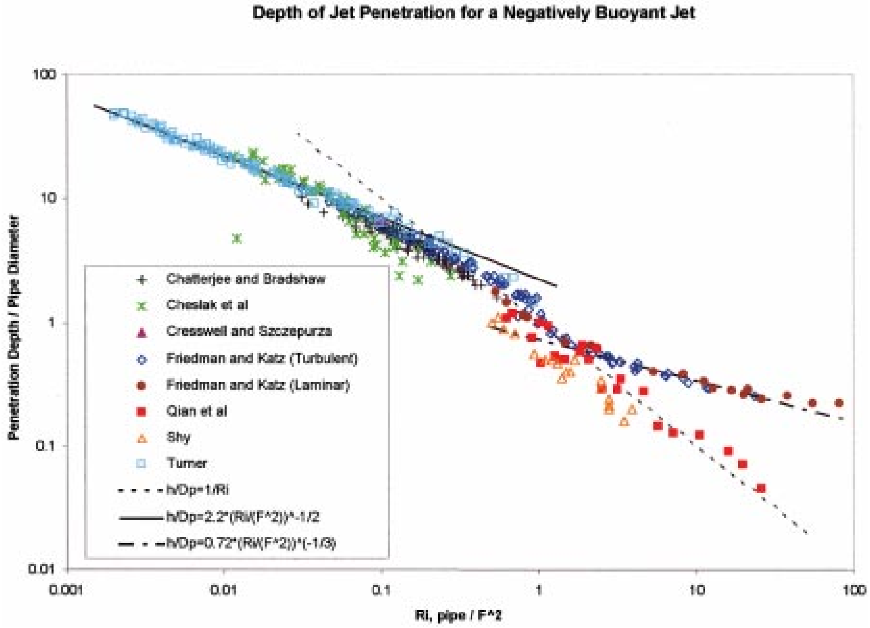

Fig. 2 Dimensionless penetration depth as a function of Ri_P/F^2. All data approach one of three power law trends. Data from Friedman and Katz at high Ri_P/F^2 follow a different trend than the rest of the data because of the radial pressure distribution established as flow turns sharply over pipe edge.

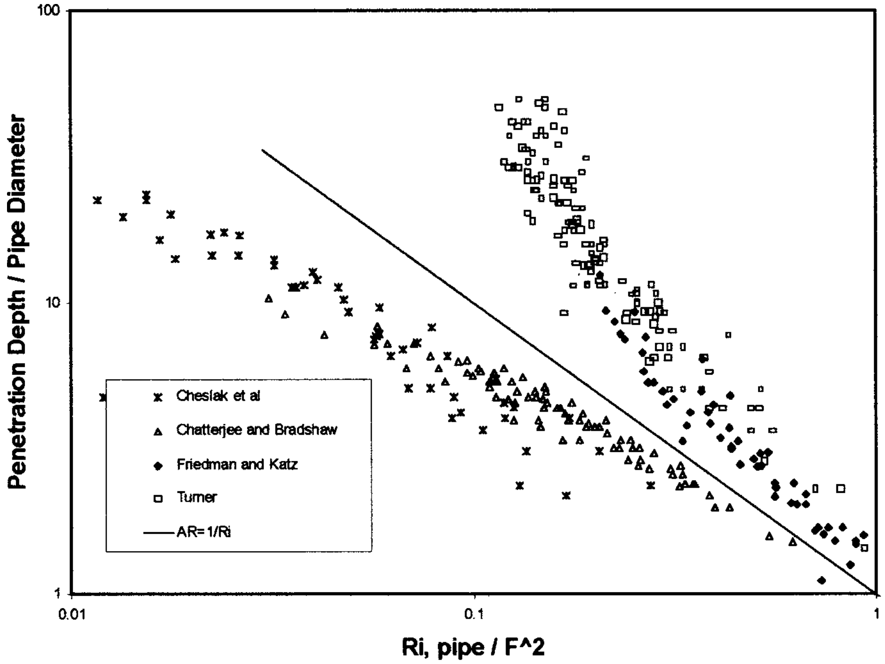

Fig. 3 Dimensionless penetration depth, h/D_P as a function Ri_P/F^2. In this case, F is based on jet spreading to the position $l+h$ [i.e., $F=D_PK_2/(1+h-x_0)$]. The correlation shows significant deviation and is not considered universal.

where $M=(U_P^2\pi D^2)/4$ is the momentum flux and $B=g\Delta\rho U_P\pi D^2/(4\rho)$ is the negative buoyancy flux. This expression is equivalent to Eq. (2) with $n=1/2$,

$$\frac{h}{D_P}=\frac{C}{\mathrm{Ri}_P^{1/2}}$$

Returning to the shallow penetration anomaly, data for $\mathrm{Ri}_P/F^2>2$ show a distinct bifurcation that is explained by the underlying physics. With the pipe exit close to the interface $(l/D_P\ll 1)$, data deviate from the $n=1$ trend because the penetration depth is governed by the radial pressure gradient associated with the sharp 90 deg change in flow direction of the jet fluid as it bends through the narrow gap between the pipe and the interface. The higher centerline pressure lifts the interface. Friedman and Katz [1] develop an expression for h/D_P by equating the radial flow through the gap with the jet flow rate. The analysis is extended here to cases with $l>0$. Equating the pipe flux with the radial flow $[\pi U_P D_P^2/4=\pi D_P u_R(l+h)]$ and substituting $u_R\propto(2gh\Delta\rho/\rho)^{1/2}$ yields

$$\frac{h}{D_P}\left(\frac{l+h}{D_P}\right)^2=\frac{C}{\mathrm{Ri}_P} \tag{6}$$

When $l=0$, Eq. (6) takes the form of Eq. (2)

$$\frac{h}{D_P}=\frac{C}{\mathrm{Ri}_P^{1/3}}$$

Reynolds number affects the penetration depth only if the flow is laminar. When compared with turbulent flow with the same mean velocity, the laminar parabolic velocity profile has more momentum and kinetic energy and thus a greater penetration depth (Friedman and Katz [1]). To account for this difference, the Richardson number can be based on the root mean square velocity, $\mathrm{Ri}_{P,\mathrm{RMS}}$ (for laminar flow $\mathrm{Ri}_{P,\mathrm{RMS}}=\mathrm{Ri}_P/2$). In Fig. 2, $\mathrm{Ri}_{P,\mathrm{RMS}}$ is used for all data from Friedman and Katz [1] with $\mathrm{Re}<2500$ and $\mathrm{Ri}_P/F^2<5$. If $\mathrm{Ri}_P/F^2>5$, then the penetration is governed by the radial pressure distribution as noted above.

Conclusions

We have shown that three power law relationships explain the penetration depth of a negatively buoyant fountain or jet,

$$\frac{h}{D_P}=\frac{C_n}{(\mathrm{Ri}_P/F^2)^n}$$

where

$$(n,C_n)=\begin{cases}(1/2,2.2), & \mathrm{Ri}_P/F^2<0.2\\ (1,1), & \mathrm{Ri}_P/F^2>0.2\\ (1/3,0.72), & \mathrm{Ri}_P/F^2>2 \text{ and } 1/D_P\ll 1\\ & \text{(i.e., Shallow penetration anomaly)}\end{cases}$$

The correlations fit a wide variety of published data, including miscible and immiscible fluids, liquid-gas interfaces, liquid-liquid interfaces and fountains with no interfaces. Weber number effects are not important in the mean flow and Reynolds number effects, which are significant only in the case of laminar flow, require only a slight modification.

A Note About the Data From Turner [11]:

There is an inconsistency between the text and plotted data on his Fig. 5. We contacted Dr. Turner and he informed us by private communication that there is a scale error on his Fig. 5. The data plotted in Fig. 2 are corrected results. We wish to thank Professor Turner for reanalyzing his 34-year-old data.

Acknowledgments

We would like to thank Naval Sea Systems Command Code 05R24, program manager Carl Adema and NSWC Carderock Division (Code 633), program manager Ray Schmitt for exceptional support and funding. Additionally, we are very grateful to Professor Stuart Turner for his review of this work and insightful comments.

Nomenclature

B = buoyancy flux
C_n = empirical constant
D_i = diameter of fluid jet at interface
D_P = diameter of fluid jet at exit
F = jet spreading velocity decay factor ($F = U_i / U_P$)
g = gravitational constant
h = depth of jet penetration in the interface or fountain rise height
K_2 = empirical jet spreading coefficient
l = distance between the jet exit and interface
M = momentum flux
n = empirical exponent
Re_P = Reynolds number based on properties at jet exit
Ri_P = Richardson number based on properties at jet exit
$\mathrm{Ri}_{P,\mathrm{RMS}}$ = Richardson number using root mean square velocity
Ri_i = Richardson number based on properties at interface
u_R = radial velocity
U_i = jet velocity at interface
U_P = jet velocity at exit
U_{RMS} = root mean square average jet velocity
We_P = Weber number based on properties at jet exit
x_o = location of virtual origin
μ_j = dynamic viscosity of jet fluid
ρ_j = density of jet fluid
$\Delta\rho$ = difference in density between lower and upper fluid
σ = interfacial surface tension

References

[1] Friedman, P. D., and Katz, J., 1999, ''The Flow and Mixing Mechanisms Caused by the Impingement of an Immiscible Interface with a Vertical Jet,'' Phys. Fluids, **11**, pp. 2598–2606.

[2] Friedman, P. D., Winthrop, A. L., and Katz, J., ''Droplet Formation and Size Distributions from an Immiscible Interface Impinged with a Vertical Negatively Buoyant Jet,'' accepted by Atom. Sprays.

[3] Cresswell, R. W., and Szczepura, R. T., 1993, ''Experimental Investigation into a Turbulent Jet with Negative Buoyancy,'' Phys. Fluids A, **5**, pp. 2865–2878.

[4] White, F. M., 1991, *Viscous Fluid Flow*, 2nd ed., McGraw-Hill, Boston, p. 474.

[5] Banks, R. B., and Chandrasekhara, D. V., 1962, ''Experimental Investigation of the Penetration of a High Velocity Gas Jet through a Liquid Surface,'' J. Fluid Mech., **15**, pp. 13–34.

[6] Papadopoulos, G., and Pitts, W., 1999, ''A Generic Centerline Velocity Decay Curve for Initially Turbulent Axisymmetric Jets,'' ASME J. Turbomach., **121**, pp. 80–85.

[7] Chatterjee, A., and Bradshaw, A. V., 1972, ''Breakup of a Liquid Surface by an Impinging Gas Jet,'' J. Iron Steel Inst., London, **210**, pp. 179–187.

[8] Cheslak, F. R., Nickolls, J. A., and Sichel, M., 1969, ''Cavities Formed on Liquid Surfaces by Impinging Gaseous Jets,'' J. Fluid Mech., **36**, pp. 55–63.

[9] Qian, F., Mutharasan, R., and Farouk, B., 1996, ''Studies of Interface Deformations in Single- and Multi-Layered Liquid Baths Due to an Impinging Gas Jet,'' Metall. Mater. Trans. B, **27**, pp. 911–920.

[10] Shy, S. S., 1995, ''Mixing Dynamics of Jet Interaction with a Sharp Density Interface,'' Exp. Therm. Fluid Sci., **10**, pp. 355–369.

[11] Turner, J. S., 1966, ''Jets and Plumes with Negative or Reversing Buoyancy,'' J. Fluid Mech., **26**, 779–792.

Philemon C. Chan
Kit K. Kan
James H. Stuhmiller

Jaycor, Inc.,
3394 Carmel Mountain Road,
San Diego, CA 92121-1002

A Computational Study of Bubble-Structure Interaction

The complex interaction between underwater explosion bubbles and nearby structures is studied using two-fluid computational fluid dynamics. Gravitational effects on bubble jetting are significantly different between jet-up and jet-down orientations. This paper presents computational results of underwater explosion bubble dynamics near a disk and a sphere. The results show that the bubble jetting and collapse phenomena and the consequent pressure loading are affected by the structure's shape, the orientation of the bubble to the structure, and the bubble depth. A unifying notion emerges connecting jet strength at impact to bubble curvature at the time of jet formation.
[S0098-2202(00)01804-6]

1 Introduction

Over the past decade, two-fluid Computational Fluid Dynamics (CFD) effort has contributed to the phenomenological understanding of explosion bubble dynamics and structural loading at small and large scales. The oscillation of a bubble generated by detonation of energetic materials underwater involves the exchange between the potential energy in the bubble and the kinetic energy in the water. The Rayleigh equation describes the ideal dynamics of a single bubble in an infinite water medium without gravity (Lamb [1]). Closed-form solutions cannot be obtained, however, in the presence of gravity and/or a nearby solid object. In these cases, understanding depends heavily on experiments which can be costly and difficult to perform.

A contracting bubble can produce strong loadings on a nearby structure with a reentrant waterjet followed by a high-pressure field when the bubble reaches its minimum (Kan and Stuhmiller [2], Blake and Gibson [3]). Immediately following detonation of an explosive underwater the initial, high bubble pressure accelerates the water radially outward and causes the bubble to expand to a large volume with an extremely low pressure. The ambient water pressure then causes the bubble to collapse to complete the oscillation cycle. During the bubble contraction, the hydrostatic pressure gradient due to gravity can disrupt the symmetry of the collapse process and cause the formation of a high-speed reentrant waterjet through the bubble (Cole [4], Goertner [5]).

An explosion bubble can be designed to direct its waterjet toward a nearby structure. When a bubble intersects a rigid surface during the expansion phase the bubble tends to attach itself to that surface during the contraction phase (Snay et al. [6]). The collapse is then concentrated on the side of the bubble away from the structure, leading to the formation of a reentrant waterjet that may be directed toward the structure. Therefore, a bubble is considered in a jet-up or jet-down orientation when it is below or above a rigid boundary, respectively.

While existing tests and the majority of previous computational studies have primarily addressed the collapse of bubbles generated by charges located beneath a rigid boundary in the jet-up orientation, much less is known about bubble dynamics for charges placed above a rigid boundary in the jet-down orientation. The objective of this work is to provide a comparison understanding of underwater explosion bubble behavior between these two orientations using axisymmetric computations. Simulations were performed for a disk and a sphere to also study the effects of structural geometry on bubble collapse.

Potential flow has long been used in solving two-phase flow problems with a sharp interface but increasing difficulties are encountered in modeling the bubble jetting and break up behavior (Chahine [7], Chahine and Duraiswani [8]). By taking the interface as a streamline next to a gas region with a uniform pressure, the potential flow approach can establish an air-water interface as part of the solution without numerical diffusion (Chan and Chow [9]). Potential flow method is limited to providing a solution when the bubble remains simply connected (Blake [10], Blake and Gibson [3], Blake and Prosperetti [11]). However, after jetting, the bubble becomes a doubly connected shape like a torus and eventually breaks up. Some previous numerical studies on the effect of gravity on bubble migration and jet formation near a rigid boundary were carried out by Blake et al. [10] using the potential flow method, but their simulation could not continue beyond jet touchdown or the inception of bubble splitting. Simulation of the complete bubble collapse, jetting and splitting process is essential in predicting bubble loads on the nearby structure.

We simulate the interaction of explosion bubbles with rigid boundaries by the method of finite difference solution to the two-fluid transport equations for the primitive variables. An interphase tracking algorithm is implemented to preserve the gas-liquid interface. Computational fluid dynamics (CFD) method is attractive because it poses no restriction of the bubble surface, and it can handle the jetting and subsequent fragmentation of the bubble without intervention.

2 Computational Method

The governing equations and numerical method are described in cylindrical coordinates, with r, θ, z, and t representing the radial, azimuthal, axial and temporal coordinates, respectively. It is assumed that the liquid and gas phases have equal velocity and the effects of viscosity and surface tension are negligible. Mass and energy transfers caused by cavitation can be modeled, but these effects are not encountered in the present work. The equations are presented in three-dimensional form for completeness, but computations are performed in axisymmetric r-z coordinates with all azimuthal components suppressed.

With the subscripts 1 and 2 designating the liquid and gas phases, respectively, the continuity equations are

$$\frac{\partial}{\partial t}m_1+\frac{1}{r}\frac{\partial}{\partial r}rm_1u+\frac{1}{r}\frac{\partial}{\partial \theta}m_1v+\frac{\partial}{\partial z}m_1w=0 \qquad (1)$$

$$\frac{\partial}{\partial t}m_2+\frac{1}{r}\frac{\partial}{\partial r}rm_2u+\frac{1}{r}\frac{\partial}{\partial \theta}m_2v+\frac{\partial}{\partial z}m_2w=0 \qquad (2)$$

with m being the bulk density

$$m_1=\alpha_1\rho_1 \qquad (3)$$

Contributed by the Fluids Engineering Division for publication in the JOURNAL OF FLUIDS ENGINEERING. Manuscript received by the Fluids Engineering Division November 11, 1998; revised manuscript received August 10, 2000. Associate Technical Editor: C. Merkle.

$$m_2=\alpha_2\rho_2 \tag{4}$$

where α and ρ are the volume fraction and material density of each phase, and u, v, and w are the velocities in r, θ, and z directions, respectively. By conservation of volume

$$\alpha_1+\alpha_2=1 \tag{5}$$

The equation of motion in each direction is the sum of the two phasic momentum equations

$$\frac{\partial u}{\partial t}+u\frac{\partial u}{\partial r}+\frac{v}{r}\frac{\partial u}{\partial \theta}+w\frac{\partial u}{\partial z}-\frac{v^2}{r}=-\left(\frac{1}{m_1+m_2}\right)\frac{\partial p}{\partial r}+g_r \tag{6}$$

$$\frac{\partial v}{\partial t}+u\frac{\partial v}{\partial r}+\frac{v}{r}\frac{\partial v}{\partial \theta}+w\frac{\partial v}{\partial z}-\frac{uv}{r}=-\frac{1}{r}\left(\frac{1}{m_1+m_2}\right)\frac{\partial p}{\partial \theta}+g_\theta \tag{7}$$

$$\frac{\partial w}{\partial t}+u\frac{\partial w}{\partial r}+\frac{v}{r}\frac{\partial w}{\partial \theta}+w\frac{\partial w}{\partial z}=-\left(\frac{1}{m_1+m_2}\right)\frac{\partial p}{\partial z}+g_z \tag{8}$$

where p is pressure, and g_r, g_θ, and g_z are the body forces per unit mass.

Since there is no interphase mass and energy exchange, the energy equation is not needed by assuming that the liquid phase stays at a constant temperature with a constant sound speed, c_0, and the gas obeys an adiabatic expansion

$$d\rho_1=\frac{1}{c_0^2}dp \tag{9}$$

$$\frac{p}{\rho_2^\gamma}=C \tag{10}$$

where γ is the ratio of specific heats and C is a constant determined by the initial bubble condition.

The two-fluid computational method used in this work is implemented in the Equation Independent Transient Analysis Computer Code (EITACC) developed by JAYCOR. The EITACC code has been successfully applied to single phase blast problems, as well as two-phase flows with combustion (Klein et al. [12], Chan and Klein [13]).

The system of governing equations is integrated by the pressure-based semi-implicit finite difference algorithm of Liles and Reed for two-phase flows (Liles and Reed [14]), where pressure is solved implicitly while the continuity and momentum equations are integrated explicitly. A staggered mesh convention is adopted, with scalar variables placed at cell centers and velocities across mid-cell faces. The continuity and momentum equations (1–2, 6–8) are integrated from time level n to $n+1$ with time step Δt as

$$m_1^{n+1}=m_1^n-\Delta t\left[\frac{\partial}{\partial r}rm_1^nu^{n+1}+\frac{1}{r}\frac{\partial}{\partial \theta}m_1^nv^{n+1}+\frac{\partial}{\partial z}m_1^nw^{n+1}\right] \tag{11}$$

$$m_2^{n+1}=m_2^n-\Delta t\left[\frac{\partial}{\partial r}rm_2^nu^{n+1}+\frac{1}{r}\frac{\partial}{\partial \theta}m_2^nv^{n+1}+\frac{\partial}{\partial z}m_2^nw^{n+1}\right] \tag{12}$$

$$u^{n+1}=u^n-\Delta t\left[u\frac{\partial u}{\partial r}+\frac{v}{r}\frac{\partial u}{\partial \theta}+w\frac{\partial u}{\partial z}-\frac{v^2}{r}\right]^n-\frac{\Delta t}{(m_1+m_2)^n}\frac{\partial p^{n+1}}{\partial r}+g_r^n\Delta t \tag{13}$$

$$v^{n+1}=v^n-\Delta t\left[u\frac{\partial v}{\partial r}+\frac{v}{r}\frac{\partial v}{\partial \theta}+w\frac{\partial v}{\partial z}+\frac{uv}{r}\right]^n-\frac{\Delta t}{(m_1+m_2)^n}\frac{\partial p^{n+1}}{\partial \theta}+g_\theta^n\Delta t \tag{14}$$

$$w^{n+1}=w^n-\Delta t\left[u\frac{\partial w}{\partial r}+\frac{v}{r}\frac{\partial w}{\partial \theta}+w\frac{\partial w}{\partial z}\right]^n-\frac{\Delta t}{(m_1+m_2)^n}\frac{\partial p^{n+1}}{\partial z}+g_z^n\Delta t \tag{15}$$

By Taylor's series expansion, Eqs. (5), (9), and (10) are differenced in the linearized form as

$$\left(\frac{m_1}{\rho_1}\right)^{n+1}+\left(\frac{m_2}{\rho_2}\right)^{n+1}=0 \tag{16}$$

$$\rho_1^{n+1}=\rho_1^n+\left(\frac{\partial \rho_1}{\partial p}\right)^n(p^{n+1}-p^n) \tag{17}$$

$$\rho_2^{n+1}=\rho_2^n+\left(\frac{\partial \rho_2}{\partial p}\right)^n(p^{n+1}-p^n) \tag{18}$$

Equations (11)–(18) are cast in matrix form for each computational cell

$$[A][x]=[s] \tag{19}$$

where matrices $[A]$ and $[s]$ contain known quantities from differencing and boundary conditions, and $[x]$ is the unknown column matrix

$$[x]=\begin{bmatrix}u\\v\\w\\\rho_1\\\rho_2\\m_1\\m_2\\p\end{bmatrix} \tag{20}$$

By applying Gaussian elimination to Eq. (19), a banded pressure matrix equation can be derived for the entire computational domain which is solved by the Alternating Direction Iteration (ADI) method (Peaceman and Rachford [15]). Once the pressure is known, all other dependent variables are determined by back substitution using Eq. (19). Nonlinearities can be removed by Newton-Raphson iteration (Anderson et al. [16]).

A hybrid central-upwind difference scheme is used for discretizing the advection terms in the momentum equations (13)–(15) to minimize interface dispersion while maintaining accuracy. If a computational cell is in a single-phase region, the second order Lax-Wendroff central difference is applied (Anderson et al. [16]). For cells that are part of or next to an interface, second-order upwind difference is used.

The advection terms in the continuity equations (11)–(12) are differenced by upwind fluxing compatible with the interface-sharpening algorithm. At each time step for each two-phase cell, the orientation of the interface, which is assumed as a flat plane, and its intersections with cell faces are determined. The mass fluxes of each phase crossing the cell faces are apportioned based on the old time level velocities such that a donor cell will not be overdepleted and a receptor cell not overfilled. Numerical errors will still cause minor countering effects and interphase dispersion that will be corrected by a sharpening process at the end of each time step.

The sharpening algorithm is implemented based on the conservation of volume similar to the VOF method (Hirt and Nichols [17]), but the marker-in-cell particles are not used. At the end of each calculation time step, the normals to all interfaces are determined. Water in the two-phase zones is redistributed in the directions normal to the interface to remove overfilling, overdepletion and dispersion until the gas and liquid phases are separated by no more than one layer of two-phase cells.

At a given depth, Z (including the atmospheric pressure) an explosive charge will release a certain amount of chemical energy and produce a certain maximum bubble radius, $A_{\max}$, minimum bubble radius, $A_{\min}$, and bubble oscillation period, T. The conditions for each calculation can, therefore, be expressed in terms of the inverse Froude number, $\mathrm{F}^{-1}=gT^2/A_{\max}$. It is understood that $A_{\max}$ is the radius of an equivalent sphere with the same maximum bubble volume since gravity distorts the symmetry of the bubble. Each of the calculations was started with a high pressure gas bubble of radius $A_{\min}$, with initial bubble pressure P_0, chosen according to the empirical relationships established by the Naval Surface Warfare Center (NSWC) (Snay and Christian [18]; Snay et al. [6]).

3 Validation

Validation of the computational method with grid sensitivity study was first performed for an isolated bubble corresponding to an inverse Froude number of 0.172. The calculated bubble maximum radius and period using three resolutions all agree with the NSWC data (Snay and Christian [18]) as shown in Table 1. To simulate the bubble oscillation, it is important to use uniform resolution to cover the maximum bubble volume. The three cell resolutions used in the bubble region were $A_{\max}/20$, $A_{\max}/30$, and $A_{\max}/40$, and computational cells outside of the bubble region were gradually spanned out to the outer boundary taken to be $10A_{\max}$ from the charge center. Ambient hydrostatic pressure conditions were imposed at the outer boundary. Table 1 shows that the simulation with all three resolutions agree with the empirical results within 0.1%. Our experience indicates that when the bubble radius is resolved by 40 cells, $(A_{\max}/40)$, adequate jetting resolution is achieved. For all subsequent calculations, the bubble resolution was taken as at least $A_{\max}/40$ in both r and z directions.

Table 1 Single bubble validation results

Resolution	$A_{\max}$ Calculation/Data	T Calculation/Data
$A_{\max}/20$	0.992	1.003
$A_{\max}/30$	1.000	1.003
$A_{\max}/40$	0.996	0.999

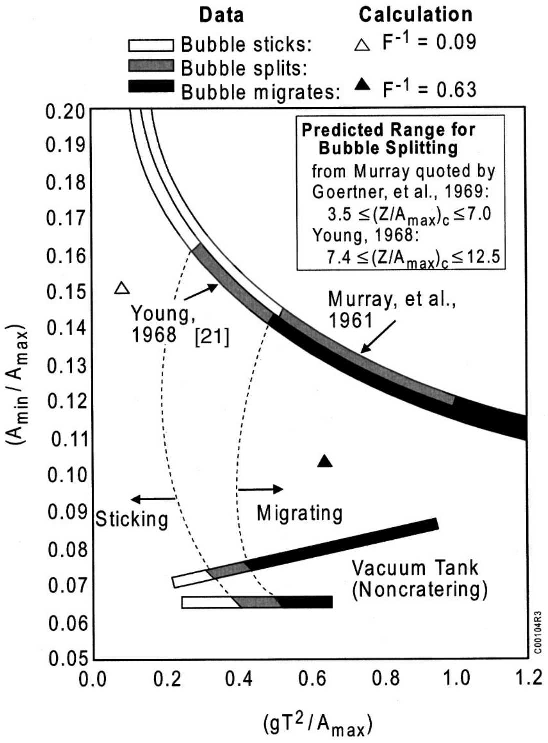

Fig. 1 Comparison of calculations for bottom explosion bubbles with data from Goertner et al. [19]. Reference cited in figure is [21].

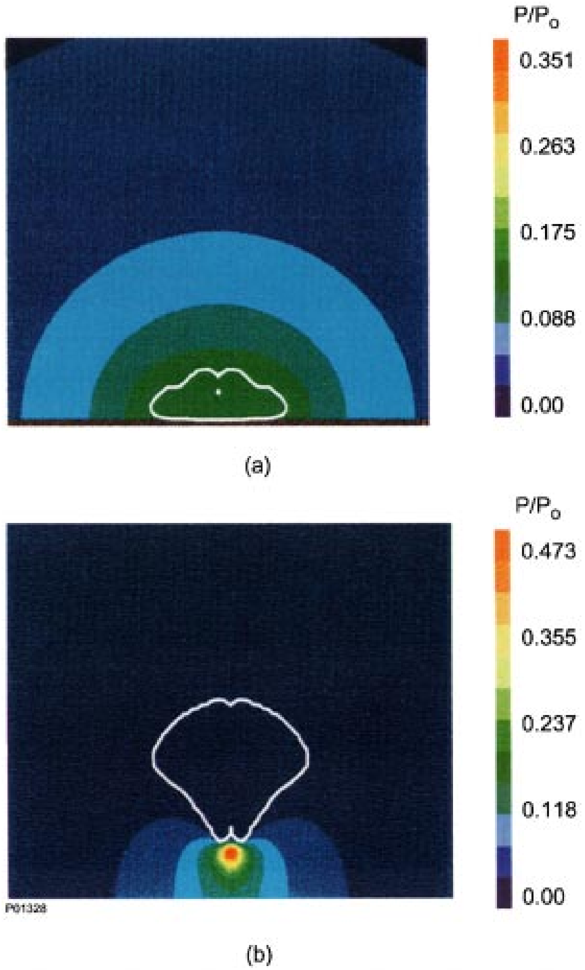

Fig. 2 Calculated bubble shapes near their minima for bottom explosion bubbles. (*a*) $\mathrm{F}^{-1}=0.09$; (*b*) $\mathrm{F}^{-1}=0.63$.

Validation calculations were also performed for explosion bubbles generated on a rigid bottom. When a bubble collapses on a rigid surface from below, gravity and geometric effects work together to cause the bubble to jet upward. When a bubble collapses on a rigid surface from above in the jet-down orientation, however, the two effects oppose one another, resulting in significant changes to the jetting process. To validate the computation method for the case of bubble collapse in the jet-down orientation, simulations were compared to experimental data (Goertner et al. [19]). Two calculations for a bubble generated on a bottom surface were made at conditions corresponding to $\mathrm{F}^{-1}=0.09$ (relatively deep), and 0.63 (shallow).

The calculated results agree with the regimes based on a collection of experimental results from Goertner et al. [19] as plotted in Fig. 1 on the coordinates of the radius ratio $(A_{\min}/A_{\max})$ and the inverse Froude number. Figure 1 shows there is a considerable spread of the compiled data. The data generally show that the bubble tends to stick to the bottom when the inverse Froude number F^{-1} is less than 0.2 (deep condition), and the bubble tends to migrate upward when F^{-1} is greater than 0.5 (shallow condition), and our validation calculations capture these two conditions (Fig. 1). Figure 2 shows the calculated bubble shapes near their

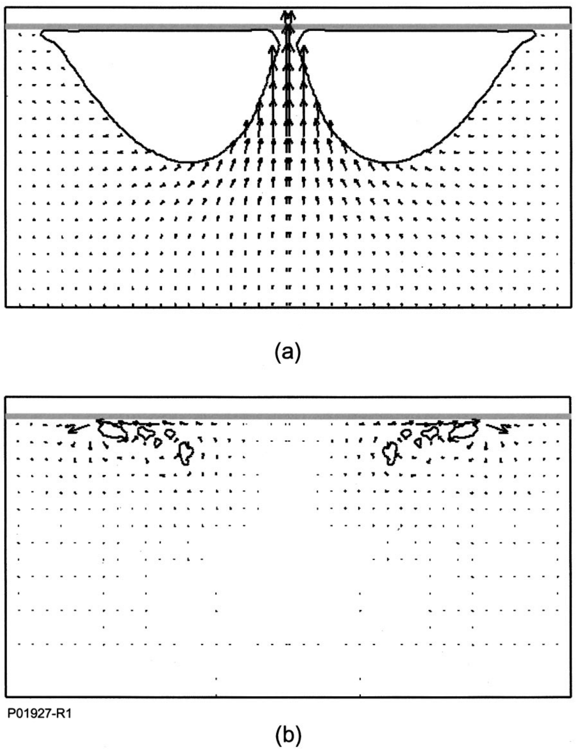

Fig. 3 Calculated flow field for jet-up test. (*a*) Jet touch down, $t/T=1.05$; (*b*) bubble fragmentation near minimum, $t/T=1.17$.

minima. The deep bubble collapses in a flattened shape on the bottom ($F^{-1}=0.09$), and the shallow bubble collapses into an inverted cone with a high pressure zone at the bottom that moves it upward ($F^{-1}=0.63$) (Fig. 2). These data comparisons, although qualitative due to the spread of the data, validate the computation method in capturing the dynamic behavior of jet-down bubbles. Detailed jet-down data are very limited at present.

A jet-up computation was validated against test data obtained by Goertner et al. [20] at the NSWC Hydrotank facility. The tests were conducted by placing small explosives below the center of a submersed rigid circular plate at different standoffs with detailed pressure measurements taken on the plate. The Hydrotank pressure can be controlled to simulate different depth conditions. Calculation was performed for a test conducted at normal atmospheric condition with the bubble placed at 0.75 $A_{\max}$ below the plate.

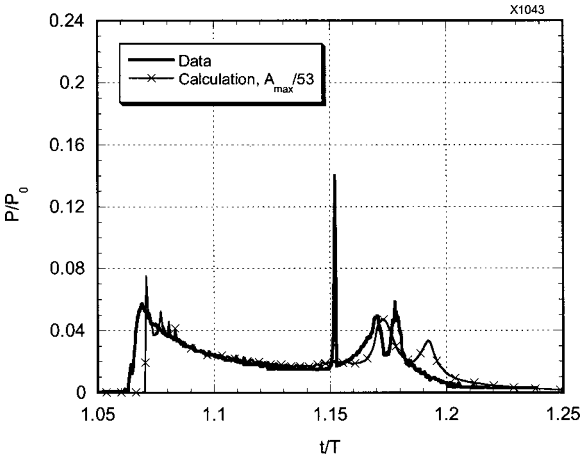

Fig. 4 Validation for jet-up test with resolution at $A_{max}/53$

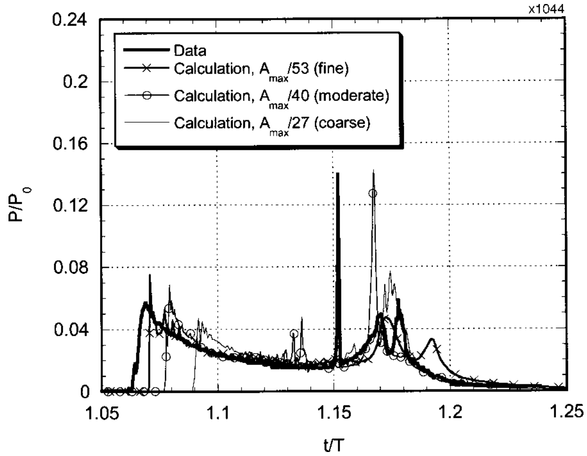

Fig. 5 Grid sensitivity study for jet-up test

Figures 3(*a*) and (*b*), respectively, present the calculated flow fields of the jet touching down on the plate, with the bubble shortly forming a torus and becoming fragmented near the minimum. Figure 4 shows the data comparison for the plate center pressure with the calculation performed at a resolution of $A_{\max}/53$. As shown in Fig. 4, pressure and time are normalized by the bubble initial pressure and the Raleigh (free) bubble period, respectively. The data show that the jet touch down and bubble minimum occur at t/T of about 1.07 and 1.17, respectively, and this behavior is well reproduced by the calculation (Fig. 4). The presence of the structure has lengthened the bubble period by about 17% (Fig. 4). The calculation overshoots the jet impingement peak, but the overall pressure feature compares favorably with data (Fig. 4). The double peak behavior from $1.15T<t<1.2T$ shown in Fig. 4 is due to the fragmentation of the torus near the bubble minimum (Fig. 3(*b*)). We note that in the present axisymmetric simulation, any fragmentation of the bubble in the azimuthal direction is precluded, and this limitation of the bubble dynamics might have slowed down the outward spread of the jet, hence making the calculated double peaks broader than the data (Fig. 4). The data spike near $t/T=1.15$ was due to gauge anomaly.

Grid sensitivity calculations were performed for the jet-up test with fine, moderate and coarse resolutions, respectively taken as $A_{\max}/53$, $A_{\max}/40$, and $A_{\max}/27$. As shown in Fig. 5, the calculated separation time between jet touch down and bubble minimum decreases by about 15% between the fine and coarse resolutions, which is a common trend that we have observed from computational results. However, the bubble minimum time does not seem to change to any significant extent between the fine and coarse resolutions (Fig. 5). The results for the moderate resolution ($A_{\max}/40$) compare favorably with the data, with a significant improvement over the coarse resolution in jet loading and timing (Fig. 5). Compared to $A_{\max}/53$, the resolution at $A_{\max}/40$ captured the bubble minimum near $t/T=1.17$ as a single peak, but the entire collapse phase from jet touch down through the bubble minimum agrees with data well (Fig. 5). These trends are consistent with those presented earlier for the single bubble with gravity that $A_{\max}/40$ is a reasonable resolution for modeling bubble dynamics (Table 1). We chose this resolution to carry out all subsequent calculations to perform a phenomenological trend study using an extensive series of calculations involving jet-up and jet-down conditions at various inverse Froude numbers with different geometries.

4 Single Bubbles Above and Below a Disk

To understand the difference between bubbles contracting in jet-up and jet-down orientations, two-dimensional axisymmetric calculations were performed for a flat circular disk with diameter D equal to $A_{\max}$. The bubble was placed either below or above the disk for the jet-up or jet-down orientations, respectively (Fig. 6). In the latter case, some calculations included a rigid bottom below the disk at a distance equal to the disk diameter (Fig. 6(*b*)). The standoff distance between the center of the bubble and the disk was 0.75 $A_{\max}$. The bubble depth was varied, corresponding to inverse Froude numbers ranging from 0.1 to 0.36.

Because of gravity, a much sharper jet is formed by a bubble in the jet-down than the jet-up orientation, as shown by the results at $\mathrm{F}^{-1}=0.237$ (Fig. 7). Figure 7 also shows the calculated pressure contours. For a bubble below a disk, the fluids are in a stable configuration with the gas above the water, and the bubble contracts evenly, like a hemisphere, with the water flowing primarily towards the disk (Figs. 7(*a*) and (*b*)). The relatively flat bottom surface of the bubble results in a broad, relatively slow jet. Conversely, for a bubble above the disk, the fluids are in an unstable configuration with the gas below the water. In this situation, the bubble, although attached to the plate below, migrates partially upwards due to its buoyancy and, as a result, is elongated and attains a high curvature at the top surface (Fig. 7(*c*)). As the

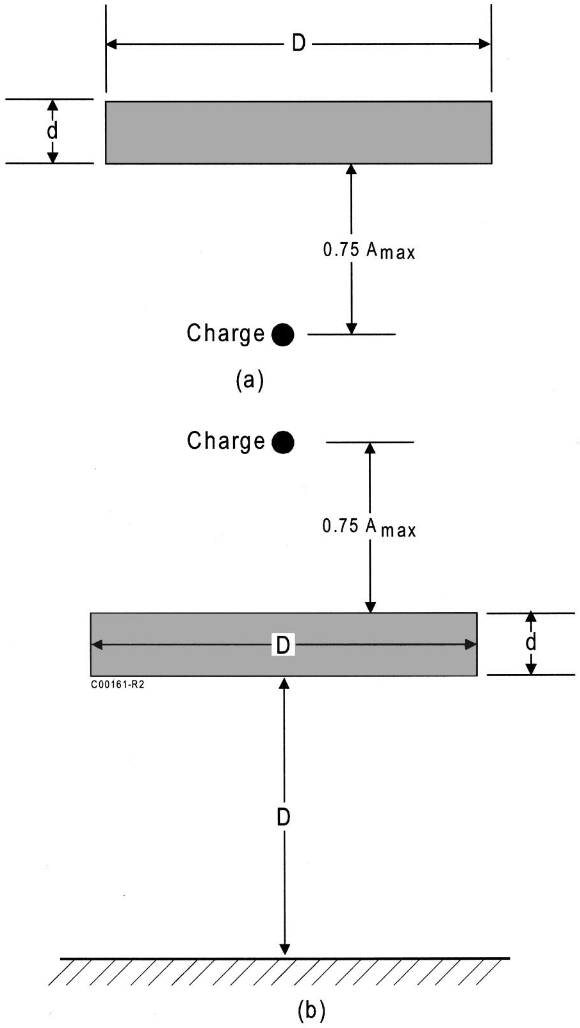

Fig. 6 Schematic diagram for calculations for bubble-disk interaction

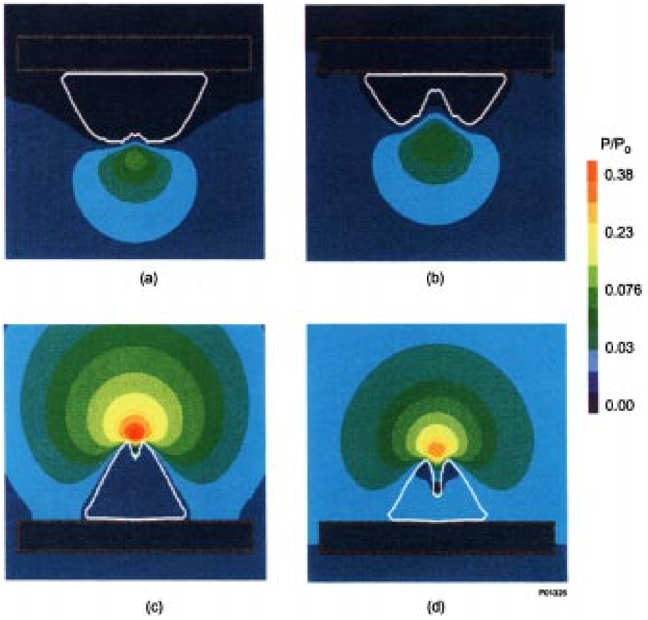

Fig. 7 Jet formation comparison between jet-up and jet-down orientations for the disk at $\mathrm{F}^{-1}=0.237$. (*a*) Early jet formation (jet-up); (*b*) fully developed (jet-up); (*c*) early jet formation (jet-down); (*d*) fully developed (jet-down).

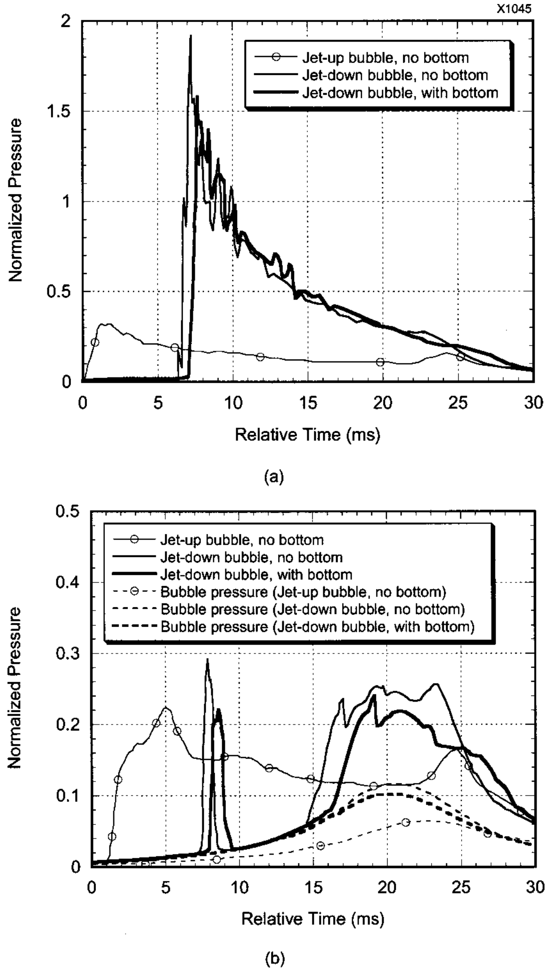

Fig. 8 Pressure loading comparison between jet-up and jet-down orientations for the disk at $\mathrm{F}^{-1}=0.237$. (*a*) Center loading on the disk; (*b*) off-center loading on the disk ($r=A_{\max}/15$).

bubble contracts, a high pressure region forms above the bubble tip, which eventually drives a sharp, high speed downward jet towards the disk (Figs. 7(*c*) and (*d*)).

Analysis of the pressure loadings on the disk confirms the sharp intensity of the downward jet. Figure 8 shows the comparison between jet-up and jet-down pressure loadings, where all pressures are normalized by the initial bubble pressure. The abscissa for time shows only the jetting phase of interest, but the relative timings of all results are preserved. Compared to the jet-up orientation, the jet-down bubble delivers a four times stronger peak center pressure on the disk (Fig. 8(*a*)), showing that the downward jet is much faster. However, at an off-center location, $A_{\max}/15$ from the plate center, the pressure loading for the jet-down orientation drops off much more rapidly than the jet-up orientation, Fig. 8(*b*), confirming the narrow nature of the downward jet. The second pulse of the off-center jet-down loading is primarily due to the bubble reaching its minimum in a torus shape as indicated by the corresponding bubble pressure behavior (Fig. 8(*b*)). Figures 8(*a*)–(*b*) also show that the presence of a solid bottom with $D = A_{\max}$ below the disk slightly delays and weakens the jet impact on the plate, but the fast, sharp nature of the downward jet is preserved.

A series of calculations were performed for the disk with no solid bottom at jet-up and jet-down conditions at F^{-1} of 0.107, 0.172, and 0.237, respectively. The calculated pressures at the disk center are shown in Fig. 9 for comparison between jet-up and jet-down conditions with the trend lines representing F^{-1} effects indicated. In addition, the results shown in Fig. 9 labeled as ''no gravity'' were calculated with gravity set to zero, but the ambient pressures were set to the same hydrostatic values corresponding to the respective inverse Froude numbers if gravity was present. The results under no gravity are ''neutral'' cases since jet-up and jet-down are immaterial if there is no gravity. Figure 9 also shows that the load duration increases with F^{-1} (stronger buoyancy).

As shown in Fig. 9, as the bubble depth increases, the difference between the collapse behavior of jet-up and jet-down bubbles diminishes. With increasing depth (smaller F^{-1}), the pressure loading from the jet-down bubble decreases, but that from the jet-up bubble increases (Fig. 9). Both bubble orientations should produce identical loadings at infinite depth, $F^{-1}=0$, as indicated by the trend lines (Fig. 9). Furthermore, as F^{-1} approaches 0, the loadings should all approach that calculated with no gravity, as suggested by the merging of the three trend lines in Fig. 9.

These trends support the notion discussed earlier, that gravity increases the bubble curvature, hence the jet velocity, for the jet-down orientation, while blunting the curvature and reducing the jet velocity for the jet-up orientation. As depth increases, these differences are reduced and the jet behavior becomes independent of orientation, depending only on the geometric effects of the nearby structure.

A comparison with the previous potential flow results obtained by Blake [10] is noteworthy. The present study has shown that strong jet-down conditions are possible when the bubble center standoff is at 0.75 $A_{\max}$ above a target. The simulations of Blake et al. [10] under quiescent ambient conditions were performed with the standoff at 1 and 2 $A_{\max}$ with the emphasis on the migration trend of the bubbles. Based on Kelvin impulse arguments and a summary of their numerical results, Blake et al. [10] hypothesized that a bubble will move away or toward a flat boundary when $\gamma\delta$ is greater or less than 0.42, where γ is the normalized standoff and δ is $(\rho_1 g A_{\max}/\Delta p)^{1/2}$ with Δp being the difference between the ambient pressure and the bubble vapor pressure. For our present study for the disk, $\gamma\delta$ is less than 0.24, and our simulated cases indicate all bubbles migrate toward the flat surface in agreement with Blake et al. [10]. Our results also agree with Blake et al. [10] that a jet-up bubble tends to be more oblate with a slower and broader jet. Our simulations were carried out further than those of Blake et al. in studying the trends of the bubble loading from jetting through the bubble collapse beyond the minimum (Fig. 9). Furthermore, the effects of structural curvature on the bubble loading are studied as presented in the next section.

5 Single Bubble Above a Sphere

To study the effect of structural shape on jet-down bubble dynamics, calculations were performed for a sphere with diameter same as the disk and sitting on a rigid bottom. The same initial bubble mass and energy were used with F^{-1} varied from 0.107 to 0.363. The bubble standoff distance from the sphere was 0.75 $A_{\max}$ and the grid resolution was the same as the disk calculations.

A jet-down bubble develops a sharper jet on the sphere than the disk. Figure 10 shows the calculated bubble shapes shortly after jet touch down on the sphere for four bubble depths, corresponding to $F^{-1}=0.237$, 0.172, 0.134, and 0.107. Due to the curvature of the sphere, the bubble becomes more conical during the contraction phase and does not attach as closely to the sphere as to the disk as shown by comparing Fig. 10 with Fig. 7. The higher curvature at the top of the bubble produces a faster, narrower jet for the sphere. Consequently, at shallow depth, $F^{-1}=0.237$, the

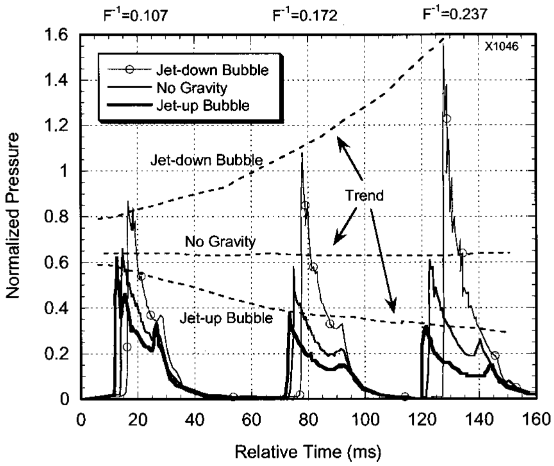

Fig. 9 Effect of bubble orientation and depth on pressure loading on the disk

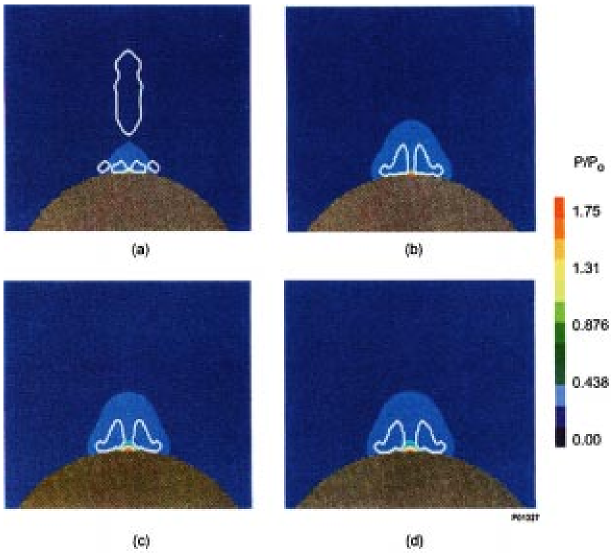

Fig. 10 Effect of depth on bubble collapse above a sphere. (*a*) $F^{-1}=0.237$; (*b*) $F^{-1}=0.172$; (*c*) $F^{-1}=0.134$; (*d*) $F^{-1}=0.107$.

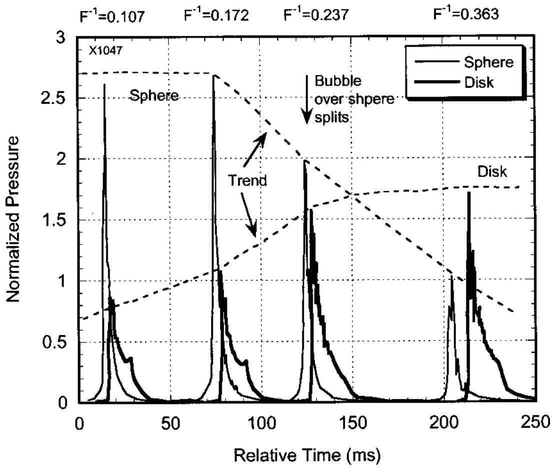

Fig. 11 Effect of structural shape and bubble depth on pressure loading for jet-down orientation

bubble splits above the sphere (Fig. 10(*a*)), while a disk would keep the bubble attached at the same depth (Fig. 7(*c*)).

Compared to a disk, the bubble jets down even sharper onto the sphere. Figure 11 shows the comparison of the jet center loadings between the disk and the sphere at four F^{-1} conditions as indicated by the trend lines. As shown in Fig. 11 for all four bubble depths, the jet center loading on the sphere is higher but with shorter duration than that on the disk. Furthermore, the jet touchdown time for the sphere nearly coincides with the bubble minimum, resulting in a pressure loading that is nearly single peaked (Fig. 11). At shallower depths (larger F^{-1}), the bubble above the sphere becomes so elongated that the jetting process is impeded and finally disrupted altogether due to bubble splitting (Fig. 10(*a*)). Consequently, the pressure loading on the sphere decreases significantly for F^{-1} higher than 0.172 due to bubble splitting (Fig. 11).

These results demonstrate that for the jet-down orientation the structural shape affects the shape of the bubble and the dynamics of the collapsing jet. The greater the curvature of the structure, the greater the curvature of the jet-down bubble and the faster and narrower the jet. On the other hand, the greater structural curvature makes the bubble more likely to split at shallow depths, reducing or potentially eliminating the jetting behavior.

6 Conclusion

Two-fluid CFD calculations have been carried out to study the interaction of underwater explosion bubbles with nearby structures. Building on previous validation results for jet-up bubbles (Kan and Stuhmiller [2]), validation calculations for an isolated bubble, explosion bubbles on a rigid bottom and a jet-up test show favorable agreement with experimental data. A phenomenological study was then carried out using a series of computations over a wide range of conditions.

In the analysis of each study, a pattern has been noted: the curvature of the bubble at the time of jet formation correlates directly with the speed of the resulting jet and the peak pressure at impact. Many of the relative timing features can be explained by noting that Rayleigh's equation shows that the bubble period, hence the time of impact, increases with the maximum bubble volume, which in turn is increased by reduced depth or the presence of the bottom. The studies involved only a single charge weight and, despite the use of dimensionless parameters to characterize the conditions, may only apply to a limited range. Nonetheless, we recount the findings of these studies, pointing out where the observed trends can be explained by these concepts.

1 Peak impact pressures are higher for jet-down than jet-up bubble orientations for all structural shapes and depths as studied (Figs. 8 and 9). This result follows from the increase in the jet-down bubble curvature caused by gravity.

2 Peak impact pressures in jet-down orientations are reduced by the presence of the bottom and are delayed in time (Fig. 8). The influence of the bottom flattens the bubble and effectively reduces the structural curvature. The resulting jet is reduced in speed.

3 Peak impact pressures for jet-up bubbles increase with depth, while jet-down bubbles behave conversely (Fig. 9). Gravity increases the curvature of jet-down bubbles and decreases that of jet-up bubbles. Gravitational effects are reduced with depth.

4 Peak impact pressures on the sphere are stronger than the disk (Fig. 11). The bubble curvature follows the effective structural curvature.

Each of the qualitative trends found in the computational studies can be understood in terms of a notional concept: the velocity of the jet (hence peak pressure loading at impact) varies directly as the curvature of the bubble at the time of jet formation. The flow field is observed to develop high pressures around the high curvature regions which accelerate the jet in its early formation. As a corollary arising from momentum conservation: the jets with higher velocity are narrower and have a shorter duration.

To understand the factors controlling the bubble curvature we propose a second notional concept: the bubble curvature is greater for structures with greater effective curvature, and is either decreased by gravity in the jet-up orientation or increased by gravity in the jet-down orientation. Since the bottom is a large, relatively distant flat surface: the bottom reduces the effective curvature for jet-down bubbles.

Acknowledgments

This work was sponsored by the Naval Surface Warfare Center under contract number N60921-92-0048 with Mr. Ken Kiddy serving as the project manager. The support of Mr. Ken Kiddy and Mr. Greg Harris of NSWC during the course of this investigation is appreciated.

References

[1] Lamb, H., 1945, *Hydrodynamics*, 6th Ed., Dover, New York, pp. 122–123.
[2] Kan, K. K., and Stuhmiller, J. H., 1994, ''The Phenomena of an Underwater Explosion Bubble Under a Circular Plate,'' JAYCOR Final Report for NSWC.
[3] Blake, J. R., and Gibson, D. C., 1987, ''Cavitation Bubbles Near Boundaries,'' Annu. Rev. Fluid Mech., **19**, pp. 99–123.
[4] Cole, R. H., *Underwater Explosions*, 1948, Princeton University Press.
[5] Goertner, J. F., 1956, ''Vacuum Tank Studies of Gravity Migration of Underwater Explosion Bubbles,'' NAVORD Report 3902, US Naval Ordnance Laboratory.
[6] Snay, H. G., Goertner, J. F., and Price, R. S., 1952, ''Small Scale Experiments to Determine Migration of Explosion Gas Globes Towards Submarines,'' NAVORD Report 2280, US Naval Ordinance Laboratory.
[7] Chahine, G. L., 1989, ''A Numerical Model for Three-Dimensional Bubble Dynamics in Complex Flow Configurations,'' 22nd ATIC meeting, St. John's, Newfoundland, Canada, Aug. 1989.
[8] Chahine, G. L., and Duraiswani, R., 1994, ''Boundary Element Method for Calculating 2D and 3D Underwater Explosion Bubble Behavior in Free Water and Near Structures,'' NSWC Report NSWCDD/TR-93/44 [Limited Distribution].
[9] Chan, P. C., and Chow, W. L., 1984, ''The Study of Gravitational Nozzle Flows by Hodograph Transformations,'' ASME J. Appl. Mech., **51**, No. 3.
[10] Blake, J. R., Taib, B. B., and Doherty, G., 1986, ''Transient Cavities Near Boundaries, Part 1, Rigid Boundary,'' J. Fluid Mech., **170**, pp. 479–499.
[11] Blake, J. R., and Prosperetti, A., 1989, ''Dynamics of Underwater Explosion Bubbles,'' Final Report to the Office of Naval Research, Grant. No. N00014-89-J-1791, May 1989.
[12] Klein, H. H., Chan, P. C., and Chan, R. K.-C., 1989, ''JAYCOR CFD Analysis of the Hydrogen Disposal System at the Vandenberg Space Shuttle Launch Site,'' AIAA-89-0579, 27th Aerospace Sciences Meeting, Reno, Nevada, January 9–12, 1989.
[13] Chan, P. C., and Klein, H. H., 1994, ''A Study of Blast Effects Inside an Enclosure,'' ASME J. Fluids Eng., **116**, pp. 450–455.
[14] Liles, D. R., and Reed, W. H., 1978, ''A Semi-Implicit Method for Two-Phase Fluid Dynamics,'' J. Comput. Phys., **26**, No.3, pp. 390–407.

[15] Peaceman, D. W., and Rachford, H. H., 1955, ''The Numerical Solution of Parabolic and Elliptic Differential Equations,'' J. SIAM., **3**, pp. 28–41.
[16] Anderson, D. A., Tannehill, J. C., and Pletcher, R. H., 1984, *Computational Fluid Mechanics and Heat Transfer*, Hemisphere Publishing, N.Y.
[17] Hirt, C. W., and Nichols, B. D., 1981, ''Volume of Fluid (VOF) Method for the Dynamics of Free Boundaries,'' J. Comput. Phys., **39**, pp. 201–225.
[18] Snay, H. G., and Christian, E. A., 1952, ''Underwater Explosion Phenomena: The Parameters of a Non-migrating Bubble Oscillating in an Incompressible Medium,'' NAVORD Report 2437.
[19] Goertner, J. F., Hendrickson, J. R., and Leamon, R. G., 1969, ''Model Studies of the Behavior of Underwater Explosion Bubbles in Contact with a Rigid Bottom,'' NOLTR 68-207, US Naval Ordinance Laboratory.
[20] Goertner, J. F., Thrun, R., and Berry, J. E., 1993, ''Underwater Explosion Bubble Collapse Against a Flat Plate. 1987 NSWC Hydrotank Test Series Pressure Data Report,'' NSWC Report NSWCDD/TR-93/98 (Limited Distribution).
[21] Young, G. A., 1968, ''The Transport of the Products of Very Deep Underwater Explosions,'' NOLTR 67-179.

R. A. Bunnell
Graduate Research Assistant

S. D. Heister
Professor

School of Aeronautics and Astronautics,
Purdue University,
W. Lafayette, IN 47907-1282

Three-Dimensional Unsteady Simulation of Cavitating Flows in Injector Passages

Fully 3-D, unsteady, viscous simulations are performed on a plain-orifice pressure atomizer being fed by a manifold with a crossflow. This geometry replicates features present in both liquid rocket and diesel engine injectors. Both noncavitating and cavitating conditions are considered to determine the role of cavitation on the orifice discharge characteristics. The presence of cavitation is shown to affect both the mean and unsteady components of the orifice discharge coefficient. The presence of a significant cavitation zone can inhibit vorticity transport causing nearly all the fluid to be ejected through a crescent-shaped sector of the orifice exit plane. [S0098-2202(00)01604-7]

Introduction

The influence of injector orifice design has long been known to be a key feature influencing the jet/spray characteristics from these devices. In spite of this fact, relatively little analysis or experiments have been focused on this area in favor of scores of studies on the effects which have taken place outside the orifice passage. This state of affairs is explained by the difficulty in observing these internal flows; transparent test articles must be manufactured and even in this case light refraction can make visual observations challenging. In addition, the tiny length scales involved also complicate visualizations and surface-mounted instrumentation.

Despite these complications, there is ample motivation to perform such experiments since the flow in the internal passages provides the initial condition for jet/spray development. In many high-pressure injectors, cavitation has been believed to provide a substantial contribution to the internal flows. The diesel engine and liquid rocket engine industries have conducted the bulk of the experimental studies to date. Several experiments have been conducted over the years using transparent orifices of super-scale (Bergwerk [1], Nurick [2], Lichtarowicz et al. [3], He and Ruiz [4], Strakey et al. [5], Acroumanis et al. [6]) and actual scale (Tamaki [7], Chaves et al. [8], Henry [9], Li and Collicott [10], Chandra and Collicott [11], Sanchez and Collicott [12], Karasawa et al. [13]) sizes. These experiments have not only shown the presence of cavitation over a wide array of experimental conditions, but have documented the unsteadiness created by the alternating growth and collapse of the cavity in the vena-contracta region just downstream of the orifice inlet. Recent experimental results have quantified the length of the cavity (Henry [9], Sanchez and Collicott [12]) as well as the frequencies of oscillations (Chandra and Collicott [11]).

Modeling efforts have also progressed over the past decade or so such that arbitrary single or multiphase flow can be considered in a single computation. The bulk of these approaches has relied on a homogeneous fluid approximation in which the fluid is assigned a pseudo-density which varies in extent from the liquid to the vapor extremes. The creation of this fictitious variable necessitates a constitutive relation to close the set of equations. Several treatments have been utilized (Delannoy and Kueny [14], Kubota et al. [15], Chen and Heister [16], Alajbegovic et al. [17], Schmidt et al. [18], Ahuja et al. [19], most of these have appeared within the past few years. The present studies focus on a treatment due to Chen and Heister [16] which casts the physics of the Rayleigh-Plesset equation for bubble dynamics into an expression for pseudo-density. Over the past three years, 2-D simulations using this approach have been validated extensively against experimental results showing good comparisons with cavitation inception, length, and characteristic frequencies (Bunnell et al. [20], Xu et al. [21]).

Despite these successes, the full 3-D problem has received little attention due primarily to a limitation in computational resources. The ever-increasing computational speeds and use of parallel processing has now enabled fully 3-D, time-accurate simulations within the past few years. It has long been known that the presence of a crossflow at the orifice entrance can substantially alter the orifice flow patterns and discharge characteristics. The present studies are aimed at shedding some light on this flow which is common to liquid rocket engine injectors and diesel engines. The following section provides a brief description of the model, followed by the validation of the code and a summary of results.

Model Description

While most atomizers operate in a turbulent flow regime, the present calculations are for a laminar fluid assumption. In the strongly accelerated region near the lip of the inlet where the minimum pressure occurs, turbulence is not believed to be of critical influence. However, downstream of the contraction where flow reattachment and boundary layer development occurs, turbulence can have an influence on the flowfield. Unfortunately, there is a real lack of turbulence models for cavitating flows. This factor, combined with the promising results obtained with previous 2-D simulations noted previously, support the use of a laminar flow assumption. Obviously, this is an area requiring further study since turbulence itself remains largely unexplained.

The main innovation developed in this model is in the treatment of the cavitation region itself. Individual bubbles appearing in the cavitation region are not resolved, rather an average void fraction (measured by the local mixture density) is predicted by the code. A single fluid is employed by defining a fluid pseudo-density which varies in magnitude between the liquid and vapor extremes. If we nondimensionalize variables using the liquid density, the pseudo-density becomes a parameter which varies from $\approx 10^{-3}$ to unity over the range from pure vapor to pure liquid. The advantage of this approach is that it does not require tracking of the large number of individual bubbles formed in the cavitation region and that results can be obtained for a fixed computational mesh.

We choose liquid density, the orifice radius, and the ideal (Bernoulli) velocity as dimensions. Following Kubota et al. [15] the viscosity of the mixture is written: $\mu = \alpha\mu_g + (1-\alpha)\mu_l$ where μ_g

---

Contributed by the Fluids Engineering Division for publication in the JOURNAL OF FLUIDS ENGINEERING. Manuscript received by the Fluids Engineering Division December 6, 1999; revised manuscript received July 11, 1999. Associate Technical Editor: J. Katz.

and μ_l are the vapor and liquid viscosities, and α is the void fraction. Since $\mu_g \ll \mu_l$ and $(1-\alpha)$ is the dimensionless pseudo-density, this result reduces to

$$\mu \approx \rho \mu_l \tag{1}$$

The two dimensionless variables pertaining to this flow are the Reynolds and cavitation numbers

$$\mathrm{Re}=\rho_l V a/\mu_l \quad K=\frac{P_1-P_v}{P_1-P_2} \tag{2}$$

where V is the Bernoulli velocity based on the liquid density (ρ_l) and the orifice pressure drop (P_1-P_2), i.e. $V=\sqrt{2(P_1-P_2)/\rho_l}$. Finally, in Eq. (2), P_v is the fluid vapor pressure.

Under these assumptions, the dimensionless governing equations take on the following form:

$$\frac{\partial \rho}{\partial t}+\frac{\partial \rho u}{\partial x}+\frac{\partial \rho v}{\partial y}+\frac{\partial \rho w}{\partial z}=0 \tag{3}$$

$$\frac{\partial \rho u}{\partial t}+\frac{\partial \rho u^2}{\partial x}+\frac{\partial \rho u v}{\partial y}+\frac{\partial \rho u w}{\partial z}+\frac{\partial P}{\partial x} = \frac{1}{\mathrm{Re}}\left(\frac{\partial}{\partial x}\rho\frac{\partial u}{\partial x}+\frac{\partial}{\partial y}\rho\frac{\partial u}{\partial y}+\frac{\partial}{\partial z}\rho\frac{\partial u}{\partial z}\right) \tag{4}$$

$$\frac{\partial \rho v}{\partial t}+\frac{\partial \rho u v}{\partial x}+\frac{\partial \rho v^2}{\partial y}+\frac{\partial \rho v w}{\partial z}+\frac{\partial P}{\partial y} = \frac{1}{\mathrm{Re}}\left(\frac{\partial}{\partial x}\rho\frac{\partial v}{\partial x}+\frac{\partial}{\partial y}\rho\frac{\partial v}{\partial y}+\frac{\partial}{\partial z}\rho\frac{\partial v}{\partial z}\right) \tag{5}$$

$$\frac{\partial \rho w}{\partial t}+\frac{\partial \rho u w}{\partial x}+\frac{\partial \rho v w}{\partial y}+\frac{\partial \rho w^2}{\partial z}+\frac{\partial P}{\partial z} = \frac{1}{\mathrm{Re}}\left(\frac{\partial}{\partial x}\rho\frac{\partial w}{\partial x}+\frac{\partial}{\partial y}\rho\frac{\partial w}{\partial y}+\frac{\partial}{\partial z}\rho\frac{\partial w}{\partial z}\right) \tag{6}$$

While the real flow is most certainly turbulent, previous 2-D and axisymmetric laminar results have compared well with measured cavity shapes (Chen and Heister [16], Bunnell et al. [20]), oscillation frequencies (Bunnell et al. [20]) and inception pressures (Xu et al. [21]). The favorable pressure gradients on the inflow to the orifice suppress turbulence and the hydrodynamic instability of the venacontracta, a key element in these flows, is resolved with a laminar calculation.

The governing equations are solved via a second-order spatial and 1st-order temporal Marker and Cell discretization which is described in Chen and Heister [16]. The two-phase treatment requires an additional relation for the pseudo-density, ρ, in order to obtain closure for the governing equations. The current treatment (Chen and Heister [22]) is based on the dynamic response of a single bubble to changes in external pressure as it is convected through the flowfield. The constitutive relation represents the physics described in the Rayleigh-Plesset equation which govern the dynamics of a single bubble in a quiescent field.

The model presumes that all bubbles are of the same size. Furthermore, coalescence, bubble breakup, surface tension effects, and slip between the phases are not considered. This greatly simplifies the physics of the flow, but still provides a gross response to the spatial and time varying pressure field. The resulting constitutive relation for the pseudo-density is similar to the Rayleigh-Plesset equation in that changes in pseudo-density are governed by pressure and inertial forces:

$$\frac{D^2\rho}{Dt^2}=\frac{6\alpha'(1+\alpha'+\alpha'^2)^2}{L_0^2(2+\alpha')(1-\alpha'^3)^{1/3}}(P-P_v)+\left[\frac{11\alpha'^3-\alpha'^2-\alpha'-1}{6\alpha'^3(1-\alpha'^3)} - \frac{1+4\alpha'+\alpha'^2}{6\alpha'^2(2+\alpha')(1+\alpha'+\alpha'^2)}\right]\left(\frac{D\rho}{Dt}\right)^2 \tag{7}$$

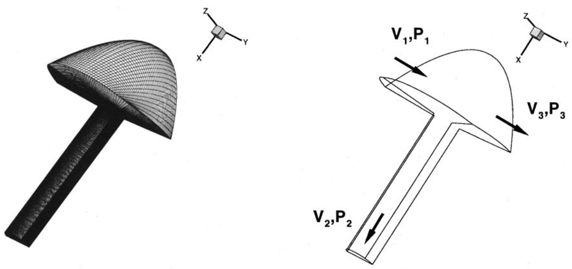

Fig. 1 Boundary mesh and schematic representation of crossflow imposed by the manifold

Here, $\alpha'=\sqrt[3]{1-\rho}$ and P is the local pressure returned by the Navier-Stokes solver and P_a is the fluid vapor pressure under our assumption of negligible surface tension effects. The relation does account for hydrodynamic nonequilibrium effects in that the inertia term ($D\rho/Dt$ term on RHS of Eq. (7)) does become important at very small length scales. Scaling effects have been addressed successfully using the model (Chen and Heister [16]). Finally, in Eq. (7) L_0 is a characteristic length scale which is a function of the site density:

$$L_0^2=\left(\frac{3}{4\pi n_0}\right)^{2/3} \tag{8}$$

Here, n_0 is the nondimensional site density. Letting the dimensional site density be represented by $\hat{n}_0$, then

$$n_0=\hat{n}_0\hat{D}^3 \tag{9}$$

where $\hat{D}$ is a characteristic length used in the nondimensionalization of the governing equations. Physically, $\hat{n}_0$ represents the number of active cavitation sites per unit volume. It has been estimated to be about 10^8–10^{12} sites/m^3 by Fujimoto et al. [23] for small scale internal flows. However, because currently it is impossible to measure submicron scale bubbles and site density depends on the type of liquid, the degree to which it is filtered, and surface structure, additional sites may exist. Prior studies by Bunnell et al. [20] have shown that results are not sensitive to this parameter; a value of 10^{12} sites/m^3 is assumed for this work.

Computational Mesh and Boundary Conditions. A mesh was developed to treat a circular orifice machined perpendicular to the local manifold. Flow in the manifold imposes a crossflow at the entry to the orifice as shown in Fig. 1. The mesh was constructed to take advantage of the symmetry about a plane intercepting the center of the orifice passage in alignment with the crossflow direction (see Fig. 1). Note that this assumption does not allow us to treat a ''cyclone effect'' in which a vortex enters the orifice and is convected downstream. While this flow is certainly possible, our computational resources do not permit gridding of the entire physical domain at this time. The mesh was generated algebraically by warping a square into a circle via use of exponential stretching. The resulting circular mesh is then rotated through various angles to form the paraboloid inflow boundary depicted in Fig. 1. Additional exponential stretching was employed to enhance resolution in the region near the inlet lip. Here, experience gained from prior 2-D models (Bunnell et al. [20], Xu et al. [21]) aided immensely.

Flows on both inflow and outflow boundaries are assumed to be steady in formulating boundary conditions for the problem. Along the walls of the manifold injector, the no-slip condition was used. Symmetry conditions were used along the plane of symmetry. At the exit plane zeroth order extrapolation is used for velocities, assuming that viscous interactions are unimportant far downstream of the orifice lip, and a constant pressure (P_2) outflow condition.

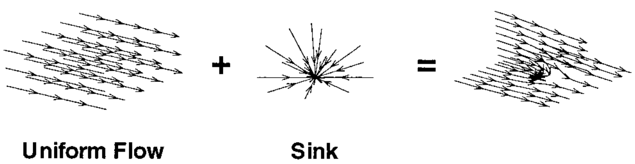

Fig. 2 3-D potential flow theory for inlet conditions for manifold cross-flow

The upstream boundary represents a unique challenge. Since the orifice extracts some massflow from the manifold duct the manifold conditions downstream of the orifice (P_3, V_3 in Fig. 1) are unknown. Appropriate conditions on this paraboloid surface were generated by modeling the inflow as a potential flow formed by a sink in a uniform crossflow. The sink was assumed to lie at the center of the orifice within the orifice entry plane as shown in Fig. 2. The velocity potential (ϕ) for a uniform flow superposed with a sink can be written

$$\phi(r,\theta) = V_1 r \cos\theta - \frac{Q}{4\pi r} \tag{10}$$

where V_1 is the specified crossflow velocity, r is the radial coordinate measured from the sink location, θ is the angle measured from the sink/manifold plane and the volume flux, $Q=\pi a^2 V$. Writing the Bernoulli velocity, V, in terms of the pressure drop, $P_1 - P_2$ gives

$$Q = \pi a^2 \sqrt{\frac{2(P_1 - P_2)}{\rho} + V_1^2} \tag{11}$$

where P_1 is the pressure upstream of the orifice inlet and P_2 is the exit pressure of the orifice, see Fig. 1.

This procedure gives an approximate pressure distribution on the upstream boundary. The resulting velocity components on the inflow boundary are determined directly from the velocity potential ($\vec{v} = \nabla\phi$) and the pressure on the inflow boundary, P, can be determined from Bernoulli's equation:

$$\frac{P}{\rho} + \frac{1}{2}\nabla\phi\cdot\nabla\phi = \frac{P_1}{\rho} + \frac{1}{2}V_1^2 \tag{12}$$

Note that the velocities that are set on the upstream boundary are only used to solve for the viscous terms in the momentum equations. Since the gradients in this region are small, the error in using potential flow velocities in this region is negligible. Investigation of solutions showed smooth velocity profiles in the inlet region, thereby confirming the supposition that viscous stresses were of little importance in setting the inflow boundary conditions. Continuity is solved for the entire domain minus the boundary upstream. Thus, the actual inlet velocity is one position in the mesh upstream of the boundary, and is calculated from the full equation set (Eqs. (3)–(6)) in order to maintain continuity through out the domain.

Convergence Study

In order to determine if the solution methodology led to convergence when refining the mesh, and also to determine a satisfactory mesh for subsequent simulations, a simple grid convergence study was undertaken. A coarse mesh consisting of 80 ×21×21 grid points (32,000 cells) and a fine mesh of 120 ×42×42 grid points (200,039 cells) was used. Simulations were performed for a manifold cross-flow over a sharp edged orifice, as discussed in the next section.

The code was parallelized as described in Bunnell [24] to speed up the computation. Two dual-450 Pentiums were used in the computation. The use of 4 processors required an average of 12 seconds of computation time per time step on the 200,039 node grid for the cases that were simulated. This number is cut in half when the solver is used for single phase flow. Thus, for the first 30,000 time steps or more, which is equivalent to the amount of time it would take for a fluid particle to transverse the the injector 6 or more times, the simulation is run as a single phase flow. This flow field is then used as an initial condition for the two-phase simulation. This approach saves several days worth of computation time. Typical runs on the 200,039 cell fine mesh take 2–3 weeks.

Figure 3 shows the cavitation length and discharge coefficient obtained for the two meshes plotted as a function of time. Here, the discharge coefficient, C_d, is defined as the ratio of the computed and ideal massflows. The ideal massflow assumes a flow with the Bernoulli velocity ($\sqrt{2(P_1 - P_2)/\rho}$) through the available orifice exit area. The computed massflow is determined via quadrature of the massflux over the orifice exit plane. Note that for the coarse mesh the simulation was run as a single phase flow until a non dimensional time of 20; for the fine mesh single phase was assumed until a time of 60. A time step of 0.001 was used in all cases; previous studies (Bunnell et al. [20]) confirmed that results are insensitive to this parameter at this level. This explains why the discharge coefficient begins to adjust for the two phase phenomena at these times in Fig. 3. The coarse mesh has the effect of smoothing the cavitation length and discharge coefficient. The mesh is not fine enough to capture the unsteady behavior of these two parameters of interest. The cavitation length is also predicted to be less and the discharge coefficient greater than that obtained by the finer mesh. The behavior is quite similar to the results obtained from the 2-D convergence study in Bunnell et al. [20]. In the 2-D convergence study it was found that once the mesh was refined until the oscillatory behavior was obtained that the overall integral (discharge coefficient) or averaged solu-

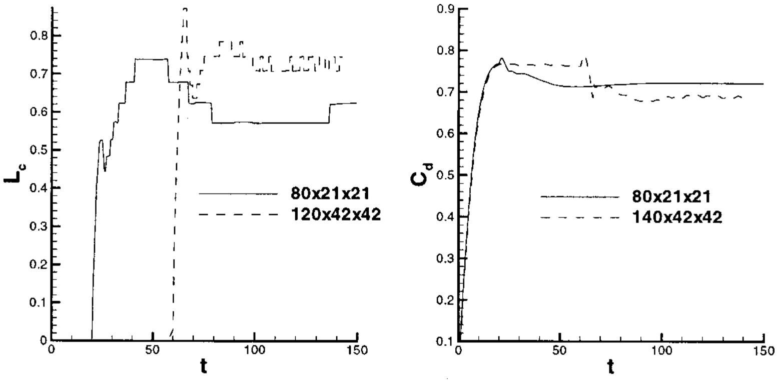

Fig. 3 Cavitation length, L_c, and orifice discharge coefficient, C_d for two meshes ($K=1.2$)

tions were fairly independent of more grid refinement. Therefore, the 120×42×42 was used in all of the subsequent simulations.

Results

There are very few experimental measurements suitable for comparison with calculations from this model. One notable exception is the recent experiments of Strakey and Talley [5] which aimed at measuring orifice discharge characteristics in a manifold similar to those used in liquid rocket engines. An orifice with a diameter of 2.03 mm and a length of 10.15 mm ($L/D=5$) was modeled. The inlet pressure, P_1, was 0.69 MPa and the inlet crossflow velocity, V_1, was 8.9 m/s. By changing the back pressure, the cavitation number was varied over a wide range of values. Water was used as the fluid in the tests. Three separate conditions were modeled: $K=1.2$, Re=85, 400; $K=1.8$, Re=70, 850; and $K=6.0$, Re=42, 800.

Cavitation length (L_c) and discharge coefficient (C_d) results are summarized in Figs. 4 and 5. For the case where the cavitation number $K=6.0$, no cavitation of any significance was present. When $K=1.8$ cavitation developed around the lip of the orifice, extending only 2 percent of the total length of the injector at its maximum extent. A small cavity did develop downstream of the lip at about 16 percent of the injector length early in the simulation, but this quickly reverted back to liquid. This is most likely due to the fact that when the simulation begins with the single-phase solution, the cavitation tends to overshoot. It then settles into a characteristic periodic growth and collapse at some shorter extent. Finally, for $K=1.2$ the flow field becomes extremely cavitated extending about 80 percent of the length of the channel. Here, the cavity length was taken as the furthest extent in the orifice that the local pseudo-density was found to contain at least 2 percent gas. While this choice is somewhat arbitrary, the L_c was quite insensitive to the threshold selected because the density varies rapidly at the outermost edge of the cavity.

The discharge coefficient is shown in Fig. 5. For the two cavitating cases, calculations up to $t=60$ were for single-phase flow. One can note a dramatic decrease in C_d in the $K=1.2$ case as the two-phase computations are initiated. Clearly, the presence of the cavitation is to reduce the effective mass flux out of the injector. Even when $K=1.8$ and the cavitation is only visible about the lip, the discharge coefficient drops about 2 percent. In all three cases the discharge coefficient is found to reach a quasi-periodic state with oscillations roughly 1–2 percent of the mean. Note that even under noncavitating conditions ($K=6$) discharge oscillations are present due to instabilities in the vena contracta formed at the orifice entrance.

Comparison of the discharge coefficient results with the experimental results of Strakey and Talley [5] shows good agreement as noted in Table 1. Values of C_d change rapidly with K at the low K value of 1.2 which can lead to a substantial change in discharge for a small change in K.

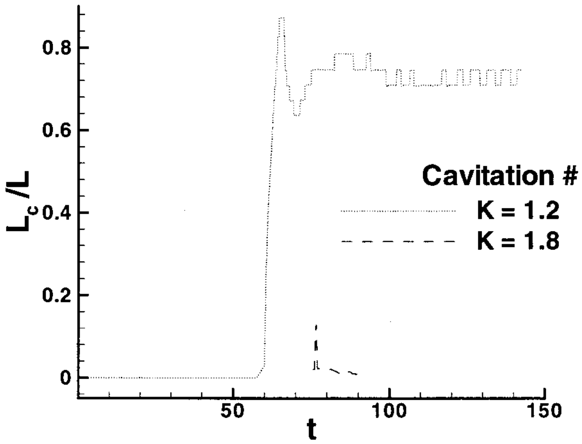

Fig. 4 Cavitation length histories for $K=6$, 1.8, 1.2

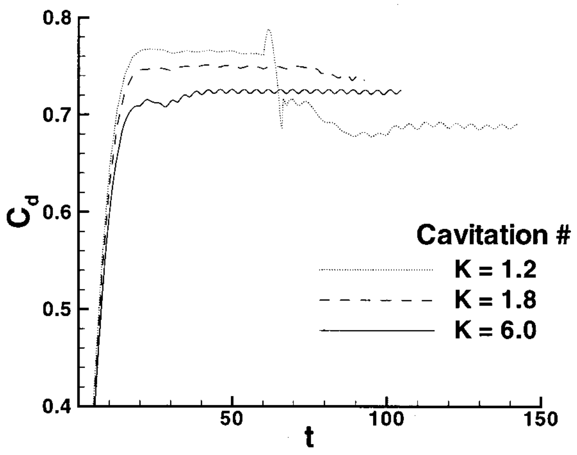

Fig. 5 Discharge coefficient histories for $K=6$, 1.8, 1.2

Table 1 Comparison of time-averaged discharge coefficients

Cavitation No. K	Strakey/Talley	Computational
K	$\overline{C_d}$	$\overline{C_d}$
6.0	0.68	0.72
1.8	0.74	0.73
1.2	0.65	0.68

The value of C_d is over predicted by the code under noncavitating conditions when boundary layer losses on the surface of the passage play a larger role. Similar effects were noted in axisymmetric calculations and are generally attributed to the fact that the present code is laminar while the boundary layers in the device are turbulent. In addition, the effect of orifice geometry also plays a key role. Slight rounding or canting of the orifice lip can have a significant effect on the resulting flow field (Xu et al. [21], Chen and Heister [25]). The numerical results assumed a sharp edged orifice, where as in practice the manufacture of a truly sharp edged orifice is not possible. Another source of error could lie in the mesh used for this simulation. Recall Fig. 3, as the mesh was refined the discharge coefficient fell in value. It is conceivable that refining the mesh may bring the results somewhat closer in value.

The frequency of fluctuation for both the discharge coefficient, C_d, and the cavitation length, L_c, are found to be the same, 3589 Hz, for the cavitating $K=1.2$ simulation. Physically, this oscillation is caused by hydrodynamic instability of the vena-contracta. We have investigated the instability in detail in axisymmetric geometries (Xu et al. [21]) and found it to exist in both cavitating and noncavitating flows. When the cavitation length is a maximum, the discharge coefficient is at its maximum amplitude. As the cavitation length decreases so to does the discharge coefficient. This is likely do to the increase in volume downstream of the cavity region as the cavitation length decreases allowing the liquid to backfill thus reducing the mass flux exiting the orifice. This correlation between the cavity length and the mass flow exiting the orifice has previously been seen in the axisymmetric simulations of Xu et al. [21].

When $K=1.2$, a highly developed, quasi-periodic cavity forms in the orifice. Figure 6 shows the cavitation via contours of the pseudo-density at four instances in time.[1] The cavity region initially begins growing from the lip of the orifice and precedes downstream. After the cavity reaches its furthest extent, the

---

[1] A color rendering of Figs. 6, 9, and 10 can be seen on the JFE website.

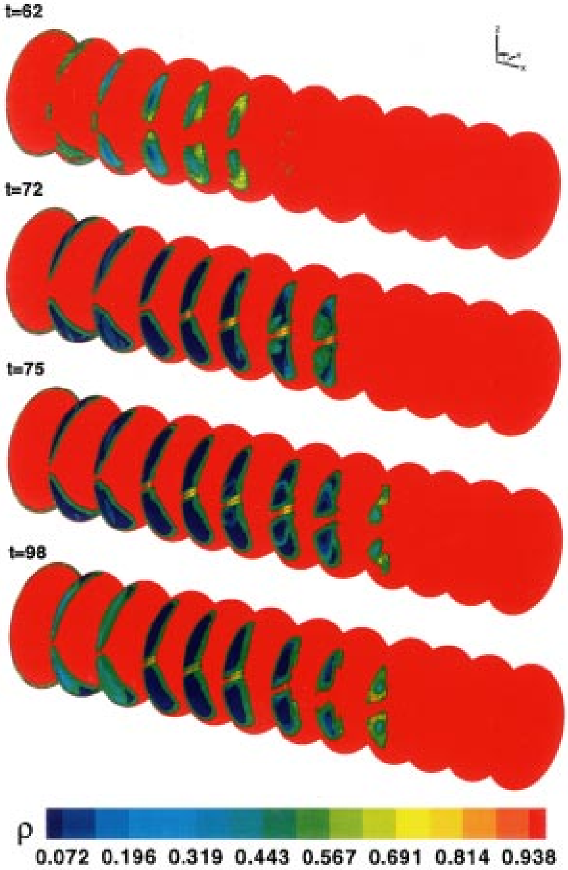

Fig. 6 Cavitation profiles at four different instances in time ($K=1.2$)

bubbles in the region approximately one diameter downstream of the lip begins to collapse. In this region the pseudodensity is about 0.5 in magnitude. In other words, about half of the cavity region is liquid. Beyond this point, a full cavity develops about 2 diameters further downstream. The next diameter downstream is highly active with the collapse and reformation of cavitation. In this region the cavitation actually separates from the wall due to the circulation of liquid about the circumference of the orifice.

In this case, the period of oscillation is found to be 0.28 msec. Similar behavior has been noted in both 2-D simulations (Bunnell et al. [24], Xu et al. [21]) and experiments (Chandra and Collicott [11]). The present results are consistent with the notion that the frequency is related to the time a fluid element spends in the orifice passageway.

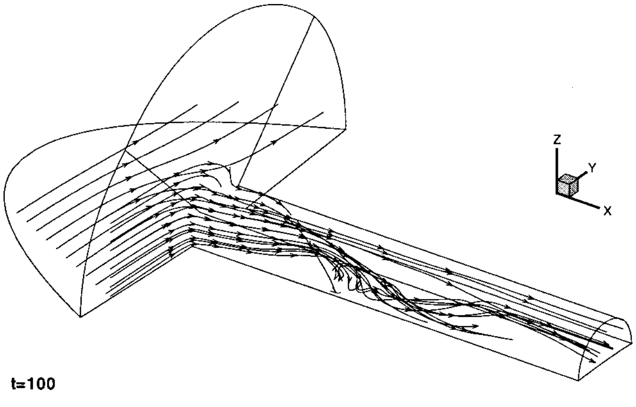

Fig. 7 Typical streamline patterns ($K=6.0$: noncavitating)

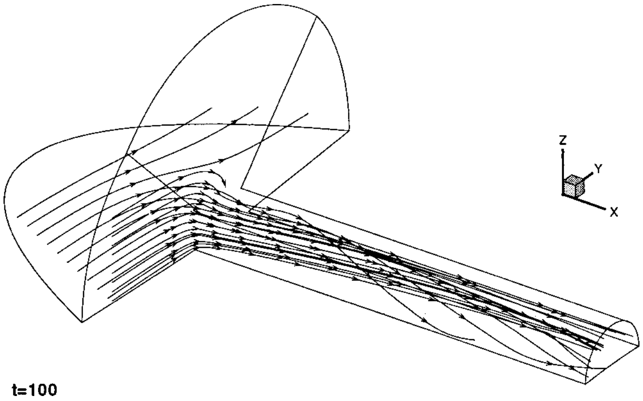

Fig. 8 Typical streamline patterns ($K=1.2$: cavitating)

Streamlines and Velocity Fields. Figures 7 and 8 show the typical streamlines for a given instant in time. In the noncavitating case ($K=6.0$) a strong vortex develops about one diameter downstream of the lip. For the cavitating case the vortex develops farther downstream. The cavity region tends to act as a slipstream, as can be seen from the streamlines in Fig. 8. The effect this has on the exit flow conditions of the injector orifice can be seen in Figs. 9(*a*) and 10(*a*). The figures show orifice exit streamline patterns for cavitating and noncavitating cases. The crossflow from the manifold would come from the left in the views shown in these figures.

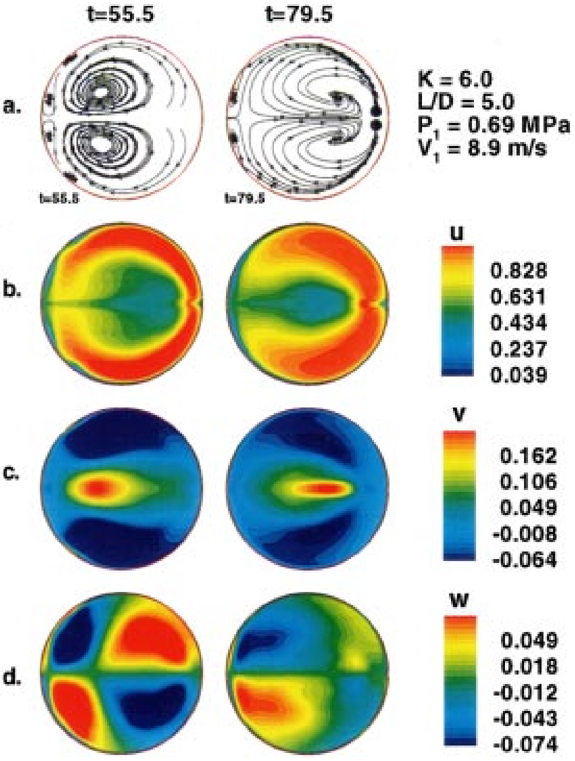

Fig. 9 Exit plane velocity characteristics (*a*) streamlines; (*b*) axial velocity contours; (*c*) transverse velocity, (in direction of cross-flow); (*d*) transverse velocity, (normal to cross-flow); $K=6.0$: noncavitating)

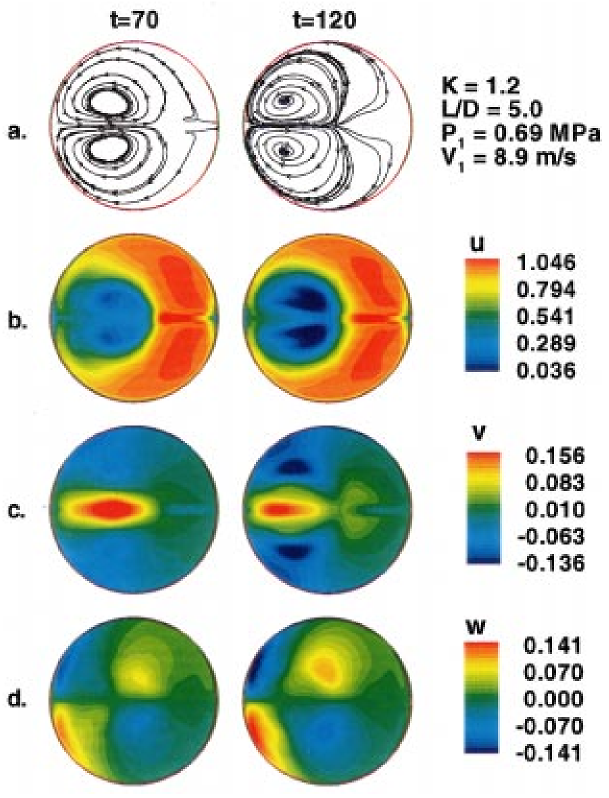

Fig. 10 Exit plane velocity characteristics (*a*) streamlines; (b) axial velocity contours; (*c*) transverse velocity, (in direction of cross-flow); (*d*) transverse velocity (normal to cross-flow); *K* =1.2: cavitating)

For the noncavitating flow (Fig. 9(*a*)), a greater amount of structure is present, revealing extensive vorticity transport as a result of the crossflow at the inlet. Several smaller recirculation zones develop along the edge of the orifice. In the cavitating flow, these smaller cells of circulation are not present (Fig. 10(*a*)). Formation of cavitation tends to reduce exit plane gradients and inhibit development of streamwise vorticity. The vortical structure at the exit also tends to move about more in the noncavitating case. The presence of significant cavitation appears to inhibit this behavior as well.

Part (b) of Figs. 9 and 10 shows contours of the axial velocity at two instances in time for $K=6.0$ and $K=1.2$. This can be thought of as a representation of the mass flux from the injector. In both cases, the maximum flux forms a crescent moon shape or horseshoe like structure on the side of at the exit plane which is downstream from the crossflow. This region contracts and grows with time. In the cavitating case, there is a significant stagnant region where little or no mass flux is present. For the noncavitating simulation this region has a mass flux which is still approximately 50 percent of the maximum exit velocity. The peak axial velocity in the cavitating case is nearly 20 percent higher than in the noncavitating case due to the fact that substantial flow is observed over a smaller fraction of the orifice exit plane.

Parts (c) and (d) of Figs. 9 and 10 show contours of the transverse velocities. Part (c) shows the crossflow velocity v, and Part (d) shows the vertical velocity w. In the noncavitating case, the transverse velocities in the region of the symmetry plane reach about 20 percent of the maximum axial velocity at the exit. Outside of the this region the transverse velocities are $\leqslant 10$ percent of the maximum axial velocity. In the cavitating flow the transverse velocities comparable; on the order of 10 to 15 percent of the maximum axial velocity.

Implications on Atomization. Determining the effects on overall atomization produced by these orifice flows is a complex task. The most obvious notion is that the spray will be biased to the side of the orifice which lies downstream of the crossflow. Variations induced by the crossflow are known to persist unless the orifice passage is very long ($L/D > 10$).

The effect of cavitation on the spray is much more difficult to assess. While the cavitated region tends to serve as a blockage for a greater fraction of the orifice exit area, this fact leads to higher exit velocities as compared to a noncavitating case. While temporal variations in injector massflow occur in both cases, these effects are more prominent in cavitating orifices. This behavior could enhance atomization for cavitated flows. However, the slipstream behavior of the cavitation surface tends to inhibit vorticity transport and transverse velocities which can serve to break-up the exiting flow. In comparing Parts (c) and (d) of Figs. 9 and 10, one can see that there is a large region of negligible transverse velocity in the cavitated flow. The lack of appreciable radial/tangential velocities in this region will serve to inhibit atomization.

Overall, the presence of cavitation tends to accentuate the presence of the crossflow; nonaxisymmetric discharge characteristics will be much more evident in an orifice which is cavitating an appreciable amount. The lack of knowledge of the importance of all these factors makes it very difficult to assess how the drop sizes might be affected by these varying conditions.

Conclusions

A series of numerical studies have been performed to assess the flowfield inside a plain-orifice atomizer driven by a manifold flow with crossflow. The influence of cavitation within the passage has been addressed. Results indicate that for a given flow condition, the presence of cavitation tends to decrease orifice massflow in addition to contributing noticeable massflow variations in the 1–2 percent range. Comparison of a highly-cavitated case with a noncavitated case shows the cavitation boundary to act as a slipstream which inhibits vorticity transport within the orifice passage. The cavitation region restricts the orifice discharge to a relatively small crescent-shaped region in the orifice exit plane. Axial discharge velocities are higher for a cavitated orifice, while transverse velocities and exit plane vorticity are smaller than a noncavitated passage. The overall repercussions of these differences on the atomization process are difficult to assess due to the large number of considerations and relative lack of knowledge of atomization itself.

Acknowledgment

The authors gratefully acknowledge the support of this work by Cummins Engine Company under the guidance of Dr. Wayne Eckerle and by the Army Research Office under Contract DAAGG-98-1-0318 monitored by Dr. David Mann.

Nomenclature

a = orifice radius
C_d = orifice discharge coefficient
K = cavitation number
L = orifice length
L_c = cavitation length
n = bubble number density
P = pressure
Re = Reynolds number
r = radial or transverse coordinate
t = time
u = axial velocity
v = ‘‘y’’ velocity (Fig. 1)
V = velocity
w = ‘‘z’’ velocity (Fig. 1)
x = axial coordinate
y,z = transverse coordinates (Fig. 1)

α = void fraction
μ = viscosity
ρ = fluid pseudo-density

Subscripts

1 = inlet side of manifold (Fig. 1)
2 = orifice outlet (Fig. 1)
3 = outlet side of manifold (Fig. 1)
v = vapor

References

[1] Bergwerk, W., 1959, ''Flow Pattern in Diesel Nozzle Spray Holes,'' Proc. Inst. Mech. Eng., **173**, pp. 655–660.
[2] Nurick, W. H., 1976, ''Orifice Cavitation and Its Effect on Spray Mixing,'' ASME J. Fluids Eng., pp. 681–687.
[3] Lichtarowicz, A., Duggins, R. K., and Markland, E., 1965, ''Discharge Coefficients for Incompressible Non-Cavitating Flow Through Long Orifices,'' J. Mech. Eng. Sci., **7**, No. 2, pp. 210–219.
[4] He, L., and Ruiz, F., 1996, ''Effect of Cavitation on Flow and Turbulence in Plain Orifices for High-Speed Atomization,'' Atom. Sprays, **5**, pp. 569–584.
[5] Strakey, P. A., Olson, K. M., and Talley, D. G., 1997, ''The Effect of Manifold Cross-Flow on the Discharge Coefficient of Sharp-Edged Orifices,'' ILASS-97 Conference Proceedings, Ottawa, Canada.
[6] Acroumanis, C., Gavaises, M., Nouri, J. M., Abdul-Wahab, E., and Horrocks, R. W., 1998, ''Analysis of the Flow in the Nozzle of a Vertical Multi Hole Diesel Injector,'' SAE Paper 980811.
[7] Tamaki, N., Shimizu, M., Nishida, K., and Hiroyasu, H., 1998, ''Effects of Cavitation and Internal Flow on Atomization of a Liquid Jet,'' Atom. Sprays, **8**, pp. 179–197.
[8] Chaves, H., Knapp, M. and Kubitzek, A., 1995, ''Experimental Study of Cavitation in the Nozzle Hole of Diesel Injectors Using Transparent Nozzles,'' SAE Paper No. 950290.
[9] Henry, Mark E., 1997, *An Experimental Investigation of a Cavitation Slot Orifice*, Thesis, May.
[10] Li., Haiyun, and Collicott, S. H., 1999, ''Initial Images of Cavitation Inside High-Pressure Atomizers,'' *ILASS-99 Conference Proceedings*, pp. 409–413, Indianapolis, IN.
[11] Chandra, B. W., and Collicott, S. H., 1999, ''Experimental Investigation of Cavitation Frequency in a Slot Orifice,'' *ILASS-99 Conference Proceedings*, pp. 379–384, Indianapolis, IN.
[12] Sanchez, P. K., and Collicott, S. H., 1999, ''Statistics of Cavitation Length in a 2-D Slot Orifice,'' ILASS-99 Conference Proceedings, pp. 403–408, Indianapolis, IN.
[13] Karasawa, T., Tanaka, M., Abe, K., and Kurabayashi, T., 1992, ''Effect of Nozzle Configuration on the Atomization of a Steady Spray,'' Atom. Sprays, **2**, pp. 411–426.
[14] Delannoy, Y., and Kueny, J. L., 1990, ''Two Phase Flow Approach in Unsteady Cavitation Modeling,'' *Cavitation and Multiphase Flow Forum*, ASME, FED Vol. 98.
[15] Kubota, A., Kato, H., and Yamaguchi, H., 1992, ''A New Modeling of Cavitating Flows: A Numerical Study of Unsteady Cavitation on a Hydrofoil Section,'' J. Fluid Mech., **240**, pp. 59–96.
[16] Chen, Y., and Heister, S. D., 1995, ''Modeling Hydrodynamic Non-Equilibrium in Bubbly and Cavitating Flows,'' ASME J. Fluids Eng., **118**, No. 1, pp. 172–178.
[17] Alajbegovic, A., Grogger, H. A., and Philipp, H., 1999, ''Calculation of Transient Cavitation in Nozzle Using the Two-Fluid Model,'' ILASS-99 Conference Proceedings, pp. 373–377, Indianapolis, IN.
[18] Schmidt, D. P., Rutland, C. J., and Corradini, M. L., 1999, ''A Fully Compressible, Two-Dimensional Model of Small, High-Speed, Cavitating Nozzles,'' Atom. Sprays, **9**, No. 3, pp. 255–276.
[19] Ahuja, V., Hosangadi, A., Ungewitter, R., and Dash, S. M., 1999, ''A Hybrid Unstructured Mesh Solver for Multi-Fluid Mixtures,'' AIAA 99-3330, *14th Computational Fluid Dynamics Conference*.
[20] Bunnell, R. A., Heister, S. D., Yen, C., and Collicott, S. C., 1999, ''Cavitating Injector Flows: Validation of Numerical Models and Simulations of High-Pressure Injectors,'' in Review, Atom. Sprays.
[21] Xu, C., Bunnell, R. A., and Heister, S. D., 1999, ''On the Influence of Internal Flow Structure on Performance of Plain-Orifice Atomizers,'' In Review, Atom. Sprays.
[22] Chen, Y., and Heister, S. D., 1995, ''Two-Phase Modeling of Cavitated Flows,'' Comput. Fluids, **24**, No. 7, pp. 799–809.
[23] Fujimoto, H., Mishikori, T., Tsukamoto, T., and Senda, J., 1994, ''Modeling of Atomization and Vaporization Process in Flash Boiling Spray,'' ICLASS-94, Paper VI-13.
[24] Bunnell, R. A., 1999, ''Unsteady, Viscous, Cavitating Simulation of Injector Internal Flows,'' Ph.D. dissertation, Purdue University.
[25] Chen, Y., and Heister, S. D., 1996, ''Modeling Cavitating Flows in Diesel Injectors,'' Atom. Sprays, **6**, pp. 709–726.

Hironori Horiguchi
Research Associate,
Faculty of Engineering,
Tokushima University,
2-1 Minami-josanjima,
Tokushima, 770-8506 Japan
e-mail: horiguti@me.tokuhsima-u.ac.jp

Satoshi Watanabe
Lecturer,
Graduate School of Engineering,
Kyushu University,
6-10-1 Hakozaki,
Fukuoka, 812-8581 Japan
e-mail: fmnabe@mech.kyushu-u.ac.jp

Yoshinobu Tsujimoto
Professor,
Graduate School of Engineering Science,
Osaka University,
1-3 Machikaneyama,
Toyonaka, Osaka, 560-8531 Japan
e-mail: tujimoto@me.es.osaka-u.ac.jp

A Linear Stability Analysis of Cavitation in a Finite Blade Count Impeller

The linear stability analysis of cavitation in flat plate cascades corresponding to 2, 3, 4, and 5-bladed impeller was carried out to clarify the effect of the blade count on cavitation instabilities. Each blade is treated independently so that all possible modes in those impellers can be found. In steady flow analysis the alternate blade cavitation was found only for impellers with even number of blades. For 2 or 4-bladed impeller, it was confirmed that there exists no additional destabilizing mode to those found in the previous analysis in which the inter-blade phase difference of disturbance was assumed. It was shown that the modes with total cavity volume fluctuation depend on the inlet duct length while the modes without total cavity volume fluctuation are independent on the system. [S0098-2202(00)01304-3]

Introduction

Various kinds of cavitation related phenomena such as alternate blade cavitation [1,2], cavitation surge [3], and rotating cavitation [4–7] were examined by a series of our theoretical analyses [8–11]. In the early studies of cavitation surge, the effect of cavities are modeled by cavitation compliance and mass flow gain factor and extensive studies have been made to determine these factors [12]. It was further found in the actuator disk analysis of rotating cavitation [13] that positive mass flow gain factor is the cause of rotating cavitation as well as cavitation surge. In these analyses modeling the effects of cavities by those factors, the relationship between the flow details around the cavity and the instabilities cannot be discussed. To clarify the relationships, Watanabe et al. [8,9] first proposed a method for the stability analysis of two-dimensional cavitating flow in cascades. This method has been applied to various cases by the present authors [10,11]. In these analyses, the inter-blade phase difference of disturbance is assumed for the purpose of reducing computational time. These analyses can predict only the instabilities of assumed modes, and we need to generalize the treatment to find all possible modes.

It is well known that the alternate blade cavitation, in which the cavity length changes alternately from blade to blade, occurs in impellers with even number of blades [1,2,5]. It was found that alternate blade cavitation can be simulated by a potential flow calculation [10], but the effect of blade count has not been clarified theoretically. On the other hand, it is also known that an asymmetric steady cavitation pattern with one cell occurs at a cavitation number slightly smaller than that of rotating cavitation onset. This occurs in 3-bladed inducers [7] as well as in 4-bladed inducers [5]. No attempts have been made to simulate the asymmetric steady cavitation.

In the present study, under the above circumstances, attempts are made to obtain all possible steady and unsteady cavitation modes in finite blade count impellers. We generalized our previous stability analysis by removing the assumption on the inter-blade phase difference. The analysis is made for the cavitation in flat plate cascades corresponding to 2, 3, 4, and 5-bladed impellers and discussions are made on the effect of the blade count on possible destabilizing modes. The system dependence of the cavitation surge modes is also discussed.

Analysis Model

We consider a cascade of flat plates with the chord length C, the spacing h and the stagger angle β as shown in Fig. 1, with a mean flow of magnitude U and the angle of attack α at upstream. The index of blades is defined by taking account of the periodicity of blade row for the inducer with blade number Z_N: the blade located on x-axis is given the index zero, and the index increases in positive direction of y-axis and the index of Z_Nth blade returns to zero.

We consider the case of partial cavitation with cavity length l_n on the nth blade. It is assumed that steady and unsteady flow disturbances due to blades and cavities are both small. Based on this assumption, quadratic and higher order terms of those disturbance components are neglected. Inviscid, linear closed cavity model is employed and the boundary conditions on the cavity surface are applied approximately on the blade surface. From these assumptions, the re-entrant jets often observed in experiments are not included in the present analysis. No cavity shedding is assumed but the cavity length is allowed to oscillate freely.

Assuming the periodicity of the disturbances over Z_N blades, we represent the velocity disturbance due to the blades and cavi-

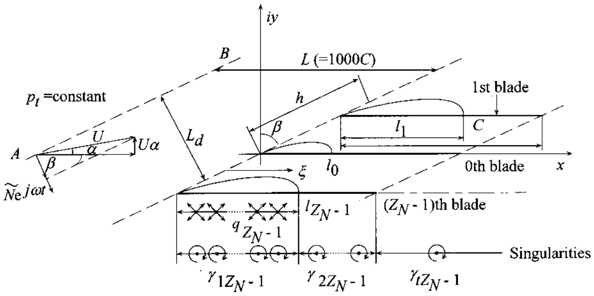

Fig. 1 Model for present analysis

Contributed by the Fluids Engineering Division for publication in the JOURNAL OF FLUIDS ENGINEERING. Manuscript received by the Fluids Engineering Division June 3, 1999; revised manuscript received July 18, 2000. Associate Technical Editor: J. Katz.

ties as follows by source distributions q_n on the cavity region, vortex distributions γ_{1n} and γ_{2n} on the blade and trailing vortices γ_{tn} on wake surface of the blades.

$$
\begin{aligned}
w(z,t)&=u-iv\\
&=U\mathrm{e}^{-i\alpha}+\tilde{N}\mathrm{e}^{i\beta}\mathrm{e}^{j\omega t}+\frac{1}{2\pi}\sum_{n=0}^{Z_N-1}\Bigg\{\Bigg[\int_0^1[q_n(s_1)+i\gamma_{1n}(s_1)]\\
&\quad\times[f_n(z,l_ns_1)-f_n(-L,l_ns_1)]l_nds_1\\
&\quad+i\int_1^2\gamma_{2n}(s_2)[f_n\{z,(C-l_n)s_2+(2l_n-C)\}\\
&\quad-f_n\{-L,(C-l_n)s_2+(2l_n-C)\}](C-l_n)ds_2\\
&\quad+i\int_C^\infty\gamma_{tn}(\xi)[f_n(z,\xi)-f_n(-L,\xi)]d\xi\Bigg]\Bigg\}
\end{aligned}
\tag{1}
$$

$$
f_n(z,\xi)=\frac{\pi}{Z_Nh}\mathrm{e}^{-i(\pi/2-\beta)}\cos\left\{\frac{\pi}{Z_Nh}(z-\xi)\mathrm{e}^{-i(\pi/2-\beta)}-\frac{n}{Z_N}\pi\right\}
\tag{2}
$$

where s_1 and s_2 are introduced in order to take account of the variable cavity length l_n and defined by

$$
\xi=l_ns_1\quad(0<\xi<l_n,\quad 0<s_1<1,\quad n=0,1,\ldots,Z_N-1)\tag{3}
$$

$$
\begin{aligned}
&\xi=(C-l_n)s_2+(2l_n-C)\\
&\qquad(l_n<\xi<C,\quad 1<s_2<2,\quad n=0,1,\ldots,Z_N-1)
\end{aligned}
\tag{4}
$$

The function $f_n(z,\xi)$ represents the effects of infinite number of singularities of equal strength located at $z=\xi+mZ_Nhe^{j\omega t}$, $m=-\infty,\ldots,-1,0,1,\infty$. The strength of singularities are specified on these coordinates s_1 and s_2 moving in accord with the variable cavity length l_n. In the present analysis with larger L $(L=1000C)$, $f(-L,\xi)$ is approximated by $-\pi\mathrm{e}^{i\beta}/h$.

The strength of singularities and the cavity length are divided into the steady and unsteady components. We consider unsteady components with the time dependence of $\mathrm{e}^{j\omega t}$, where $\omega=\omega_R+j\omega_I$ is the complex frequency with its real part ω_R signifying the frequency and the imaginary part ω_I the decay rate.

In the previous analyses of alternate blade cavitation, cavitation surge and rotating cavitation, the phase of the disturbance on each blade is assumed depending on the instability considered. In these analyses only the stability of the phenomenon assumed can be examined, but the phenomenon with other mode cannot be predicted even if it exists. To find out all possible modes, we removed the assumption on the phase of disturbance on each blade.

We assume that the outlet duct length is infinite and there exists no velocity fluctuation at downstream infinity. The inlet duct length L is assumed to be finite and set to be $L=1000C$ in this study. The inlet duct is connected to a space with constant total (=static) pressure p_t along AB at the duct inlet. The complex conjugate velocity fluctuation there is denoted by $\tilde{N}\mathrm{e}^{i\beta}\mathrm{e}^{j\omega t}$, where $\tilde{N}$ represents the amplitude of axial velocity fluctuation.

The velocity around the blades is divided into the uniform steady component $(U,U\alpha)$, the steady disturbance (u_s,v_s), and the unsteady disturbance $(\tilde{u},\tilde{v})$ components as follows, with the complex frequency $\omega=\omega_R+j\omega_I$ to be determined from the analysis.

$$
\begin{aligned}
u&=U+u_s+\tilde{u}\mathrm{e}^{j\omega t}\\
v&=U\alpha+v_s+\tilde{v}\mathrm{e}^{j\omega t}
\end{aligned}
\tag{5}
$$

Here, we assume that $\alpha\ll1$, $U\gg|u_s|$, $|v_s|\gg|\tilde{u}|$, $|\tilde{v}|$ and linearizations are made based on these assumptions throughout the present study.

Because the fundamental flow field and the formulation are the same as those used in the study [10], we do not get into details in the present paper.

Boundary Conditions

All the singularities are distributed on the blades and their extensions assuming that the flow disturbance is small. The following five boundary and complimentary conditions are applied.

1 The pressure on the cavity surface equals to the vapor pressure. From the suggestion of a reviewer, it was found that a term representing the effect of the centrifugal force due to the curvature of the steady cavity surface is neglected as second order small quantity in the present analysis. Wang and Wu [14] pointed out that this term causes surface waves on the cavity surface. So, the present analysis cannot predict the instabilities related to the surface waves.

2 The velocity component normal to the wetted surface should be zero.

3 Cavity thickness at cavity trailing edge is zero (closed cavity model).

4 The pressure difference between the pressure and suction surfaces of blade vanishes at the trailing edge of blade (unsteady Kutta's condition).

5 Downstream condition: As the downstream duct length is assumed to be infinite, the downstream flow rate fluctuation is suppressed due to the infinite inertia effect. Thus, the fluctuation of cavity volume is related to the upstream velocity fluctuation.

Analytical Method

We specify the strength of singularities at discrete points $s=S_{1k}$ $(k=1\sim N_C)$ on cavity surface and S_{2k} $(k=1\sim N_B)$ on wetted surface in the coordinates stretching with the variable cavity length as unknowns as well as the variable cavity length. The boundary conditions are applied at the middle of those discrete points. After linearization, the boundary conditions are reduced to the following set of linear equations.

For steady components,

$$
[A_s(l_{sn})]\begin{Bmatrix}C_{q_n}(S_{11})\\ \vdots\\ C_{\gamma_{1n}}(S_{11})\\ \vdots\\ C_{\gamma_{2n}}(S_{21})\\ \vdots\\ \sigma/2\alpha\end{Bmatrix}=\{B_s\}\quad(n=0,1,\ldots,Z_N-1)\tag{6}
$$

and for unsteady components,

$$
[A_u(l_{sn},\omega)]\begin{Bmatrix}\tilde{q}_n(S_{11})\\ \vdots\\ \tilde{\gamma}_{1n}(S_{11})\\ \vdots\\ \tilde{\gamma}_{2n}(S_{21})\\ \vdots\\ \tilde{u}_{cn}\\ \vdots\\ \alpha l_n\\ \vdots\\ \tilde{N}\end{Bmatrix}=\{0\}\quad(n=0,1,\ldots,Z_N-1)\tag{7}
$$

where $A_s(l_{sn})$, $A_u(l_{sn},\omega)$ are coefficient matrices, B_s is a constant vector. C_{qn}, $C_{\gamma1n}$, and $C_{\gamma2n}$ are the functions of steady components of singularities and defined as follows.

$$
\begin{aligned}
C_{qn}&=q_{sn}(s_1)/(U\alpha)\\
C_{\gamma1n}&=\gamma_{1sn}(s_1)/(U\alpha)\\
C_{\gamma2n}&=\gamma_{2sn}(s_1)/(U\alpha)
\end{aligned}
\tag{8}
$$

The value of unknowns on *n*th blade are shown by the index n $(=0,1,\ldots,Z_N-1)$. In the previous analyses, we assumed the inter-blade phase difference of the disturbance to decrease the number of unknowns. In the present study, we consider the unknowns on all blades as independent variables to obtain all possible destabilizing modes in a cascade corresponding to an impeller with finite number of blades.

The steady flow is determined from Eq. (6), which shows the steady cavity length l_{sn} is a function of $\sigma/2\alpha$. Equation (7) is a set of linear homogeneous equations. For the cases with externally forced disturbances, Eq. (7) has nonzero vector in the right hand side. In the present study without any external disturbances, the determinant of the coefficient matrix $A_u(l_{sn},\omega)$ should satisfy

$$|A_u(l_{sn},\omega)|=0 \tag{9}$$

so that we have nontrivial solutions. The complex frequency $\omega=\omega_R+j\omega_I$ is determined from Eq. (9). Thus, the angular frequency ω_R and the stability of cavitation depend on the steady cavity length l_{sn} or equivalently $\sigma/2\alpha$.

We use the following Strouhal number based on steady cavity length l_{se}.

$$\mathrm{St}=\frac{\omega_R/2\pi}{U/l_{se}}, \quad \mathrm{St}_I=\frac{\omega_I/2\pi}{U/l_{se}} \tag{10}$$

where St_I represents the nondimensional decay rate.

For rotating cavitation, we define the following normalized frequency.

$$k_R+jk_I=\frac{(\omega/2\pi)Z_N h}{U_T} \tag{11}$$

The real part k_R represents the ratio of propagation velocity of disturbance to the peripheral velocity U_T of cascade, observed in a frame moving with the cascade. Here, we define the phase difference $\theta_{m,n}$ of the disturbance on nth blade relative to mth blade. The propagation velocity ratio observed in the stationary frame k_R^* can be determined from the following equations for $k_R>0$.

$$\begin{aligned} k_R^* &= 1+k_R \quad (0<\theta_{0,1}<\pi) \\ k_R^* &= 1-k_R \quad (-\pi<\theta_{0,1}<0) \end{aligned} \tag{12}$$

Results and Discussions

Steady Cavitation. The following three types of steady cavitation have been observed in experiments; the equal length cavitation in which the cavities on all blades are identical, the alternate blade cavitation in which the cavity length differs alternatively, and the asymmetric cavitation as sketched in Fig. 2. In the present study a systematic research has been made to determine if steady solutions exist corresponding to these cavitation patterns in finite blade count impellers.

The cavity lengths l_{sn} $(n=0,1,\ldots,Z_N-1)$ are determined for a given value of $\sigma/2\alpha$ using the following procedure. To determine the approximate values, we assume the cavity length l_{sn} as follows.

$$l_{sn}=A+B\sin\left(2\pi\frac{n}{Z_N}m\right) \tag{13}$$

or

$$l_{sn}=A+B\cos\left(2\pi\frac{n}{Z_N}m\right) \tag{14}$$

where m is a number of cell. By solving Eq. (6) excluding the cavity closure conditions for these cavity length l_{sn}, we obtain the cavity thickness η_n at cavity trailing edge. We define the residual of the cavity closure conditions as follows.

$$\frac{\delta(A,B)}{C}=\frac{1}{CZ_N}\sum_{n=0}^{Z_N-1}|\eta_n(A,B)| \tag{15}$$

The approximate values of cavity length can be determined from the values of A and B which minimize the residual $\delta(A,B)$. Using them as initial values, the cavity length l_{sn} which satisfies the cavity closure condition can be found by iterative methods such as Newton's method.

Figures 3(*a*) and (*b*) show the residual $\delta(A,B)/C$ of the cavity closure condition for the cavitation in the cascade with the solidity of $C/h=2.0$ and the stagger of $\beta=80.0$ deg for the blade number of $Z_N=3$ and 4, respectively. These are the results for $\sigma/2\alpha=2.4$ and the number of cell m is set to be unity, to obtain a solution corresponding to asymmetric cavitation. In these figures,

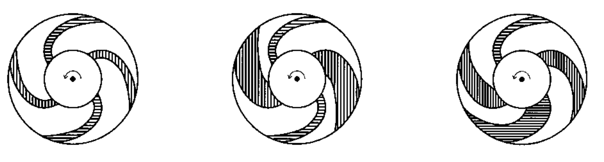

(a) Equal length cavitation (b) Alternate blade cavitation (c) Asymmetric cavitation

Fig. 2 Various types of steady cavitation, adopted from B. Goiland et al. [5]. (*a*) Equal length cavitation; (*b*) alternate blade cavitation; (*c*) asymmetric cavitation

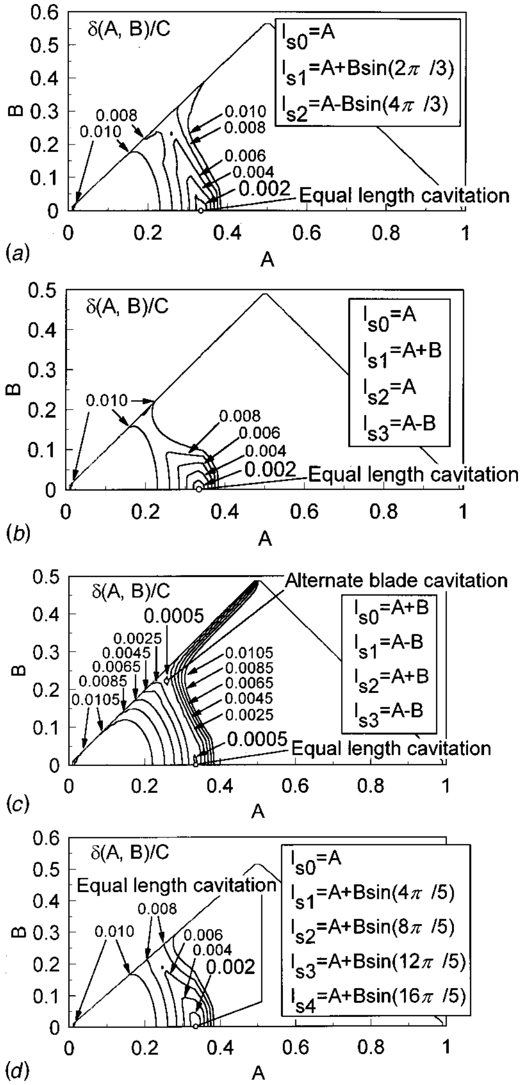

Fig. 3 Residual of cavity closure condition at $\sigma/2\alpha=2.4$. (*a*) $Z_N=3$, $m=1$; (*b*) $Z_N=4$, $m=1$; (*c*) $Z_N=4$, $m=2$; (*d*) $Z_N=5$, $m=2$

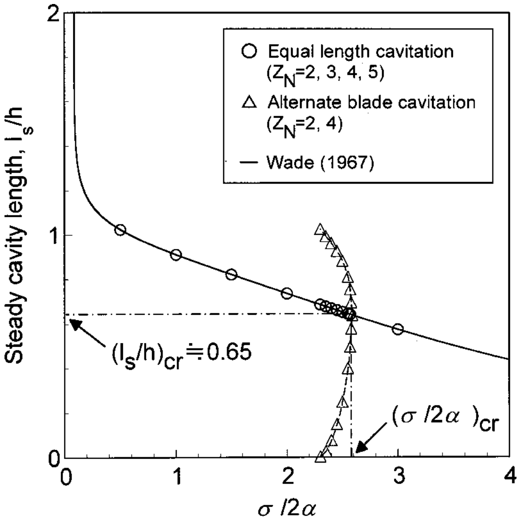

Fig. 4 Steady cavity length for the cascade with $Z_N=2,3,4,5$, $C/h=2.0$ and $\beta=80$ deg

the residual $\delta(A,B)/C$ is locally minimum only near $A=0.33$ and $B=0$. This indicates that only the equal length cavitation exists, and no solutions corresponding to the asymmetric cavitation are obtained.

Figures 3(*c*) and (*d*) show the residual $\delta(A,B)/C$ of the cavity closure condition for $\sigma/2\alpha=2.4$ and $m=2$ in Eq. (14) and Eq. (13) for the cascades with $Z_N=4$ and 5, respectively. In Fig. 3(*c*), $\delta(A,B)/C$ becomes minimum not only at $A=0.33$ and $B=0$ corresponding to the equal length cavitation but also at $A=0.26$ and $B=0.22$ corresponding to the alternate blade cavitation. From this result, it is found that the alternate blade cavitation can exist in addition to the equal length cavitation for $Z_N=4$.

In Fig. 3(*d*), the minimum point of $\delta(A,B)/C$ is not found except that near $A=0.33$, $B=0$. Thus, for $Z_N=5$, only the equal length cavitation was found and the cavitation pattern corresponding to alternate blade cavitation or asymmetric cavitation was not found.

We also made other trial calculations for various combinations of Z_N and m at various values of $\sigma/2\alpha$ in the case of the cascades with $Z_N=2$, 3, 4, and 5. From these results, it was found that the alternate blade cavitation occurs only in the impeller with even number of blades. This fact agrees with experimental observations. However, no steady solution corresponding to asymmetric cavitation was found.

Giving the cavity length l_{sn} predicted by the method mentioned above as initial value, we obtained the solution for cavity length l_{sn} by repeating the correction on the cavity length until the cavity closure condition was satisfied to the order of $\delta(A,B)/C \ll 10^{-8}$. Figure 4 shows the results of steady cavity length obtained finally. The symbol ○ in Fig. 4 represents the equal length cavitation and the solid line represents the results obtained by conformal mapping method [15]. Symbol △ shows the solutions corresponding to alternate blade cavitation found in the cascades with even number of blades, $Z_N=2$ and 4. No other type of steady solution was obtained.

Unstable Modes of Cavitation

Figures 5, 6, 7, and 8 show the reduced frequency St of unstable modes and the phase difference $\theta_{n,n+1}(\theta_{n,n+2})$ for the case of the cascade with the number of blades, $Z_N=2$, 3, 4, and 5, respectively. Many unstable modes are obtained but only the lower order modes are shown in the figures. In the previous analyses [10,11], the stability of the cavitation with assumed mode was examined. In the present analysis, we can examine the all possible

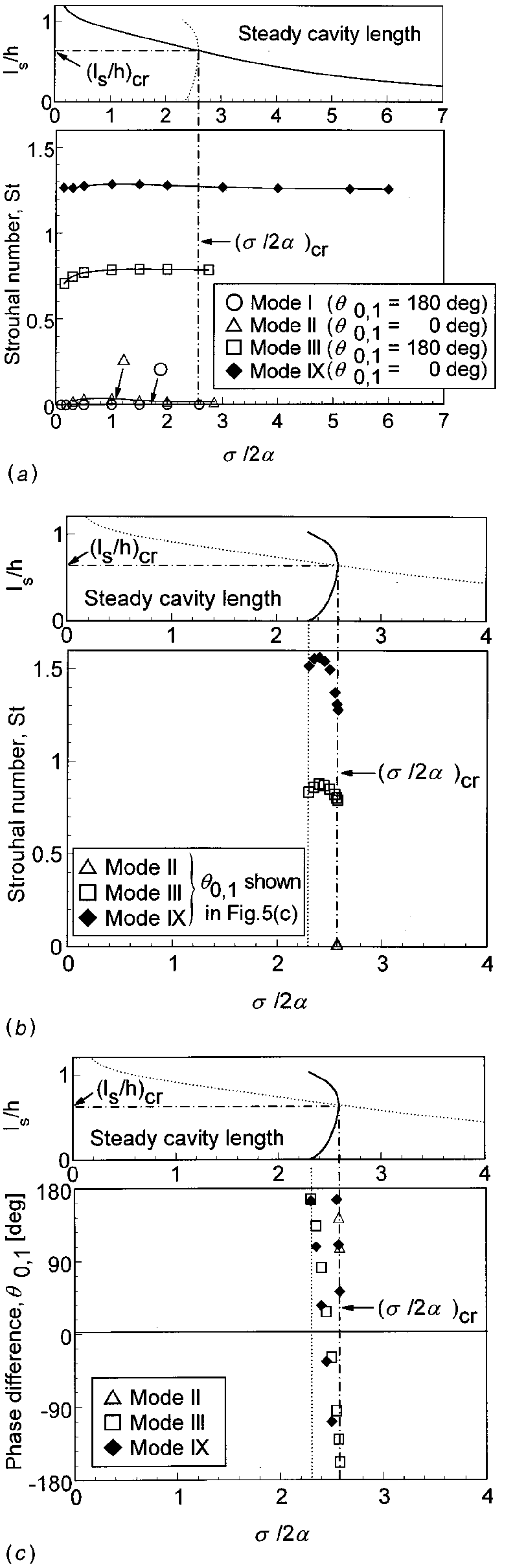

Fig. 5 Unstable modes of the cavitation in the cascade with $Z_N=2$, $C/h=2.0$ and $\beta=80$ deg. (*a*) Strouhal number for equal length cavitation; (*b*) Strouhal number for alternate blade cavitation (*c*) Phase difference for alternate blade cavitation

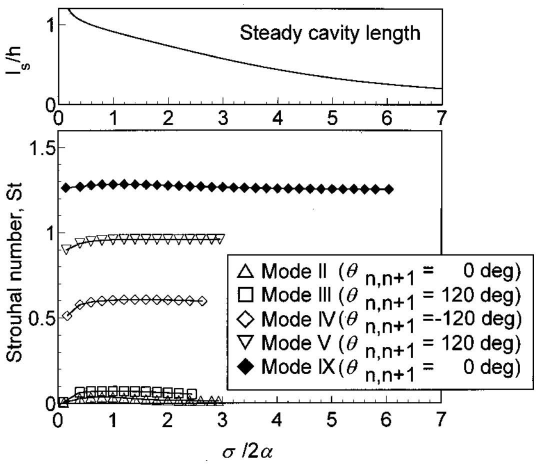

Fig. 6 Unstable modes of the cavitation in the cascade with $Z_N=3$, $C/h=2.0$ and $\beta=80$ deg

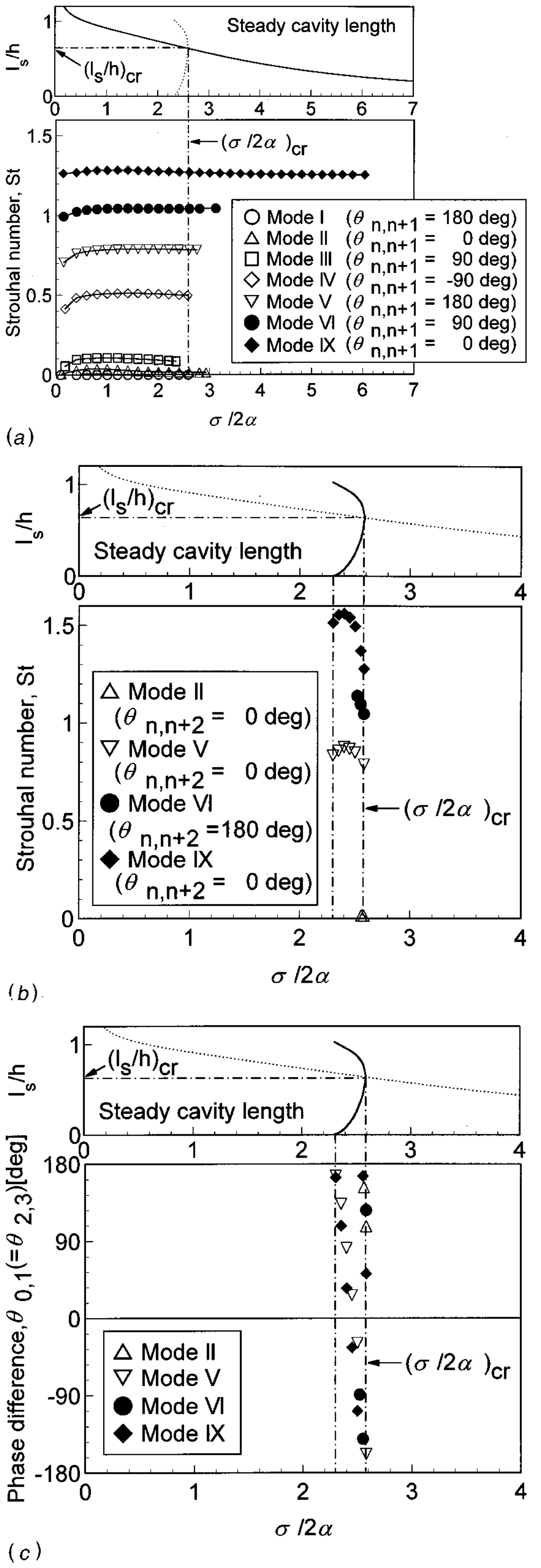

Fig. 7 Unstable modes of the cavitation in the cascade with $Z_N=4$, $C/h=2.0$ and $\beta=80$ deg. (*a*) Strouhal number for equal length cavitation; (*b*) Strouhal number for alternate blade cavitation; (*c*) Phase difference for alternate blade cavitation

modes without any restrictions on the phase of the disturbance. The length of steady cavity examined is shown in the upper part of Figs. 5–8.

First, let us focus on the results for the case of $Z_N=2$ and 4, shown in Figs. 5 and 7. In the case of equal length cavitation, the phase difference $\theta_{n,n+1}$ is found to be identical in each mode for any blade index *n*. On the other hand, for the case of alternate blade cavitation with $Z_N=4$, we have to refer to two phase differences $\theta_{n,n+1}$ and $\theta_{n,n+2}$ because the phase differences are different alternately. For simplicity, we assume a longer cavity on the 0th (2nd) blade. The phase difference $\theta_{0,1}$ ($\theta_{2,3}$) is shown in Fig. 5(*c*) and Fig. 7(*c*). The phase difference $\theta_{n,n+2}$ for the case of $Z_N=4$ is indicated in Fig. 7(*b*).

Mode I shown by the symbol ○ in Fig. 5(*a*) and Fig. 7(*a*), obtained for the case of equal length cavitation in the cascade with even number of blades, is a mode in which the frequency equals to zero and the phase angle $\theta_{0,1}(=\theta_{2,3})$ is 180 deg. This suggests that the cavity on one blade becomes longer exponentially and the cavity on the neighboring blades shorter. Mode I indicates the transition of equal length cavitation to the alternate blade cavitation. Thus, in the region where Mode I exists, the equal length cavitation is statically unstable. On the other hand, in the results shown in Fig. 5(*b*) and Fig. 7(*b*) for the alternate blade cavitation, Mode I is not found. Thus, the alternate blade cavitation is statically stable.

In the results shown in Figs. 6 and 8 for the cascades with odd number of blades, $Z_N=3$ and 5, the divergence type mode with the frequency 0 is not found. This shows that the equal length cavitation in the cascade with odd number of blades is statically stable for all values of $\sigma/2\alpha$. This corresponds to the nonexistence of steady ‘‘alternate blade cavitation’’ for the impellers with odd number of blades.

Mode II and Mode IX, denoted by symbols △ and ◆, respectively, in Figs. 5(*a*), 6, 7(*a*), and 8, are the cavitation surge modes with the same phase for all blades. The Strouhal number of lower mode, Mode II, depends on the length *L* of the inlet duct while that of the higher order mode, Mode IX, is independent of the length *L* [9]. Here, we examine the reason. Figures 9(*a*) and (*b*) show the cavity shapes of Mode II and Mode IX at $\sigma/2\alpha=2.0$ for $\alpha=4.0$ deg, respectively. The cavity shapes in one period are shown in every one fourth period from the time [(i) in Fig. 9] when the cavity length is 1.05 times as long as steady cavity length. And also the ratio $\widetilde{V}_C/V_{CS}$ of fluctuation of cavity volume to the steady cavity volume is shown in the figure. The fluctuation of cavity volume in Mode IX is significantly smaller than that in

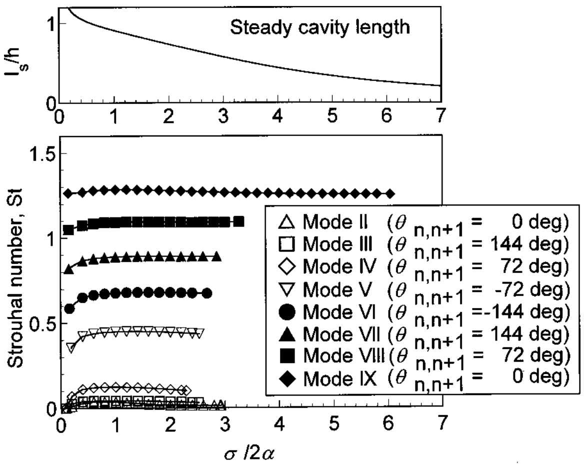

Fig. 8 Unstable modes of the cavitation in the cascade with $Z_N=5$, $C/h=2.0$ and $\beta=80$ deg

Mode II. Therefore, the mass flow fluctuation in the inlet duct does not occur and the frequency of Mode IX is not affected by the length of the inlet duct.

Mode III–VIII in Figs. 5(*a*), 6, 7(*a*), and 8 correspond to the modes of rotating cavitation. They are discussed in the next section.

The results in Fig. 7 agree with the results obtained by assuming inter-blade phase difference [10,11]. This proves that there are no extra unstable modes in addition to the modes which had already been obtained.

Rotating Cavitation

In this section, we discuss the effect of the number of blade for the mode corresponding to rotating cavitation. The frequencies of the lower order modes of rotating cavitation, Mode I and Mode III–VIII in Figs. 5(*a*), 6, 7(*a*), and 8, are replotted in Figs. 10(*a*), (*b*), and (*c*) in terms of the propagation velocity ratio k_R^* observed in stationary frame.

The first mode shown in Fig. 10(*a*) represents the conventional forward rotating cavitation observed in experiments, and the second and third modes shown in Figs. 10(*b*) and (*c*), respectively, represent the backward rotating cavitation and higher order mode of forward rotating cavitation respectively. As has been indicated by Watanabe et al. [8], the absolute value of propagation velocity ratio k_R^* of these modes increase as the inter-blade phase difference $2\pi m/Z_N$ of disturbance decreases. As $2\pi m/Z_N$ decreases, the regions in which first and second modes appear become smaller and that in which third mode appears becomes larger.

The results obtained by the present analysis agree with the results which have been obtained so far using the assumption of phase of disturbance. Thus, it is found that the unstable modes can be predicted by the conventional analyses if appropriate phase difference of disturbance is assumed.

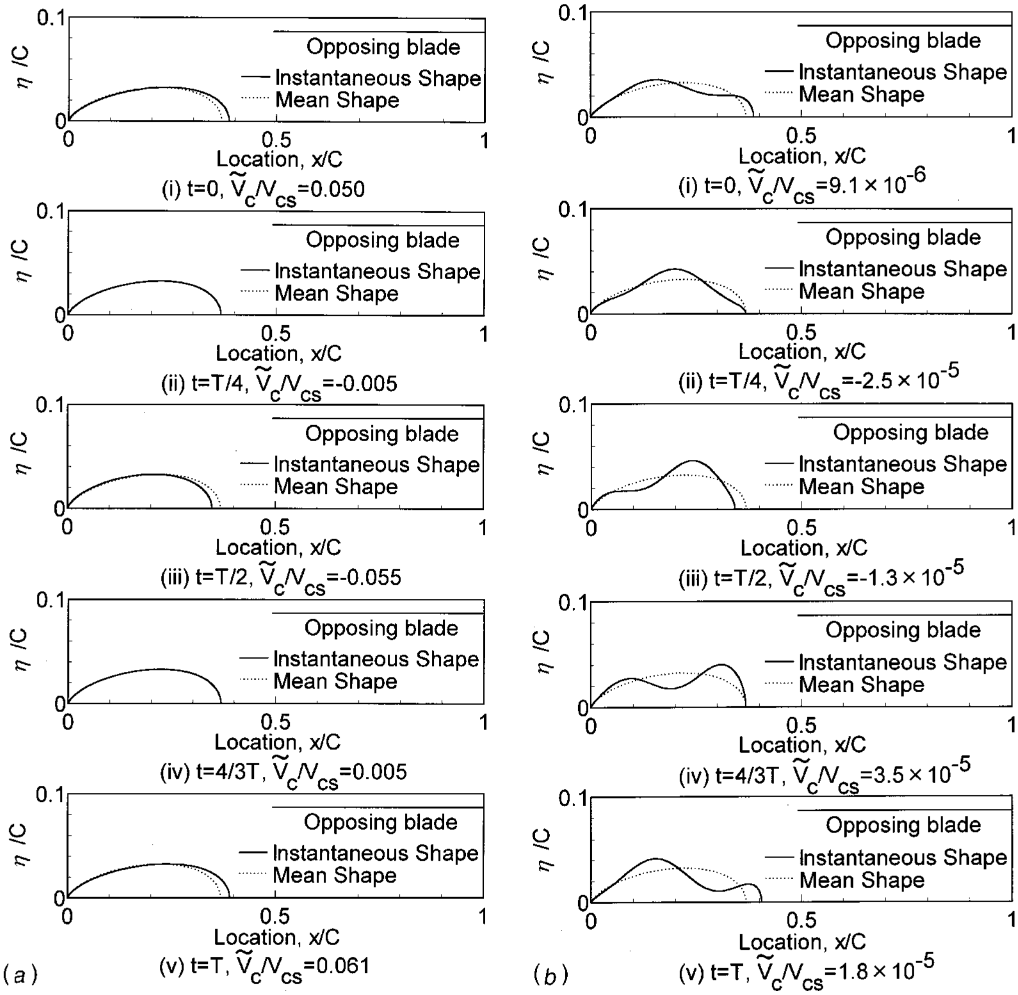

Fig. 9 Unsteady cavity shapes in first and second modes with $\theta_{n,n+1}=0$ deg at $\sigma/2\alpha=2.0$ for $\alpha=4.0$ deg. (*a*) Mode II; (*b*) Mode IX

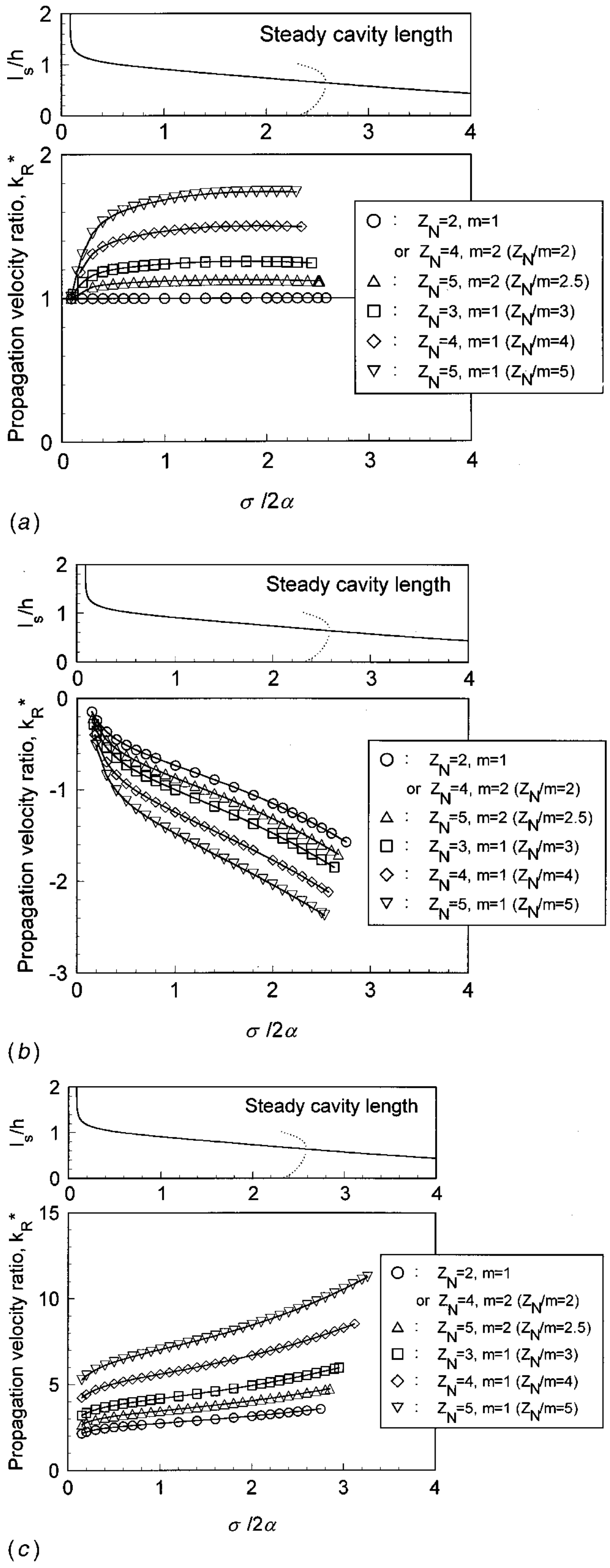

Fig. 10 Destabilizing roots of rotating cavitation. (*a*) First mode; (*b*) second mode; (*c*) third mode

As shown in Figs. 5–10, many various unstable modes appear when the cavity length of equal length cavitation becomes longer than 65% of the pitch. This means that the equal length cavitation with longer cavity is unstable both statically and dynamically. It has been shown in [10] that these instabilities are caused by the interaction of the local flow with small angle of attack near the cavity closure with the leading edge of the opposing blade. We should note here that a term representing the effect of the centrifugal force due to the curvature of the steady cavity surface is not included in the present analysis. This term may affect the higher frequency modes and may cause additional modes related with the surface waves on the cavity.

Conclusions

A systematic study has been made to examine all possible steady cavitation modes for impellers with finite blade count. In this survey only alternate blade cavitation in even number of blades cascades was found in addition to the equal cavity mode: unfortunately, the asymmetric cavitation mode observed in experiments could not be predicted in the present analysis.

Linear stability analyses were then carried out for all the steady cavitation modes. For even number of blades, it was found that the equal cavities are statically unstable in the region where the stable alternate blade cavitation exists. However, the equal cavitation is statistically stable for the case with odd number of blades for which the alternate blade cavitation does not exist. This shows clearly that the blade count affects the stability of steady cavitation modes.

All possible instabilities in impellers with finite blade count were determined by treating each blade independently. No substantially new instabilities were found. This shows that previous methods assuming inter-blade phase difference can be perfect as long as all possible mode is examined.

In the present analysis, the effects of the centrifugal force caused by the curvature of the steady cavity surface is not taken into account. This effect may cause additional cavitation instabilities related to the surface wave on the cavity boundary as well as affecting the higher frequency modes found in the present analysis. The authors would like to study the effect of surface waves on the cavitation instabilities in the near future.

Acknowledgment

This study was partly supported by the Grant-in-Aid for Scientific Research from the Ministry of Education, Science, Sports and Culture. The author would like to thank the reviewers for their valuable suggestions especially to refer to the important work [14].

Nomenclature

A = coefficient matrix, or mean cavity length
B = constant vector, or cavity length deviated from mean cavity length
C = chord length
f = function used in equation of complex velocity
h = pitch
i = imaginary unit in space, $i^2=-1$
j = imaginary unit in time, $j^2=-1$
k = complex propagation velocity ratio in a frame moving with a cascade, $k_R+jk_I=[(\omega/2\pi)Z_Nh]/U_T$
k_R = propagation velocity ratio in a frame moving with a cascade
k_I = decay ratio
k_R^* = propagation velocity ratio in a stationary frame, $1+k_R$ or $1-k_R$
L = distance between the leading edge of blade and the space with constant total pressure, $1000C$
L_d = inlet duct length, $L\cos\beta$
l = cavity length

m = number of cell
N = amplitude of upstream axial velocity fluctuation
N_C, N_B = number of discrete points on coordinate s
n = blade index
p_{-L} = pressure at $\xi = -L$
p_t = total pressure at $\xi = -L$
p_v = vapor pressure
q = strength of source distribution
S = location of discrete point on coordinate s
St = Strouhal number, $(\omega_R/2\pi)/(U/l_{se})$
St_I = decay rate, $(\omega_I/2\pi)/(U/l_{se})$
T = one period of fluctuation
t = time
U = upstream mean velocity
U_T = peripheral velocity (moving speed) of cascade, $U \sin(\alpha+\beta)$
u = flow velocity in x-direction
V_C = cavity volume
v = flow velocity in y-direction
w = complex velocity, $u - iv$
Z_N = number of blade
z = complex coordinate, $x + iy$
α = angle of attack
β = stagger
γ = strength of vortex distribution
η = cavity thickness
δ = residual of closure condition
$\theta_{m,n}$ = phase angle of the fluctuation of cavity length on nth blade relative to mth blade
ξ = distance from the leading edge along blade
ρ = density
σ = cavitation number, $(p_{-Ls} - p_v)/(\frac{1}{2}\rho U^2)$
ω = complex angular frequency, $\omega_R + j\omega_I$
ω_R = angular frequency
ω_I = decay ratio

Superscript

$\tilde{}$ = unsteady component

Subscript

1,2 = index of cavitating and noncavitating region in terms of coordinate s
cr = turning point between the equal length cavitation and alternate blade cavitation
e = equal length cavitation
k = index of discrete point
m, n = blade index
s = steady component
t = trailing free vortex
u = unsteady component

References

[1] Acosta, A. J., 1958, ''An Experimental Study of Cavitating Inducers,'' *Proceedings of the 2nd Symposium on Naval Hydrodynamics*, ONR/ACR-38, pp. 537–557.

[2] Huang, J. D., Aoki, M., and Zhang, J. T., 1998, ''Alternate Blade Cavitation on Inducer,'' JSME Int. J., Ser. B, **41**, No. 1, pp. 1–6.

[3] Young, W. E., 1972, ''Study of Cavitating Inducer Instabilities, Final report,'' NASA-CR-123939.

[4] Kamijo, K., Shimura, T., and Watanabe, M., 1977, ''An Experimental Investigation of Cavitating Inducer Instability,'' ASME Paper 77–Wa/FW-14.

[5] Goirand, B., Mertz, A. L., Joussellin, F., and Rebattet, C., 1992, ''Experimental Investigations of Radial Loads Induced by Partial Cavitation With a Liquid Hydrogen Inducer,'' IMechE, C453/056, pp. 263–269.

[6] Ryan, R. S., Gross, L. A., Mills, D., and Mitchell, P., 1994, ''The Space Shuttle Main Engine Liquid Oxygen Pump High-Synchronous Vibration Issue, the Problem, the Resolution Approach, the Solution,'' AIAA Paper 94-3153.

[7] Tsujimoto, Y., Yoshida, Y., Maekawa, Y., Watanabe, S., and Hashimoto, T., 1997, ''Observations of Oscillating Cavitation of an Inducer,'' ASME J. Fluids Eng., **119**, No. 4, pp. 775–781.

[8] Watanabe, S., Sato, K., Tsujimoto, Y., and Kamijo, K., 1999, ''Analysis of Rotating Cavitation in a Finite Pitch Cascade Using a Closed Cavity Model and Singularity Method,'' ASME J. Fluids Eng., **121**, No. 4, pp. 834–840.

[9] Watanabe, S., Tsujimoto, Y., Franc, J. P., and Michel, J. M., 1998, ''Linear Analysis of Cavitation Instabilities,'' *Proceedings of the 3rd International Symposium on Cavitation*, Vol. 1, pp. 347–352.

[10] Horiguchi, H., Watanabe, S., Tsujimoto, Y., and Aoki, M., 2000, ''A Theoretical Analysis of Alternate Blade Cavitation in Inducers,'' ASME J. Fluids Eng., **122**, No. 1, pp. 156–163.

[11] Horiguchi, H., Watanabe, S., and Tsujimoto, Y., 2000, ''Theoretical Analysis of Cavitation in Inducers with Unequal Blades with Alternate Leading Edge Cut-Back, Part I: Analytical Methods and the Results for Smaller Amount of Cutback,'' ASME J. Fluids Eng., **122**, No. 2, pp. 412–418.

[12] Brennen, C. E., and Acosta, A. J., 1976, ''The Dynamic Transfer Function for a Cavitating Inducer,'' ASME J. Fluids Eng., **98**, No. 2, pp. 182–191.

[13] Tsujimoto, Y., Kamijo, K., and Yoshida, Y., 1993, ''A Theoretical Analysis of Rotating Cavitation in Inducers,'' ASME J. Fluids Eng., **115**, No. 1, pp. 135–141.

[14] Wang, D. P., and Wu, T. Y., 1965, ''General Formulation of a Perturbation Theory for Unsteady Cavity Flows,'' ASME J. Basic Eng., **87**, No. 4, pp. 1006–1010.

[15] Wade, R. B., 1967, ''Linearized Theory of a Partially Cavitating Cascade of Flat Plate Hydrofoils,'' Appl. Sci. Res., **17**, pp. 169–188.

Hong-Hui Shi
Lecturer

Motoyuki Itoh
Professor

Takuya Takami[1]
Graduate Student

Department of Mechanical Engineering,
Nagoya Institute of Technology,
Gokiso-cho, Showa-ku, Nagoya 466-8555
Japan

Optical Observation of the Supercavitation Induced by High-Speed Water Entry

When a high-speed projectile penetrates into water, a cavity is formed behind the projectile. The gas enclosed in the cavity experiences a nonequilibrium process, i.e., the gas pressure decreases as the projectile moves more deeply into water. As a result, the cavity is sealed near the free surface (surface closure) and subsequently the cavity breaks up in water (deep closure). Accompanying the break-up of the cavity, secondary shock waves appear. This is the so-called supercavitation in water entry. This paper describes an experimental investigation into the water entry phenomenon. Projectiles of 342 m/s were generated from a small-bore rifle that was fixed vertically in the experimental facility. The projectiles were fired into a windowed water tank. A shadowgraph optical observation was performed to observe the entry process of the projectile and the formation and collapse of the cavity behind the projectile. A number of interesting observations relating to the motion of the free surface, the splash, the underwater bubbly flow and so on were found. [S0098-2202(00)00204-2]

1 Introduction

The study of water entry of a high-speed blunt solid body and the body's underwater motion has wide applications to industry, natural science, and defense technology. These include the landing of the space vehicle and satellites on the sea surface, the contact of a high-speed ship with a water surface, the formation of the earth geometry due to the impact of meteorites with the sea, the supercavitation around the rotating blades of hydraulic machines, and the flow field around underwater weapons.

Because of the importance of the phenomenon, it has been studied since the beginning of this century (Worthington and Cole [1]). With the long history of research, the water entry problem has been considered as a classic problem in fluid mechanics. Past research activities are mainly focused on three topics characterized by different entry stages. The first topic is the impact force on solid bodies in the initial stage of water entry. The most recent work can be seen from Lin and Shieh [2], and Korobkin [3]. The air cushioning and the compressible behavior of liquid are key factors influencing the impact pressure. The second topic is the fluid dynamics of the supercavitation formed behind the solid body when it has penetrated into water at some distance. The drag coefficient, the scaling relationship, the shape of the cavity, and other characteristics need to be determined. Actually, there have been some results in this area, for example, May [4], Glasheen and McMahan [5], Lee et al. [6]. However, because too many factors are involved in the complicated flow field, the cavity dynamics has not been understood well. A satisfactorily generalized theory to describe this stage of water entry is required. The third topic of past research is the trajectory of the solid body when it has moved more deeply into water. In this stage of water entry, the deep closure of the cavity occurs. The closure causes a jet that is moving along the direction of the penetration of the body. It is possible that the trajectory of the body may be deflected by the impact of the jet on the back of the body. On the other hand, the three-dimensional cavitation and the chaotic turbulent flow around the body may also cause the trajectory deflection (Shi and Takami [7]).

It has been known that in an axisymmetric flow, if the cavitation parameter K is not large, the drag coefficient of an underwater body can be approximated by a linear relationship (Batchelor [8]),

$$C_D(K)=C_D(0)(1+K) \tag{1}$$

$$K=(p_0-p_b)/(0.5\rho V_0^2) \tag{2}$$

where $C_D(0)$ is the drag coefficient without cavitation, p_0 is pressure in the undisturbed liquid at the depth of the nose of the entering body, p_b is cavity pressure, ρ is the liquid density, and V_0 is the velocity of the body. In a high-speed water entry, the cavity pressure p_b is negative and decreases as the penetration depth of the underwater body increases (Abelson [9], Shi and Kume [10]). As the body goes downwards in water, p_0 is increased, while V_0 does not change so much within a limited distance because of high inertia of the body. Thus, the cavitation parameter K increases as water depth increases. Consequently not only the surface sealing but also the deep sealing of the cavity occurs. That was why Knapp et al. [11] used the words *supercavity* and *cavitation* to describe this flow field of water entry.

This paper presents a flow visualization of the supercavitation in water entry. The work belongs to the second research topic of water entry which has been mentioned above. Extensive photography was performed to try to catch the sequence of the complicated cavitation flow. The obtained experimental results can be compared with other experimental data such as pressure measurements and underwater impact tests (Shi and Kume [10], Shi and Takami [7]). They can also serve as a reference for modeling or numerical simulations.

2 Experiment

Figure 1(*a*) illustrates the optical system for flow visualization of the water entry. A projectile was vertically fired downwards from an Anschutz rifle (made in Germany). The projectile has 5.7 mm diameter, 12.3 mm total length, and 2.67 g mass. It is a lead slug with density of 11.4 g/cm^3. In this experiment, the ''pistol match'' slugs with the muzzle velocity of 342±5 m/s made by Dynamit Nobel (Germany) were used. The front curve of the projectile was profiled by using least square method

---

[1] Current address: Space Station Engineering Division, Space Engineering Development Co., Ltd., Issei Build., Takezono 2-3-12, Tsukuba 305-0032, Japan.

Contributed by the Fluids Engineering and presented at the Symposium on Non-invasive Measurements in Multiphase Flows, ASME Fluids Engineering Summer Meeting, Boston, MA, June 11–15, 2000, of THE AMERICAN SOCIETY OF MECHANICAL ENGINEERS. Manuscript received by the Fluids Engineering Division January 28, 2000; revised manuscript received July 10, 2000. Associate Technical Editor: J. Katz.

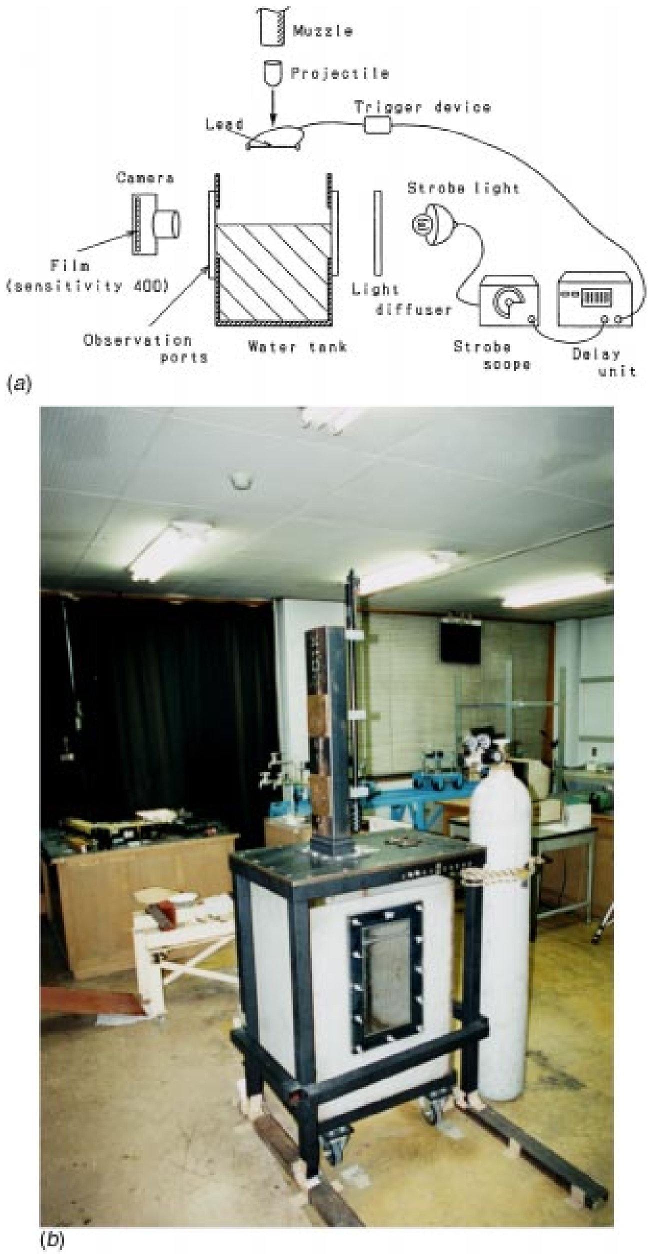

Fig. 1 (*a*) Experimental setup for optical observation of high-speed water entry. (*b*) Photograph of the experimental setup for water entry tests

$$z=0.010r^6+0.010r^4+0.14r^2,$$
$$(0\leqq z\leqq 5.2\text{ mm}) \qquad (3)$$

Here z is the central axis in mm and r is the radius in mm.

The projectile entered a water tank of 60 cm×60 cm×80 cm made from 5 mm thick stainless plates. The water tank was windowed at two sides for optical observation. The impact velocities just before the water entry were measured by cutting two laser beams (Takami [12], Shi and Takami [7]). The measured velocities were calibrated by the method of cutting two thin electric wires (0.2 mm diameter copper wires). Using a strobe light (PS-240 & PL240, Sugahara Research Laboratory, Japan) and an open shutter camera (Nikon), the entry sequences, the underwater projectile motion, the splash and the cavitation were photographed. The height of the camera was adjusted until the free surface was visible on the screen of the camera. The lens of the camera was focused on the impact axis where the projectile was passing along. A light diffuser of 1.5 mm PMMA plate was put in front of the strobe light to get a background of uniform light intensity. The strobe light was triggered by a pulse signal from a 0.5 mm diameter carbon rod when it was broken by the impact of the projectile before entering the water, Fig. 1(*a*). Other details can be seen in the photograph of the experimental facility shown in Fig. 1(*b*).

3 Results

Figure 2 shows the entire process from the beginning of entry at the water surface to the formation of a cavity behind the projectile and finally the collapse of the cavity into bubbles. The first significant phenomenon is that, shortly after the impact of the projectile on the water surface (Fig. 2(*b*)), upward moving jettings and a laterally expanding splash are formed above the surface, and the projectile is suddenly surrounded by the splash. The second significant phenomenon is that, as the projectile penetrates into water, a cavity under the surface is formed (Figs. 2(*c*)–2(*g*)). During this time period, the air from atmosphere comes into the cavity continually. Initially, the air entrainment is due to the gas flow induced by the high-speed projectile. Then the air is entrained into the cavity by the negative pressure of the cavity (Abelson [9]). The reason for the negative pressure is that in a high-speed water entry, the volume of the cavity increases rapidly and the cavity cannot keep its thermodynamic state in equilibrium (Knapp et al. [11]). Later, the airflow into the cavity is ended by the surface closure by the splash (seen from Fig. 2(*g*)) and the enclosed cavity is pulled away from the surface by the downward moving projectile (Fig. 2(*j*)).

The helical streaks seen on the cavity wall (Figs. 2(*e*)–2(*h*)) are evidence that the projectile was rotating as it moved along the firing trajectory. The deep closure of the cavity (May [4]) was not observed in this experiment because of the high velocity of the projectile. As a result, the deep closure of the cavity occurred beyond the windowed area of the tank. In Figs. 2(*j*)–2(*l*), the lower part of the cavity is seen to be expanded. This is thought to be caused by the hitting of the projectile on the bottom of the water tank before the collapse of the cavity. This impact can add an extra pressure in the cavity. When the cavity disappears from the window, the splash which has moved upward above the water surface starts to fall down under the action of gravity (Fig. 2(*p*)). The falling splash forms a re-entry jet composed of air and water. The water surface is disturbed severely by the re-entry jet and some water forms drops spreading on the surface (Figs. 2(*p*)–2(*q*)). Moreover, air is entrained into water by the re-entry jet (Clanet and Lasheras [13]) and finally, smaller bubbles are formed when the jet breaks up (Figs. 2(*r*)–2(*t*)). Afterwards, the bubbles float toward the surface due to buoyancy but some of the bubbles may immediately dissipate in water because their sizes are too tiny. From the pictures of Figs. 2(*p*)–2(*t*), it is known that the flow created by the re-entry of the falling splash is a very complicated air/water two-phase flow.

Figure 3 shows the evolution of the splash shape with time. Once the splash is generated, it experiences three stages. The first stage is the radially fast spreading, which is caused by the high-speed liquid/solid impact on the surface (Shi [14]). This can be seen in Figs. 3(*a*)–3(*b*). The second stage occurs when the fast upward moving splash is atomized into spray, followed by a vertical upward cylindrical splash whose diameter is almost same as that of the cavity. The formation of the cylindrical splash is a result of the inertia of the upward moving spray (Figs. 3(*b*)–3(*c*)). The final stage is the smooth connection between the splash cylinder and the free surface because of the meniscus effect. During this stage, there is a shortage in the flow rate of transportation from the free surface to the cylindrical splash, since the water near the free surface has a larger mass and a lower speed due to the effect of surface tension. Therefore, the cross-section in the middle of the hollow cylinder begins to contract and to form a throat as in a Laval nozzle (Figs. 3(*c*)–3(*f*)).

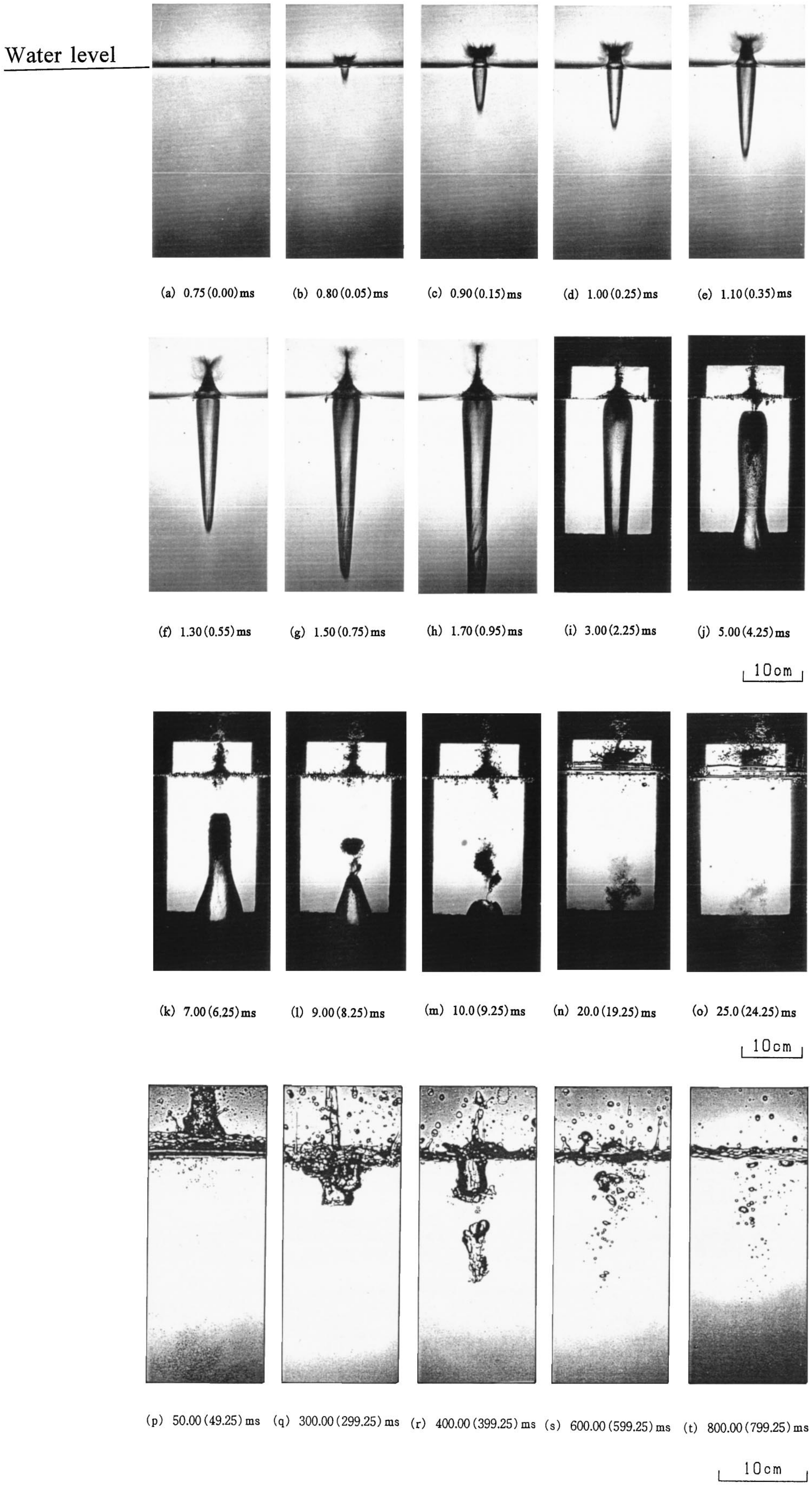

(a) 0.75(0.00)ms (b) 0.80(0.05)ms (c) 0.90(0.15)ms (d) 1.00(0.25)ms (e) 1.10(0.35)ms

(f) 1.30(0.55)ms (g) 1.50(0.75)ms (h) 1.70(0.95)ms (i) 3.00(2.25)ms (j) 5.00(4.25)ms

(k) 7.00(6.25)ms (l) 9.00(8.25)ms (m) 10.0(9.25)ms (n) 20.0(19.25)ms (o) 25.0(24.25)ms

(p) 50.00(49.25)ms (q) 300.00(299.25)ms (r) 400.00(399.25)ms (s) 600.00(599.25)ms (t) 800.00(799.25)ms

Fig. 2 Time history of phenomena accompanying water entry. The frames show production of splash, cavity, surface closure, and disappearance of cavity.

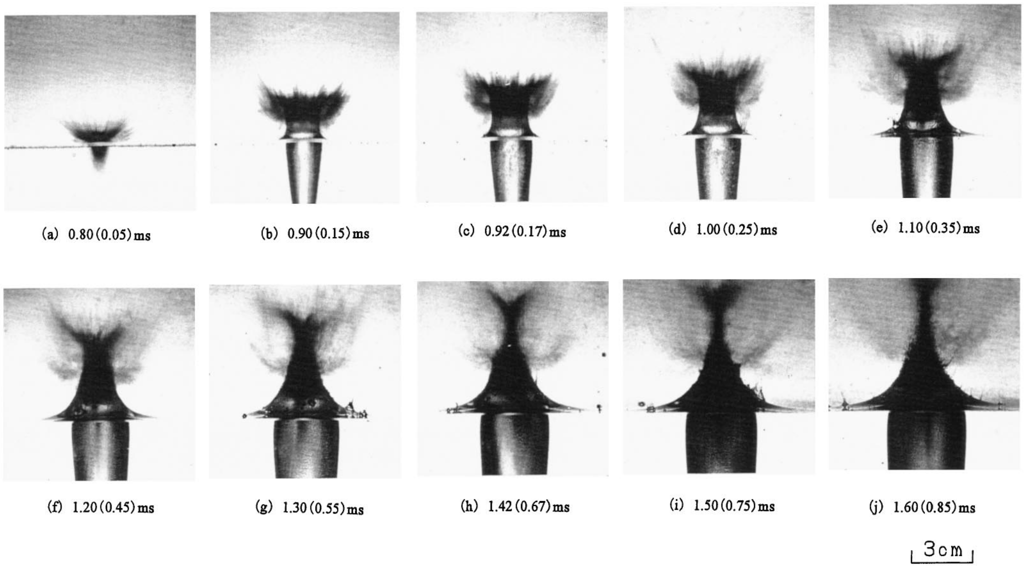
(a) 0.80 (0.05) ms (b) 0.90 (0.15) ms (c) 0.92 (0.17) ms (d) 1.00 (0.25) ms (e) 1.10 (0.35) ms

(f) 1.20 (0.45) ms (g) 1.30 (0.55) ms (h) 1.42 (0.67) ms (i) 1.50 (0.75) ms (j) 1.60 (0.85) ms

Fig. 3 Motion of splash. Upper splash changes upward jets and other splash domes over to cause surface seal of cavity.

During the period seen in Fig. 3(*c*) to Fig. 3(*f*), the air is still flowing into the cavity. However, the air flow will be stopped when the throat cross-sectional area of the splash cylinder becomes zero. This change in the throat area has been shown in Figs. 3(*g*)–3(*i*). The mechanism of this process is that the interior pressure at the throat is lower than atmosphere, so the pressure difference between the inside and the outside of the hollow cylinder creates the contraction of the throat area. Then a dome-like closure of the splash occurs, which is the so-called surface closure. Accompanying the surface closure, an up-jet moving upward and a down-jet moving downward are simultaneously generated from the dome's top (see also May [4]). In Fig. 3(*j*), a thin down-

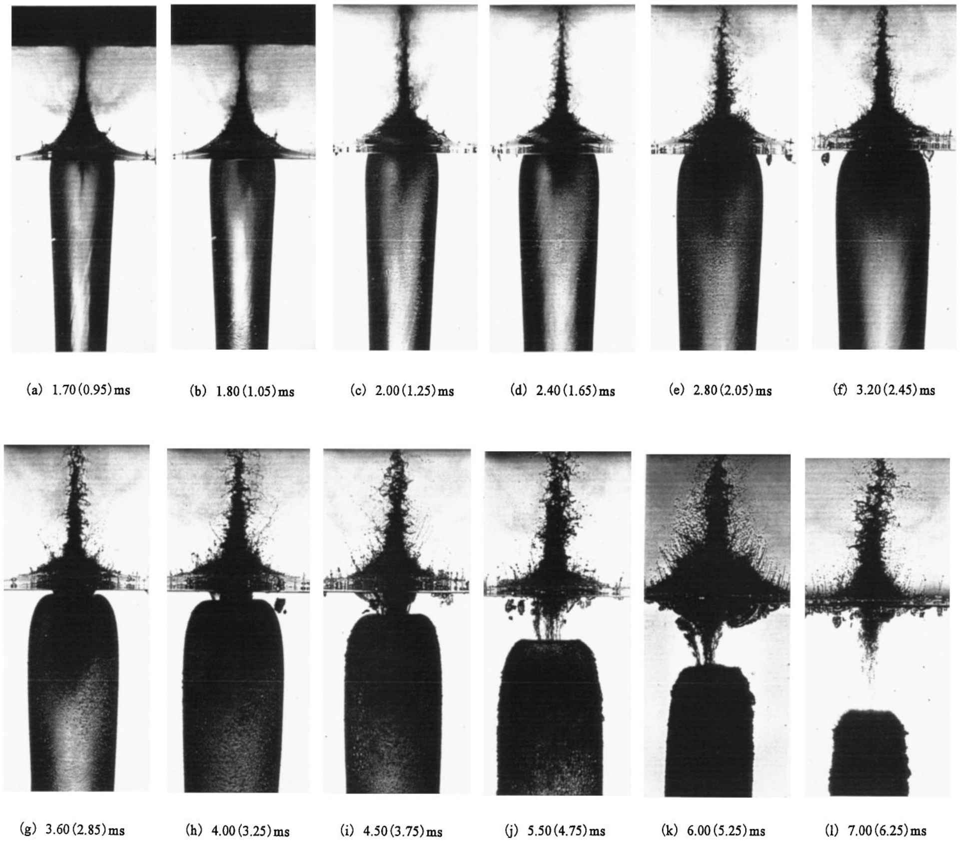
(a) 1.70 (0.95) ms (b) 1.80 (1.05) ms (c) 2.00 (1.25) ms (d) 2.40 (1.65) ms (e) 2.80 (2.05) ms (f) 3.20 (2.45) ms

(g) 3.60 (2.85) ms (h) 4.00 (3.25) ms (i) 4.50 (3.75) ms (j) 5.50 (4.75) ms (k) 6.00 (5.25) ms (l) 7.00 (6.25) ms

Fig. 4 Motion of cavity. Cavity pulled away from the water surface and then the flat cavity top is characteristic of cavity development.

jet is visible in the cavity. The thicker up-jet shown in Fig. 3(*j*) was found to reach 400 mm above the surface.

The evolution of the cavity with time has been shown in Fig. 4. There are two distinguishable processes: one is that the cavity diameter changes; another is that the cavity is pulled away from the free surface. The cavity diameter increases about 1.5 times from Fig. 4(*a*)–Fig. 4(*f*). The maximum diameter of the cavity can be measured as ~50 mm, which is about 9 times the diameter of the projectile. However, although the increase of the cavity diameter is significant, it is much slower than the increase of the cavity length. The down-jet is relatively thin in the cavity at the beginning (Fig. 4(*a*)) but it becomes thicker in the cavity as the cavity diameter increases. After the down-jet impacts the cavity wall, many hollows appear on the wall. In fact, the hollows may be droplets because the tip of the down-jet is thin and composed of spray. It is believed that the impact between the down-jet and the cavity wall does not make a contribution to the increase of the cavity diameter.

Before the cavity is pulled away from the free surface by the underwater projectile, as shown in Fig. 4(*e*), the cavity has started to collapse. This convergence is driven by the pressure difference between the vapor pressure of the cavity and the pressure of the surrounding water. The gravity of the dome-like splash on the surface also exerts a static pressure on the cavity. Furthermore, the vapor pressure of the cavity continues to fall after the surface closure occurs because the volume of the cavity is still increasing. Meanwhile, the down jet becomes larger, which causes the bottom of the cavity to contract in order to supply water into the jet. One of the results is that the upper part of the cavity becomes more and more opaque (Figs. 4(*e*)–4(*h*)). The other result is that the cavity is completely separated from the free surface and pulled farther into the water by the downward momentum induced by the projectile (Figs. 4(*i*)–4(*l*)). This separation not only disturbs the free surface (see the increased areas which are occupied by the splash above the free surface and the bubbles under the free surface shown in Fig. 4(*k*)), but also causes instability of the cavity (see the wave-like shape of the cavity shown in Figs. 4(*j*)–4(*l*)). The measurement of the underwater acoustic field has confirmed that the separation of the cavity from the free surface generates secondary shock waves (Shi and Kume [10]). It is believed that the convergence of the bottom of the cavity produces strong vortex rings and the surrounding water is entrained inward to the cavity by the vortex rings. During the separation, the surrounding water particles collide with each other so that shock waves are generated.

4 Conclusions

In the present experiment, the entry velocity of the projectile is within a range of a few m/s ~tens m/s in the experiments conducted by May [4], Gilbarg and Anderson [15] and the experiment of ~1 km/s water entry conducted by McMillen [16]. The cavity, splash, up-jet and down-jet observed in the present experiment are basically identical to those done by the previous researchers. However, the use of a near field camera, the intense illumination by the strobe light, and the patient photographic work have provided some new information on the details of the process in water entry. The expansion of the lower part of the cavity, the gravity re-entry of the splash after the projectile is far away from the surface, the wide expansion of the down-jet in the cavity, the severe vibration of the cavity wall and the free surface during the pull-away of the cavity are newly documented by the authors.

The slender shape of the cavity is attributed to the high velocity of the water entry, but it is not like the conical shaped cavity produced by a ~1 km/s entry projectile (McMillen [16]). However, the speed of the surface closure is comparable to the stretching speed of the cavity length which has been shown in the experiment. Therefore, the back end of the cavity and the front of the cavity are all curved. It must be remembered that the projectile used in this experiment is not either a sphere or a disc, it has a parabolic front and a cylindrical back section. This geometry of the projectile will bring about a rather different shape of the splash. The radially spreading splash shown in Figs. 3(*a*)–3(*b*) is generated during the contact of the curved front of the projectile with the water surface since the spray occurs in the gap between the liquid and the concave solid (Batchelor [8]). This has been understood well. However, the formation of the vertical hollow splash cylinder shown in Figs. 3(*b*)–3(*c*) depends on the shape of back section of the projectile. In the experiment of Bivin et al. [17], it was shown that the splash of a sphere was different from the splash of a disk. Naturally, it is emphasized that the flow field in the water entry of this experiment combines the characteristics in the water entries of a sphere and a disk. The supercavitation process is more complicated than originally thought. The optical visualization method described in this paper better shows the complexity caused by the various factors.

Acknowledgments

Funding for this work has been provided by the Japan Society for the Promotion of Science, under a Grant-in-Aid for Scientific Research (C) (grant no. 12650162). Misters T. Sakakura, M. Kume, H. Sobue, and S. Hashimoto are thanked for their assistance in the experiment. The referees are thanked for their comments on the manuscript of this paper.

References

[1] Worthington, A. M., and Cole, R. S., 1900, Phil. Trans. Roy. Soc. (London), **194A**, pp. 175–199.

[2] Lin, M.-C., and Shieh, L.-D., 1997, ''Simultaneous Measurements of Water Impact on a Two-Dimensional Body,'' Fluid Dyn. Res., **19**, pp. 125–148.

[3] Korobkin, A., 1998, ''Elastic Response of Catamaran Wetdeck to Liquid Impact,'' Ocean Eng., **25**, pp. 687–714.

[4] May, A., 1952, ''Vertical Entry of Missiles into Water,'' J. Appl. Phys., **23**, pp. 1362–1372.

[5] Glasheen, J. W., and McMahon, T. A., 1996, ''Vertical Water Entry of Disks at Low Froude Numbers,'' Phys. Fluids, **8**, pp. 2078–2083.

[6] Lee, M., Longoria, R. G., and Wilson, D. E., 1997, ''Cavity Dynamics in High-Speed Water Entry,'' Phys. Fluids, **9**, pp. 540–550.

[7] Shi, H. H., and Takami, T., 2000, ''Hydrodynamic Behavior of an Underwater Moving Body after Water Entry,'' Acta Mech. Sin., **16**, No. 3, Sept.

[8] Batchelor, G. K., 1967, *An Introduction to Fluid Dynamics*, Cambridge University Press, U.K.

[9] Abelson, H. I., 1970, ''Pressure Measurements in Water-Entry Cavity,'' J. Fluid Mech., **44**, pp. 129–144.

[10] Shi, H. H., and Kume, M., 2000, ''An Experimental Research on the Flow Field of Water Entry by Pressure Measurements,'' Phys. Fluids, in review, Sept.

[11] Knapp, R. T., Daily, J. W., and Hammitt, F. G., 1970, *Cavitation*, McGraw-Hill, New York.

[12] Takami, T., 1999, ''Study on Water Entry of High Speed Blunt Body,'' Masters thesis, Nagoya Institute of Technology, Japan, Feb.

[13] Clanet, C., and Lasheras, J. C., 1997, ''Depth of Penetration of Bubbles Entrained by a Plunging Water Jet,'' Phys. Fluids, **9**, pp. 1864–1866.

[14] Shi, H. H., 1997, ''Fast Water Entry of Blunt Solid Projectile,'' *Proc. 74th JSME Spring Annual Meeting*, Tokyo, Vol. VI, pp. 1–4.

[15] Gilbarg, D., and Anderson, R. A., 1948, ''Influence of Atmosphere Pressure on the Phenomena Accompanying the Entry of Sphere into Water,'' J. Appl. Phys., **19**, pp. 127–139.

[16] McMillen, J. H., 1945, ''Shock Wave Pressures in Water Produced by Impact of Small Spheres,'' Phys. Rev., **68**, pp. 198–209.

[17] Bivin, K. Yu., Glukhov, M. Yu., and Permyakov, V. Yu., 1985, ''Vertical Entry of Solid into Water,'' Izv. Akad. Nauk SSSR, Mekh. Zhidk. Gaza, No. 6, Nov.–Dec., pp. 3–9.

PIV Technique for the Simultaneous Measurement of Dilute Two-Phase Flows

K. T. Kiger
e-mail: kkiger@eng.umd.edu

C. Pan

Department of Mechanical Engineering,
University of Maryland,
College Park, MD 20742

A Particle Image Velocimetry (PIV) image processing technique has been developed which can be applied to solid-liquid two-phase turbulent flows. The main principle of the technique is to utilize a two-dimensional median filter to generate separate images of the two phases, thus eliminating the errors induced by the distinct motion of the dispersed component. The accuracy and validity of the technique have been studied in the present research for different filter widths, f, and for 4 groups of different sized dispersed particles ranging from an effective image diameter of $d_p = 2.9$ pixels to 13 pixels in combination with tracer particles with an effective image size of $d_t \sim 2.4$ pixels. The results have shown that the errors introduced by the filter are negligible, and mainly arise in regions of large velocity gradients that are sensitive to the slight loss of information incurred by the processing. The filter width f also affects the algorithm's ability to correctly separate and identify the dispersed phase particles from the two-phase images, with the main result that above a critical particle image size ratio, $d_p/d_t \approx 3.0$, the particle size had no significant influence on the number of particles identified, or the accuracy of the displacement calculation. Sample results of particle-fluid interaction and cross-correlation terms which can be obtained from the method are also presented. [S0098-2202(00)01104-4]

1 Introduction

Particle-laden turbulent flows cover a wide range of applications from pollution control and sediment transport, to combustion processes and erosion effects in gas turbines. In the last two decades, many improvements have been made in measurement technology to advance the knowledge of physical mechanisms and dynamics of such flows. The most commonly used measurement techniques, such as Laser Doppler Anemometry and Phase Doppler Anemometry, are single point measurements which provide useful statistical information of fluid velocity, particle velocity, particle size, and concentration. One limitation of single-point measurements, however, is the difficulty associated with interpreting the data into meaningful physical mechanisms which control the dynamics between the phases. Thus to reach a good understanding of multi-phase flows, the microscale spatial information of the inter-phase dynamics and its structure relative to the carrier fluid is essential.

In contrast to single point measurements, PIV represents an instantaneous whole field technique which makes it possible to detect spatial flow structure and provide a direct indication of the inter-phase coupling. One of the critical requirements of PIV measurement is to calculate the displacement of tracer particles by means of cross-correlation or auto-correlation performed within an interrogation volume. For multi-phase flows, however, the presence of the discrete particles will affect the PIV evaluation. Figure 1(*a*) shows a sample two-phase image of a particle-laden channel flow seeded with hollow, silver-coated, glass beads as PIV tracer particles (diameter≈15 μm), and transparent glass beads as discrete particles (diameter≈330 μm). The velocity field computed by standard PIV techniques without any specialized treatment is illustrated in Fig. 1(*b*). Erroneous vectors occur in the vicinity of the discrete particles, due to the fact that there are significant differences between the motion of the dispersed phase and the carrier fluid. In order to utilize PIV in the measurement of multi-phase flows, standard PIV processing techniques need to be modified to eliminate the interference effects caused by the disparate motions of each phase.

In surveying recent literature, several examples can be found where PIV has been applied to the simultaneous measurement of both phases using four different fundamental techniques: 1) fluorescence tagging, 2) amplitude discrimination, 3) phase dynamics, and 4) geometrical characteristics.

Fluorescent particle tagging has been extensively used for the study of bubbly flows, and is perhaps one of the most mature of phase separations techniques. Examples of this method can be found in the work of Hassan et al. [1], Sridhar and Katz [2], and Fujiwara [3], and commercial systems are even available (Dantec [4]). With this method, one phase is composed of particles which have a fluorescent dye that can be excited by the illumination source. Two cameras are then used, one which records light directly scattered by both phases, the other which only records fluorescent images. One drawback to this method is that it requires the use of two synchronized cameras and a powerful laser to produce adequate intensity fluorescent images.

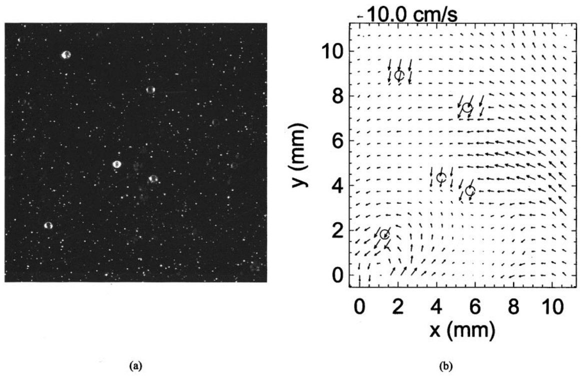

Fig. 1 (*a*) Sample two-phase image. (*b*) Corresponding displacement vector field of carrier phase using standard PIV. Circles represent locations of dispersed phase particles.

Contributed by the Fluids Engineering Division for publication in the JOURNAL OF FLUIDS ENGINEERING. Manuscript received by the Fluids Engineering Division May 23, 2000; revised manuscript received July 26, 2000. Associate Technical Editor: J. Lasheras.

Amplitude discrimination techniques rely on a strong difference in the scattering amplitude between the continuous and carrier phase particles to perform the phase separation (Paris and Eaton [5]; Anderson and Longmire [6]). This requires that the maximum scattering cross-section of the seed for the carrier phase and the smallest of the dispersed phase particles are different by more than an order of magnitude to prevent significant cross-talk between the phases. Even with properly selected seeding particles, this method requires careful tuning and patience to optimize the imaging to eliminate the interference between the phases.

A more recent method developed by Delnoij et al. [7] relies on the inherent differences in the motion of the two phases to discriminate between them. The separation is performed in correlation space by identifying the two dominant correlation peaks, one which represents the motion of the tracers while the other provides the displacement of the dispersed phase. This technique promises to be useful for high concentration flows of very fine particles and can even provide carrier phase turbulence statistics; but, because the method is based upon the bulk average motion of the dispersed phase, the details of the interaction terms may not always be clear.

The last class of methods rely on the geometrical properties of the particles to separate the phases. For example, Sato et al. [8] used two CCD cameras with optical filters combined with multi-volume illumination to accurately detect discrete phase particulates relative to tracer particles in a water channel flow. However, due to the correlation influence between the phases, no carrier phase vectors could be detected in the vicinity of the discrete particles. Gui et al. [9] used a particle mask function to eliminate the cross-talk between the phases from influencing the correlation calculations. The mask was formed based upon a threshold calculation of the particle's cross-sectional area, and hence a significant difference between the size of the partices is required for good separation.

The technique for the current study is also based on geometrical properties of the dispersed and tracer particles. The motivation for the present study is to provide a reliable, single-camera technique that can resolve the local particle/fluid interaction within the flow, and to quantify the performance of the separation process as a function of the particle size and image resolution. To accomplish this goal, an image processing technique has been developed to eliminate the dispersed phase influence in the displacement calculation through the use of a two-dimensional median filter. The following section describe the details of the technique, the test procedure used to evaluate the filter performance, and summarizes the type of correlated particle/fluid turbulence statistics that can be obtained.

2 Experimental Setup

The experimental test cases for the technique all examine heavy particle sedimentation in the turbulent wake of a cylinder. A vertical, recirculating water channel (Fig. 2) with a 100 mm by 100 mm square cross-section and a maximum velocity of 100 mm/s is used to conduct the tests. The images are acquired 25 mm downstream of a 12 mm diameter cylinder, at a Reynolds number of 840 based on the cylinder diameter. The test section is illuminated by a high speed pulsed Nd:YAG laser ($\lambda=532$ nm) with a pulse intensity of 15 mJ focused to a sheet of width $\delta z \sim 0.8\,\text{mm}$. The image area is approximately 27 mm×27 mm, and recorded using a Kodak Megaplus ES1.0 camera (1008×1018 pixel array; 9 μm pixel spacing) with a 200 mm focal length lens ($f^{\#}=8$) and a time separation of 3 ms between image pairs. Hollow silver-coated glass spheres with an average diameter of 15 μm, and a specific gravity around 1.5 are seeded as PIV tracer particles in the flow. All tracer displacements are calculated using a 40×40 pixel interrogation window, which is found to be the minimum size for reliable processing at the current seeding concentration levels. This was determined empirically by processing the images with correlation window sizes ranging from 24×24 pixels to 128×128 pixels and selecting the minimum window size that produced no obvious spurious vectors. When examining the particle seeding density statistics, the 40×40 pixel correlation window resulted in an average of 38 particles per subimage, with less than 0.5 percent of the correlation regions containing less than 8 particles per window. This provides a comfortable margin with respect to the the optimal number of particles sufficient to obtain a good correlation, even when accounting for in-plane loss-of-pairs due to velocity gradients and out-of-plane loss-of-pairs due to motion perpendicular to the light sheet (Keane and Adrian [10]).

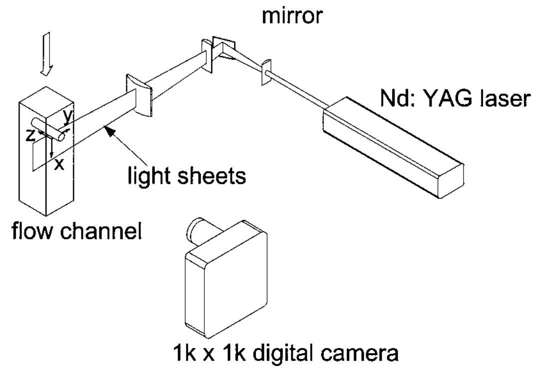

Fig. 2 Sketch of the experimental setup

Four groups of different size transparent glass spheres with diameters ranging from 45 μm to 360 μm and a specific gravity of 2.5 are used as dispersed phase particles. The particles were obtained by running nominally spherical industrial glass beads through a mechanical shaker sieve system, using standard stainless steel mesh sieves. Although this method is not as reliable as inertial classification, the tolerance is sufficient to generate distinct size classes of particles. The geometrical properties of the particles based on the mean sieved sizes and optical configuration, as well as the empirically observed values, are listed in Table 1. Owing to the optical configuration, the minimum particle image size, d_e, is constrained by the point spread function of the system, d_s, as given by Adrian [11]

$$d_e=\sqrt{M^2D_p^2+d_s^2} \tag{1}$$

$$d_s=2.44(1+M)f^{\#}\lambda, \tag{2}$$

where M is the magnification and D_p is the actual particle diameter (here assumed to be the mean of the sieve sizes). In general, the observed size is systematically larger than what was measured on the images, which is likely due to a combination of uncertainty in the actual size of the particles (i.e., accuracy of the sieve procedure), noise in the image digitization process, and slight aberrations in the lens system. Since the filtering procedure operates on the digitized image size, the effective particle diameters recorded by the system are the important parameter to consider, and used consistently throughout the current work.

Table 1 Properties of particles used in the present study. The theoretical image diameter is calculated using the average sieve diameter and Eqs. (1) and (2).

Particle type	Sieve Diameter, $D_p(\mu m)$	Theoretical image diameter, d_e (pixels)	Measured image diameter, d_p (pixels)	d_p/d_{p0} (measured)
PIV tracer, $d_{p0}=d_t$	15	1.6	2.4	1
discrete, d_{p1}	45–53	2.4	3.4	1.4
discrete, d_{p2}	90–106	3.9	6.5	2.7
discrete, d_{p3}	180-212	7.4	8.5	3.5
discrete, d_{p4}	300-360	12.3	13	5.4

3 The Principle of Phase Separation

To eliminate the effect of two coexistent phases, a two-dimensional median filter is employed to separate the larger dispersed phase particle image from the carrier phase tracer particle image. A median filter is a nonlinear signal processing technique that has been found effective in reducing random noise and periodic interference patterns without severely degrading the signal (Huang [12]). In PIV image processing, the property of preserving sharp edges makes the filter useful because it allows more information about the original image to be maintained. This is especially important in regions of high shear, where the ratio of signal to noise is relatively low. For a two-phase image with both small tracer particles and big discrete particles, the small tracer particles can be regarded as noise scattered over a uniform background.

To remove the small tracer particles, a median filter is performed by convolving a rectangular two-dimensional filter stencil *A*, of width $N_f \times M_f$ pixels, over all the pixels within the image. For the case of a square stencil, the filter width, *f*, is taken to be the width of the window, N_f. For each position (i_o, j_o) of the window *A*, the filter sorts the gray level values of region *A* into ascending order and then selects the median value to replace pixel (i_o, j_o). This is stated mathematically by Eq. (3):

$$X_{i,j}^1 < \ldots < X_{i,j}^k \ldots < X_{i,j}^{N_f^2} \quad (i,j) \in A$$
$$Y_{i_o,j_o} = X_{i,j}^k \tag{3}$$

where Y_{i_o,j_o} is the filtered value, $X_{i,j}$ is an element of the input stencil image, and the superscript *k* represents the median value of the region. This implies that the effect of the median filter is to reduce the variance, and increase the ratio of signal to noise in the image. The median value computed at one window position is independent of the value computed at another window position.

For typical PIV images, the tracer particles usually occupy a region of only several pixels. The gray level values within any given stencil will therefore be dominated by the image background. Only a small portion of pixels (at the location of the tracer particles) in the window will have a large intensity, and hence will be sorted to an extreme rank position and removed. When the filter window is convolved with a region containing a larger discrete particle, the image intensity sampled by a small stencil will be dominated by the pattern of the discrete particle, which will result in a median value that is relatively unchanged from the original. Thus after filtering, the small tracer particles are removed, leaving only the discrete particles. The filter width is a critical parameter to determine whether the two phases are separated properly.

With regard to computational expense, the heart of a median filter will be composed of a sorting routine to organize the elements into ascending rank order. The generic versions of sort routines typical scale as $N \ln N$ (Press et al. [13]), where *N* is the number of elements to be sorted. With the standard median filter routine available in data processing packages, specially optimized routines may be used. The data reported within the current work was processed using Interactive Data Language (IDL), which is an interpreted matrix operation code. Tests were run in which a square 3, 5, 7, and 9 pixel median filter was convolved with a 1008×1018 pixel image, requiring approximately 0.37, 0.49, 0.62, and 0.77 seconds on a conventional desktop system. These results scale better than the standard sorting algorithm, and represents a relatively inconsequential difference in computational time in comparison to the PIV calculations.

3.1 Evaluation of the Discrete Particles. After filtering, only discrete particles remain on the image, and their motion is calculated using a correlation tracking algorithm similar to the Particle Mask Correlation (PMC) method described by Takehara and Etoh [14] and Takehara et al. [15] as shown in Fig. 3. First, a reference particle is selected as a template and convoluted with the whole image to identify discrete particles (Fig. 3(*b*)). This differs from the PMC method in that an actual representative particle image is used, instead of a modeled function, due to the more complex image map required to obtain a good correlation. The reference particle is selected such that it is distinct, well-formed, and nonoverlapping with other dispersed-phase particles. Since the discrete particles have a form similar to the reference particle, the peaks in the convolution correspond to center locations of the individual dispersed particles. A peak-finding algorithm is then used to identify discrete particles, and a cross-correlation tracking method is performed to calculate the displacements between the discrete particle image pairs (see Fig. 3(*c*)).

A sensitivity analysis was performed to determine the effect of particle selection on the resulting displacement vectors, and it was found that the magnitudes typically varied from 0.013 to 0.05 pixels depending on the particle size and the filter width used. Although the above method will tend to discriminate against particles only partially illuminated by the sheet, this effect will be compensated by the increased volume of detection due to their larger scattering cross-section.

3.2 Evaluation of the Tracer Particles. The motion of the carrier phase is determined using an extraction technique which obtains a single-phase image of tracer particles, $S_{i,j}$, from the original two-phase image, $T_{i,j}$, by subtraction:

$$S_{i,j} = T_{i,j} - median(T_{i,j}, f) \quad (i,j) \in Z^2 \tag{4}$$

where *median* $(T_{i,j})$ is the two-dimensional median filtered output (of filter width *f*) of the original image, and *Z* is the domain of the image. The velocity field of the carrier phase is calculated through a standard cross-correlation method applied to the tracer particle images.

4 Validation of the Technique

The median filter width will affect the information of both phases extracted from a two-phase image. In turn, this may influence the accurate calculation of the displacement through residual ''artifacts'' left by the image separation process. Figure 4 illustrates how the information content within a carrier phase image changes with the filter width. For small filter width, the discrete particle is completely removed, whereas for increasing filter width, a residual image around the periphery of the discrete particle remains. This results from an erosion of the particle by the larger filter, and hence an incomplete removal when it is subtracted from the original image. These slight changes may induce errors in the displacement calculation of both phases. The goal of the present work is to quantify these effects and assess the optimal filter parameters to ensure accurate calculations.

In order to achieve these goals, the phase separation technique has been tested by using a series of artificial two-phase images for each size class composed of two separate single phase images; one which contains only PIV tracer particles, the other which contains only discrete particles. The images were selected from 72 independent image pairs for all size classes (1 tracer and 4 dispersed phase), which were randomly combined to produce 72 pairs of artificial two-phase images for each of the 4 dispersed phase sizes. The results of the composition process are illustrated in Fig. 5, which is obtained from equation:

$$T_{i,j} = W - (W - S_{i,j}) \times \left(1 - \frac{P_{i,j} - N_{\text{noise}}}{\max[P_{i,j} - N_{\text{noise}}]}\right), \tag{5}$$

where *W* is the white-field intensity of the image ($W = 2^8 = 255$ for an 8-bit image), N_{noise} is the average background noise of the dispersed phase, and $P_{i,j}$ is the image of the dispersed phase particles. Equation (5) adds the two images such that the tracer images are reduced in magnitude in the vicinity of the dispersed phase to prevent a bias in favor of the tracer displacements, and to ensure similarity of the image characteristics between the real and artificial two-phase images. The velocity field of the carrier phase is then calculated in two ways: 1) by applying standard PIV tech-

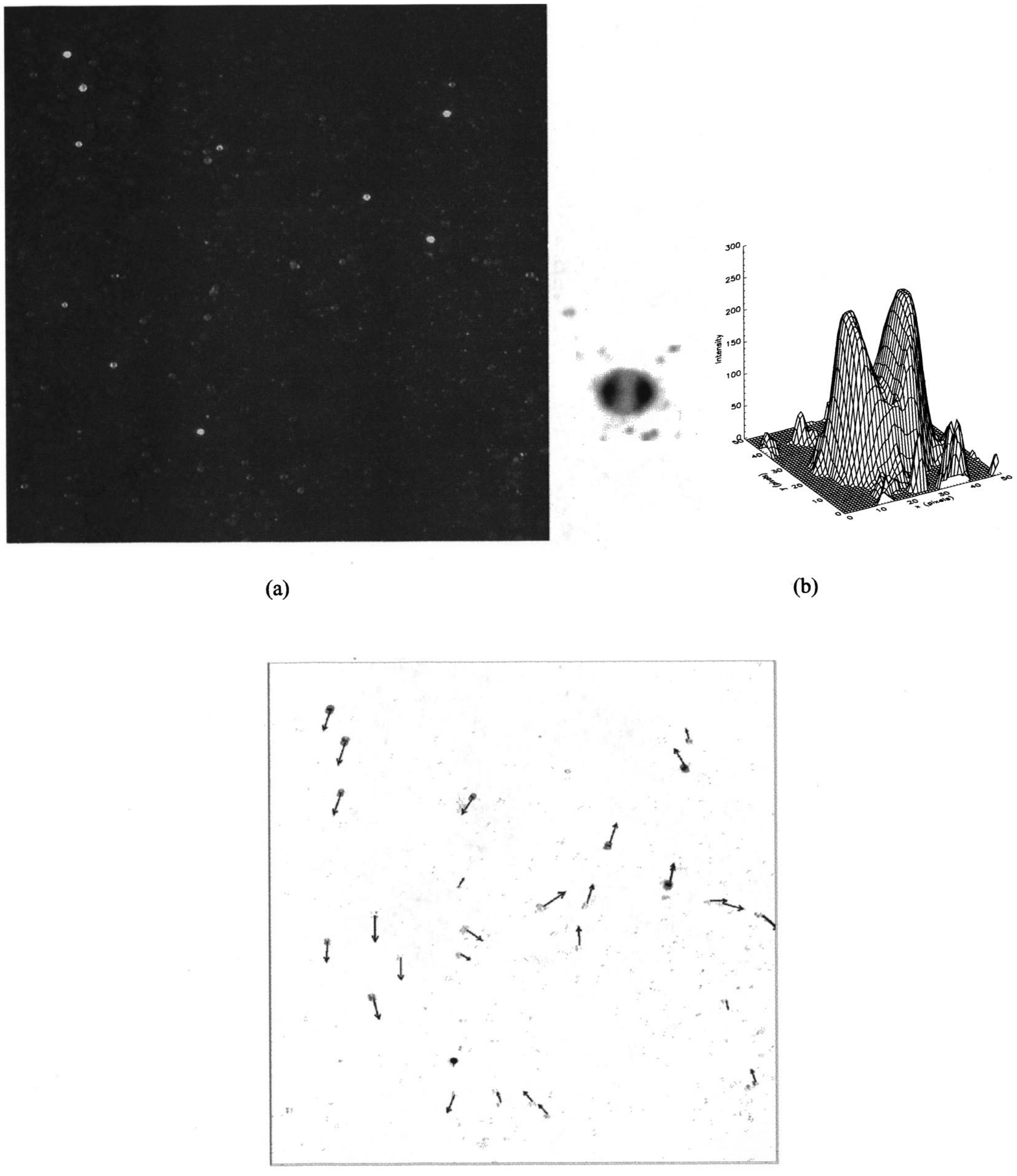

(a) (b)

(c)

Fig. 3 (*a*) Dispersed phase (filtered) image. (*b*) Enlarged image and image intensity surface plot of the dispersed phase reference particle. (*c*) The corresponding vector displacement field for the dispersed phase.

nique to the original single phase image, and 2) by applying the separation technique to the artificial two-phase image and recalculating the tracer particle displacements (see Fig. 6). The errors induced by the median filter are investigated by computing the absolute variance between the two displacement fields in the direction of streamwise and spanwise coordinates of the fluid motion. Filter widths of 3, 5, and 7 pixels are tested for 4 different groups of discrete particle size. The average error is then calculated using

$$x_{err}=\frac{1}{MN}\sum_{i=1}^{i=N}\sum_{j=1}^{j=M}|\Delta x_{(i,j),\Delta_f}-\Delta x_{(i,j),o}| \tag{6}$$

$$y_{err}=\frac{1}{MN}\sum_{i=1}^{i=N}\sum_{j=1}^{j=M}|\Delta y_{(i,j),\Delta_f}-\Delta y_{(i,j),o}| \tag{7}$$

$$s_{err}=\sqrt{x_{err}^2+y_{err}^2} \tag{8}$$

where $M\times N$ is the number of carrier fluid vectors in each image, and the subscripts o and Δf represents the original displacement field and the displacements obtained after separation, respectively. The total error is then calculated for 72 independent image pairs for each case. This represents 152,400 velocity measurements for the carrier fluid and approximately 2300 to 3,900 measurements for the particles depending on their size. The results are shown in Figs. 7–11. A spurious vector filtering algorithm based on the local median test of the normalized residual displacement (Westerweel [16]) is applied to the tracer vector field prior to the error calculation. The threshold parameters for bad vector detection are set large enough such that only obviously bad vectors are removed from the displacement field. This was done to remove the influence of the detectable errors from those that cannot be discrimi-

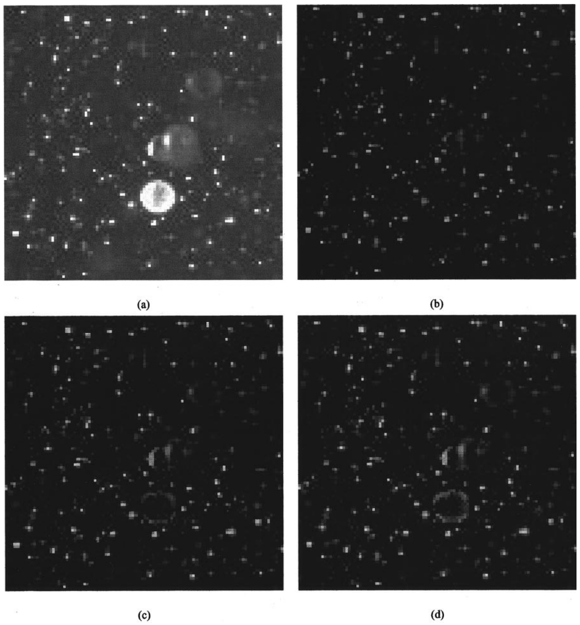

Fig. 4 (*a*) **Original two-phase image.** (*b*) **Carrier phase image obtained with the filter width** $f/d_t=1.3$. (*c*) **Carrier phase image obtained with the filter width** $f/d_t=2.1$. (*d*) **Carrier phase image obtained with the filter width** $f/d_t=2.9$. $d_p=13$ **pixels,** $d_t=2.4$ **pixels.**

nated by standard statistical methods. The quality of the images was sufficient such that typically less than 0.02 percent of the calculated vectors were eliminated by the detection routine.

As a final comment, it should be noted that the error reported for these experiments gives the relative contribution due to the median filter, and not the total error inclusive of the inherent uncertainties associated with standard PIV algorithms. The results are thus independent of the PIV procedure used, as the same algorithms are applied to both the original single-phase and artificial two-phase images. The authors would also like to note that preliminary results of this work were presented at a conference elsewhere [17]. While there are several differences in the details of the results, due to both a reduced statistical convergence and a plotting error, the main conclusions presented by the data remain unchanged. The conclusions reported within this paper represent the definitive quantitative results of the work.

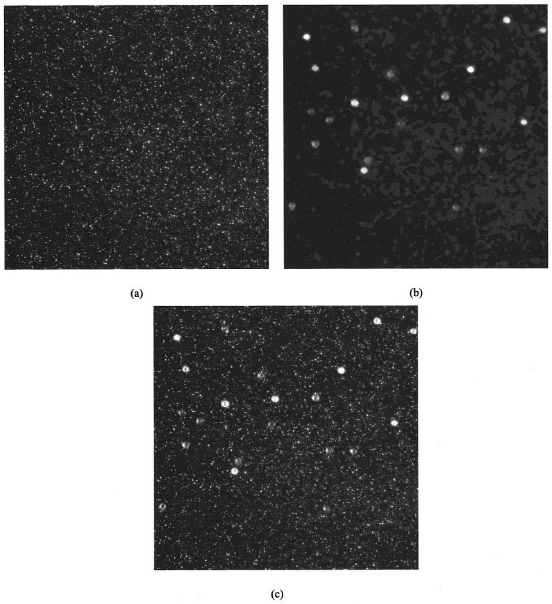

Fig. 5 Artificial two-phase image creation: (*a*) **single-phase tracer particle image,** (*b*) **single-phase dispersed phase particle image,** (*c*) **the artificial image reconstructed by adding** (*a*) **to** (*b*) **as given by Eq.** (**5**)

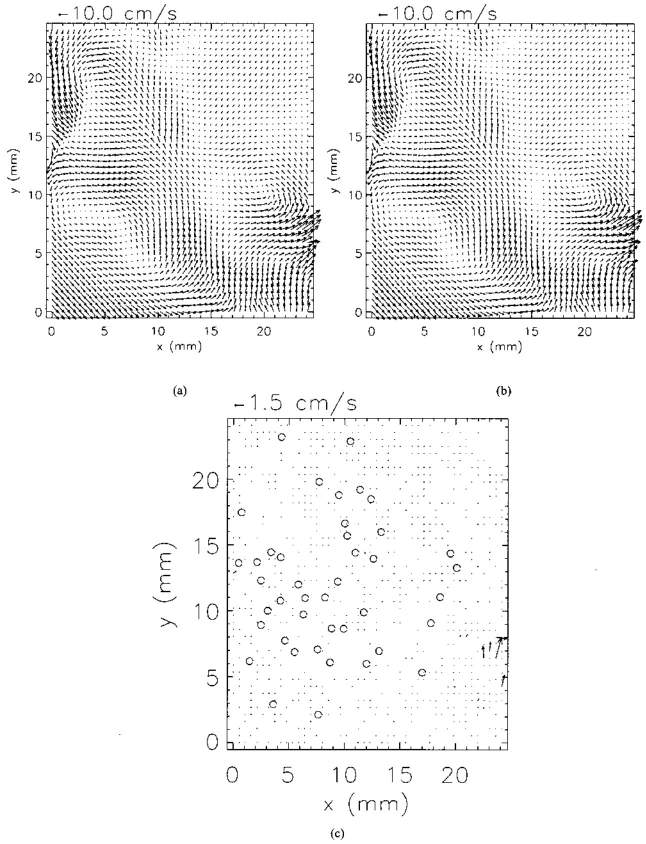

Fig. 6 Errors induced by a median filter of width $f/d_t=2.1$ **for a single image pair.** (*a*) **Single phase image** $\vec{u}_s$, (*b*) **Composite filtered image** $\vec{u}_c$, (*c*) $\vec{u}_s-\vec{u}_c$ **with location of dispersed phase particles shown by the open circles.**

4.1 Filter Influence on Tracer Displacements. The effect of the filter width and discrete particle size on the calculation of the tracer particle displacement is shown for a specific example in Fig. 6, and the average error results are shown in Fig. 7. The main conclusion from these results is that the filtering process produces a negligible error in the carrier phase displacement. From the

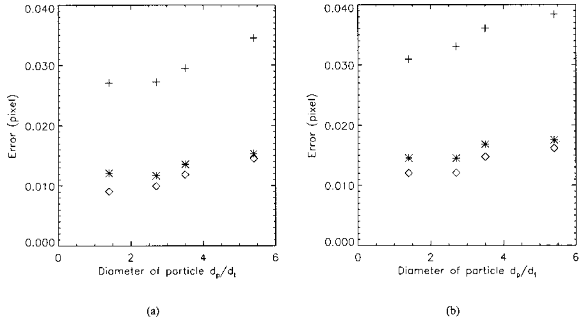

Fig. 7 Average absolute displacement error of carrier phase. (*a*) **Spanwise direction.** (*b*) **Streamwise direction.** +, **filter width** $f/d_t=1.3$; *, **filter width** $f/d_t=2.4$; ◇, **filter width** $f/d_t=2.9$.

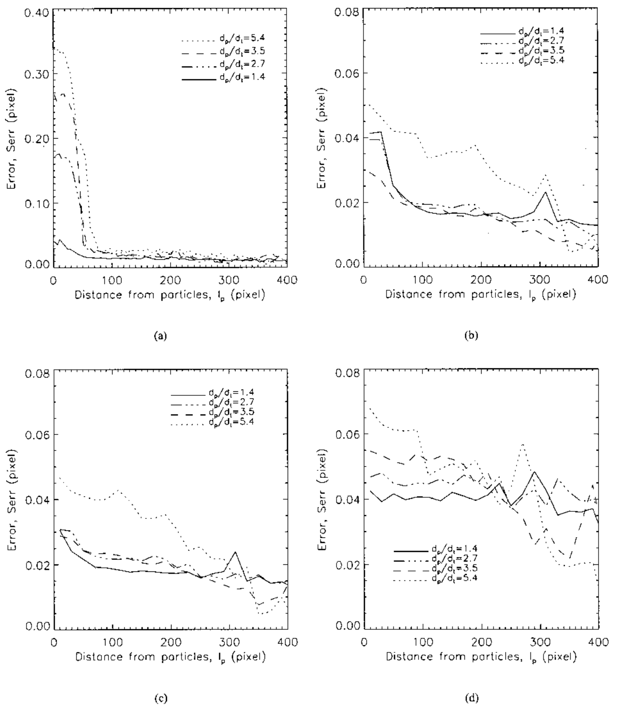

Fig. 8 Average displacement error ($s_{err}=\sqrt{x_{err}^2+y_{err}^2}$) as a function of distance to the nearest neighboring dispersed phase particle. (*a*) No separation filter, (*b*) filter width $f/d_t=2.9$, (*c*) filter width $f/d_t=2.4$, and (*d*) filter width $f/d_t=1.3$ pixels.

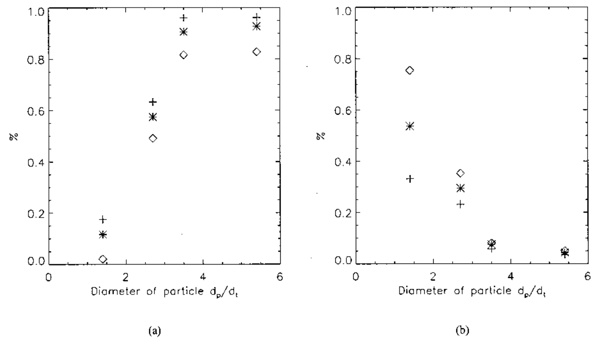

Fig. 10 (*a*) The percentage of correctly identified particles (normalized by the actual number present in the image) versus the different size of particles. (*b*) Percentage of incorrectly identified particles (normalized by the actual number present in the image) versus the different size of particles. +, filter width $f/d_t=1.3$; $*$, filter width $f/d_t=2.4$; ◇, filter width $f/d_t=2.9$.

average results in Fig. 7, it is observed that the absolute value of the error is less than 0.015 pixels for the optimal filter. Normalized with respect to the actual displacement, this corresponds to an error of around 0.2 percent for the selected experimental conditions (the mean displacement was around 8 pixels). This is encouraging when one considers the fact that typical PIV uncertainties are usually on the order of 0.1 pixels for quality experiments, and that minimal values of approximately 0.04 pixels have been demonstrated under ideal conditions (Westerweel et al. [18]). It can also be seen that the errors are very small for the majority of the flow map (Fig. 6(*c*)), and sizable errors only occur in limited regions not associated with a dispersed phase particle. This observation is further supported by measurement of the mean displacement error calculated as a function of distance to the nearest neighboring dispersed phase particle (Fig. 8). When no separation filter is used, the largest mean errors occur within the width of the correlation window (40 pixels), and then drop to negligibly small levels (Fig. 8(*a*)). It is also noted that the amount of the error is proportional to the dispersed phase particle diameter, which is likely due to a stronger influence on the correlation function owing to its larger size. When a separation filter with a width of 7 pixels ($f/d_t=2.9$) is applied, the peaks are still visible, but are reduced to levels comparable to the background noise influence (Fig. 8(*b*)). If the filter width is further decreased, the peak in the error which corresponds to the proximity of a dispersed phase particle is lost (Fig. 8(*c*)), and at small enough filter values, a general rise occurs over all distances from the dispersed phase (Fig. 8(*d*)). This indicates that the increased error at small *f* is not correlated with the dispersed phase.

The source of the increased noise at the small filter width is instead observed to correspond with regions of large velocity gradients. Evidence of this can be confirmed when the mean error is plotted as a function of the carrier phase vorticity (Fig. 9). The plots show generally similar trends for all of the sizes, with a

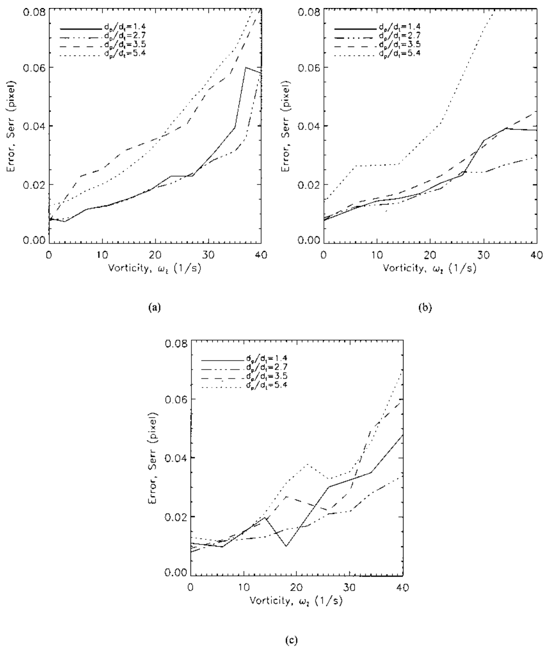

Fig. 9 Average displacement error ($s_{err}=\sqrt{x_{err}^2+y_{err}^2}$) as a function of carrier phase vorticity magnitude. (*a*) Filter width $f/d_t=1.3$, (*b*) filter width $f/d_t=2.4$, (*c*) filter width $f/d_t=2.9$

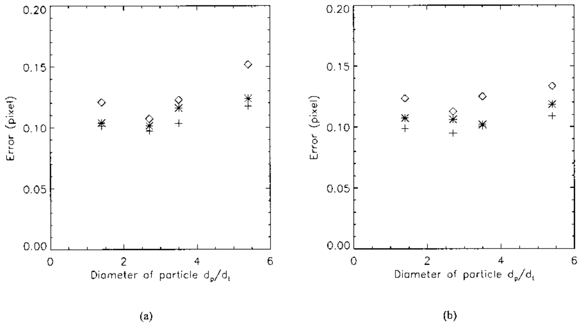

Fig. 11 Average absolute displacement error of dispersed phase. (*a*) Spanwise direction. (*b*) Streamwise direction. +, filter width $f/d_t=1.3$; $*$, filter width $f/d_t=2.4$; ◇, filter width $f/d_t=2.9$.

minimum error occurring at the low vorticity magnitudes and increasing error for large magnitudes. The smallest filter width of $f=3$ $(f/d_t=1.3)$ pixels demonstrates the largest sensitivity to the velocity gradients, with errors greater than the other filter widths over much of the measured vorticity range. High shear regions typically have low signal to noise ratios which produce poorly resolved correlation peaks. When the separation procedure is applied, it slightly reduces the correlation peak, and hence makes the area more susceptible to errors. The filter width of 3 pixels is slightly larger than the size of the tracer particles images, and therefore generates the greatest degradation during the separation process.

The optimum filter width is observed to consistently be a 5–7 pixel window, which corresponds to a nondimensional size of $f/d_t \approx 2$ to 3. Filter widths smaller than this value decrease the correlation peak through the removal of some of the larger tracer particles, while larger filter sizes leave residual ‘‘artifacts’’ of the discrete particles as shown in Fig. 4. In general, there is also a slight increase in the error as the size of the discrete particles is increased. This may be due to the increased amount of ‘‘voids’’ in the single phase image after removal of the discrete particles, which decreases the number of tracer particles available to construct the proper correlation.

4.2 Filter Influence on Phase Separation. One of the most important assessments provided by the artificial image tests is to gauge the ability of the method to successfully separate the two phases. The effect of f and d_p on the accurate identification of the dispersed phase is shown in Fig. 10, using the results from the same random image pairs discussed in the previous section. In each image, the program is told to search for a specified number of particles that must be determined by the operator in advance. The subsequent images are assumed to contain a similar number of particles, and thus there will be some difference between the total number of particles identified and the actual number present. When processing data for quantitative experiments, user intervention must be used to audit the identification of the particles, but selecting the appropriate filter size can minimize the work required. The results indicate that the smaller filter widths do a better job of separating the phases, and that above a critical discrete particle size of $d_p/d_t>3$, little change is observed in the percentage of particles correctly identified. This confirms the fairly intuitive observation that the greater the separation in size between the filter and the particles (large d_p/d_t, small f/d_t), then a greater number of the discrete particles will be retained by the separation process, but more importantly, places a quantitative estimate of the required parameter values for effective identification.

4.3 Filter Influence on Discrete Phase Displacement. The effect of the filter width on the displacement of the discrete particles is shown in Fig. 11. The error for these displacements is about an order of magnitude larger than those for the tracer particle calculation. This is consistent with the fact that only a single particle is used in the estimate of the displacement (in contrast to the tracer phase which typically has on the order of 10 particles), and hence will have a larger uncertainty. Additionally, theoretical estimates on the lower bounds of the uncertainty in the particle location are shown to vary in proportion with the particle diameter (Westerweel [19], Wernet and Pline [20]). Thus the average absolute error is about 0.1 pixel. Considering that the typical uncertainty of a subpixel interpolation estimate is on the order of 0.1 pixel, this does not represent a major increase in the particle's calculated displacement. The optimal filter width corresponds to the smallest filter, $f/d_t \approx 1.3$, but is closely matched by the intermediate size, $f/d_t \approx 2$.

5 Sample Results: Two-Phase Wake

Several sample results of the type of important closure-term measurements the method can provide are illustrated in Figs. 12, 13, and 14. These measurements were obtained from a sequence of 80 independent two-phase images acquired approximately 1 diameter downstream of a cylindrical wake (gravity aligned in the streamwise direction). The dispersed phase consisted of 330 μm glass spheres with a specific gravity of 2.5 and a mean volume fraction of approximately 1×10^{-4}. For these tests, a median filter width of 5 pixels was used, with a correlation window of 40×40 pixels.

Figure 12 depicts the Reynolds stress of both the carrier fluid, $\langle uv\rangle$, and the dispersed phase, $\langle u_p v_p\rangle$, which is important for the calculation of turbulent transport of both phases within two-fluid models. For the current flow conditions, the magnitude of both terms is qualitatively similar in shape, and quantitatively similar in magnitude. Note that the mean recirculation zone is clearly visible just downstream of the cylinder near the top of the figure.

Figure 13 shows the conditionally-averaged mean-square slip velocity between the dispersed phase and the carrier fluid. This term is representative of the amount of kinetic energy being dissipated by the net drag force acting on each particle. There is a net equilibrium dissipation level of 50 cm^2/s^2 due to buoyancy induced slip, and increased levels up to 175 cm^2/s^2 close to the cylinder as a result of the particles' inability to adjust to the strong spatial gradients within the recirculation zone.

One important consideration in multiphase particle/turbulence interaction is a measure of the local inhomogeneities of the dispersed phase that can be caused by the rotational and straining fields of the flow. This phenomena is commonly referred to as ‘‘preferential concentration’’ (Eaton and Fessler [21]), and occurs when the viscous response time of the particle, $\tau_p=\rho_p d_p^2/18\rho_f \nu$, is of order 1 relative to the fluid timescales, τ_f, for large particle/fluid density ratio systems. Under these conditions, the particles respond sufficiently to the fluid motions to avoid regions of strong rotational flow (high vorticity) while tending to accumulate in regions of large strain (Wang and Maxey [22]). One measure of the amount of preferential concentration would be to compare the probability distribution function (PDF) of the carrier fluid vorticity and strain rate sampled from an ensemble of measurements to a similar PDF conditionally sampled at the locations of the dispersed-phase particles. If the particles are exhibiting preferential concentration effects, there should be a reduced probability of finding large vorticity values and an increased probability of finding low vorticity values in the conditionally-sampled PDF. The converse should hold for the strain rate PDF. Figure 14 depicts the PDF of the velocity gradients sampled over the entire spatial extent of the image, and the corresponding PDF sampled conditionally only at the particle locations. For the current flow conditions, no net preferential concentration is observed, as the mean and conditionally sampled histograms match within the experimental uncertainty. This is to be expected, however, as the Stokes number, $\mathrm{St}=\tau_p/\tau_f$, based on the large-scale eddy turnover time is

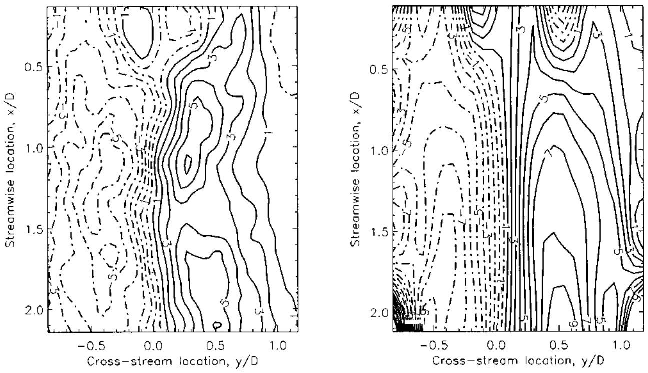

Fig. 12 Reynolds stress of (*a*) fluid and (*b*) particulates in near wake of cylinder. Units associated with the contours lines are in cm^2/s^2. Dashed lines represent negative stress values.

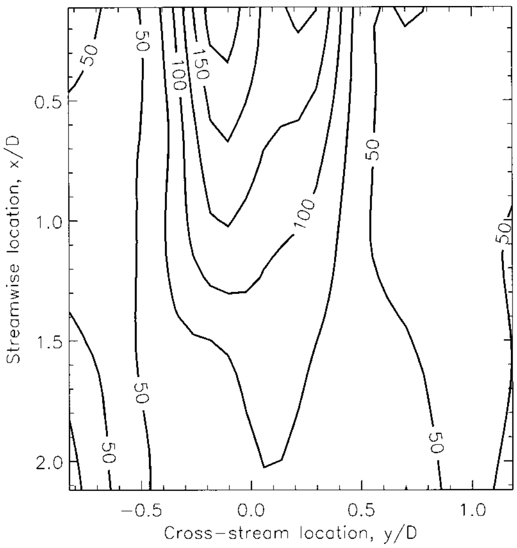

Fig. 13 Conditionally-averaged mean square slip velocity between the dispersed phase and the fluid. Units associated with the contour lines are in $\mathrm{cm}^2/\mathrm{s}^2$.

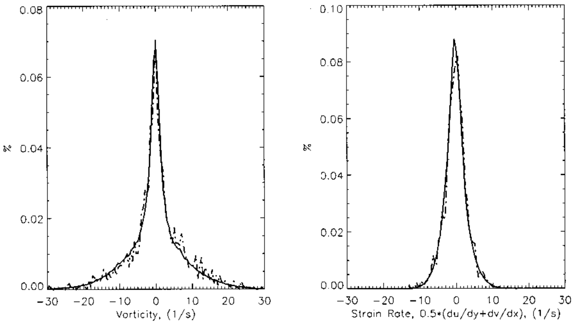

Fig. 14 Probability distribution function of vorticity, ω_z, and strain rate, $\partial v/\partial x+\partial u/\partial y$, for all fluid elements (——), and for particle-conditioned samples (--)

approximately 0.09 (taking $\tau_f \approx l/U \approx 1.2\ \mathrm{cm}/7\ \mathrm{cm/s}=0.17\ \mathrm{s}$). For small St, the dispersed phase begins to track the motion of the flow as a fluid particle. While these particular results do not demonstrate a strong preferential concentration effect, they do illustrate a possible experimental method by which it could be measured.

6 Conclusions

The results of the validation study indicate that the median filter width should be selected to optimize the minimum error incurred on both the carrier phase displacement and to maximize the correct identification of the dispersed phase particles. The optimal value for the tracer particle evaluation is given by a filter width of $f/d_t \geqslant 2$ for all discrete particle sizes. These conditions give average displacement errors in the tracer flow field of on the order of 0.02 pixels, but the errors are primarily caused by a small number of vectors which are modified in the region of large shear. The optimal filter width for dispersed phase evaluation corresponds to $f/d_t = 1.3$, for $d_p/d_t > 3$, which will ensure that 95 percent of the particles are correctly identified with an accuracy of 0.1 pixels. This method can be usefully applied to a wide range of two-phase flows to produce detailed information about the structure of the particle/turbulence interaction, and the nature of the important cross-correlation terms required for two-fluid modeling.

Acknowledgments

The authors would like to thank the National Science Foundation for their generous support of this work under grant numbers CTS9702723 and CTS9871156. We would also like to acknowledge the competent assistance of Mr. Holger Rhör, Mr. Markus Slupianek, and Mr. Neil Zuckerman in the preliminary development of the experiments, and the thoughtful and constructive comments provided by the anonymous reviewers of this article.

References

[1] Hassan, Y., Philip O., and Schmidl W., 1993, ''Bubble Collapse Velocity Measurements Using a Particle Image Velocimetry Technique with Fluorescent Tracers,'' ASME-FED 172, pp. 85–92.

[2] Sridhar, G., and Katz, J., 1995, ''Drag and Lift Forces on Microscopic Bubbles Entrained by a Vortex,'' Phys. Fluids, **7**, pp. 389–399.

[3] Fujiwara, A., Tokuhiro, A., Hishida, K., and Maeda, M., 1998, ''Investigation of Oscillatory Bubble Motion Using a Dual Shadow Technique and its Surrounding Flow Field by LIF-PIV,'' Third Int. Conf. on Multiphase Flow, ICMF'98, Lyon, France, June 8–12.

[4] Dantec Measurement Technology A/S, 1997 http://www.dantecmt.com/PIV/System/PIVPLIF/Index.html, Jan. 5, 2000.

[5] Paris A., and Eaton, J., 1999, ''Measuring Velocity Gradients in a Particle-Laden Channel Flow,'' Proceedings of the Third International Workshop on Particle Image Velocimetry PIV'99 Santa Barbara, CA, September 16–18, pp. 513–518.

[6] Anderson, S., and Longmire, E., 1996, ''Interpretation of Autocorrelation PIV Measurements in Complex Particle-Laden Flows,'' Exp. Fluids, **20**, No. 4, pp. 314–317.

[7] Delnoij, E., Westerweel, J., Deen, N., Kuipers, J., and Swaaij, W., 1999, ''Ensemble-Correlation PIV Applied to Bubble Plumes Rising in a Bubble Column,'' Chem. Eng. Sci., **54**, pp. 5159–5171.

[8] Sato, Y., Hanzawa, A., Hishida, K., and Maeda, M., 1995, ''Interactions Between Particle Wake and Turbulence in a Water Channel Flow (PIV Measurements and Modeling for Turbulence Modification).'' Proceedings of the 2nd Int. Conf. on Multiphse Flow, Kyoto, Japan, April 3–7, 1995, Elsevier, Amsterdam, The Netherlands.

[9] Gui, L., Lindken, R., and Merzkirch, W., 1997, ''Phase-Separated PIV Measurements of the Flow Around Systems of Bubbles Rising in Water,'' ASME FEDSM'97, June 22–26 paper FEDSM97-3103.

[10] Keane, R., and Adrian, R., 1992, ''Theory of Cross-Correlation Analysis of PIV Images,'' Appl. Sci. Res., **49**, pp. 191–215.

[11] Adrian, R., 1991, ''Particle Imaging Techniques for Experimental Fluid Mechanics,'' Annu. Rev. Fluid Mech., **23**, pp. 261–304.

[12] Huang, T. S., 1981, *Two-Dimensional Digital Signal Processing II*, Springer-Verlag, Berlin.

[13] Press, W., Flannery, B., Teukolsky, S., and Vetterling, 1989, *Numerical Recipes: The Art of Scientific Computing*, Cambridge University Press, Cambridge.

[14] Takehara, K., and Etoh, T., 1999, ''A Study on Particle Identification in PTV—Particle Mask Correlation Method,'' J. of Visualization, **1**, No. 1, pp. 313–323.

[15] Takehara, K., Adrian, R., and Etoh T., 1999, ''A Hybrid Correlation/Kalman Filter/χ^2-Test Method of Super Resolution PIV,'' Proceedings of the Third International Workshop on Particle Image Velocimetry PIV'99 Santa Barbara, CA, Sep. 16–18, pp. 163–169.

[16] Westerweel, J., 1994, ''Efficient Detection of Spurious Vectors in Particle Image Velocimetry Data,'' Exp. Fluids, **16**, pp. 236–247.

[17] Kiger, K. T., and Pan, C., 1999, ''Two-Phase PIV for Particle-Laden Flows,'' Turbulence on Shear Flow-1, S. Banerjee and J. Eaton, eds., Begell House, New York, pp. 843–848.

[18] Westerweel, J., Dabiri, D., and Gharib, M., 1997, ''The Effect of Discreet Window Offset on the Accuracy of Cross-Correlation Analysis of Digital PIV Recordings,'' Exp. Fluids, **10**, pp. 181–193

[19] Westerweel, J., 1999, ''Theoretical Analysis of the Measurement Precision and Reliability of PIV,'' Proceedings of the Third International Workshop on Particle Image Velocimetry PIV'99 Santa Barbara, CA, Sep. 16–18, pp. 9–14.

[20] Wernet, M., and Pline, A., 1993, ''Particle Displacement Tracking Technique and Cramer-Rao Lower Bound Error in Centroid Estimates from CCD Imagery,'' Exp. Fluids, **15**, pp. 295–307.

[21] Eaton, J., and Fessler, J., 1994, ''Preferential Concentration of Particles by Turbulence,'' Int. J. Multiphase Flow, **277**, pp. 109–134.

[22] Wang, L.-P., and Maxey, M., 1993, ''Settling Velocity and Concentration Distribution of Heavy Particles in Homogeneous Isotropic Turbulence,'' J. Fluid Mech., **256**, pp. 27–68.

James F. Klausner

Feng Fu

Department of Mechanical Engineering,
University of Florida,
Gainesville, FL 32611

Renwei Mei

Department of Aerospace Engineering,
Mechanics and Engineering Science,
University of Florida,
Gainesville, FL 32611

A Conductance Based Solids Concentration Sensor for Large Diameter Slurry Pipelines

An instrument has been developed that measures the solids concentration in slurry pipelines ranging in diameter from 5–150 cm. The operating principle is based on conductance, and in contrast to the gamma densitometer, the instrument does not require a nuclear radiation source. The instrument operates on-line, is nonintrusive, and provides real-time output. The instrument measures local concentration around the pipe periphery, and the local values are integrated to obtain the area-average concentration. A graphical display shows the variation of concentration from the top of the pipe to the bottom as well as the area-average concentration history. The instrument has been extensively tested in an experimental slurry transport facility as well as on-line at the Swift Creek phosphate mine in the state of Florida. When compared with a quick-closing valve measuring technique, the mean deviation of solids concentration measured with the conductance based instrument is 0.81 percent based on mass. [S0098-2202(00)00704-5]

1 Introduction

The transport of particulate materials in slurry form is prevalent in many industries. In the mining industry slurry pipelines are used to transport raw material (ore or matrix) to the industrial processing facilities and to transport the waste material (tailings) to be used for land reclamation. The industrial facilities that process the ore or matrix also contain numerous slurry transport lines. Specifically, the utilization of slurry transport pipelines within the phosphate mining industry is standard practice. A substantial operating cost associated with mining and processing involves paying for the electricity powering the slurry pumps. The optimal operating condition for ore, matrix, and tailings lines is to pump as high a slurry concentration as possible without plugging the pipeline. Knowledge of the slurry concentration within the pipeline is essential for efficient and reliable operation. The current practice in the phosphate mining industry is to use gamma densitometry to measure the slurry concentration in large diameter pipes. However, due to safety concerns of radiation exposure to workers and fear of litigation, gamma densitometers are typically placed in remote locations within the processing plant where mine operators will not have routine access. The problem associated with such an installation is that the water jet operator, who continually mixes the slurry, does not know the slurry concentration until the slurry reaches the processing plant, which may involve a delay time of thirty minutes to an hour. Since the water jet operator does not have instantaneous feedback from the gamma densitometer, the current practice is to use the slurry pump amperage as an indicator of slurry concentration. Because there are many other factors which can influence the current drawn by the slurry pump, the method is not very accurate, and there exist large variations of slurry concentration with flow through the pipeline. In order for the water jet operator to maintain the slurry concentration near optimum conditions or in order to automate the slurry mixing process, it is necessary to have a robust instrument which can give accurate and instantaneous feedback on the slurry concentration entering the pipeline.

A review article by Williams et al. [1] on multiphase flow measurements discusses the following techniques which have been applied to measuring particulate concentration in flowing slurry suspensions: radiation attenuation, ultrasonics, microwave resonance, capacitance, conductance, laser radar, light scattering, and light attenuation. When considering high concentration (typically 40 percent by weight) slurries in large diameter (typically 500 mm) pipelines used for mining operations, optical techniques are not useful since the slurry is essentially opaque to radiation in the visible spectrum. Radiation attenuation techniques using gamma-rays or X-rays are suitable, but they are typically kept out of reach of operating personnel, and are considered undesirable by those that work with them. An intrusive sensor is not feasible since it would be rapidly destroyed by the abrasive flowing slurry. In what follows, the development of a suitable slurry solids concentration sensor, which utilizes electrical conductance as the basis for measuring the solids concentration, is discussed in detail. The design, fabrication, wear characteristics, and performance of the solids concentration sensor are presented. The sensor has been extensively tested in the laboratory and in the field at the Swift Creek phosphate mine in the state of Florida. The results of these tests, which validate the sensor performance, are discussed.

2 Basis for Slurry Solids Concentration Measurement

The concept that has been successfully implemented to measure the slurry solids concentration is to fabricate a nonintrusive sensor that measures the local slurry concentration around the periphery of a sensor flow tube using conductance (impedance). For high specific gravity solids the slurry concentration is typically uniform in a horizontal plane due to gravitational stratification. Thus, the integrated local concentration around the pipe periphery approximates the average pipe concentration. The sensor configuration is similar to the impedance tomography sensor developed by Klug and Mayinger [2] for concentration measurements of gas/liquid flow. However, the current solids concentration sensor only utilizes conductance (impedance) measurements between adjacent electrodes, which distinguishes it from a tomography sensor. Tomography is not useful for the present application since the signal to noise ratio for the conductance measured between electrodes mounted diametrically opposed would be restrictively low, considering the pipe diameter is large and the slurry is dense.

Although the conductivity of a slurry mixture depends on both the solids concentration and carrier liquid conductivity, the solids concentration may be deduced from measurements of both the mixture conductivity and the carrier liquid conductivity. Conductivity methods employed to measure solids concentrations in slurry flows have been discussed by many researchers such as

---

Contributed by the Fluids Engineering Division for publication in the JOURNAL OF FLUIDS ENGINEERING. Manuscript received by the Fluids Engineering Division September 13, 1999; revised manuscript received June 19, 2000. Associate Technical Editor: S. Banerjee.

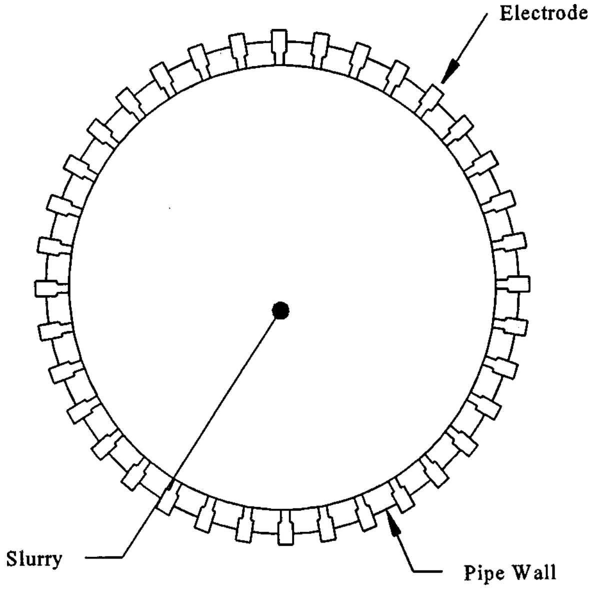

Fig. 1 Cross-section of conductance sensor depicting electrode array

Beck et al. [3], Lee et al. [4], Ong and Beck [5], Nasr-El-Din et al. [6,7], Colwell and Shook [8], and Uribe-Salas et al. [9]. As is the case with tomography, these methods rely on measuring the conductivity across a slurry flowing through a channel, which is not practical for the current application.

The conductivity sensor used for measuring slurry solids concentration in large diameter pipes consists of a circular cross section conduit in which equally spaced electrodes are placed around the pipe periphery as shown in Fig. 1. The conductivity of a slurry mixture measured between any two electrodes relative to the conductivity measured for the carrier liquid may be related to the local slurry concentration flowing between adjacent electrodes. A solution of Maxwell's equations suggests that the solids concentration, C_v, is related to the mixture and carrier liquid conductivities through (Uribe-Salas et al. [9])

$$K=\frac{1-C_v}{1+0.5C_v} \tag{1}$$

where $K=k_m/k_c$, k_m is the mixture conductivity, k_c is the conductivity of the carrier liquid (typically water for mining applications), and it is assumed the solids are nonconducting. Since conductivity sensors require calibration, C is typically expressed as

$$C_v=1-K^{1/n} \tag{2}$$

where n must be determined through calibration.

An electronic bridge circuit, shown schematically in Fig. 2, is used to measure the mixture-to-liquid conductivity ratio, K, using two electrode pairs. One electrode pair measures the conductivity of the slurry mixture while the other measures the conductivity of the carrier liquid. The reference potential, V_a, to the bridge circuit is a 1 kHz, 5 volt peak-to-peak signal. The conductivity ratio K may be expressed in terms of the electrode geometry and electrical resistance as,

$$K=\frac{k_m}{k_c}=\left(\frac{A_c}{A_m}\frac{d_m}{d_c}\right)\frac{R_c}{R_m} \tag{3}$$

where A is the electrode surface area, d is the distance between electrodes, R is the resistance across electrodes, m denotes the mixture, and c denotes the carrier liquid. Using bridge theory it may be shown that

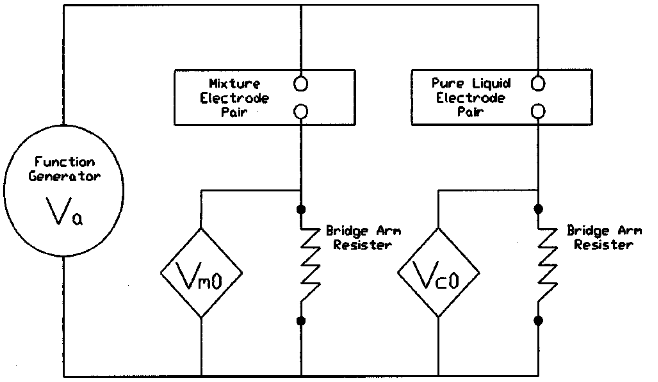

Fig. 2 Schematic diagram of bridge circuit used for conductance measurement

$$K=K_0\left(\frac{V_a}{V_{c0}}-1\right)\Big/\left(\frac{V_a}{V_{m0}}-1\right) \tag{4}$$

where V_{m0} and V_{c0} are the measured bridge arm voltages, and $K_0=(A_c/A_m)\ (d_m/d_c)$ is a constant for a given electrode pair. Ideally, if all electrodes are identically manufactured and equally spaced, $K_0=1.0$. In practice, manufacturing imperfections necessitate that K_0 is determined through calibration for each electrode pair.

3 Sensor Design

During the course of development, three concentration sensors of different size were fabricated and tested: 100 mm ID, 150 mm ID, and 500 mm ID sensors. All three sensors are geometrically similar and thus only the 500 mm sensor will be described here. An assembled drawing of the 500 mm ID sensor is shown in Fig. 3. The sensor flow tube is 1.2 m in length and is constructed from a dielectric composite, G-10 Garolite. It has an inner diameter of 489 mm with a wall thickness of 19 mm. 48 electrodes are equally spaced around the circumference of the flow tube as shown in Fig. 1. All of the stainless steel electrodes are 6.4 mm in diameter and are mounted flush to the inner sensor wall. The conductance sensor flow tube is connected to the pipeline via slip flanges. A pictorial view of the 500 mm assembled sensor is shown in Fig. 4. The reference electrodes shown in Fig. 3 are mounted at the top of the flow tube and are displaced in the direction of flow. For coarse and high specific gravity solids the concentration is very low at the top of the pipe due to gravitational settling, and the measured conductance at the top of the pipe using these reference electrodes is taken to be that of the carrier liquid. The occurrence of zero concentration at the top of the sensor flow tube has been verified experimentally for the slurry flow applications considered in this investigation. Whether or not solids are present at the top of the flow tube for other applications depends on particulate size, specific gravity, and pipe Reynolds number.

The measurement of the local and average solids concentration is obtained using a data acquisition, control and processing system (DACPS) that utilizes a microprocessor at its core. A block diagram showing the DACPS circuitry is shown in Fig. 5. An industrial 100 MHz microprocessor houses a signal generator, a 48 channel I/O board, an analog-to-digital converter, and a digital-to-analog converter. The sensor electrodes are connected to a 48 channel relay panel and are sequentially switched into the electronic bridge circuit using the 48 channel I/O board. The 1 kHz, 5 Volt peak-to-peak reference signal sent to the bridge circuit is controlled by the programmable signal generator. The bridge circuit arm voltages are measured with the analog-to-digital converter. After the mixture to liquid conductivity ratio, K, is measured for all adjacent electrodes, Eqs. (2) and (4) are used to compute the local slurry solids concentration between electrodes.

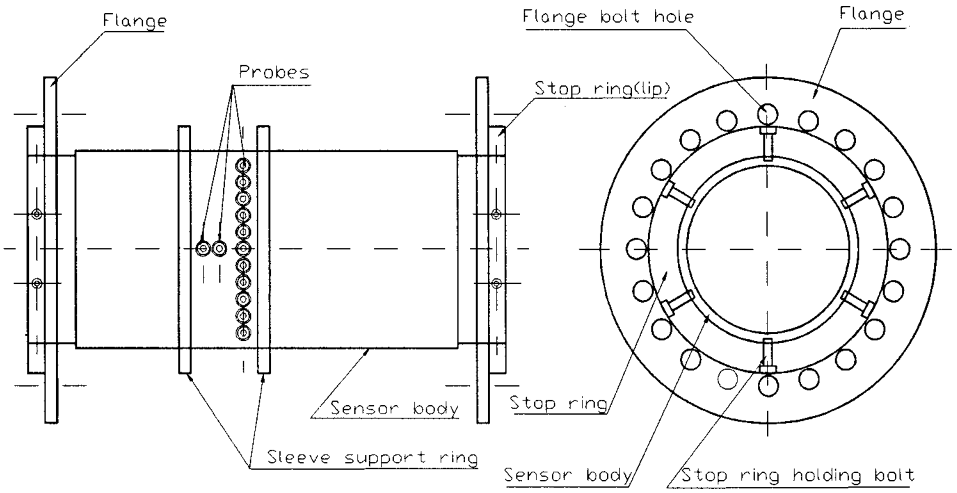

Fig. 3 Assembly diagram of 500 mm conductance sensor

In order to convert the local concentration to an average concentration, the following area averaging procedure is used

$$\overline{C_v}=\frac{1}{A}\int_A C_v(A)dA \tag{5}$$

where A denotes the cross sectional area of the flow tube and $C_v(A)$ is the local concentration. In applying Eq. (5) to the current instrument, it is noted that $C_v(A)$ is actually measured near the sensor wall. It is assumed that C_v is uniform in any horizontal plane due to gravitational stratification. The concentration data are displayed numerically, pictorially, and graphically in real time on a digital monitor. A 4-20 milliamp analog output is also supplied for remote monitoring or industrial control.

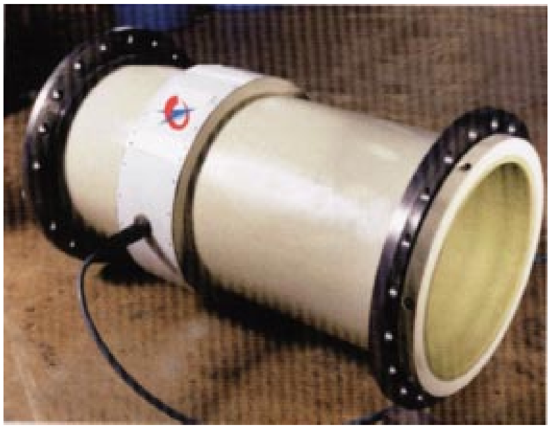

Fig. 4 Assembled view of conductance sensor body

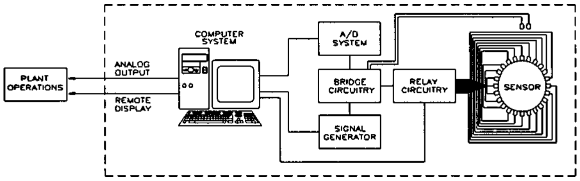

Fig. 5 Block diagram of data acquisition, control, and processing system

4 Sensor Calibration

The measurement of the slurry solids concentration requires Eqs. (2) and (4) and thus two constants, K_0 and n, need to be determined empirically through calibration. The determination of K_0 is discussed first. Although an attempt has been made to manufacture all electrodes identically, because of machining and assembly imperfections, the conductivities measured between sensor electrode pairs and the reference electrode pair with pure liquid flowing through the sensor may not be identical. Thus the constant K_0, which appears in Eq. (4), will not equal 1.0. In order to measure the local solids concentration accurately, K_0 must be known for each electrode pair. K_0 is determined by running pure liquid through the sensor and measuring V_{m0}, V_{c0}, and V_a for a given electrode pair. For each electrode pair K_0 is calculated according to

$$K_0=\left.\frac{1}{\left(\dfrac{V_a}{V_{c0}}-1\right)\Big/\left(\dfrac{V_a}{V_{m0}}-1\right)}\right|_{\text{pure liquid}} . \tag{6}$$

In practice, it is found that K_0 is typically within 5 percent of unity.

The calibration constant, n, is determined using a static calibration. An end-plate is bolted to one end of the sensor flow tube, and the sensor flow tube is positioned so that its center line is oriented vertically. A water-solids mixture is placed inside the sensor flow tube so that the saturated particle bed just covers the electrode array, and the reference electrodes remain in contact with only liquid. Values for V_{m0}, V_{c0}, and V_a are measured using the sensor DACPS (data acquisition, control and processing system). Equation (4) is used to compute K, and based on the known saturated particle bed volumetric concentration, n is computed from Eq. (2).

Calibrations have been performed for all the sensors fabricated. The particulate solids used to calibrate the sensors are silica sand and phosphoric tails. Five different particle size ranges were considered, which vary from 0.1 mm to 15 mm. The calibration results reveal that the calibration constant, n, is independent of sensor inner diameter and independent of particle size, provided the particle size is less than 5 mm (Klausner et al. [10]). It is also found that the signal source frequency has no effect on the calibration constant provided the frequency does not exceed a threshold value. A signal source frequency of 1 kHz works well for all cases considered. It has been found that $n=1.3$ for all of the particulate solids considered in this investigation. While in the pipeline, a large portion of solids flow as a moving bed in the bottom section of the sensor body. Therefore, the accuracy of the concentration measurement is relatively insensitive to the shape of the function given by Eq. (2) since *n* is calibrated for a solids bed.

5 Slurry Solids Concentration Sensor Performance

5.1 Laboratory Test. The different size conductance based slurry solids concentration sensors were tested over a variety of operating conditions. Here the results of a laboratory test and a field test are reported. The schematic diagram of a 150 mm diameter slurry test facility is shown in Fig. 6. The inside diameter of the test facility piping is 145 mm. During operation of the slurry flow test facility, the slurry mixture is drawn from a 1900-liter conical bottom PVC tank. The discharge of the tank feeds a 45 kW centrifugal slurry pump. The slurry pump is driven by a 45 kW 4-cylinder diesel engine. The slurry flow can be directed either through the 150 mm diameter test loop pipeline or to a bypass line via two 150 mm knife valves. The slurry flow first passes through a magnetic flow meter manufactured by Advanced Flow Technology, Lakeland, Florida. For single phase flow the uncertainty of the flow meter is ±0.5 percent of full scale (3208 l/m). However, for two-phase horizontal flow the solids are significantly stratified and the uncertainty for the mean volumetric flow rate is not known. Therefore, the flow rate reported for these experiments is that of single-phase flow through the facility prior to loading it with solids. Following a 180 deg bend the slurry flows through a quick-closing valve section. This section is used to measure the slurry concentration by simultaneously closing the two knife valves at both ends of this 1.56-meter-long pipe section. Following the quick-closing valve section, the slurry flows through the conductance sensor where the solids concentration of the slurry is measured in-line. Finally, the slurry flow is either directed back to the 1900-liter tank, where it is either recirculated or diverted to the 760-liter flow rate calibration tank.

A typical test was initiated by establishing the desired single-phase flow rate, which was measured with the magnetic flow meter. For all tests conducted in the slurry flow test facility industrial grade sand was used as the slurry solids. Next, the desired concentration was obtained by adding solids to the 1900-liter tank. The slurry was circulated through the test facility until steady flow conditions were established. The conductance based solids concentration sensor continually monitored the slurry concentration using the DACPS at a frequency of seven samples per second and the slurry concentration time history was graphically displayed and stored for future analysis.

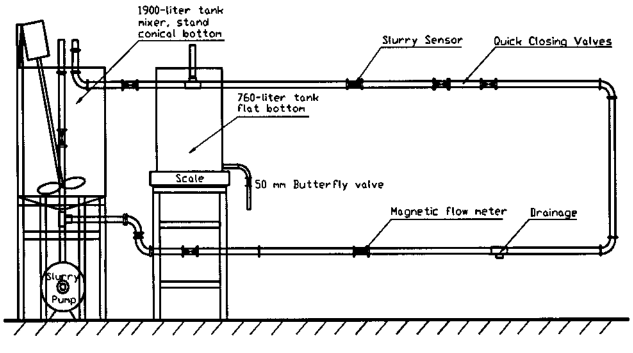

Fig. 6 Schematic diagram of the slurry transport test facility

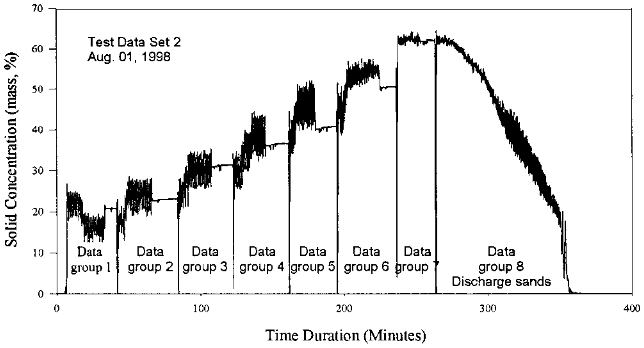

Fig. 7 Solids concentration history upon loading and unloading slurry transport test facility

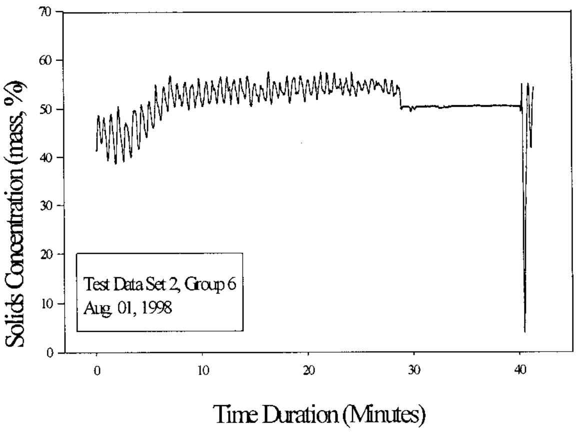

Fig. 8 Typical measured solids concentration history for a single test using 150 mm conductance sensor

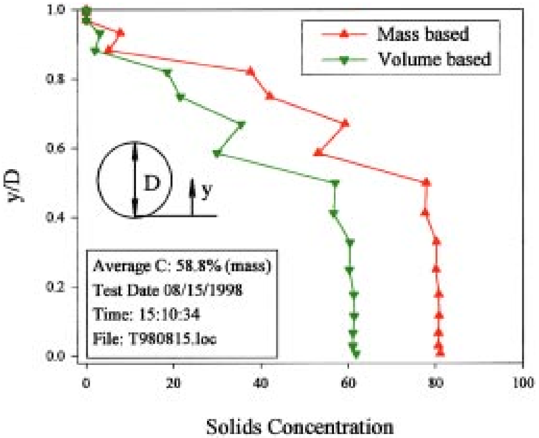

Fig. 9 Local variation of solids concentration in 150 mm conductance sensor

Figure 7 shows the time history of the sand concentration flowing through the test facility upon loading and discharging the facility. Each data group shown represents the response of the sensor to the addition of solids in the slurry flow system. The last data group shows the sand solids being discharged from the system. These results demonstrate that the concentration sensor is very good at capturing the correct trend. Figure 8 shows the solids concentration history measured by the sensor for a typical test. Once a steady-state concentration was reached, it is observed that the concentration fluctuates around a mean. These fluctuations are not random; in fact, they are due to the fact that there was a wavy sand bed moving along the bottom of the pipeline. The fluctuations shown capture the wave structure of the sand bed. These data demonstrate that the conductivity sensor is also very sensitive to small changes in particle concentration. After approximately 30 minutes, the quick-closing valves were activated and the flow was stopped. It is seen that while there was no flow, the sensor gave a very constant signal for the particles remaining in the sensor flow tube. At about the 40 minute mark the flow was again initiated through the pipeline and the sensor showed a spike in concentration ($C\rightarrow 0$). This spike represents a slug of water that moved through the pipeline which was introduced when the quick-closing valve section was removed from the pipeline and emptied of all solids. Again these data demonstrate that the sensor is extremely sensitive in capturing changes in concentration. Figure 9 shows the concentration profile within the 150 mm slurry pipeline for a mean volumetric flow rate of 1938 liters/min and a mean mass solids concentration of 58.8 percent. It is clearly seen that the solids were significantly stratified, and the majority of solids travel along the bottom of the pipeline in the form of a moving bed.

The solids captured in the quick-closing section were collected in a container for analysis. The solid samples were dried in an oven and then weighed using a digital scale with a 0.1 g resolution. The volumetric solids concentration using the quick-closing section is computed from

$$C_v=\frac{M_p/\rho_p}{\nu_q} \tag{7}$$

where $\nu_q=0.0258\ \mathrm{m}^3$ is the quick-closing valve volume, M_p is the mass of solids captured in the quick-closing section, and $\rho_p=2560\ \mathrm{kg/m}^3$ is the material density of the solids. It is typical industrial practice to report the solids concentration on a mass basis. The relation between the mass and volumetric concentration is

$$C_m=\frac{1}{1+\frac{\rho_c}{\rho_p}\left(\frac{1}{C_v}-1\right)} \tag{8}$$

where C_m is the solids concentration on a mass basis and ρ_c is the density of the carrier liquid.

The average solids concentrations measured using the in-line conductance sensor are compared with measurements obtained with the quick-closing valve section in Fig. 10. A total of 38 tests were performed with flow rates ranging from 2006 to 2877 l/m and mass solids concentration ranging from 5 to 60 percent. As seen from Fig. 10 the agreement is quite good. The mean deviation between the two measuring techniques is defined as

$$\varepsilon_c=\frac{1}{N}\sum_{N}^{i=1}|C_{\mathrm{msi}}-C_{\mathrm{mqi}}| \tag{9}$$

where C_{msi} is the mass concentration measured with the conductance sensor and C_{mqi} is that measured with the quick-closing valve method. For these data $\varepsilon_c=0.81$ percent. The uncertainty associated with the quick-closing valve method is approximately ± 1 percent. Therefore, it may be concluded that the conductance sensor is at least as accurate as the quick-closing valve method in measuring the solids concentration.

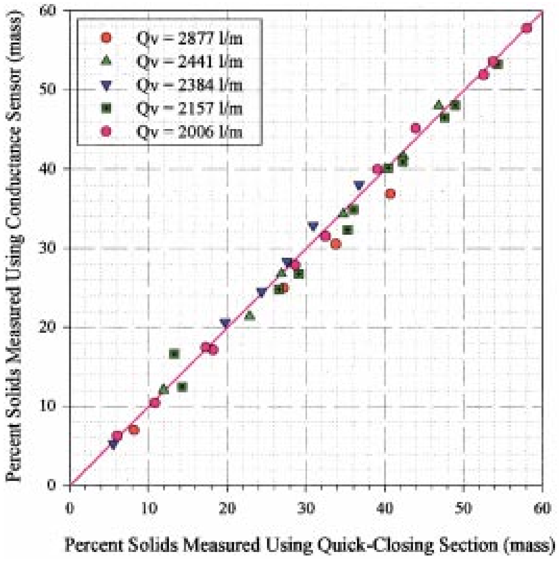

Fig. 10 **Comparison of measured solids concentration using conductance sensor and quick-closing valve method in the slurry transport test facility**

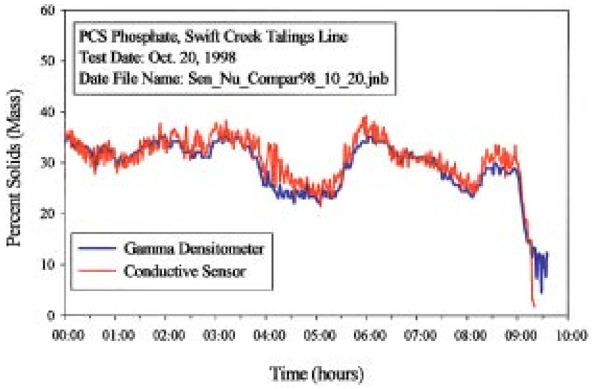

Fig. 11 **Comparison of measured solids concentration using conductance sensor and gamma densitometer at the PCS phosphate swift creek mine, Florida**

5.2 Field Test. The 500 mm diameter slurry solids concentration sensor was installed for a three month period at the Swift Creek phosphate mine in the state of Florida. On-line testing has been conducted for both a tailings and a matrix slurry transport line. Flow conditions in the matrix and tailings lines ranged from 34,000 to 53,000 liters per minute. Figure 11 shows the measured solids concentration by mass in the tailings line using the conductance based solids concentration sensor compared with that using a gamma densitometer over a 10 hour time period. As observed, the agreement between the instruments is excellent. The gamma densitometer was mounted on a horizontal pipeline and appears to be well calibrated. For the duration of the testing, the conductance based sensor was very stable and maintained its calibration, despite serious erosion. It was found that the sensor flow tube had excessive wear in the bottom portion of the tube. Near the bottom of the tube, approximately 13 mm of wall thickness were eroded during the three months of field testing. Therefore, Garolite is not a suitable material for the sensor flow tube for mining applications. It is recommended that future conductance sensors be manufactured with high density, very high molecular weight polyethylene.

6 Concluding Remarks

This paper describes the successful development of a slurry solids concentration sensor that is suitable for large diameter pipes, which are typically encountered in the mining industry. A sophisticated data acquisition, control, and processing system has been developed that implements the algorithms necessary to measure the local and average slurry concentration. The sensor has been demonstrated to be very accurate under a wide range of operating conditions.

Acknowledgments

This work was funded by the Florida Institute of Phosphate Research under Contract Number 96-04-056R and Cargill Fertilizer under Contract Number 41040449.

Nomenclature

A = area (m^2)
d = distance between electrodes (m)
C_m = mass basis concentration
C_v = volumetric concentration
k = conductivity $(\text{ohm-m})^{-1}$
K = mixture to liquid conductivity ratio
M = mass (Kg)
R = resistance (ohm)
V_a = reference potential (volt)
V_{c0} = continuous phase bridge arm voltage (volt)
V_{m0} = mixture bridge arm voltage (volt)
ρ = density ($\mathrm{kg/m}^3$)
ν_q = volume of quick-closing section (m)

Subscripts

c = carrier liquid
m = mixture

References

[1] Williams, R. A., Xie, C. G., Dickin, F. J., Simons, Jr., S., and Beck, M. S., 1991, ''Multi-Phase Flow Measurements in Powder Processing,'' Powder Technol., **66**, pp. 203–224.
[2] Klug, F., and Mayinger, F., 1994, ''Impedance Based Flow Reconstruction—A Novel Flow Composition Measuring Technique for Multi-Phase Flows,'' Nucl. Eng. Des., **146**, pp. 35–42.
[3] Beck, M. S., Calvert, G., Hobson, J. H., Lee, K. T., and Mendies, P. J., 1971, ''Total Volume and Component Flow Measurement in Industrial Slurries and Suspension Using Correlation Techniques,'' Trans. Inst. Meas. Control (London), **4**, pp. 133–138.
[4] Lee, K. T., Beck, M. S., and McKeown, K. J., 1974, ''An On-Line Instrument for Measuring Small Quantities of Dispersed Non-Conducting Liquid in a Conducting Liquid,'' Trans. Inst. Meas. Control (London), **7**, pp. 341–345.
[5] Ong, K. H., and Beck, M. S., 1975, ''Slurry Flow Velocity, Concentration and Particle Size Measuring Using Flow Noise and Correlation Techniques,'' Trans. Inst. Meas. Control (London), **8**, pp. 453–463.
[6] Nasr-El-Din, H., Shook, C. A., and Colwell, J. M., 1987, ''A Conductivity Probe for Measuring Local Concentrations in Slurry Systems,'' Int. J. Multiphase Flow, **13**, pp. 365–378.
[7] Nasr-El-Din, H., Shook, C. A., and Colwell, J. M., 1987, ''The Lateral Concentration Distributions in Horizontal Slurry Pipelines Flow,'' Int. J. Multiphase Flow, **13**, pp. 661–670.
[8] Colwell, J. M., and Shook, C. A., 1988, ''The Entry Length for Slurries in Horizontal Pipeline Flow,'' Can. J. Chem. Eng., **13**, pp. 714–720.
[9] Uribe-Salas, A., Gomez, C. O., and Finch, J. A., 1994, ''A Conductivity Technique for Gas and Solids Holdup Determination in Three-Phase Reactors,'' Chem. Eng. Sci., **49**, pp. 1–10.
[10] Klausner, J. F., Fu, F., and Mei, R., 1998, ''Development of An On-Line Concentration Sensor for Slurry Flow Through Large Diameter Pipes,'' Florida Institute of Phosphate Research, Publication No. 04-056-152.

M. Gutman
202 N. First Street, #1002,
Marshall, MN 56258

Optimization of a Deepening Load Acting on a Flexible Cable Towed Under Water

In this paper we examine the problem of flexible cable equilibrium in water flow, when the cable is loaded with an arbitrarily distributed load which is directed perpendicular to the flow. We define optimal value and distribution of this load and parameters of cable equilibrium corresponding to this load. The optimal load provides maximum deflection of the rear end of the cable in relation to front end in the direction perpendicular to the flow direction, provided the tension is limited. [S0098-2202(00)01204-9]

Discussion

There are several ways to deflect a flexible cable in flowing water. One is to apply concentrated force perpendicular to the flow to the cable's rear end. This takes place when a so-called hydrodynamic apparatus is located at the end of the cable, to create the concentrated force applied at the end. Another is to apply load, distributed along the cable, also perpendicular to the flow. We assume that we can change the load along the cable. This can be accomplished, for example, by attaching small wings along a fairing which is mounted onto the cable. Hydrodynamic forces acting on those wings imitate a distributed load. An example of this arrangement was actually designed and tested in the Soviet Union, and has proved to be performing quite well [1]. Another possibility is to change the weight-in-water along the cable.

It may seem that the first way is preferable because it is easiest to create. However, there may be situations when an apparatus located at the end of the cable cannot ensure the necessary depth, for instance, when the deepening load which is necessary to achieve the required depth is too big and destroys the cable. Probably, we can increase the depth by distributing the deepening force along the cable when we choose the optimal form of such distribution. If this is true, it is interesting and important to estimate the result quantitatively since it can be useful to have a more complicated arrangement in order to improve the technical characteristics of such a cable.

There are a number of works solving the problem of optimization for the first case [2,3]. In this article the problem is formulated and solved for the second case. The problem is being solved for a two-dimensional (plane) case; therefore, the cable is considered to be in the vertical plane and the distributed load is a deepening load. We will suppose that all wings have the same size, the same angle of attack, and so form the same force. Under these conditions, to find the optimal distributed load is to find that force and number of wings per unit of length, such as the function of the distance from one of the cable's ends.

As in Eames and Egorov [2,3], we will assume that the optimal load is the one which provides maximum deepening of the rear end with a given tension on the cable at its front end. This optimization allows us to get the most benefit out of the cable's strength.

Consider a segment of flexible cable with a wing (Fig. 1). This element is small enough to be viewed as a straight line. On this figure,

α_τ is the angle of attack of a fairing, equal in this case to the slope of the cable,

α_w is the angle of attack of the wing, and

α_f is the rigging angle of incidence of wings as follows from Fig. 1.

It is obvious that:

$$\alpha_w = \alpha_f - \alpha_\tau \tag{1}$$

The hydrodynamic force acting on a segment may be represented as the sum of two forces: R_1, the force acting on a segment of cable with fairing and R_2, the force acting on a wing. We can assume that hydrodynamic interaction between these two parts is small, because of big distances between wings and their very small sizes. So hereafter we will count that interaction as absent.

Let us project these forces on normal n and tangent τ to the element of a cable and find the nondimensional coefficients of the projections. The product of fairing chord length by the cable's length unit is taken to be the characteristic area. C_{1N} is a normal coefficient for force R_1, and C_{2N} is a normal coefficient for force R_2. $C_{1\tau}$ and $C_{2\tau}$ are tangent coefficients for those forces.

$$C_{1n} = 2R_{1n}/\rho v^2 b$$

$$C_{1\tau} = 2R_{1\tau}/\rho v^2 b$$

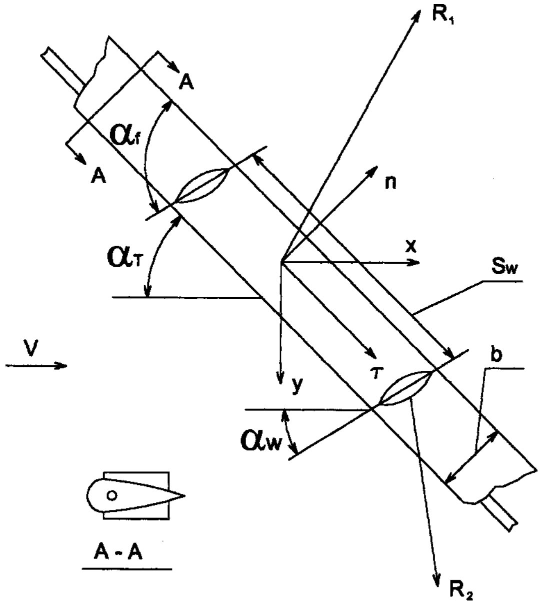

Fig. 1 Acting forces scheme

Contributed by the Fluids Engineering Division for publication in the JOURNAL OF FLUIDS ENGINEERING. Manuscript received by the Fluids Engineering Division June 21, 1998; revised manuscript received July 19, 2000. Associate Technical Editor: M. Taiantafyllov.

$$C_{2n}=2R_{2n}/\rho v^2 b$$

$$C_{2\tau}=2R_{2\tau}/\rho v^2 b$$

where ρ is the water density, v is the speed of towing, and b is a fairing chord.

We can write C_{2n} and $C_{2\tau}$ as follows:

$$C_{2n}=[C_{yw}(\alpha_w)\cos\alpha_\tau-C_{xw}(\alpha_w)\sin\alpha_\tau]F_w/bS_w$$

and

$$C_{2\tau}=[C_{yw}(\alpha_w)\sin\alpha_\tau+C_{xw}(\alpha_w)\cos\alpha_\tau]F_w/bS_w \tag{2}$$

where C_{yw} and C_{xw} are the lift and drag coefficients of the wing; F_w is the wing plan area; and S_w is the distance between two nearest wings at this point of the cable.

To assign an equilibrium position means to define for any point on the cable an angle, $\alpha_\tau(S)$, where S is the distance along the cable at this point from one of the ends of the cable. Knowing this function we can find the inverse function, $S(\alpha_\tau)$. Then, if we arrange the small wings along a cable in such a way that the ratio $W=F_w/bS_w$ is a function of $W=W(S)$, for any equilibrium position of the cable,

$$F_w/bS_w=W(S(\alpha_\tau)). \tag{3}$$

Let us have a function $C_{2n}(\alpha_\tau)$. We can easily find the equilibrium which corresponds to the load with C_{2n}, i.e., find a function $\alpha_\tau=\alpha_\tau(S)$ related to the above equilibrium. Having Eq. (1) and Eq. (2) and using Eq. (3) we can find a function $W(S)$ which gives us the predetermined distribution of the load. Obviously, the ratio $\kappa=C_{2\tau}/C_{2n}$ does not depend upon W and, therefore, is a known specific function of $\alpha_\tau=\alpha_\tau(S)$ if the wing profile and angle α_τ are given.

Another way to create varied load distributed along the cable is to change its weight-in-water along the cable. In this case, Eq. (2) can be rewritten as follows:

$$C_{2n}=2g(S)/\rho v^2 b\cos\alpha_\tau$$

$$C_{2\tau}=2g(S)/\rho v^2 b\sin\alpha_\tau.$$

Here $g(S)$ is weight-in-water of the cable's unit length at the point with the coordinate of S. If the cable has uniform weight-in-water which we are not going to change, it should be included in C_{1n} and $C_{1\tau}$ using analogous formulas. It is necessary to note that for the distributed wings case, the optimal distribution of wings does not depend on tow velocity v, while optimal $g(S)$ would change with variation of v.

Therefore, the problem is to determine a function $C_{2n}(\alpha_\tau)$ which gives the maximum magnitude of the optimization value. Considering the above statement and the work of Egorov [3], we take a nondimensional parameter

$$\eta=C_x\rho v^2 bY/2T \tag{4}$$

as the optimization value. Here, C_x is the drag coefficient of a cable which is perpendicular to water flow, Y is the depth of the rear end in relation to the front end, and T is the tension in the cable at the front end.

Using integral representation of the equilibrium equation for a flexible cable in water flow, as in Eames [2], we can write η as a functional (i.e., a function whose argument is itself a function) of $C_{2n}(\alpha_\tau)$:

$$\eta=\frac{\displaystyle\int_{\alpha_{\tau K}}^{\alpha_{\tau 0}}\frac{\sin u}{C_{1n}(u)-C_{2n}(u)}\exp\left[\int_u^{\alpha_{\tau 0}}\frac{C_{1\tau}(v)+\kappa(v)C_{2n}(v)}{C_{1n}(v)-C_{2n}(v)}dv\right]du}{\displaystyle\exp\int_{\alpha_{\tau K}}^{\alpha_{\tau 0}}\frac{C_{1\tau}(u)+\kappa(u)C_{2n}(u)}{C_{1n}(u)-C_{2n}(u)}du} \tag{5}$$

where $\alpha_{\tau 0}$ and $\alpha_{\tau K}$ are the angles between cable and flow direction at the rear and front ends respectively.

The value of $\alpha_{\tau 0}$ is determined by the direction of the force with which the hydrodynamic apparatus acts on the cable. Ultimately, $\alpha_{\tau 0}$ is the angle between this force and the flow direction. The value of $\alpha_{\tau K}$ is determined by cable length and for an arbitrary $\alpha_{\tau K}$ from interval $(0<\alpha_{\tau K}<\alpha_{\tau 0})$ we can find a cable length which corresponds to that. Because we are trying to find the optimal distribution of the load independent of the cable length we have to optimize η for any value of $\alpha_{\tau K}$. Therefore, $\alpha_{\tau 0}$ and $\alpha_{\tau K}$ do not depend upon C_{2n}, and the outer integrals in Eq. (5) have to be considered integrals with constant limits.

To simplify ''composition'' of Euler's equation let us introduce a new function $\Phi(u)$:

$$\Phi(u)=\frac{C_{1\tau}(u)+\kappa(u)C_{2n}(u)}{C_{1n}(u)-C_{2n}(u)} \tag{6}$$

and substituting $\Phi(u)$ into Eq. (5) gives us:

$$\eta=\int_{\alpha_{\tau k}}^{\alpha_{\tau 0}}\frac{[\kappa(u)+\Phi(u)]\sin u}{\kappa(u)C_{1n}(u)+C_{1\tau}(u)}\exp\int_u^{\alpha_{\tau K}}\Phi(v)\,dv\,du \tag{7}$$

This can be converted by a new change of the variable $G(u)=\int_u^{a_{\tau k}}\Phi(v)dv$ to classical form:

$$\eta=\int_{\alpha\tau\kappa}^{\alpha_{\tau 0}}\frac{[\kappa(u)-G'(u)]\sin u\,e^{G(u)}}{\kappa(u)C_{in}(u)+C_{1\tau}(u)}du=\int_{\alpha_{\tau K}}^{\alpha_{\tau 0}}\Pi(u,G,G')du \tag{8}$$

For this case, Euler's equation looks like:

$$\partial\Pi/\partial G-d(\partial\Pi/\partial G')/du=0.$$

It means that for functional η the Euler equation is:

$$e^{G(u)}\left[\frac{\kappa(u)\sin u}{C_{1n}(u)\kappa(u)+C_{1\tau}(u)}+\frac{d}{du}\,\frac{\sin u}{C_{1n}(u)\kappa(u)+C_{1\tau}(u)}\right]=0. \tag{9}$$

The expression in brackets does not depend on the optimized function $G(u)$, so the unique solution of Eq. (9) is $G(u)=-\infty$. It means that if u and $\alpha_{\tau 0}$ are finite, then

$$C_{2n}(\alpha_\tau)=C_{1n}(\alpha_\tau)$$

for every magnitude of an angle α_τ.

Therefore, the load of optimally distributed wings must balance the normal forces acting on the fairing. If the normal load acting on the cable becomes zero, the cable becomes a straight line. Hence, optimal configuration of the flexible cable in water flow is a straight line.

Now we have to define the optimal angle, α_τ, with which this line has to be inclined to water flow. If the cable is a straight line, the value η can be determined from the simple formula

$$\eta=\frac{C_x \sin \alpha_\tau}{C_{1\tau}(\alpha_\tau)+C_{2\tau}(\alpha_\tau,\alpha_f,W)} \tag{10}$$

where here η is not a functional, but a function of three arguments α_τ, α_f, and W. Equation (10) flows from the two obvious expressions for T and Y of the straight cable:

$$Y=L\sin\alpha_\tau$$

$$T=(C_{1\tau}+C_{2\tau})v^2bL/2.$$

Let us define the relative extreme of this function under the condition

$$C_{1n}(\alpha_\tau)=C_{2n}(\alpha_\tau,\alpha_f,W).$$

Using La Grange's method of indeterminate coefficients we can have the system of four equations,

$$\begin{gathered} C_{1n}-C_{2n}=0 \\ \partial\eta/\partial\alpha_f=\lambda\,\partial(C_{1n}-C_{2n})/\partial\alpha_f \\ \partial\eta/W=\lambda\,\partial(C_{1n}-C_{2n})/\partial W \\ \partial\eta/\partial\alpha_\tau=\lambda\,\partial(C_{1n}-C_{2n})/\partial\alpha_\tau \end{gathered} \tag{11}$$

with four unknown variables α_τ, α_f, W and the undetermined coefficient λ. It is easy to see that

$$\partial C_{1n}/\partial\alpha_f=0 \quad \text{and} \quad \partial C_{1n}/\partial W=0. \tag{12}$$

Based on Eq. (2) and Eq. (10) we can write the following:

$$\partial C_{2n}/\partial W=C_{2n}/W; \quad \text{and} \quad \partial\eta/\partial W=-\eta^2C_{2\tau}/(C_xW\sin\alpha_\tau). \tag{13}$$

The third equation of the Eq. System (11) gives us

$$\lambda=\eta^2C_{2\tau}/(C_xC_{2n}\sin\alpha_\tau). \tag{14}$$

Using Eq. (12) and Eq. (14) we can rewrite the second equation of Eq. System (11) in the following form

$$\partial C_{2\tau}/\partial\alpha_f-(C_{2\tau}/C_{2n})(\partial C_{2n}/\partial\alpha_f)=0. \tag{15}$$

Taking into account the relationship between angles α_τ, α_f, and α_W in Eq. (1) we will get

$$\partial C_{2\tau}/\partial\alpha_f=\partial C_{2\tau}/\partial\alpha_w \quad \text{and} \quad \partial C_{2n}/\partial\alpha_f=\partial C_{2n}/\partial\alpha_w$$

and it means that Eq. (15) is equivalent to the condition

$$d(C_{yw}/C_{xw})/d\alpha_w=0. \tag{16}$$

In other words the little wings have to be arranged under the angle of attack ensuring maximal aerodynamic efficiency. If we call this angle α_{ME} we can write down

$$\alpha_f=\alpha_{ME}+\alpha_\tau. \tag{17}$$

Since κ is a function of only α_τ we can write

$$\kappa=\frac{K_M\sin\alpha_\tau+\cos\alpha_\tau}{K_M\cos\alpha_\tau-\sin\alpha_\tau},$$

where

$$K_M=C_{yw}(\alpha_{ME})/C_{xw}(\alpha_{ME}).$$

If deepening is realized only by the cable weight-in-water, $K_M=\infty$ and $\kappa=\tan\alpha_\tau$. Using the first equation of Eq. System (11) and the expression in Eq. (2) we can define W as:

$$W=\frac{C_{1n}(\alpha_\tau)}{C_{yw}(\alpha_{ME})\cos\alpha_\tau-C_{xw}(\alpha_{ME})\sin\alpha_\tau}. \tag{18}$$

Thus, we have expressed all unknown variables of Eq. System (11) as functions of α_τ and now we will define α_τ out of the last equation of system (11). Substituting Eq. (14) into the last equation of Eq. System (11), and using Eq. (10), we can arrive at:

$$\begin{aligned} &C_{2n}\partial C_{2\tau}/\partial\alpha_\tau-C_{2\tau}\partial C_{2n}/\partial\alpha_\tau+C_{2n}\partial C_{1\tau}/\partial\alpha_\psi+C_{2\tau}\partial C_{1n}/\partial\alpha_\tau \\ &\quad =C_{2n}(C_{1\tau}+C_{2\tau})\cot\alpha_\tau. \end{aligned} \tag{19}$$

Considering Eq. (1), we will write down the following expressions:

$$\partial C_{2n}/\partial\alpha_\tau=-\partial C_{2n}/\partial\alpha_f+\partial\widetilde{C}_{2n}/\partial\alpha_\tau$$

and (20)

$$\partial C_{2\tau}/\partial\alpha_\tau=-\partial C_{2\tau}/\partial\alpha_f+\partial\widetilde{C}_{2\tau}/\partial\alpha_\tau$$

where the sign ~ means that a derivative is calculated based on the assumption that C_{xw} and C_{yw} do not depend on α_τ. Differentiating Eq. (2) with respect to α_τ on the condition that C_{xw} and C_{yw} do not depend on α_τ, we have:

$$\partial\widetilde{C}_{2n}/\partial\alpha_\tau=(-C_{yw}\sin\alpha_\tau-C_{xw}\cos\alpha_\tau)W,$$

and

$$\partial\widetilde{C}_{2\tau}/\partial\alpha_\tau=(C_{yw}\cos\alpha_\tau-C_{xw}\sin\alpha_\tau)W.$$

Using Eqs. (15) and (20) it is possible to get the following

$$C_{2n}\partial C_{2\tau}/\partial\alpha_\tau-C_{2\tau}\partial C_{2n}/\partial\alpha_\tau=C_{2n}\partial\widetilde{C}_{2\tau}/\partial\alpha_\tau-C_{2\tau}\partial\widetilde{C}_{2n}/\partial\alpha_\tau.$$

Whence:

$$\begin{aligned} C_{2n}\partial C_{2\tau}/\partial\alpha_\tau-C_{2\tau}\partial C_{2n}/\partial\alpha_\tau&=(C_{xw}^2+C_{yw}^2)W^2 \\ &=(C_{2n})^2+(C_{2\tau})^2. \end{aligned}$$

Using the above expression and the first equation of Eq. System (11) we will rearrange Eq. (19) to the following:

$$\begin{aligned} &dC_{1\tau}/d\alpha_\tau+\kappa(\alpha_\tau)dC_{1n}/d\alpha_\tau+C_{1n}(\alpha_\tau)[1+\kappa^2(\alpha_\tau) \\ &\quad -\kappa(\alpha_\tau)\cot\alpha_\tau]-C_{1\tau}(\alpha_\tau)\cot\alpha_\tau=0. \end{aligned} \tag{21}$$

Since all terms of Eq. (21) depend just on α_τ, Eq. (21) is a transcendental equation with one unknown variable α_τ. The solution of this equation, along with α_f from Eq. (17) and W from Eq. (18), completely defines the optimized parameters of equilibrium, and solves the problem set up in this article.

To illustrate the solution, we consider it for the special case when coefficients C_{1n} and $C_{1\tau}$ depend on α_τ in the following way, as described by Gorshkov [4]:

$$\begin{gathered} C_{1n}=C_\Phi\sin^2\alpha_\tau+C_f\sin\alpha_\tau; \\ C_{1\tau}=C_f\cos\alpha_\tau; \\ C_x=C_\Phi+C_f \end{gathered} \tag{22}$$

where C_Φ and C_f are constants. Using Eq. (22) to define the derivatives $dC_{1\tau}/d\alpha_\tau$ and $dC_{1n}/d\alpha_\tau$, we can substitute them in Eq. (21) and finally get the quadratic equation. The unknown variable in this equation is the ratio $C_{2\tau}/C_{1n}$.

We can write down the solution of the quadratic equation as follows:

$$C_{2\tau}/C_{1n}=\kappa(\widetilde{C}_f,\alpha_\tau)=1/2[\cot(\alpha_\tau)-f(\widetilde{C}_f,\alpha_\tau)+\sqrt{(\cot\alpha_\tau-f(\widetilde{C}_f,\alpha_\tau))^2-4[1-2\widetilde{C}_ff(\widetilde{C}_f,\alpha_\tau)/(\sin 2\alpha_\tau(2\sin\alpha_\tau+\widetilde{C}_f))]}], \tag{23}$$

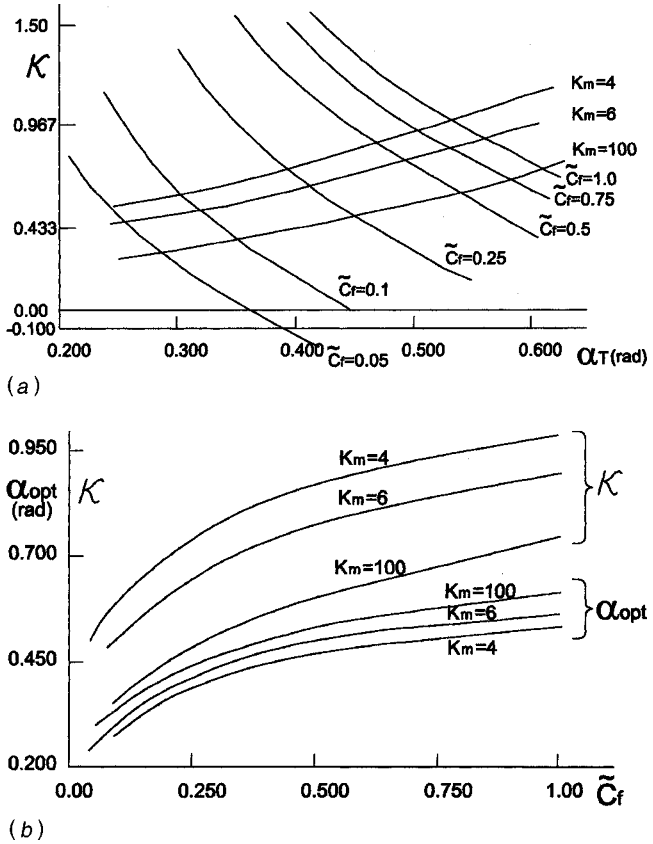

Fig. 2 (*a*) **Graphic representation of Eq. (23) and (24); (*b*) plot of α and κ as functions of C_f and K_M**

where $\tilde{C}_f = C_f/C_\Phi$, and

$$f(\tilde{C}_f,\alpha_\tau)=\frac{\sin 2\alpha_\tau+\tilde{C}_f\cos\alpha_\tau}{\sin\alpha_\tau(1+\tilde{C}_f)}.$$

On the other hand, using the first equation of Eq. System (11), we can state

$$C_{2\tau}/C_{1n}=\kappa(\alpha_\tau,K_M). \tag{24}$$

Having the right parts of Eqs. (23) and (24) equal, we will get an equation for defining α_τ. Figure 2(*a*) is a graphic representation of the solution for the above defined equation. There are two families of curves F and κ as functions of α_τ. Different curves F correspond to different values of $\tilde{C}_f$ and different curves κ correspond to different values of K_M. Each intersection point determines the value of $\alpha_{\text{opt}}=\alpha_\tau$ at predetermined values of $\tilde{C}_f$ and K_M. Figure 2(*b*) represents a plot of the functions $\alpha_{\text{opt}}(\tilde{C}_f)$ and $\kappa_{\text{opt}}(\tilde{C}_f)$ for different K_M. If we know α_τ and κ, we can define the corresponding α_f and W and also the maximum value η using the formula

$$\eta=[(1+\tilde{C}_f)\sin\alpha_\tau]/[\tilde{C}_f\cos\alpha_\tau+\kappa(\sin\alpha_\tau+\tilde{C}_f\sin\alpha_\tau)] \tag{25}$$

which can be easily obtained from Eqs. (10), (22), and (24).

Figure 3 shows the dependence η and α_{opt} of $\tilde{C}_f$ under different values of K_M as a solid curve. The dotted curve is η calculated for the situation when the deflection of the cable is accomplished by setting a deepening apparatus or concentrated weight on the rear end of the cable. The dotted curve is created under the assumptions that Eq. System (22) is right, the apparatus forms only deepening force (i.e., its hydrodynamic resistance equals zero), and the weight-in-water of the cable is equal to zero. The optimization in this case is made by the approach described in Egorov [3]. All the curves on Fig. 3 are shown in logarithmic scale.

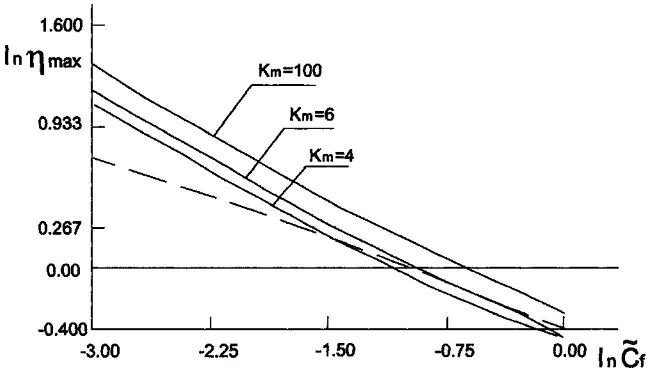

Fig. 3 Maximum value of η

The points of intersection of the dotted curve with the continuous curves give us a bound value of $\tilde{C}_f$ for different K_M. If $\tilde{C}_f$ is less than this value, using a distributed load is more beneficial than a concentrated one. The benefit which we can get using a distributed load is defined by the ratio of η_d/η_c, where η_d is η for a distributed load, and η_c is η for a concentrated one.

All the above results are also true for a cable with no wings or special deepening apparatus at the end but which has an additional weight-in-water. So we can say that the best distribution of added weight-in-water along the cable is a uniform distribution $g(S)=g=\text{const}$. For this case, $K_M=\infty$ because the force of weight-in-water is always directed vertically, and so $\kappa=\tan\alpha_\tau$. Seeing that, we can rewrite Eq. (25) for this case in the form

$$\eta=[(1+\tilde{C}_f)\sin 2\alpha_\tau]/[2(\tilde{C}_f+\sin^3\alpha_\tau)],$$

and the equation for determination of α_{opt} in the form

$$\tilde{C}_f=\sin^3\alpha_\tau(1+\cos^2\alpha_\tau)/\cos 2\alpha_\tau. \tag{26}$$

For cables with a round profile (the ones without fairing), $\tilde{C}_f=0.015-0.025$. In the book of V. I. Egorov [3] the author points out that for a round cable $C_f=0.022$ and $C_\Phi=1.8$; this means that $\tilde{C}_f=0.012$. But tests which were carried out on long segments of cables in the Soviet Union later showed that C_f is greater, and for a cable which has a small angle of attack, C_Φ can be less, so that $\tilde{C}_f=0.015$–0.025. Knowing this and using Eq. (26) we can determine α_{opt} for that case and get $\alpha_{\text{opt}}=11$–13 deg. It is not difficult to show that for a round cable which has a diameter d the optimal weight-in-water, if speed of towing is v, is approximately $g_{\text{opt}}=(33$–$47)v^2d$, where g_{opt} is in N, v is in m/s, and d is in m. Here, and below, g is the complete weight-in-water of the cable.

Each towing cable which does not bear an apparatus makes a straight line. The angle between this line and the flow direction is called the critical angle. So the result we have now is that the optimal added weight-in-water should make the critical angle equal to the optimal one; for a round cable it is 11–13 deg. In other words, by making the cable heavier, or lighter if necessary, we can improve the capability of the towing system. For example, we can reach a higher velocity of towing if the depth of the rear end does not vary.

Example #1. Let us take a round cable with $b=d=0.025$ m, and let $T=100{,}000$ N, $v=5$ m/s, $C_\Phi=1.8$, and $C_f=0.03$; then $\tilde{C}_f=0.017$. For this $\tilde{C}_f$ we can define $\alpha_{\tau\text{opt}}=0.2015$, and $\eta=7.97$, so $Y_{\max}=1390$ m, and to have this we need to have $g_{\text{opt}}=24$ N/m.

For comparison, let us calculate $Y_{\max}$ for the same initial data but under the condition that cable deepening is accomplished by the special apparatus on its end. For that calculation, we can use the equilibrium formulas from Egorov [3] which are appropriate for a weightless cable. If the hydrodynamic load is defined by Eq. (22) and the apparatus yields a force acting in the vertical direction, the equilibrium formulas can be written as follows:

$$Y_c = T/r \ln[\cot(\alpha_\tau/2)]\{\sin\alpha_\tau/[\sin\alpha_\tau(1-\tilde{C}_f)+\tilde{C}_f]\};$$

$$L_c = T/r \cot\alpha_\tau\{\sin\alpha_\tau/[\sin\alpha_\tau(1-\tilde{C}_f)+\tilde{C}_f]\};$$

and (27)

$$\eta_c = \ln[\cot(\alpha_\tau/2)]\{\sin\alpha_\tau/[\sin\alpha_\tau(1-\tilde{C}_f)+\tilde{C}_f]\}$$

where $r = 0.5Cx\rho v^2 b$ and α_τ is the angle of attack of the front cable end.

Using Eq. (27) we can calculate that $\alpha_{\tau\text{opt}} = 0.05$, $\eta_c = 2.79$, and $Y_{c\,\max} = 487$ m. If the cable had weight-in-water not equal to zero, the result would be even worse: for $g = 13$ N/m and the optimal weight on the cable end, $Y_{c\,\max} = 310$ m. So, using a distributed load we can increase $Y_{\max}$ by 2.7 times. It is pertinent to remark here that the ''optimal'' critical angle is not the best one for a practical use. If we increase the angle 3–5 degrees, the Y which can be reached will be, of course, less than $Y_{\max}$ but only about 7–15 percent less, still much more than $Y_{c\,\max}$, but L will be lower by 26–40 percent.

Example #2. As an example, let us calculate S_w for the cable with fairing with the following characteristics: $C_x = 0.15$, $C_f = 0.05$, $C_\Phi = 0.1$ and then $\tilde{C}_f = 0.5$. Let the wings be rectangular with chord $b_w = 0.8b$ and $\lambda_w = 2$ and have a profile like a circle arc with $f = 0.1$. For a wing like this, $\alpha_{ME} = 5$, $K_M = 6.5$, $C_{yw}(\alpha_{ME}) = 0.85$, and $C_x(\alpha_{ME}) = 0.13$. For $\tilde{C}_f = 0.5$ and $K_M = 6.5$, from Fig. 3 we can find that $\alpha_{\text{opt}} = 0.525 = 30$ deg. Using Eq. (22) we define that $C_{1n}(\alpha_{\text{opt}}) = 0.05$. From Eq. (18) and putting $\alpha_\tau = \alpha_{\text{opt}}$ we will get $W = 0.75$. The value of S_w we can find now from Eq. (3) if we take into consideration that $F_w = \lambda_w(b_w)^2$. The result of calculations is that $S_w = 17b$; that is to say, the optimal distance between two neighboring wings should be equal to 17 chords of the fairing.

Conclusions

(a) Optimal distribution of a deepening load is a uniform load. It means that wings should be located uniformly and a cable would be a straight line in water flow.

(b) Use of the distributed deepening load can be beneficial in comparison with a concentrated force applied at the end of the cable, in the case of a relatively poorly streamlined form of the cable. In particular, a distributed load is right for a round cable.

(c) For each round cable with a certain diameter and strength, there is an optimal weight-in-water which ensures the maximum depth of the rear cable end. The amount of the optimal weight-in-water depends on the tow speed. The optimal critical angle of any round cable is 11–13 degrees.

Nomenclature

b = chord of a fairing (m)
b_w = chord of a wing (m)
C_f = friction coefficient of a fairing
C_ϕ = form coefficient of a fairing
$\tilde{C}_f$ = comparative friction coefficient of a fairing
C_{1n} = normal hydrodynamic coefficient of a fairing
$C_{1\tau}$ = tangent hydrodynamic coefficient of a fairing
C_{2n} = normal hydrodynamic coefficient of a wing
$C_{2\tau}$ = tangent hydrodynamic coefficient of a wing
C_x = drag coefficient of the cable which is perpendicular to water flow
C_{xw} = drag coefficient of a wing
C_{yw} = lift coefficient of a wing
d = diameter of a round cable (m)
F_w = wing plan area (m^2)
f = circle arc of a wing
$f(\tilde{C}_f, \alpha_\tau)$ = ancillary function in Eq. (23)
$G(u)$ = ancillary function in Eq. (8)
$g(s)$ = weight-in-water of the cable's unit (N/m)
g_{opt} = optimal amount of g (N/m)
k_m = maximal aerodynamic efficiency of a wing
L = length of the cable (m)
L_c = length of the cable with deepening apparatus (m)
r = $.5C_x\rho v^2 b$ (N/m)
R_{1n} = normal force acting on a segment of the cable (N)
$R_{1\tau}$ = tangent force acting on a segment of the cable (N)
R_{2n} = normal force acting on a wing (N)
$R_{2\tau}$ = tangent force acting on a wing (N)
S = coordinate of a point, i.e., the distance to this point from front end along the cable (m)
S_w = distance between two nearest wings (m)
T = tension in the cable at the front end (N)
W = F_w/bs_w
Y = depth of the rear end of the cable (m)
Y_c = depth of the rear end of the cable with apparatus (m)
$Y_{c\,\max}$ = maximal depth of the rear end of the cable with apparatus (m)
Y_m = maximal depth of the rear end of the cable (m)
α_f = rigging angle of incidence
α_{ME} = angle of maximal aerodynamic efficiency
α_τ = angle of a fairing
$\alpha_{\tau K}$ = angle of a fairing on its front end
$\alpha_{\tau 0}$ = angle of a fairing on its rear end
α_{opt} = optimal angle of a fairing
α_w = angle of attack of a wing
κ = $C_{2\tau}/C_{2n}$
κ_{opt} = optimal amount of κ
λ = indeterminate coefficient
ρ = mass density of water (kg/m^3)
η = optimization value
η_c = maximal amount of η for the cable deepened by the apparatus
η_d = maximal amount of η for the cable deepened by the distributed load

References

[1] Juravlev, V. F., Puzyrev, G. V., and Tilman A. X., 1968, ''Underwater Towing Systems,'' Sudostroenie, **11**, pp. 12–17, in Russian.

[2] Eames, M., 1968, ''The Steady-State Theory of Towing Cables,'' Quart. Trans. R. Inst. Naval Arch., **109**, pp. 185–206.

[3] Egorov, V. I., 1981, ''Underwater Towing Systems,'' Sudostroenie, **96**, pp. 236–240, in Russian.

[4] Gorshkov, A. S., 1969, ''A Generalization of A. N. Krylov's Formulas for Calculation of Tension and Form of a Flexible Cable in the Flow,'' Oceanology, **6**, pp. 29–33, in Russian.

Turbulent Mixing, Viscosity, Diffusion, and Gravity in the Formation of Cosmological Structures: The Fluid Mechanics of Dark Matter

C. H. Gibson
Professor,
Departments of MAE and SIO, Center for
Astrophysics and Space Sciences,
University of California at San Diego,
La Jolla, CA 92093-0411
e-mail, website: cgibson@ucsd.edu,
http://www-acs.ucsd.edu/~ir118

Self-gravitational structure formation theory for astrophysics and cosmology is revised using nonlinear fluid mechanics. Gibson's 1996–2000 theory balances fluid mechanical forces with gravitational forces and density diffusion with gravitational diffusion at critical viscous, turbulent, magnetic, and diffusion length scales termed Schwarz scales. Condensation and fragmentation occur for scales exceeding the largest Schwarz scale rather than L_J*, the length scale introduced by Jeans in his 1902 inviscid-linear-acoustic theory. The largest Schwarz scale is often larger or smaller than* L_J*. From the new theory, the inner-halo* $(10^{21}\,\mathrm{m})$ *dark-matter of galaxies comprises* $\sim 10^5$ *fossil-*L_J*-scale clumps of* 10^{12} *Earth-mass fossil-*L_{SV}*-scale planets called primordial fog particles (PFPs) condensed soon after the cooling transition from plasma to neutral gas, 300,000 years after the Big Bang, with PFPs tidally disrupted from their clumps forming the interstellar medium. PFPs explain Schild's 1996 ''rogue planets . . . likely to be the missing mass'' of a quasar lens-galaxy, inferred from twinkling frequencies of the quasar mirages, giving 30 million planets per star. The non-baryonic dark matter is super-diffusive and fragments at large* L_{SD} *scales to form massive outer-galaxy-halos. In the beginning of structure formation 30,000 years after the Big Bang, with photon viscosity values* ν *of* $5\times 10^{26}\,\mathrm{m^2\,s^{-1}}$*, the viscous Schwarz scale matched the horizon scale* $(L_{SV}\approx L_H<L_J)$*, giving* $10^{46}\,\mathrm{kg}$ *proto-superclusters and finally* $10^{42}\,\mathrm{kg}$ *proto-galaxies. Non-baryonic fluid diffusivities* $D\sim 10^{28}\,\mathrm{m^2\,s^{-1}}$ *from galaxy-outer-halo* (L_{SD}) *scales* $(10^{22}\,\mathrm{m})$ *measured in a dense galaxy cluster by Tyson, J. A., and Fischer, P., 1995, ''Measurement of the Mass profile of Abell 1689,'' Ap. J., 446, pp. L55–L58, indicate non-baryonic dark matter particles must have small mass* $(\sim 10^{-35}\,\mathrm{kg})$ *to avoid detection.*

[S0098-2202(00)01504-2]

Keywords: Turbulence, Mixing, Fluid Mechanics, Gravitational Instability, Cosmology, Astrophysics

Introduction

Information about the early universe has been flooding in with spectacular resolution from bigger and better telescopes on earth, on high altitude balloons, and in space, covering spectral bands previously unobservable. The 1989 COsmic Background Explorer (COBE) satellite and the other instruments reveal a color photograph of the universe as it existed 300,000 years after the hot Big Bang when the cooling opaque plasma formed a transparent H-He gas. Hubble Space Telescope (HST) images show evolved structures earlier than expected from standard linear cosmological models of Weinberg [1], Zel'dovich and Novikov [2], Silk [3,4], Kolb and Turner [5], Peebles [6], Padmanabhan [7], and Rees [8]. However, the most remarkable conclusion from all these observations of galaxies and galaxy clusters is that 99% or more of the matter is not in stars but is in unknown ''dark matter'' forms. What is this dark matter? From measured ratios of the light elements (H, D, He, Li) and nucleosynthesis theory of the Big Bang, only 4% or less of the total mass in a ''flat'' universe can be ordinary ''baryonic'' matter that interacts by the strong force, comprised of protons and neutrons in atoms and plasmas. The remaining 96% is truly exotic as an engineering fluid because it has the ghostly behavior of neutrinos that interact by the weak force, and may indeed be neutrinos. Most of the energy of the 1987 southern hemisphere supernova was radiated by a powerful neutrino blast wave that passed through the earth as though it wasn't there, producing only a handful of collisions in great pools of water and cleaning fluid buried under mountains in the northern hemisphere that serve as neutrino detectors. Several neutrino species have been identified and some of their mass differences have been measured; so that presently, neutrinos are the only known form of non-baryonic dark matter. Dozens of nonbaryonic particles have been proposed but none detected in a new discipline, termed astro-particle-physics, whose major goal is the solution of the non-baryonic dark matter problem. Gibson [9] suggests that many aspects of the dark matter paradox of astrophysics and cosmology may be resolved by a better job of fluids engineering. When was the first turbulence? What was the viscosity? Won't the weakly collisional non-baryonic dark matter have a large diffusivity that dominates and delays its gravitational instability, independent of its temperature and sound speed? Won't this render concepts like cold and hot dark matter obsolete? Present cosmology relies on Jeans's 1902 inviscid linear theory that reduces the problem of structure formation by gravity to one of gravitational acoustics.

In the following we review two theories of gravitational insta-

---

Contributed by the Fluids Engineering Division for publication in the JOURNAL OF FLUIDS ENGINEERING. Manuscript received by the Fluids Engineering Division June 15, 1999; revised manuscript received June 12, 2000. Associate Technical Editor: S. Banerjee.

bility. The linear acoustic Jeans theory is strongly modified by a nonlinear theory based on the mechanics of real fluids. Cosmological differences between the theories are discussed, and comparisons are made with observations. Finally, a summary and conclusions are provided.

Problems With Jeans's Theory

Jeans's [10] theory of self-gravitational instability poorly describes this highly nonlinear phenomenon because its truncated momentum-mass equations and linear perturbation stability analysis exclude turbulence, turbulent mixing, viscous, Coriolis and magnetic forces, and molecular and gravitational diffusivity. In fluid mechanics it is well known that linear theories may give vast errors when applied to nonlinear processes. For example, neglect of the inertial-vortex forces in the Navier Stokes equations gives constant laminar flow velocity profiles that are independent of time and Reynolds number, contrary to observations that such flows always become turbulent when the Reynolds number exceeds a critical value. It is argued by Gibson [9,11–16] that the dark matter paradox is one of several cosmological misconceptions resulting from the application of Jeans's instability criterion to the development of structure by gravitational forces in the early universe.

Jeans's [10] theory predicts only acoustic instabilities, where sound waves of wavelength λ require a time λ/V_S to propagate a distance of one wavelength and gravitational response requires a free fall time of $(\rho G)^{-1/2}$, with ρ the density, G Newton's constant of gravitation, and V_S the speed of sound. Sound waves provide density nuclei for condensation and fragmentation for wavelengths $\lambda \geqslant \mathrm{L_J}$ by setting these two times equal to each other, so the Jeans criterion for gravitational instability of density perturbations on scale L is $\mathrm{L} \geqslant \mathrm{L_J} \equiv V_S/(\rho \mathrm{G})^{1/2}$. By the Jeans theory all density nuclei propagate with velocity V_S as sound waves. Waves with $\lambda \leqslant \mathrm{L_J}$ move away before gravity can act.

However, most density nuclei in natural fluids are nonacoustic, drifting with the local fluid speed $v \approx 0$ rather than V_S. Such density extrema generally result from turbulent scrambling of temperature and chemical species gradients, which produce density fluctuations $\delta\rho/\rho$ much larger than acoustic levels. The reference pressure fluctuation δp for sound in air is $2 \times 10^{-5}\,\mathrm{kg/m\,s^2}$, corresponding to $\delta T/T$ of 6×10^{-11} and $\delta\rho/\rho$ of 1.4×10^{-10}. Measurements by COBE of the cosmic microwave background (CMB) show $\delta T/T$ is $\sim 10^{-5}$. This small value proves the primordial plasma was not strongly turbulent, but it is large enough to make any acoustic interpretation (e.g., Hu [17]) highly questionable. Maximum local $\delta T/T \sim 10^{-4}$ values of 124 dB mapped by the BOOMERanG telescope (de Bernardis et al. [18]) nearly match those for the 125 dB sonic threshold of pain.

Because no local sources of sound existed in the hot plasma epoch, viscous damping was strong with short viscous attenuation lengths $V_s\lambda^2/\nu$, and because BOOMERanG δT spectra show small or nonexistent harmonic ''sonic'' peaks it seems likely that all $\delta T/T$ fluctuations measured are nonacoustic. The observed spectral peak at subhorizon scales $\mathrm{L} < \mathrm{L_H}$ is more likely a fossil of the first gravitational structure, Gibson [9], nucleated by fossils of Big Bang ''turbulent'' δT mixing in the quantum gravitational dynamics (QGD) epoch. QGD mixing is between a chaotic source of the space-time-energy (and δT) of the universe at the Planck temperature $T_P = (c^5 h/\mathrm{G}k^2)^{1/2} \approx 10^{32}\ K$, Planck length scale $\mathrm{L_P} = (h\mathrm{G}/c^3)^{1/2} \approx 10^{-35}\,\mathrm{m}$ and Planck time $t_P = (h\mathrm{G}/c^5)^{1/2} \approx 10^{-43}\,\mathrm{s}$ terminated by the strong force freeze-out temperature $10^{28}\,\mathrm{K}$ at $10^{-35}\,\mathrm{s}$ and $10^{-27}\,\mathrm{m}$, with inflation by a factor of 10^{49} to the fossil Planck scale $10^{14}\,\mathrm{m}$ and fossil strong force horizon $\mathrm{L_H} = 10^{22}\,\mathrm{m}$ (see website http://www-acs.ucsd.edu/~ir118 for figures). The intermediate QGD ''turbulence'' δT spectrum $k^2\phi_T = \beta\chi\varepsilon^{-1/3}k^{1/3}$ (not the Harrison-Zel'dovich spectrum $\phi_T \sim k^{-3}$) is fossilized by inflation (Guth [19]) stretching the fluctuations outside their scales of causal connection, where χ and ε are dissipation rates of temperature and velocity variance that represent rates of entropy production at the beginning of inflation.

According to the turbulent mixing theory of Gibson [20], constant density surfaces move with the local fluid velocity except for their velocity $-\vec{r}D\nabla^2\rho/|\nabla\rho|$ with respect to the fluid due to molecular diffusion D, where $\vec{r}$ is a unit vector in the direction of the density gradient. The scale of the smallest density fluctuation is set by an equilibrium between this diffusion velocity D/L and the convection velocity γL at distances L away from points of maximum and minimum density, giving the Batchelor scale $\mathrm{L_B} \equiv (\mathrm{D}/\gamma)^{1/2}$ independent of the ratio $\mathrm{Pr} \equiv \nu/\mathrm{D}$, where γ is the local rate-of-strain and ν is the kinematic viscosity. This prediction has been confirmed by measurements in air, water and mercury for $0.02 \leqslant \mathrm{Pr} \leqslant 700$ and by numerical simulations at smaller $\mathrm{Re} \approx 2500$ for $10^{-2} \leqslant \mathrm{Pr} \leqslant 1$, Gibson et al. [21]. Even if gravitational condensation of mass were to take place on a sound wave moving in a stationary fluid, it would immediately produce a nonacoustic density maximum from the conservation of momentum. Since the ambient condensing fluid is not moving, its momentum (zero) would immediately dominate the tiny momentum of the sound wave crest.

Gibson [9] shows that gravitational fragmentation at a non-acoustic density minimum or condensation on a non-acoustic density maximum is limited by viscous or turbulent forces at either the viscous Schwarz scale $\mathrm{L_{SV}} \equiv (\gamma\nu/\rho\mathrm{G})^{1/2}$ or the turbulent Schwarz scale $\mathrm{L_{ST}} \equiv \varepsilon^{1/2}/(\rho\mathrm{G})^{3/4}$, whichever is larger, where ε is the viscous dissipation rate of the turbulence. For the super-diffusive non-baryonic dark matter that constitutes most of mass of the universe, the diffusive Schwarz scale $\mathrm{L_{SD}} \equiv [\mathrm{D}^2/\rho\mathrm{G}]^{1/4}$ limits instability. The criterion for gravitational instability at scale L is thus $L \geqslant \mathrm{L_{SX\,max}} = \max[\mathrm{L_{SV}}, \mathrm{L_{ST}}, \mathrm{L_{SD}}]$, where only viscous and turbulent forces are assumed to prevent instability in the early universe (magnetic forces are negligible) for the baryonic matter, and $\mathrm{L_{SD}}$ sets the maximum scale for fragmentation of the non-baryonic matter $(\gamma < [\rho\mathrm{G}]^{1/2})$. Because the universe is expanding, the largest scale structures form by fragmentation, which is assisted by the expansion, rather than condensation which is resisted.

$\mathrm{L_{SD}} \equiv [\mathrm{D}^2/\rho\mathrm{G}]^{1/4}$ is derived by setting the diffusion velocity D/L equal to the gravitational velocity $\mathrm{L}(\rho\mathrm{G})^{1/2}$. The diffusivity D of a gas is the particle collision length 1 times the particle velocity v. If $1 \geqslant \mathrm{L_H}$ the particle is considered collisionless and more complex methods are required using the collisionless Boltzmann equation and general relativity theory. Density perturbations in collisionless species are subject to Landau damping, also termed collisionless phase mixing or free streaming, Kolb and Turner [[5] p. 351]. The free-streaming length $\mathrm{L_{FS}}$ is about $10^{24}\,\mathrm{m}$ for neutrinos assuming a neutrino mass of $10^{-35}\,\mathrm{kg}$ corresponding to that required for a flat universe, giving an effective diffusivity of $3 \times 10^{35}\,\mathrm{m^2\,s^{-1}}$ from $\mathrm{L_{SD}}$. Thus if neutrinos are the missing non-baryonic mass and collisionless, they are irrelevant to structure formation until $\mathrm{L_{FS}} = \mathrm{L_H}$ at $\sim 10^8$ years. From observations and $\mathrm{L_{SD}}$ it appears that whatever the non-baryonic fluid may be, its diffusivity D is too small for its particles to be collisionless but too large for them to have the mass of any known particles besides neutrinos or they would have been observed.

In the early universe, the sound speed V_S was large because of the high temperatures, and horizon scale Reynolds numbers $\mathrm{Re} \approx c^2 t/\nu$ were small because the viscosity ν was large and t was small. Therefore, $\mathrm{L_{SV}}$ and $\mathrm{L_{ST}}$ were both smaller than $\mathrm{L_J}$, giving sub-Jeans-mass fragments in this period of time. From linear cosmology, no such fragmentation is possible with $t \leqslant 300{,}000$ years ($10^{13}\,\mathrm{s}$) in the plasma epoch following the Big Bang because $\mathrm{L_J} > \mathrm{L_H} \equiv \mathrm{ct}$. No structures can form by causal processes on scales larger than $\mathrm{L_H}$ because the speed of information transfer is limited by the speed of light c. Star formation is prevented by the Jeans criterion until the Jeans mass $\mathrm{M_J} = (\mathrm{RT}/\rho\mathrm{G})^{3/2}\rho$ decreases below a solar mass as the temperature of the universe decreases, but this requires $\sim 10^8$ years contrary to recent observations showing not only stars but galaxies and galaxy clusters existed at the earliest times observable; that is, at times $t < 10^9$ years with redshifts z of 4 and larger. By the present nonlinear theory, viscous and turbulent forces permit fragmentations beginning at about 30,000 years ($t = 10^{12}$ s, $z = 4000$) when decreasing L_{SV} values first match the increasing horizon scale L_H with rate of strain $\gamma = 1/t$ and ν values more than $10^{26}\ m^2\ s^{-1}$, Gibson [11,12]. At this time the horizon mass $L_H{}^3\rho$ equaled the Schwarz viscous mass $M_{SV} = L_{SV}{}^3\rho$ at the observed supercluster mass of 10^{46} kg, Kolb and Turner [5], the largest structure in the universe. Density as a function of time can be computed from Einstein's equations of general relativity assuming a flat universe with kinetic energy always just matching gravitational potential energy, Weinberg ([1], Table 15.4). The horizon Reynolds number c^2t/ν therefore was ~ 150, near the turbulent transition value.

This enormous $\nu = 10^{26}\ m^2\ s^{-1}$ can be explained as due to photon collisions with electrons of the plasma of H and He ions by Thomson scattering, with Thomson cross section $\sigma_T = 6.7 \times 10^{-29}\ m^2$. Fluctuations of plasma velocity are smoothed by the intense radiation since the ions remain closely coupled to the electrons by electric forces. We can estimate the kinematic viscosity $\nu \approx lc = 5\times 10^{26}\ m^2\ s^{-1}$ using a collision length l of 10^{18} m from $l = 1/\sigma_T n$, with number density n of electrons about $10^{10}\ m^{-3}$ assuming the baryon (ordinary) matter density is 10^{-2} less than the critical density $\rho_C = 10^{-15}\ kg\ m^{-3}$ at the time ($\rho_C = 10^{-26}$ at present), from Weinberg [1]. Between 30,000 years and 300,000 years during the plasma epoch of the universe the temperature decreased from 10^5 to 3000 K, decreasing the viscosity ν for the baryonic matter with its expansion gravitationally arrested at $\rho = 10^{-17}\ kg\ m^{-3}$, and decreasing the viscous Schwarz scale L_{SV} of condensation due to decreases in both ν and γ. The final fragmentation mass by this scenario is about 10^{42} kg, the mass of a galaxy. As mentioned, the primordial plasma was not strongly turbulent from CMB observations of $\delta T/T \sim 10^{-5}$. If the flow were strongly turbulent, $\delta T/T$ values would be 3–4 orders of magnitude larger. Gravitational structure formation results in suppression of turbulence by buoyancy forces within the structures, Gibson [22].

Because the non-baryonic matter decouples from the fragmenting baryonic plasma by lack of collisional mechanisms while $L_{SD} \geqslant L_H$, it diffuses to fill the expanding proto-voids between the proto-superclusters, proto-clusters, and proto-galaxies developed during the plasma epoch, suppressing the gravitational driving force. The average density of galaxies of $10^{-21}\ kg\ m^{-3}$ today is 10^4 less than the initial protogalactic baryonic density of $10^{-17}\ kg\ m^{-3}$ estimated in the present scenario, so galaxies never collapsed but expanded slowly and sometimes merged. The density $10^{-17}\ kg\ m^{-3}$ matches the density of globular star clusters, which is no coincidence since both ρ and γ at this time of first fragmentation should be preserved as hydrodynamic fossils, Gibson [14,15]. At some later time $\sim 10^8\ y$ gravitational forces caused fragmentation of the non-baryonic matter at L_{SD} scales to form halos of the evolving baryonic structures with galaxy to supercluster masses, as an effect rather than the cause.

Because the Jeans criterion does not permit baryonic matter to condense to form the observed structures, standard linear cosmology requires ''cold'' non-baryonic dark matter (CDM) to condense early in the plasma epoch, forming gravitational potential wells to guide the late collapse of the baryonic matter to form galaxies at $z \approx 5$ ($\sim 0.7\times 10^9\ y$). This is accomplished by assuming the weakly interacting massive particles (WIMPs) have large masses, about 10^{-25} kg, giving small sound velocities and small Jeans CDM condensation masses in the galaxy mass range. Mixtures of such ''cold dark matter'' with less massive ''warm'' and ''hot'' dark matter particles are used to match observations of the actual universe structure. Such curve fitting is no longer required if the Jeans criterion is abandoned in favor of the recommended Schwarz length scale criteria.

Theory of Gravitational Instability

Gravitational condensation for scales smaller than the horizon L_H in the early universe can be described by the Navier Stokes equations of momentum conservation

$$\frac{\partial \vec{v}}{\partial t} = -\nabla B + \vec{v}\times\vec{\omega} + \overrightarrow{F_g} + \overrightarrow{F_v} + \overrightarrow{F_m} + \overrightarrow{F_{\text{etc.}}} \tag{1}$$

where $\vec{v}$ is the velocity, $B = p/\rho + v^2/2$ is the Bernoulli group, $\vec{v}\times\vec{\omega}$ is the inertial vortex force, $\vec{\omega}$ is the vorticity, $\overrightarrow{F_g}$ is the gravitational force, $\overrightarrow{F_v}$ is the viscous force, and the magnetic and other forces $\overrightarrow{F_m} + \overrightarrow{F_{\text{etc.}}}$ are assumed to be negligible. The gravitational force per unit mass $\overrightarrow{F_g} = -\nabla\phi$, where ϕ is the gravitational potential in the expression

$$\nabla^2\phi = 4\pi\rho G \tag{2}$$

in a fluid of density ρ. The density conservation equation in the vicinity of a density maximum or minimum is

$$\frac{\partial\rho}{\partial t} + \vec{v}\cdot\nabla\rho = D_{\text{eff}}\nabla^2\rho \tag{3}$$

where the effective diffusivity D_{eff}

$$D_{\text{eff}} = D - L^2/\tau_g \tag{4}$$

includes the molecular diffusivity D of the gas and a negative gravitational term depending on the distance $L \geqslant L_{SX\ max}$ from the nonacoustic density nucleus and the gravitational free fall time $\tau_g = (\rho G)^{-1/2}$. Turbulence is driven by $\vec{v}\times\vec{\omega}$ forces.

For scales smaller than L_H gravitational effects on space-time are described by Einstein's equations of general relativity

$$G_{ij} = R_{ij} - g_{ij}R = -(8\pi G/c^4)T_{ij} \tag{5}$$

where R_{ij} is the Ricci tensor, R is its trace, a term Λg_{ij} on the right has been set to zero (the cosmological constant Λ introduced by Einstein and later dropped has recently been resurrected in attempts to reconcile observations with theory), G is Newton's gravitational constant, T_{ij} is the energy-momentum tensor, g_{ij} is the metric tensor, and indices i and j are 0, 1, 2, and 3. The Ricci tensor was developed to account for curvature problems of non-Euclidean geometry by Riemann and Christoffel and is formed by contracting the fourth-order curvature tensor so that Einstein's gravitational field tensor G_{ij} on the left of (5) has only terms linear in second derivatives or quadratic in first derivatives of g_{ij}, Weinberg [[1] p. 153]. G_{ij} was adapted from R_{ij} to preserve Lorentz invariance and the equivalence of inertia and gravitation in mechanics and electromechanics. An expanding universe with critical density monotonically decelerates and is called flat by its mathematical analogy to zero curvature geometry. Classical solutions of the Einstein equations are given by standard cosmology texts such as Weinberg [1], Peebles [6], Kolb and Turner [5], Padmanabhan [7], and Coles [23].

The homogeneous-isotropic Robertson-Walker metric describes the universe after the Big Bang, where the cosmic scale factor $a(t) = R(t)/R(t_0)$ gives the time evolution of spatial scales in ''comoving'' coordinates $x' = x/a$ as the universe expands to the present time t_0. Variations in curvature of space can result in acausal changes of density for scales larger than L_H. Isocurvature fluctuations may not grow after inflationary expansion beyond the horizon and reenter the horizon at a later time with the same amplitude, Kolb and Turner [[5] p. 238]. Curvature fluctuations grow with the cosmological scale $R(t)\alpha t^{2/3}$ until they reenter the horizon. Strain rates diverge at zero time and in proper coordinates the horizon expands faster than c.

Jeans [10] considered the problem of gravitational condensation in a stagnant, inviscid gas with small perturbations of density, potential, pressure, and velocity so that the nonlinear term in (1) could be neglected along with all other terms except $\overrightarrow{F_g}$. He assumed that the pressure p is a function only of the density ρ. Either the linear perturbation assumptions or this barotropic assumption are sufficient to reduce the problem to one of acoustics. Details of the Jeans derivation and its corrections from (5) are given in Kolb and Turner [[5] pp. 342–344] and in most other standard textbooks on cosmology, so they will not be repeated here. Diffusion terms are neglected in Eq. (3), and the adiabatic sound speed $V_S = (\partial p/\partial \rho)^{1/2}$ reflects an assumption that there are no variations in the equation of state. Cross differentiation with respect to space and time of the perturbed equations neglecting second order terms gives a wave equation for the density perturbation ρ_1

$$\frac{\partial^2 \rho_1}{\partial t^2} - V_S^2 \nabla^2 \rho_1 = 4\pi G \rho_0 \rho_1 \tag{6}$$

where ρ_0 is the unperturbed density. The solutions of (6) are of the form

$$\rho_1(\vec{r},t) = \delta(\vec{r},t)\rho_0 = A \exp[-i\vec{k}\cdot\vec{r} + i\omega t]\rho_0 \tag{7}$$

which are sound waves of amplitude A for large $k \geqslant k_J$ which obey a dispersion relation

$$\omega^2 = V_S^2 k^2 - 4\pi \mathrm{G} \rho_0 \tag{8}$$

where $k = |\vec{k}|$ and the critical wavenumber

$$k_J = (4\pi G \rho_0 / V_S^2)^{1/2} \tag{9}$$

has been interpreted as the criterion for gravitational instability. All solutions of (6) with wavelength larger than $\mathrm{L_J}$ are imaginary and are termed gravitationally unstable in linear cosmologies. Only such modes are considered to be eligible for condensation to form structure. Void formation is very badly modeled by linear cosmologies, and is not mentioned in standard treatments such as Kolb and Turner [5].

Consider the problem of gravitational instability for a nonacoustic density nucleus of diameter L and mass $M' = \delta \rho L^3$, where $\mathrm{L_J} > \mathrm{L} > \mathrm{L_{SX\,max}}$. For scales smaller than $\mathrm{L_J}$ the pressure adjusts rapidly compared to the gravitational time $\tau_g \equiv (\rho \mathrm{G})^{-1/2}$. For scales larger than the largest Schwarz scale $\mathrm{L_{SX\,max}}$ fluid mechanical forces and molecular diffusion are negligible compared to gravitational forces toward or away from the nucleus. Starting from rest, we see that the system is absolutely unstable to gravitational condensation or void formation, depending on whether M' is positive or negative.

The radial velocity v_r will be negative or positive depending on the sign of M', and will increase linearly with time since the gravitational acceleration at radius r from the center of the nucleus is constant with value $-M'\mathrm{G}/r^2$. Thus

$$v_r = -M'\mathrm{G}t/r^2 \tag{10}$$

shows the mass flux

$$dM'/dt = -\rho v_r 4\pi r^2 = M' \rho G t 4\pi \tag{11}$$

into or away from the nucleus is constant with radius. Integrating (11) gives two solutions

$$M'(t) = |M'(t_0)| \exp[\pm 2\pi \rho G t^2] = |M'(t_0)| \exp[\pm 2\pi (t/\tau_g)^2] \tag{12}$$

where $M'(t_0)$ is the initial mass of the density nucleus. For condensation the only place where the density changes appreciably is at the core. We can define the core radius r_c as

$$r_c = -v_r'' t = M'\mathrm{G}t^2/r_c^2, \tag{13}$$

where r_c is the distance from which core material has fallen in time t toward the core. The core mass change M'' is then

$$M'' = \rho r_c^3 = M' \rho \mathrm{G} t^2 = M'(t_0)(t/\tau_g)^2 \exp[2\pi (t/\tau_g)^2] \tag{14}$$

from (13) and (12).

For $M' < 0$, the velocity of the rarefaction wave is limited by the sound speed V_S, but for $M' > 0$ velocities become large for small r according to (10). This may cause turbulence and inhibit condensation at times t of order τ_g, depending on $\mathrm{L_{SV}}$ and $\mathrm{L_{ST}}$.

The viscous Schwarz scale $\mathrm{L_{SV}}$ is derived by setting the viscous force $F_V = \rho \nu \gamma L^2$ at scale L equal to the gravitational force $F_g = \mathrm{G}\rho L^3 \rho L^3/L^2$, so

$$\mathrm{L_{SV}} \equiv (\nu\gamma/\rho G)^{1/2} \tag{15}$$

where γ is the rate of strain. Viscous forces overcome gravitational forces for scales smaller than $\mathrm{L_{SV}}$. The turbulent Schwarz scale $\mathrm{L_{ST}}$ is derived by setting the inertial vortex forces of turbulence $F_I = \rho V^2 L^2$ equal to $F_g = G\rho^2 L^4$, substituting the Kolmogorov expression $V = (\varepsilon L)^{1/3}$ for the velocity at scale L,

$$\mathrm{L_{ST}} \equiv \varepsilon^{1/2}/(\rho \mathrm{G})^{3/4} \tag{16}$$

where ε is the viscous dissipation rate of the turbulence. These two scales become equal when the inertial, viscous, and gravitational forces coincide. The gravitational inertial viscous scale

$$\mathrm{L_{GIV}} = [\nu^2/\rho \mathrm{G}]^{1/4} \tag{17}$$

corresponds to this equality, where $\mathrm{L_{GIV}} = \mathrm{L_{SD}}$ if $D = \nu$.

We can compare these expressions with the Jeans scale

$$\mathrm{L_J} \equiv V_S/(\rho \mathrm{G})^{1/2} = [RT/\rho \mathrm{G}]^{1/2} = [(p/\rho)/\rho \mathrm{G}]^{1/2} \tag{18}$$

in terms of the temperature and pressure. The two forms for the sound velocity V_S in (18) have led to the erroneous concepts of pressure support and thermal support, since by the Jeans criterion high temperature or pressure in a gas prevent the formation of structure. The length scale $\mathrm{L_{IC}} \equiv [RT/\rho \mathrm{G}]^{1/2}$ has the physical significance of an initial fragmentation scale in a uniform gas based on the ideal gas law $p = \rho RT$, where decreases in density are matched by rapid decreases in pressure so that the temperature remains constant on scales less than $\mathrm{L_J}$. Thus cooling occurs for $\mathrm{L} \geqslant \mathrm{L_{IC}}$ when the finite speed of sound limits the pressure adjustment in such voids, so that fragmentation is accelerated by radiative heat transfer from the warmer surroundings. The length scale $\mathrm{L_{HS}} \equiv [(\mathrm{p}/\rho)/\rho \mathrm{G}]^{1/2}$ is a hydrostatic scale that arises if an isolated blob of gas approaches hydrostatic equilibrium, with zero pressure outside. Neither $\mathrm{L_{IC}}$ nor $\mathrm{L_{HS}}$ have any physical connection to Jeans's theory. $\mathrm{L_{IC}}$ and $\mathrm{L_{SV}}$ are the initial gravitational fragmentation scales of the primordial gas to form PGCs and PFPs. $\mathrm{L_{HS}}$ appears at the final stages of primordial-fog-particle formation as their size, but as an effect of the formation not the cause.

Cosmology

The conditions of the primordial gas emerging from the plasma epoch are well specified. The composition is 75% hydrogen-1 and 25% helium-4 by mass, at a temperature of 3000 K. This gives a dynamical viscosity μ of $2.4 \times 10^{-5}\,\mathrm{kg\,m^{-1}\,s^{-1}}$ by extrapolation of the mass averaged μ values for the components to 3000 K, so the kinematic viscosity $\nu = \mu/\rho$ depends on the density ρ assumed. The most likely ρ for the baryonic gas is $10^{-17}\,\mathrm{kg\,m^{-3}}$, the fossil-density-turbulence value at the time 10^{12} s of first structure formation, with fossil-vorticity-turbulence $\gamma \approx 10^{-12}\,\mathrm{s^{-1}}$. We find $\mathrm{L_{SV}} = (\nu\gamma/\rho G)^{1/2} = 6 \times 10^{13}$ m and $\mathrm{M_{SV}} = \mathrm{L_{SV}}^3 \rho = 2 \times 10^{24}$ kg as the most likely mass of the first gravitationally condensing objects of the universe, termed primordial fog particles or PFPs. With this density the gravitational time $\tau_g = (\rho G)^{-1/2}$ is 4×10^{13} s, or 1.3 million years. However, the time required for the voids to isolate the individual PFPs should be much less since the speed of void boundaries represent rarefaction waves, and may thus approach the sound speed $V_S = 3\times10^3$ m s^{-1}, giving an isolation time $L_{SV}/V_S = 2\times10^{10}$ s, or 700 years. The viscous dissipation rate $\varepsilon = \nu\gamma^2 = 2\times10^{-12}$ m^2 s^{-3}. The range of estimated PFP masses for various densities and turbulence levels 10^{24} to 10^{26} kg includes the Earth-mass of 6.0×10^{24}. Kolmogorov and Batchelor scales $L_K = L_B = 1.4\times10^{12}$ m.

Thus the entire baryonic universe of hydrogen and helium gas rapidly turned to PGC clumps of fog as the cooling plasma universe neutralized, with resulting primordial fog particle masses near that of the earth, separated by distances about 10^{14} m (10^3 AU). These PFPs constitute the basic materials of construction for everything else. Those that have failed to accrete to star mass, and this should be about 97%, constitute the baryonic dark matter. The mass of the inner halos of galaxies should be dominated by the mass of such PFPs, since the non-baryonic component diffuses to L_{SD} scales that are much larger.

Observations

Quasars are the most luminous objects in the sky. They are generally thought to represent black holes in cores of cannibal galaxies at an early stage of their formation when they were ingesting other galaxies, one or two billion years after the Big Bang. Quasar microlensing occurs when a galaxy is precisely on our line of sight to the quasar, so that it acts as a gravitational lens. The quasar image is split into two or more mirage-like images which twinkle at frequencies determined by the mass of the objects making up the lens galaxy. Schild [24] reports the results of a 15 year study of the brightness fluctuations of the two images of the QSO Q0957+561 A,B gravitational lens, amounting to over 1000 nights of observations. The time delay of 1.1 years was determined to subtract out any intrinsic quasar variability. The dominant microlensing mass was shown by frequency analysis to be 6.3×10^{24} kg, close to the primordial fog particle mass estimated above and by Gibson [9]. Three observatories have since independently reported the same time delay and microlensing signals for this lensed quasar. Thus it is an observational fact that the mass of at least one galaxy is dominated by planetary mass objects, with 3×10^7 planets per star. Star-microlensing searches for planetary mass MACHOs (massive compact halo objects) have failed because PFPs are sequestered in PGC clumps, and have highly intermittent lognormal particle density distributions as a result of their nonlinear self-similar gravitational accretion cascades to form larger objects and ultimately stars, Gibson and Schild [16].

Planetary nebula (PN) appear when ordinary stars are in a hot dying stage on their way to becoming white dwarfs. Strong stellar winds and intense radiation from the central star should cause ambient PFPs to reevaporate and reveal themselves. Hubble Space Telescope observations of the nearest planetary nebula Helix (NGC 7293), by O'Dell and Handron [26], show a halo of $>6500 \sim 10^{25}$ kg ''cometary knots'' with tails pointing away from hot central star like ''comets brought out of cold storage.'' Thousands of PFP-like ''particles'' also appear in HST photographs (PRC97-29, 9/18/97) of the recurring Nova T Pyxidis by M. Shara, R. Williams, and R. Gilmozzi, and as radial ''comets'' in recent HST photographs of the Eskimo PN (NGC 2392, A. Fructer et al., PRC00-07, 1/24/00).

Tyson and Fischer [25] report the first mass profile of a dense galaxy cluster Abel 1689 from tomographic inversion of 6000 gravitational arcs of 4000 background galaxies. The mass of the cluster is 10^{45} kg, with density 5×10^{-21} kg m^{-3}. From the reported mass contours the cluster halo thickness is about 6×10^{21} m. Setting this size equal to $L_{SD} = [D^2/\rho G]^{1/4}$ gives a diffusivity $D = 2\times10^{28}$ m^2 s^{-1}, more than a trillion times larger than that of any baryonic gas component. A virial particle velocity $v = (GM/r)^{1/2} = 3.3\times10^6$ m s^{-1} with mean collision distance $l = D/v = 6\times10^{21}\, m = m_p/\rho\sigma$ gives a collision cross section $\sigma = m_p(GM/r)^{1/2}/\rho D = 10^{-37}$ m^2 taking a particle mass $m_p = 10^{-35}$ kg corresponding to the neutrino mass required to produce a flat universe. If the particles are nearly relativistic, l is 7×10^{19} m and $\sigma = 10^{-35}$ m^2.

Conclusions

The Jeans length L_J determines the formation of Jeans-mass-PGCs (Proto-Globular-star-Clusters), but it overestimates the minimum mass of baryonic fragmentation by 2–5 orders of magnitude during the plasma epoch when proto-supercluster to proto-galaxy objects were formed, and by 12 orders of magnitude in the hot gas epoch for PFPs (Primordial-Fog-Particles). In the cold, dense, turbulent molecular clouds of galactic disks where modern stars condense, the Jeans mass is generally smaller than the turbulent Schwarz mass by an order of magnitude, and is therefore irrelevant. The Gibson [11–16] hydro-gravitational criteria are recommended instead of Jeans's; that is, $L \geqslant L_{SX\,\max} = \max[L_{SV}, L_{ST}, L_{SD}]$, where structure formation occurs at scales L larger than the largest Schwarz scale.

According to the new theory, gravitational structure formation in the universe began in the plasma epoch at a time about 30,000 years after the Big Bang with the formation of proto-supercluster-voids and proto-superclusters in the baryonic component, triggered by inflated fossil ''turbulence'' density fluctuations from the QGD epoch ($t < 10^{-35}$ s). The fragmentation mass decreased to that of a proto-galaxy by the time of plasma neutralization at 300,000 years. Immediately after atoms formed, the baryonic fragmentation mass decreased to that of a small planet and the universe of neutral primordial hydrogen and helium gas turned to fog within L_J scale PGCs. Some of these primordial fog particles have aggregated to form stars and everything else, but most are now frozen as rogue planets and sequestered in clumps within PGC clumps as the dominant form of dark matter within 10^{21} m (30 kpc) galaxy-inner-halos. Many PFPs have probably been disrupted from their PGCs by tidal forces to form the dominant interstellar mass component of galaxy disks and galaxy cores. The non-baryonic part of the universe does not drive the formation of baryonic structures even though it is more massive, but is instead driven by them. It is highly diffusive from its small collision cross section σ, and diffuses to large L_{SD} scales near 10^{22} m to form the outer halos of isolated galaxies and galaxy cluster halos in response to these large baryonic structures. Indicated σ values near 10^{-36} m^2 are reasonable for small particles like neutrinos, but $\sigma = m_p(GM/r)^{1/2}/\rho D \approx 10^{-26}$ m^2 indicated for more massive non-baryonic candidates like 10^{-25} kg neutralinos are much larger than theoretical $\sigma \approx 10^{-46}$ values or recent $\sigma \leqslant 10^{-42}$ m^2 values excluded by observations using sensitive WIMP detectors (Dark Matter 2000 Conference, Marina del Rey, February 2000).

Nomenclature

AU = astronomical unit (solar distance), 1.4960×10^{11} m
$a(t)$ = cosmological scale factor as a function of time t
c = speed of light, 2.9979×10^8 m s^{-1}
D = molecular diffusivity of density, m^2 s^{-1}
ε = viscous dissipation rate, m^2 s^{-3}
G = Newton's gravitational constant, 6.7×10^{-11} m^3 kg^{-1} s^{-2}
γ = rate of strain, s^{-1}
k_B = Boltzmann's constant, 1.38×10^{-23} J K^{-1}
h = Planck's constant, $2\pi\ 1.05\times10^{-34}$ kg m^2 s^{-1}
l = collision length, m
ly = light year, 9.461×10^{15} m
L_{GIV} = gravitational-inertial-viscous scale, $[\nu^2/\rho G]^{1/4}$
L_{SV} = viscous Schwarz scale, $(\nu\gamma/\rho G)^{1/2}$
L_{ST} = turbulent Schwarz scale, $\varepsilon^{1/2}/(\rho G)^{3/4}$
L_{SD} = diffusive Schwarz scale, $(D^2/\rho G)^{1/4}$
L_H = Hubble or horizon scale of causal connection, ct
L_J = Jeans scale, $V_S/(\rho G)^{1/2}$

λ = wavelength, m
m_p = proton mass, 1.661×10^{-27} kg
M_{sun} = solar mass, 1.99×10^{30} kg
M_{earth} = earth mass, 5.977×10^{24} kg
υ = kinematic viscosity, $\text{m}^2\,\text{s}^{-1}$
pc = pars, 3.0856×10^{16} m
R = gas constant, $\text{m}^2\,\text{s}^{-2}\,\text{K}^{-1}$
$R(t)$ = cosmological scale, $a(t)=R(t)/R(t_0)$
ρ = density, $\text{kg}\,\text{m}^{-3}$
ρ_C = critical density, $10^{-26}\,\text{kg}\,\text{m}^{-3}$ at present for flat universe
σ = collision cross section, m^2
σ_T = Thomson cross section, $6.6524\times10^{-29}\,\text{m}^2$
t = time since Big Bang
t_0 = present time, 4.6×10^{17} s
T = temperature, K
V_S = sound speed, $\text{m}\,\text{s}^{-1}$
z = redshift$=\lambda/\lambda_0-1$

References

[1] Weinberg, S., 1972, *Gravitation and Cosmology: Principles and Applications of the General Theory of Relativity*, Wiley, NY.

[2] Zel'dovich, Ya. B., and Novikov, I. D. 1983, *The Structure and Evolution of the Universe*, G. Steigman, ed., The University of Chicago Press, Chicago.

[3] Silk, Joseph, 1989, *The Big Bang*, revised and updated edition, W. H. Freeman and Company, NY.

[4] Silk, Joseph, 1994, *A Short History of the Universe*, Scientific American Library, New York.

[5] Kolb, E. W., and Turner, M. S., 1993, *The Early Universe*, paperback edition, Addison-Wesley, NY.

[6] Peebles, P. J. E., 1993, *Principles of Physical Cosmology*, Princeton U. Press, Princeton, NJ.

[7] Padmanabhan, T., 1993, *Structure Formation in the Universe*, Cambridge U. Press, UK.

[8] Rees, Martin, 2000, *New Perspectives in Astrophysical Cosmology*, Second Edition, Cambridge U. Press, UK.

[9] Gibson, C. H., 1996, ''Turbulence in the ocean, atmosphere, galaxy and universe,'' Appl. Mech. Rev., **49**, pp. 299–316, xxx.lanl.gov: astro-ph/9904260.

[10] Jeans, J. H., 1902, ''The stability of a spherical nebula,'' Philos. Trans. R. Soc. London, **199**, pp. 1–53.

[11] Gibson, C. H., 1997, ''Dark matter at viscous-gravitational Schwarz scales: theory and observations,'' *Dark Matter in Astro- and Particle Physics*, H. V. Klapdor-Kleingrothaus and Y. Ramachers, eds., World Scientific, New Jersey, pp. 409–416, astro-ph/9904284.

[12] Gibson, C. H., 1997, ''Dark matter formation at Schwarz scales: primordial fog particles and WIMP superhalos,'' *The Identification of Dark Matter*, Neil J. C. Spooner, ed., World Scientific, New Jersey, pp. 114–119, astro-ph/9904283.

[13] Gibson, C. H., 1998, A fluid mechanical explanation of dark matter, *Sources and detection of dark matter in the universe*, Cline, D. B., ed., Elsevier, North-Holland, pp. 409–411, astro-ph/9904317.

[14] Gibson, C. H., 2000, ''Turbulence and diffusion: fossil turbulence,'' *Encyclopedia of Ocean Science*, Steele, Thorpe, and Terekian, eds., to be published, astro-ph/0003147.

[15] Gibson, C. H., 2000, ''Primordial viscosity, diffusivity, Reynolds numbers, sound and turbulence at the onset of gravitational structure formation,'' astro-ph/9911264.

[16] Gibson, C. H., and Schild, R. E., 2000, ''Quasar-microlensing versus star-microlensing evidence of small-planetary-mass objects as the dominant inner-halo galactic dark matter,'' astro-ph/9904362.

[17] Hu, Wayne, 2000, ''Ringing in the new cosmology,'' Nature, **404**, pp. 939–940.

[18] de Bernardis, P., et al., 2000, ''A flat Universe from high-resolution maps of the cosmic microwave background radiation,'' Nature, **404**, 955–959.

[19] Guth, Alan H., 1997, *The Inflationary Universe*, Helix Books, Addison-Wesley, NY.

[20] Gibson, C. H., 1968, ''Fine structure of scalar fields mixed by turbulence: I. Zero-gradient points and minimal gradient surfaces,'' Phys. Fluids, **11**, pp. 2305–2315.

[21] Gibson, C. H., Ashurst, W. T., and Kerstein, A. R., 1988, ''Mixing of strongly diffusive passive scalars like temperature by turbulence,'' J. Fluid Mech., **1**, pp. 261–293.

[22] Gibson, C. H., 1988, ''Oceanic and interstellar fossil turbulence, in Radio Wave Scattering in the Interstellar Medium,'' *AIP Conference Proceedings 174*, R. G. Lerner, American Institute of Physics, New York, pp. 74–79.

[23] Coles, P., ed., 1999, Critical Dictionary of the New Cosmology, Routledge, NY.

[24] Schild, R. E., 1996, ''Microlensing variability of the gravitationally lensed quasar Q0957+561 A,B,'' Astrophys. J., **464**, pp. 125–130.

[25] Tyson, J. A., and Fischer, P., 1995, ''Measurement of the mass profile of Abell 1689,'' Ap. J., **446**, pp. L55–L58.

[26] O'Dell, C. R., and Handron, K. D., 1996, ''Cometary knots in the Helix Nebula,'' Astrophys. J., **111**, pp. 1630–1640.